The Mechanical Properties of Auxetic Foams

Yan Na Xin (Nancy) Chan

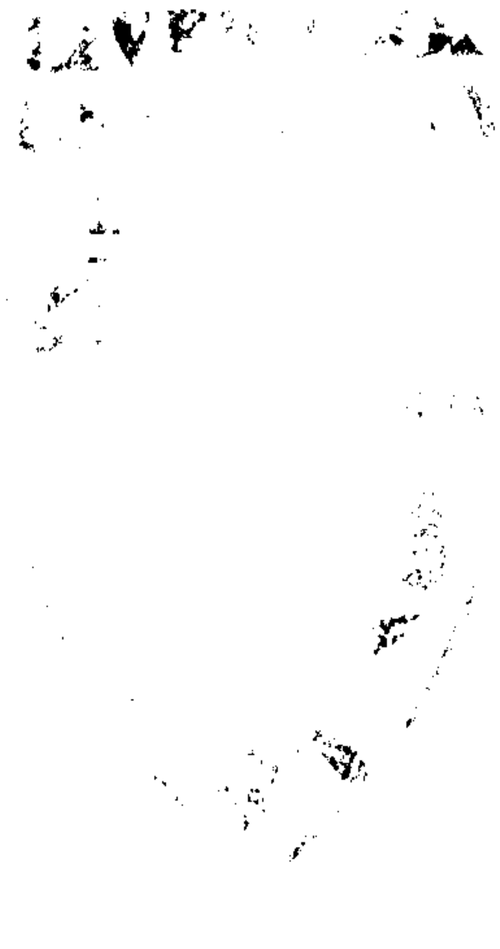

This thesis is submitted in accordance with the requirements of the University of Liverpool, for the degree of Doctor of philosophy by Yan Na Xin (Nancy) Chan.

March 1995

Department of Material Science and Engineering,
University of Liverpool.

To

My Mother and Father

Acknowledgements

First, I would like to say that I like Liverpool very much and have enjoyed studying here. When I first started my Ph.D study in Liverpool my little baby was just six months old, and I could only speak a few words of English. The people in Liverpool have been extremely friendly. Now, I have finished my final year of study. Just before I go back to China, I would like to make the following acknowledgements:

I should like to thank Profs. D. J. Bacon and P. J. Goodhew, Heads of the Department of Materials Science and Engineering, for their encouragement and also for provision of departmental facilities.

Principally, I wish to thank my supervisor Prof. K. E. Evans for his encouragement and guidance, and to thank my official supervisor Prof. Bacon for his kind help after Prof. Evans left for Exeter University. Special thanks also to: Dr. B. D. Caddock, Dr. A. Alderson, and Dr. A. Roach for their general advice, helpful discussions, and critical readings.

I am very grateful to many other members of the department. Thanks must also given to Mr. R. J. Smith, Mr. C. Baker, and to Mr. D. Whitehurst for their general advice and assistance with making the fabrication moulds.

Finally, I would like to thank my mother and father in-laws, and my parents in China for their support and encouragement.

Special thanks also to the China-British Educational Centre for the hardship funding during my final year of study.

Abstract

Auxetic materials have a negative Poisson's ratio, that is, they expand laterally when stretched longitudinally. Negative Poisson's ratio is an unusual property that affects many of the mechanical properties of the material, such as indentation resistance, compression, tension and shear stiffness, and certain aspects of the dynamic performance. Auxetic foam was fabricated from a conventional polymeric foam. The unusual mechanical properties of auxetic foams are attributed to the deformation characteristics of re-entrant microstructures.

There are four main aspects to the project. Firstly, the fabrication method for auxetic foams has been examined and developed further. Secondly, the microstructure of the foams has been characterised using electron and optical microscopy. Thirdly, the foams have been tested for their static and dynamic mechanical properties. Comparative tests have also been performed on conventional, non-auxetic foams. Fourthly, theoretical models have been developed to relate the observed microstructures to their properties.

Contents

Page

Preface i
Acknowledgements ii
Abstract iii
Contents iv
Notation viii

1. Introduction 1
    1.1 The Nature and Classification of Conventional Foams 2
    1.2 Manufacture of Polymeric Conventional Foams 3
    1.3 Properties of Conventional Polymeric Foams 3
    1.4 The Applications of Polymeric Foams 4
    1.5 The Deformation Mechanisms of Foam 5
    1.6 Limitation of the Conventional Hexagonal Cell Shape 6

2. Review of Literature 7
    2.1 Introduction 7
    2.2 General Review of Conventional Polymeric Foams 7
    2.3 Cell Geometry and Most Appropriate Cells 8
    2.4 Theoretical Models for the Deformation of Conventional Foams 10
    2.5 Mechanical Testing 15
    2.6 General Review of Auxetic Foams 25
    2.7 Fabrication and Mechanical Test Methods for the Auxetic Foams 29
    2.8 Applications of Auxetic Foams 30

3. Fabrication Method 33
    3.1 Introduction 33
    3.2 Fabricating the Small Size Auxetic Polymeric Foams 34
        3.2.1 General Fabrication Procedure 34
        3.2.2 The Heating Temperature 35
        3.2.3 The Heating Time 36
        3.2.4 Volumetric Compression Ratio 41
    3.3 Fabricating Large Auxetic Foam Blocks 46
    3.4 To Summarise the Fabrication Method 53

4. Microscopic Examination of the Microstructure and
Deformation of Foams 55
4.1 Introduction 55
4.2 The Microstructure of Conventional Foam 57
4.3 The Microstructure of Auxetic Foams 60
4.4 Characterisation of Polymeric Foams 61
4.5 The Use of Sodium Hydroxide for
Thinning Down the Cell Rib Thickness 69
4.6 Microscopic Examination of Foam Deformation 72
4.6.1 Conventional Foam Deformation under Tension 72
4.6.2 Conventional Foam Deformation under Compression 73
4.6.3 Shearing of Conventional Foam 75
4.6.4 Auxetic Foams under Axial Loading Conditions 76
4.6.5 Shearing an Auxetic Foam 78
4.7 Comparison of an Auxetic Foam and
its Parent Conventional Foam 79

5. Theoretical Models for the Deformation of Foams 80
5.1 Introduction 80
5.2 Anisotropic Elongated Rhombic
Dodecahedron Cells Geometry 82
5.3 The Flexure Model for the 3D Foam Cell Structure 86
5.3.1 Introduction 86
5.3.2 Loading in the X-Direction 86
5.3.3 Loading in the Z-Direction 89
5.3.4 Loading in the Y-Direction 91
5.3.5 The Shear Modulus of the Flexure Model 94
5.3.5.1 Introduction 94
5.3.5.2 Shearing in the X-Z Plane 94
5.3.5.3 Shearing in the Z-Y Plane 96
5.3.5.4 Shearing in the X-Y Plane 100
5.3.6 Summary of the Flexure Model 100
5.4 The Hinging Model for the Foam Cell Structure 102
5.4.1 Introduction 102
5.4.2 Loading in the X-Direction 102
5.4.3 Loading in the Z-Direction 105
5.4.4 Loading in the Y-Direction 105
5.4.5 Shear Modulus of the Hinging Model 107
5.4.5.1 Shearing in the Z-Y Plane 107

5.4.5.2 Shearing in the X-Y Plane 109
5.4.5.3 Shearing in the X-Z Plane 109
5.4.5.4 The Determination of K_h 111
5.4.6 Summary of the Hinging Model 112
5.5 The Stretching Model for the Foam Cell Structure 113
5.5.1 Loading in the X-Direction 113
5.5.2 Loading in the Z-Direction 115
5.5.3 Loading in the Y-Direction 116
5.5.4 Shearing in the X-Z Plane 119
5.5.5 Shearing in the Z-Y Plane 119
5.5.6 Shearing in the X-Y Plane 119
5.5.7 Summary of the Stretching Model 120
5.6 The Combined Model for the Foam Cell Structure 121
5.6.1 Loading in the X-Direction 121
5.6.2 Loading in the Z-Direction 122
5.6.3 Loading in the Y-Direction 122
5.6.4 Shearing in the Z-Y Plane 124
5.6.5 Shearing in the X-Y Plane 125
5.6.6 Shearing in the X-Z Plane 125
5.6.7 Summary of the Combined Analytical Model 126
5.7 Conclusion 127

6. The Mechanical Properties of Foams (I) 128
6.1 Introduction 128
6.2 Compression 128
6.2.1 Introduction 128
6.2.2 Compressive Creep 128
6.2.3 Strain Rate Effect 130
6.2.4 Specimen Geometry Effect 132
6.2.5 The Compressive Stress-Strain Behaviour 134
6.3 Tensile Test 143
6.3.1 Introduction 143
6.3.2 Strain Rate Effect 144
6.3.3 Specimen Geometry Effect 145
6.3.4 Tensile Creep 147
6.3.5 The Tensile Stress-Strain Behaviour 149
6.3.6 The Effect of Cell Rib Thickness 154
6.4 Poisson's Ratio 154
6.4.1 The Tensile Poisson's Ratio 154

6.4.2 The Compressive Poisson's Ratio 158
6.5 Shear Test 161
6.5.1 Introduction 161
6.5.2 Static Shear Modulus Measurement 161
6.5.3 Calculation of the Shear Modulus 163
6.5.4 Dynamic Shear Modulus Measurement 166

7. The Mechanical Properties of Foams (II) 172
7.1 Introduction 172
7.1 The Ball Indentation Test (Static Indentation Resilience) 172
7.2 The Indentation Stress-Strain Curves 183
7.3 Hysteresis Loop 188
7.4 The Ball Rebound Test (Dynamic Indentation Resilience) 190
7.5 DMTA - Loss Tangent 192

8. Discussion 197
8.1 Introduction 197
8.2 Comparison of the 3D Model with the 2D Model 197
8.3 Examination of the Special Cases 199
8.4 Examination of the Combined Model 200
8.5 Effects of Cell Geometry on the Flexure Model 202
8.6 Effects of Cell Geometry on the Hinging Model 209
8.7 Effects of Cell Geometry on the Stretching Model 213
8.8 Effects of Cell Geometry on the Combined Model 217
8.9 The Stress-Strain Behaviour of Foams under Small Strains 223
8.10 Comparison of Experimental and Theoretical Results 227
8.11 The Mechanical Properties in Terms of Relative Density 235
8.12 The Cross Sectional Area of the Cell Ribs 239
8.13 Elastic Theory of the Ball Indentation Test 241
8.14 Elastic Theory of the Ball Rebound Test 247
8.15 Relate the Loss Tangent with
the Ball Rebound Measurements 250

9. Conclusions and Future work 252
9.1 Conclusion 252
9.2 Future Work 253

References 255

Notation

A, B, C	= Foam block orientation factors
$A_{cross\text{-}section}$	= Cross sectional area of the cell ribs (mm^2)
A_o	= Initial cross-sectional area (mm^2)
a	= Chordal radius of the indentation profile (mm)
b	= Thickness of cell rib (mm)
C, c	= Constants
d	= Chordal diameter of the indentation profile, or deflection (mm)
D	= Diameter of the ball, or diameter of a circular plate (mm)
E, E_x, E_y, E_z	= Young's moduli in the principle directions of foam (kN/m^2)
E_B	= Young's modulus of the ball (kN/m^2)
E_s	= Young's modulus of the base solid (kN/m^2)
E_M	= Young's modulus of the testing material (kN/m^2)
E'	= Storage Young's modulus ($dyne/cm^2$)
E''	= Loss Young's modulus ($dyne/cm^2$)
E*	= Complex Young's modulus ($dyne/cm^2$)
F	= Force (kN)
f	= Frequency (Hz)
g	= Acceleration due to gravity ($9.81 m/s^2$)
G, G_{ij}	= Shear moduli of foam (kN/m^2)
G_s	= Shear modulus of the base solid (kN/m^2)
G'	= Storage shear modulus ($dyne/cm^2$)
G''	= Loss shear modulus ($dyne/cm^2$)
G*	= Complex shear modulus ($dyne/cm^2$)
H	= Static indentation resilience or hardness (kN/m^2)
h	= length of vertical rib in foam cell, or the depth of impression, or height of the specimen (mm)
h_1	= The dropping height, or the height of fall (mm)
h_2	= The ball rebound height (mm)
I	= Second moment of area of cell rib for foam (mm^4)
K_f, K_h, K_s	= Flexure, hinging, and stretching force constants (kN/m)
K	= Bulk modulus (kN/m^2)
L, L_i	= Length in the principle directions of foam specimen, or length of cell rib in foam cell, or the length of cylinder (mm)
ΔL	= The change in length (mm)
M	= Moment (kNm)
m	= mass (kg)

O	= Initial Point of a line (or curve)
P	= Pressure (kN/m^2) or Force (kN)
P_m	= Mean pressure (kN/m^2)
R_c	= Volumetric compression ratio
R	= The radius of the cylinder (ball) (mm)
r, r_1	= The radius of the ball (mm)
r_B	= The radius of the ball (mm)
S	= Shearing area (mm^2)
t	= Cell rib thickness, or the thickness of a circular plate (mm)
T	= Temperature (^oC), or Force (kN)
T_g	= Glass transition temperature (^oC)
Tm	= Melting temperature (^oC)
V_o	= Initial volume of specimen (mm^3)
V_1	= Final volume of specimen (mm^3)
W	= Energy absorbed per unit volume (J), or the normal load (kN)
w	= the width of the specimen (mm)
x, y, z	= Co-ordinates
X, Y, Z	= Co-ordinates
X_o, y_o	= The original length (mm)
X', y', X'', y''	= The changing length (mm)
α	= The ratio of h/L. Where: L, is the length of the angled rib at the end of the vertical rib whose length is h.
α_y	= The angle subtended by the chordal diameter of the indentation
β	= The ratio of t/L. Where: t, is the cell rib thickness and L, is the length of angled rib.
γ	= Geometric angle of foam cell or re-entrant cell face, or the shear strain
δ, δ_i	= Deflection (mm), or the phase angle (Deg.)
δ_x, δ_y, δ_z	= Maximum compression displacement of the foam rise direction and the other two direction.
ε, ε_i	= Principle strains
ε_Q	= The critical elastic collapse strain, or maximum output strain
ε_m	= The maximum elastic strain
ε_o	= Maximum output strain
θ	= Cell rib angle with x direction (Deg.)
ν, ν_{ij}	= Poisson's ratio in the principle directions of foam
ν_B	= Poisson's ratio of the ball

ν_m = Poisson's ratio of the material

ρ = Density of foam (kg/m^3)

ρ_s = Density of cell rib solid (kg/m^3)

ρ^* = Relative density

σ, σ_i = Principal stresses (kN/m^2)

σ_y = Yield stress of foam (kN/m^2)

σ_o = Maximum output stress ($dyne/cm^2$)

σ_p = Plateau stress (kN/m^2)

τ, τ_i = Shear stresses (kN/m^2)

ϕ = Geometric angle of foam cell, or re-entrant cell face, or the volume fraction of material

ξ = A measure of filler phase, structural factor.

ω = Angular frequency (radians/sec.)

Chapter 1 Introduction

1.1 The Nature and Classification of Conventional Foams

Cellular materials are widespread. Such materials are common in nature as bread, cork, sponge and bone. Man has made use of these natural cellular materials for many centuries. Wood is the world's oldest structural material and cork was used as stoppers for wine bottles in Roman times. More recently man has made his own cellular materials such as honeycombs and foams. The unusual mechanical properties of foams come from their porous cellular structure. Foams can be stiff, yet light, and they are also capable of absorbing large amounts of energy. For this reason, therefore, they are an important class of engineering materials as they extend the range of mechanical properties available to the engineers. It has been suggested that changing the cell geometry to optimise the cell shape, size, and cell rib thickness will improve the mechanical properties of the foams (Gibson and Ashby 1988).

A cellular material is a low density porous solid, made up of an interconnected network of solid struts or plates which form the edges and faces of cells. The simplest structure is a two-dimensional array of polygons which pack to fill a plane area similar to the hexagonal cells of a bee's honeycomb; for this reason, such two-dimensional cellular materials are called honeycombs. Cellular material made up of three-dimensional polyhedral cells are termed foams. An open-cell foam resembles an assembly of beam-column elements which forms the edges of the cells, while a closed-cell foam has solid closure distributed on the face of each cell as well as its edges. Depending on the nature of the cell wall material, cellular materials can also be characterised as elastic (e.g. rubbers), plastic (rigid polymers and metals), and brittle (e.g. ceramics and glasses).

Polymeric foams are usually classified according to their stiffness: rigidity and flexibility. Sckochdopole and Rubens (1965) have defined a rigid foam as one in which the polymer matrix exists in the crystalline state, or if amorphous, is below its glass transition temperature. Following on from this, a flexible foam is a system in which the matrix polymer is above its glass transition temperature. Polymeric foams are multiphase systems that consist of a polymer matrix and a fluid phase; the fluid usually being a gas. Most polymers can be expanded into a cellular product, but only a small number have been exploited commercially. In terms of volume consumed, polyurethane, polystyrene, poly(vinyl chloride) and the polyolefins have dominated the markets. This thesis is concerned with the mechanical properties of elastic, flexible, polyurethane foams.

1.2 Manufacture of Polymeric Conventional Foams

The chemical and technological aspects of the manufacture of polymer foams have been described in detail in publications edited by Frisch and Saunders (1972). Although foams can be produced in a variety of ways, the most commonly employed method is the expansion process. In principle, this consists of (1) the nucleation of gas bubbles in a liquid polymer system, (2) the growth and stabilisation of these bubbles and (3) the solidification of the polymeric phase by crosslinking or cooling to give a structurally stable cellular system. Details of this process will depend upon the nature of the starting materials, i.e. thermoplastic or thermosetting plastic. The structures resulting from this expansion process may be open cell or closed cell. In some cases, such as with some flexible cellular polyurethanes, the foam undergoes a chemical treatment, called 'reticulation', which causes the disappearance of all the membranes between adjacent cells and produces a completely open-cell structure.

Polyurethane foams have been described as being unique in the family of cellular polymers. They are manufactured by accurate metering and mixing of two catalysed liquid components: a polyol and an isocyanate. The polyol component has either a polyether or a polyester backbone chain and contains either a chain extender or crosslinking agent and a catalyst. Once the components have been mixed the polymerisation and expansion take place simultaneously. It is to be noted that physical blowing agents are often included in the formulation which are completely responsible for, or assist in, the blowing of the foam.

The structural parameters of a foam such as the size, the structural geometry, and the orientation of the cells are all controlled by the way the foam has been made.

1.3 Properties of Conventional Polymeric Foams

The properties of foams can vary widely depending on the choice of the solid from which they are originally made. Also important are the volume fraction of the solid and the geometry of the cells. The properties: density, thermal conductivity, Young's modulus, and the compressive strength as collated by Gibson and Ashby (1988) are shown in *Figure* 1.1 along with their ranges. The bar with dotted shading shows the range of the property spanned by fully dense solids; the heavy shading bar shows the extension of this range made possible by foaming. The enormous extension in these properties creates new and interesting applications for foams, and offers potential for engineering ingenuity.

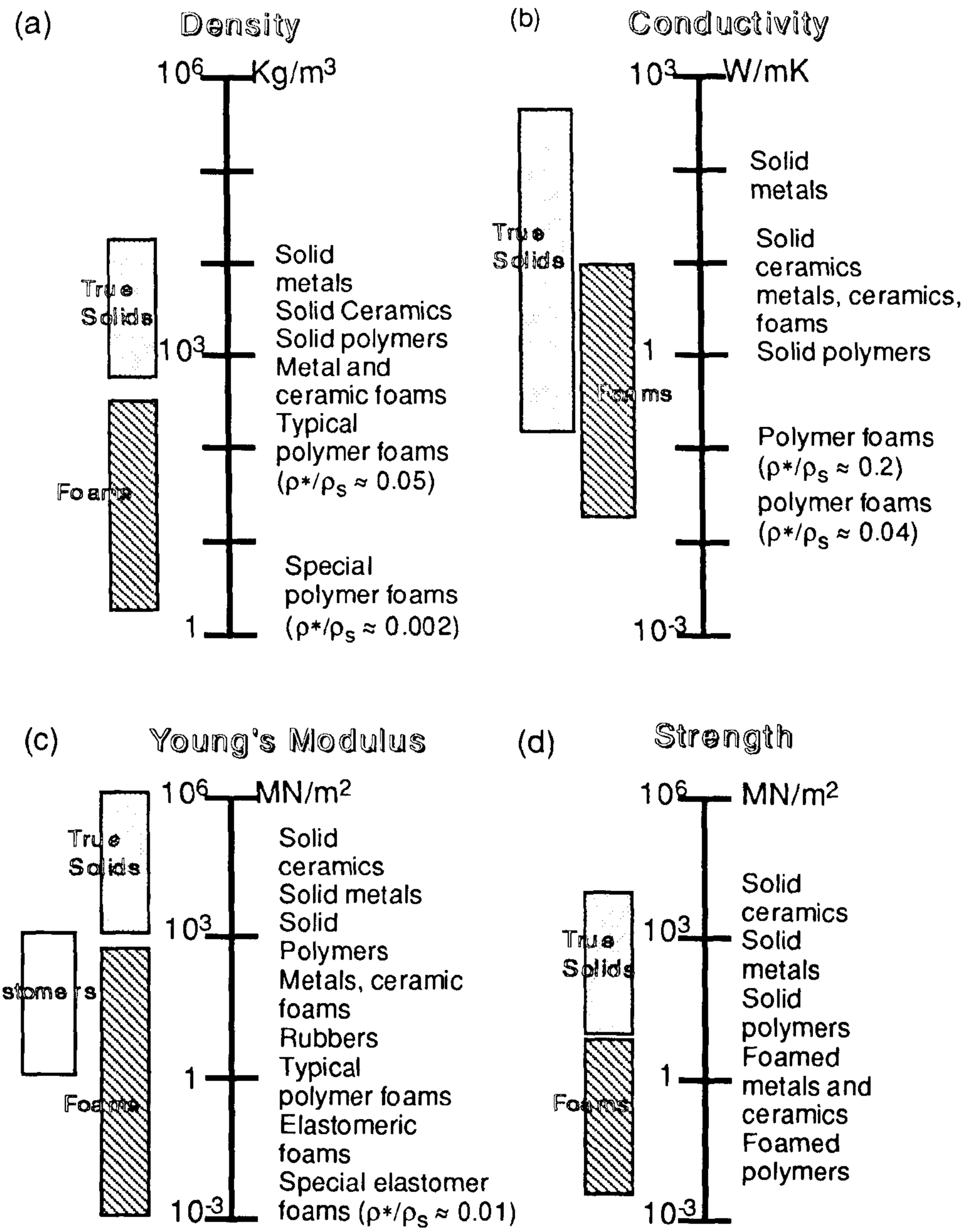

Fig. 1.1 The range of properties available to the engineer through foaming: (a) density; (b) thermal conductivity; (c) Young's modulus; (d) compressive strength. (Gibson and Ashby, 1988)

1.4 The Applications of Polymeric Foams

Recently, foams have become very important in sandwich panel fabrication. The common skin materials used in sandwich panels are fibre-reinforced plastics, whilst a light weight foam is used in the core. The core acts as a filler to separate the stiff faces, increasing the second moment of area of the panel. The principle of a sandwich panel is the same as an 'I' beam, i.e. the amount of material in the region of the neutral axis is reduced to minimum. The increase in the moment of inertia gives sandwich panels a high ratio of bending stiffness to weight. As a result, they are used

in applications where weight is critical, e.g. as structural components in aircraft, space vehicles, skis, racing yachts and portable buildings The bending stiffness of a sandwich beam depends upon two factors: its flexural rigidity and on its shear rigidity. This is different from isotropic beams where shear deflections are usually negligible. To obtain the sandwich effect, the core material must be stiff enough in shear to prevent the skins from sliding over each other and stiff enough in compression to keep the skins the correct distance apart (Gibson, 1984).

Over the last few years, there has been an increased utilisation of foams for thermal insulation, vibrational damping, buoyancy, cushioning and packaging applications. An effective package must absorb the energy of impacts. Foams are particularly well suited for this. The strength of a foam can be adjusted over a wide range by controlling the cell geometry and the properties of the polymer matrix. The details of cushioning, packaging and energy absorption of foams are discussed in Chapter 7. Here, it is noted that foams also offer a secondary advantage as packaging materials. Their low density means that the package is light, reducing handling and shipping cost. Currently, the foams most widely used in packaging are polystyrene, polyurethane and polyethylene (Suh and Skochdopole, 1980).

1.5 The Deformation Mechanisms of Foam

It is obvious from the examination of a 3D foam structure that deformation of the cells can arise from bending, hinging or stretching of the cell ribs. Commercially available foams are considered to deform elastically by flexing of the cell walls. This behaviour has been quite accurately described by a flexure model based on the assumption that the cell walls bend like beams (Gibson and Ashby, 1982 and 1988). For a rigid plastic foam, hinging might be the dominant mechanism, i.e. deformation occurs by a change in the cell angle alone. The final mechanism is stretching, in which the cell angles are considered fixed and deformation occurs by axial extension of transversely stiff cell walls. Gent and Thomas (1959, and 1963), Lederman (1971), and Chan and Nakamura (1969) have used stretching mechanism to describe the mechanical behaviour of foams.

In general, macro-foam structures will deform by either flexing or hinging, the particular mechanism being determined by the properties of the cell wall material and the cell geometry. However, it is feasible to imagine that all three mechanisms could operate concurrently and that a general elastic deformation model can be obtained by combining the appropriate equations. The details of the deformation mechanisms of foams are discussed in Chapter 4 and 5 of this study.

1.6 Limitation of the Conventional Hexagonal Cell Shape

It can be seen from *Figure* 1.2(a) (Evans, 1990) that a sandwich panel comprises of stiff composite laminate skins of carbon or glass fibre reinforced plastic sandwiching a light, porous core material, which may be a foam or a honeycomb material. Such a panel is very stiff, but it has the disadvantage that, when a sheet of core is bent out-of-plane, it produces the anticlastic or the saddle shaped curvature shown in *Figure* 1.2(b). This is a direct result of the in-plane positive Poisson's ratio of the core material. Currently, the only way to overcome this problem is to machine a block of conventional core to the required contours, but this is obviously expensive, and also damaging to the core material.

Synclastic curvatures (*Figure* 1.2(c)) will occur naturally if the core structure has a negative Poisson's ratio. This can be achieved by making the cells re-entrant in shape. The synclastic, or dome shaped curvature can be of obvious benefit when making aircraft bodies, wings, car doors and body panels (Evans, 1990; Masters, 1994)

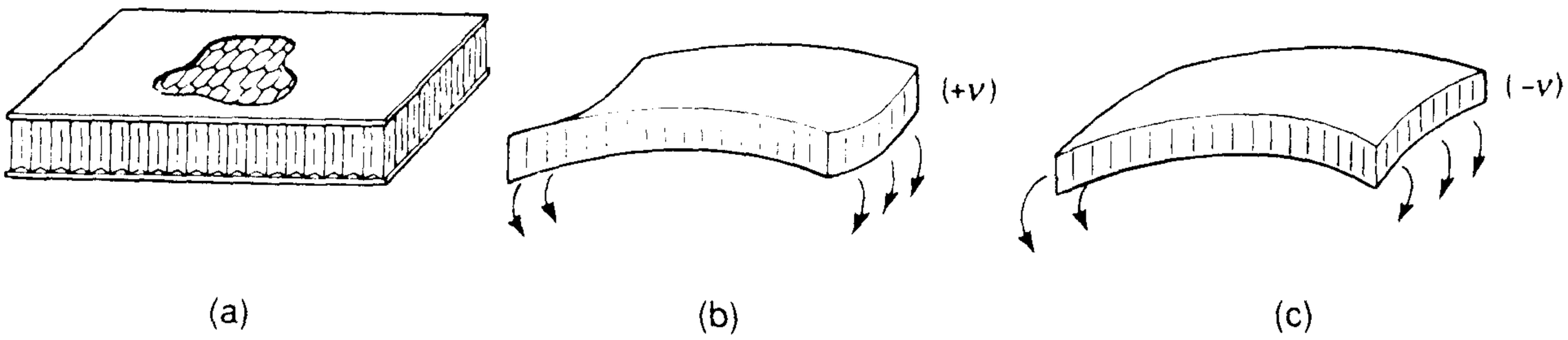

Fig. 1.2 A sandwich pane. (a) comprising of high stiffness composite laminate skins and a honeycomb core; (b) a conventional hexagonal honeycomb deforms to a saddle shape when it is flexed, whereas (c) a re-entrant honeycomb produces a dome-like double curvature on flexing. (Evans, 1990)

In 1987, a conventional hexagonal celled PUR (polyurethane) foam was converted into a re-entrant celled foam by Lakes (1987). This material was reported as isotropic and had a Poisson's ratio of -0.7. A negative Poisson's ratio is produced from a re-entrant cell structure. However, very little experimental work has been carried out on re-entrant celled foams.

The primary purpose of the research presented in this thesis is, therefore, to investigate the properties of the re-entrant celled foam using both mathematical modelling and practical experimentation and to compare them with their parent conventional foams. To enable this objective to be achieved considerable research into developing the fabrication route for the auxetic foam was also required.

This chapter has served as a brief introduction to this project. *Chapter* 2 reviews the literature concerned with previous theories and the mechanical testing methods involved, with particular emphasis on both conventional and auxetic polymeric foams. *Chapter* 3 explains the experimental method for the fabrication of auxetic foams. Extensive experiments on a wide range of foams are reported. A multi-stage fabrication method is developed. *Chapter* 4 details the microstructure of auxetic and conventional foams. Examples of the microstructural deformation mechanisms observed are presented. The results of optical and scanning electron microscopy studies for the geometric parameters of different foams are analysed. *Chapter* 5 is concerned with the development of a three dimensional foam model, and develops a theory for the mechanism involved in the deformation of both auxetic and conventional foams. Theoretically, the mechanical properties of an open-cell foam are calculated by analysing a representative elongated rhombic dodecahedral cell. The different deformation mechanisms, such as flexure, hinging and stretching are also analysed using classical beam theory. Finally, the general mechanical properties of the anisotropic foams are derived in terms of the solid properties and the cell geometrical factors. *Chapter* 6 describes the experimental methods used, and the results obtained from the static tests. Extensive experimental results such as compressive modulus, tensile modulus, shear modulus, the Poisson's ratio, creep and Dynamic Mechanical Thermal Analysis (DMTA) are reported. *Chapter* 7 studies the indentation resilience and the energy loss of the foams. *Chapter* 8, the discussion chapter, draws together all the information gained both experimentally and theoretically and discusses the results. This leads to the conclusions of this research. Finally, areas of future research are listed in *Chapter* 9.

Chapter 2. Literature Review

2.1 Introduction

A critical discussion of the results obtained for this thesis requires an understanding of the current state of knowledge in these areas. A survey has therefore been made of published work that is relevant to the chosen project area.

To provide a background for the study of auxetic foams, I shall first review conventional cellular foams. Then follows a more detailed review on auxetic foams.

2.2 General Review of Conventional Polymeric Foams

Almost any material can be foamed. Polymers are common materials to be foamed, but metals, ceramics, glasses and even composites can also be fabricated into cells. Descriptions of the foaming processes can be found in Harding (1965) and Suh and Skochdopole(1980). Foams are made using different techniques for different types of solid. Polymers are foamed by introducing a gas into the liquid monomer or hot polymer with a blowing agent, allowing the bubbles to grow and stabilise, then solidifying the foam by cross-linking or cooling (Hilyard, 1982). Metallic foams are made by mixing carbon beads into a metal melt in an inert atmosphere. When the metal has cooled and solidified, the carbon is burnt off, leaving a cellular matrix (Davis and Zhen, 1983). Ceramic foams are made by infiltrating an open-cell polymer foam with a fine slurry of ceramic in water or some other fluid, when the aggregate is fired, the slurry bonds to give an image of the original foam, and finally the original polymer foam is burnt off (Gibson and Ashby, 1988). Foaming dramatically extends the range of properties such as: density, thermal conductivity, Young's modulus, and compressive strength available to the engineer. The extension of these properties creates applications for foams which cannot easily be filled by dense solids. The low density permits the design of light structural components (Gibson et al. 1989; Triantafillo et al. 1989). The low thermal conductivity allows cheap and reliable thermal insulation (Hanhi and Stenberg, 1993). The low stiffness makes foams ideal for cushioning (Chessin and Driver, 1967; Throne et al. 1985; Campbell, 1979; Neet, 1975). Finally, the low strengths for large compressive strains make foams attractive for packaging and energy-absorbing applications (Zhang and Ashby, 1994; Schwaber et al. 1971; Mills and Hwang, 1989; Meineck and Schwaber, 1970). Their uses exploit the unique combination of properties offered by cellular foams. For a more detailed description of the applications of natural and man-made cellular materials, readers may refer to a book by Gibson and Ashby (1988) and a review by Gibson (1989).

In recent years, significant effort and resources have been devoted to characterise the mechanical properties of plastic foams used as cushioning materials. The major requirement of these foams is to protect fragile products during handling and transportation. The properties sought include: Force-Deformation (or stress-strain) in compression and shock and vibration transmissibility curves. Acquisition of the data however requires highly sophisticated and costly equipment and involves a tremendous amount of experimental work. As a result of this, published data on the mechanical properties of plastic foams as related to their protective characteristics and on the relationship between structure and performance of cushioning materials is quite limited, despite the amount of literature on conventional polymeric foams is a large one. However, the approaches of relevant work are summarised in the following sections.

2.3 Cell Geometry and Most Appropriate Cells

Unit cells are often used in modelling cell shape in foams. The non-prismatic polyhedra which pack to fill space are rhombic dodecahedra, with 12 regular faces (Plateau, 1873), and tetrakaidecahedra, with six square and eight hexagonal faces (Kelvin, 1887; Smith, 1952; Thompson, 1961; Ko, 1965). Other polyhedra which do not pack to fill space properly unless distorted have been suggested at various times for the unit cells of foams; these include the tetrahedron, the icosahedron and the pentagonal dodecahedron (Jones and Fesman, 1965; Harding, 1967; Chan and Nakamura, 1969; Menges and Knipschild, 1975; Barma et al., 1978).

We assume that a foam is made up of a collection of the three dimensional array of cells, and that the shape of each single cell may well be different. Normally man-made polymeric foams have cells which are anisotropic. However, for a first approximation of the theoretical model the structure can be thought of as typified by one of the regular units. In 1988, Gibson and Ashby investigated the microstructures of conventional foams. From their work on foam cell geometries, they summarised the most appropriate cells used for modelling as shown in *Figure 2.1*. Their mathematical model for foams was actually based on a box-like structure shown in *Figure 2.2*.

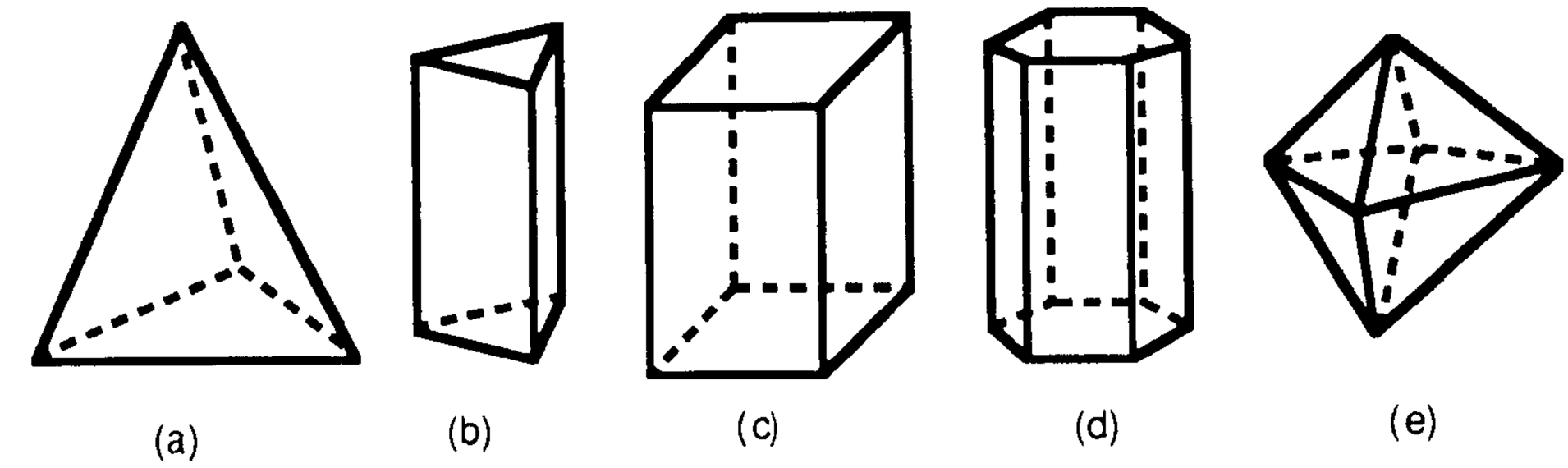

Fig. 2.1 Stet polyhedral cells: (a) tetrahedron, (b) triangular prism, (c) rectangular prism, (d) hexagonal prism, (e) octahedron, (f) rhombic dodecahedron, (g) pentagonal dodecahedron, (h) tetrakaidecahedron, (i) icosahedron. (Gibson and Ashby, 1988)

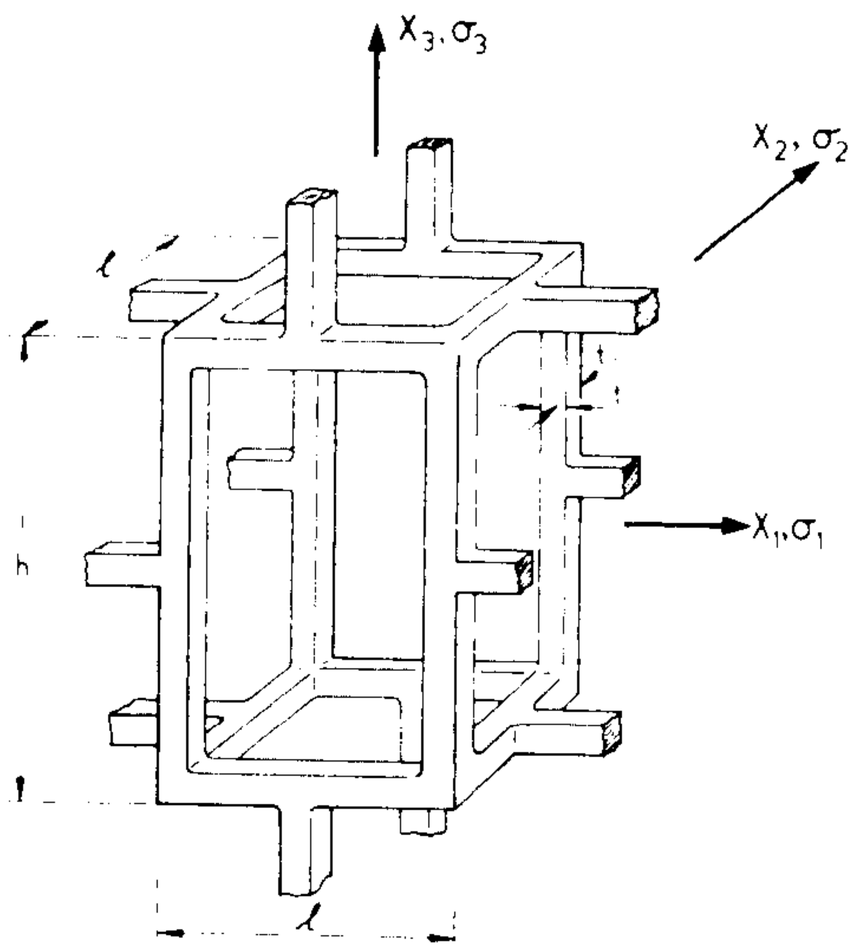

Fig 2.2 A box-like model for an open-cell foam showing the edge length , h and L, and the edge thickness, t. (Gibson and Ashby, 1988; and Huber and Gibson, 1988.)

The cell structure of low density conventional plastic foams was suggested by Gent and Thomas (1963). They used a simple cubic lattice of struts which Kanakkanatt (1973) modified to include anisotropy. The microstructure of rigid polyurethane foams was studied by Dawson and Shortall (1982). They found that the foams with a density of the order of 35 kg/m^3 are shown to be best represented by pentagonal dodecahedra. Waterman and Phillips (1974) stated that the structure of foams of density higher than about 200 kg/m^3 was one of isolated spherical holes in a polymer matrix, low-density foams had a polyhedral structure. Chaffanjon and Verhelst (1992) proposed an automated image analysis method for the characterisation

of flexible foam cellular structure. This method was used by Huang and Gibson (1993) to measure the cell size and the mean dimension of the conventional foam cells. The degree of microstructural orientation in a foam is a fundamental quantity of wide interest to those studying mechanical properties of both natural and man-made foams.

2.4 Theoretical Models for the Deformation of Conventional Foams

Foams, with complicated geometry, are difficult to model. One of the earliest attempts at incorporating anisotropy into a model of foam behaviour was that of Lederman (1971). The foam was modelled by bars oriented in random directions connected by rigid spheres. The orientation of the bars is specified by a direction distribution function. Loads are assumed to be carried axially by the bars and only stretching is considered. The Young's modulus of the foam is then correlated to the distribution function. Lederman only considered two extremes: (a) complete alignment of the bars with the loading direction, and (b) complete alignment perpendicular to the loading direction. The first case gives a modulus of 0.6 times that of an unoriented foam, while the second gives a modulus of zero. No experimental data was presented for the function or any method suggested to obtain it for a general oriented foam.

Early studies assumed that the cell walls carried axial loading only (Gent and Thomas 1959, 1963 and Lederman, 1971). This assumption leads to a conclusion which is inconsistent with experimental data, that the Young's moduli of a foam should vary linearly with its density. Later work recognised the dominant contributions of cell wall bending to the mechanical properties, and the linear elastic moduli of cellular materials has been considered to reflect mainly the bending of the cell members (Ko, 1965; Patel and Finnie, 1970; Menges and Knipschild, 1975; Abdd El-sayed et al, 1979; Gibson et al, 1982; Gibson and Ashby, 1982; Green,1985; Warren and Kraynik, 1987, 1988; Klintworth and Stronge, 1988, 1989).

Ko (1965) assumed that the morphology of a three-dimensional foam could be represented by the topology of interstices that is determined by the idealized arrangement of uniform spheres in hexagonal close packing (hcp) or face-centred-cubic packing (fccp). Since these structures are inherently anisotropic, he arbitrarily chose a principle direction of uniaxial strain and calculated the effective Young's modulus of the foam from a three-dimensional beam analysis of the structure. For a hcp and low relative density foam, Ko obtained:

$$\frac{E}{E_s} = \frac{\sqrt{3}}{4}\left[1 + \frac{9}{4\left(13 + 8\nu + 2\sqrt{3}\,\frac{L^2}{A}\right)}\right]\left(\frac{A}{L^2}\right) \qquad (2.1)$$

$$\nu \approx \frac{1}{4} \qquad (2.2)$$

where E/Es, is the relative Young's modulus, ν, is the Poisson's ratio, and A/L^2, is the slenderness of the cell rib.

For a fccp and low relative density foam, he obtained:

$$\frac{E}{E_s} = \frac{63\sqrt{3}}{71 + 16\nu + \sqrt{3}\,\frac{L^2}{A}}\left(\frac{A}{L^2}\right) \qquad (2.3)$$

$$\nu \approx \frac{7}{8} \qquad (2.4)$$

Ko considered both stretching and bending of the cell ribs. The difference in his asymptotic results reflects a change in the dominant deformation mechanism, which depends upon the morphology of the structure and its orientation with respect to the principle axes of strain. To explain his experiments, he had to suppose that real foams are a mixture of 67% hcp and 33% fccp.

Chan and Nakamura (1969) derived expressions for E/E_S and ν for open and closed- cell foams based on the bending deflection of an initially bent column or plate loaded axially. This method breaks down if the columns or plates are initially straight: because they are loaded axially and no bending occurs. Therefore, their derivation does not analyse the actual mechanism of deformation for the linear elastic behaviour of foams.

Menges and Knipschild (1975, 1982) noticed from microscopic examination that the faces of closed cell foams have very little stiffness and strength and conclude that the membrane closures do not contribute significantly to the stiffness or strength of the foam. They then treated open and closed- cell foams identically. The choice of microstructural element: four identical struts meeting at a tetrahedral junction is a noteworthy feature of their model. Their analysis of the bending and axial deformation of the cell edges gave:

$$E / E_s = \frac{C_1(\rho / \rho_s)^2}{(\rho / \rho_s) + C_2} \qquad (2.5)$$

Where: C_1 and C_2, are constants, to be determined by experiment. E / E_s, is the

relative Young's modulus, and ρ/ρ_s, is the relative density. Their experimental results for rigid, closed cell polyurethane are in good agreement with this expression.

Barma et al.(1978) have derived an expression for the Young's modulus of rigid polyurethane foams by modelling these foams as pentagonal dodecahedra with open faces and with some initial curvature in the cell edges. Like Chan and Nakamura, they calculated the bending deflection of the initially curved cell edges under an axial load and then related this to the axial displacement. However, they neglected the bending of members loaded perpendicularly to their length. This derivation does not therefore analyse the actual mechanism of deformation for the linear elastic behaviour of the foams.

Warren and Kraynik (1988, 1991) attempted a more exact analysis for the properties of low-density foams. A three-dimensional open-cell foam is considered as an aggregate of tetrahedral structural elements, which consists of four half-beams of length L meeting at equal angles of $\cos^{-1}(-1/3)$ or 109^0. Their analysis for both assumed a homogeneous deformation at the cell level, whereas, in reality, cell walls which lie parallel to the loading axis deform less than those which lie at an angle to it. Their method is a 'geometry' method in principle, which gives a conservative estimate of displacement, and an upper bound for Young's modulus. They supposed an admissible deformation mode, which is a homogeneous deformation in their particular case. The elastic moduli for their isotropic model were derived as:

$$\frac{E}{E_s} = \frac{\phi^2(11+4\phi)}{(10+31\phi+4\phi^2)} \qquad (2.6)$$

$$\nu = \frac{(1-\phi)(5+4\phi)}{(10+31\phi+4\phi^2)} \qquad (2.7)$$

$$\frac{G}{E_s} = \frac{\phi^2(11+4\phi)}{30(1+2\phi)} \qquad (2.8)$$

$$\frac{K}{E_s} = \frac{\phi}{9} \qquad (2.9)$$

Where: ϕ, is the volume fraction of the material, and is equal to the relative density ρ/ρ_s. G, is the effective shear modulus, K, is the bulk modulus.

Kanakkanatt (1973) used a repeating unit cell, an axisymmetric box, to model an anisotropic foam. Average cell dimensions were introduced to characterize the structural anisotropy of the foam. The anisotropy in Young's moduli were calculated in terms of these average cell dimensions.

Tension:

$$\frac{E_y}{E_x} = \frac{\left(t/h\right)^2\left(1 + t/h\right)}{\left(t/L\right)^2\left(1 + t/L\right)} \qquad (2.10)$$

Compression:

$$\frac{E_y}{E_x} = \frac{\left(t/h\right)\left(1 + t/L\right)}{\left(t/L\right)\left(1 + t/h\right)} \qquad (2.11)$$

Where: E_x and E_y, are the Young's modulus of the foam in the x and y direction respectively. L and h, are the cell rib length in the x and y direction respectively. t, is the cell rib thickness.

Hilyard (1982) assumed a model similar to that of Kanakkanatt (1973). A rhombic box was employed as a representative cell. Hilyard further considered the anisotropy in elastic collapse stress, σ_c by relating it to the aspect ratios of the rhombic cell.

$$\frac{\sigma_c}{E_s} \approx \frac{0.2285\phi^2 a}{\sqrt{1 - \nu_p^{\,2}}} \qquad (2.12)$$

Where: a, takes account of the influence of the specimen preparation, and is assumed to be approx. 0.8. ν_p, is the Poisson's ratio of the base material.

Mehta and Colombo (1976) considered a foam as a composite of solid matrix and a 'filler' of liquid or gas. They further extended the Halpin-Tsai equation (1968) for predicting the composite modulus to the foam, obtaining the ratio of the solid modulus E_s to the foam modulus E as:

$$\frac{E_s}{E} = \frac{1}{\xi} + \frac{\rho_s}{\rho}\left(1 + \frac{1}{\xi}\right) \qquad (2.13)$$

Where: the factor ξ, is a measure of filler phase (i.e. cell geometry and orientation). An exponential function was assumed between this structure factor ξ and the aspect ratio h/L of the cell geometry, which, in turn, is related to experimental shrinkage data. A foam sample was immersed in a hot oil bath and the change in dimensions measured after cooling. The ratio of foam moduli parallel and perpendicular to the foam rise direction, E_y/E_x, was calculated in terms of the shrinkage data sh_y and sh_x. The experimental data generally fall within $\pm 20\%$ of the predicted values for these ratios. The method of using shrinkage data to decide the aspect ratio of the cell may provide an alternative way to that of measuring the mean intercept lengths, proposed by Kanakkanatt (1973), Harrigan and Mann (1984) and Huber and Gibson (1988).

Harrigan and Mann (1984) found that a second rank tensor can describe the degree of anisotropy in orthotropic materials. They also demonstrated that this material anisotropy tensor is symmetric and adequately represents the mean intercept length measurements. The experimental techniques and data of this tensor on five human bones can also be found from the paper.

In 1988, Gibson and Ashby illustrated the microstructures of honeycomb and foams, and at the same time they have successfully developed a very basic model of the deformation of conventional foams, which is based on flexure. This three dimensional anisotropic model has been represented as shown in *Figure 2.2*.
Gibson and Ashby (1982, 1988) have derived the equations for open cell foams as:

$$E_1 = \frac{cE_s}{2}\left(\frac{t}{l}\right)^4 \frac{l}{h}\left(1+\left(\frac{l}{h}\right)^3\right) \qquad (2.14)$$

$$E_3 = c\,E_s\left(\frac{t}{l}\right)^4 \frac{h}{l} \qquad (2.15)$$

Where: E_s, is the Young's modulus of the solid material, E_3, is the Young's modulus of the foam rise direction, E_1, is the Young's modulus in the other two directions, C, is a constant, t is the cell rib thickness, h, is the height of the cell, and l, is the width of the cell. Poisson's ratio, ν, is predicted solely as a function of cell geometry and is independent of relative density. Gibson and Ashby (1988) did not give the equation for the shear modulus in the three directions, but they derived a formula showing the relation between two directions as:

$$\frac{G_{31}}{G_{12}} = \frac{2}{1+\frac{h}{l}} \qquad (2.16)$$

Huber and Gibson (1988) further studied the anisotropy in shear modulus by relating it to the aspect ratios of the rhombic cell.

$$G_{12} = CE_s\left(\frac{t}{L}\right)^4\left(\frac{L}{h}\right) \qquad (2.17)$$

$$G_{13} = 2CE_s\left(\frac{t}{L}\right)^4\left(\frac{L}{h}\right)\frac{1}{(h/L)+1} \qquad (2.18)$$

Their experimental results for polyurethane foams are reported to be in good agreement with these expressions. But real cells in foams are not cubical, they are far more complicated. The cubic is only an approximation for real cell shapes. However, as a result of using this over simplified cell model (a cubic cell shape), Gibson and

Ashby failed to take cell wall orientation into account. Therefore, a good model incorporating both cell wall length variation and cell wall orientation is needed.

2.5 Mechanical Testing

Methods for tension, compression, shear and ball rebound testing of foams have been published by the ASTM (D-3574). Test methods on foams for ball indentation, and the DMTA test (Dynamic Mechanical Thermal Analyst) are not available from the ASTM. The Ball Indentation Test is in stark contrast to similar tests associated with metals where many books are already in print, such as: Hertz (1882), O'Neill (1934, 1967), Tabor (1951), Johnson (1985). The same method of DMTA testing of polymers can be used for testing the polymeric foams (see Murayama, 1978).

The properties of cellular solids can vary widely depending on the choice of the solid from which they are made, the volume fraction of the solid and the geometry of the cells. The physical properties of flexible foams are generally believed to depend upon the structure of both the polymer network and the cells formed as a result of the blowing process. The foams may not be homogeneous, isotropic materials. Their use as structural materials in complex geometries requires either a good stress analysis or large safety factors. For elastic stress analysis, Young's modulus, shear modulus and Poisson's ratio are commonly required. (e.g. $E_x, E_y, E_z, \nu_{xy}, \nu_{yx}, \nu_{xz}, \nu_{zx}, \nu_{zy}, \nu_{yz}, G_{xy}$, $G_{yx}, G_{xz}, G_{zx}, G_{zy}$, and G_{yz}). Although anisotropy in foams was noticed by Gibson and Ashby (1982, 1988), little experimental work was carried out to investigate this observation. Nearly all flexible polymeric foams have an extremely high elastic limit at room temperature, with the result that deformations of most flexible foams are nearly always within the elastic region. For example, when a flexible polyurethane foam is fully deformed by an external load, it can be restored to its original length after the external load is removed. Since there is a large amount of published data on stress-strain performance in compression, it is instructive to review this data. (e.g. Gibson and Ashby (1988), Gibson (1989), Gibson and Ashby (1982), Feng and Christensen (1982), Patel and Finnie (1970), Throne and Progelhof (1985), Gent and Thomas (1959, 1963), Whittaker (1971), Cunningham (1984), Tsai (1982), and Gibson et. al. (1989)). However, the shapes of those stress-strain curves are similar, and most of the researchers have only tested the foam in one direction. It is the aim of this study to test the behaviour of foams in three directions and investigate any anisotropy in the mechanical properties.

Several experimental studies of creep in polyurethane and polystyrene foams have been carried out. Findly and Stanley (1968) measured the creep response over a

2 hours period for a rigid polyurethane foam under uniaxial tension and compression. Huang and Gibson (1991) measured the creep behaviour of rigid polyurethane foams under constant shear. The foams creep at room temperature, thus, limiting their use in structural applications.

Few reports concerning rate effects on polystyrene foams in compression are available. The results of Benjamin (1965) are in disagreement with the results of this study, showing a decrease in modulus and a slight increase in yield stress for PSB foam. Results of Hoge and Wasley (1969) and Rinde and Hoge (1971) on PSB foam do, however, show good agreement with the results of this study. Foam properties vary according to the different polymers involved, and also depend upon the cell size and cell shape.

Poisson's ratio is one of the fundamental mechanical properties of an engineering material. When a material is stretched, the normal expectation is that it will become thinner in the direction perpendicular to the stretching direction. Almost all naturally occurring materials appear to exhibit this property which is defined by the quantity known as Poisson's ratio, ν (1829).

$$\nu_{yx} = -\frac{\varepsilon_x}{\varepsilon_y} \qquad (2.19)$$

Where: ε_y, is the tensile strain in the stretching direction, ε_x, is the tensile strain perpendicular to this. Since most materials contract in the perpendicular direction, the presence of a minus sign in the definition ensures that the ratio is positive. Conversely, a material with a negative Poisson's ratio is one which expands in all directions when pulled in only one, thus increasing its volume. Although it is generally believed that all materials have a positive ν, it has been known for over a century that a negative ν is theoretically possible (Love 1944). Most naturally occurring materials have Poisson' s ratio ν between 1/4 ~ 1/3. Rinde (1970) reported the Poisson's ratio for anisotropic flexible polyethylene foam was 0.37 in the foam rise direction and 0.68 for the transverse direction. His data also showed the time dependence of lateral straining at several strain rates. Ko (1965) has determined Poisson's ratio in tension on a flexible polyurethane foam rubber containing 47% voids and found a value of 1/4. Gent and Thomas (1959) found Poisson's ratio to be 1/3 for flexible foam rubbers and independent of void content in the range of 50-90% voids. Show and Sata (1966) found the Poisson's ratio of some undefined polystyrene foam to be 0.03 in compression at high strains. Gibson and Ashby (1988) have investigated the Poisson's ratio for rigid and flexible polyurethane foams. Their analysis shows Poisson's ratio to be independent upon the relative density and the value is about 0.33. Rigbi (1967) presents the temperature dependence of Poisson's

ratio for several plastics. Poisson's ratio was shown to be nearly constant at 0.33-0.35 for the temperature range -50 to 40^0C, and then rises to about 0.45 at 80^0C.

Structural foams used in many practical applications are often subjected to shear stresses. For example, the use of sandwich panels in aircraft construction is now a fairly widespread practice and one of the most commonly used types of core material is the polymer foam. To be effective in a sandwich panel, the core must have sufficient shear stiffness to prevent the skins from sliding over one another. Direct shear tests can be conducted to obtain a measure of shear rigidity for specific foams. However, most of the researchers assume that the foams are isotropic materials and they calculated the shear moduli using the equations shown in Figure 2.8. There is very few experimental data reported. Moore and Couzens (1974) and Gibson and Ashby (1988) measured the shear modulus of plastic foams and their data together with mine are shown in *Figure* 8.30 in this study.

Cellular solids are widely used for cushioning and energy absorption because they are highly compressible, even at very large strains. Shock mitigating cellular solids are typically subjected to indentation loads that crush some cells owing to complex multi-dimensional stress states. Some attempts have been made to correlate these features with the cushioning performance of the foam, using relatively simple tests. For example, Meinecke and Schwaber (1970, 1971) compared the energy absorption characteristics of PUR and Nitrile rubber foams as determined from compressive and pendulum-impact measurements; Rusch (1969, 1970) studied the compressive behaviour of several flexible and brittle foams; Gibson and Ashby (1988), and Zhang and Ashby (1994) suggested equations for predicting the compressive strength and failure envelope of plastic PUR foams as a function of density. Klintworth and Stronge (1989) estimated the force for flat punches indenting honeycombs by assuming that yield occurs when the maximum principal stress reaches a particular value. Cousins (1976) and Orringer et al. (1985) modelled the half-space beneath a spherical punch as independent concentric circular cylinders deforming in uniaxial compression, and estimated the force-deflection behaviour of the punch using experimental material data. Foam behaviour under dynamic impact loading were reported by many researchers such as: Throne et al. (1985); Mills and Hwang (1989); Sherwood (1992); Richardson and Nandra (1985); Ramon and Miltz (1990); Yossifon and Szanto (1987, 1989) and Shuttleworth et al. (1985). They have examined the effect of distributed and concentrated loads on many different brittle and flexible foams.

O'Neill (1934, 1967) has wisely observed that hardness, ' like the storminess

of the seas, is easily appreciated but not readily measured'. In general hardness implies the resistance to deformation. Hardness measurements usually fall into two main categories: indentation hardness, and rebound or dynamic hardness.

The first satisfactory analysis of the stresses at the contact of two elastic solids was due to Hertz (1882). Being guided by his observations of interference fringes, Hertz first made the hypothesis that the contact area is, in general, elliptical. He then introduced the simplification that, for the purpose of calculating the local deformations, each body can be regarded as an elastic half-space loaded over a small elliptical region of its plane surface. By using this simplification, generally used in contact stress theory, the highly concentrated contact stresses are treated separately from the general distribution of stress in the two bodies, which arises from their shape, and the way in which they are supported. In order for this simplification to be justifiable two conditions must be satisfied: the significant dimensions of the contact area must be small compared with (a) the dimensions of each body and (b) the relative radii of curvature of the surfaces. The first condition is obviously necessary to ensure that the stress field calculated on the basis of a solid which is infinite in extent is not seriously influenced by the proximity of its boundaries to the highly stressed region. The second condition is necessary to ensure firstly, that the surface just outside the contact region approximates roughly to the plane surface of a half-space, and secondly that the strains in the contact region are sufficiently small to lie within the scope of the linear theory of elasticity. Metallic solids loaded within their elastic limit inevitably comply with this latter restriction. However, caution must be used in applying the results of the theory to low modulus materials like rubber and foams where it is to produce deformations which exceed the restriction to small strains. The Hertz theory is restricted to frictionless surfaces and perfectly elastic solids.

The methods most widely used in determining the hardness of metals are static indentation methods. In the Brinell test (Brinell, 1900; Meyer, 1908) the indenter consists of a hard steel ball. Another type of indenter which has received wide use is the conical or pyramidal indenter as used in the Ludwik (1908) and Vickers (1925) hardness tests respectively. These tests involve the formation of a permanent indentation in the surface of the metal to be examined, the hardness being determined by the load and size of the indentation formed.

The Brinell hardness number is expressed as the ratio of the load, W, to the curved area of the indentation.

$$\text{Brinell hardness number} = \frac{2W}{\pi D^2\left[1-\sqrt{1-\left(\frac{d}{D}\right)^2}\right]} \qquad (2.22)$$

Where: W, is the normal load, D, is the diameter of the ball and d the chordal diameter of the indentation.

The Meyer hardness is expressed as the ratio of the load, W, to the projected area of the indentation.

$$\text{Meyer hardness} = \frac{W}{\pi a^2} = \frac{4W}{\pi d^2} \qquad (2.23)$$

Where: 2a (or d), is the chordal diameter of the projected area (indentation profile).

Tabor (1951) proposed the indentation strain as:

$$\varepsilon = f\left(d/D\right) \qquad (2.24)$$

and the mean pressure P_m is:

$$P_m = \frac{4W}{\pi d^2} = \varphi\left(d/D\right) \qquad (2.25)$$

Where: $\varphi\left(d/D\right)$, is some function of d/D that still has to be determined. This is the same as saying that geometrically similar indentations have the same hardness whatever the absolute size of the indentation.

O'Neill (1934) reported that there is a variation in yield stress at various depths in the bulk of the material. It would therefore appear difficult to assign a 'representative' value to the yield stress of the whole material. However, empirical tests by Tabor (1951) suggest that,

$$P_m \approx 3\sigma_y \qquad (2.26)$$

Where: P_m, is hardness of the material and σ_y, is the yield stress of the material.

Shaw and Sata (1966) and Wilsea et al. (1975) found that the hardness, H, of their foams were almost equal to σ_y. This is because the foam is compressible under the indent, a column of foam collapses, in a way which is hardly influenced by the surrounding material. The fact that the factor of 3 associated with completely solid materials arises as a result of the restraint offered by the surrounding elastic material as the plastic region attempts to extend laterally in accordance with a Poisson's ratio of 1/2 suggests that the restraint factor should be a function of Poisson's ratio. If Poisson's ratio were to be zero or negative the elastic material would offer no resistance to plastic flow, since there would be no tendency for the material to extend laterally as it undergoes plastic deformation. Therefore, the restraint factor should in this case be 1. Finally, Shaw and Sata (1966) pointed out that the mean strain beneath the indenter is much larger for a cellular material, and the strain is also far more

uniform over the plastically deformed region.

Wilsea et al. (1975) analysed a plastic foam indented by cylindrical and spherical indenters (see *Figure* 2.4) and found that

For the cylinder Indentation test:

$$\varepsilon_m = \frac{d}{h_y} \approx \frac{a}{2R\cot\left(\alpha_y/2\right)} \qquad (2.27)$$

and

$$H = \frac{P}{2aL} = \frac{\pi\sigma_y}{\alpha_y + \sin\alpha_y} \qquad (2.28)$$

For the ball indentation test:

$$\varepsilon_m = \frac{d}{h_y} \approx \frac{a^2}{2Rh} \qquad (2.29)$$

and $$H = \frac{P}{\pi a^2} = \sigma_y\left(1 - \frac{\left(h/a\right)^3}{\left[1+\left(h/a\right)^2\right]^{3/2}}\right)^{-1} . \qquad (2.30)$$

Where: AB=2a, the diameter of the indentation profile. The foam yields when the maximum principle stress reaches the value $-\sigma_y$, α_y, is the angle subtended by AB. The trajectories of maximum principle stress bisect the angle α_y. R, is the radius of the ball. h, is the height of the indentation profile. d, is the displacement. P, is the uniform normal indentation pressure. L, is the length of the cylinder. ε_m, is the maximum elastic strain. H, is the hardness of the foam.

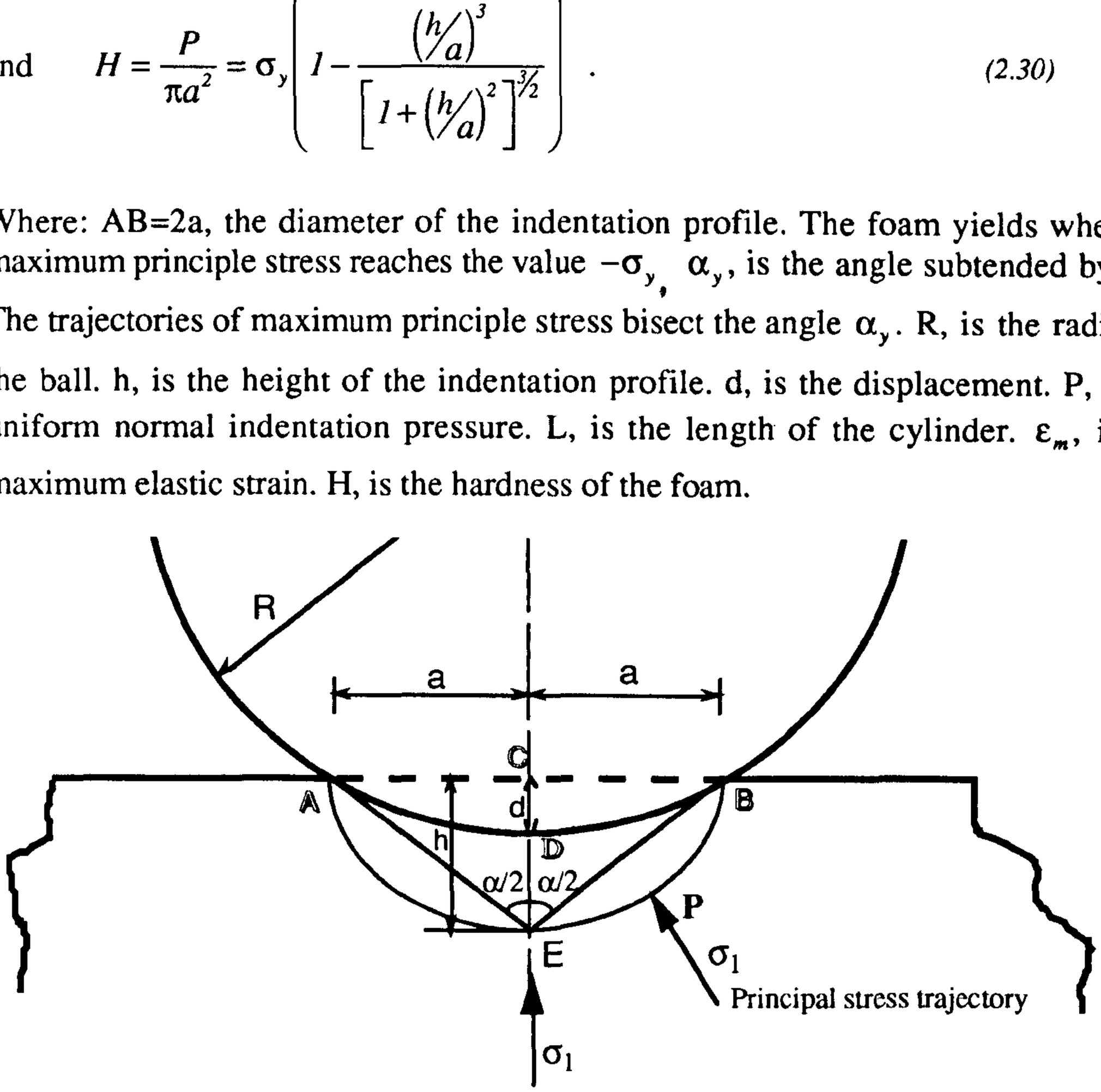

Fig. 2.4 The stress system beneath a cylindrical indenter having a uniform indentation pressure. (Wilsea et al., 1975).

The ball rebound test is deceptively simple in the sense that it is very easy to visualise and carry out, but the interpretation of the results requires great care. Static indentation tests such as the Ball Indentation Test provide a good way of characterising the static hardness of materials. But it requires the use a test machine that applies the indentation load to the ball in a controlled manner. The ball rebound test was introduced by Shore in 1918 to enable hardness tests to be made on metal structures or components without the need to cut specimens from the material. It was an early example of non-destructive testing, and provide a simple way of accurately providing a known load to a ball that was capable of indenting the material.

The principle of the test is that a ball, usually of hardened steel and with a diameter of 5-10 mm, is dropped from a prescribed height onto the surface of the test material. At impact, the ball indents the surface and kinetic energy is either converted into stored strain energy, or, if the local yield stress is exceeded, promotes the plastic flow that results in a permanent indentation in the material. When the kinetic energy has been dissipated, the specimen relaxes and the ball rebounds to a height proportional to the amount of energy stored elastically by the specimen. It is thus possible to obtain a measure of indentation resilience of the materials without the need to obtain a measure of the size or depth of the indentation.

Polymeric foams are usually made from viscoelastic polymers. Viscoelastic materials have some of the characteristics of both viscous liquids and elastic solids. Elastic materials have a capacity to store mechanical energy with no dissipation of energy; on the other hand, a viscous fluid in a nonhydrostatic stress state has a capacity for dissipating energy, but none for storing it. When a polymeric foam is deformed, part of its energy is stored as potential energy and part is dissipated as heat. A number of mechanisms are at work in absorbing energy. Some of the mechanisms are related to the elastic, plastic, or brittle deformation of the cell walls (Gibson and Ashby, 1988); some, to the viscoelastic energy absorption (Meinecke and Clark, 1973); and others, to the compression or flow of the fluid within the cells (Zhang, 1993). The plateau stress for an elastomeric foam used in cushions and in soft padding (see Figure 2.5) is determined by the elastic buckling of the cell ribs. Much of the external work stored during loading is released when the foam is unloaded. Friction is dissipated as heat, as a result of the intrinsic damping or hysteresis of the elastomer and of losses caused by the flow of cell fluid. But, despite this, there is usually some rebound on impact. In the case of plastic and brittle foams, the work done in the plateau region is completely dissipated as plastic work or as work of fracture, with almost no rebound after impact (Hilyard, 1982).

The static energy absorption mechanisms were carefully studied by Gibson

and Ashby (1988). When a foam is loaded, work is done by the forces applied to it. The work per unit volume in deforming to a strain ε is the area under the stress-strain curve up to ε (*Figure* 2.5).

$$W = \int_o^{\varepsilon} \sigma(\varepsilon) d\varepsilon \qquad (2.33)$$

when the plateau is flat, the plateau stress, σ_p, is almost constant and W is given approximately by:

$$W \approx \sigma_p \varepsilon \qquad (2.34)$$

The energy, W, and stress, σ_p, depend on the strain-rate, and on the temperature.

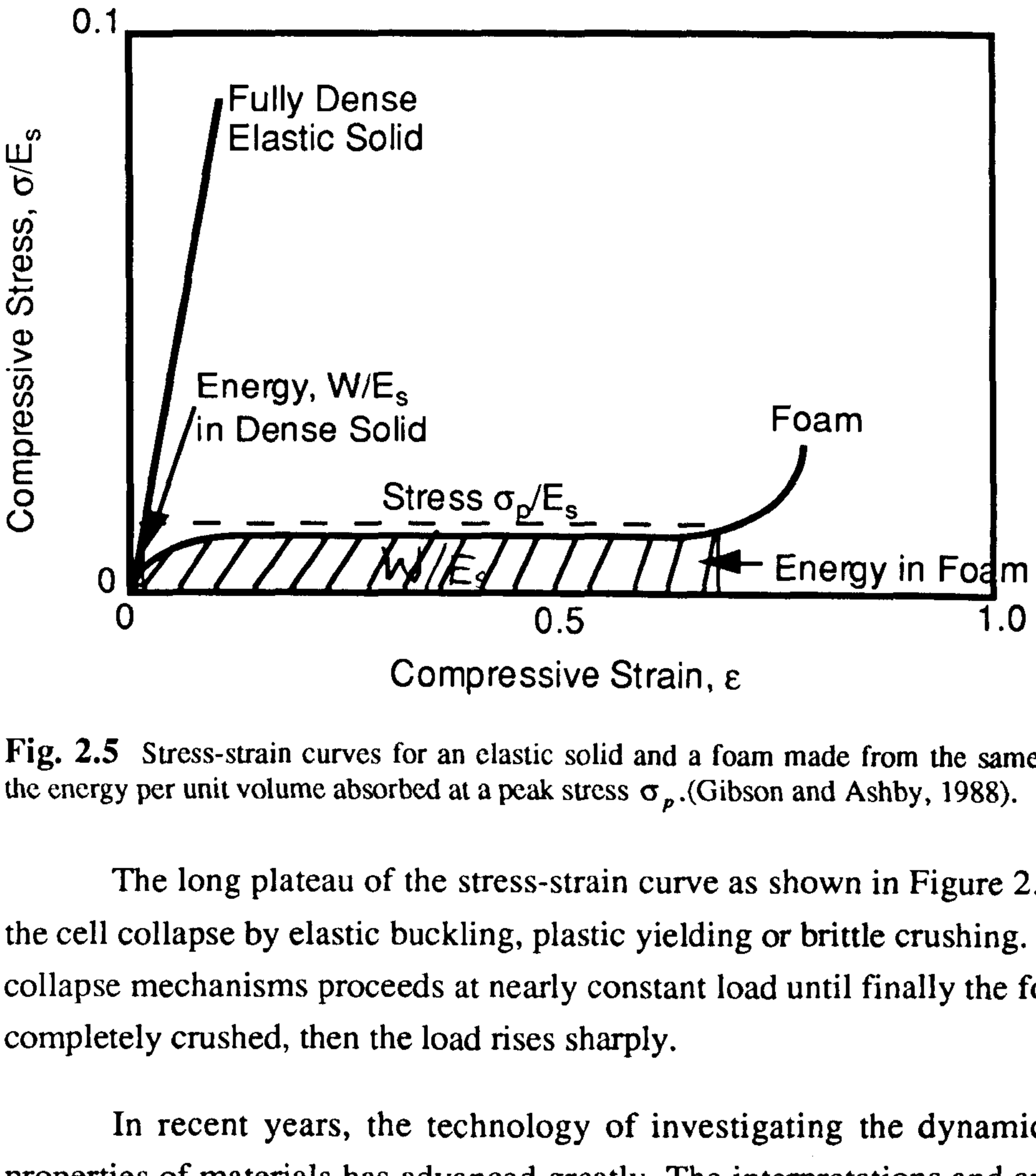

Fig. 2.5 Stress-strain curves for an elastic solid and a foam made from the same solid, showing the energy per unit volume absorbed at a peak stress σ_p.(Gibson and Ashby, 1988).

The long plateau of the stress-strain curve as shown in Figure 2.5 arises from the cell collapse by elastic buckling, plastic yielding or brittle crushing. Each of these collapse mechanisms proceeds at nearly constant load until finally the foam is almost completely crushed, then the load rises sharply.

In recent years, the technology of investigating the dynamic mechanical properties of materials has advanced greatly. The interpretations and applications of dynamic data have stimulated interest from both the practical and the scientific stand point. The stiffness of a flexible foam is related to its composition and structure. As a result of being a viscoelastic material, it would be expected that the small-strain dynamic properties of a foam will depend on the frequency of deformation and the temperature.

Viscoelastic materials are temperature dependent i.e. flexible foams are soft at room temperature, but become harder at low temperature (e.g. -30^0). Viscoelastic materials are also time (or frequency) dependent i.e. modulus measurements over short times result in high values, whereas, measurements over long times result in low values. In the viscoelastic studies of polymeric materials, the method of sinusoidal excitation and response is very useful (Ferry, 1961; Kolsky, 1953; and Murayama, 1978). In this case, the applied force and the resulting deformation both vary sinusoidally with time, the rate usually being specified by the frequency f in cycles/sec (Hz). or $\omega = 2\pi f$ in radians/sec. For linear viscoelastic behaviour, the strain will alternate sinusoidally but will be out of phase with the stress, as shown in *Figure* 2.6(B).

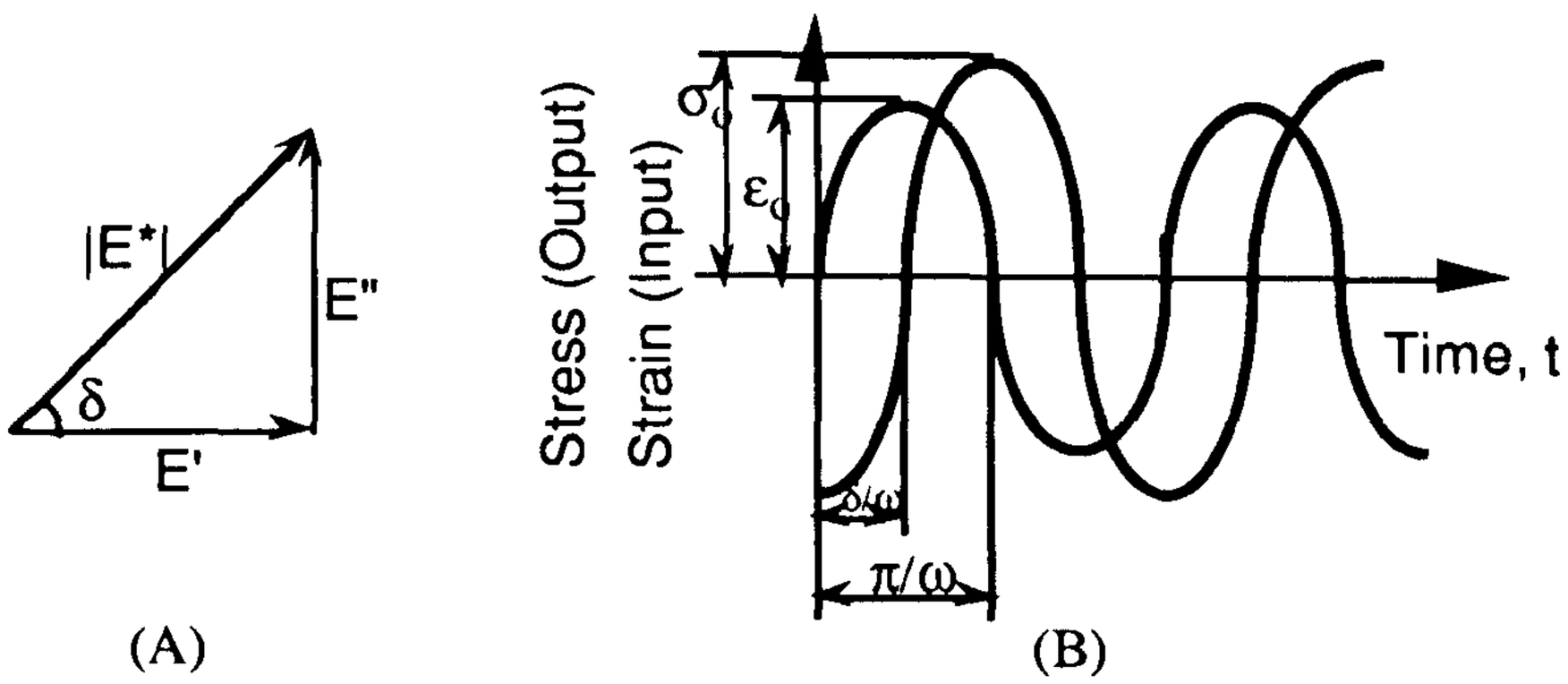

Fig. 2.6 Relations between various parameters used to express the results of a dynamic mechanical measurements.

This phase lag results from the time necessary for molecular rearrangements is associated with relaxation phenomena (McCrum et al., 1967). The stress, σ, and strain ε, can be expressed as follows:

$$\sigma = \sigma_o \sin(\omega t + \delta) \qquad (2.35)$$

$$\varepsilon = \varepsilon_o \sin \omega t \qquad (2.36)$$

Where: ω, is the angular frequency, and δ, is the phase angle.

$$\sigma = \sigma_o \sin \omega t \cos \delta + \sigma_o \cos \omega t \sin \delta \qquad (2.37)$$

The stress can be considered to consist of two components, one in phase with the strain ($\sigma_o \cos \delta$), and the other 90^0 out of phase ($\sigma_o \sin \delta$). When these are divided by the strain, the modulus can be separated into an in-phase (real) and out-of-phase (imaginary) component. These relationships are:

$$\sigma = \varepsilon_o E' \sin \omega t + \varepsilon_o E'' \cos \omega t \qquad (2.38)$$

$$E' = \frac{\sigma_o}{\varepsilon_o} cos\delta \qquad \text{and} \qquad E'' = \frac{\sigma_o}{\varepsilon_o} sin\delta \qquad (2.39)$$

Where: the real part of the modulus, E', is called the storage modulus, because it is related to the storage of potential energy and its release in the periodic deformation. The imaginary part of the modulus, E", is called the loss modulus, and is associated with the dissipation of energy as heat when materials are deformed. The phase angle, δ (see Figure 2.6(A)) is given by:

$$tan\delta = \frac{E''}{E'}. \qquad (2.40)$$

The dynamic complex modulus, $|E^*|$, is therefore equal to $\sqrt{E'^2 + E''^2}$. Where the loss tangent, $\tan\delta$, is proportional to the ratio of the energy dissipated to the energy stored during one deformation cycle.

The impact data can be related directly to the deformation energy (area under the loading curve) and the hysteresis loop (area between the loading and unloading curves). However, the rate dependence limits the direct comparison of the data obtained at one strain rate with the impact data, since in the impact test the rate of deformation decreases with penetration distance.

Flom (1960) attempted to relate the time dependant loss $tan\delta$ to the ball rebound measurements, and obtained the following equation:

$$tan\delta = 9.212\pi log\left(h_1/h_2\right) / \left(4\pi^2 - (2.303 log(h_1/h_2))^2\right) \qquad (2.41)$$

Where: $tan\delta$, is the energy dissipated as heat and manifests itself as mechanical damping or internal friction. h_1, is the dropping height, and h_2, is the ball rebound height.

The loss $tan\delta$, can be obtained using a DMTA (Dynamic Mechanical Thermal Analyser). DMTA is a commonly used dynamic mechanical instrument which can measure the deformation of a material in response to vibrational forces. The dynamic modulus, the loss modulus, and a mechanical damping are determined from these measurements. The modulus indicates stiffness of material, and it may be a shear, a tensile or a flexible modulus, depending upon the experimental equipment. The mechanical damping (internal friction) gives the amount of energy dissipated as heat during the deformation.

2.6 General Review of Auxetic Foams

In theory, there are two ways of improving the mechanical properties of conventional polymeric foams— either by altering the chemical constituents of the solid struts or by changing the cell geometry. A lot of the work done in this area has concentrated on changing the chemical composition of the foam. Many different types of polymeric foam, such as PUR (polyurethane) foam, and PS (polystyrene) foam have been widely used all over the world. Most recently, attempts have been made to look for a new way to improve the mechanical properties based on changing the foam cell geometry.

In 1987, a very interesting new type of foam was developed by R. S. Lakes. This new type of polymeric foam has a re-entrant cell shape which had a Poisson's ratio of -0.7. The distinction between this new foam and a conventional foam was that when this foam was stretched in one direction, it became fatter in all directions, whereas, the conventional foam became thinner in all other directions. Although it is generally believed that all materials have a positive Poisson's ratio, it has been known for a very long time that a negative Poisson's ratio, is theoretically possible (Love, 1944). Nye (1960) pointed out that theoretical bounds on Poisson's ratio can be obtained by requiring that the strain energy of an elastic isotropic solid remains positive under any set of deformations. This gives the bounds $-1 \leq \nu \leq 0.5$ for isotropic materials. The upper limit corresponds to materials that cannot change volume, and the lower limit applies to materials that cannot change shape. The bounds on Poisson's ratio of anisotropic material are much wider (Rothenburg et al. 1991, and Lakes, 1993). Typical values are nearly 1/2 for rubber and nearly 1/3 for steel. Negative Poisson's ratio materials are of interest because of their unusual nature, and because they deform in ways unexpected on the basis of experience with ordinary materials.

In 1991, Evans proposed the designation "auxetic" (from the Ancient Greek word auxetos: "that may be increased") for such material. He claimed that the unusual behaviour of auxetic foam comes from its unusual cell structure: the cell-ribs of conventional foam are protruding outward, whereas, that of auxetic foam are permanently protruding inward. Evans also pointed out that a simple two dimensional model for a conventional open-celled polymeric foam is that of a hexagonal honeycomb which is shown in *Figure 2.7* . When such a honeycomb is pulled, the cells elongate and thin down, thus giving rise to a positive Poisson's ratio. However, if the cells are made re-entrant, that is the upper and lower apices are made obtuse, then when this honeycomb is stretched, the cross-section broadens and a negative

Poisson's ratio results.

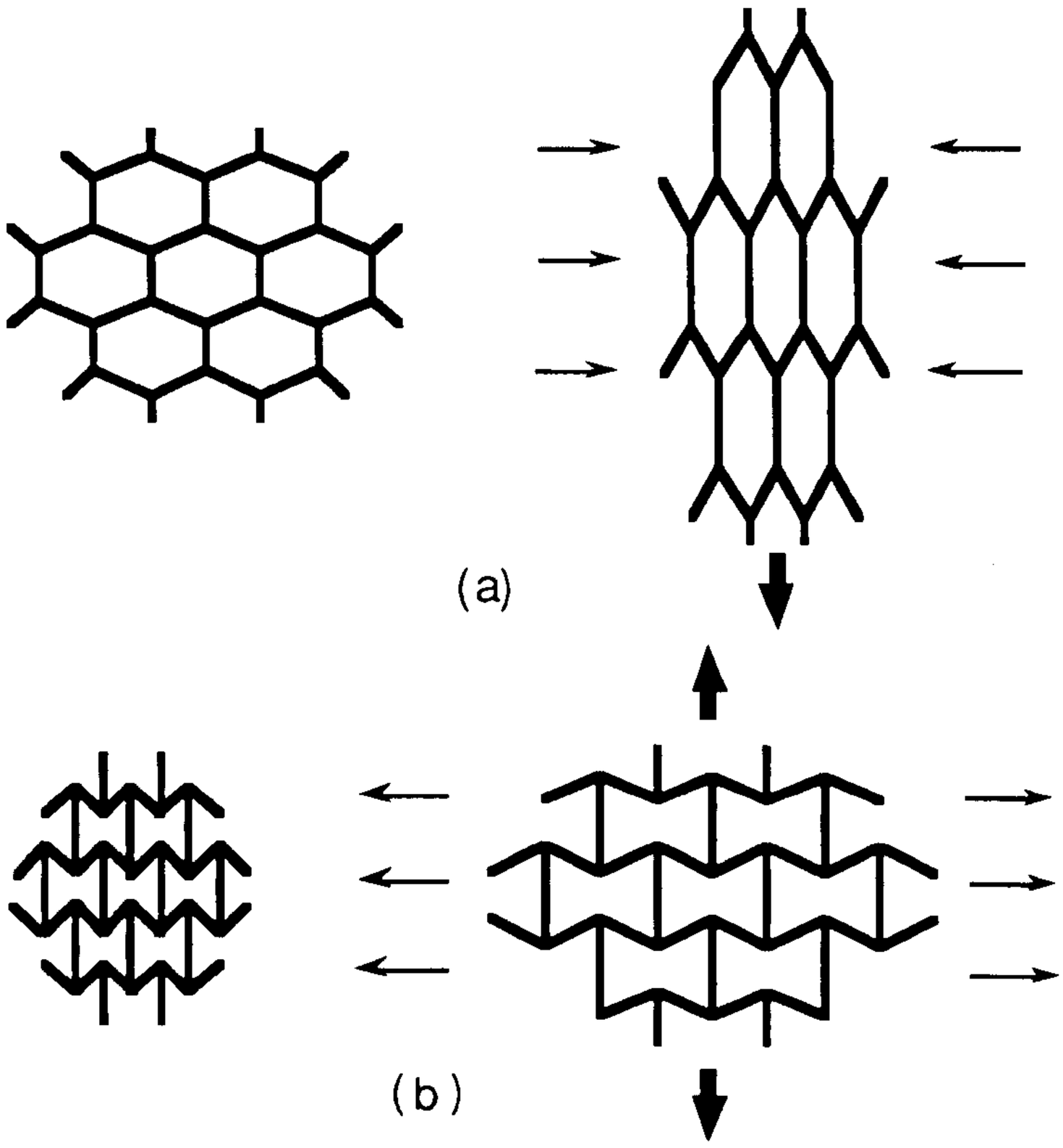

Fig. 2.7 (a) A schematic diagram of a conventional hexagonal structure and how it deforms when stretched, producing a conventional positive Poisson's ratio. (b) A re-entrant honeycomb producing a negative Poisson's ratio. (Evans, 1991).

Foams with negative Poisson's ratios can be produced from a variety of conventional materials, these include thermoplastic foams such as polyurethane foams (Lakes, 1987, Choi and Lakes, 1992), silicone rubber (Friis, Lakes and park 1988) and metallic foams based on copper and aluminium (Lakes, 1987, Choi and Lakes, 1992). More recent findings of negative Poisson's ratio are in composite laminates (Milton, 1992), in honeycombs (Gibson and Ashby, 1988; and Masters 1994), in polymer/water gels (Hirotsu, 1991), and in anisotropic microcellular polymers such as expanded polytetrafluoroethylene (Evans and Caddock, 1989) and UHMWPE (Alderson and Evans, 1993).

In 1988, Gibson and Ashby developed a flexure model for describing the mechanics of 2D honeycombs to show how a re-entrant honeycomb exhibits a negative Poisson's ratio. Masters (1994) further considered the mechanics of a two-dimensional re-entrant honeycomb consisting of thin planar walls of uniform thickness but different lengths. He employed a beam analysis to obtain the effective in-plane elastic constants for a particular orientation of the cells with respect to the principle axes of strain. Hinging and stretching were found to be the preferred deformation mechanism for the re-entrant cardboard honeycombs in tension and flexure is the

dominant mechanism in compression.

Hinging Model:

$$\begin{cases} \dfrac{E_1}{E_s} = \dfrac{K_h(h/L + \sin\theta)}{b\cos^3\theta} \\ \dfrac{E_2}{E_s} = \dfrac{K_h\cos\theta}{b\sin^2\theta(h/L + \sin\theta)} \end{cases} \qquad (2.42)$$

Stretching Model:

$$\begin{cases} \dfrac{E_1}{E_s} = \dfrac{K_s(h/L + \sin\theta)}{b\cos\theta(2h/L + \sin^2\theta)} \\ \dfrac{E_2}{E_s} = \dfrac{K_s}{b\cos\theta(h/L + \sin\theta)} \end{cases} \qquad (2.43)$$

Flexure Model:

$$\begin{cases} \dfrac{E_1}{E_s} = \dfrac{K_f(h/L + \sin\theta)}{b\cos^3\theta} \\ \dfrac{E_2}{E_s} = \dfrac{K_f\cos\theta}{b\sin^2\theta(h/L + \sin\theta)} \end{cases} \qquad (2.44)$$

Where: E_1/E_s and E_2/E_s, are the relative Young's moduli in the 1 and 2 directions respectively, K_f, K_h and K_S, are the flexure, hinging and stretching force constant respectively, h/L, is the ratio of lengths of the cell ribs, b, is the cell rib thickness, and θ, is the angle between the two connected ribs.

Almgren (1985) used a 2-D array of rigid rods joined by elastic hinges from which he developed a 3-D model which is isotropic in its macroscopic elastic properties. This model gives $\nu = -1$, and $G = \infty$. Almgren showed that the 2-D model is not isotropic in the plane although the properties in the 1 and 2 directions are equal i.e. $\nu_{12} = \nu_{21} = -1$ when h/L=2 and $\theta = -30^{o}$. Evans (1991) describes this condition as square symmetric since measuring Poisson's ratio along directions away from the principle axes yields values differing from -1. Wojciechowski and Branka (1989) investigated theoretically the negative Poisson's ratios in a 2-D molecular system of hard cyclic hexamers in the high-density phase, i.e. with a tilt of the molecular axes relative to the crystalline ones. The Poisson's ratio, ν_p is

$$\nu_p \equiv \frac{4\lambda_{\xi\eta\xi\eta} - 2\lambda_{\xi\xi\eta\eta} + p}{4\lambda_{\xi\eta\xi\eta} + 2\lambda_{\xi\xi\eta\eta} - p} \qquad (2.45)$$

Where: $\lambda_{\xi\eta\xi\eta}$ and $\lambda_{\xi\xi\eta\eta}$, are the compressibility-related and shear-related modulus respectively.

Further theoretical and computational work along this line involving anisotropic and isotropic particles, molecular networks, tensile springs, and topologically constraining rods or strings can be found in references: Rothenburg et al. (1991); Evans et al. (1991); Boal et al. (1993) Warren (1990) and Wei (1992).

In 1988, Lakes et al. proposed the 3D re-entrant foam structure as shown in *Figure 2.8*. Although this geometry produces re-entrancy in three dimensions, there are problems with the connectivity of these cells. They cannot be connected together to fill space without the presence of an equal number of non re-entrant cells. In this situation, it is not clear whether or not the combined structure will still produce a negative Poisson's ratio. However, there was no mathematical calculations for this model reported.

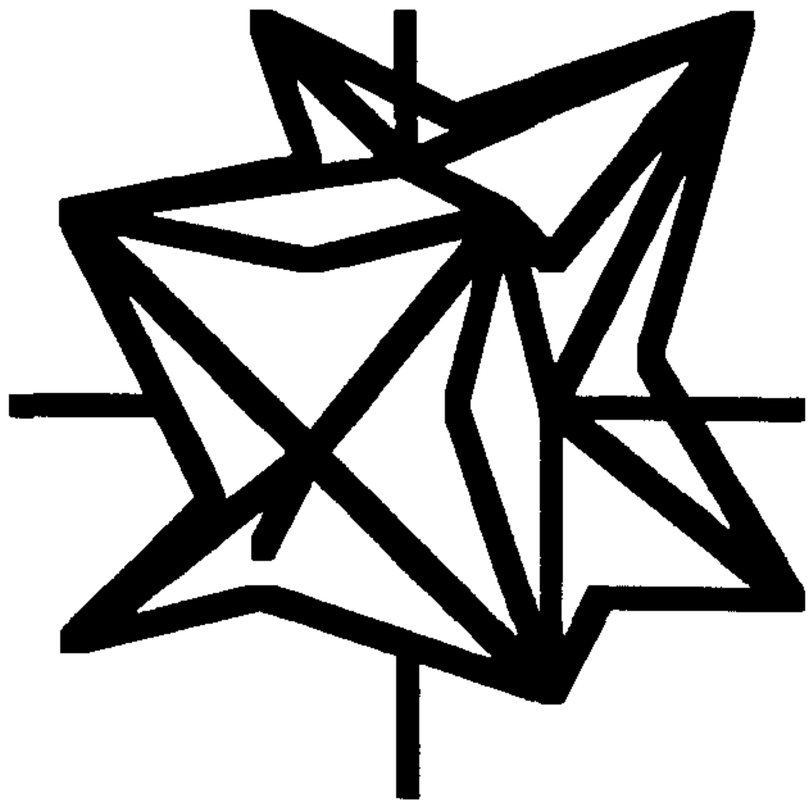

Fig 2.8 Idealized re-entrant unit cell produced by Lakes, 1988.

In order to understand the behaviour of auxetic materials, we need to know how co-operative interactions with the material structure produce the novel mechanical effects. So far in the current literature there is no three-dimensional anisotropic foam model available to analyse the unusual mechanical performance of auxetic foams until a 3D re-entrant foam model was developed for this thesis.

2.7 Fabrication and Mechanical Test Methods for the Auxetic Foams

Recently, a discussion on fabricating auxetic foam has been given by Friis, Lakes, and Park (1988). According to their report, the re-entrant cell structure is obtained by triaxial compression at elevated temperature. The method involves compressing a foam block into a rectangular mould to reduce the volume of the foam by a factor of up to 3.4. The structure of the compressed foam is then 'set' by an appropriate thermal treatment. Lakes' method only works for small size specimens with a 2.54cm cross section. When the required specimen is larger than this, the specified thermal treatment is no longer suitable. As a result of this, the fabrication method of auxetic foams requires further development, so that large size auxetic foam blocks can be produced. So far only Lakes group has reported on the fabrication method for the auxetic foams.

In 1992, Choi and Lakes reported some mechanical test results on polymeric foams. As noted above however, the specimen sizes used were very small, such as: 10mm x 10mm x 12.5mm for the tensile test; and 10mm x 10mm x 6mm for the compression test. As a result of the relatively large pore size (10 pores per inch) of the cellular foams used in this work, there may be large end effects involved in these tests. To improve the accuracy of the static test results, larger auxetic foam specimens with higher aspect ratios need to be fabricated and tested.

In the same paper, Choi and Lakes also detailed a method for measuring the Poisson's ratio of the foams. This was described as: "..... during the test, two lines 10mm apart were drawn in the middle of the lateral surface of the foam, and the longitudinal strain was changed by 5% and lateral deformation was measured with a micrometer". This implies that they have only measured the movement of the foam surface, instead of measuring the movement of the entire block of foam. Although the paper gives some data, it can be seen that no shear measurements have been carried out. They assumed that the foam material is isotropic, and derive the shear modulus, G, by using the equation $G = E/2(1+\nu)$. But this assumption may be incorrect because of the anisotropic microstructure of the foams. So far, the Lakes group is the only one that has reported results on the mechanical properties of auxetic foams.

In 1993, Dubbelday reported the results of a literature search on auxetic materials. The conclusion reached was that: "..... there is no complete set of explicit data on the elastic moduli of various auxetic foams. Thus, it was not possible to judge how far progress was made in obtaining materials with a large value of G compared

with conventional stiff materials". This is one of the issues that will be addressed in this thesis.

2.8 Applications of Auxetic Foams

Because of the unusual behaviour of auxetic foams under tension or compression, as shown in *Figure 2.7*, Lakes (1987, 1991) and Evans (1990, 1991) have made predictions concerning these new materials.

As a first step in acquiring an understanding of the nature of the auxetic property, we first study the relationship between elastic moduli and Poisson's ratio. *Figure 2.9* is condensed from Evans (1991) paper and shows the four equations relating the constitutive properties.

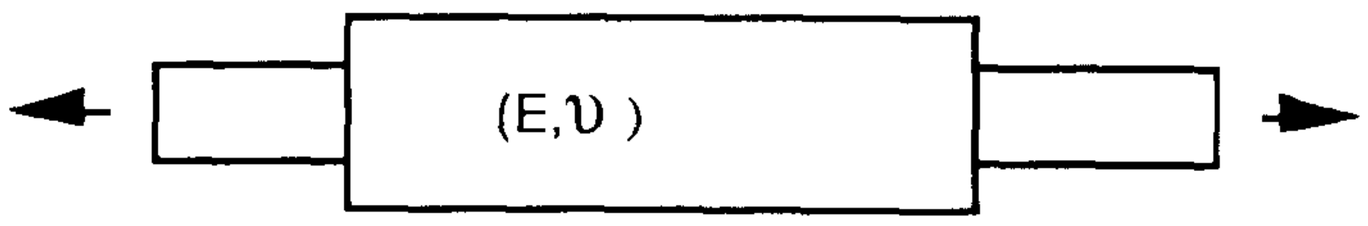

E measure of resistance to tensile load

υ measure of change in cross-section under tension

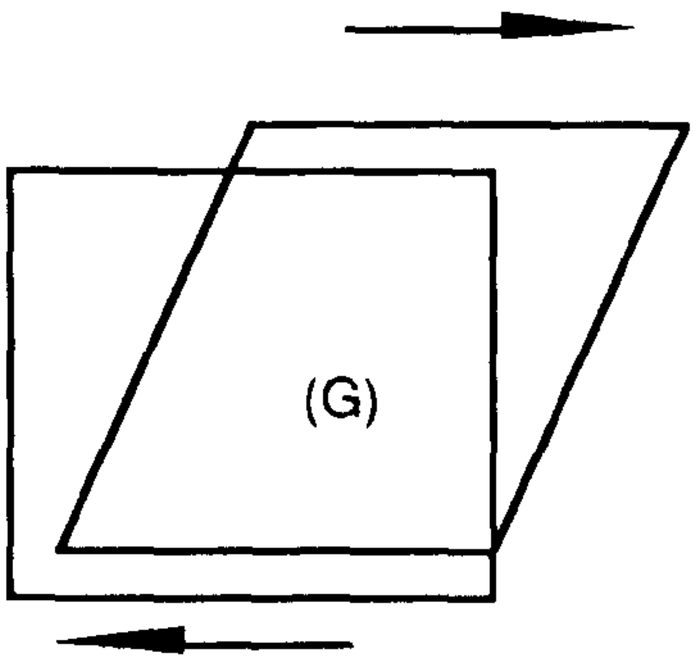

G measure of resistance to applied shear load

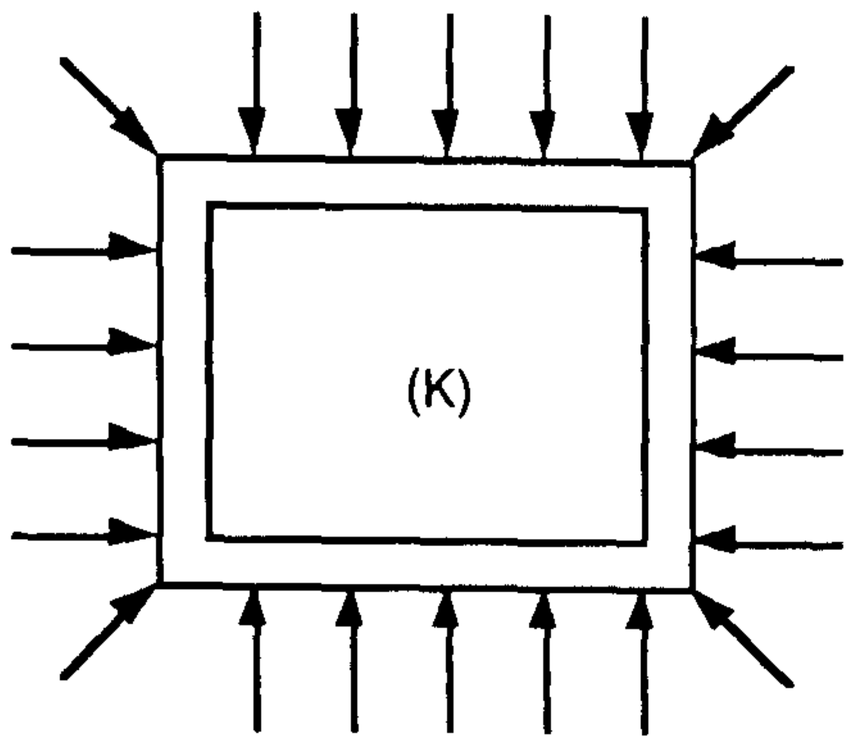

K measure of resistance to an appiled pressure

$$K = \frac{E}{3(1-\nu)} \qquad G = \frac{E}{2(1+\nu)}$$

$$E = \frac{9KG}{(3K+G)} \qquad \nu = \frac{3K-2G}{2(3K+G)}$$

Fig 2.9 The relationship between the fundamental elastic constants, the tensile or Young's modulus, E, the Poisson's ratio, ν, the bulk modulus, K, and the shear modulus G, for an isotropic material. (Evans, 1991)

For an isotropic perfectly elastic material only two of these quantities need to be measured as the other two can be determined from them. Evans (1991) therefore suggests that if we have a material with a particular fixed value for its Young's modulus, E, we can vary the Poisson's ratio, ν. Then as ν approaches 0.5, the bulk modulus, K, will become very large. On the other hand, if ν approaches -1 the shear modulus, G, will become very large. Thus Evans predicted that a large negative ν would produce a benefit by increasing G at the expense of K. For example, a solid with $\nu \approx -1$ would be the opposite of rubber: difficult to shear but easy to deform volumetrically, G>>K. It is clear that a large negative Poisson's ratio ($-1.0 \leq \nu \leq -0.5$) will improve the ratio G/E. If a material can be modified to alter ν without significantly altering E then this will result in large increases in the shear modulus.

A further example of the benefits of a negative ν, is the case of the deflection of a fixed circular plate which is illustrated by Evans (1991) and shown in *Figure 2.10*. As υ approaches -1 the deflection of the circular plate becomes smaller and smaller for a given load. Hence the plate becomes effectively stiffer as a result of simply altering the Poisson's ratio.

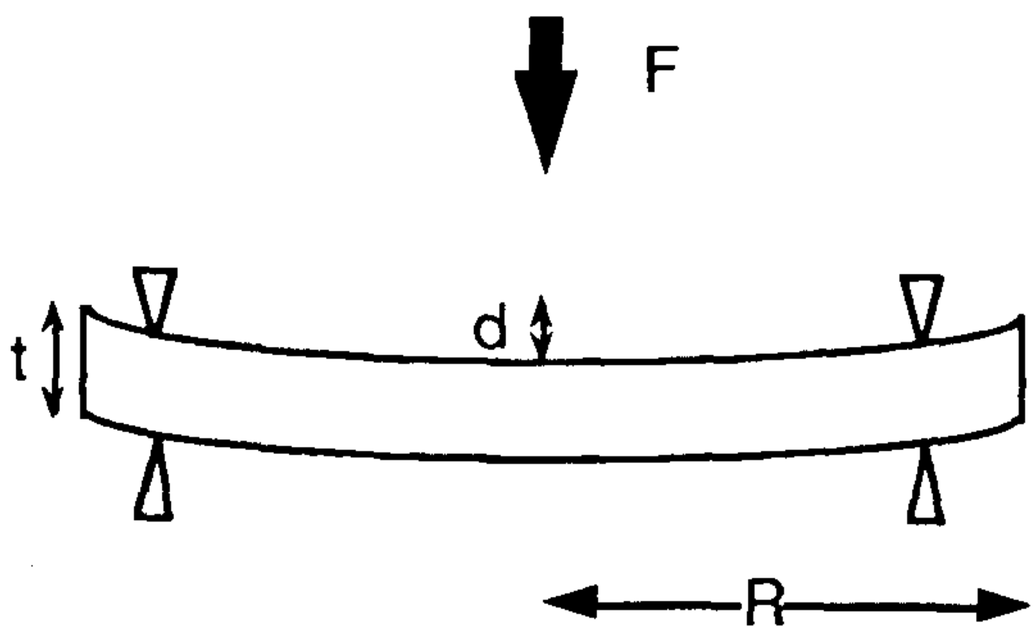

$$d = \frac{3FR^2(1-\nu^2)}{16Et^3}$$

Fig. 2.10 A circular plate, radius R, thickness t, with a Young's modulus E, and Poisson's ratio υ, will deflected a distance d, by applying a force F. When υ approaches -1 the deflection approaches zero. (Evans, 1991)

Another advantage of a sheet of auxetic foam, predicted by Evans (1990), is its dome shape curvature under flexure, as shown in *Figure 1.2*. When a sheet of ordinary foam is curved downwards, it natural tendency is to curve up in the transverse direction to form a saddle shape. A material with a negative Poisson's ratio, because of its unusual cell structure will however curve downwards in both directions producing a dome shape. Currently the only way of using honeycombs in curved geometries is either by machining them - a costly process, or by forcing them into shape and damaging the core material.

Choi and Lakes (1991) designed a fastener which consists of a hollow

circular cylindrical core, made of negative Poisson's ratio material, and a socket with a corresponding cylindrical hole. The fastener is made bigger than the hole. When it is inserted, the longitudinal force of insertion causes its diameter (transverse dimension) to become smaller by virtue of the negative Poisson's ratio. With sufficient force, the core diameter becomes equal to the hole diameter and the core can be inserted into the hole. As axial force is applied to remove the fastener this causes the core to expand laterally, generating an increased frictional force which resists removal. Lakes (1991) and Evans (1991) also pointed out that the same principle would apply in minimising fibre pullout in fibre reinforced composites .

In order to justify further work on the development of applications of auxetic foams and to examine the veracity of previous predictions, we need to investigate the basic mechanical properties of these new materials. These include such properties as compression stiffness, tensile stiffness, shear stiffness, Poisson's ratio, creep, resilience, indentation resistance, dynamic damping, and kinetic energy absorption during impact. All these mechanical properties have been studied in this thesis, and a comparison has also been made with the properties of the parent conventional foams.

Chapter 3
Fabrication Methods

3.1 Introduction

One way of obtaining negative Poisson's ratio is by using a re-entrant cell structure. Various features of the re-entrant cell shape can be controlled by processing techniques. In 1987, Lakes converted an open cell polymeric foam into an auxetic foam with a Poisson's ratio of -0.7, and developed the fabrication method for making a small auxetic foam specimen of dimensions: 22mm × 22mm × 125mm. The method used involved four stages: compression, heating, cooling and relaxation.

To transform a conventional flexible foam into an auxetic one using this method requires that the foam is compressed simultaneously in three dimensions to force the cell ribs to buckle. This produces a re-entrant structure which is then heated to its softening temperature to preserve the new configuration. Different types of polymeric foam (e.g. open or closed-cell) and differing densities of conventional foams require different heating times and temperatures. The conventional foams used in this work are listed in the *Table* 3.1. The process used by Lakes is a one-stage compression and has several problems. An auxetic foam produced in this way may exhibit long term instability, with the material reverting to its original structure. The one-stage compression also promotes severe surface creasing. To improve the quality of the auxetic product, and to fabricate larger specimens the process was developed as described below.

Type	Short hand name	Supplier	Density (Kg/m^3)
60ppi closed-cell polyester urethane foam	PECC	Caligen, Britain.	37.9±2.1
60ppi reticulated polyester urethane foam	PECO	Caligen, Britain	33.7±1.3
10ppi open-cell polyether urethane foam	10CO	Reticel Via Caligen, Belgium.	24.1±3.1
30ppi open-cell polyether urethane foam	30CO	Reticel Via Caligen, Belgium	24.5±2.7
60ppi open-cell polyether urethane foam	60CO	Reticel Via Caligen, Belgium	21.7±1.9

Table 3.1 Specify materials used such as: types, suppliers, densities. note: ppi means pores per inch.

3.2 Fabricating the Small Size Auxetic Polymeric Foams

3.2.1 General Fabrication Procedure

All the foam specimens used in this work were cut to size using a Burgess band saw fitted with a knife blade. This enabled accurate rectangular blocks to be cut with smooth faces. As a result of the foam being flexible and having a very low Young's modulus it can easily be squeezed into a small rectangular mould to achieve a 3-dimensional compression. The starting point for the investigation was the method published by Friis and Lakes (1988), described below.

A Gallenkamp BS oven was pre-heated to 200^0C. Next, A square aluminium tube (e.g. with inner dimensions: 25.4mm × 25.4mm × 80mm) was used as a mould for the foam which was cut oversize (38mm × 38mm × 110mm in the case of the open-cell polyether urethane foam). The inner walls of the mould were then treated with a general purpose lubricant (WD 40) to aid in the insertion of the foam. At this point the foam can be inserted into the tube with the aid of a spatula to help eliminate surface wrinkles. This procedure gives compression in two transverse directions. Two end-plates made of aluminium (dimensions 1.5mm × 25.4mm × 25.4mm) can then be used to block up the ends of the mould, so that the foam is compressed in the third, longitudinal direction as shown in *Figure* 3.1. The compressed foam with the buckled cell ribs was then placed in the oven at 200^0C for eight minutes to 'set' the new configuration. The heating time is very critical since the transformation temperature of the foam does not reach the oven temperature. The establishment of the correct heating time is discussed later. The mould was then removed from the oven and was cooled at room temperature for 15 minutes. Finally, the foam was taken out of the mould by hand, and was stretched gently in each of three orthogonal directions to overcome any adhesion of the cell ribs.

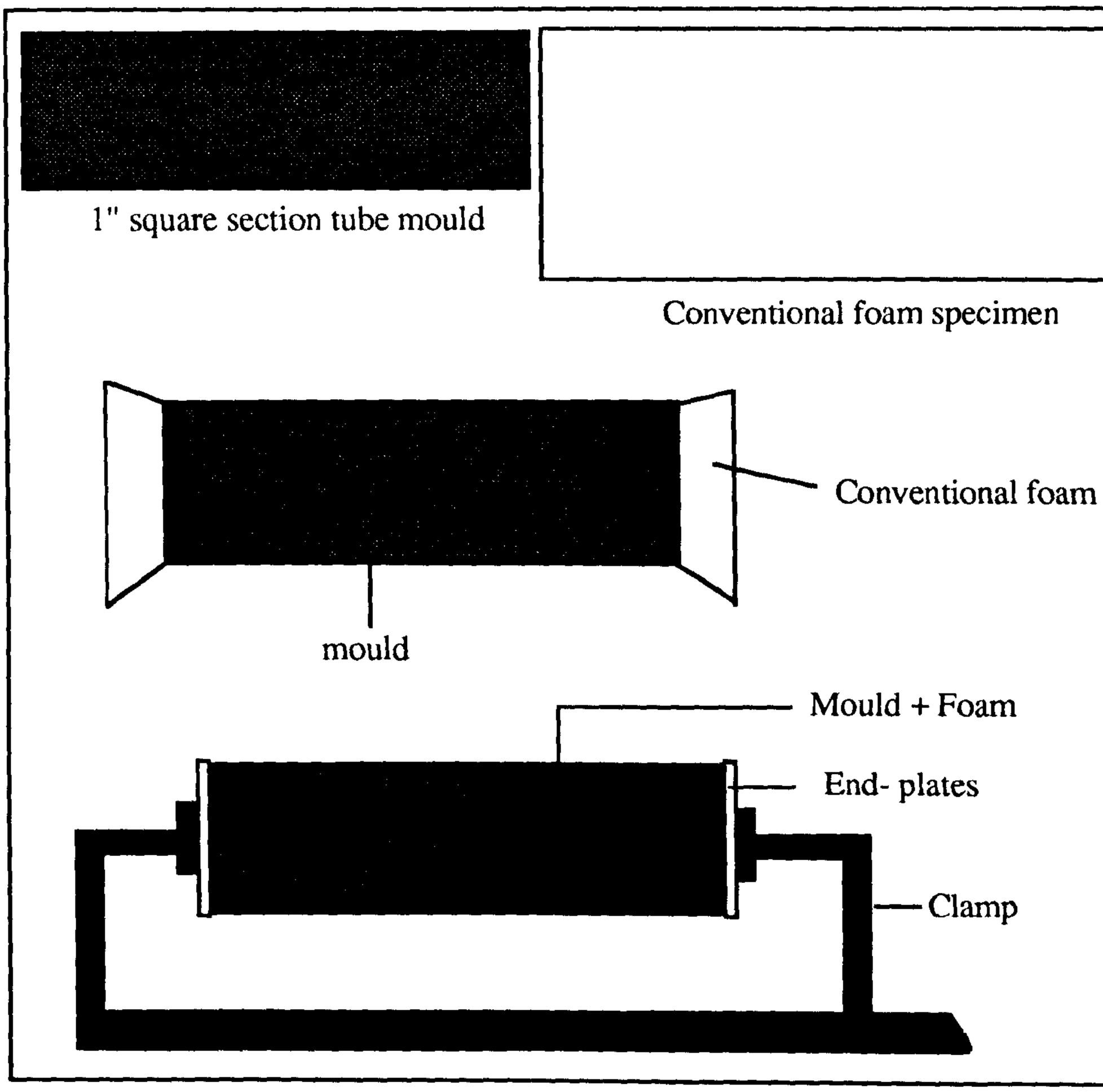

Fig. 3.1 Schematic diagram for fabricating the small size auxetic foam technique .

3.2.2 The Heating Temperature

Friis and Lakes (1988) carried out their work at an oven temperature of 200^0C. However, Lakes did not report how and why he decided on this temperature. As an attempt to investigate this, an experiment was performed to determine the transformation temperature required by the foam. A small specimen of foam was placed inside a test tube, and heated using a Bunsen burner. A thermocouple was inserted in the middle of the foam to measure the temperature, and the whole procedure was carried out inside a fume cupboard as shown in *Figure* 3.2. The foam softening temperature was recorded when the cell ribs began to collapse. Three specimens were tested for each type of foam, and the average temperature was taken. Although this method is not very accurate, it was possible to obtain estimates of the softening, liquefaction and decomposition temperatures respectively.

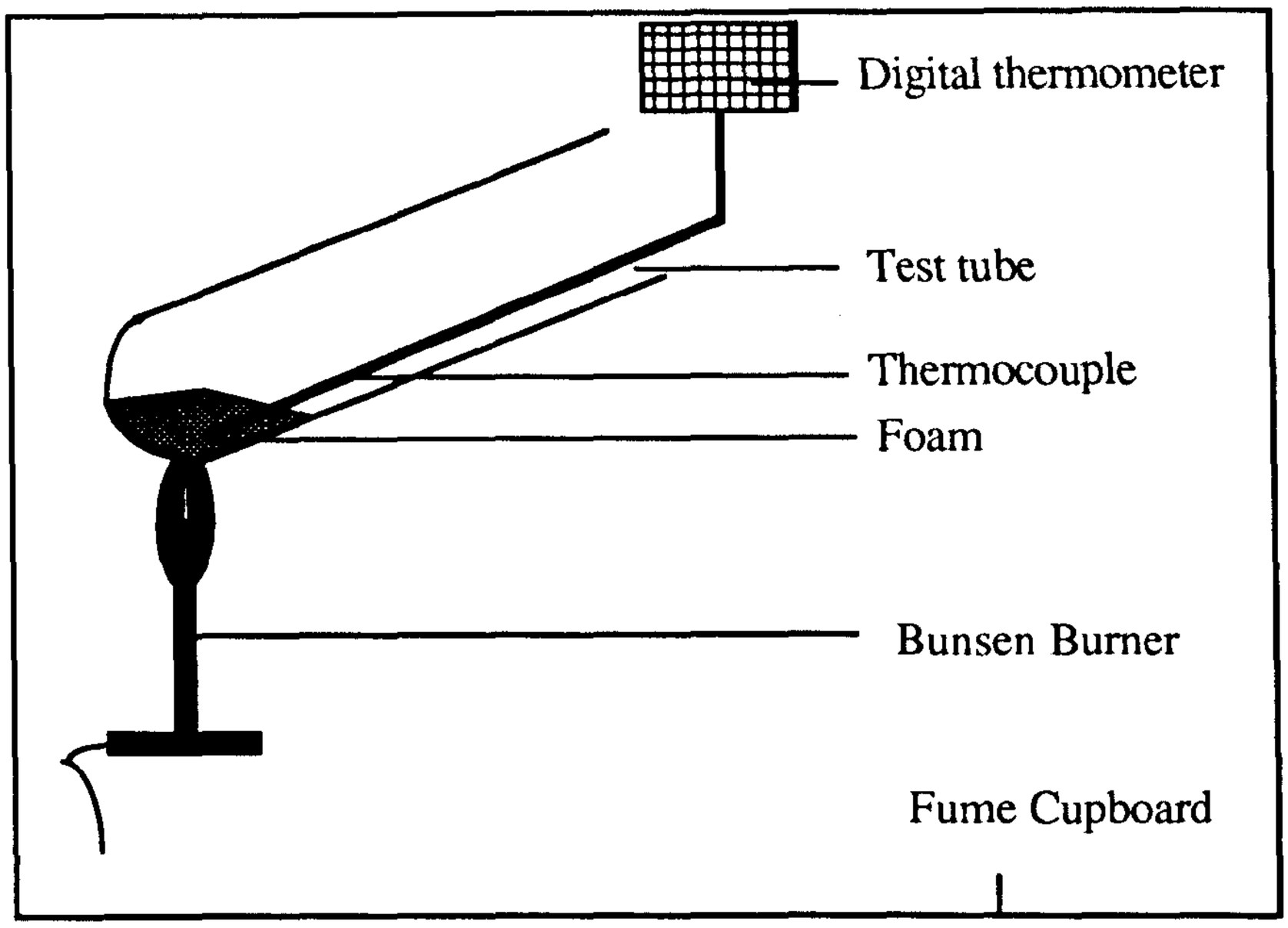

Fig. 3.2 Schematic diagram for examining the heating conditions of the foam specimen.

It was noticed that the softening temperature of PECO is around 180^0C (at this temperature, the cell ribs started to collapse), the liquefied temperature 270^0C, and the decomposed temperature 300^0C. There appears to be no sharp melting temperature for these polymeric foams. Therefore, a suitable oven temperature for this foam may be considered to be 180^0C, which was perhaps why Friis et al. (1988) used 200^0C as the oven temperature for their foam fabrication. As a rough guide to the conversion temperature I suggest that this should be about 5~20^0C lower than the softening temperature in order to maximise stress relaxation and minimise cell rib adhesion.

The different values of softening, liquefaction and decomposition temperatures for different materials are shown in *Table* 3.2.

Type of the foam	Softening Temp. (°C)	Liquefied Temp. (°C)	Decomposed Temp. (°C)	Oven Temp. (°C)
PECC	200 ±5.6	290 ±3.8	320 ±6.7	200
PECO	180 ±5.2	270 ±4.0	300 ±5.8	180
10CO	175 ±7.7	240 ±6.5	270 ±4.2	175
30CO	175 ±5.5	240 ±4.3	270 ±5.1	175
60CO	182 ±7.3	270 ±6.2	295 ±4.8	182

Table 3.2 Investigation of the heating temperature of the foam.

3.2.3 The Heating Time

In addition to the heating temperature the heating time (which determines how

long the foam takes to reach its softening temperature) is another very useful factor which directly affects the fabrication result.

Under static external loading conditions, one of the remarkable influences of sustained exposure to high temperatures is to produce a permanent deformation of the strained foam. At the softening point, the stress of the foam relaxes to zero, therefore, a conventional foam with an outward cell structure can be converted into auxetic foam with an inward cell structure. This is similar in a sense to making a spring from iron wire .

The experiments show that if the heating time is too short, the foam cannot be 'set', with the result that after it comes out of the mould, the foam soon expands to its original size. If, on the other hand, the time at the softening point is too long, the foam will be either melted, so that the cell ribs stick together to form a block of dense material (this was observed with the 60ppi closed-cell polyester urethane foam); or alternatively, the foam may decompose (as in the case of the open-cell polyether urethane foams). In order to maximise the stress relaxation and minimise sticking and structural collapse it is very important to establish the correct heating time for the foam being used.

The time-temperature profiles for fabricating the auxetic foams have been studied. In order to determine the time-temperature profile that is required to produce an auxetic foam we performed the following experiment. Starting with the small one inch (25.4 mm) square tubular section we fitted one thermocouple sandwiched between the mould and the foam, and another thermocouple was inserted into the middle of the specimen (*Figure* 3.3). The time and temperature were measured starting from the moment that the block was exposed to the high temperature and was continued after the block was removed from the oven until the temperature had fallen to well below the foam softening temperature (e.g. 30^0C). Three specimens were tested for each type of foam, the average was taken and shown in *Figures* 3.4, 3.5 3.6, 3.7, 3.8.

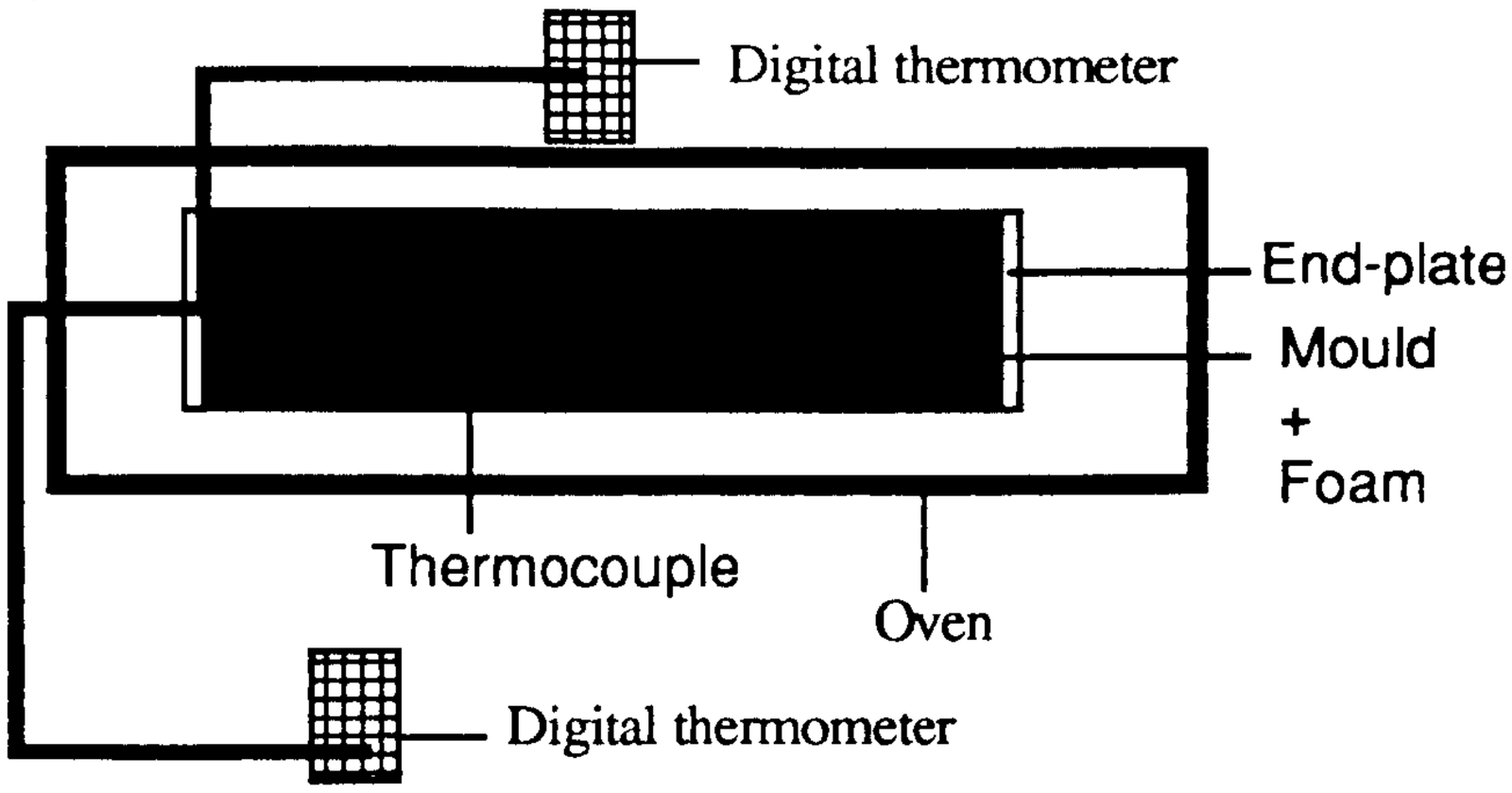

Fig. 3.3 Schematic diagram of recording the time-temperature profile for fabricating a small 1" square sectional rectangular auxetic foam specimen (dimensions: 25.4 x 25.4 x 80 mm).

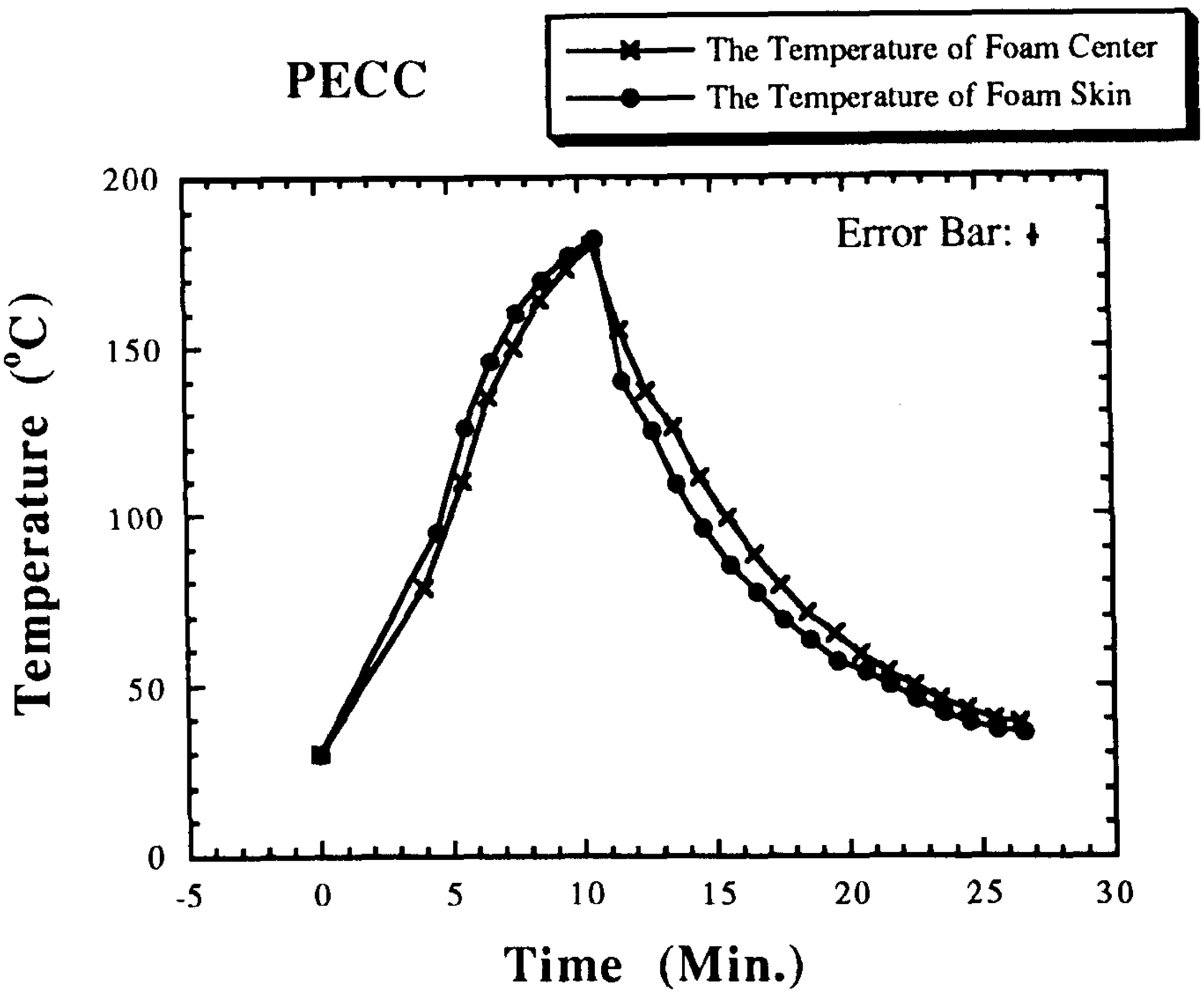

Fig. 3.4 The time-temperature profile for making a 1" square sectional rectangular 60ppi closed-cell polyester urethane auxetic foam (dimensions: 25.4 x 25.4 x 80 mm).

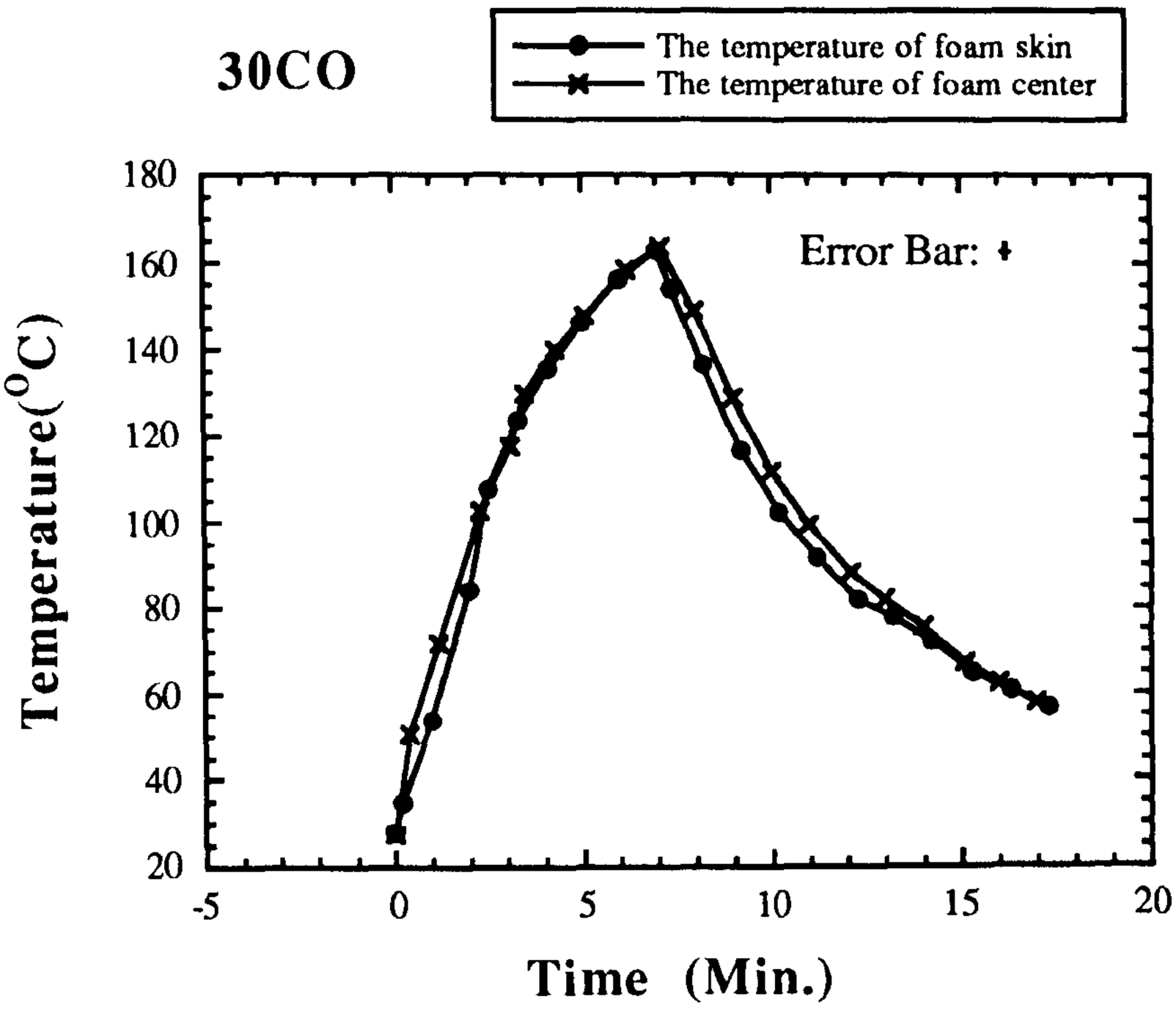

Fig. 3.5 The time-temperature profile for making a 1" square sectional rectangular 30ppi open-cell polyether urethane auxetic foam (dimensions: 25.4 x 25.4 x 80 mm).

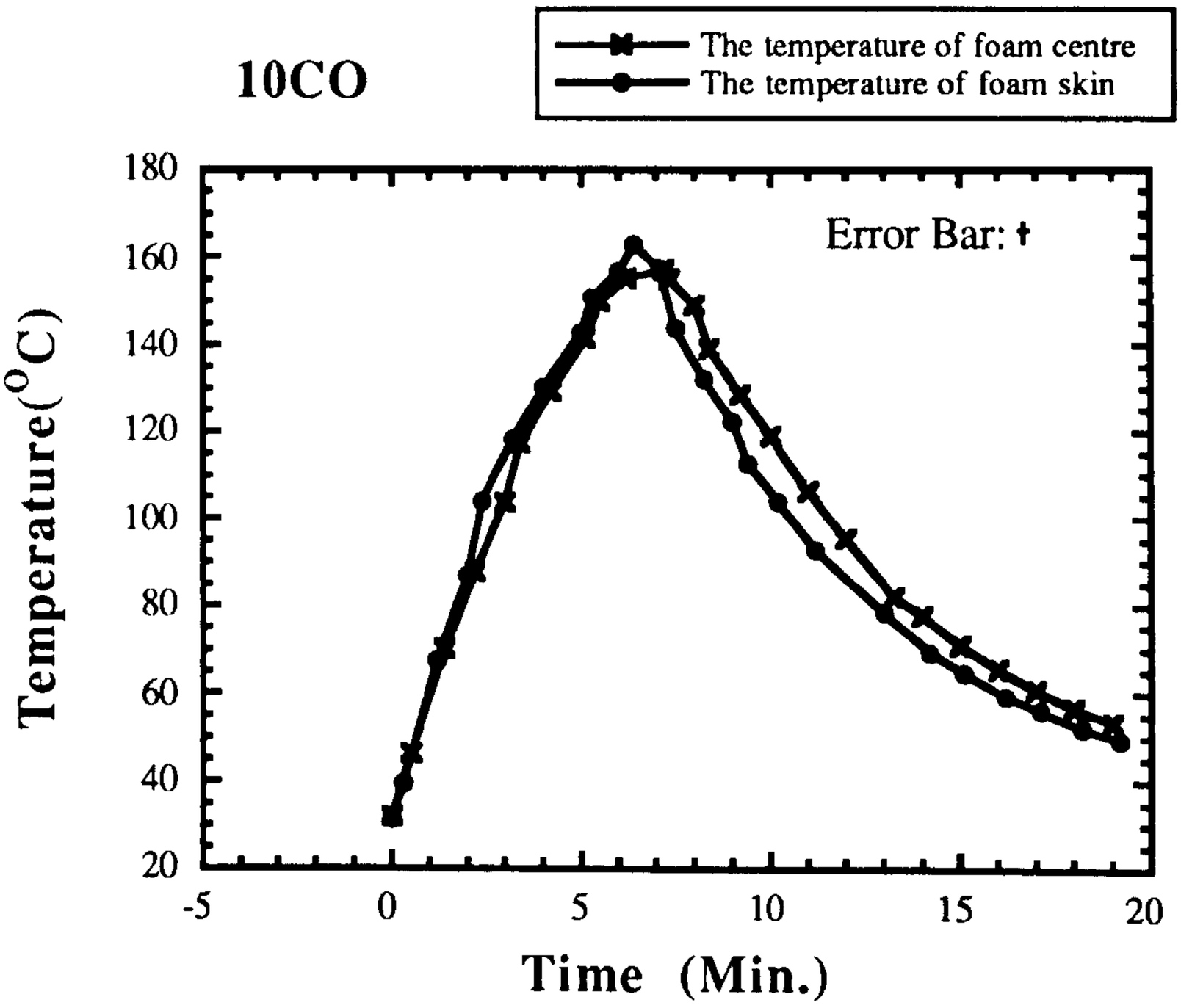

Fig. 3.6 The time-temperature profile for making a 1" square sectional rectangular 10ppi open-cell polyether urethane auxetic foam (dimensions: 25.4 x 25.4 x 80 mm).

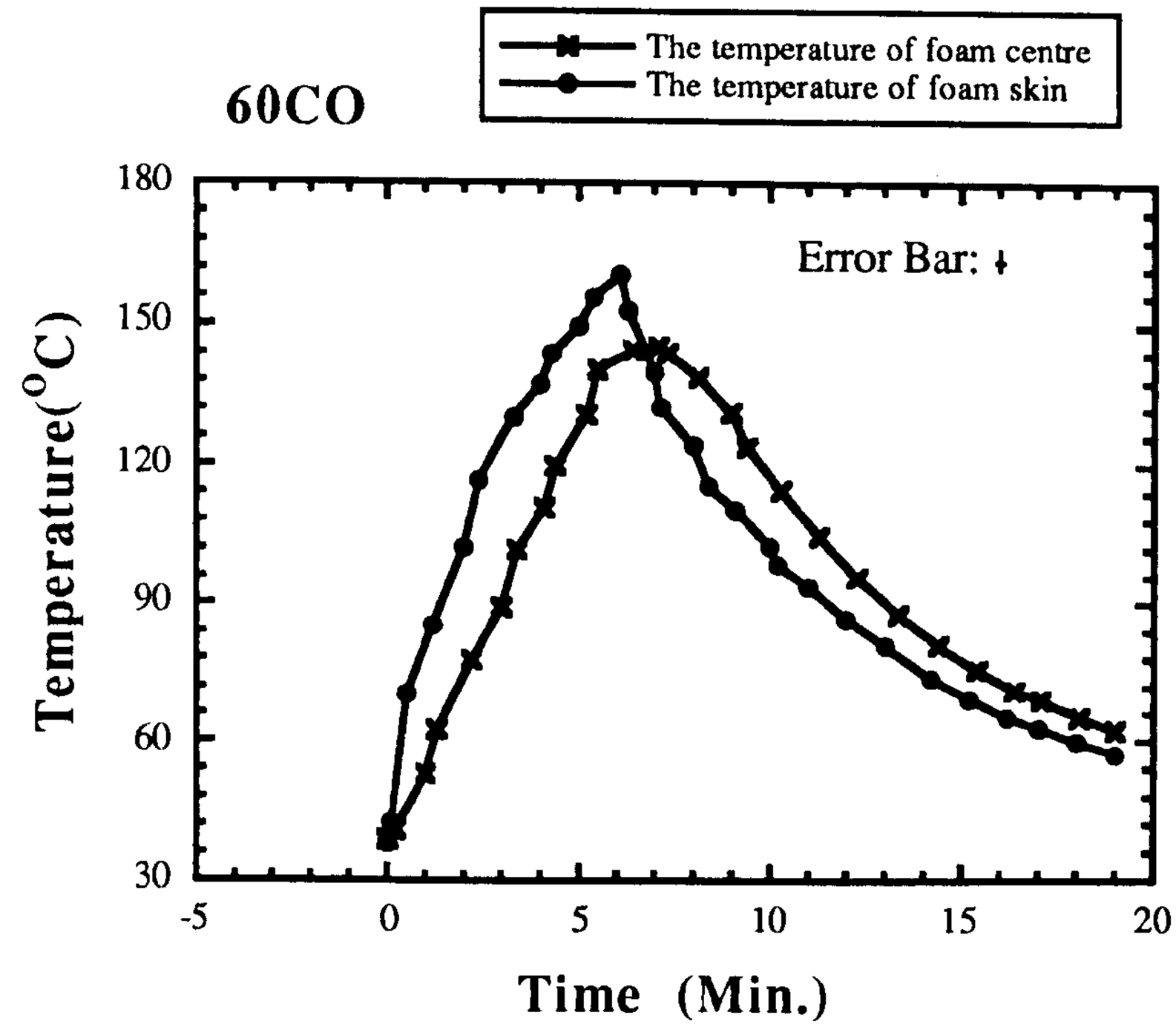

Fig. 3.7 The time-temperature profile for making a 1" square sectional rectangular 60ppi open-cell polyether urethane auxetic foam (dimensions: 25.4 x 25.4 x 80 mm).

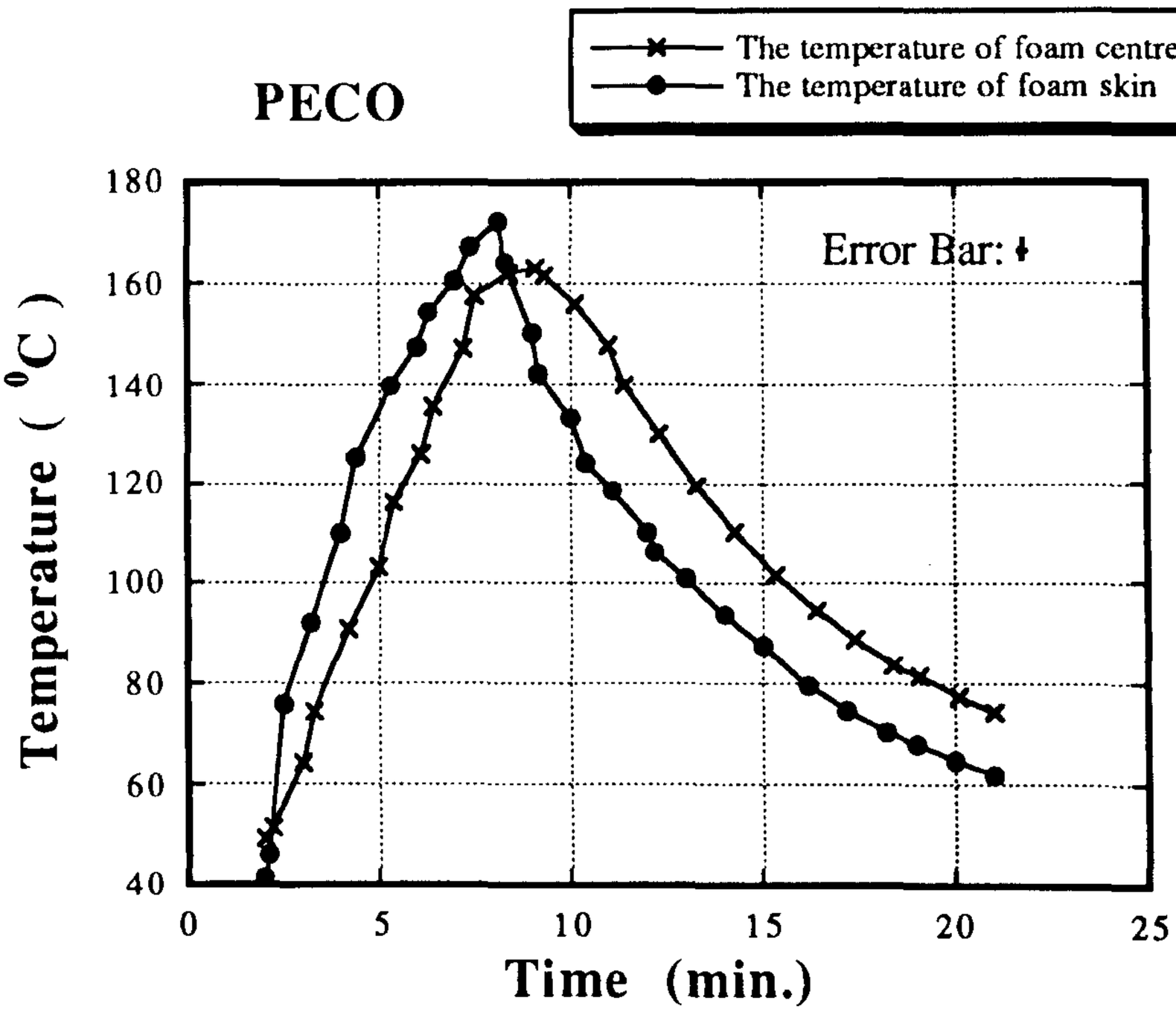

Fig. 3.8 The time-temperature profile for making a 1" square sectional rectangular 60ppi reticulate polyether urethane auxetic foam (dimensions: 25.4 x 25.4 x 80 mm).

During the heating time the specimen was left to 'set' in the oven at a constant oven temperature (i.e. 200^{0}C). It has been found that the heating time required to transform a conventional foam into an auxetic one depends upon the type of foam being used. *Table 3.3* lists the heating time required for a foam to reach its conversion temperature.

Type	Heating Time (minute)	Oven Temp. (^{o}C)	Conversion Temp. (^{o}C)	Starting Size (mm^3)	Finish Size (mm^3)
10CO	6.2 ±0.5	175 ±2	170 ±8	38 × 38 × 110	25.4 × 25.4 × 80
30CO	7.1 ±0.3	175 ±2	168 ±6	38 × 38 × 110	25.4 × 25.4 × 80
60CO	6.0 ±0.3	182 ±2	175 ±8	38 × 38 × 110	25.4 × 25.4 × 80
PECC	11 ±0.2	200 ±2	185 ±6	38 × 38 × 110	25.4 × 25.4 × 80
PECO	8 ±0.4	180 ±2	173 ±8	38 × 38 × 110	25.4 × 25.4 × 80

Table 3.3 The typical time-temperature combinations for making small auxetic foam with a volumetric compression ratio of 3.1. Note: the average error on the sample dimension is ±1 mm.

3.2.4 Volumetric Compression Ratio

From a theoretical point of view, changing the compression ratio of foams enables us to fabricate auxetic foams with a range of negative Poisson's ratios. This is because this determines the proportion of the cells that will become re-entrant. The foams exhibit a characteristic distribution of cell sizes so that the maximum effective volumetric compression ratios of the foams are not the same.

An investigation was carried out to determine the deformation characteristics of the foams, using compression in different directions. The conventional foam was first cut to the dimensions: $L_x \times L_y \times L_z$ (e.g. 50mm × 50mm × 50mm), using a band saw with a knife blade. During the cutting, particular attention was made to ensure that all surfaces were flat. Then, using an Instron 4505 testing machine, the sample was tested at a cross-head speed of 2 mm min^{-1} to attain the compression deformation. The values for load and displacement were taken directly from the load cell and cross-head movement respectively, and were recorded on the Instron chart recorder. With the trace from the chart recorder the compression modulus, the elastic collapse load and the elastic densification displacement could be determined. Tests were carried out in each of the three dimensions of the conventional foam specimens, to determine the point of maximum densification, without significant cell concact, δ, in *Figure* 3.11.

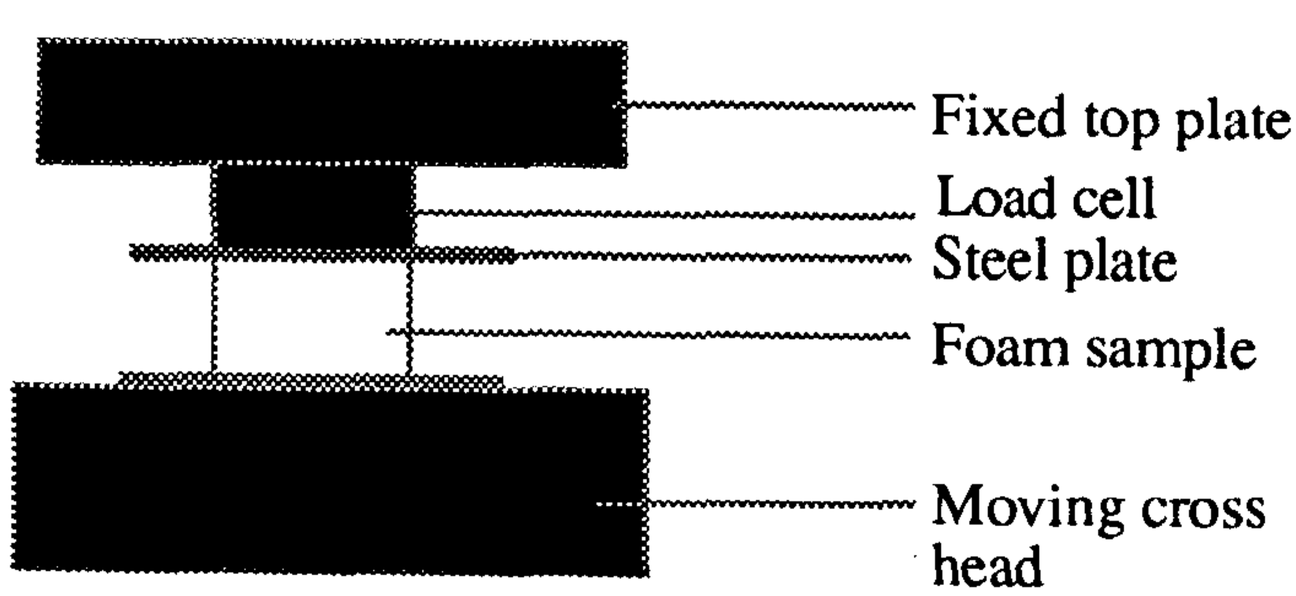

Fig. 3.9 Schematic diagram for compression testing the foam.

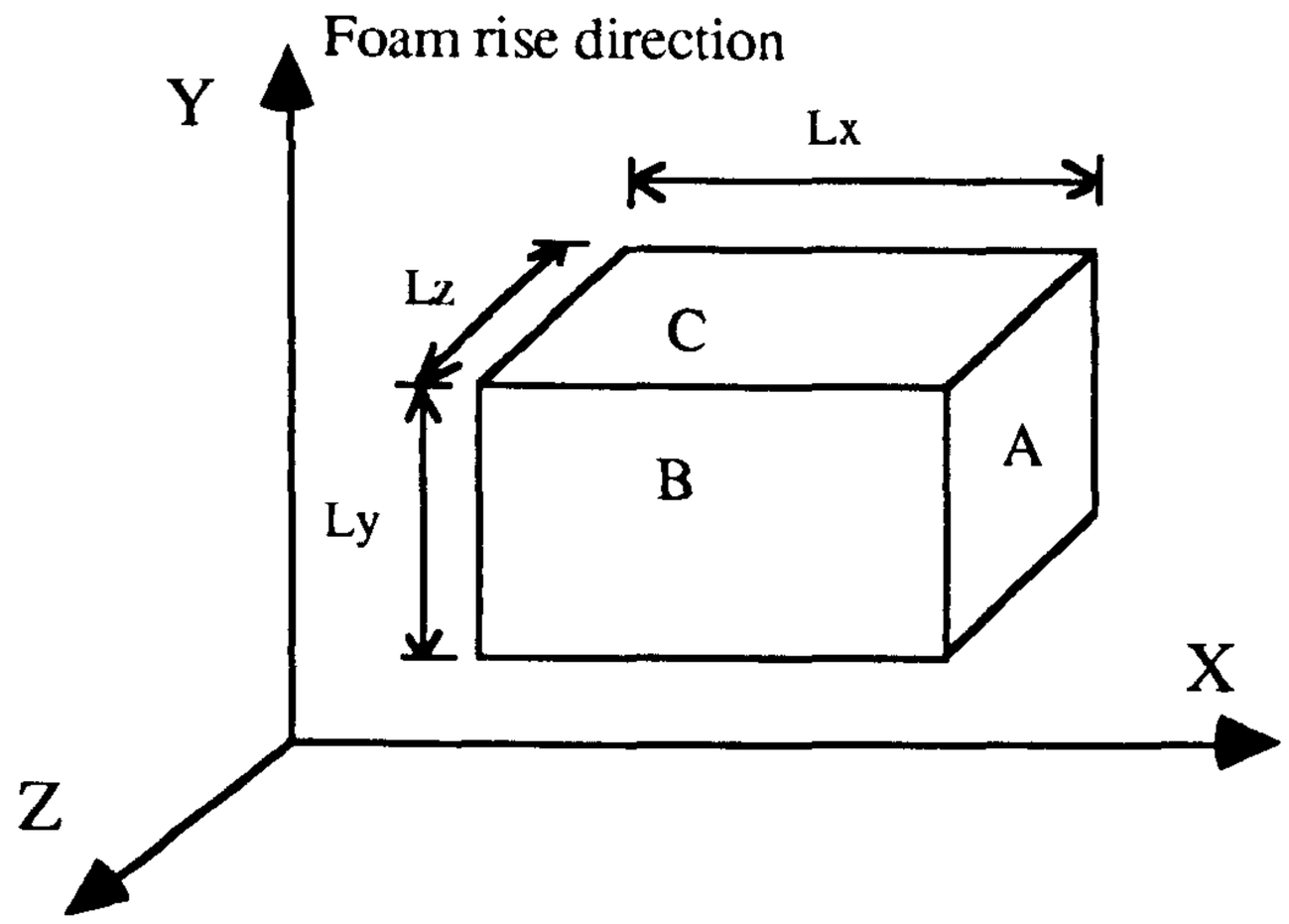

Fig. 3.10 Schematic diagram of the three dimensional conventional foam block.

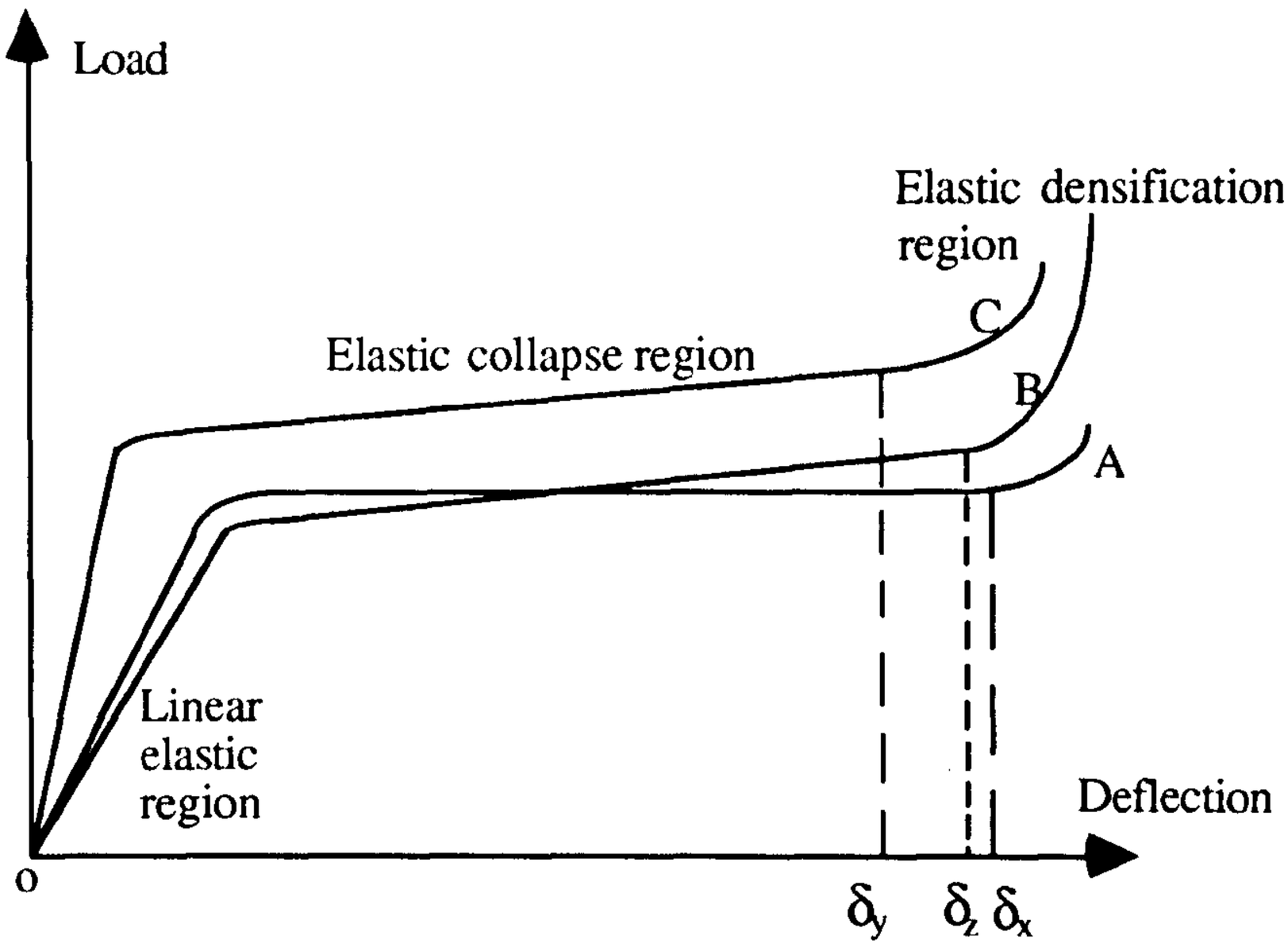

Fig. 3.11 A schematic of the load-deflection curve of the three dimensional conventional foam. (A) Compress along the x-direction. (B) Compress along the z-direction. (C) Compress along the y-direction.

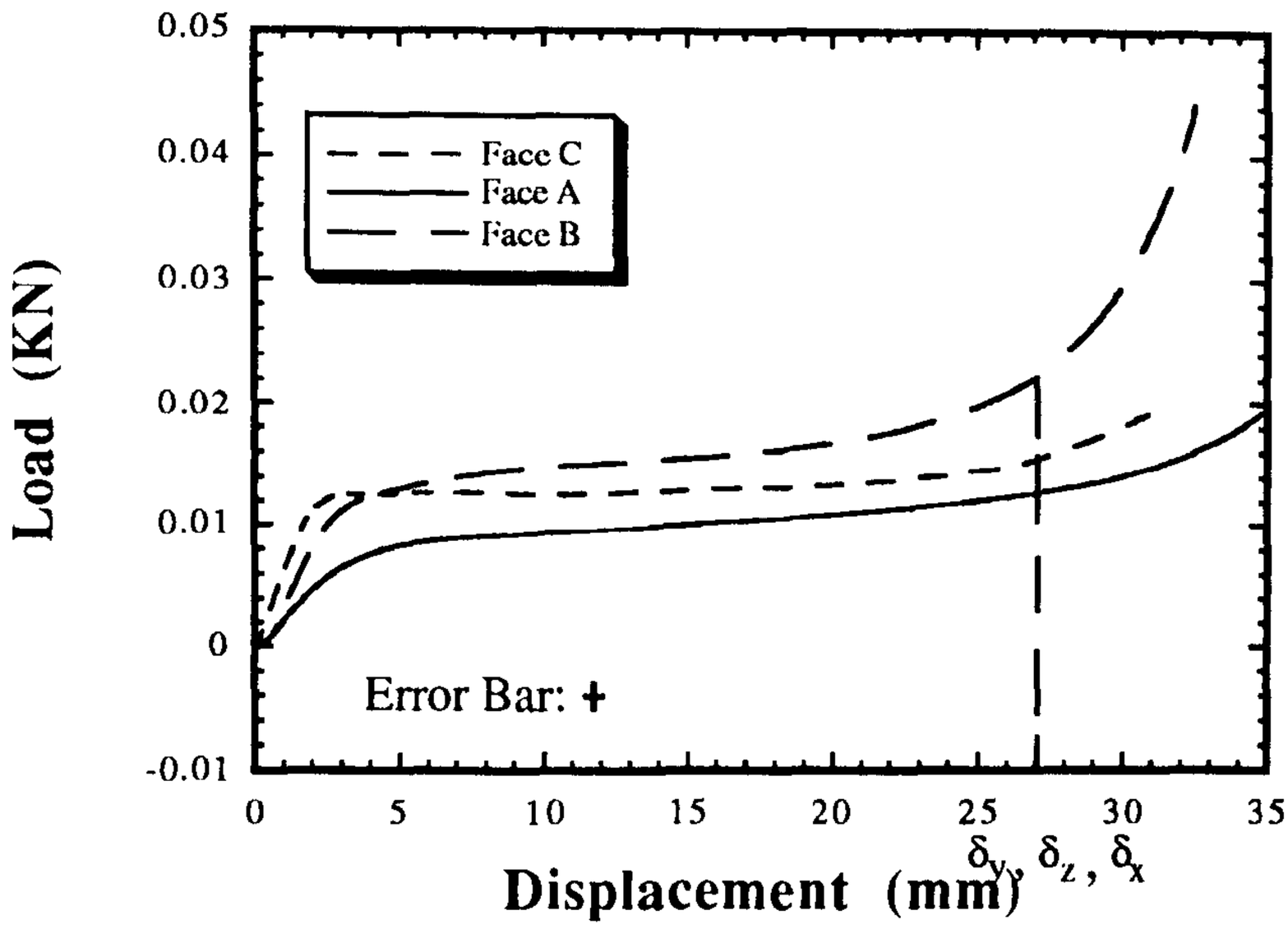

Fig. 3.12 Compressive Load-Displacement curves in two orthogonal directions in the planes normal to the rise direction (Face A and Face B) and in the rise direction (Face C) for the 60ppi closed cell polyester urethane foam (PECC).

10ppi Open-Cell Polyether Urethane Foam

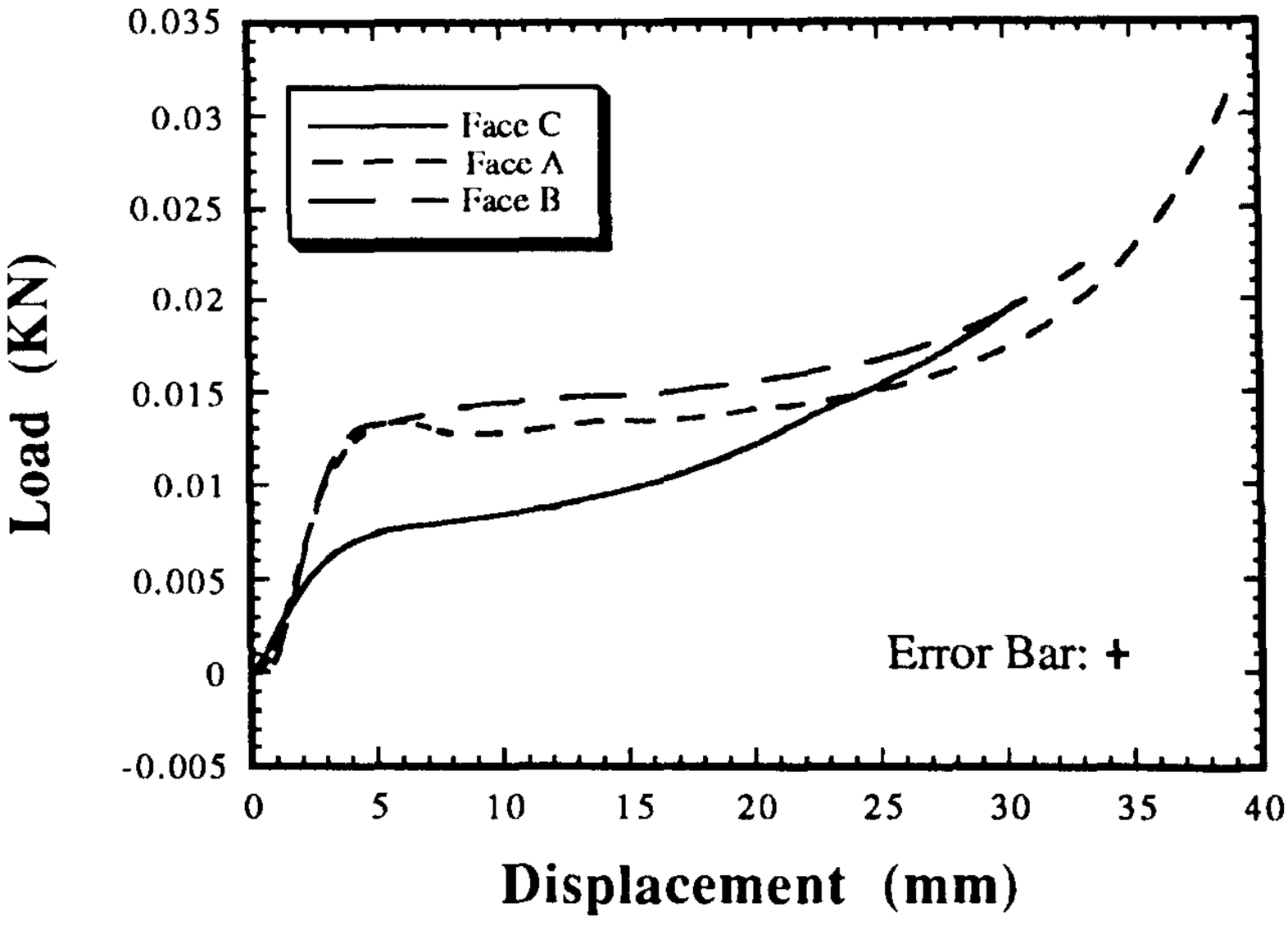

Fig. 3.13 Compressive Load-Displacement curves in two orthogonal directions in the planes normal to the rise direction (Face A and Face B) and in the rise direction (Face C) for the 10ppi open-cell polyether urethane foam (10CO).

30ppi Open-Cell Polyether Urethane Foam

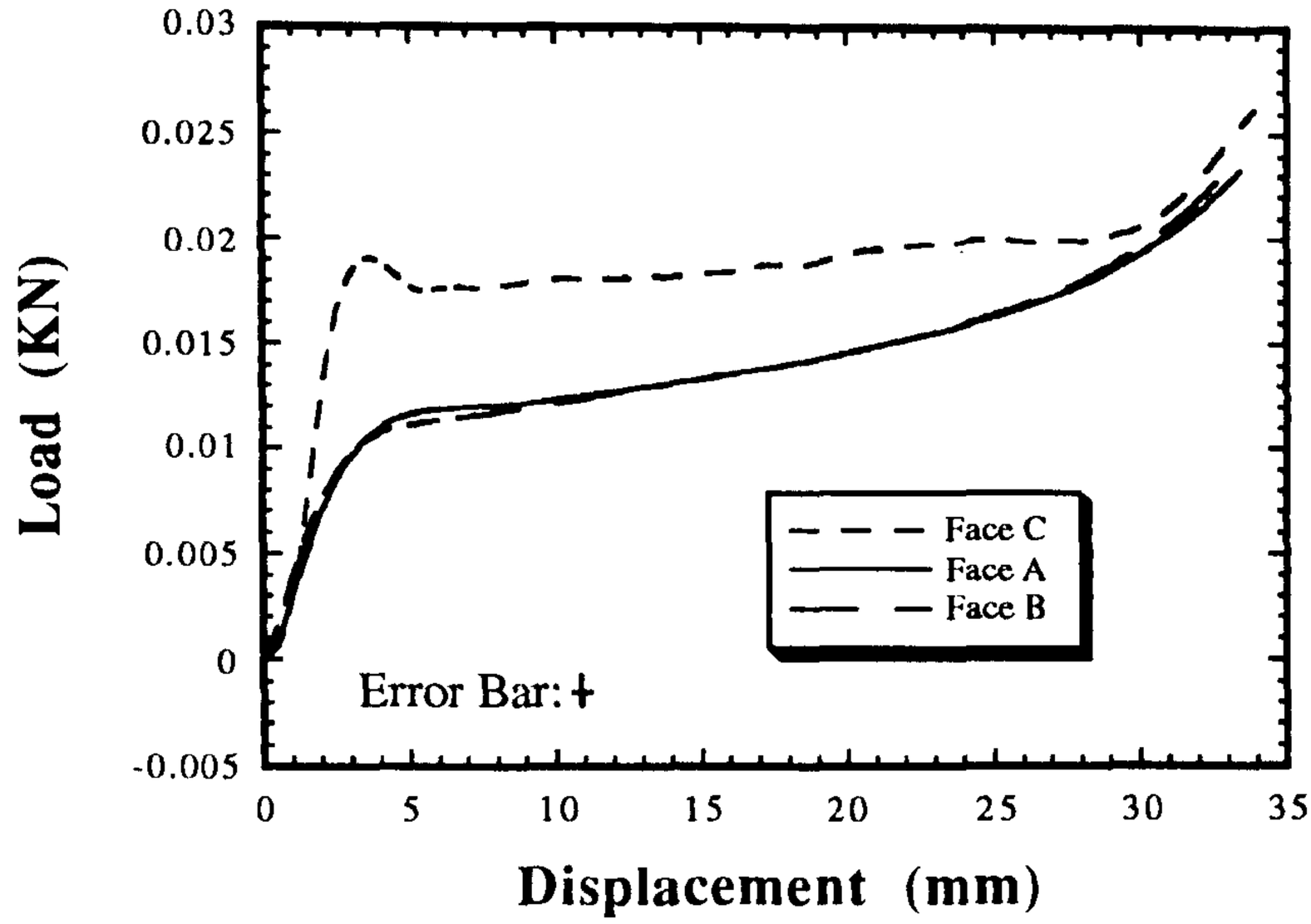

Fig. 3.14 Compressive Load-Displacement curves in two orthogonal directions in the planes normal to the rise direction (Face A and Face B) and in the rise direction (Face C) for the 30ppi open-cell polyether urethane foam (30CO).

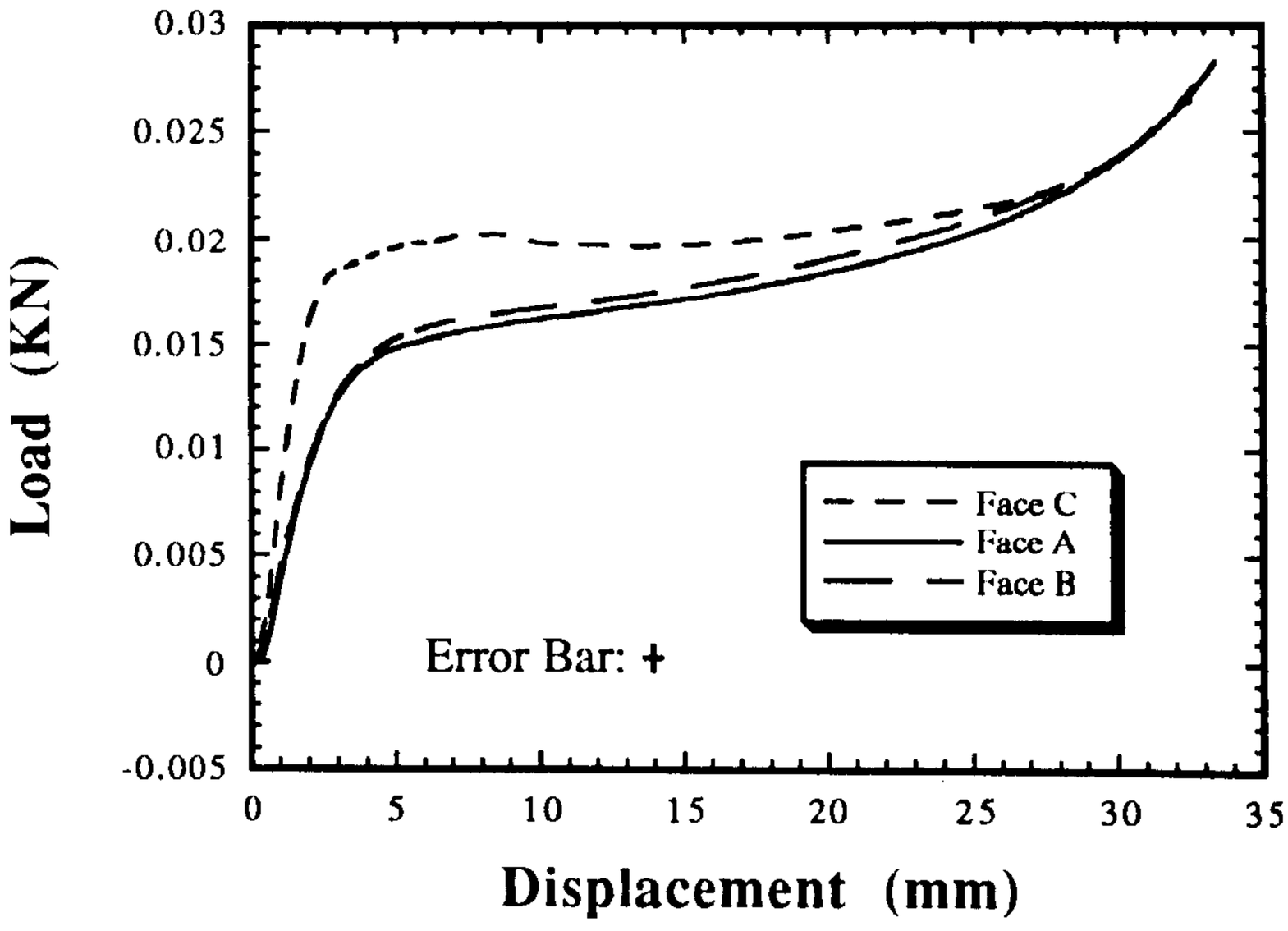

Fig. 3.15 Compressive Load-Displacement curves in two orthogonal directions in the planes normal to the rise direction (Face A and Face B) and in the rise direction (Face C) for the 60ppi open-cell polyether urethane foam (60CO).

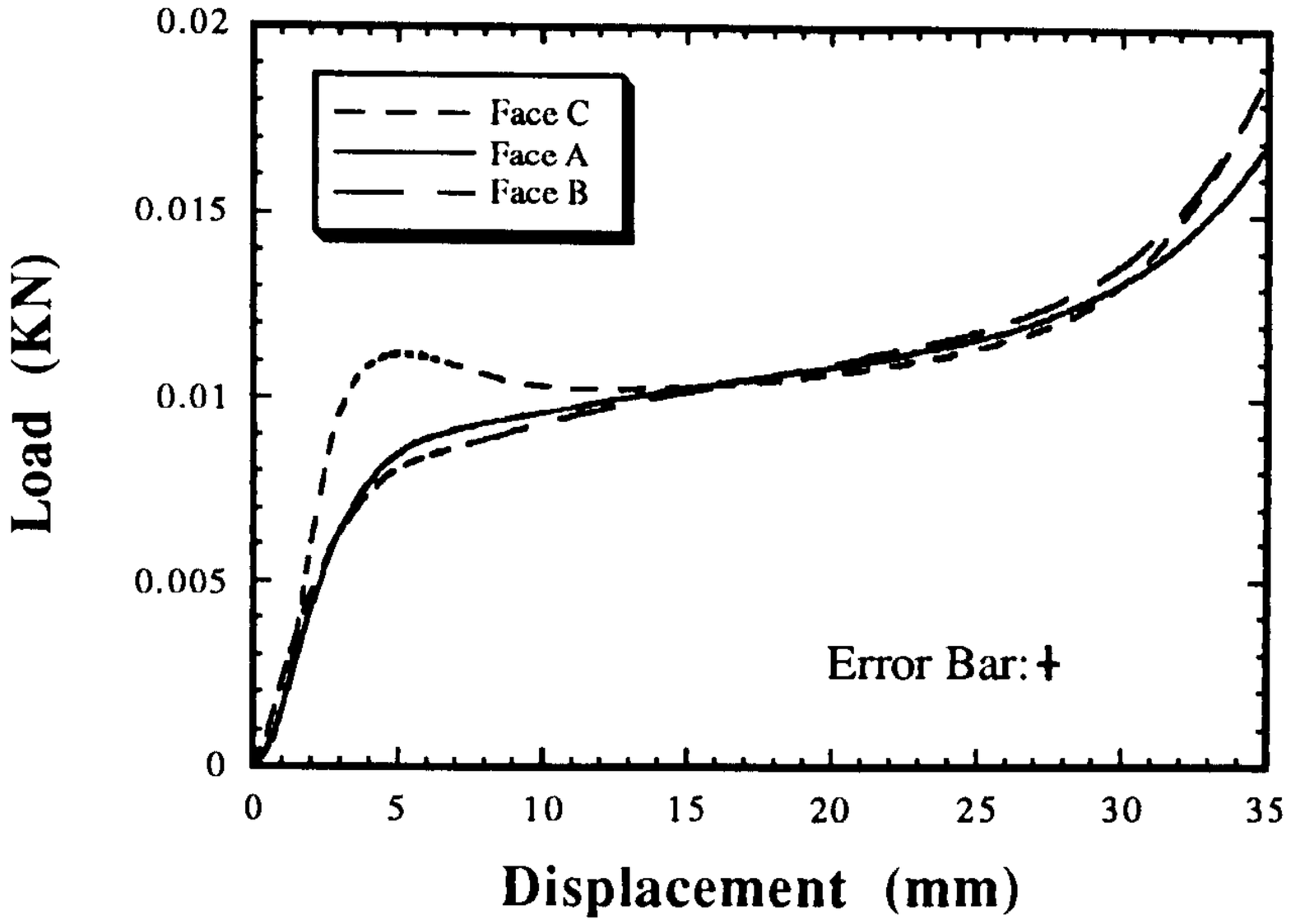

Fig. 3.16 Compressive Load-Displacement curves in two orthogonal directions in the planes normal to the rise direction (Face A and Face B) and in the rise direction (Face C) for the 60ppi reticulated polyester urethane foam (PECO).

The original volume for the conventional foam specimen is:

$$V_o = L_x \times L_y \times L_z$$

when the foam reaches the elastic densification region, the minimum volume of the compressed foam becomes:

$$V_1 = (L_x - \delta_x) \times (L_y - \delta_y) \times (L_z - \delta_z)$$

Where: δ_y, is the maximum compression displacement of the foam rise direction and δ_x and δ_z, are the maximum displacements of the other two directions. The maximum auxetic effect is expected when all the cell ribs have buckled and this occurs at the elastic densification displacement. Therefore, the maximum effective volumetric compression ratio is given by:

$$R_C = V_o / V_1$$

Experiments have shown (see *Figures* 3.12 to 3.16) that different types of foam have various maximum volumetric reductions which are due to their differing mechanical performance. The results are listed in the *Table 3.4*.

Type	V_0 (mm^3)	δ_x (mm)	δ_y (mm)	δ_z (mm)	V_1 (mm^3)	R_c
10CO	52 × 52 × 51	25	25	25	27 × 27 × 26	7.276
30CO	50 × 51 × 51	30	30	30	20 × 21 × 21	14.75
60CO	50 × 51 × 50	29	29	29	21 × 22 × 21	13.4
PECC	49 × 50 × 42	27	27	27	22 × 23 × 15	13.55
PECO	50 × 51 × 51	28	28	28	22 × 23 × 23	11.17

Table 3.4 The theoretical maximum volumetric compression ratio of various types of foam. Note: the average error on sample dimension is ±1 mm.

Note: (1) the experiments described above have been conducted under conditions of uniaxial loading, whilst the fabrication method involves triaxial loading. As a result of this, the volumetric compression ratios found in the experimental work are smaller than that of the maximum values expected. (2) From a practical point of view, we need to give considerations to the visco-elastic behaviour of polymeric foams especially at high temperatures.

Further study in this area has led to another finding. By compressing different size starting blocks in the same mould followed by heating, cooling and relaxation of the foams, a range of auxetic foams can be made with a variety of Poisson's ratios. The results obtained on the 60ppi blue polyether urethane foams are shown in *Table* 3.5 and show how the Poisson's ratio varies with the compression ratio.

	Starting Size (mm^3)	Finish Size (mm^3)	Volumetric Compression Ratio	Tensile Poisson's Ratio, υ_{yx}
PEAO-1	38 × 38 × 100	25.4 × 25.4 × 70	3.2	-0.78 ± 0.13
PEAO-2	33 × 33 × 100	25.4 × 25.4 × 70	2.4	-0.57 ± 0.10
PEAO-3	30 × 30 × 100	25.4 × 25.4 × 70	2.0	-0.34 ± 0.04
PEAO-4	38 × 38 × 120	25.4 × 25.4 × 70	3.8	-0.82 ± 0.03
PEAO-5	25.4 × 25.4 × 100	25.4 × 25.4 × 70	1.4	+0.1 ± 0.03

Table 3.5 Various compression ratios of the 60ppi reticulated polyester urethane foams (PECO).
Note: the average error on sample dimension is ±1 mm.

3.3 Fabricating Large Auxetic Foam Blocks.

In order to fabricate larger specimens, it was necessary to develop a new fabrication process. Clearly, the force now required to compress such a large block of foam (dimensions: 300 × 300 × 100 mm) needs to be increased. For this reason, the mould has to be strong enough to withstand this extra force. *Figure* 3.17 shows the arrangement. Although the low moduli of the foams allows the use of a mould to achieve our purpose, it does however present another problem i.e. the creasing effect. This creasing effect is due to the increased surface area of the larger block. By inspection, it is clear that the large volume reduction indicated will require large compression of the sides. Clearly, to expect to achieve this in one step without creasing the surface is unrealistic. The surface creasing is due to the non-uniform local collapse of the foam. In order to overcome this problem, a multi-stage process method was developed, featuring a substantially smaller compression ratio for each stage, thus minimising the risk of creasing. One stage of this approach is illustrated in *Figure* 3.18.

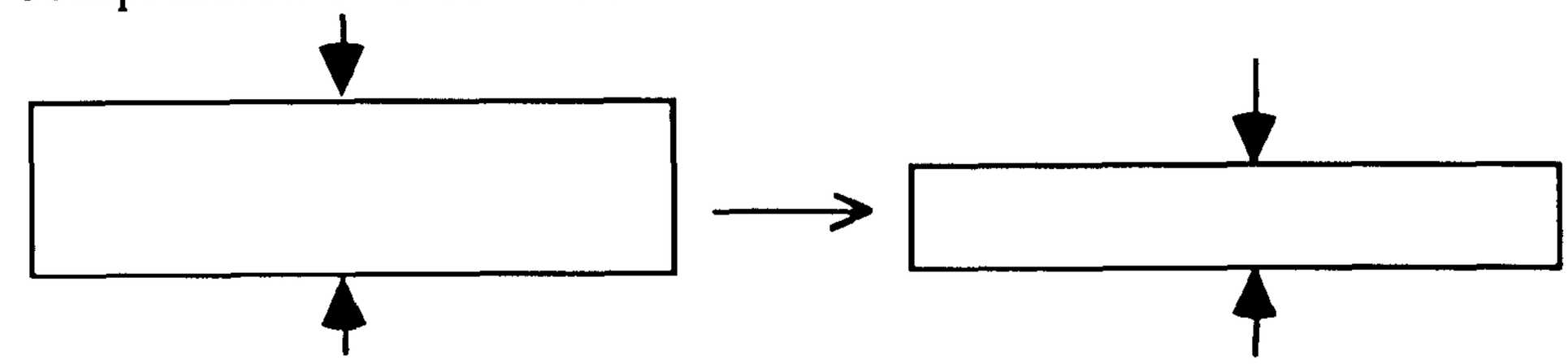

Fig. 3.17 Schematic diagram of the arrangement for fabricating a large auxetic foam block.

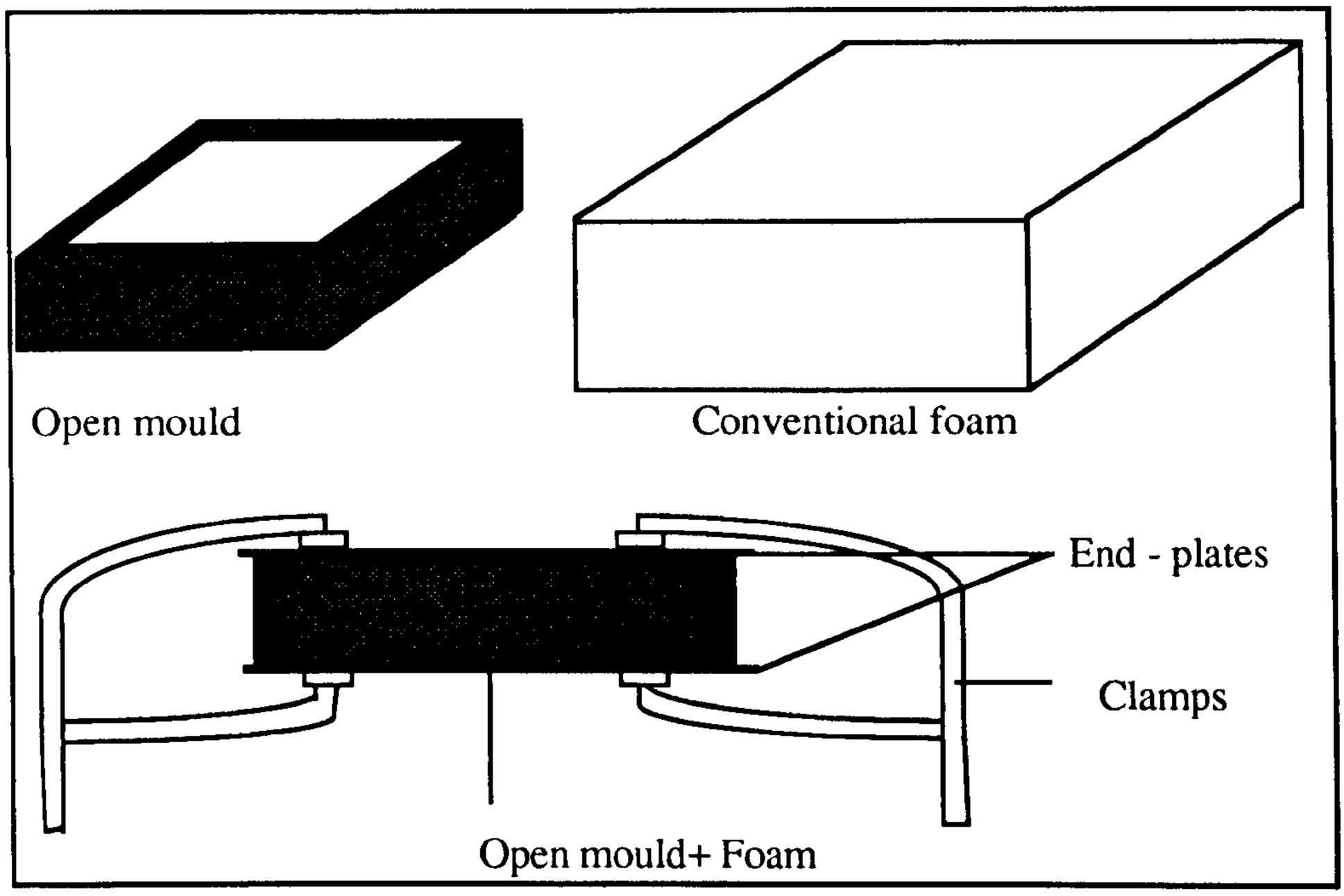

Fig. 3.18 Schematic diagram for processing the large auxetic foam block.

We can achieve the desired compression by carrying out the procedure in four stages. For example, if we consider the conventional foam to have the initial dimensions of: 300 × 300 × 76 mm. Then the four stages involved in the reduction would be to first reduce its dimensions to 275 × 275 × 69.5 mm, then 250 × 250 × 63 mm, followed by 225 × 225 × 56.5 mm and then finally, 200 × 200 × 50 mm. This will achieve a total compression ratio of 3.4. The open-ended mould was made by screwing four 5mm thick polished stainless steel plates together. The four stages require four different sized moulds for which the inner dimensions were as given above. Prior to use the inner walls of the mould were lubricated with WD 40, so that the foam can be slid into position despite the restraining effect of the pressure-induced friction. The top and bottom pressure plates were also made of 5mm thick polished stainless steel, and were lubricated with WD 40.

The first step in using the moulds involved squeezing the 300 × 300 × 76 mm block into place in the 275 × 275 × 69.5 mm mould by hand. The top plate was carefully manipulated into position to achieve a uniform distribution of cell pressure, to avoid surface creasing in the mould, and then it was clamped down. The whole assembly was then placed into the lab oven at 200^0C.

From the moment the foam was put into the preheated oven the time and temperature of the skin and the middle of the foam specimen, were recorded (see *Figure* 3.19). From these measurements a plot of the time-temperature profile (*Figure* 3.20) was produced. At the end of the heating time the specimen and mould

assembly were removed from the oven and were cooled at room temperature for 2 hours. Finally, the foam with a volume of 275 × 275 × 69.5 mm was taken out of the mould, and gently stretched by hand in each of the three orthogonal directions to relax the cell ribs. The temperatures used here to establish the heating time, compared with the temperatures used to convert the small specimens, are lower, because the heating time of the larger moulds is much longer than that for the single stage method.

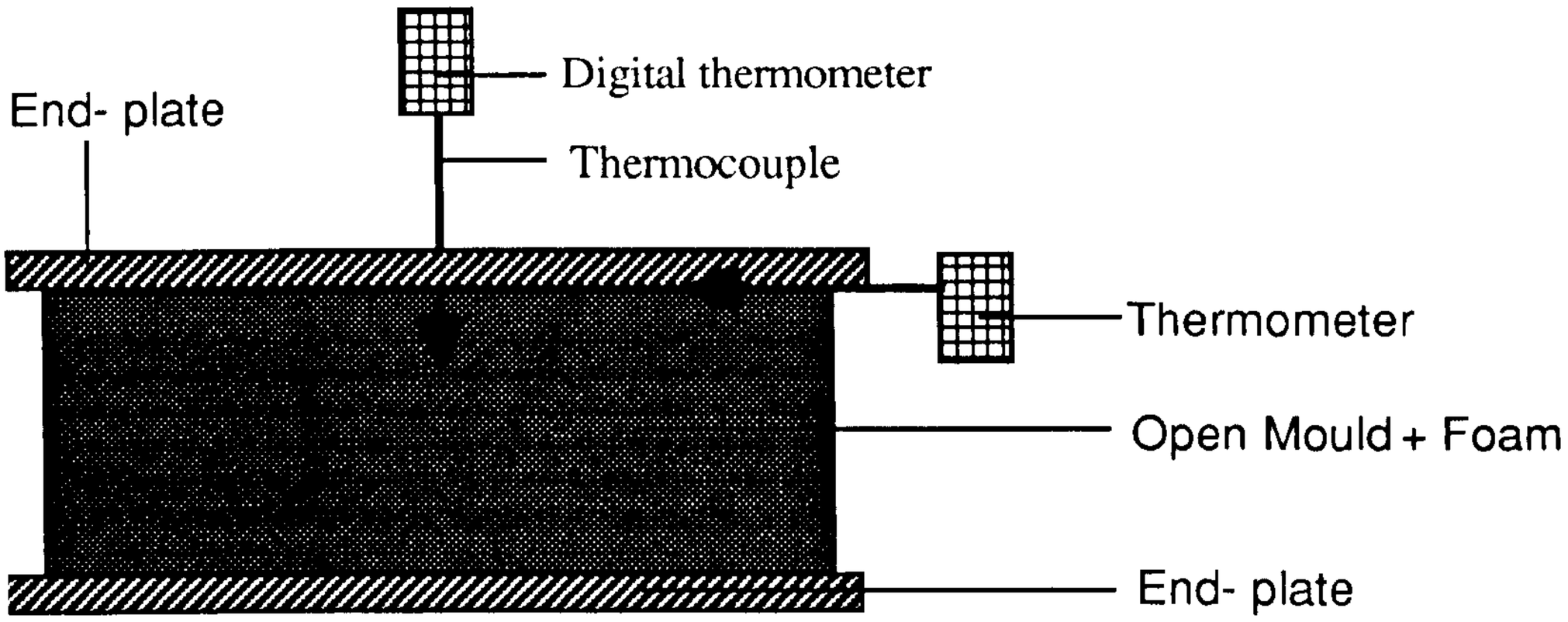

Fig. 3.19 Schematic diagram of examining the time-temperature profile for fabricating the large auxetic foam block.

A new time-temperature profile has to be recorded at each of the four compression stages. This is because the density of the foam is changing at each stage and therefore the time taken to reach the conversion temperature will also be changing.

The 10ppi Open-Cell Polyether Urethane Foam

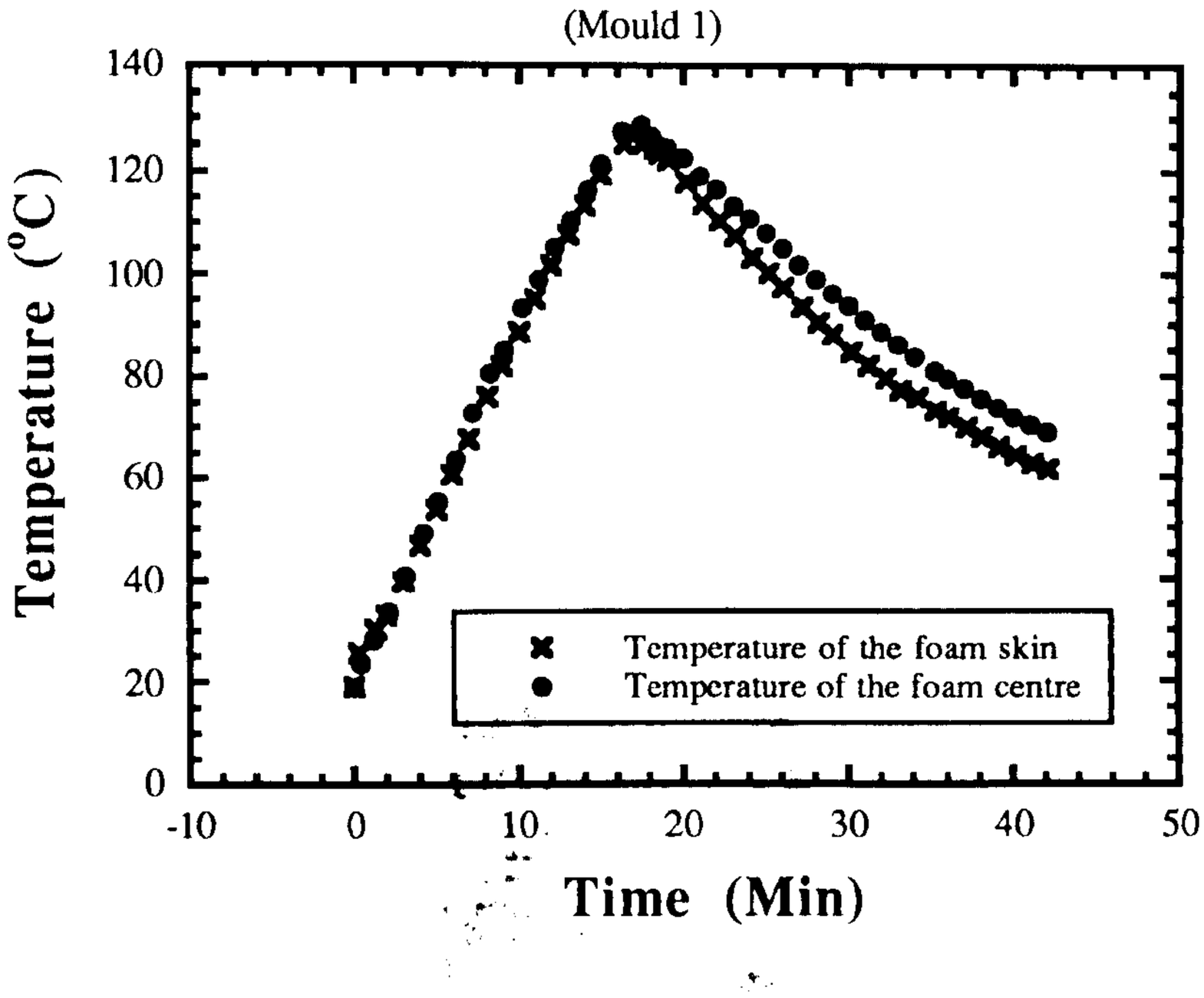

Fig. 3.20(a) The Time-Temperature profile of the 10ppi open-cell polyether urethane foam heated in the mould 1. Note: The average error of the temperature measurements is $\pm 1.2^0$C.

The 10ppi Open-Cell Polyether Urethane Foam

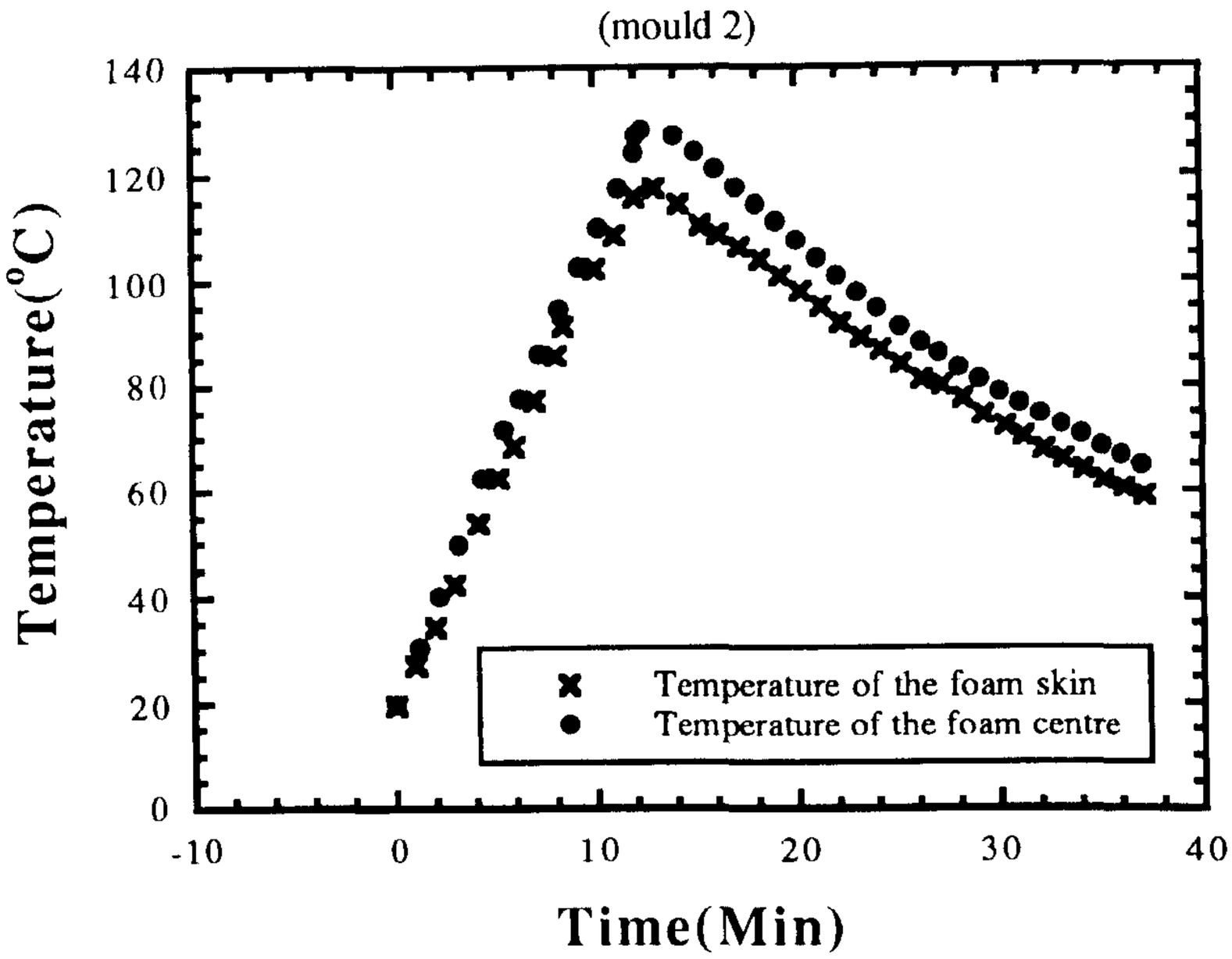

Fig. 3.20(b) The Time-Temperature profile of the 10ppi open-cell polyether urethane foam heated in the mould 2. Note: The average error of the temperature measurements is $\pm 1.5^{0}$C.

The 10ppi Open-Cell Polyether Urethane Foam

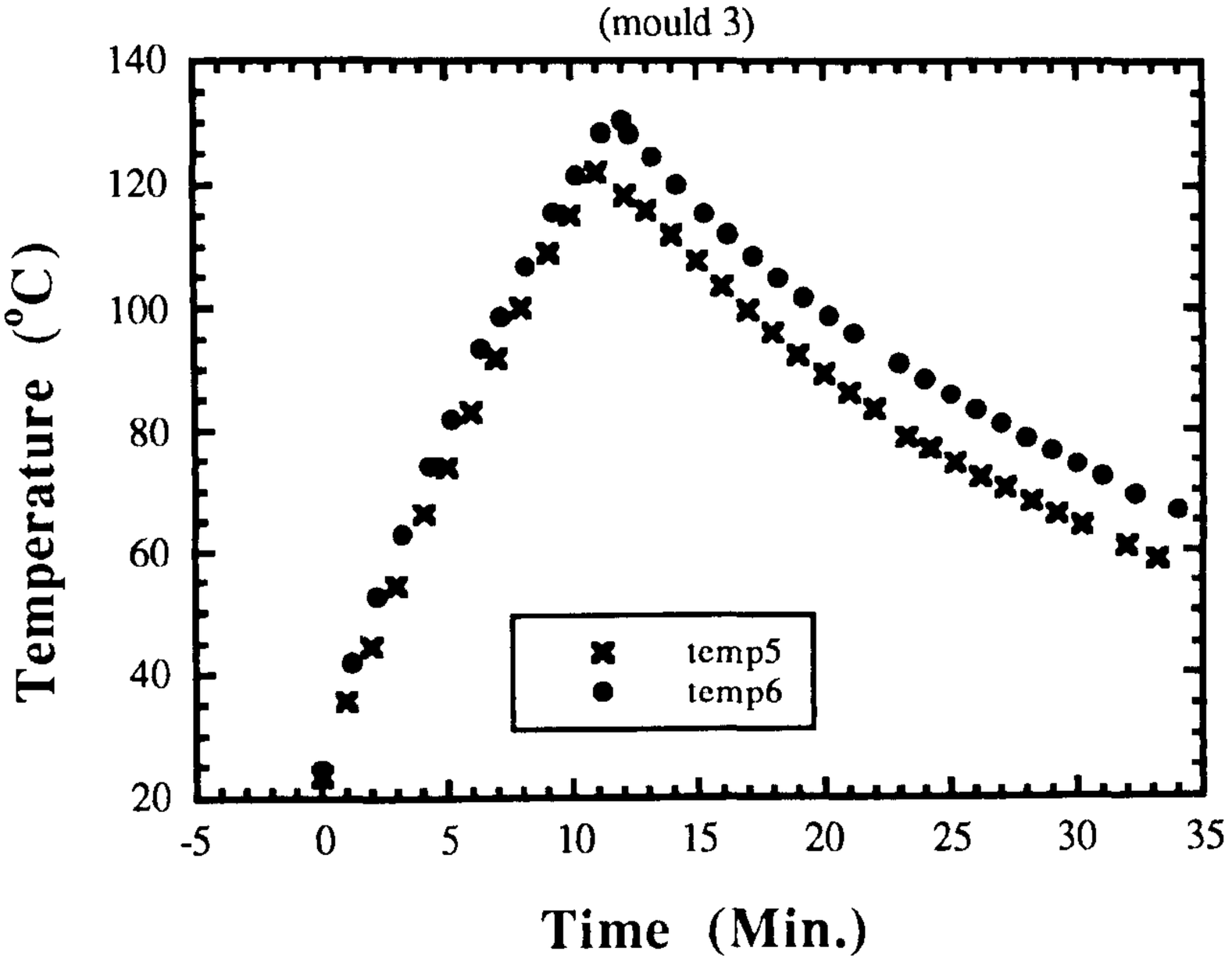

Fig. 3.20(c) The Time-Temperature profile of the 10ppi open-cell polyether urethane foam heated in the mould 3. Note: The average error of the temperature measurements is $\pm 2.1^{0}$C.

The 10ppi Open-Cell Polyether Urethane Foam

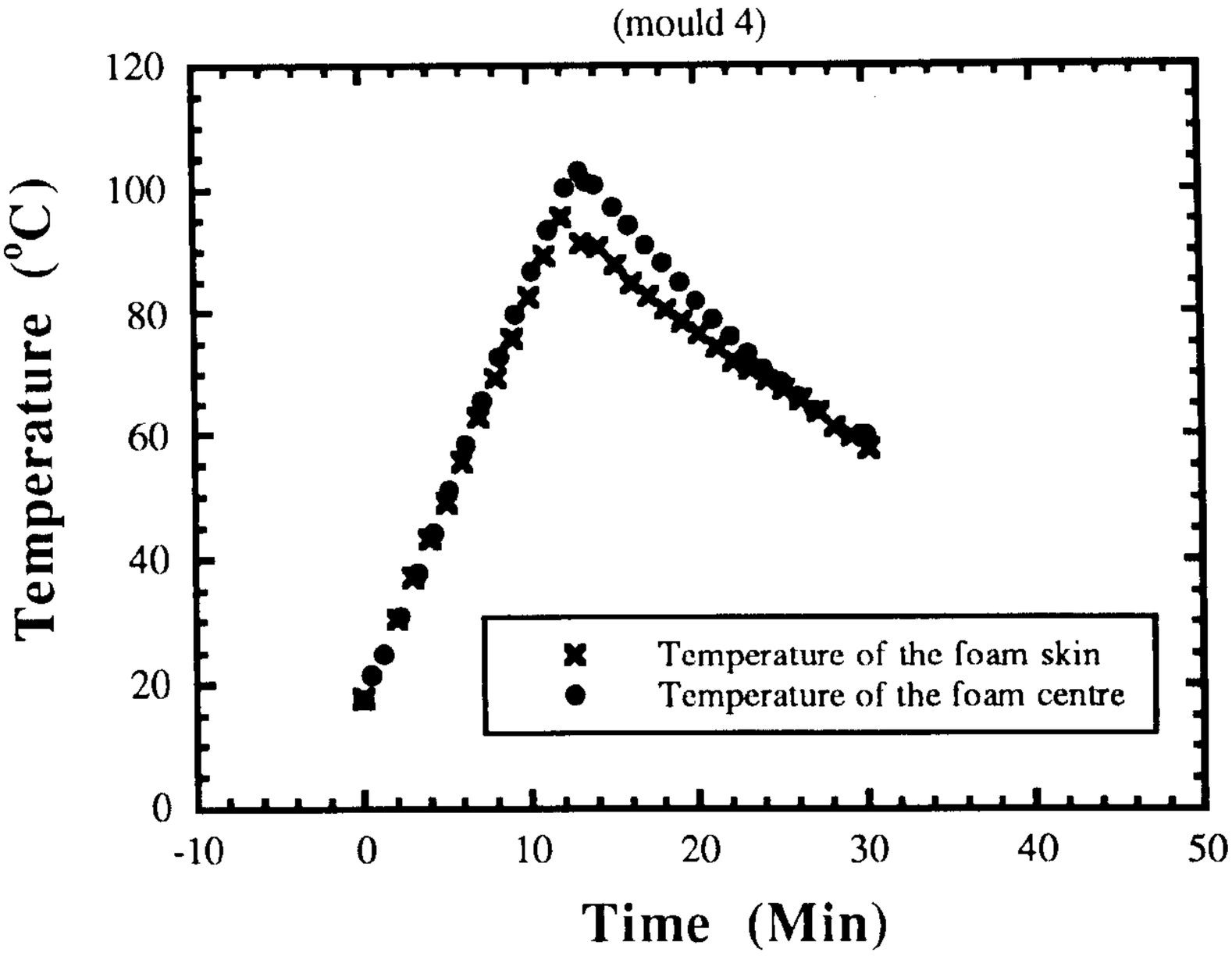

Fig. 3.20(d) The Time-Temperature profile of the 10ppi open-cell polyether urethane foam heated in the mould 4. Note: The average error of the temperature measurements is $\pm 1.7^{0}$C.

Similar curves were obtained for all the open-celled polyether urethane foams. The results are shown in Table 3.6.

The block started to cool as soon as it was removed from the oven. After allowing the specimen to cool to the room temperature, the assembly was dismantled. It was found that the final block had 'set' at the reduced dimensions defined by the final mould (200 × 200 × 50 mm). By the same fabrication method, the 60ppi closed-cell polyester urethane foam block (*Figure 3.21*), was converted.

Type of foam	Heating time of mould 1 (minute)	Heating time of mould 2 (minute)	Heating time of mould 3 (minute)	Heating time of mould 4 (minute)	Total heating time (min.)
10CO	17.1±0.35	12±0.27	12±0.21	11.8±0.33	52.9±1.16
30CO	16.8±0.23	15±0.32	14.1±0.28	13±0.25	58.9±1.08
60CO	20.8±0.34	18.2±0.24	16.3±0.19	15.5±0.21	70.8±0.98

Table 3.6 The heating time for fabricating the 10, 30, and 60ppi open-celled polyether urethane foam blocks. (Starting conventional foam dimensions: 300 × 300 × 76mm. Finished auxetic foam dimensions: 200 × 200 × 50mm). Note: The average error on sample dimension is ±1 mm.

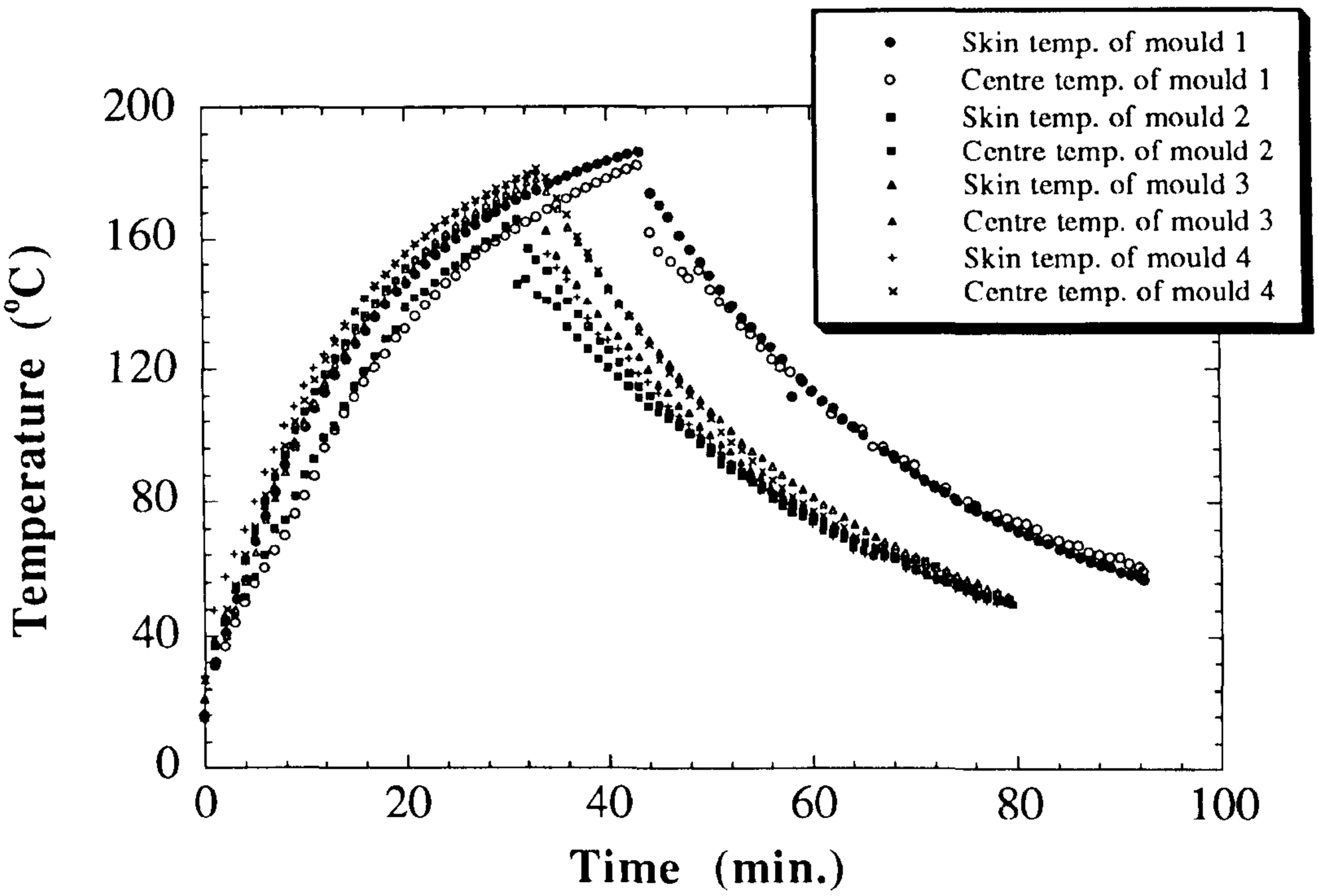

Fig. 3.21 The Time-Temperature profiles for fabricating the large 60ppi polyester urethane auxetic foam block. Note: The average error of the temperature measurements is $\pm 2.4^0$C.

It was found that the time-temperature profiles of the foam blocks were repeatable to a high degree. As a consequence, the thermocouple was no longer required once the time-temperature profile for the foam had been established. This means that the thermocouple does not have to be used for the production runs. This avoids the introduction of surface gouges in the foam at the centre of the large faces. This method works well for the fabrication of large auxetic foam blocks. Obviously, the moulds could be made to conform to any reasonable size or shape.

It has been found that by simply changing the starting conventional foam sizes, the volumetric compression ratio also changes, and a range of auxetic foams with various negative Poisson's ratio can be made. The results of varying the compression ratio to obtain different values of Poisson's ratio (measure at each stage) are shown in *Table 3.7, 3.8, and 3.9*.

Starting Type	Finish Type	Starting Volume mm^3	Finish Volume mm^3	$\frac{Lx}{Lx-\delta x}$ (x = z)	$\frac{Ly}{Ly-\delta y}$	R_c	Tensile Poisson's Ratio (ν_{yx})
10CO	100AO	300 × 300 × 100	200 × 200 × 50	1.5	2	4.5	-0.82 ± 0.05
10CO	90AO	300 × 300 × 90	200 × 200 × 50	1.5	1.8	4.05	-0.78 ± 0.04
10CO	80AO	300 × 300 × 80	200 × 200 × 50	1.5	1.6	3.6	-0.68 ± 0.02
10CO	70AO	300 × 300 × 70	200 × 200 × 50	1.5	1.4	3.15	-0.53 ± 0.011

Table 3.7 Transform the 10ppi open-cell polyether urethane foam blocks into a range of auxetic foams with different negative Poisson's ratios. The average error on sample dimension is ±2 mm.

Starting Type	Finish Type	Starting Volume mm^3	Finish Volume mm^3	$\frac{Lx}{Lx-\delta x}$ (x = z)	$\frac{Ly}{Ly-\delta y}$	R_c	Tensile Poisson's Ratio (ν_{yx})
30CO	100AO	300 × 300 × 100	200 × 200 × 50	1.5	2	4.5	-0.75 ± 0.10
30CO	90AO	300 × 300 × 90	200 × 200 × 50	1.5	1.8	4.05	-0.67 ± 0.11
30CO	80AO	300 × 300 × 80	200 × 200 × 50	1.5	1.6	3.6	-0.56 ± 0.02
30CO	70AO	300 × 300 × 70	200 × 200 × 50	1.5	1.4	3.15	-0.50 ± 0.03

Table 3.8 Transform the 30ppi open-cell polyether urethane foam blocks into a range of auxetic foams with different negative Poisson's ratios. The average error on sample dimension is ± 1 mm.

Starting Type	Finish Type	Starting Volume mm^3	Finish Volume mm^3	$\frac{Lx}{Lx-\delta x}$ (x = z)	$\frac{Ly}{Ly-\delta y}$	R_c	Tensile Poisson's Ratio (ν_{yx})
PECC	PEAC-1	300 × 300 × 100	200 × 200 × 50	1.5	2	4.5	-0.68 ± 0.11
PECC	PEAC-2	300 × 300 × 90	200 × 200 × 50	1.5	1.8	4.05	-0.63 ± 0.1
PECC	PEAC-3	300 × 300 × 80	200 × 200 × 50	1.5	1.6	3.6	-0.55 ± 0.04
PECC	PEAC-4	300 × 300 × 70	200 × 200 × 50	1.5	1.4	3.15	-0.49 ± 0.03

Table 3.9 Transform the 60ppi closed-cell polyester urethane foam blocks into a range of auxetic foams with different negative Poisson's ratios. The average error on sample dimension is ± 1 mm.

3.4 To Summarise the Fabrication Method

1. The fabrication method for auxetic foams has been developed further. We can now not only transform the small size conventional foam into an auxetic one, but also can

produce large auxetic foam blocks. The stability of the auxetic foams has been improved by using the multi-stage method.

2. The processing conditions such as the heating time, conversion temperature and volumetric compression ratios, have been examined on both small size specimens and the larger foam blocks. Fabricating a small size specimen requires a shorter heating time and less compression load, whereas, fabricating the large auxetic foam block needs a much longer heating time and requires a much bigger compression force. The multi-stage processing method is preferred for such specimens.

3. The multi-stage processing technique, which separates the transformation process into several stages, can be used to minimize the risk of surface creasing, and therefore is a more controlled technique than the one-stage processing method.

4. By changing the volumetric compression ratio, different values for Poisson's ratio of the foam can be obtained.

Chapter 4

Microscopic Examination of the Microstructure and Deformation of Foams

4.1 Introduction

A cellular foam is produced by dispersing a gas within a semi-liquid solid material which is allowed to solidify whilst the gas bubbles are still present. The direction in which the bubbles rise though the semi-liquid phase is known as the rise direction. Usually, the bubbles elongate as they rise and in the solidified foam and the bubble shape is often different in the rise and transverse directions. This effect can lead to a lack of isotropy. Assuming similar mechanical properties for the solid material comprising the foams, the principle variables affecting the properties of the foam are the geometry of the cells. In this chapter the results of optical and scanning electron microscope studies of the geometrical parameters for the different foams examined are presented. Examples of the microstructural deformation mechanisms observed are also presented. Comparison between the conventional foams and their auxetic conversions are also made.

At first sight, one might suppose that the mechanical properties of a foam would depend significantly on cell size. However, it is known that cell size makes only a minor contribution. A much more significant contribution is attributed to the cell shape (see Gibson and Ashby,1988). When the cells are equiaxed the properties are isotropic, but when the cells become slightly elongated or flattened then the properties will depend on direction, often strongly so. Three dimensional foams, in which cell walls have random orientations in space, are normally anisotropic, and this is due to the way they are foamed.

There are three different types of foam cell structure: open-cell, closed-cell and reticulated foams. The distinctions between these three foams are that closed-cell foams have a membrane of variable thickness covering each face of the cell. In an open cell foam, most of these membranes are perforated, and in reticulated foams the membranes have all been removed by chemical means or with the help of heat treatment. These foams can be used as filters. In practice, these cellular morphologies can co-exist so that a polymer foam is not always completely open or closed.

Polymeric foams have been examined using both optical and scanning electron microscopy (SEM). Each foam sample was sectioned in each of the three dimensions by using a Burgess band saw (*Figure 4.1*). The specimens prepared for the SEM were coated with gold by using an Edwards Sputter Coater S150, and examined with the Philips 501 SEM (*Figure 4.2*). photographs were taken during the

scanning process. The microstructural deformation mechanisms were observed by using a Wild M8 & MPS45 Optical Microscopes. A vice was used to deform the samples under the optical microscope as shown in *Figure 4.3* .

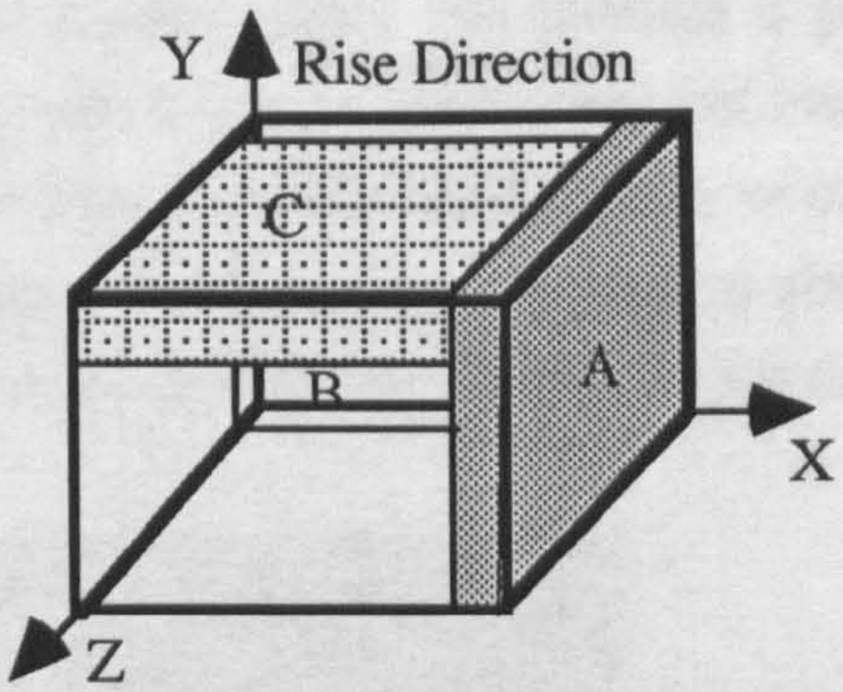

Fig. 4.1 Specimen of foam cut off the foam block in the three directions.

Fig. 4.2 The Philips 501 SEM.

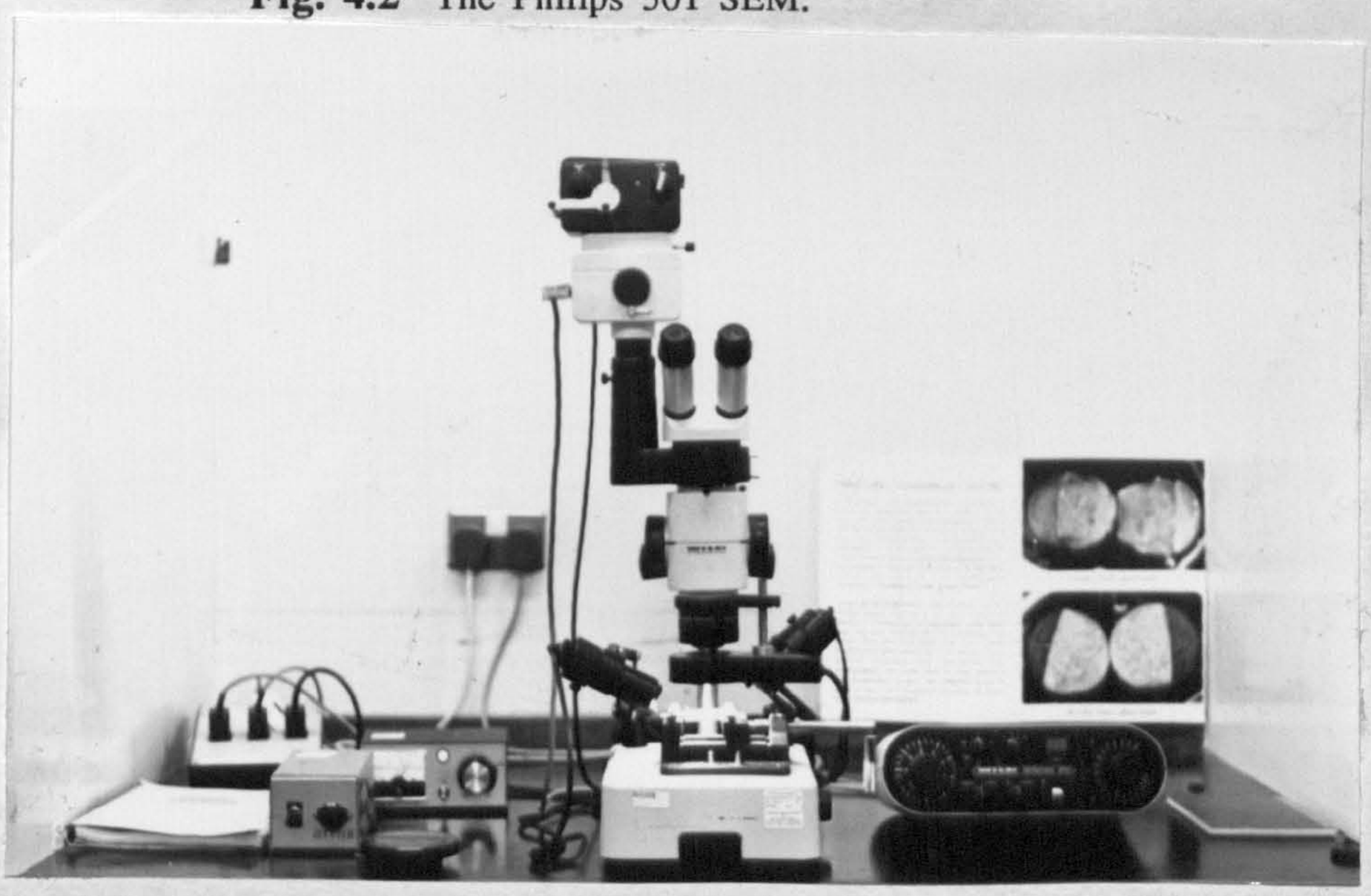

Fig. 4.3 Examination of the deformation of the foam by using a Wild M8 & MPS45 Optical Microscope.

4.2 The Microstructure of Conventional Foam

The classical example of a low density foam is reticulated PUR (polyurethane) foam, and micrographs for this type of material have been given many times in the literature (i.e. Gibson and Ashby, 1988). An example is presented in *Figure* 4.4. It is seen that the 60ppi polyester urethane foam consist of interconnecting struts, and that the predominant configuration is a dodecahedral array of cells with pentagonal faces. The foam is an anisotropic material since, as explained above, the cells in the foam rise direction when observed from above are more circular and smaller than that in the other two directions.

(a)

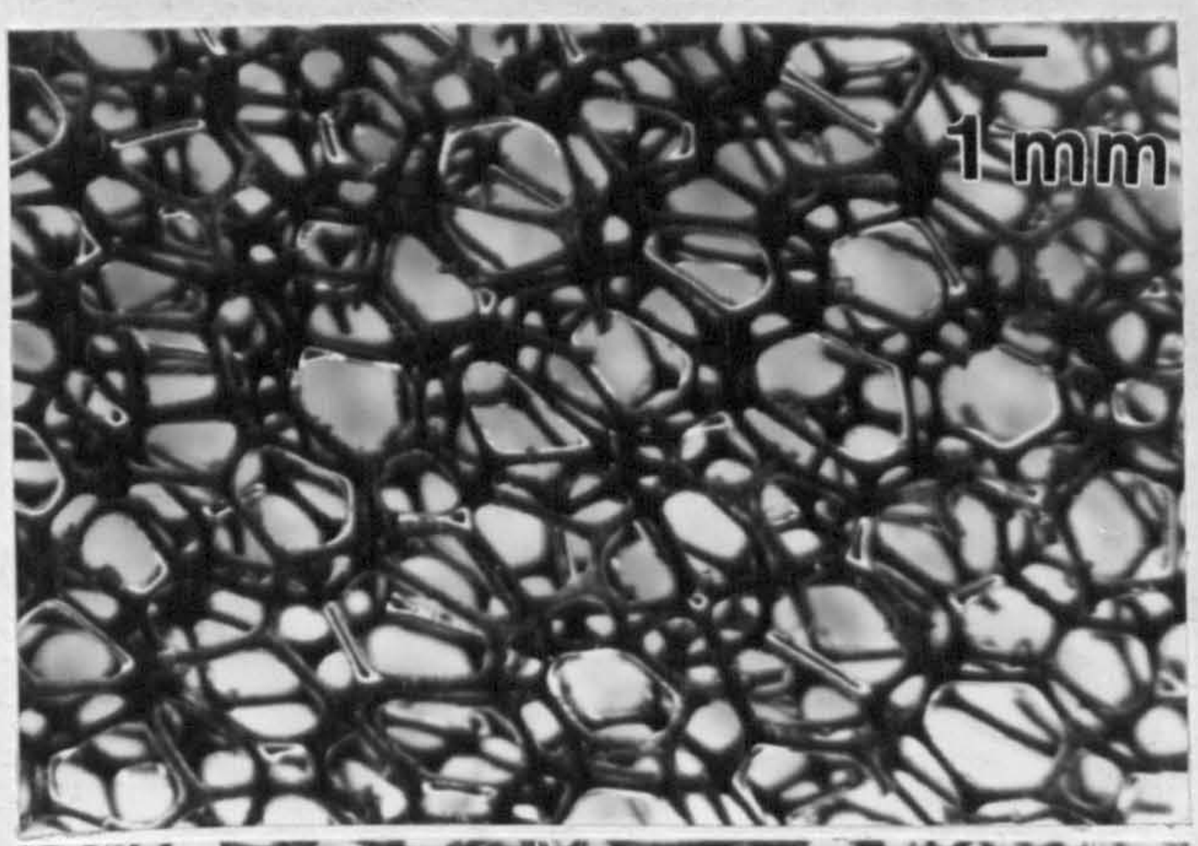

(b)

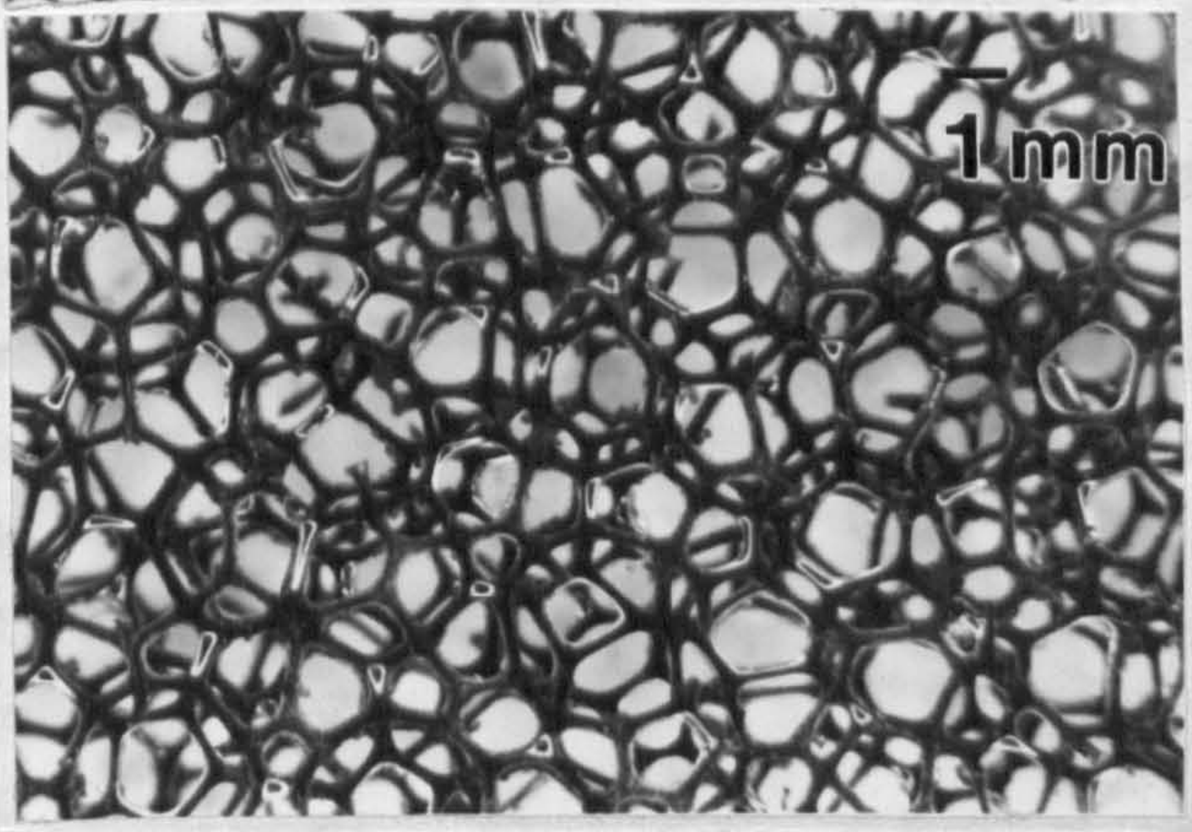

(c)

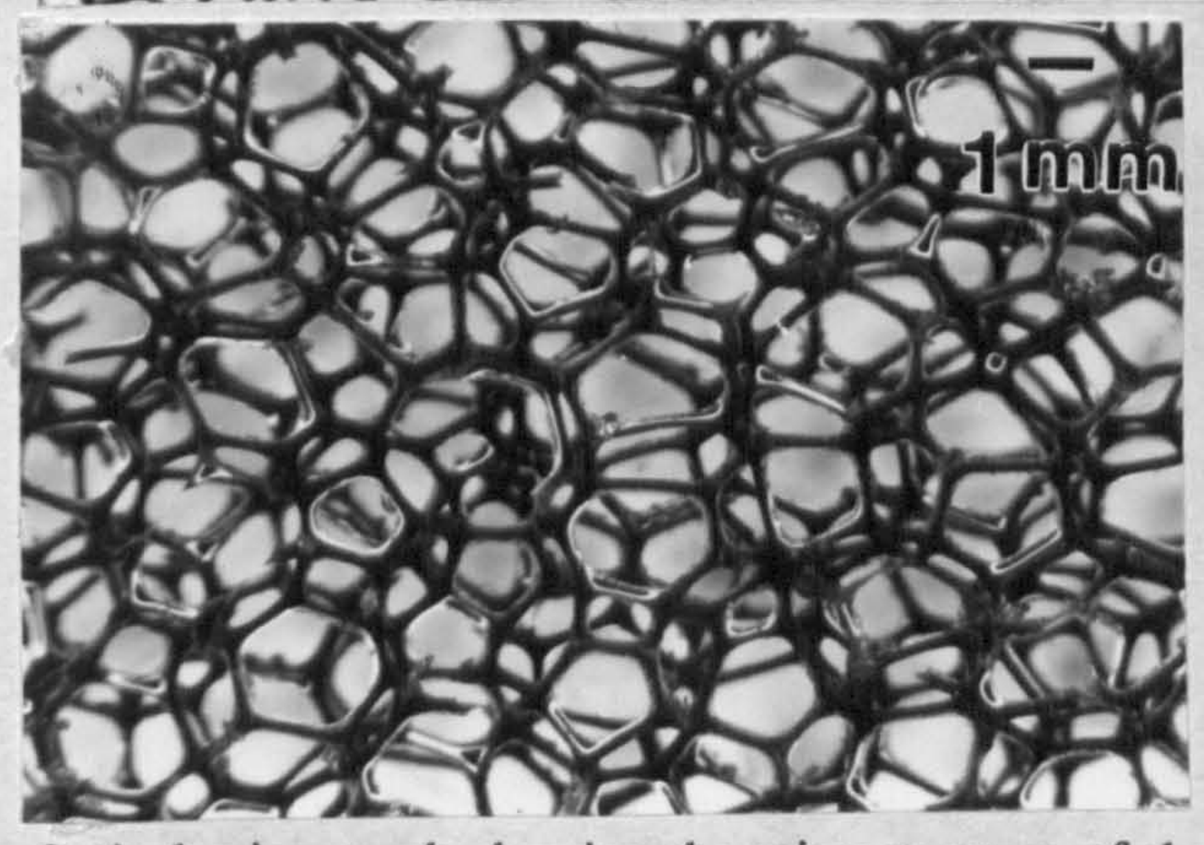

Fig. 4.4 Optical micrograph showing the microstructure of the 60ppi reticulated conventional polyester urethane foam (PECO): (a) Looking at the foam along the z axis (Face B). (b) Looking at the foam along the y axis, foam rise direction (Face C). (c) Looking at the foam along the x axis (Face A).

Figure 4.5 shows the microstructure of the 60ppi closed-cell conventional polyester urethane foam. In the closed-cell foam, most of the cell faces are closed off by thin membranes. The solid is not uniformly distributed between the edges and faces. The reason why the membranes are thinner than the cell ribs, is because during foaming. surface tension draws solid into the cell edges. Descriptions of the foaming process can be found in Suh and Skochdopole (1980).

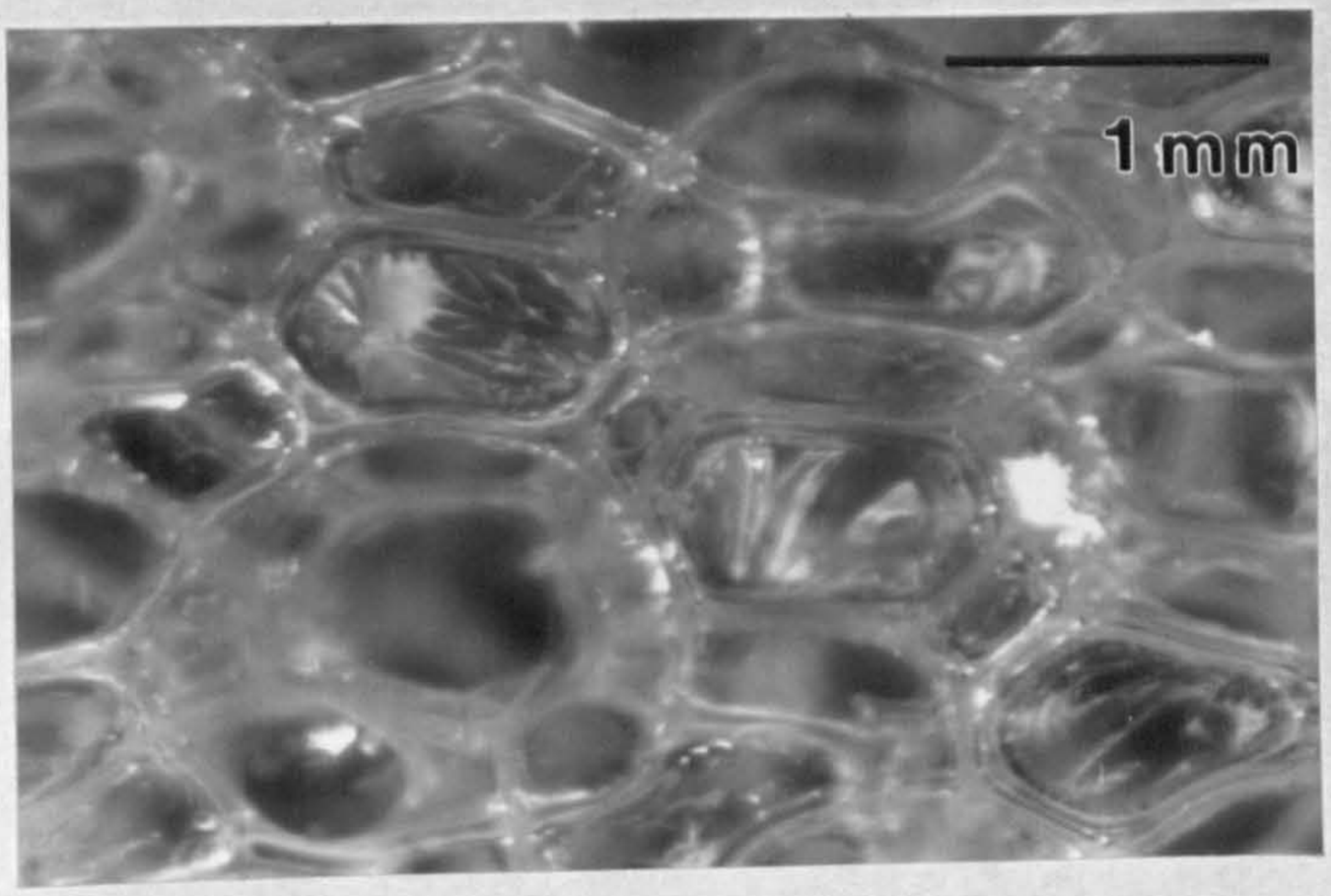

Fig. 4.5 Optical micrograph showing the microstructure of the 60ppi closed-cell conventional polyester urethane foam (PECC). Looking at the foam along the z axis (Face B).

Figures 4.6(a), (b), and (c) show the microstructures of 10ppi, 30ppi and 60ppi open-cell conventional polyether urethane foams. Although a few of the cell membranes are perfect, most of the membranes are ruptured, so the gases are not trapped inside the cells, and the porous open-cell foams allow free movement of air throughout the materials when flexed, therefore, they are classified as open-cell foams. These foams with different cell sizes as shown in *Figure* 4.6 and are made from the same type of solid material (Polyether polyurethane). However, they have various cell geometry parameters (e.g. cell rib thickness etc.)

(a)

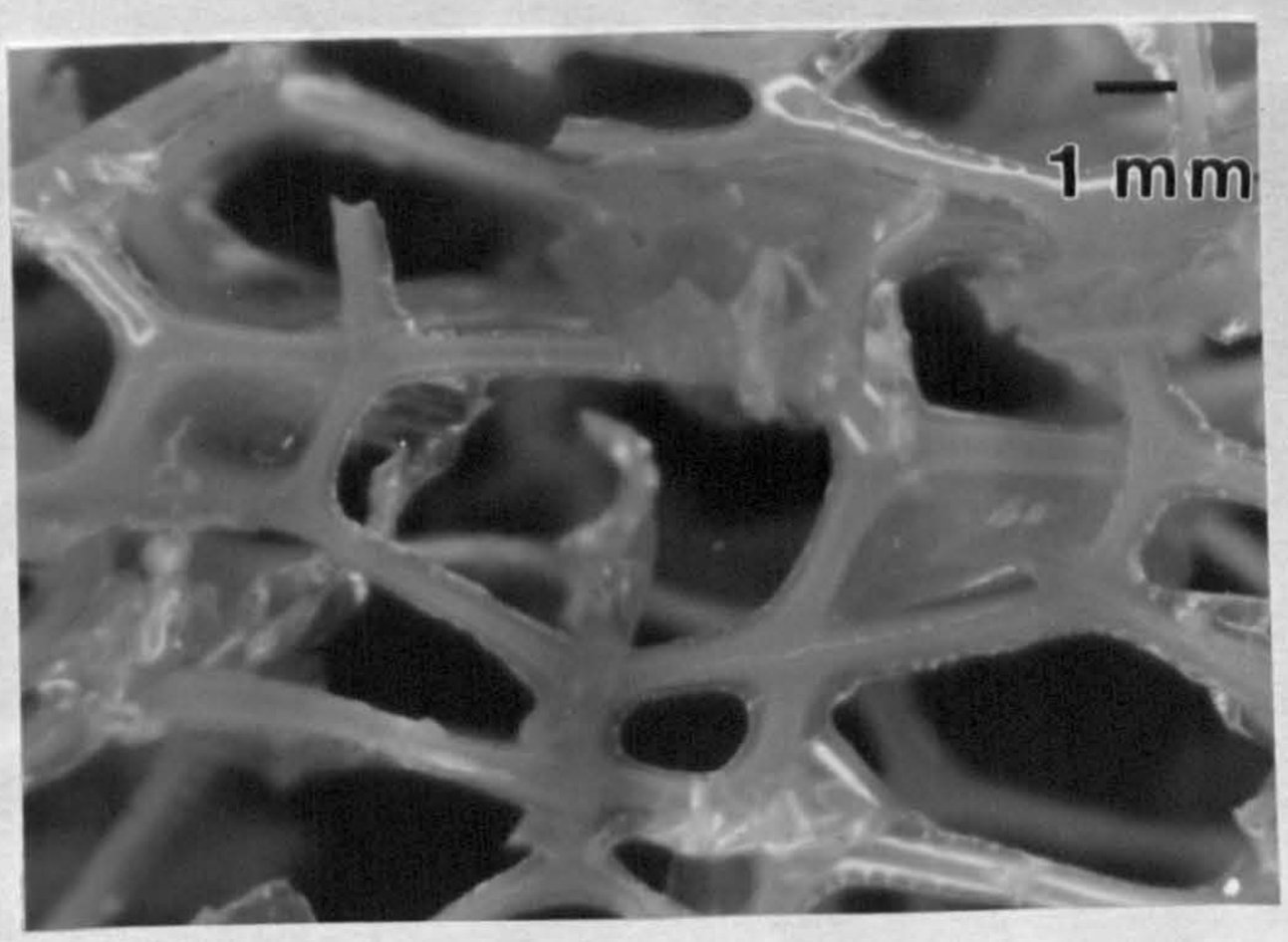

(b)

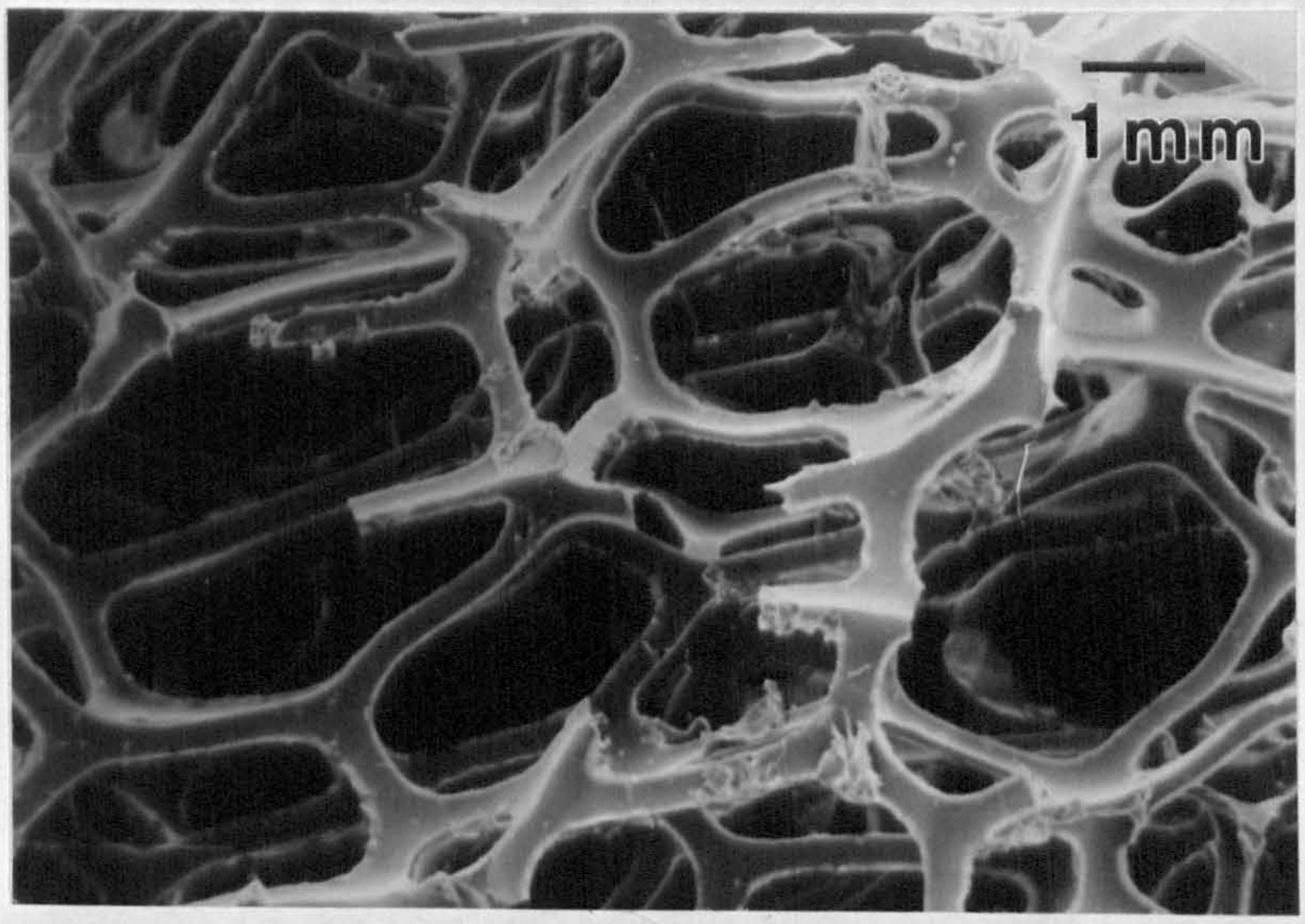

(c)

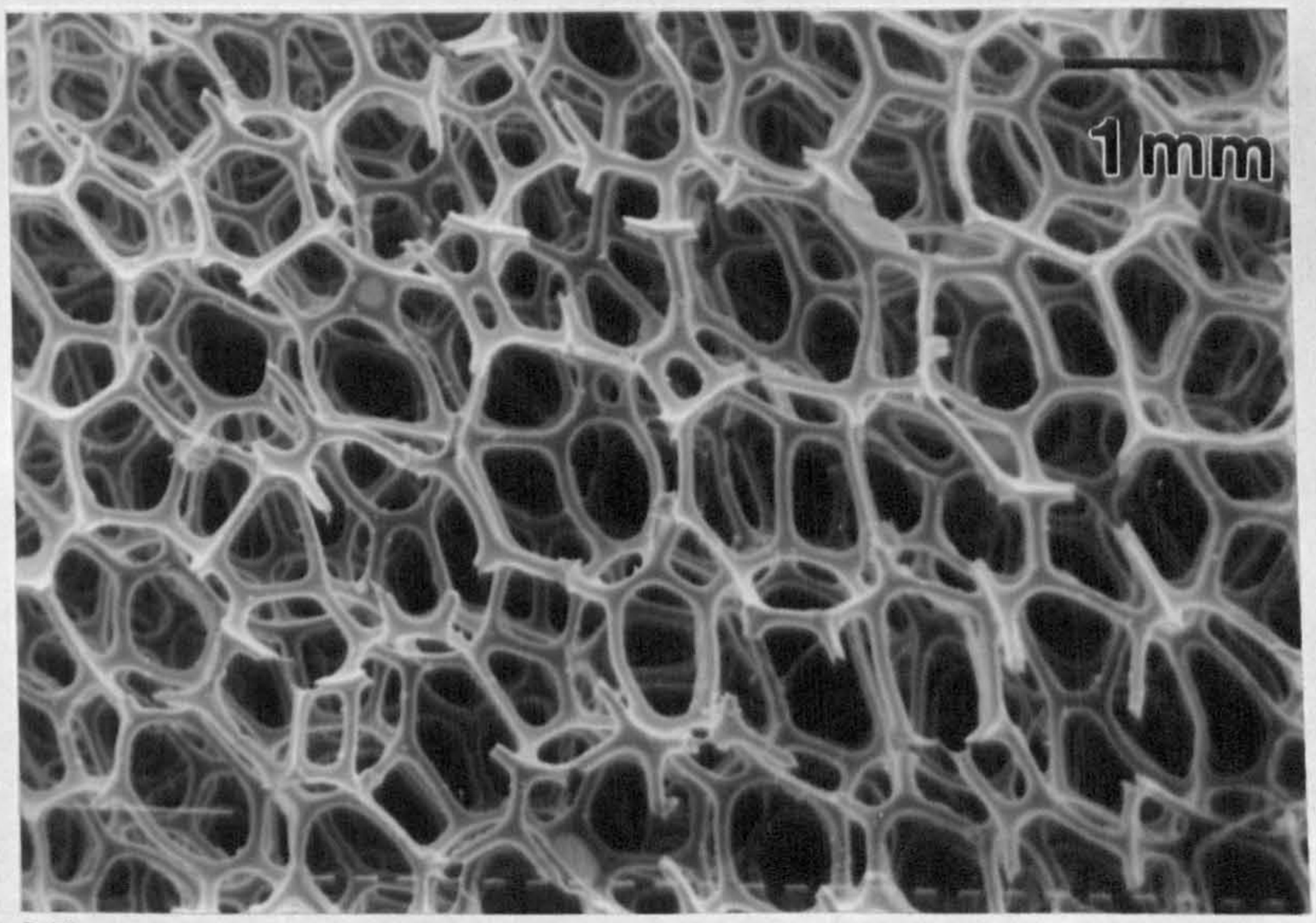

Fig. 4.6 Micrographs showing the microstructure of the open-cell conventional polyether urethane foam. (a) Looking at the 10ppi foam (10CO) along the z axis (Face B) (Optical micrograph). (b) Looking at the 30ppi foam (30CO) along the z axis (Face B) (Scanning electron micrograph). (c) Looking at the 60ppi foam (60CO) along the z axis (Face B) (Scanning electron micrograph).

Figures 4.7 and 4.8 show the microstructure of the PECC cell ribs. Two adjacent straight ribs are connected by a very short curved rib. The cross sectional area is triangular in shape. The joint of two ribs is made of two triangles.

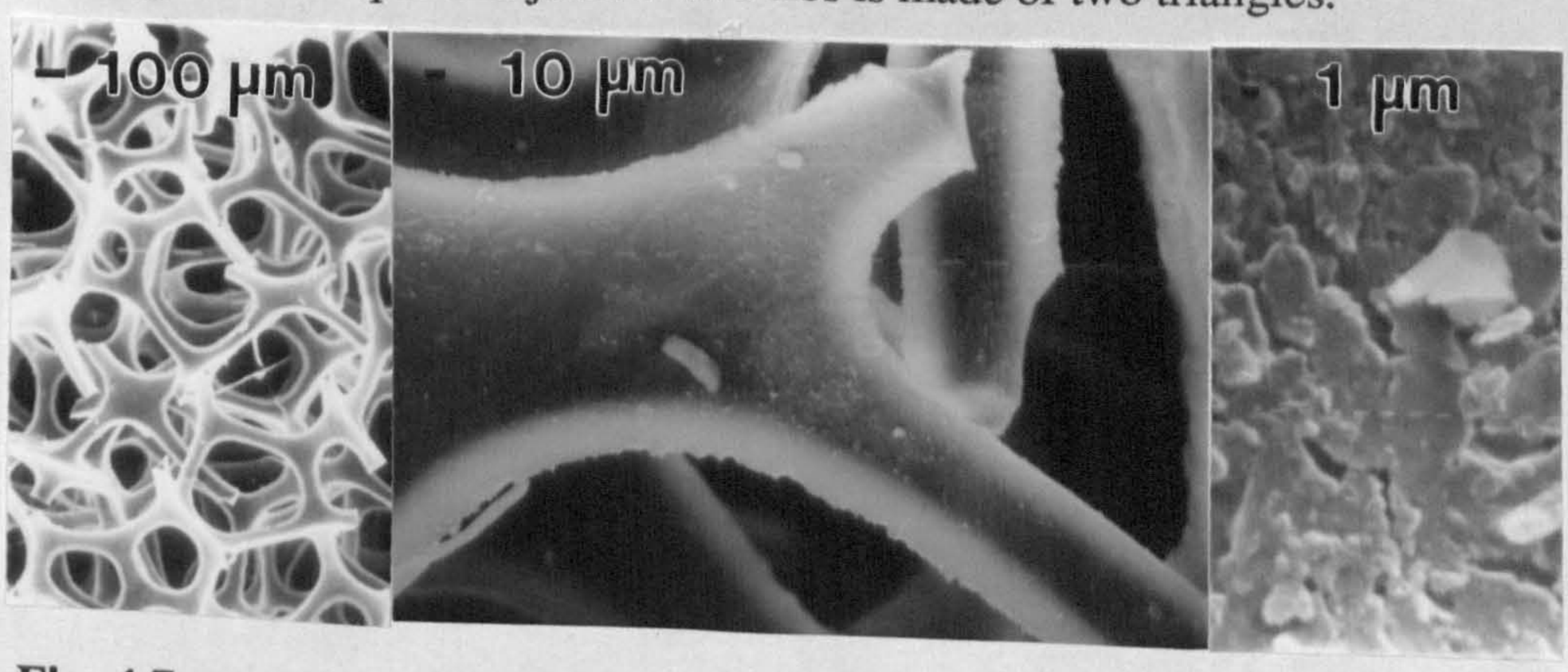

Fig. 4.7 The cell rib of the 60ppi closed-cell polyester urethane foam (PECC).

Fig. 4.8 The joint of the cell ribs of the 60ppi closed-cell polyester urethane foam (PECC). (SEM).

4.3 The Microstructure of Auxetic Foams

The microstructure of an auxetic foam were characterised by using the Philips 501 SEM and the Wild M8 & MPS45 Optical Microscopes. The micrographs of the 60ppi open cell polyether urethane foam, the 60ppi closed-cell polyether urethane foam, and the 30ppi open cell polyether urethane foam, for example, are as shown in *Figure* 4.14(a), (b) and (c).

(a)

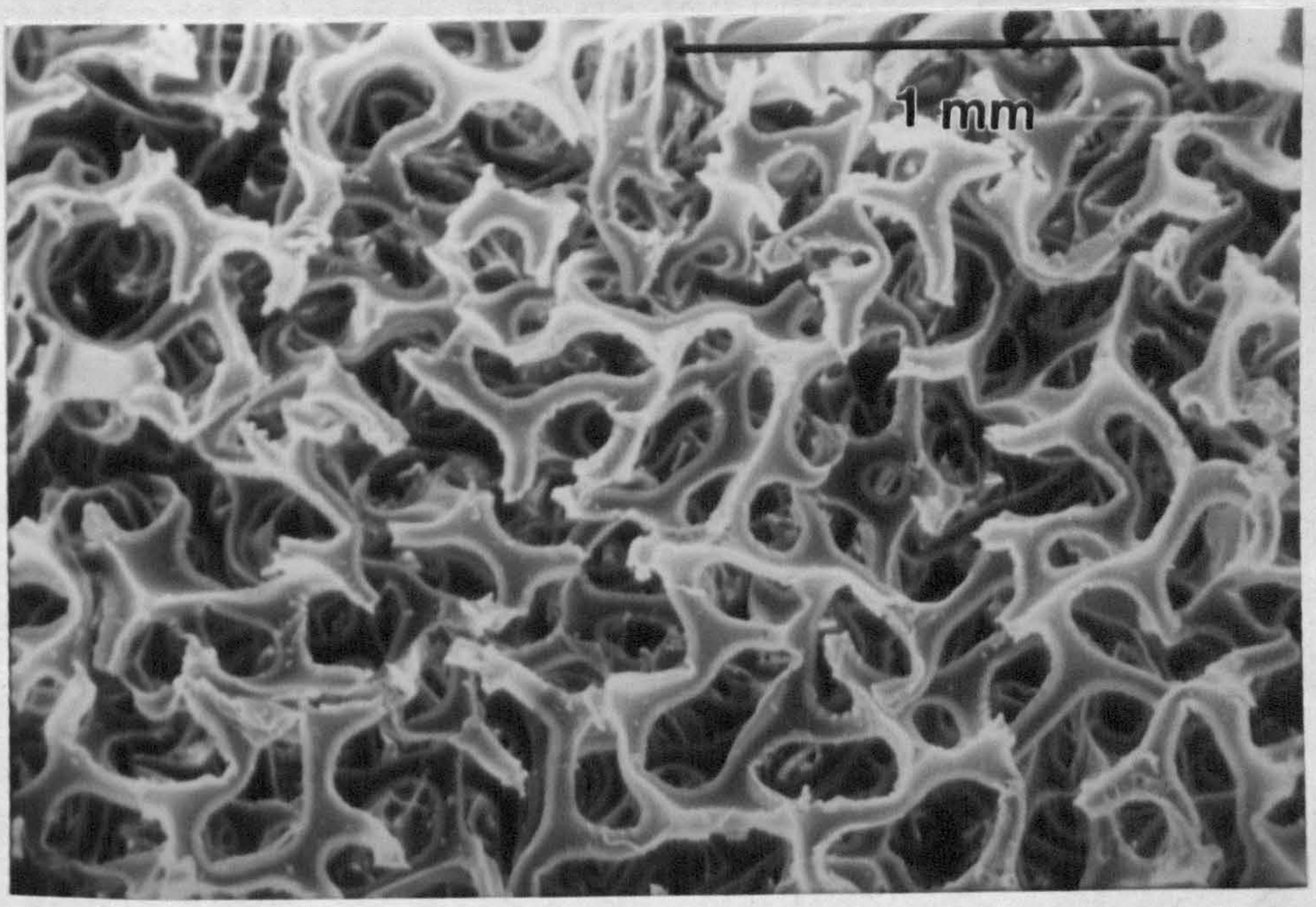

(b)

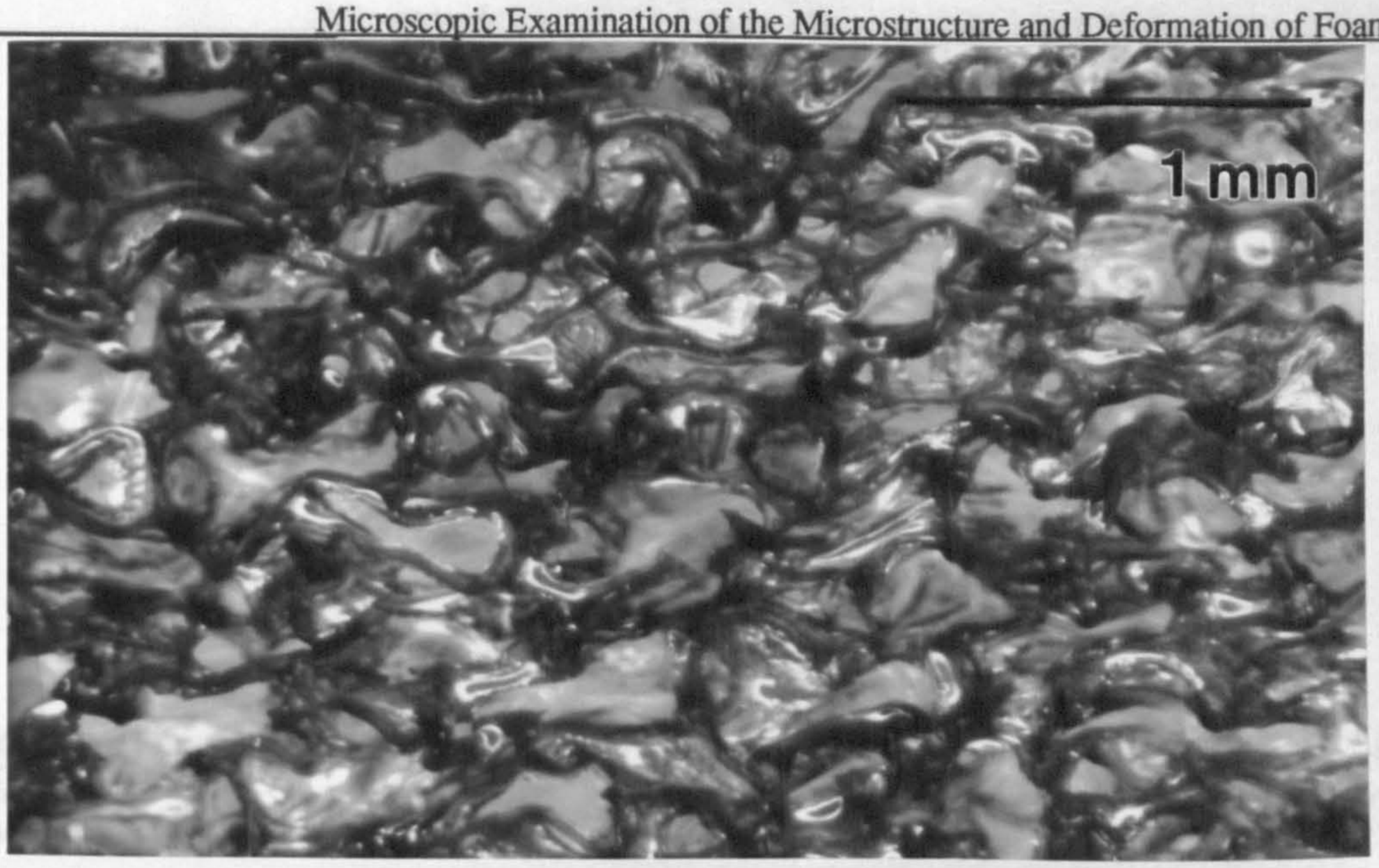

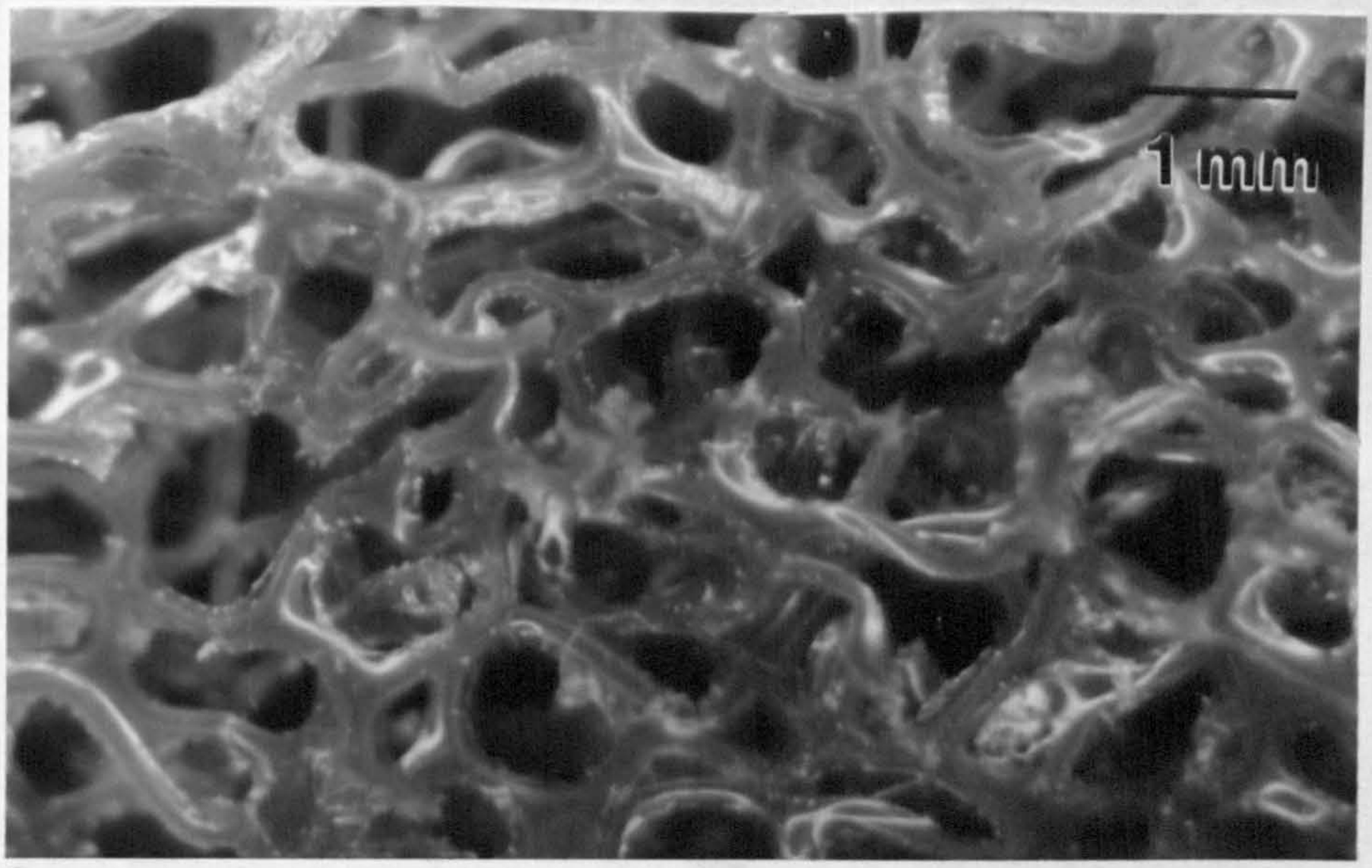

(c)

Fig. 4.9 The micrographs of auxetic foams. (a) The 60ppi open cell polyether urethane foam (60AO) (SEM). (b) The 60ppi closed-cell polyester urethane foam (PEAC) (optical microscopy). (c) The 30ppi open-cell polyether urethane foam (30AO) (optical microscopy).

4.4 Characterisation of Polymeric Foams

The microstructure of the foam is very complicated. To characterise the cell geometry of the foam, we need some way of averaging the cell geometry. To do this the foam in question was encapsulated in a resin matrix (Scandiplast 9101 resin). This was subsequently sectioned and polished, using standard metallographic methods. *Figure* 4.10 is a photograph of such a section and shows that each conventional foam cell is approximately represented by an ellipsoid. The mean dimension of the cells in the rise and transverse directions was obtained by measurement from photographs such as those in *Figure* 4.10. These data were used in conjunction with *Figure* 4.11(a) (a model of conventional foam cell) to construct EQ 4.1 and 4.2.

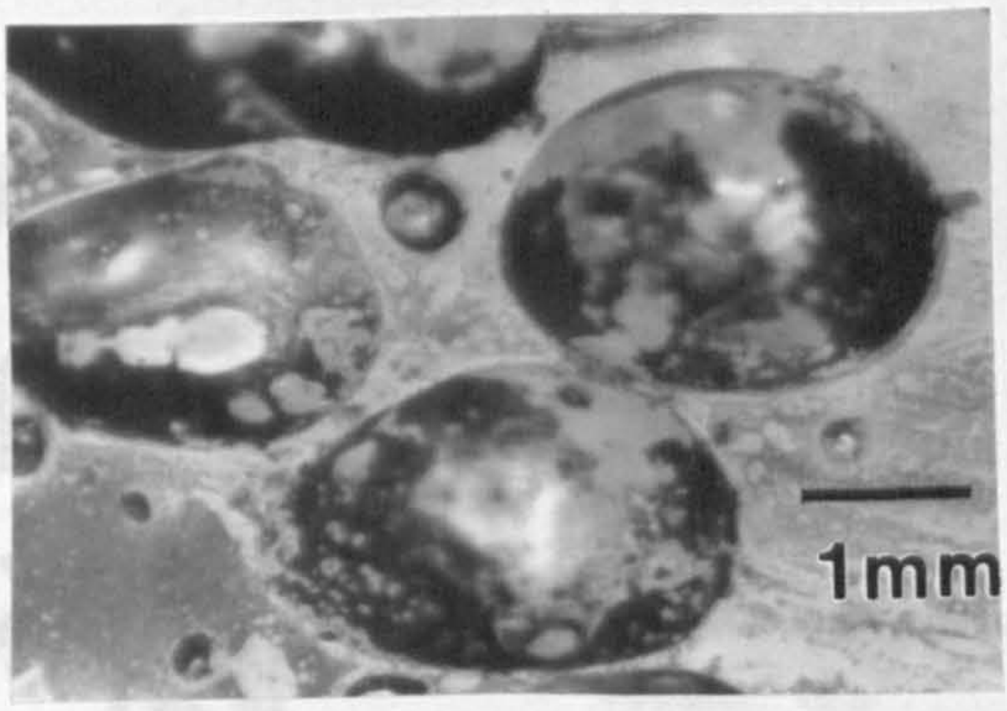

Fig. 4.10 Looking at the 60ppi reticulated polyester urethane foam (PECO) along the X axis (Face A). (Optical microscopy). This was done by using Scandiplast 9101 resin to fill the foam specimen and grinding the faces plane-parallel after hardening.

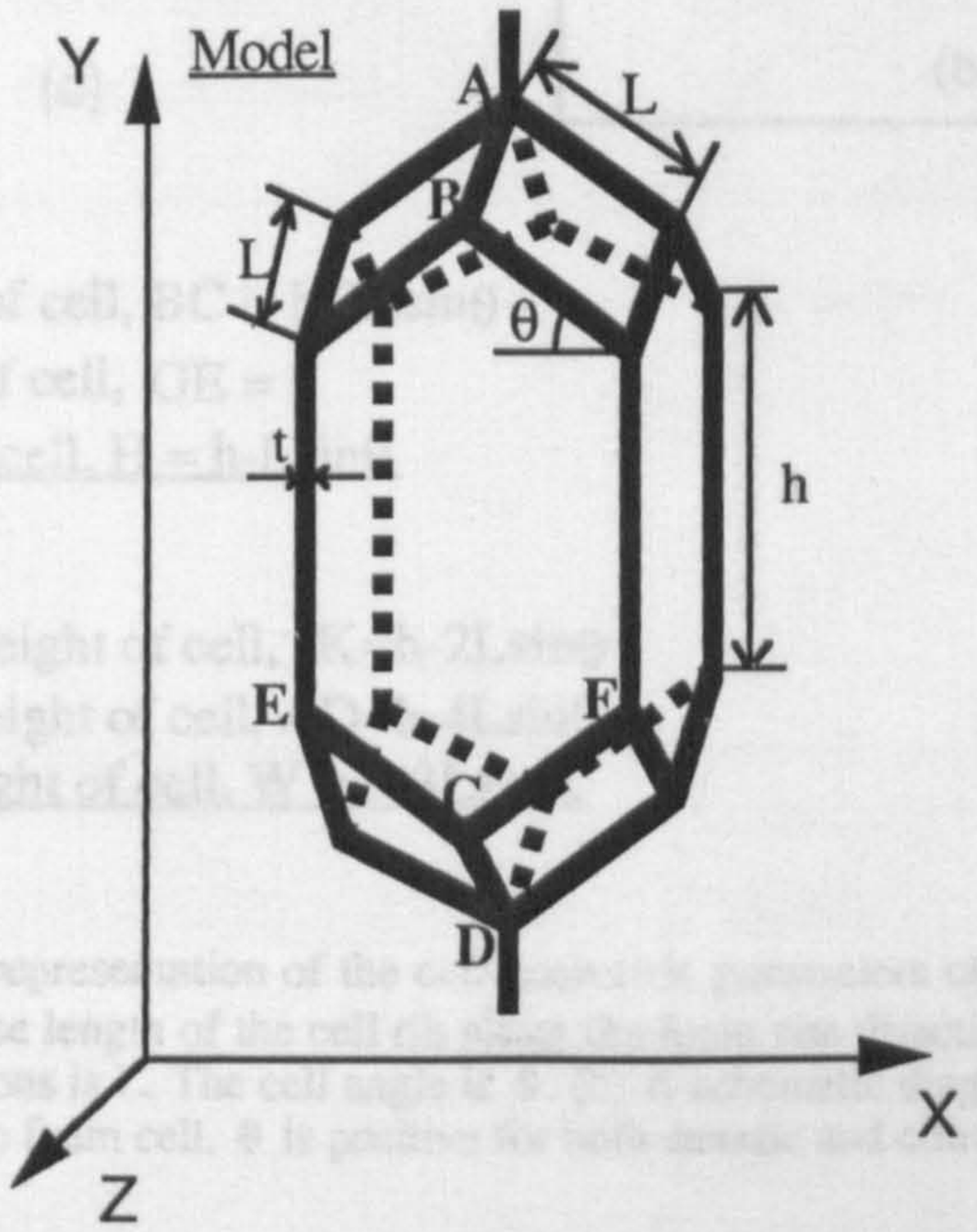

(a)

$AD = h+4L\sin\theta$

$BC = h+2L\sin\theta$

Average height of cell = the mean dimension of ellipsoids in the Y direction, $y = h+3L\sin\theta$. (EQ. 4.1)

Width of cell, EF = the mean dimension of ellipsoids in the X direction, $x = 2L\cos\theta$. (EQ. 4.2)

For same foam, after conversion to auxetic foam.

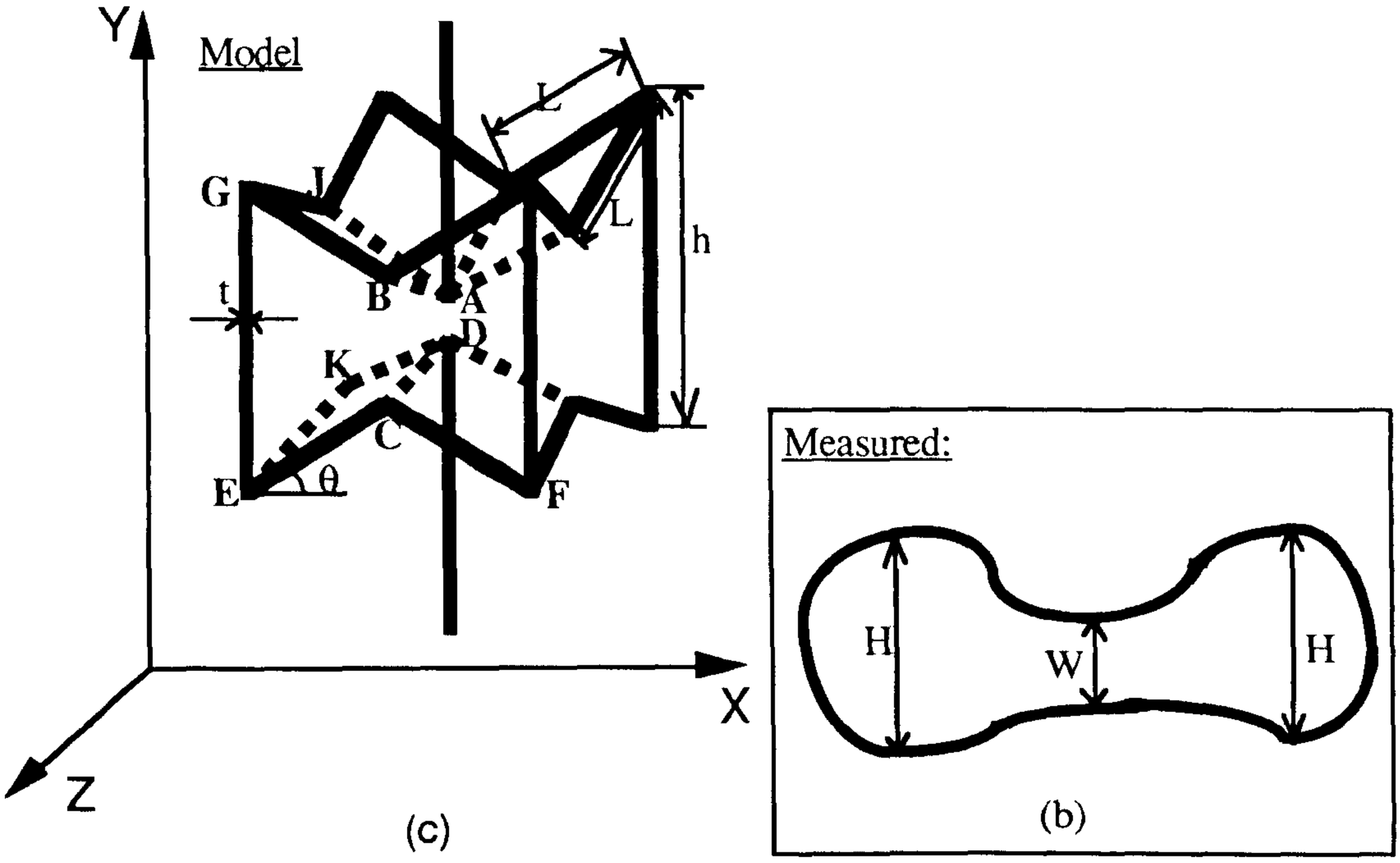

$EF=2L\cos\theta$

Maximum height of cell, $BC = h-2L\sin\theta$

Minimum height of cell, $GE = h$

Average height of cell, $H = h-L\sin\theta$. (EQ.4.3)

Maximum waist height of cell, $JK=h-2L\sin\theta$

Minimum waist height of cell, $AD=h-4L\sin\theta$

Average waist height of cell, $W = h-3L\sin\theta$. (EQ.4.4)

Fig. 4.11 A schematic representation of the cell geometric parameters of a foam. (a) A model of conventional foam cell. The length of the cell rib along the foam rise direction is h, the length of the cell rib in the other directions is L. The cell angle is θ. (b) A schematic diagram of a re-entrant foam cell. (c) A model of auxetic foam cell. θ is positive for both auxetic and conventional foams.

The data, x, y, H and W were obtained from the measurements of about one hundred cells in each direction for each foam specimen. EQ. 4.3 and 4.4 combined with earlier EQ. 4.1 and 4.2 for same foam in non-auxetic state should give all the parameters for the model. Examples of the cell size distributions and a more complete characterisation of PUR flexible foams are given in Tables 4.1 to 4.9.

Table 4.1

Material	Flexible polyester urethane (PECO)	
Density, ρ (kg/m^3)	33.7±1.3	
Open or closed cells	Reticulated	
Mean edges per face	5	
Mean faces per cell	12 or 14	
Symmetry of structure	Axisymmetry	
		Standard deviation
Mean cell edge thickness, t (mm)	0.087	0.025
Average height of cell, (mm)	2.53	0.21
Average width of cell, (mm)	1.92	0.16
Rib length along the foam rise direction, h (mm)	1.30	0.044
Rib length along the other directions, L (mm)	0.58	0.022
Cell angle, θ (degree)	32	2.2

Table 4.1 Characterisation data for the 60ppi reticulated conventional polyester urethane foam (PECO).

Table 4.2

Material	Flexible polyester urethane (PECC)	
Density, ρ (kg/m^3)	37.9±2.1	
Open or closed cells	Closed	
Mean edges per face	5	
Mean faces per cell	12 or 14	
Symmetry of structure	Axisymmetry	
		Standard Deviation
Mean cell face thickness, t_f (mm)	0.002	0.001
Mean cell edge thickness, t (mm)	0.045	0.018
Average height of cell, (mm)	1.08	0.15
Average width of cell, (mm)	0.47	0.08
Rib length along the foam rise direction, h (mm)	0.67	0.011
Rib length along the other directions, L (mm)	0.27	0.005
Cell angle, θ (degree)	30	2.6

Table 4.2 Characterisation data for the 60ppi closed-cell conventional polyester urethane foam (PECC).

Table 4.3

Material	Flexible polyether urethane (10CO)	
Density, ρ (kg/m^3)	24.1±3.1	
Open or closed cells	Open cells	
Mean edges per face	5	
Mean faces per cell	12 or 14	
Symmetry of structure	Axisymmetry	
		Standard deviation
Mean cell edge thickness, t (mm)	0.23	0.015
Average height of cell, (mm)	4.93	0.27
Average width of cell, (mm)	2.57	0.19
Rib length along the foam rise direction, h (mm)	2.33	0.047
Rib length along the other directions, L (mm)	1.55	0.021
Cell angle, θ (degree)	34	3.0

Table 4.3 Characterisation data for the 10ppi open-cell conventional polyether urethane foam (10CO).

Table 4.4

Material	Flexible polyether urethane (30CO)	
Density, ρ (kg/m^3)	24.5±2.7	
Open or closed cells	Open cells	
Mean edges per face	5	
Mean faces per cell	12 or 14	
Symmetry of structure	Axisymmetry	
		Standard deviation
Mean cell edge thickness, t (mm)	0.13	0.025
Average height of cell, (mm)	3.18	0.25
Average width of cell, (mm)	1.47	0.16
Rib length along the foam rise direction, h (mm)	1.80	0.044
Rib length along the other directions, L (mm)	0.87	0.022
Mean cell angle, θ (degree)	32	2.0

Table 4.4 Characterisation data for the 30ppi open-cell conventional polyether urethane foam (30CO).

Table 4.5

Material	Flexible polyether urethane (60CO)	
Density, ρ (kg/m^3)	21.7±1.9	
Open or closed cells	Open cells	
Mean edges per face	5	
Mean faces per cell	12 or 14	
Symmetry of structure	Axisymmetry	
		Standard deviation
Mean cell edge thickness, t (mm)	0.036	0.002
Average height of cell, (mm)	0.65	0.11
Average width of cell, (mm)	0.34	0.07
Rib length along the foam rise direction, h (mm)	0.38	0.018
Rib length along the other directions, L (mm)	0.19	0.020
Mean cell angle, θ (degree)	28	3

Table 4.5 Characterisation data for the 60ppi open-cell conventional polyether urethane foam (60CO).

Table 4.6

Material	Flexible polyether urethane (60AO)	
Density, ρ (kg/m^3)	91±2.1	
Open or closed cells	Reticulated	
Mean edges per face	6	
		Standard Deviation
Mean cell edge thickness, t (mm)	0.036	0.002
Average height of cell, H (mm)	0.285	0.08
Average waist height of cell, W (mm)	0.1	0.03
Rib length along the foam rise direction, h (mm)	0.38	0.04
Rib length along the other directions, L (mm)	0.19	0.05
Cell angle, θ (degree)	-30	2

Table 4.6 Characterisation data for the 60ppi open cell polyether urethane auxetic foam (60AO). (The volume of auxetic foam is: 25.4 x 25.4 x 80 mm, and the volume of its parent conventional foam is: 38 x 38 x 110 mm).

Table 4.7

Material	Flexible polyester urethane (PECA)	
Density, ρ (kg/m^3)	72.4±2.5	
Open or closed cells	Membranes are ruptured	
Mean edges per face	6	
		Standard Deviation
Mean cell edge thickness, t (mm)	0.045	0.015
Average height of cell, H (mm)	0.53	0.19
Average waist height of cell, W (mm)	0.24	0.09
Rib length along the foam rise direction, h (mm)	0.67	0.31
Rib length along the other directions, L (mm)	0.27	0.136
Mean cell angle, θ (degree)	-32	3

Table 4.7 Characterisation data for the 60ppi closed-cell polyester urethane auxetic foam (PEAC). (The volume of auxetic foam is: 25.4 x 25.4 x 80 mm, and the volume of its parent conventional foam is: 38 x 38 x 110 mm).

Table 4.8

Type of the foam	100AO	90AO	80AO	70AO
Material	Flexible polyether urethane			
Density, ρ (kg/m^3)	79.1±3.0	77±2.1	76.±2.2	75±2.5
Open or closed cells	Open cells			
Mean edges per face	6			
Mean cell edge thickness, t (mm)	0.19±0.05			
Average height of cell, H (mm)	1.6±0.1	1.7±0.07	1.75±0.08	1.8±0.06
Average waist height of cell, W (mm)	0.15±0.04	0.44±0.02	0.59±0.03	0.74±0.03
Rib length along the foam rise direction, h (mm)	2.33±0.71	2.33±0.83	2.33±0.8	2.33±0.96
Rib length along the other directions, L (mm)	1.55±0.6	1.55±0.49	1.55±0.43	1.55±0.28
Cell angle, θ (degree)	-28±2	-24±3	-22±2	-20±2

Table 4.8 Characterisation data for the 10ppi open-cell polyether urethane auxetic foam.

Table 4.9

Type of the foam	100AO	90AO	80AO	70AO
Material	Flexible polyether urethane			
Density, ρ (kg/m^3)	95±1.8	84±2.3	73±2.5	69±1.6
Open or closed cells	Open cells			
Mean edges per face	6			
Mean cell edge thickness, t (mm)	0.11±0.045			
Average height of cell, H (mm)	1.45±0.3	1.47±0.2	1.49±0.11	1.52±0.09
Average waist height of cell, W (mm)	0.76±0.06	0.82±0.06	0.86±0.07	0.95±0.03
Rib length along the foam rise direction, h (mm)	1.80±0.49	1.80±0.52	1.80±0.59	1.80±0.66
Rib length along the other directions, L (mm)	0.87±0.4	0.87±0.37	0.87±0.33	0.87±0.30
Mean cell angle, θ (degree)	-24±3	-22±3	-21±2	-19±2

Table 4.9 Characterisation data for the 30ppi open-cell polyether urethane auxetic foam.

The micrographs of conventional foam show that:: -

(1) Polymer foams are multiphase material systems that consist of a polymer matrix and a fluid phase- the fluid usually being gas.

(2) In low density foams, as depicted in *Figures* 4.4 to 4.6, the cell morphology is determined by energy and structural symmetry considerations. Although a tetrakaidecahedron cell, having fourteen faces, minimises the surface area of the cell, and hence the surface energy, the angular symmetry associated with the pentagonal dodecahedron cell, which has twelve five sided faces, means that this type of cell is commonly found in the foams. Invariably, there is some distribution of cell morphology within a foam specimen. For example, four and six sided faces are observed alongside the pentagonal faces. The presence of cell elements with these configurations is necessary to achieve complete packing.

(3) All the foams in this investigation are to some degree elongated, this is because of the way in which they are made.

(4) Apart from anisotropy, another important issue is the range of cell sizes in the foam. The average cell size in the foam rise direction is smaller than that in the other two directions, and there a significant proportion of cells that are so small that they will not deform and act as junction points within the foam.

(5) The section of the strut has uniform dimensions over a considerable proportion of its length, i.e. between the strut junctions.

(6) Open cell foam will naturally have thicker cell ribs than closed cell foam, since

not as much material is required to form the membranes.

(7) The cross section area of the cell rib is triangular in shape (not square or round in shape).

(8) The membranes of the closed-cell foam are thinner than the triangular prismatic ribs by a factor of ten to twenty times, so that their influence on the mechanical behaviour may be neglected.

(9) From these micrographs, estimates of the important geometric parameters for analysis of mechanical properties can be obtained. These are the cell rib thickness, cell rib length, and cell shape. The latter being defined later in this chapter.

The micrographs of auxetic foam show that:

(1) Almost all auxetic foams are anisotropic, and the orientation of the cell ribs of auxetic foam is more random than that of the conventional foam.

(2) Almost all of the membranes of the closed-cell auxetic foam are ruptured due to the fabricating process.

(3) An auxetic foam has a re-entrant shape, but not all of the foam cells can be converted into the re-entrant shape. Thus, some cells remain unchanged, particularly the smaller cells.

(4) During the fabrication process, Most of the cell ribs have either buckled or collapsed, and some are broken.

(5) An auxetic foam is denser than its parent conventional foam.

4.5 The Use of Sodium Hydroxide for Thinning Down the Cell Rib Thickness

In this section, a method is developed to enable us to vary the rib thickness. Mechanical tests on thinned foams are described elsewhere. Here we examine the effects of the thinning process.

An investigation was carried out using a water bath containing a solution of sodium hydroxide (NaOH) in water as shown in *Figure* 4.12. Specimens were cut to dimensions: 25 x 25 x 140 mm by using a Burgess band saw. The concentration of

sodium hydroxide used was 10%. The temperature of the water bath was kept at 50^0C. First, a number of specimens were put into sodium hydroxide using tongs, and a thin perforated stainless steel plate was used to hold them in position below the surface of the solution. Every five minutes a specimen was taken out of the water bath and then washed using clean water for half an hour at room temperature. Finally, all of the thinned foams were left to dry at the room temperature for about one day.

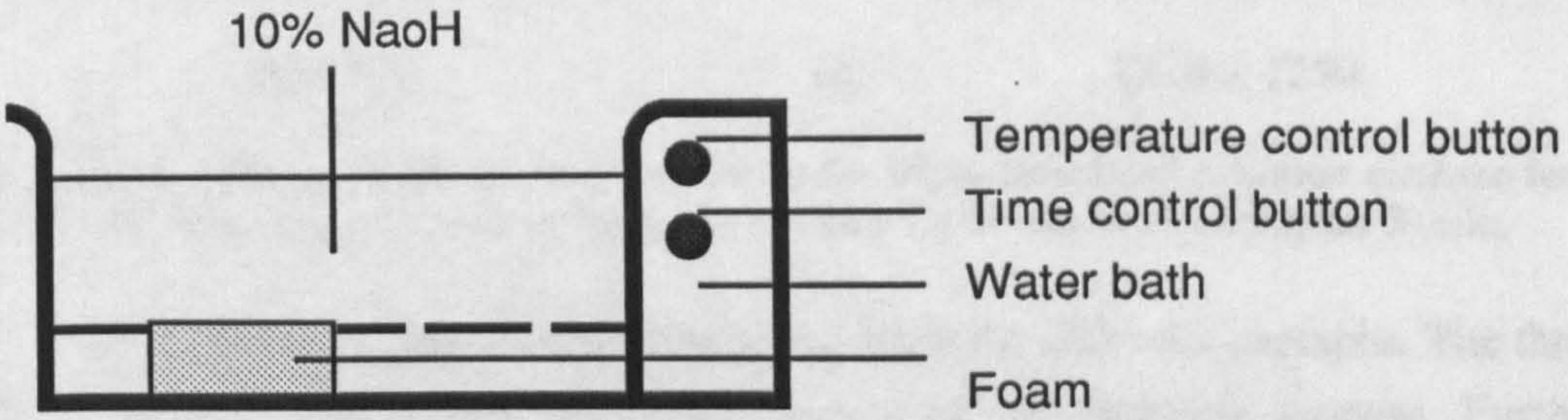

Fig. 4.12 Schematic of the foam cell rib thinning processing.

The effects of the thinning process are shown in *Figure* 4.13.

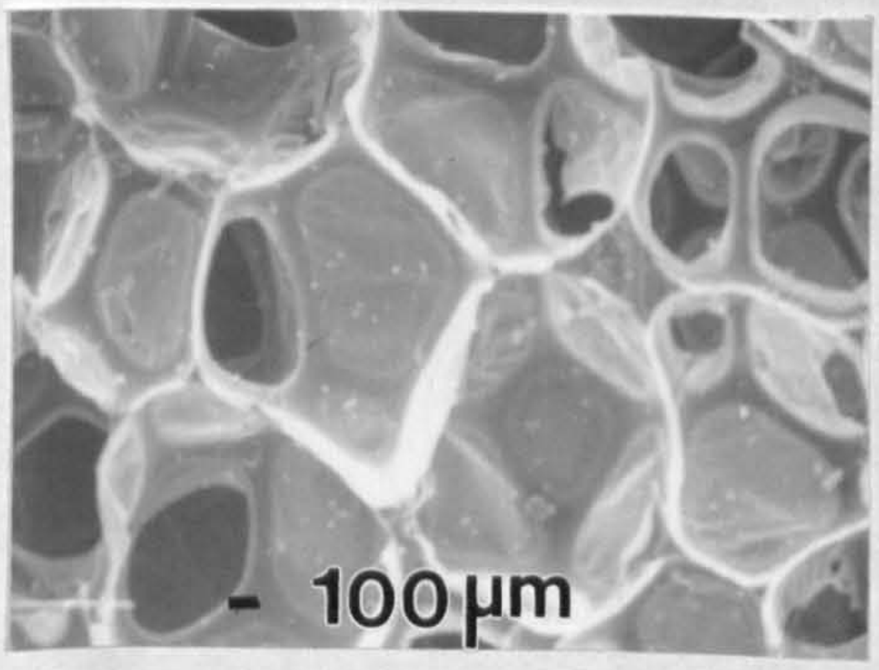

SEM x 40

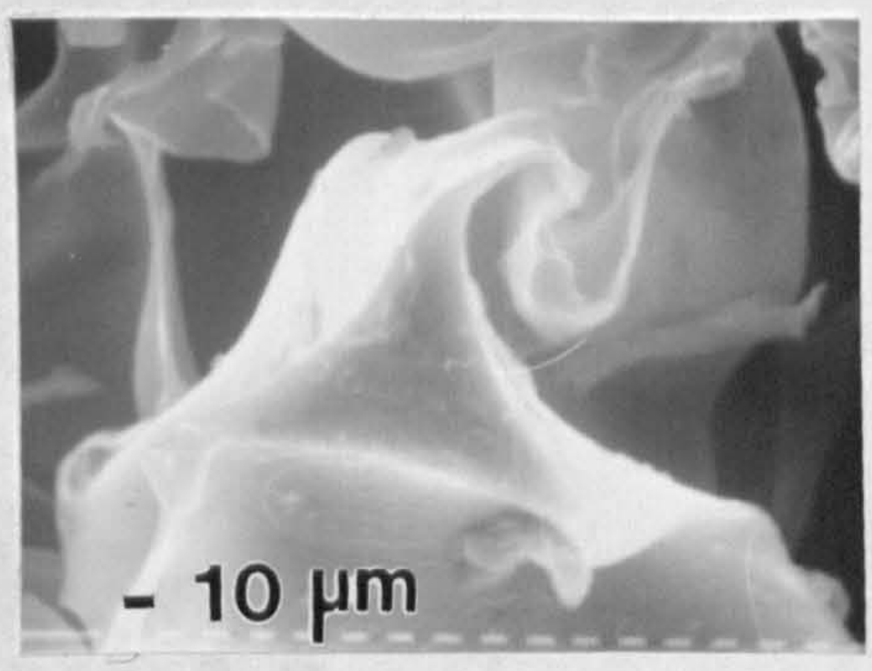

SEM x 1250

(a)

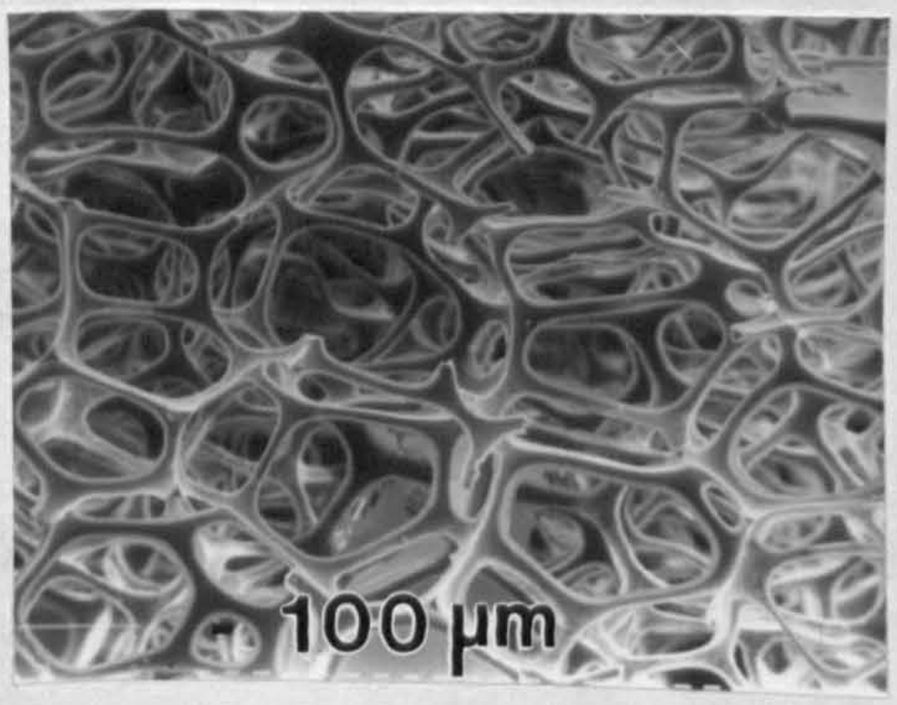

SEM x 40

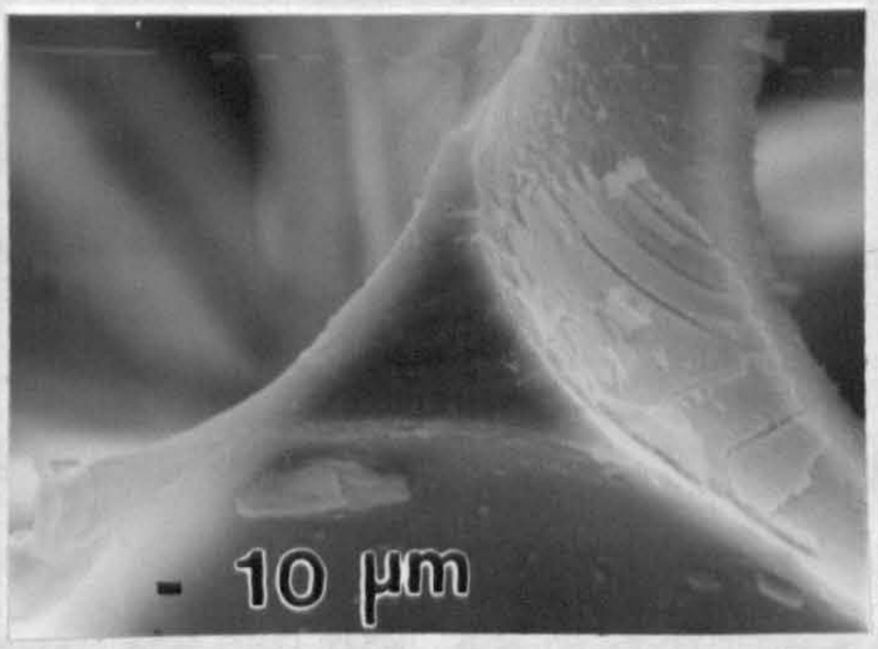

SEM x 1250

(b)

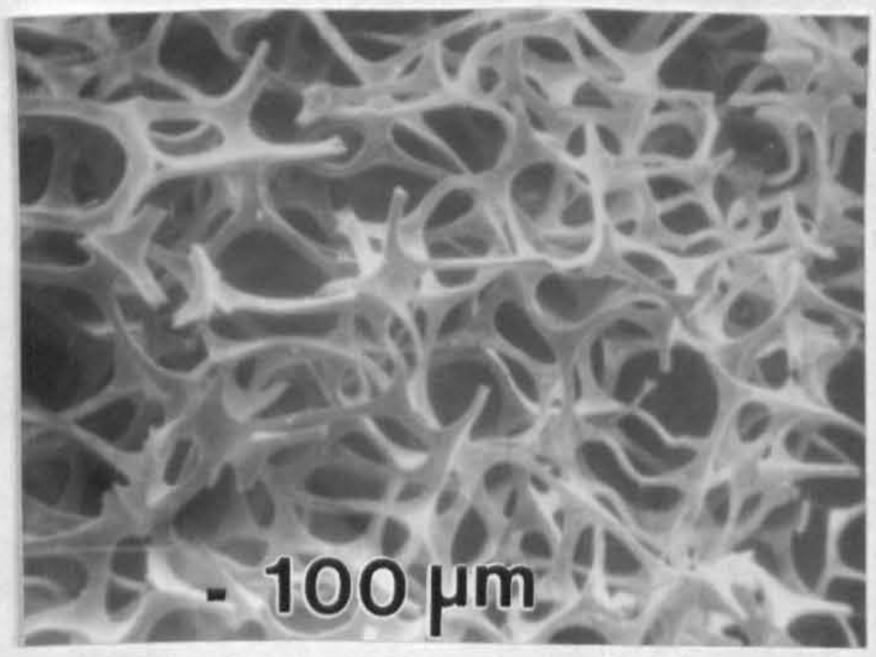

SEM x 40 (c) SEM x 1250

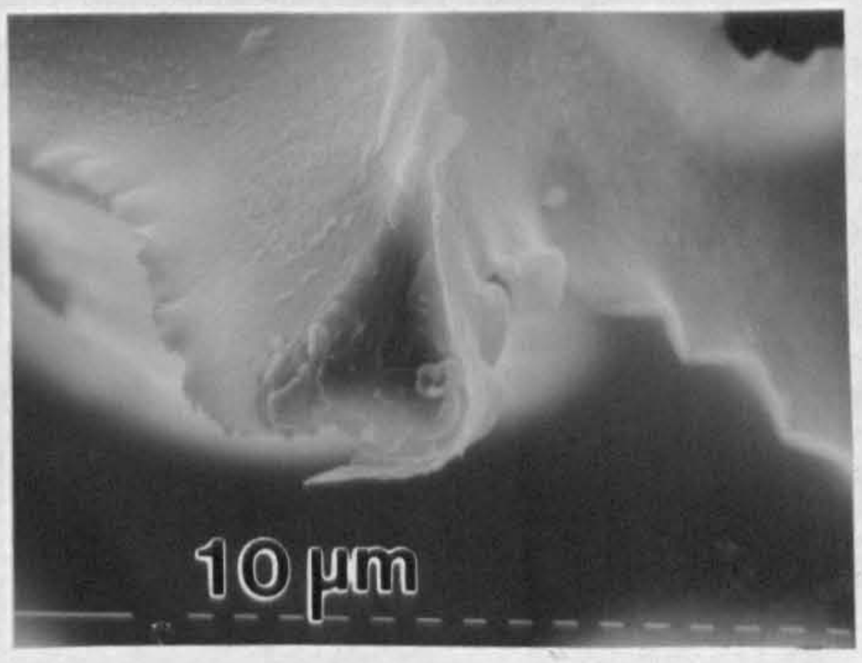

Fig. 4.13 The effects of the thinning process on the 60ppi closed-cell polyester urethane foam (PECC). (a) Conventional, as received foam. (b) Thinning for 20 min. (c) Thinning for 50 min.

The cell rib thickness can be measured from the SEM micrographs. The three pairs of photographs shown above are typical of the thinning process. Further photographs were also obtained and measured and gave the data for the thinning time versus the cell rib thickness plotted in *Figure* 4.14.

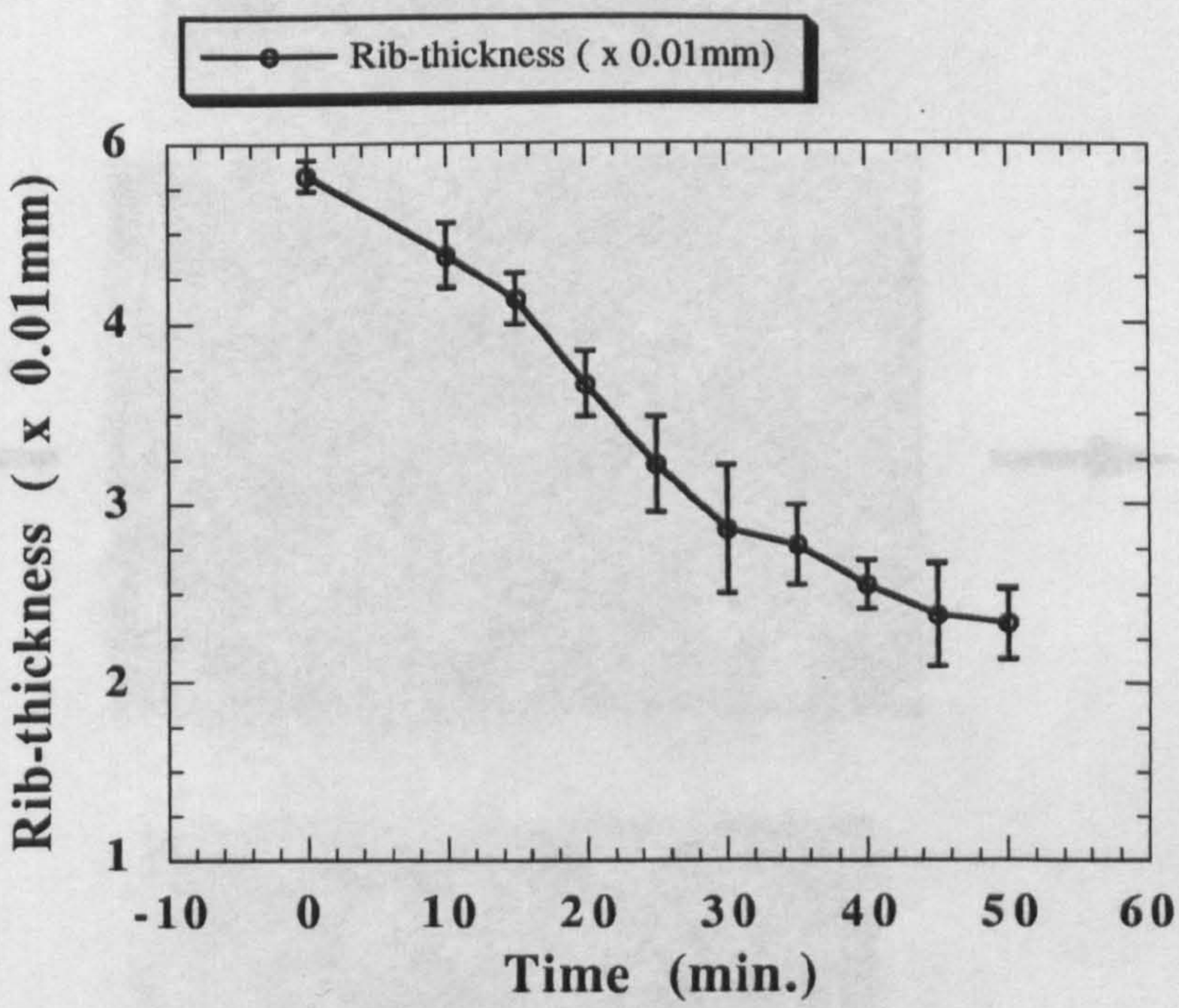

Fig. 4.14 Diagram of the cell rib thickness vs. the thinning time of the 60ppi closed-cell polyester urethane foam (PECC).

Figure 4.14 shows that the cell rib thickness is a function of the thinning time. The thinning process is affected by: the concentration of NaOH, the thinning time, the thinning temperature, and the properties of the cell ribs. An investigation on how the foam cell rib thickness may influence the mechanical property of the foam was carried out, and the results are given in Section 6.3.6.

4.6 Microscopic Examination of Foam Deformation

The deformation behaviour of the foam cell elements has been studied using a Wild M8 & MPS45 optical microscope (see Figure 4.3) for different modes of loading, i.e. tension, compression, and shear, using small specimens (dimensions, 40 x 10 x 5 mm). The investigation described here was carried out on the previously described PUR flexible foams. Various foam densities, cell sizes and cell shapes were studied.

4.6.1 Conventional Foam Deformation Under Tension

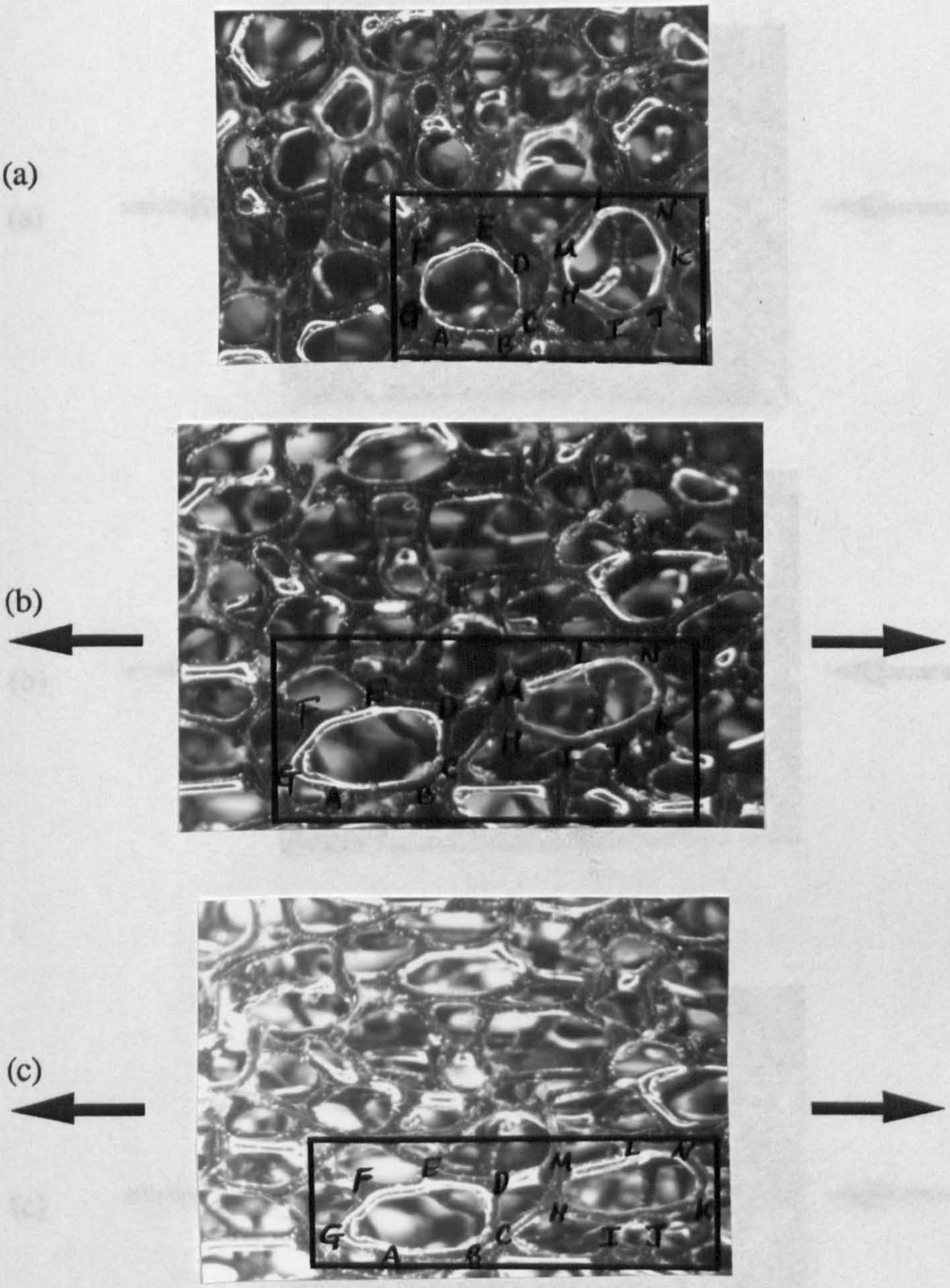

Fig. 4.15 The micrographs of the elastic tensile deformation of the 60ppi reticulated conventional polyester urethane foam (PECO) (note: looking at the foam along the y axis). Stretching, hinging and flexing of the cell ribs can be seen. The tensile strains are: (a) $\varepsilon_x = 0$ (b) $\varepsilon_x = 12\%$ (c) $\varepsilon_x = 25\%$

Under tensile loading (see Figure 4.15), the ribs AB and LN lying in the direction of the external force are stressed in tension. Failure occurs on reaching the limit of the tensile strength of the base material by the fracture of these ribs. Ribs FE, BC, ED, ML, NK, HI and IJ lying in the intermediate orientations of the applied force are stressed in bending, hinging and stretching, except for a small tensile loading, and consequently are exposed to combined normal, hinging and bending stresses. Ribs CD, FG, MN and KJ lying perpendicular to the applied force are either stressed in hinging or remain unstressed.

4.6.2 Conventional Foam Deformation Under Compression

(a)

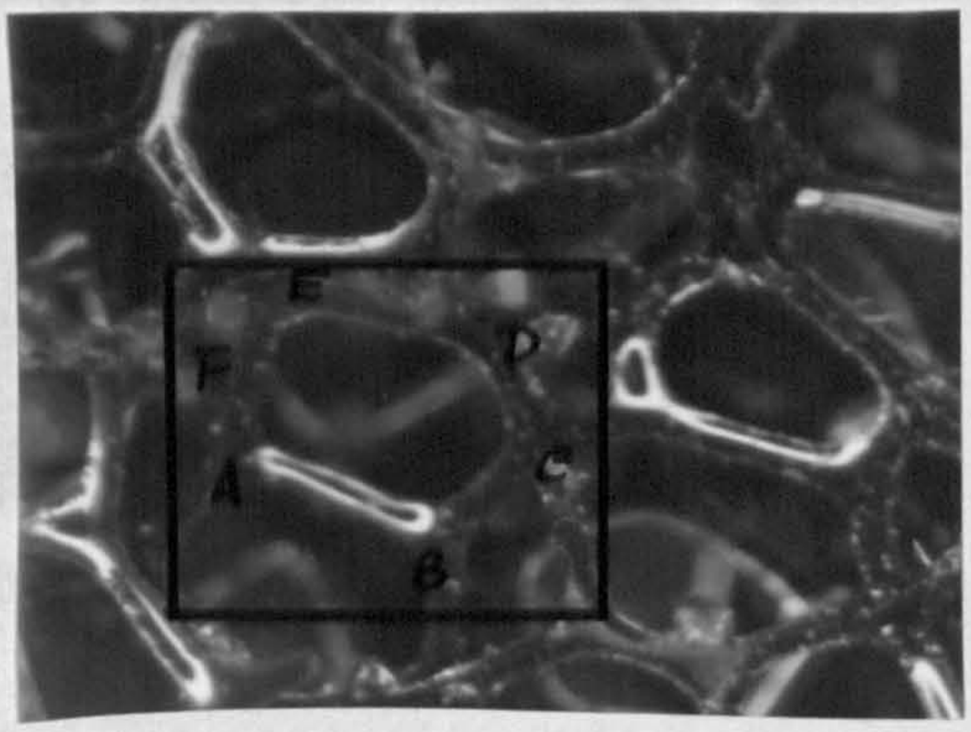

(b)

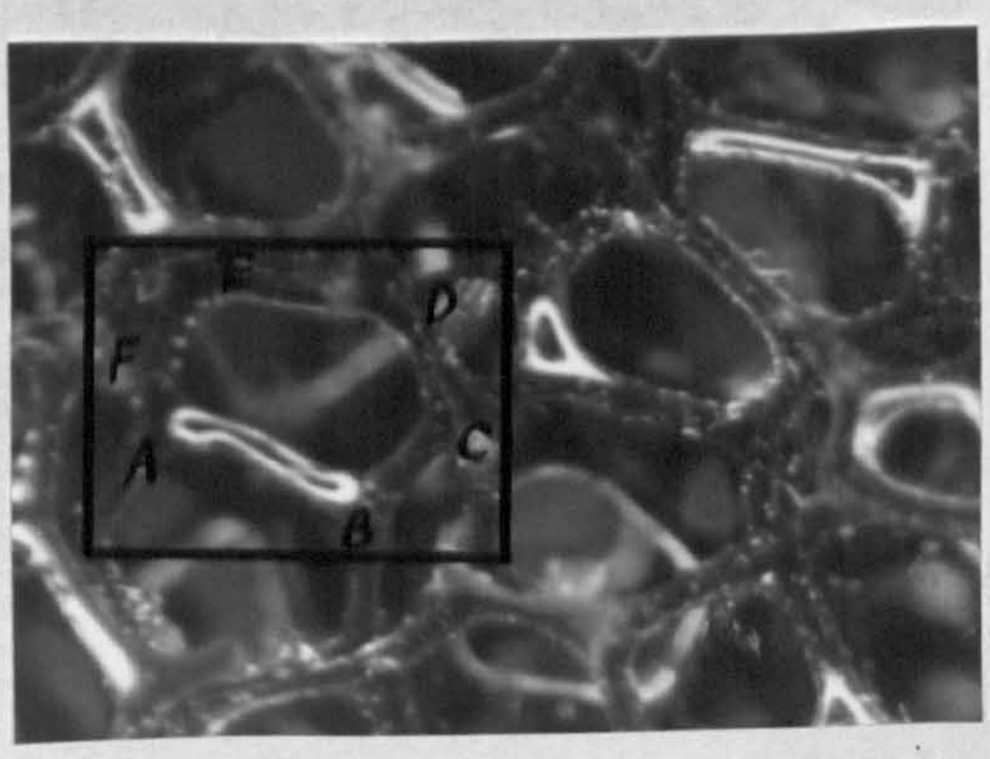

(c)

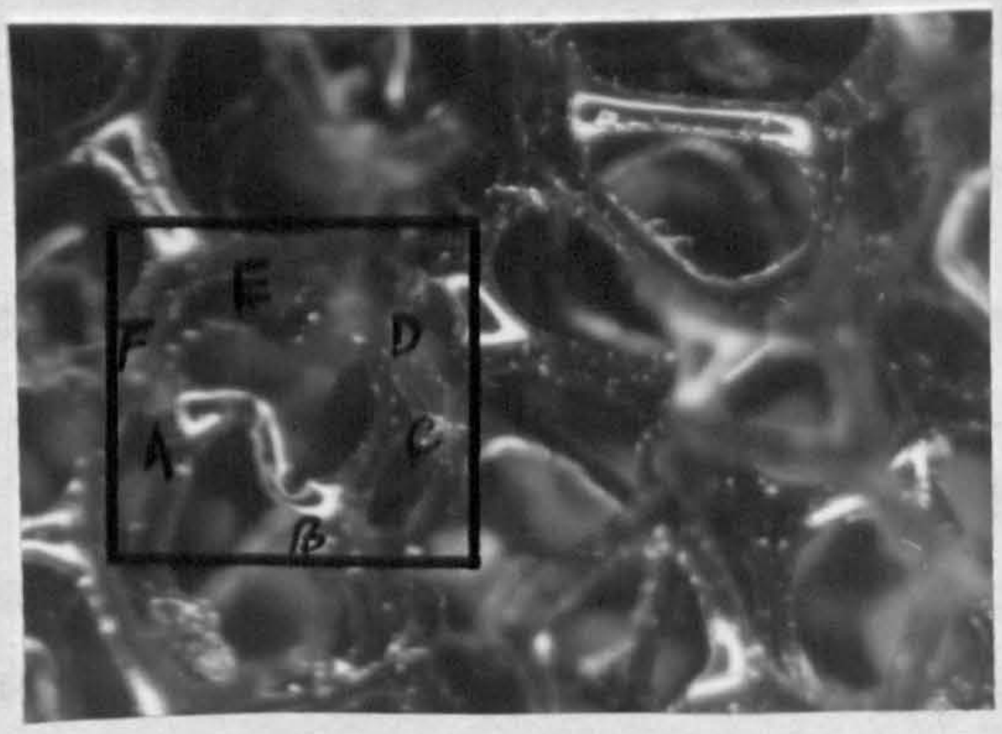

(d)

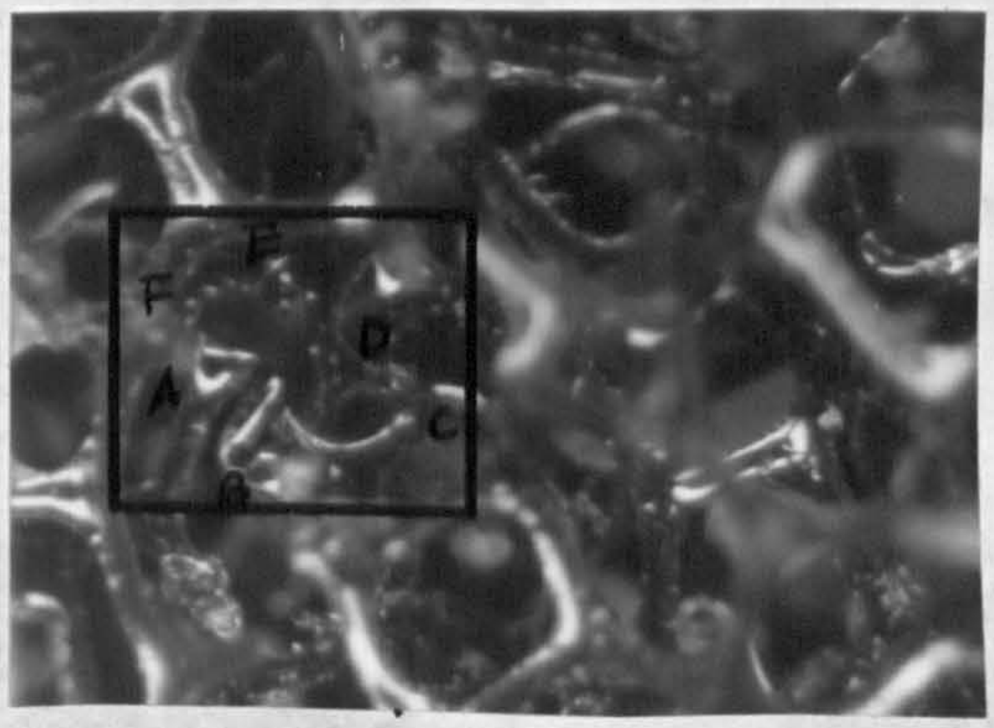

(e)

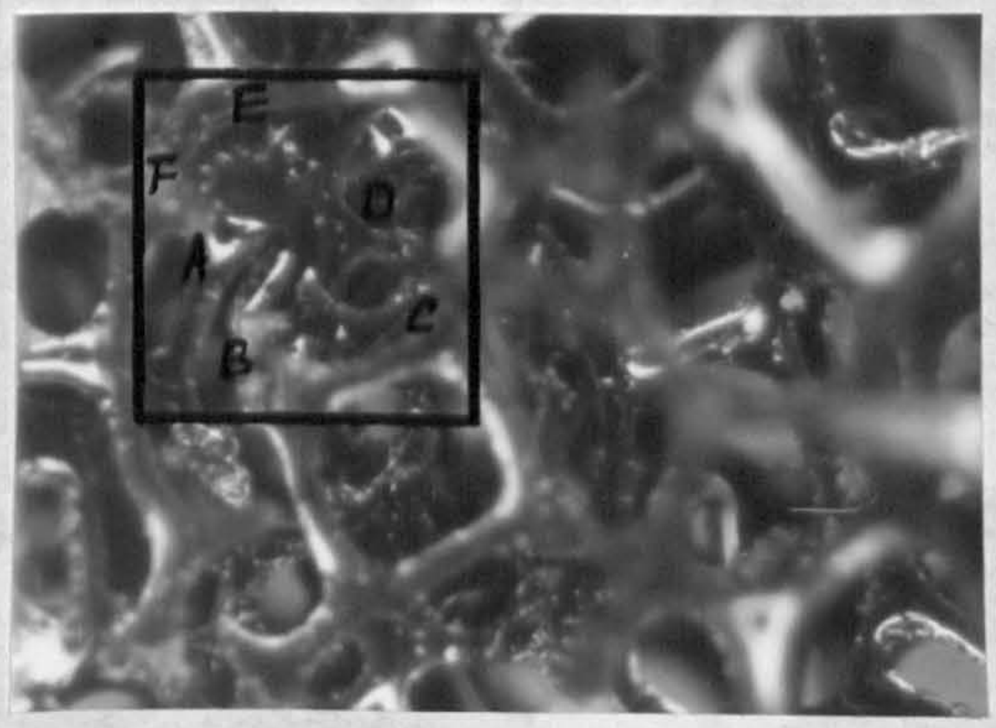

(f)

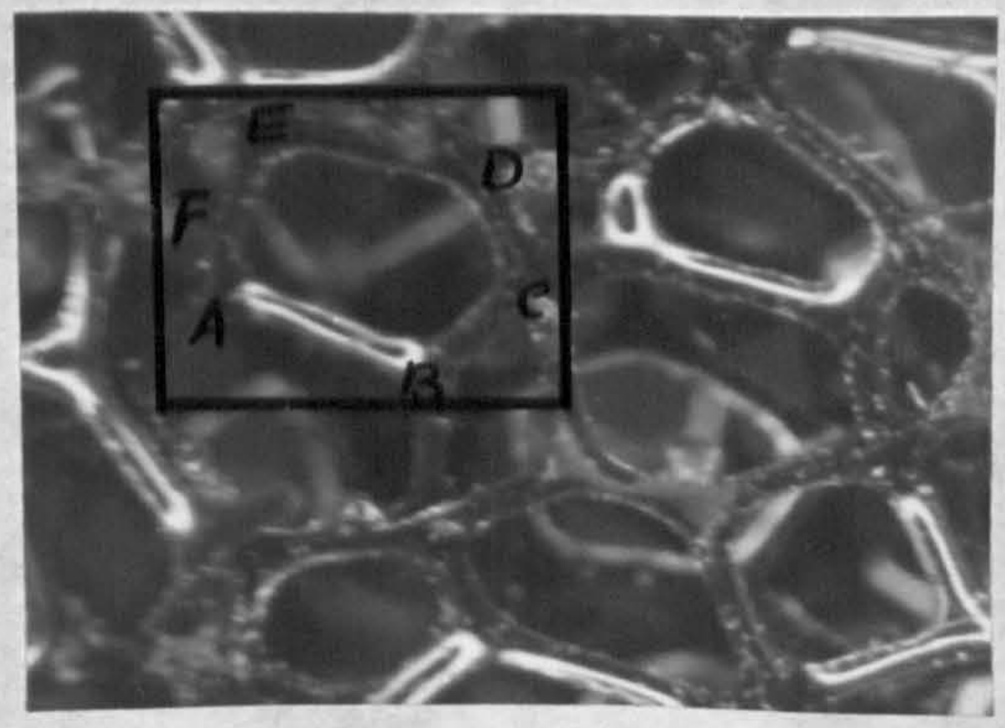

Fig. 4.16 Micrographs of the elastic compressive deformation of the 60ppi reticulated conventional polyester urethane foam (PECO) (note: looking at the foam along the y axis). The compressive strains are: (a) $\varepsilon_y = 0\%$ (b) $\varepsilon_y = 3\%$ (cell ribs bending) (c) $\varepsilon_y = 10\%$ (cell rib buckling) (d) $\varepsilon_y = 20\%$ (cell rib collapse) (e) $\varepsilon_y = 40\%$ (elastic densification occurs) (f) $\varepsilon_y = 0\%$ (restored to its original shape). Note: the load axis is the same as tension but of opposite sign.

For compression loading (see Figure 4.16), the stressing of individual ribs is similar to the case of tensile loading but of opposite sign. Flexure is the dominant mechanism. Here failure occurs in those ribs (e.g. rib AB) which lie in the intermediate orientations of the external loading. However, when investigating low density foams at large strains this happens before the limit of material strength is reached because of buckling of the cell ribs. Ribs lying in the direction or vertical to

the direction of the external loading (e.g. ribs CD and EF) are either stressed in pressing or remain unstressed. Three modes of deformation corresponding to the different buckling situations described by Euler (1746) were observed for ribs stressed only in compression.

4.6.3 Shearing of Conventional Foam

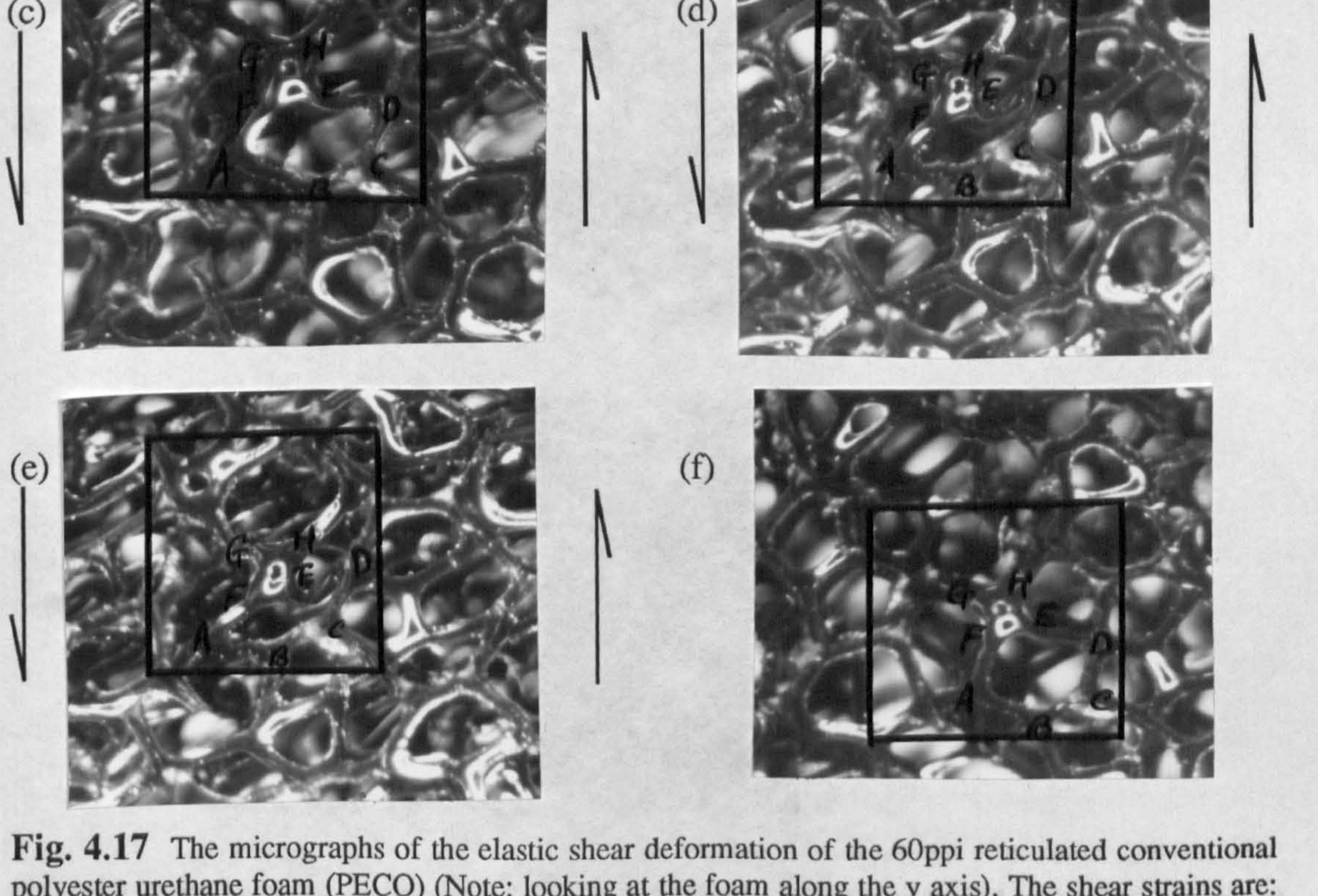

Fig. 4.17 The micrographs of the elastic shear deformation of the 60ppi reticulated conventional polyester urethane foam (PECO) (Note: looking at the foam along the y axis). The shear strains are: (a) 0% (b) 10% (c) 20% (d) 30% (e) 35% (f) 0% (resorted to its original shape).

Under shear loading (see Figure 4.17), the rib stresses may be normal stresses, bending stresses or hinging stress or a combination of the three. In this case the critical stresses for non-linear foam deformation is therefore due to a combination of stretching, hingeing and buckling. Failure then occurs because of buckling of those ribs that lie at an angle of about 45^0 to the direction of the external load (e.g. ribs AB

and ED). At higher loads, rib fracture starts to occur. *Figure* 4.17 shows a shear loaded conventional foam at different stages of deformation. It can clearly be seen that the very thin cell ribs buckle and wrinkle under small deformations. The cell in the ~~red~~ black frame rotates clockwise. The deformation under shear loading occurs in those ribs which are loaded in compression and that eventually, at large deformations, the ribs will break.

4.6.4 Auxetic Foams Under Axial Loading Conditions

Under tensile loading (see Figure 4.18), The main deformation mode of auxetic foam is hinging (e.g. ribs AB and DC). Ribs lying perpendicular to the applied force remain unstressed (e.g. rib BC). The cell expands transversely under a longitudinal tensile force.

(a)

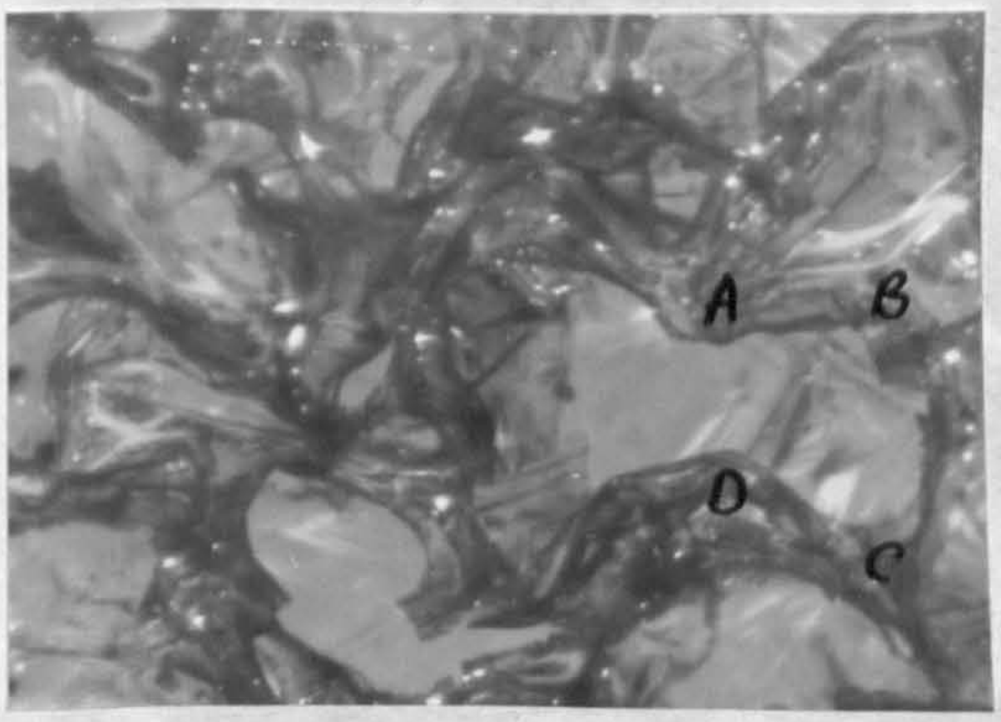

(b)

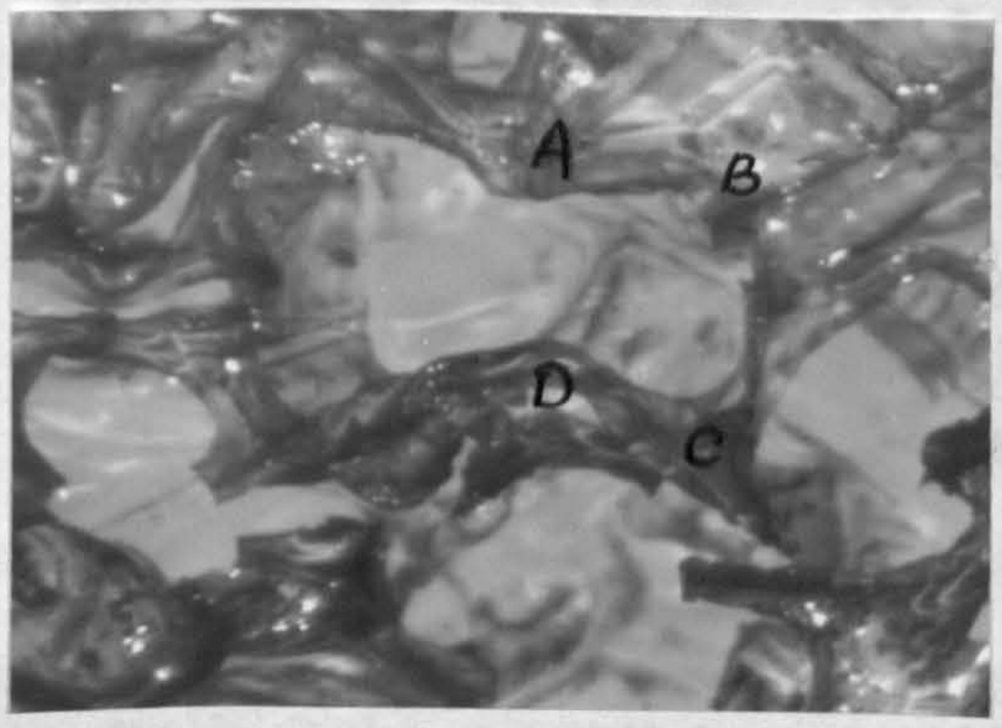

Fig. 4.18 Micrographs showing the elastic deformation of the 60ppi closed-cell auxetic polyester polyurethane foam (PEAC). (a) Unloaded. (b) Under tension.

(a)

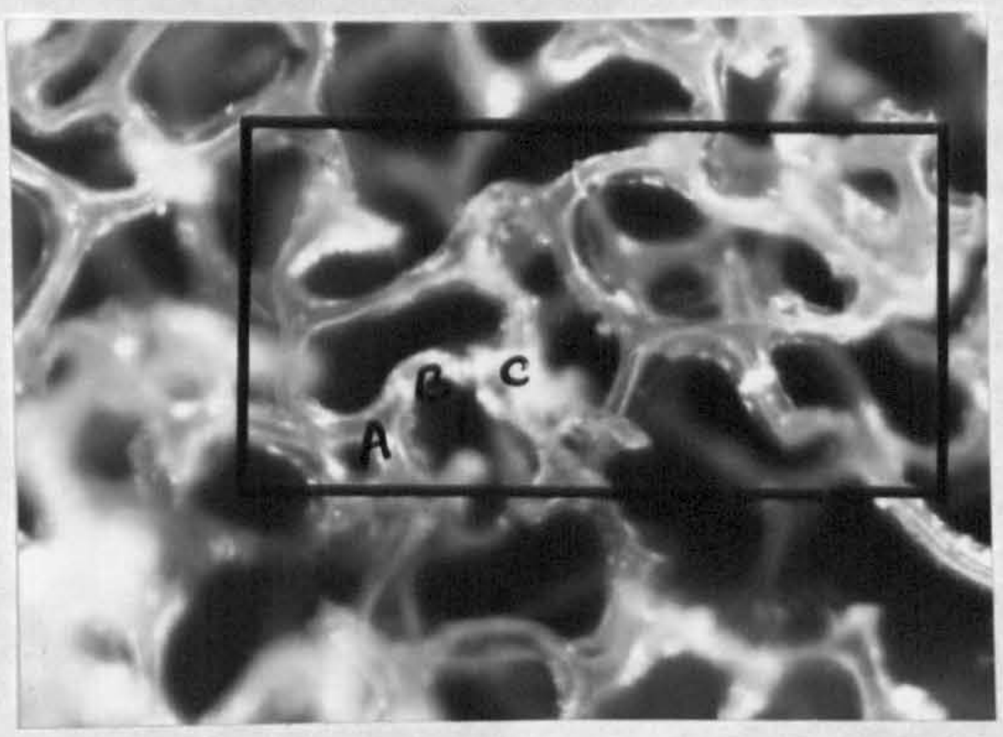

(b)

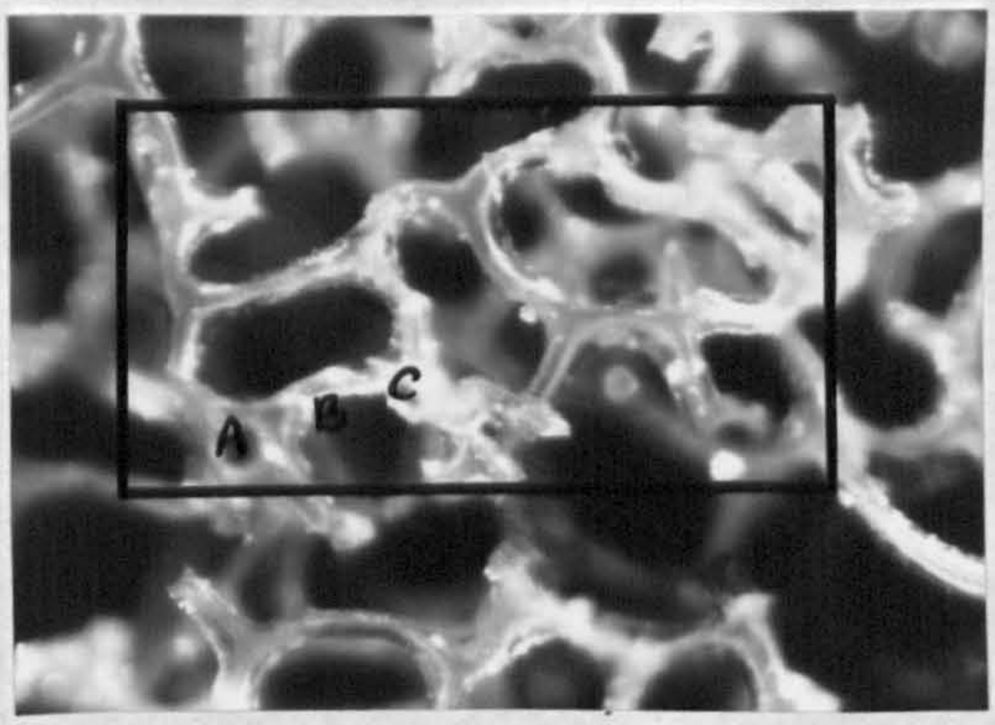

Under tensile loading, the buckled rib ABC almost 'restored' to its original undeformed length.

(c)

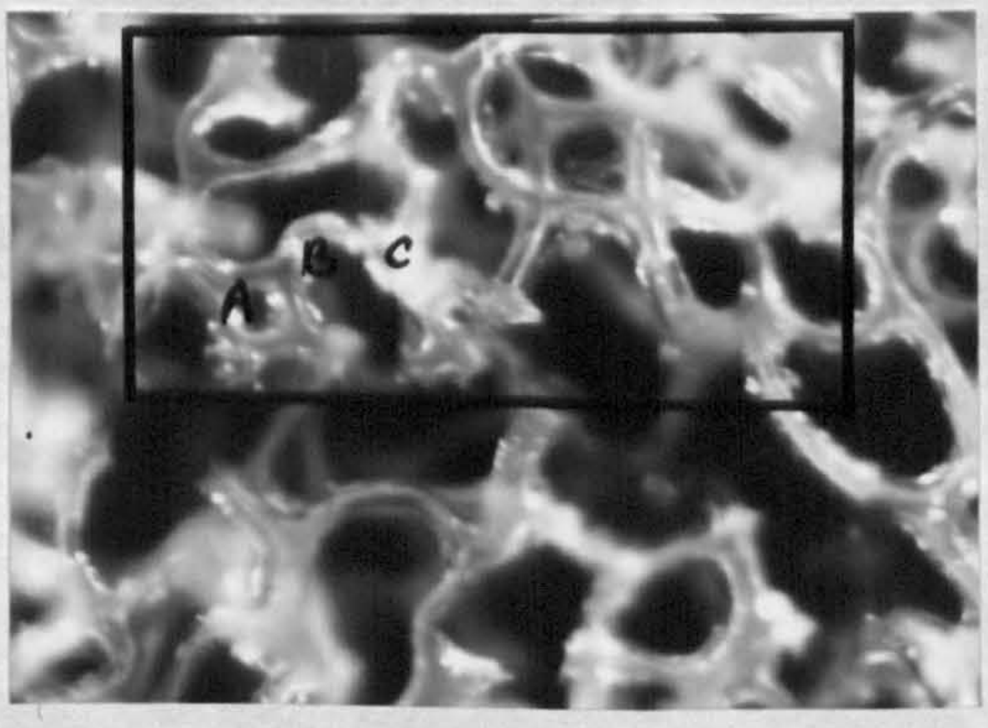

For compression loading, the buckled rib ABC buckled even further.

Fig. 4.19 Micrographs showing the elastic deformation of the 60ppi reticulated auxetic polyester polyurethane foam (PEAO). (a) Unloaded (b) Under tension (c) Under compression.

Figures 4.18 and 4.19 show that the deformation mechanism of an auxetic foam is the same as that for a conventional foam. But, because an auxetic foam cell has a concave cell shape, it therefore becomes thinner in the transverse direction in compression, and becomes fatter in tension. A conventional foam cell with a convex cell shape expands in the transverse direction under compression, but shrinks under tension. In this investigation, the specimens are elastic materials, and can therefore recover from their deformations after the deforming forces have been removed.

4.6.5 Shearing an Auxetic Foam

Figure 4.20 shows a shear loaded auxetic foam at different stages of deformation. The series of illustrations show the possible deformation modes, i.e. bending, stretching, hinging, and indicate clearly that rotation does exist.

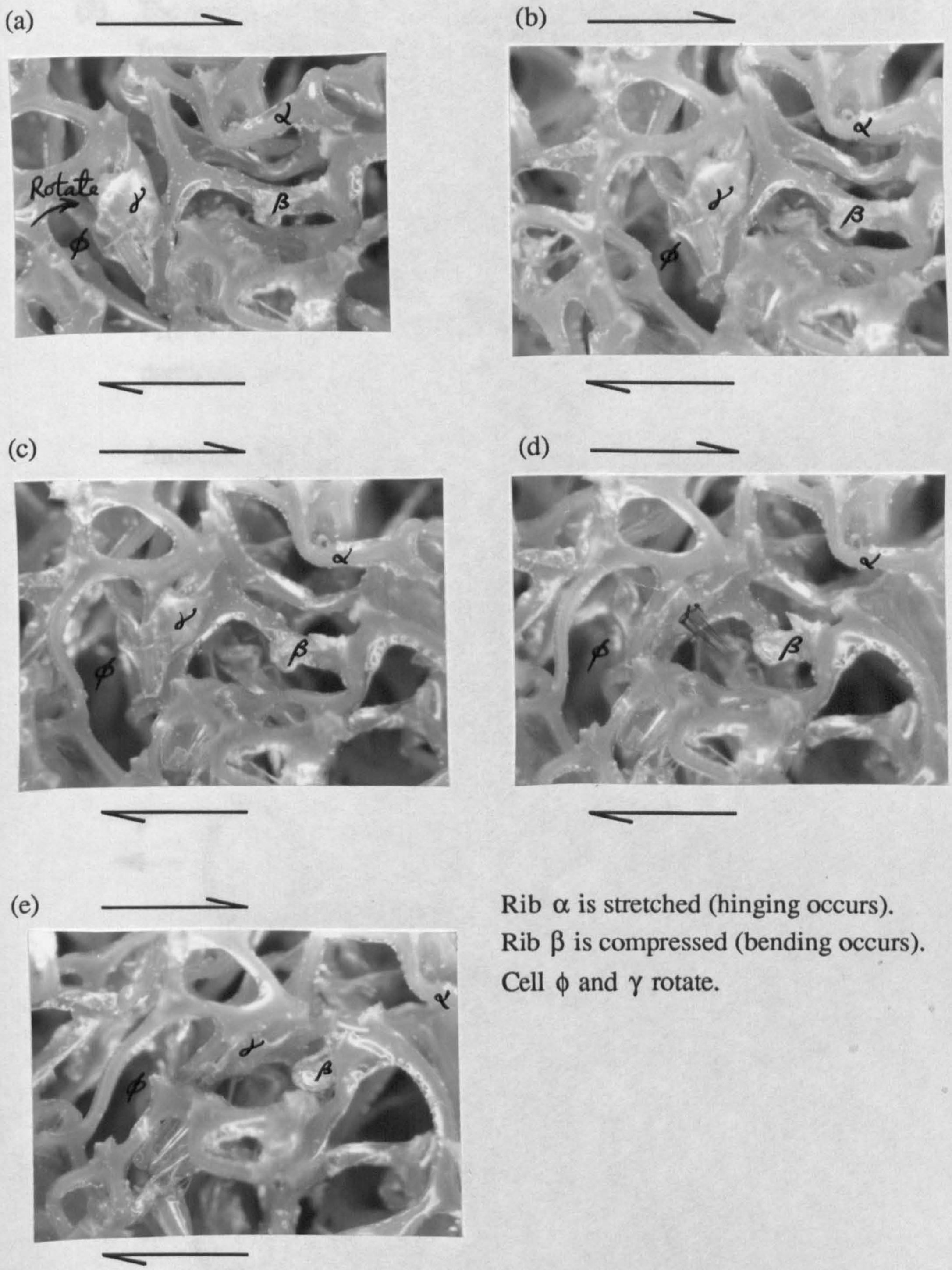

Rib α is stretched (hinging occurs).
Rib β is compressed (bending occurs).
Cell ϕ and γ rotate.

Fig. 4.20 Micrographs of the elastic deformation of the 10ppi reticulated auxetic polyether polyurethane foam (70AO). The shear strains are: (a) 0% (b) 10% (c) 20% (d) 30% (e) 40% .

4.7 Comparison of an Auxetic Foam and its Parent Conventional Foam

(1) Auxetic foam has a re-entrant cell shape, whereas conventional foam has a convex cell shape.

(2) The density of auxetic foam is much higher than its parent conventional foam.

(3) Auxetic foam shrinks under compression and expands under tension, but conventional foam shrinks under tension and expands under compression.

(5) Summary of the dominant deformation mechanisms.
Flexure, hinging and stretching all occur when the foam deforms, but
- for tension, hinging and stretching are the dominant mechanisms.
- for compression, flexure is the dominant mechanism.
- for shear, the cell rotates while the ribs are deforming. Flexure is the dominant mechanism.

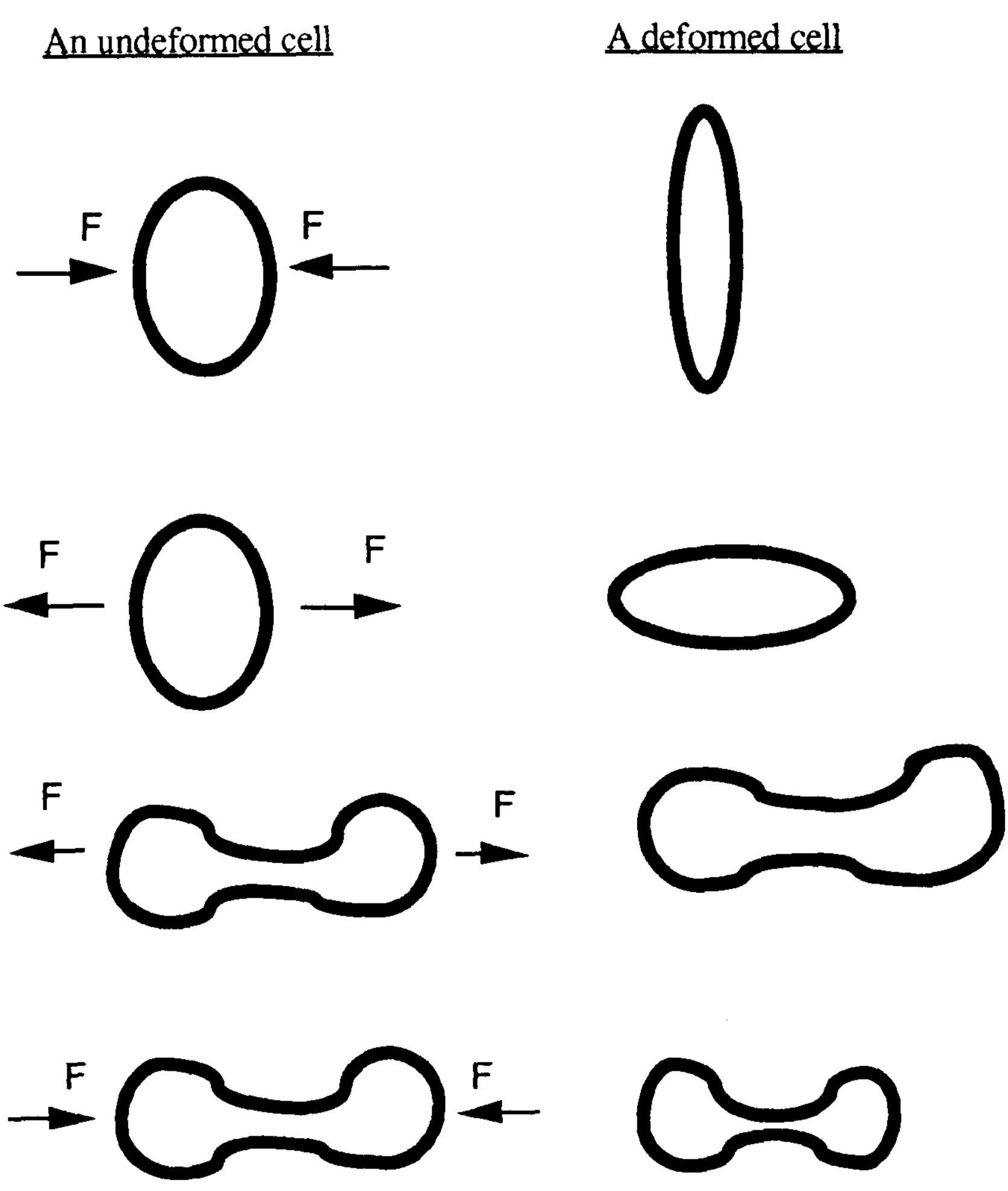

Fig. 4.21 Schematic diagram of the deformation of the foam cell under tension and compression.

Chapter 5 Theoretical Models for the Deformation of Foams

5.1 Introduction

The geometry of foams is very complicated, so in order to identify and analyse the mechanisms by which a foam deforms, we model the foam as a simple, three dimensional array of symmetrical cells. From this model we can derive the elastic moduli (e.g. tensile modulus, compression modulus, Poisson's ratio and shear modulus) for ideal three dimensional cellular foams.

The first stage in the development of a model requires us to choose the appropriate cell geometry to include in our model. Real cells in foams are neither cubical or hexagonal, they are on average tetrakaidecahedral (Thompson, 1961). Cells within the foam pack themselves to fill space and, because of surface tension requirements, try to minimize their surface area for a given volume. As the number of faces on a polyhedron increase it more closely resembles an ellipsoid, and the ratio of surface area to volume decreases (Gibson and Ashby, 1988). The microstructure of the foam has been presented in chapter 4, where it was seen that the pentagonal dodecahedron and the tetrakaidecahedron both pack to fill space, with the tetrakaidecahedra having a slightly lower surface area to volume ratio. A box-like cell model (Gent and Thomas, 1960; Kanakkanatt, 1973; and Hilyard, 1982) or a model of spheres connected by many thin bars (Lederman, 1971) does not represent the real foam structure well. Also, these two cell models tempt the researchers to use stretching as the dominant deformation mechanism in their analyses. Huber and Gibson (1988), and Gibson and Ashby (1982,1988) understand the importance of the bending mechanism but they stop short of providing a detailed mechanical analysis of the problem because of the oversimplified cell geometry (a cubic box).

To theoretically analyse the deformations of foam, we need to find suitable theoretical models for both conventional foam which has a convex cell shape, and re-entrant foam which has a concave cell structure. At the simplest level, we may consider the foam as an array of three dimensional elongated rhombic dodecahedron cells as shown in *Figure 5.1*. This model also enables anisotropy to be modelled. In this chapter, I calculate theoretically the mechanical properties of an open-cell foam by analysing a representative unit cell. I obtain the local forces acting on each rib of the cells from the external stress and derive the local deformation at the unit cell level. Then, the external strain is calculated from the local deformation, giving the global stress-strain response. The linear elastic deformation is analysed using classical beam theory. Finally, a set of moduli are derived in terms of the solid property (e.g. E_s), and

the geometric factors of the foam (e.g. t/L and θ, see *Figure* 5.1). In this chapter, my aim is to develop a general combined model to represent the modes of deformation observed in foam.

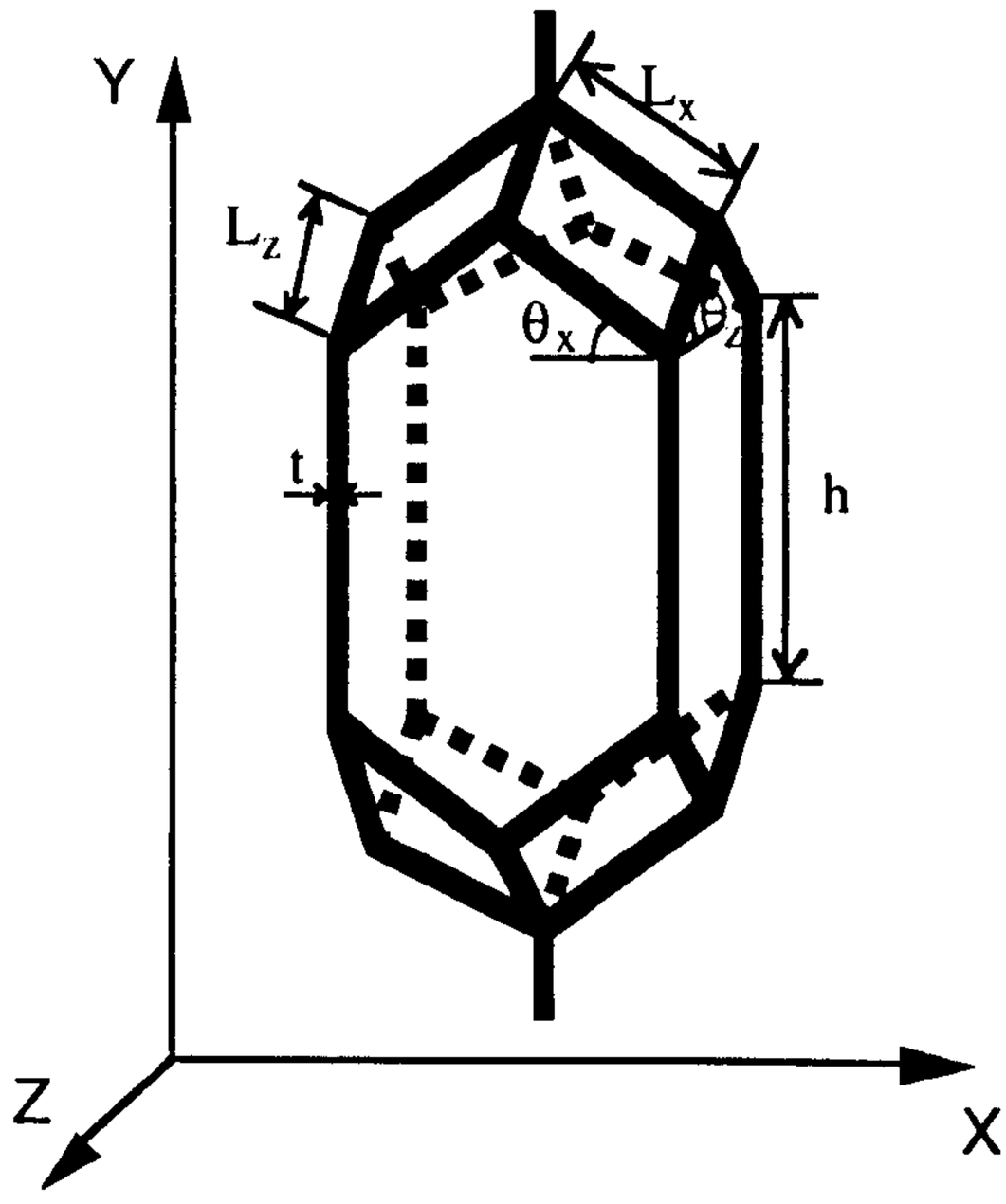

(a)

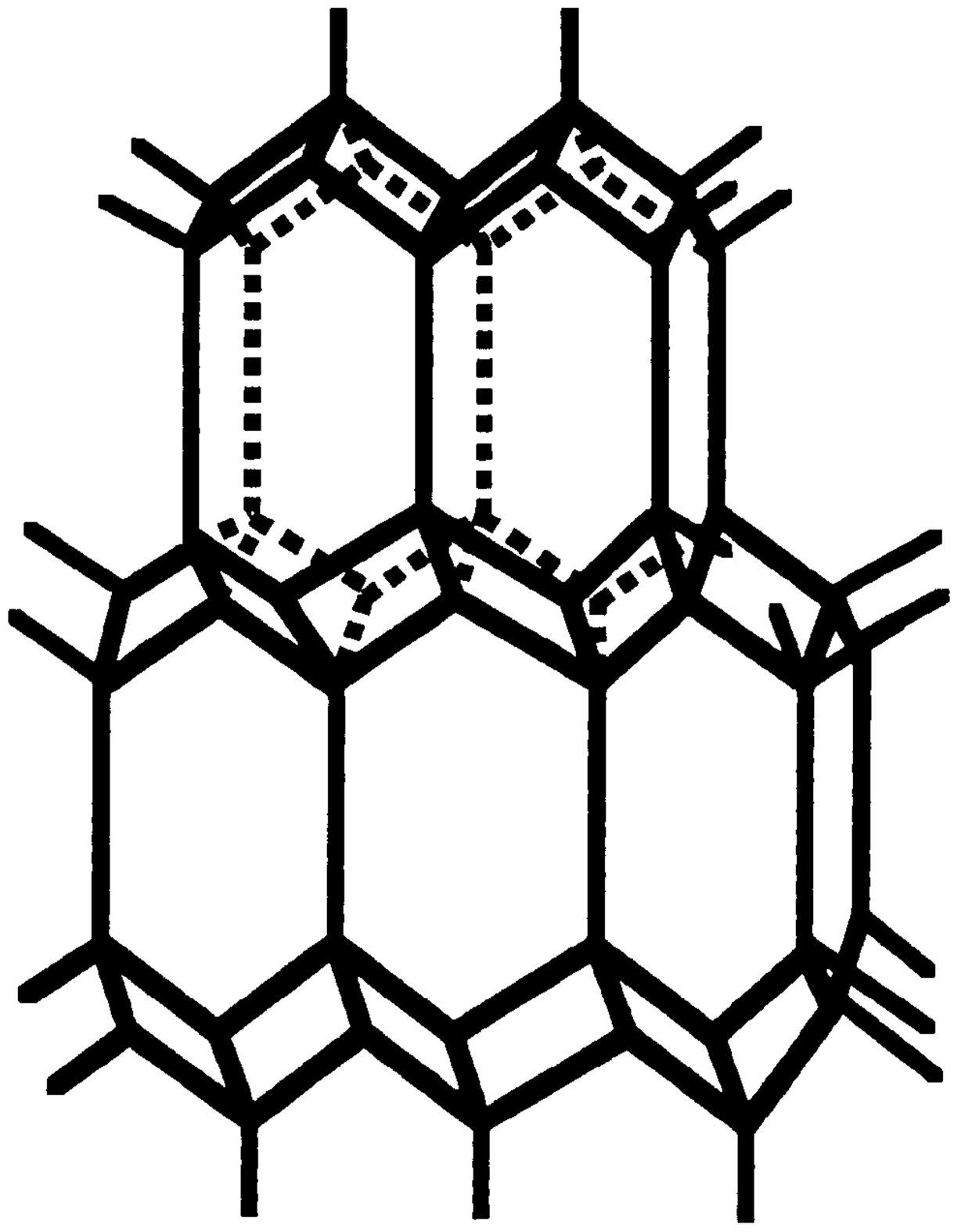

(b)

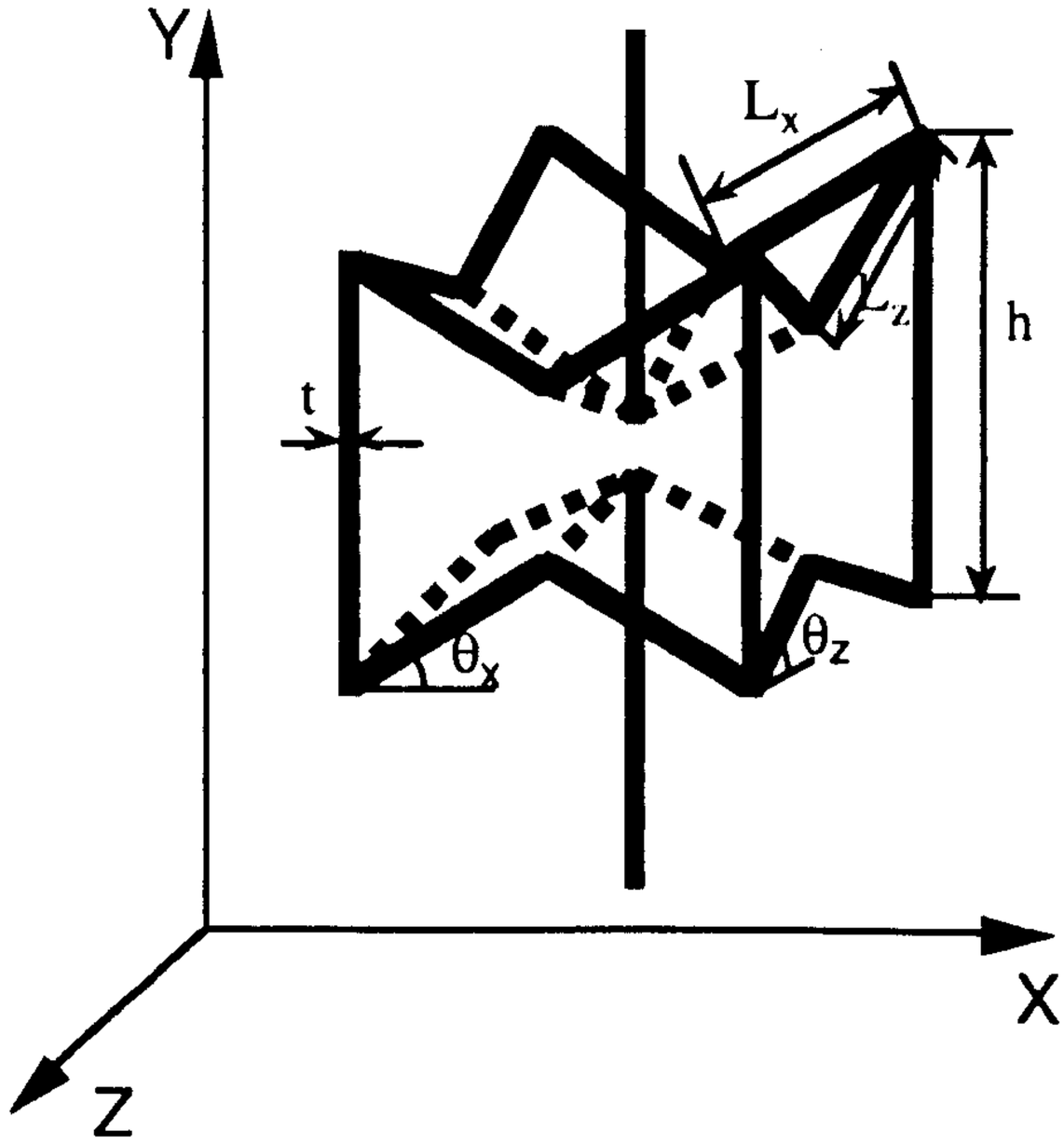

(c)

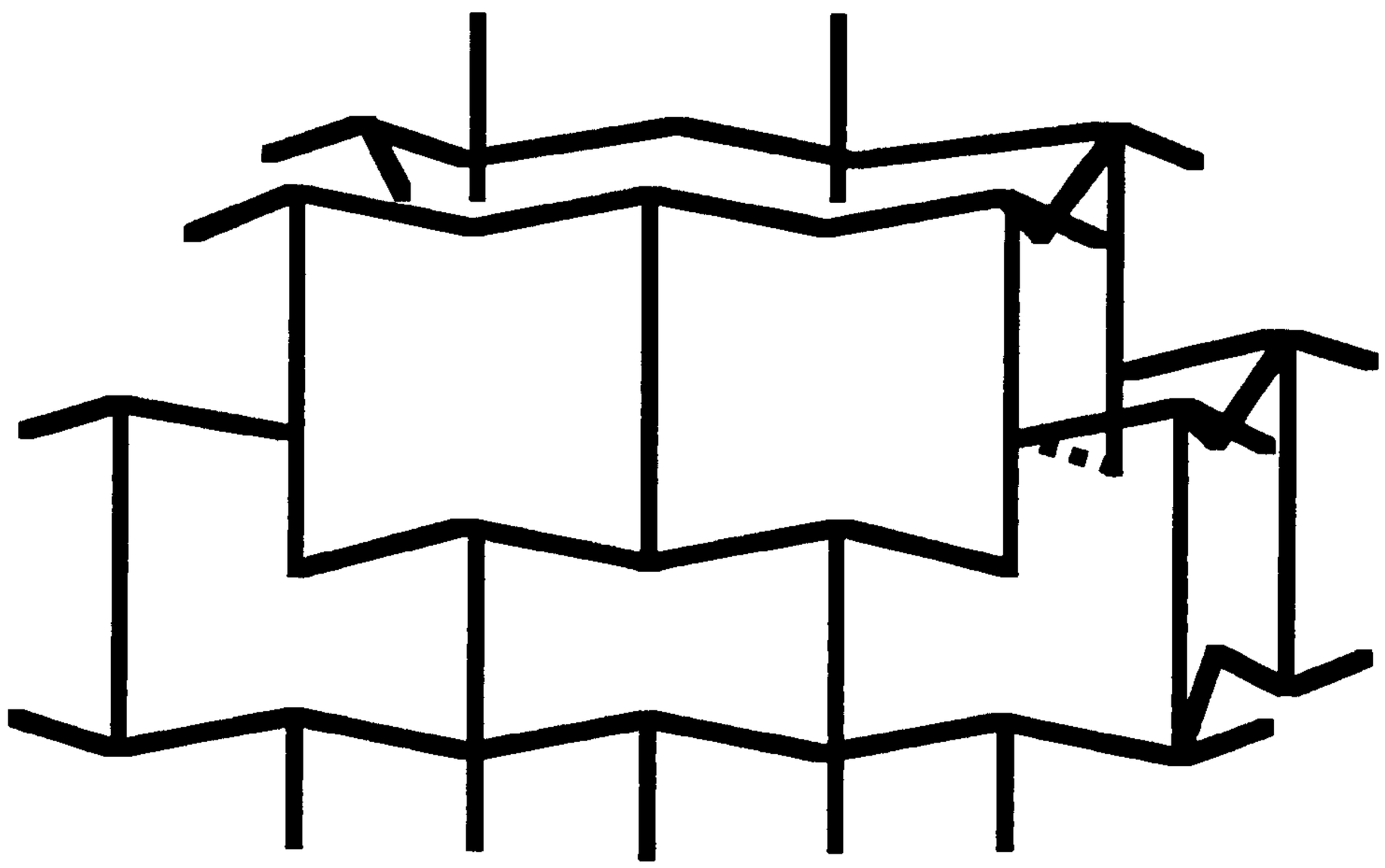

(d)

Fig. 5.1 (a) One single elongated rhombic dodecahedron cell model of conventional foam. (b) An array of elongated rhombic dodecahedron cells of conventional foam. (c) One single elongated rhombic dodecahedron cell model of auxetic foam. (d) An array of elongated rhombic dodecahedron cells of auxetic foam.

5.2 Anisotropic Elongated Rhombic Dodecahedron Cells Geometry

The projections of the three dimensional rhombic dodecahedron cell onto the reference axis planes are illustrated in *Figure 5.2, 5.3 and 5.4*.

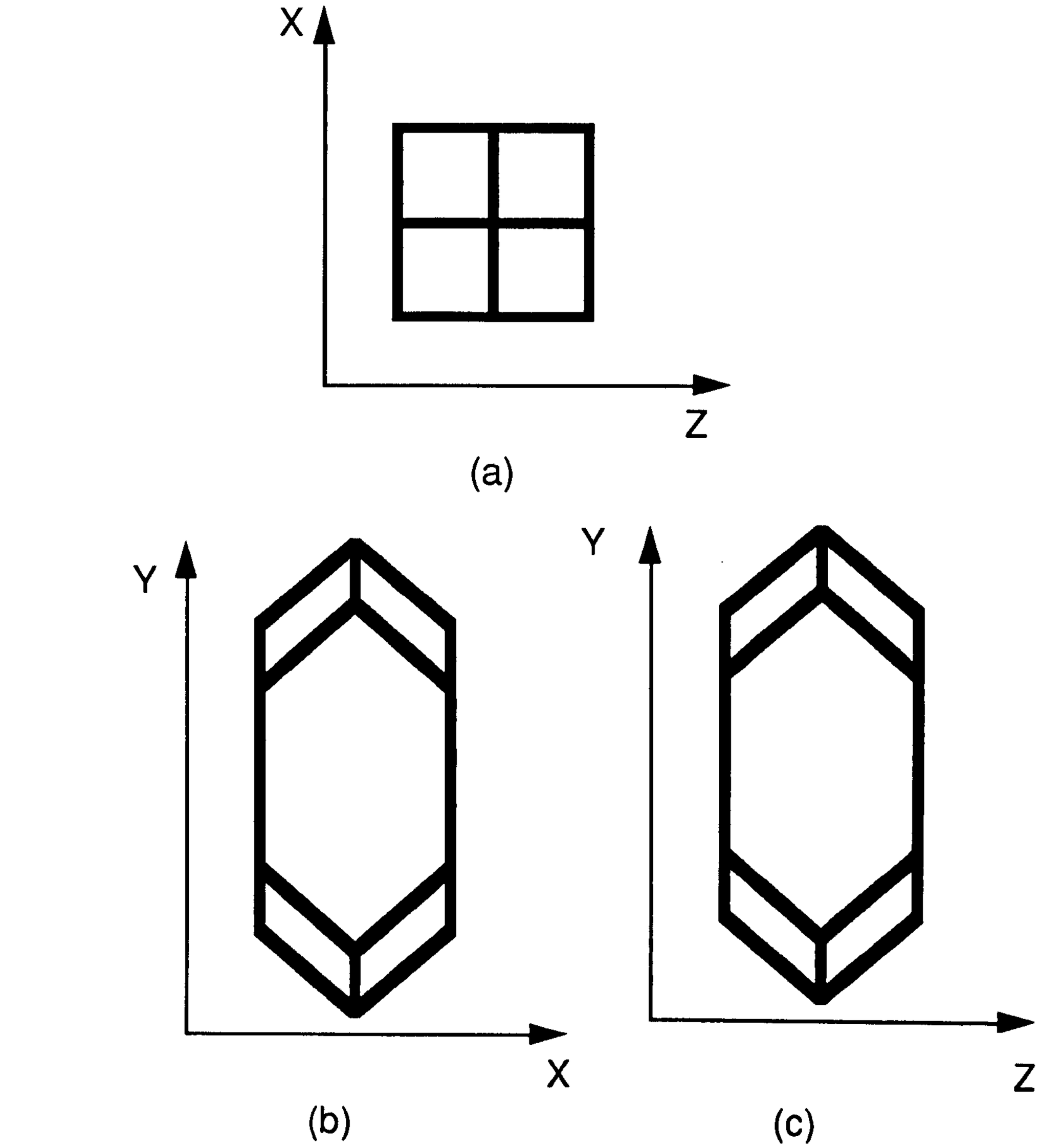

Fig. 5.2 Conventional foam cell model (a) Projection onto the x-z plane. (b) Projection onto the x-y plane. (c) Projection onto the y-z plane.

By changing the angle of the angled ribs from positive to negative, we can convert the conventional foam cell into an auxetic foam cell having a re-entrant cell shape as shown in *Figure 5.3*.

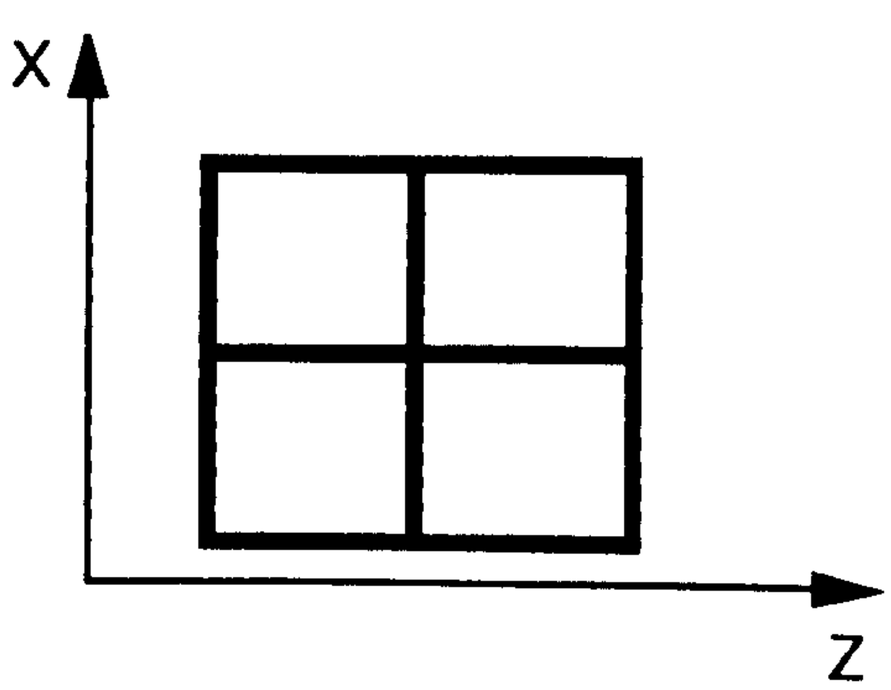

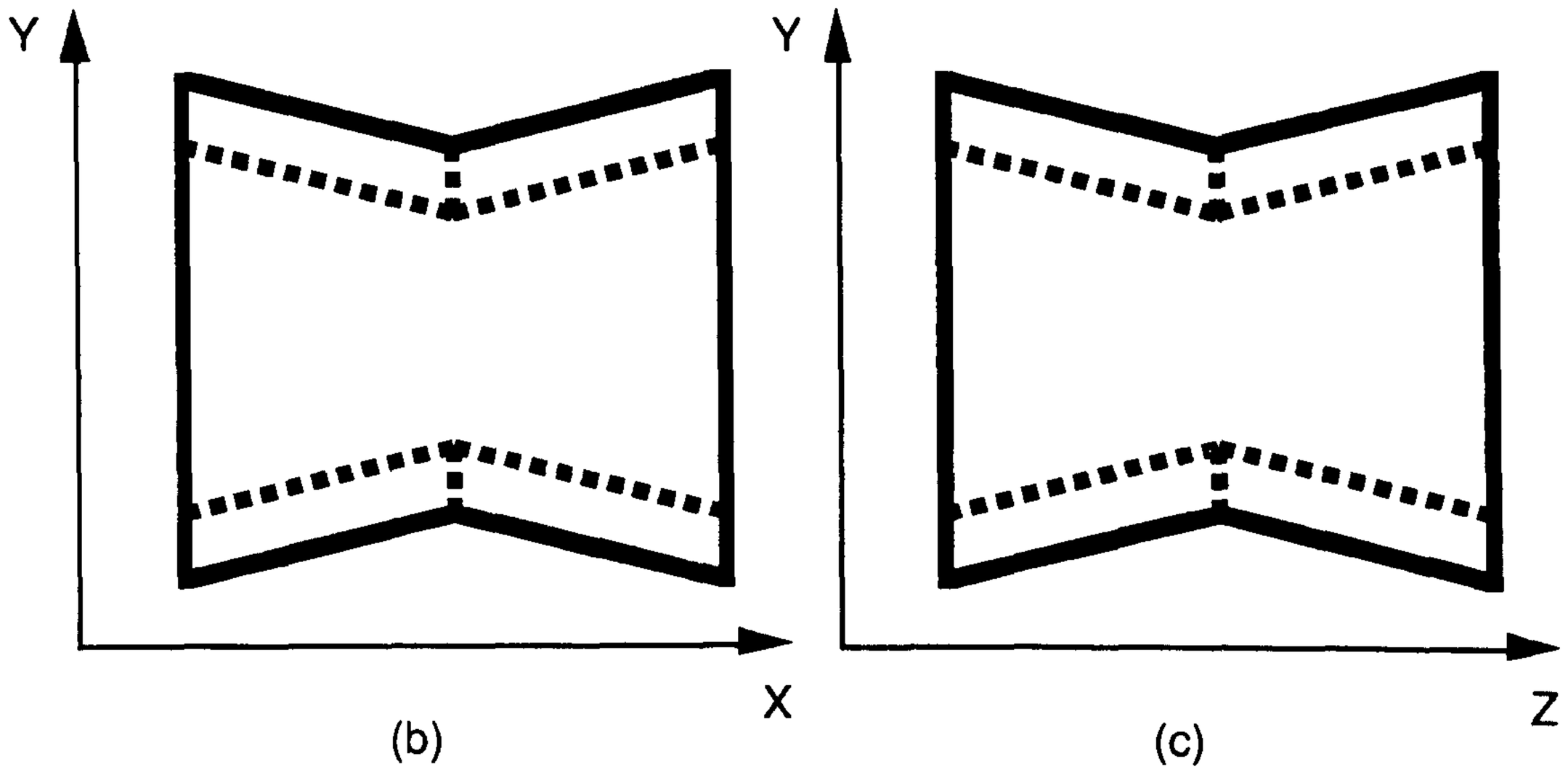

Fig. 5.3 Auxetic foam cell model (a) Projection onto the x-z plane. (b) Projection onto the x-y plane. (c) Projection onto the y-z plane.

Figure 5.4 describes projections which show how the conventional and re-entrant elongated rhombic dodecahedron cells are connected into three dimensional arrays to form a foam network microstructure.

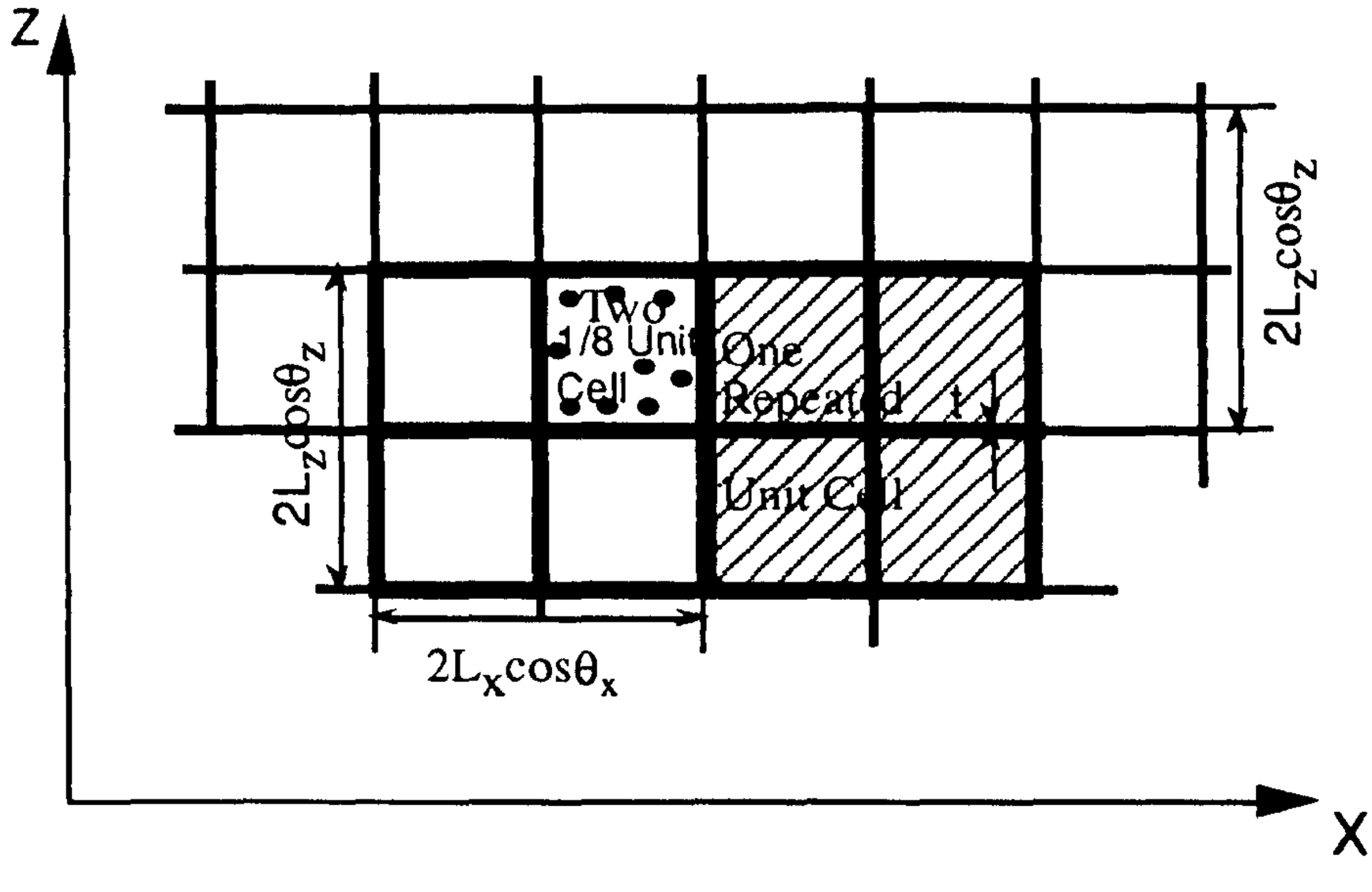

Fig. 5.4 A simple array of the three dimensional cells. (a) Projection onto the x-z plane, same for both conventional and re-entrant cell networks. (b) Projection onto the x-y plane for the conventional cell network. (c) Projection onto the x-y plane for the re-entrant cell network.

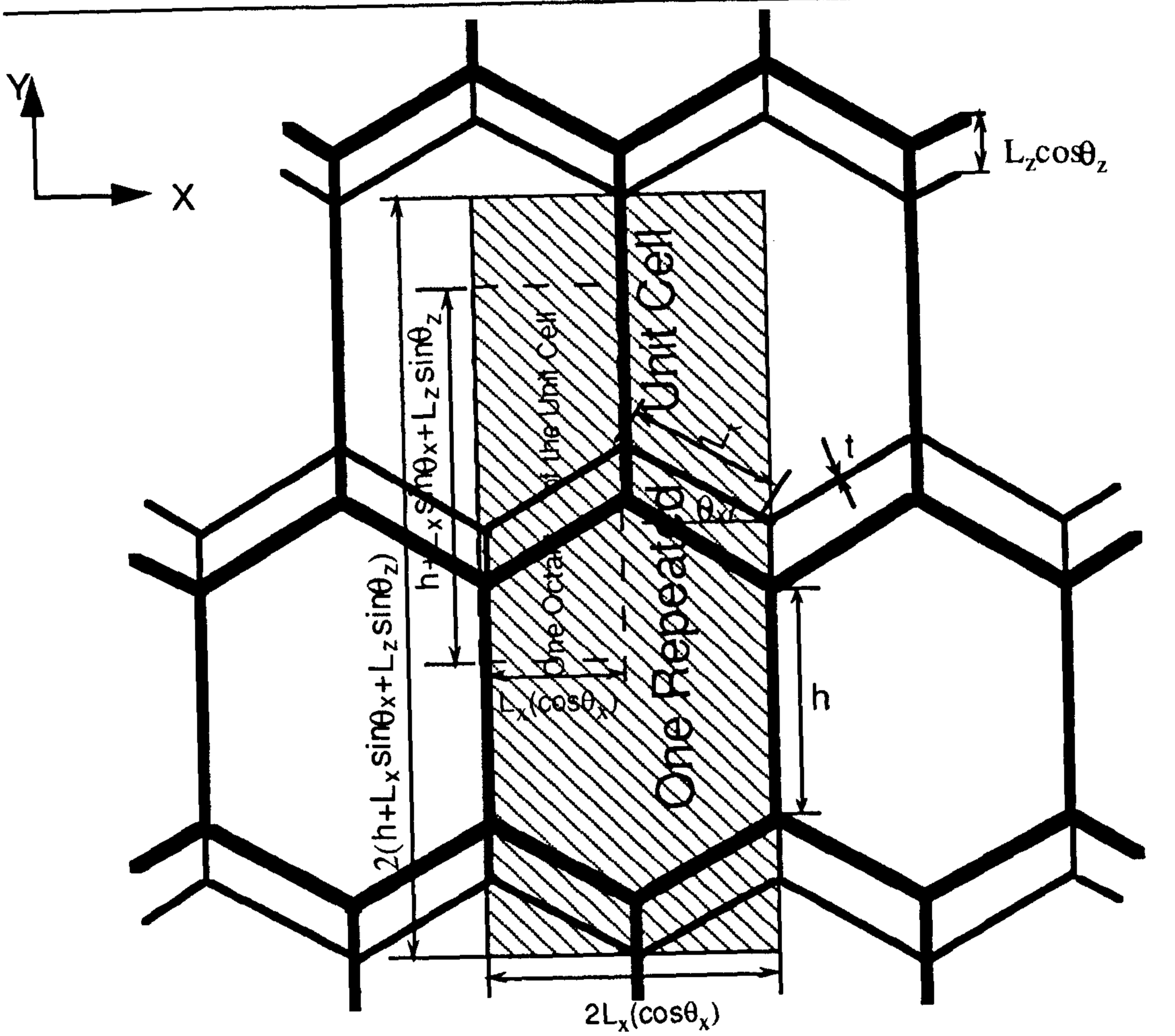

Fig.5.4(b)

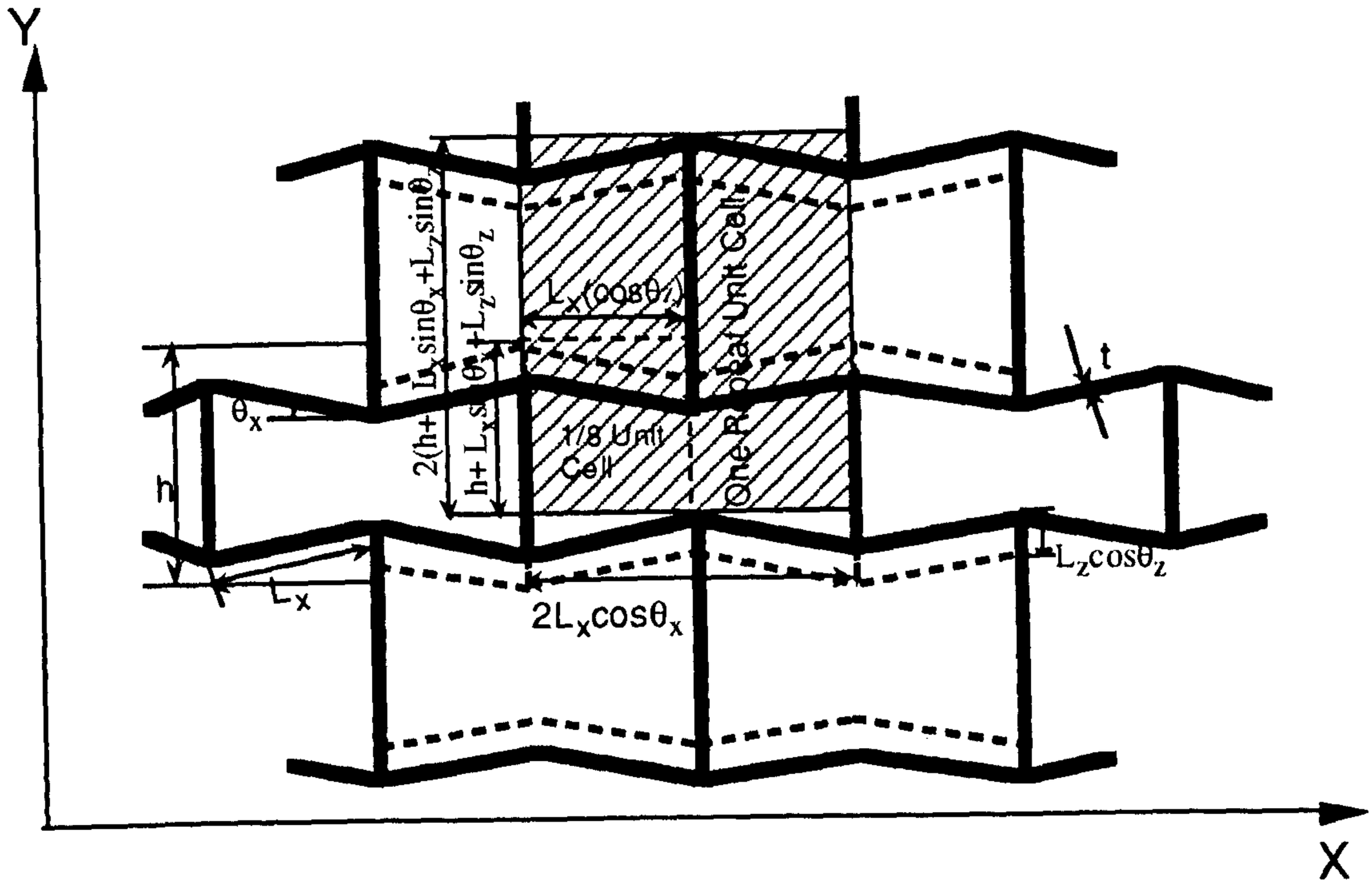

Fig.5.4(c)

The repeat unit cells for the conventional and re-entrant cell networks are also indicated in *Figure 5.4* (shaded area). In order to model the mechanical properties of foam networks it is necessary to understand the deformation of the repeat unit-cell in response to the deformation of the foams.

In *Section*s 5.3 to 5.6 the deformation of a foam network due to flexure, hinging and stretching of the ribs is modelled by considering one octant of the unit-cell for conventional and re-entrant geometric cells (see *Figure 5.5* and *Figure* 5.4 dashed outlines).

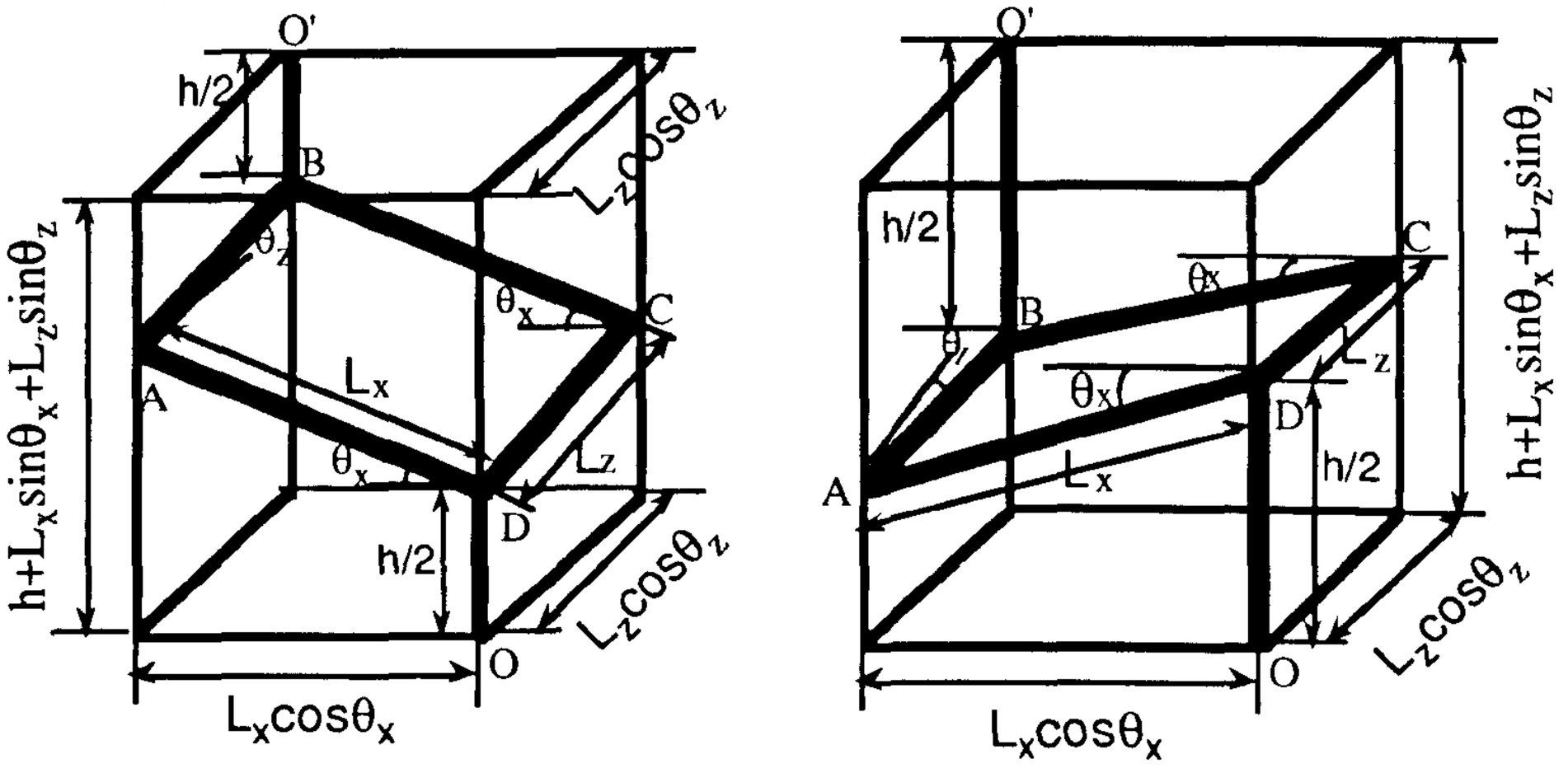

Fig. 5.5 One octant of the three dimensional unit cell. (a) One octant of conventional foam unit cell. (b) One octant of auxetic foam unit cell. θ is positive for conventional foam and θ is negative for auxetic foam.

The explanations of the theoretical model are made in *Sections 5.3 to 5.6.*

5.3 The Flexure Model for the 3D Foam Cell Structure

5.3.1 Introduction

It has been reported in chapter 4 that a flexible foam deforms by bending and buckling under a compressive loading condition and then recovers from these deformations when unloaded. Therefore, Young's modulus, E; Poisson's ratio, ν; and the shear modulus, G can be calculated from the elastic deflection, δ of the cantilevered beam under the end load, P. The flexure model for the cubic cell structure was well developed by Gibson and Ashby (1982, 1988). The flexure model for the rhombic dodecahedron cell structure is developed in this section. According to the microstructure of foams as described in Chapter 4, the cells are axisymmetric, and the experiments show that $L_z \approx L_x$ and $\theta_z \approx \theta_x$, therefore we will deal with this special case first, then develop the model more generally (e.g. when $L_z \neq L_x$ and $\theta_z \neq \theta_x$).

5.3.2 Loading in the X-Direction

Consider an octant of the unit cell for conventional foam loaded in the x

direction. Ribs AD and BC cause the deflection as shown in *Figure* 5.6.

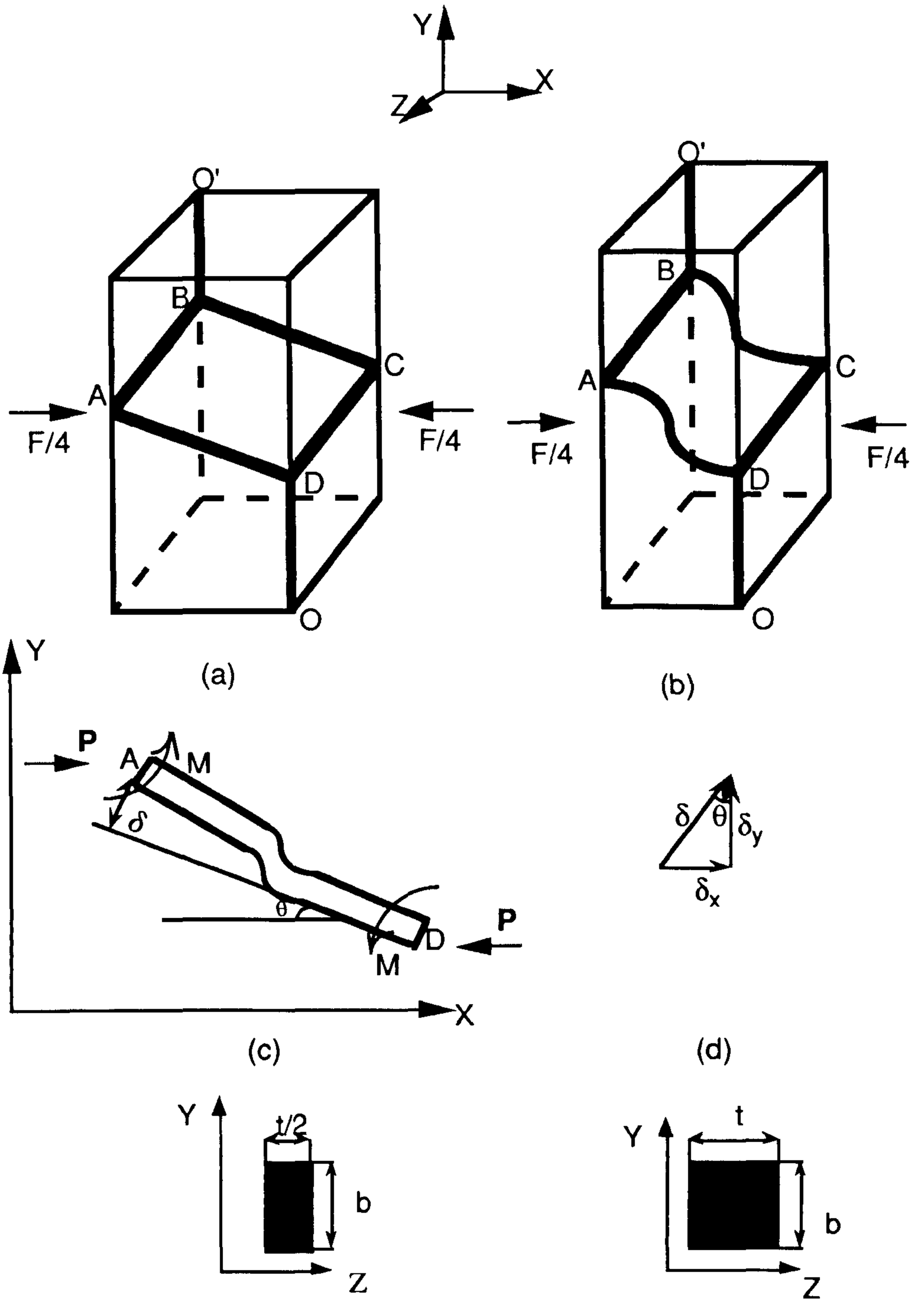

Fig. 5.6 Cell deformation by cell rib bending, giving linear-elastic compression of the foam. (Loading in the x direction) (a) An undeformed octant of the unit cell. (b) Rib bending caused by loading in the x direction. (c) Flexure of the cell rib caused by the compressive load in the x direction. (d) The deflection of the cell rib and its components along the x and y directions. (e) The cross section area of one rib in an octant of the unit cell. (f) The full cross section area of one rib in the unit cell.

In this case, only ribs AD and BC flex, and half of each cell rib is in one octant of the unit cell considered, the other half of each cell rib is in the adjacent octant

of the unit cell. Therefore, ribs AD and BC in one octant of the unit cell are equivalent to one cell rib of length l, depth t and thickness b in the unit cell. If the force in the x-direction applied to the whole unit cell is F, then that applied to an octant of the unit cell is F/4 which is defined here as P, this gives:

$$P = \frac{F}{4} = \frac{\sigma_x}{4} \times 2(h + 2L\sin\theta) \times 2L\cos\theta \qquad (5.1)$$

Where: σ_x, is negative for a compressive stress in the x direction.

From Roark and Young[1976], we know that:

$$M = P \times \frac{L}{2} \times \sin\theta \qquad (5.2)$$

Where: M, is the bending moment applied to a rib of length L at an angle θ to the x direction.

According to beam theory (Timoshenko and Goodier, 1970),

$$\delta = \frac{ML^2}{6E_sI} = \frac{PL^3\sin\theta}{12E_sI}. \qquad (5.3)$$

Where: δ, is the deflection of the cell rib, E_s is the Young's modulus of the solid polymer ribs, and I is the second moment of area of a rectangular rib.

From *Figure* 5.6(d), the deflection in the x direction is,

$$\delta_x = \delta\sin\theta = \frac{PL^3\sin^2\theta}{12E_sI} \qquad (5.4)$$

and the deflection in the y direction is,

$$\delta_y = -\delta\cos\theta = -\frac{PL^3\sin\theta\cos\theta}{12E_sI}. \qquad (5.5)$$

Since there is no component of flexure in the z-direction, then,

$$\delta_z = 0. \qquad (5.6)$$

Now we can easily calculate the engineering strain for one octant of the unit cell by using:

$$\varepsilon_x = \frac{\delta_x}{x} = \frac{\delta_x}{L\cos\theta} = \frac{PL^3\sin^2\theta}{12E_sIL\cos\theta}$$

$$= \frac{\sigma_x(h + 2L\sin\theta)L^3\sin^2\theta}{12E_sI}. \qquad (5.7)$$

$$\varepsilon_y = \frac{\delta_y}{y} = \frac{\delta_y}{h + 2L\sin\theta}$$

$$= \frac{-PL^3\sin\theta\cos\theta}{12E_sI(h + 2L\sin\theta)} = \frac{-\sigma_x(h + 2L\sin\theta)(L\cos\theta)L^3\sin\theta\cos\theta}{12E_sI(h + 2L\sin\theta)}$$

$$= -\frac{\sigma_xL^4\sin\theta\cos^2\theta}{12E_sI}. \qquad (5.8)$$

$$\varepsilon_z = \frac{\delta_z}{z} = \frac{\delta_z}{L\cos\theta} = 0. \qquad (5.9)$$

It is to be noted that a compressive stress in the x direction leads to EQ. 5.7 and EQ. 5.8 yielding negative and positive strains in the x and y directions, respectively. The Poisson's ratio, ν_{xy} , can be calculated by using the following equations:

$$\nu_{xy} = -\frac{\varepsilon_y}{\varepsilon_x} = \frac{\sigma_x L^4 \sin\theta\cos^2\theta}{12E_s I} \times \frac{12E_s I}{\sigma_x (h + 2L\sin\theta)L^3 \sin^2\theta}$$

$$= \frac{L\cos^2\theta}{(h + 2L\sin\theta)\sin\theta}. \qquad (5.10)$$

$$\nu_{xz} = -\frac{\varepsilon_z}{\varepsilon_x} = 0. \qquad (5.11)$$

Here we define the aspect ratio, α as

$$\alpha = \frac{h}{L}$$

then, $$\nu_{xy} = \frac{\cos^2\theta}{(2\sin\theta + \alpha)\sin\theta}. \qquad (5.12)$$

Combining the strain and the stress, Young's modulus for the x-direction can be obtained as:

$$E_x = \frac{\sigma_x}{\varepsilon_x} = \frac{12E_s I}{(h + 2L\sin\theta)L^3 \sin^2\theta}. \qquad (5.13)$$

From beam theory the second moment of area of a rectangular beam of thickness t, width b is $I = \frac{bt^3}{12}$. We have one flexing cell rib in the x-y plane per octant of the unit cell, and for the cell rib of equal thickness and width (t = b) we have:

$$E_x = \frac{E_s\left(\frac{t}{L}\right)^4}{(\alpha + 2\sin\theta)\sin^2\theta}. \qquad (5.14)$$

5.3.3 Loading in the Z-Direction

Figure 5.7 illustrates the one octant of the unit-cell for the conventional geometric unit loaded in the Z direction. In this case ribs AB and CD are caused to flex.

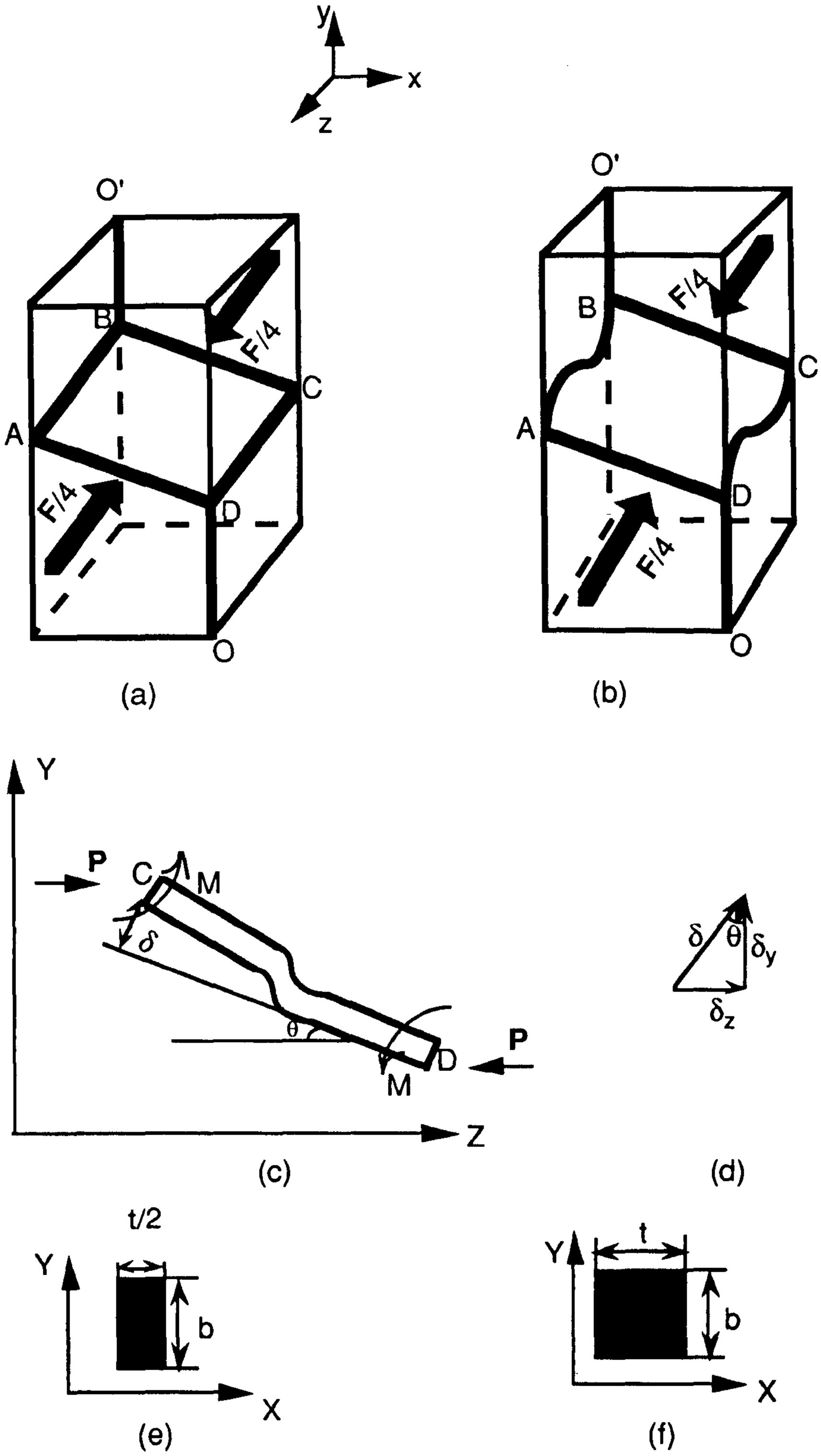

Fig. 5.7 Cell deformation by cell rib bending, giving linear-elastic compression of the foam. (Loading in the z direction). (a) An in-deformed octant of the unit cell. (b) Rib bending caused by loading in the z direction. (c) Flexure of the cell rib caused by the compressive load in the z direction. (d) The deflection of the cell rib and its components along the z and y directions. (e) the cross section area of one rib in an octant of the unit cell. (f) The cross section area of one rib in the unit cell.

By symmetry, the engineering strains are:

$$\varepsilon_z = \frac{\sigma_Z (h + 2L\sin\theta) L^3 \sin^2\theta}{12 E_s I}. \qquad (5.15)$$

$$\varepsilon_y = \frac{-\sigma_Z L^4 \sin\theta \cos^2\theta}{12 E_s I}. \qquad (5.16)$$

$$\varepsilon_X = \frac{\delta_X}{L\cos\theta} = 0. \qquad (5.17)$$

The Poisson's ratios are:

$$\nu_{zy} = \frac{\cos^2\theta}{(2\sin\theta + \alpha)\sin\theta}. \qquad (5.18)$$

$$\nu_{zx} = -\frac{\varepsilon_X}{\varepsilon_Z} = 0. \qquad (5.19)$$

The Young's modulus in the z-direction is:

$$E_Z = \frac{E_s \left(\frac{t}{L}\right)^4}{(\alpha + 2\sin\theta)\sin^2\theta}. \qquad (5.20)$$

5.3.4 Loading in the Y-Direction

Figure 5.8 illustrates one octant of the unit-cell for the conventional geometric unit loaded in the y direction. In this case ribs AD, BC, AB and CD all flex.

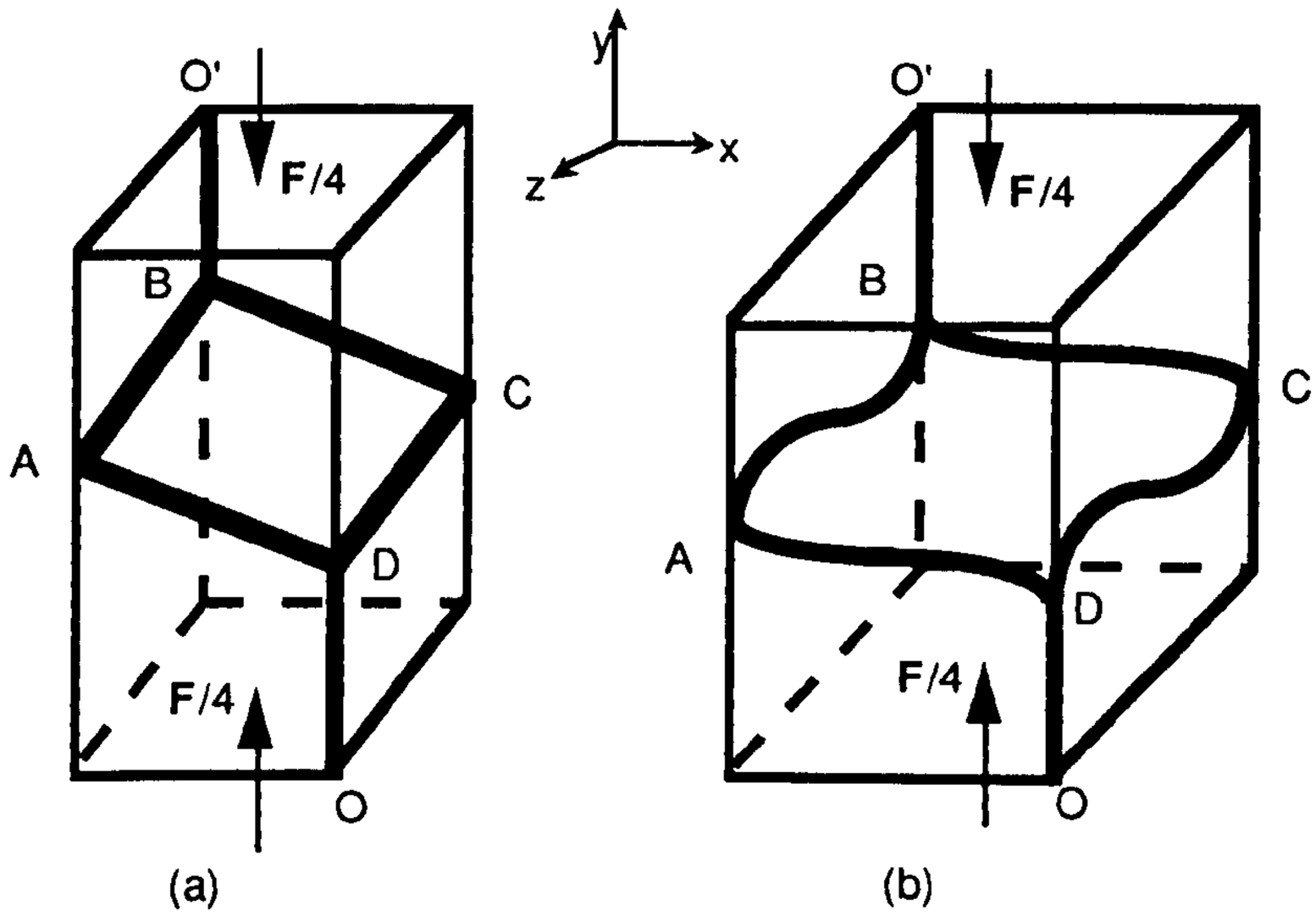

(a) (b)

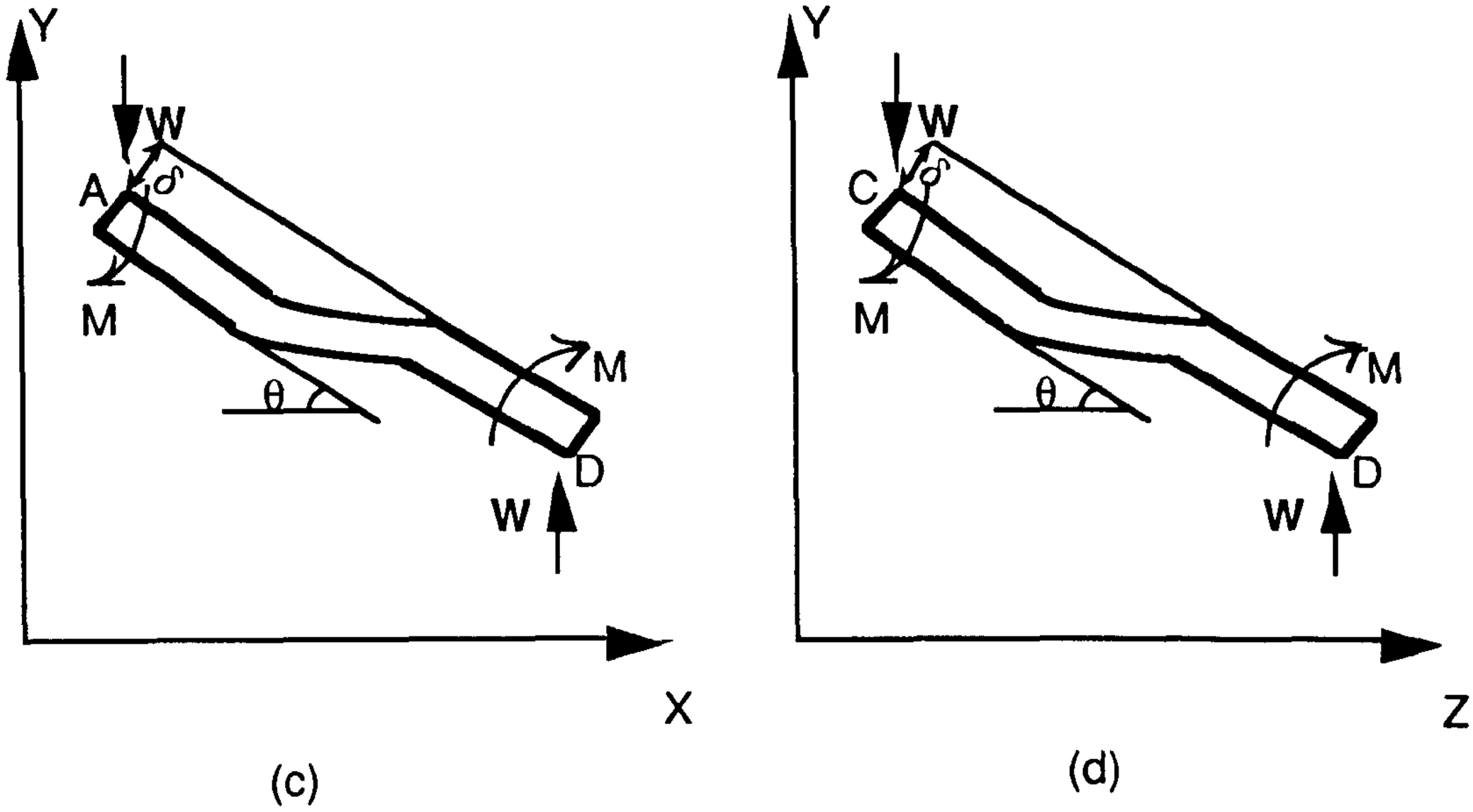

Fig. 5.8 Cell deformation by cell rib bending, giving linear-elastic compression of the foam. (Loading in the y direction) (a) An in-deformed octant of the unit cell. (b) Rib bending caused by loading in the y direction. (c) Flexure of the cell rib in the x-y plane caused by the compressive load in the y direction. (d) Flexure of the cell rib in the y-z plane caused by the compressive load in the y direction.

Figure 5.8 shows the vertical compressive loading of the flexible foam. Ribs AB, BC, CD and AD in one octant of the unit cell are equivalent to two cell ribs in the unit cell. If the force in the y-direction which is applied to the whole unit cell is F, then that applied to one octant of the unit cell will be F/4 which is defined here as W, and,

$$W = \frac{F}{4} = \frac{\sigma_y}{4} \times 2L\cos\theta \times 2L\cos\theta \qquad (5.21)$$

Where: σ_y, is negative for a compressive stress in the y direction.

From Roark and Young[1976], we know that the bending moment applied to each rib is

$$M = W \times \frac{L}{2} \times \cos\theta \qquad (5.22)$$

and according to beam theory (e.g. Timoshenko[1975]), each rib deflects by

$$\delta = \frac{ML^2}{6E_sI} = \frac{WL^3\cos\theta}{12E_sI}. \qquad (5.23)$$

In this case,

$$\delta_x = -\delta\sin\theta = -\frac{WL^3\sin\theta\cos\theta}{12E_sI} \qquad (5.24)$$

$$\delta_y = \delta_{yAD} + \delta_{yCD} = 2\delta\cos\theta = 2\left(\frac{WL^3\cos\theta\cos\theta}{12E_sI}\right) \qquad (5.25)$$

Where: δ_{yAD} and δ_{yCD} are the components of the flexure deflection in the y direction for ribs AD and CD respectively.

$$\delta_z = \frac{-WL^3\cos\theta\sin\theta}{12E_sI}. \qquad (5.26)$$

Then we can calculate the engineering strains,

$$\varepsilon_x = \frac{\delta_x}{x} = \frac{\delta_x}{L\cos\theta} = \frac{-WL^3 \sin\theta\cos\theta}{12E_sIL\cos\theta} = \frac{-\sigma_y L^2\cos^2\theta L^3\cos\theta\sin\theta}{12E_sIL\cos\theta}$$
$$= \frac{-\sigma_y L^4 \sin\theta\cos^2\theta}{12E_sI}. \qquad (5.27)$$

$$\varepsilon_y = \frac{\delta_y}{y} = \frac{\delta_y}{h+2L\sin\theta} = \frac{2WL^3\cos^2\theta}{12E_sI(h+2L\sin\theta)} = \frac{2\sigma_y(L^2\cos^2\theta)L^3\cos^2\theta}{12E_sI(h+2L\sin\theta)}$$
$$= \frac{2\sigma_y L^5\cos^4\theta}{12E_sI(h+2L\sin\theta)}. \qquad (5.28)$$

$$\varepsilon_z = \frac{\delta_z}{z} = \frac{\delta_Z}{L\cos\theta} = \frac{-WL^3\cos\theta\sin\theta}{12E_sIL\cos\theta} = \frac{-\sigma_y L^2\cos^2\theta L^3\cos\theta\sin\theta}{12E_sIL\cos\theta}$$
$$= \frac{-\sigma_y L^4\cos^2\theta\sin\theta}{12E_sI}. \qquad (5.29)$$

Hence, a compressive stress in the y direction yields a negative strain in the y direction and positive strain in the x and z direction.

Poisson's ratios can be calculated as:

$$\nu_{yx} = \frac{-\varepsilon_X}{\varepsilon_y} = \frac{\sin\theta(2\sin\theta+\alpha)}{2\cos^2\theta} \qquad (5.30)$$

and

$$\nu_{yz} = \frac{-\varepsilon_Z}{\varepsilon_y} = \frac{\sin\theta(2\sin\theta+\alpha)}{2\cos^2\theta}. \qquad (5.31)$$

From *EQ*. 5.28, the Young's modulus of the y-direction can be obtained as *EQ.5.32*.

$$E_y = \frac{\sigma_y}{\varepsilon_y} = \frac{12E_sI(h+2L\sin\theta)}{2L^5\cos^4\theta} \qquad (5.32)$$

Where: $I = \frac{bt^3}{12}$ for a rectangular beam. For the rib of equal thickness and width (t = b), E_y is,

$$E_y = \frac{E_s bt^3(h+2L\sin\theta)}{2L^5\cos^4\theta} = \frac{E_s\left(\frac{t}{L}\right)^4(\alpha+2\sin\theta)}{2\cos^4\theta}. \qquad (5.33)$$

When $\theta = 0^\circ$, $E_y = \frac{1}{2}E_s\left(\frac{t}{L}\right)^4 \times \left(\frac{h}{L}\right)$ which is the same as the result of Huber and

Gibson (1988), $E_y = CE_s\left(\frac{t}{L}\right)^4 \times \left(\frac{h}{L}\right)$ on a similar but not identical structure.

5.3.5 The Shear Modulus of the Flexure Model

5.3.5.1 Introduction

The cell rib is equivalent to a cantilever beam. And the shear modulus, G of the flexible foam can be calculated from the shear stress, τ and the shear strain, γ of one octant of the unit cell. The flexure model for the shear modulus of the foam is developed in this section. The components of stress acting on a cube are indicated in *Figure* 5.9.

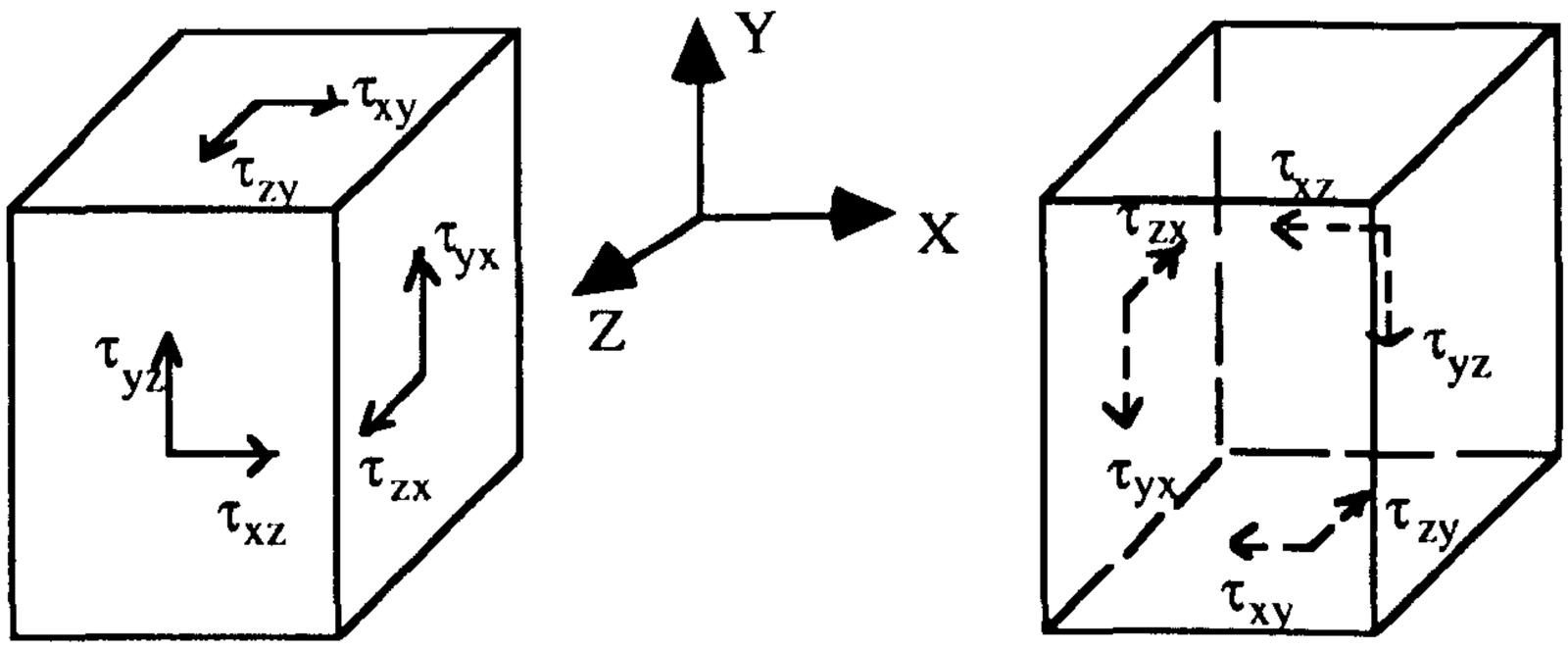

Fig. 5.9 Shear stresses acting on the unit cell.

According to the classical elasticity theory of anisotropic material (e.g. Nye (1960); when we apply a shear stress, τ_{xy}, we also are applying τ_{yx} to keep the body in equilibrium. The total moment is:

$$\underbrace{-\tau_{xy} \times (xz)}_{Force} \times y + \underbrace{\tau_{yx} \times (zy)}_{Force} \times x = 0, \qquad (5.34)$$

Therefore, $\tau_{xy} = \tau_{yx}$. (5.35)

Also, the stiffness matrix, the shear modulus G is symmetric,

$$G_{xy} = G_{yx}. \qquad (5.36)$$

As the case of shearing in the x-y plane, when we shear in the x-z plane, the shear modulus, G_{xz} is equal to the shear modulus, G_{zx}; and when we shear in the z-y plane, the shear modulus, G_{yz} is the same as the shear modulus G_{zy}.

5.3.5.2 Shearing in the X-Z Plane

In this case, the deformation caused by the shear stress which applied in the x direction on the faces with outward normal in the z direction, i.e. τ_{xz}. The shear deflection here is entirely due to flexing of the ribs AB and DC, as shown in *Figure* 5.10.

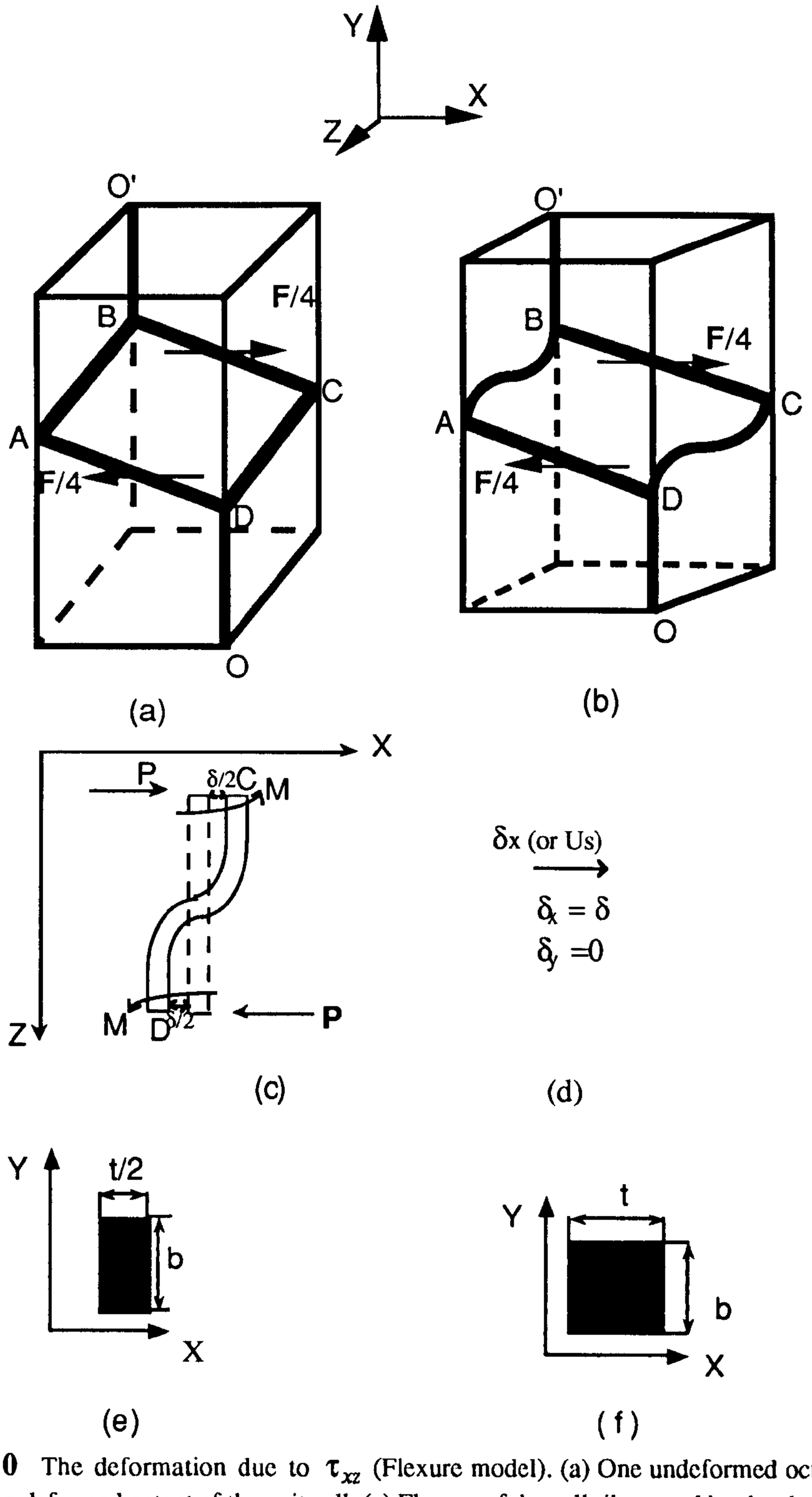

Fig. 5.10 The deformation due to τ_{xz} (Flexure model). (a) One undeformed octant of the unit cell. (b) An deformed octant of the unit cell. (c) Flexure of the cell rib caused by the shear forces along the x direction (projection onto the x-z plane). (d) The deflection of the cell rib. (e) The cross section area of one rib in an octant of the unit cell. (f) The cross section area of one rib in the unit cell.

According to beam theory,

$$M = P \times \frac{L}{2} cos\,\theta \tag{5.37}$$

and the cell rib deflects by:

$$\delta = \frac{ML^2}{6E_sI} = \frac{PL^3}{12E_sI}\cos\theta. \qquad (5.38a)$$

In the case that $\delta = \delta_x$, and

$$\delta_x = \delta = \frac{PL^3\cos\theta}{12E_sI} = U_s. \qquad (5.38b)$$

The shear strain, γ, is given by

$$\gamma = \frac{U_s}{z} = \frac{U_s}{L\cos\theta}. \qquad (5.39)$$

The shear stress, τ_{xz}, is

$$\tau_{xz} = \frac{F}{xy} = \frac{4P}{2L\cos\theta \times 2(h+2L\sin\theta)} = \frac{P}{L\cos\theta(h+2L\sin\theta)} \qquad (5.40)$$

giving the shear modulus $G = \tau / \gamma$, hence

$$G_{xz} = \frac{P}{L\cos\theta(h+2L\sin\theta)} \times \frac{12E_sI}{PL^3}$$

$$= \frac{E_s \times bt^3}{L^3\cos\theta \times (h+2L\sin\theta)} \qquad (5.41a)$$

when b=t, and $\alpha = h/L$, then:

$$G_{xz} = \frac{E_s}{\cos\theta \times (\alpha + 2\sin\theta)}\left(\frac{t}{l}\right)^4. \qquad (5.41b)$$

By symmetry, when the deformation caused by the shear stress which applied in the z direction on the faces with outward normal in the x direction, i.e. τ_{zx}. , the shear modulus

$$G_{zx} = \frac{E_s\left(\frac{t}{L}\right)^4}{\cos\theta \times (\alpha + 2\sin\theta)}. \qquad (5.41c)$$

Again, when $\theta = 0^\circ$, $G_{zx} = E_s\left(\frac{t}{L}\right)^4\left(\frac{L}{h}\right)$, which is what Huber and Gibson get on a similar (but not identical) structure (see Figure 2.2).

5.3.5.3 Shearing in the Z-Y Plane

Consider a shear stress exerted on a half of the unit cell of the foam in the z-direction on the faces with outward normal in the y direction, i.e. τ_{zy}. All ribs flex as shown in *Figure* 5.11.

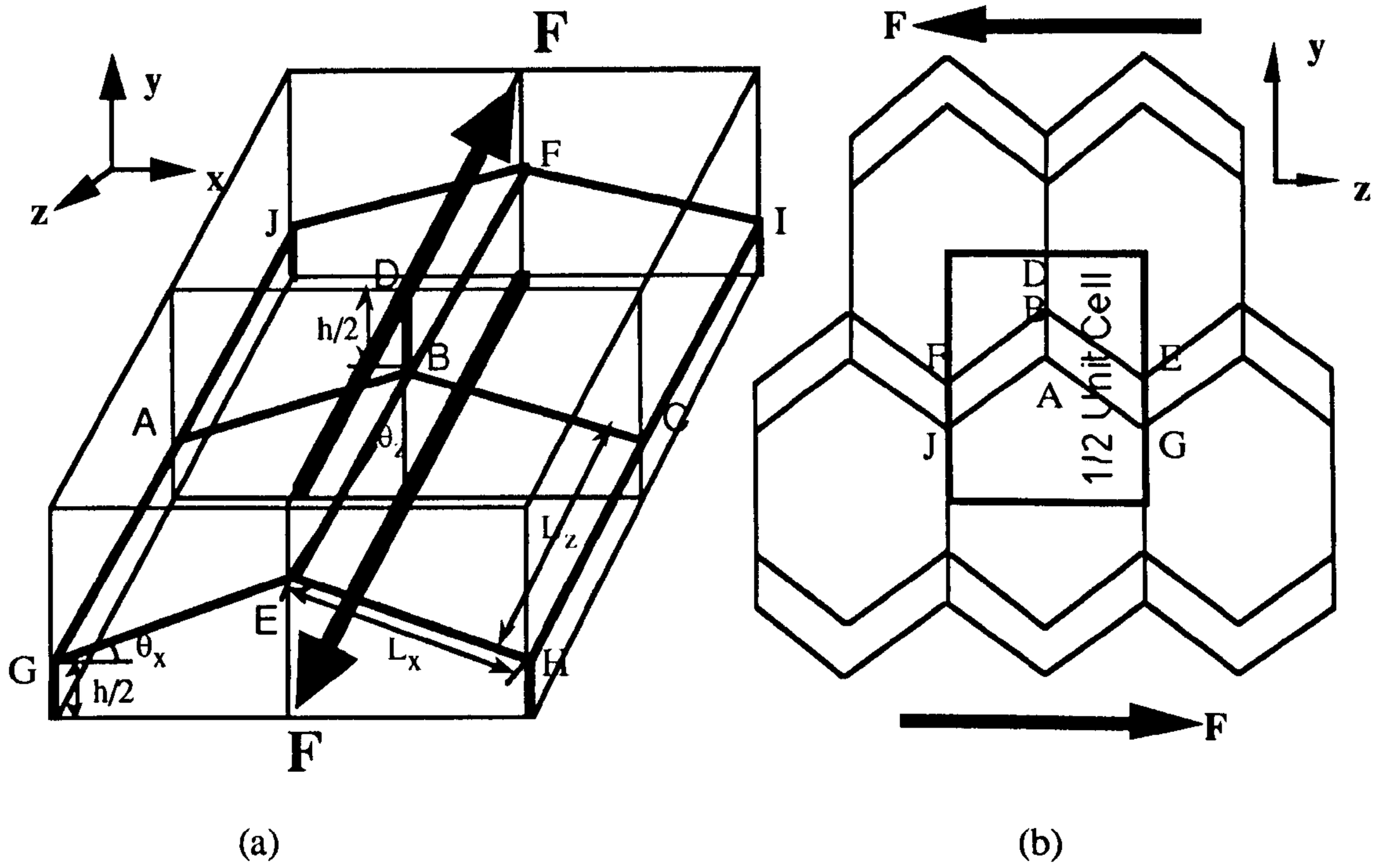

(a) (b)

Fig. 5.11 The deformation due to τ_{zy} (flexure model). (a) Half of the undeformed unit cell. (b) A simple array of the 3D cells. Projection onto the y-z plane for the conventional cell network.

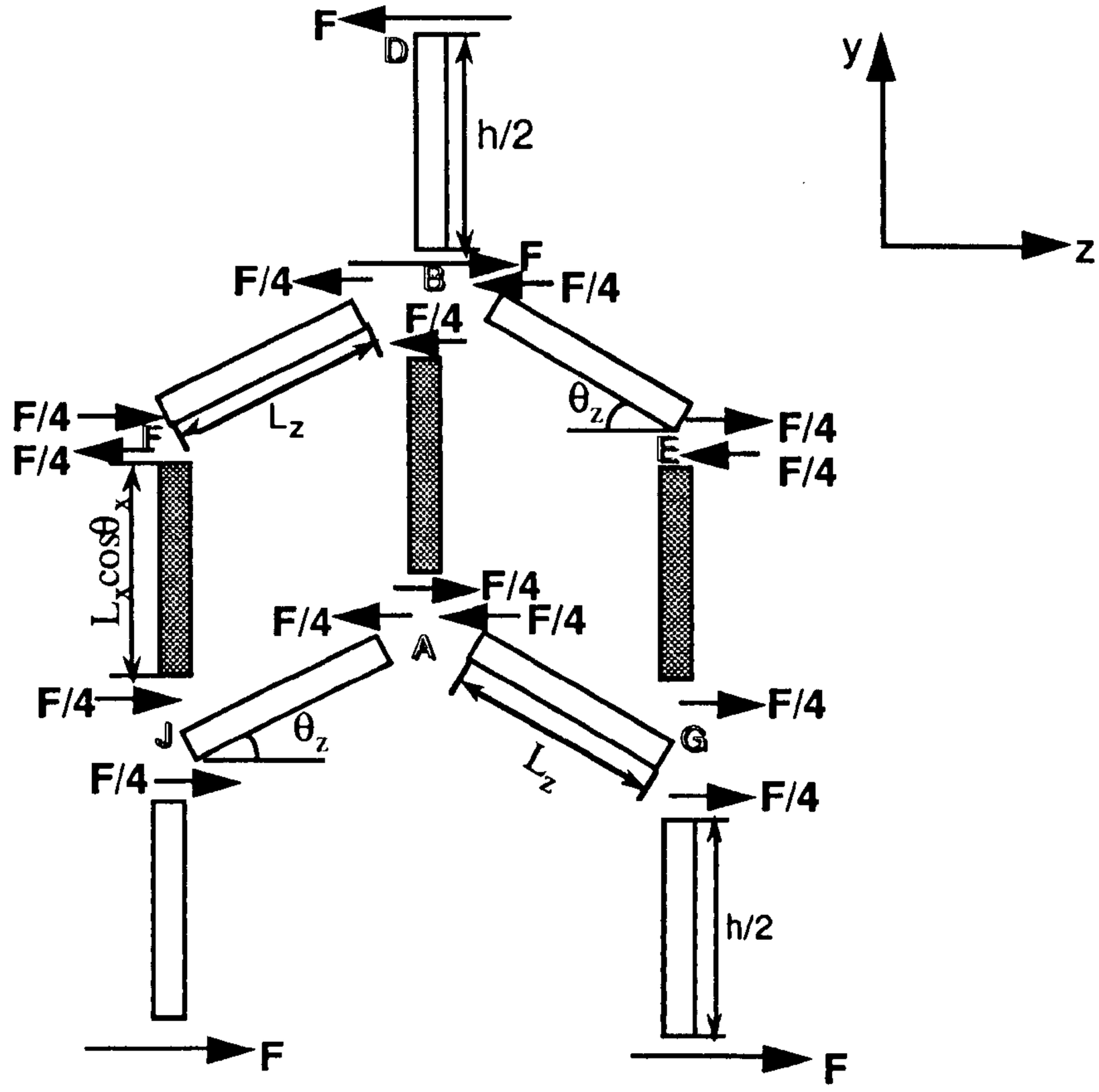

Fig. 5.11(c) Force diagram. note: shaded ribs are sloping out of the z-y plane.

Since moments applied to BD, AB and BC are all applied along the z axis, and the moment about B: $M^{BD} = 2M^{BE} + 2M_z^{AB}$, *(5.42)*

Where M^{BD}, is the moment applied to rib BD, M^{BE} (equal to M^{BF}) is the moment applied to rib BE (or BF), and M_z^{AB} (equal to M_z^{BC}) is applied moment to rib BE (or BF) along the z direction.

Let M_z be applied moment in the z direction. Then component of moment M_z at an angle β to z axis in the y-z plane is: $M_\beta = M_z \cos\beta = M_z \sin\theta$. *(5.43)*

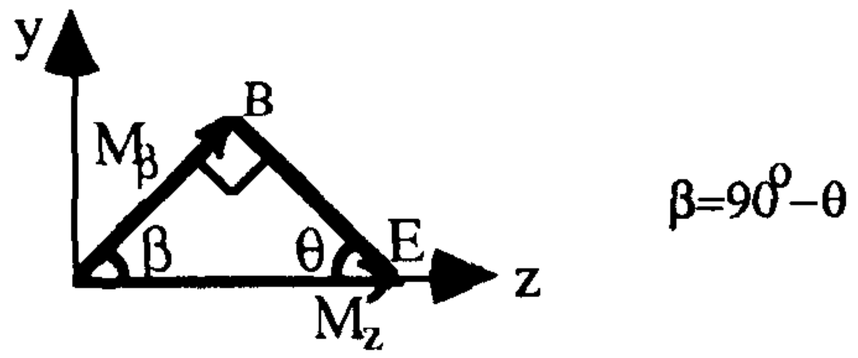

Fig. 5.11(d) The applied moment M_z in the z direction and its component M_β.

M_β is therefore the moment applied to a rib at rib angle θ at junction B.

$$M^{BE} = M_z. \qquad (5.44a)$$

$$M^{AB} = M_\beta = M_z \sin\theta \qquad (5.44b)$$

and, M_z^{AB} along z direction is,

$$M_z^{AB} = M_\beta \sin\theta = M_z \sin^2\theta, \qquad (5.45)$$

From EQ. 5.42 to 5.45,

$$M^{BD} = 2M_z + 2M_z \sin^2\theta. \qquad (5.46a)$$

Moment applied to BD is, $M^{BD} = \frac{Fh}{2}$, *(5.46b)*

hence, $M_z = \frac{Fh}{4(1+\sin^2\theta)}$. *(5.46c)*

Follow the two dimensional analysis of Gibson and Ashby (1982),

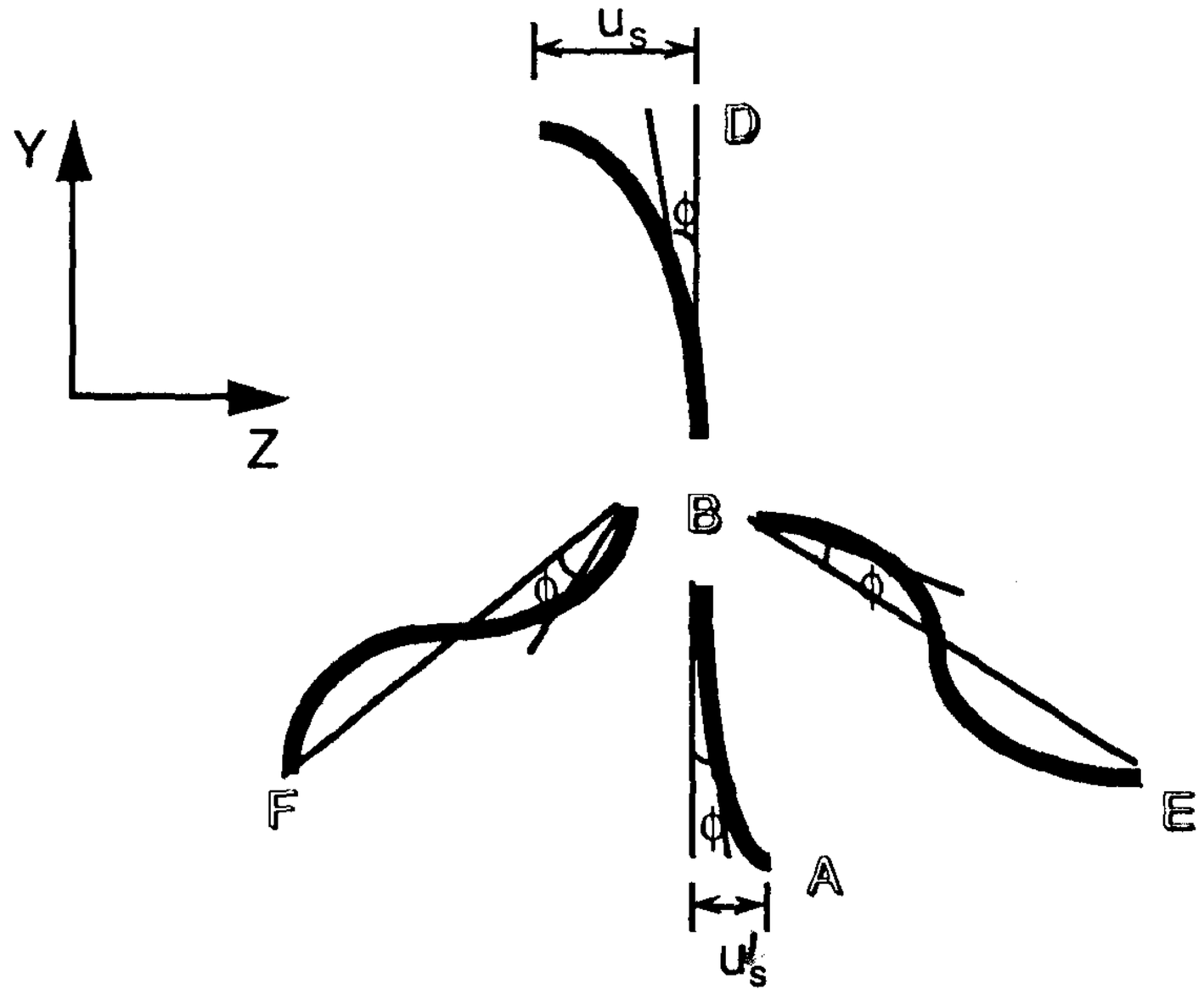

Fig. 5.11(e) Cell deformation (flexure and the internal rotation) under the shear stress, τ_{zy}.

The cell deformation under the shear stress, τ_{zy} is illustrated by *Figure* 5.11(e). There is no relative motion of the points E, B and F. The shearing deflexion of the structure is entirely due to bending of beam BD and AB (and BC), and their rotation about the point B. The forces are shown in *Figure* 5.11(c). The shear displacement of unit cell in the z direction is:

$$u_z = 2(u_s + 2u_s'). \tag{5.47}$$

All the joints rotate through an angle ϕ. The deflection of BE is:

$$\delta = \frac{M^{BE}L^2}{6E_sI} = \phi L, \tag{5.48a}$$

$$\phi L = \frac{M_z L^2}{6E_sI} = \frac{FhL^2}{24(1+\sin^2\theta)E_sI}. \tag{5.48b}$$

Shearing deflection of the point D with respect to B is:

$$u_s = \frac{1}{2}\phi h + \frac{F}{3E_sI}\left(\frac{h}{2}\right)^3. \tag{5.49a}$$

Shearing deflection of A with respect to B is:

$$u_s' = \phi L\sin\theta + \frac{M^{AB}L^2}{6E_sI} = \phi L\sin\theta + \frac{M_z\sin\theta\times L^2}{6E_sI}$$

$$= \phi L\sin\theta + \frac{FhL^2\sin\theta}{24(1+\sin^2\theta)E_sI}. \tag{5.49b}$$

Hence, $\frac{u_z}{2} = 2u_s + u_s'$

$$= \phi(h + L\sin\theta) + \frac{Fh}{12E_sI}(h^2 + \frac{L^2\sin\theta}{2(1+\sin^2\theta)})$$

$$= \frac{FhL(h+L\sin\theta)}{24(1+\sin^2\theta)E_sI} + \frac{Fh}{12E_sI}\left(h^2 + \frac{L^2\sin\theta}{2(1+\sin^2\theta)}\right)$$

$$= \frac{Fh}{12E_sI}\left(h^2 + \frac{L(h+2L\sin\theta)}{2(1+\sin^2\theta)}\right). \tag{5.50a}$$

Since, $I = \frac{bt^3}{12}$ for a rectangular beam, and when b=t, we have,

$$\frac{u_z}{2} = \frac{Fh}{E_st^4}\left(h^2 + \frac{L(h+2L\sin\theta)}{2(1+\sin^2\theta)}\right) \tag{5.50b}$$

The shear strain is, $\gamma_{zy} = \dfrac{u_z}{2(h+2L\sin\theta)}$. *(5.51)*

The shear modulus is, $G_{zy} = \dfrac{\tau_{zy}}{\gamma_{zy}} = \dfrac{F}{4L^2\cos^2\theta} \times \dfrac{2(h+2L\sin\theta)}{u_z}$

$$= \frac{E_s}{4\alpha\cos^2\theta}\left(\frac{t}{L}\right)^4 \frac{(\alpha+2\sin\theta)\left(1+\sin^2\theta\right)}{\left[\alpha^2\left(1+\sin^2\theta\right)+\left(\frac{\alpha}{2}\right)+\sin\theta\right]}. \quad (5.52a)$$

From the classical elasticity theory of anisotropic materials (e.g. Nye (1960), we know that:

$$G_{yz} = G_{zy} = \frac{E_s}{4\alpha\cos^2\theta}\left(\frac{t}{L}\right)^4 \frac{(\alpha+2\sin\theta)(1+\sin^2\theta)}{\left[\alpha^2\left(1+\sin^2\theta\right)+\frac{\alpha}{2}+\sin\theta\right]}. \quad (5.52b)$$

5.3.5.4 Shearing in the X-Y Plane.

In this case, the deformation caused by the shear stress which applied in the x direction on the faces with outward normal in the y direction, i.e. τ_{xy}. By symmetry,

$$G_{xy} = G_{yx} = \frac{E_s}{4\alpha\cos^2\theta}\left(\frac{t}{L}\right)^4 \frac{(\alpha+2\sin\theta)(1+\sin^2\theta)}{\left[\alpha^2\left(1+\sin^2\theta\right)+\frac{\alpha}{2}+\sin\theta\right]} \quad (5.52c)$$

When $\theta = 0^\circ$, $G_{xy} = \dfrac{E_s}{4}\left(\dfrac{t}{L}\right)^4 \times \dfrac{L}{h} \times \dfrac{1}{\left(\frac{h}{L}\right)+\frac{1}{2}}$ which is similar to what Huber and

Gibson (1988) get, $G_{xy} = 2CE_s\left(\dfrac{t}{L}\right)^4\left(\dfrac{L}{h}\right)\dfrac{1}{\left(\frac{h}{L}\right)+1}$ on a similar (but not identical)

structure with $\theta = 0^\circ$.

5.3.6 Summary of the Flexure Model

From *Figure 5.5*, We can see that the shape of the conventional foam unit cell differs from that of the auxetic foam unit cell only by the angle, θ; θ being positive for the conventional foam and negative for the auxetic foam. Therefore, the results are actually different for the two cases. *Table* 5.1 contains the elastic moduli due to flexure of the ribs.

(Table 5.1)

	Expressions $(\theta_x = \theta_z = \theta)$ $(L_x = L_z = L)$	General Expressions $(L_x \neq L_z)$ and $\theta_x \neq \theta_z$.
E_x	$\dfrac{E_s\left(\frac{t}{L}\right)^4}{(\alpha+2\sin\theta)\sin^2\theta}$	$\dfrac{12E_sI}{(h+L_x\sin\theta_x+L_z\sin\theta_z)L_x{}^3\sin^2\theta_x}$
E_y	$\dfrac{E_s\left(\frac{t}{L}\right)^4(\alpha+2\sin\theta)}{2\cos^4\theta}$	$\dfrac{12E_sI(h+L_z\sin\theta_z+L_x\sin\theta_x)}{\left(L_x{}^3\cos^2\theta_x+L_z{}^3\cos^2\theta_z\right)(L_x\cos\theta_x)(L_z\cos\theta_z)}$
E_z	$\dfrac{E_s\left(\frac{t}{L}\right)^4}{(\alpha+2\sin\theta)\sin^2\theta}$	$\dfrac{12E_sI}{(h+L_x\sin\theta_x+L_z\sin\theta_z)L_z{}^3\sin^2\theta_z}$
ν_{xy}	$\dfrac{\cos^2\theta}{(2\sin\theta+\alpha)\sin\theta}$	$\dfrac{L_x\cos^2\theta_x}{(h+L_x\sin\theta_x+L_z\sin\theta_z)\sin\theta_x}$
ν_{xz}	0	0
ν_{zx}	0	0
ν_{zy}	$\dfrac{\cos^2\theta}{(2\sin\theta+\alpha)\sin\theta}$	$\dfrac{L_z\cos^2\theta_z}{(h+L_x\sin\theta_x+L_z\sin\theta_z)\sin\theta_z}$
ν_{yx}	$\dfrac{\sin\theta(2\sin\theta+\alpha)}{2\cos^2\theta}$	$\dfrac{L_x{}^2\sin\theta_x\left(h+L_x\sin\theta_x+L_z\sin\theta_z\right)}{L_x{}^3\cos^2\theta_x+L_z{}^3\cos^2\theta_z}$
ν_{yz}	$\dfrac{\sin\theta(2\sin\theta+\alpha)}{2\cos^2\theta}$	$\dfrac{L_z{}^2\sin\theta_z\left(h+L_x\sin\theta_x+L_z\sin\theta_z\right)}{L_x{}^3\cos^2\theta_x+L_z{}^3\cos^2\theta_z}$
G_{xy}	$\dfrac{E_s\left(\frac{t}{L}\right)^4}{4\alpha\cos^2\theta}\dfrac{(\alpha+2\sin\theta)(1+\sin^2\theta)}{\left[\alpha^2\left(1+\sin^2\theta\right)+\frac{\alpha}{2}+\sin\theta\right]}$	$\dfrac{12E_sI(1+\sin^2\theta_z)(h+L_x\sin\theta_x+L_z\sin\theta_z)}{2h\left(L_x\cos\theta_xL_z\cos\theta_z\right)\left[L_x\left(h+L_z\sin\theta_z\right)+L_z{}^2\sin\theta_z+2h^2(1+\sin^2\theta_z)\right]}$
G_{zy}	$\dfrac{E_s\left(\frac{t}{L}\right)^4}{4\alpha\cos^2\theta}\dfrac{(\alpha+2\sin\theta)(1+\sin^2\theta)}{\left[\alpha^2\left(1+\sin^2\theta\right)+\frac{\alpha}{2}+\sin\theta\right]}$	$\dfrac{12E_sI(1+\sin^2\theta_x)(h+L_x\sin\theta_x+L_z\sin\theta_z)}{2h\left(L_x\cos\theta_xL_z\cos\theta_z\right)\left[L_z\left(h+L_x\sin\theta_x\right)+L_x{}^2\sin\theta_x+2h^2(1+\sin^2\theta_x)\right]}$
G_{yz}	$\dfrac{E_s\left(\frac{t}{L}\right)^4}{4\alpha\cos^2\theta}\dfrac{(\alpha+2\sin\theta)(1+\sin^2\theta)}{\left[\alpha^2\left(1+\sin^2\theta\right)+\frac{\alpha}{2}+\sin\theta\right]}$	$\dfrac{12E_sI(1+\sin^2\theta_x)(h+L_x\sin\theta_x+L_z\sin\theta_z)}{2h\left(L_x\cos\theta_xL_z\cos\theta_z\right)\left[L_z\left(h+L_x\sin\theta_x\right)+L_x{}^2\sin\theta_x+2h^2(1+\sin^2\theta_x)\right]}$
G_{yx}	$\dfrac{E_s\left(\frac{t}{L}\right)^4}{4\alpha\cos^2\theta}\dfrac{(\alpha+2\sin\theta)(1+\sin^2\theta)}{\left[\alpha^2\left(1+\sin^2\theta\right)+\frac{\alpha}{2}+\sin\theta\right]}$	$\dfrac{12E_sI(1+\sin^2\theta_z)(h+L_x\sin\theta_x+L_z\sin\theta_z)}{2h\left(L_x\cos\theta_xL_z\cos\theta_z\right)\left[L_x\left(h+L_z\sin\theta_z\right)+L_z{}^2\sin\theta_z+2h^2(1+\sin^2\theta_z)\right]}$
G_{xz}	$\dfrac{E_s\left(\frac{t}{L}\right)^4}{\cos\theta\times(\alpha+2\sin\theta)}$	$\dfrac{12E_sI}{L_z{}^2L_x\cos\theta_x(h+L_x\sin\theta_x+L_z\sin\theta_z)}$
G_{zx}	$\dfrac{E_s\left(\frac{t}{L}\right)^4}{\cos\theta\times(\alpha+2\sin\theta)}$	$\dfrac{12E_sI}{L_x{}^2L_z\cos\theta_z(h+L_x\sin\theta_x+L_z\sin\theta_z)}$

Table 5.1 The flexure model expressions of the Young's modulus, Poisson's ratio and the shear modulus of conventional and auxetic foams. θ is positive for conventional foam and θ is negative for auxetic foam. $\alpha = h / L$.

5.4 The Hinging Model for the Foam Cell Structure

5.4.1 Introduction

Experiments have shown that under a tensile force the flexible foam deforms not only by flexing but also by hinging of the cell ribs. In addition, when the tensile force is removed the foam recovers. It has been noticed that each member behaved as if it was fixed at one end, and the other end was free to translate horizontally. The cell rib is equivalent to a cantilever beam. Therefore, Young's modulus, E, Poisson's ratio, ν, and the shear modulus, G can be calculated from the linear elastic deflection, δ of the cantilevered beam under the end force, T. The hinging model is developed in this section. From the examination of the microstructure of foams as described in Chapter 4, the cells are axisymmetry, and the experiments show that $L_z \approx L_x$ and $\theta_z \approx \theta_x$, therefore we will deal with this special case first, then develop the model more generally (e.g. when $L_z \neq L_x$ and $\theta_z \neq \theta_x$).

5.4.2 Loading in the X-Direction

When the cell deforms by hinging of the ribs, we assume that each cell rib is rigid along its length and deflection occurs at the junction with another cell rib by a change of angle $\Delta\theta$.

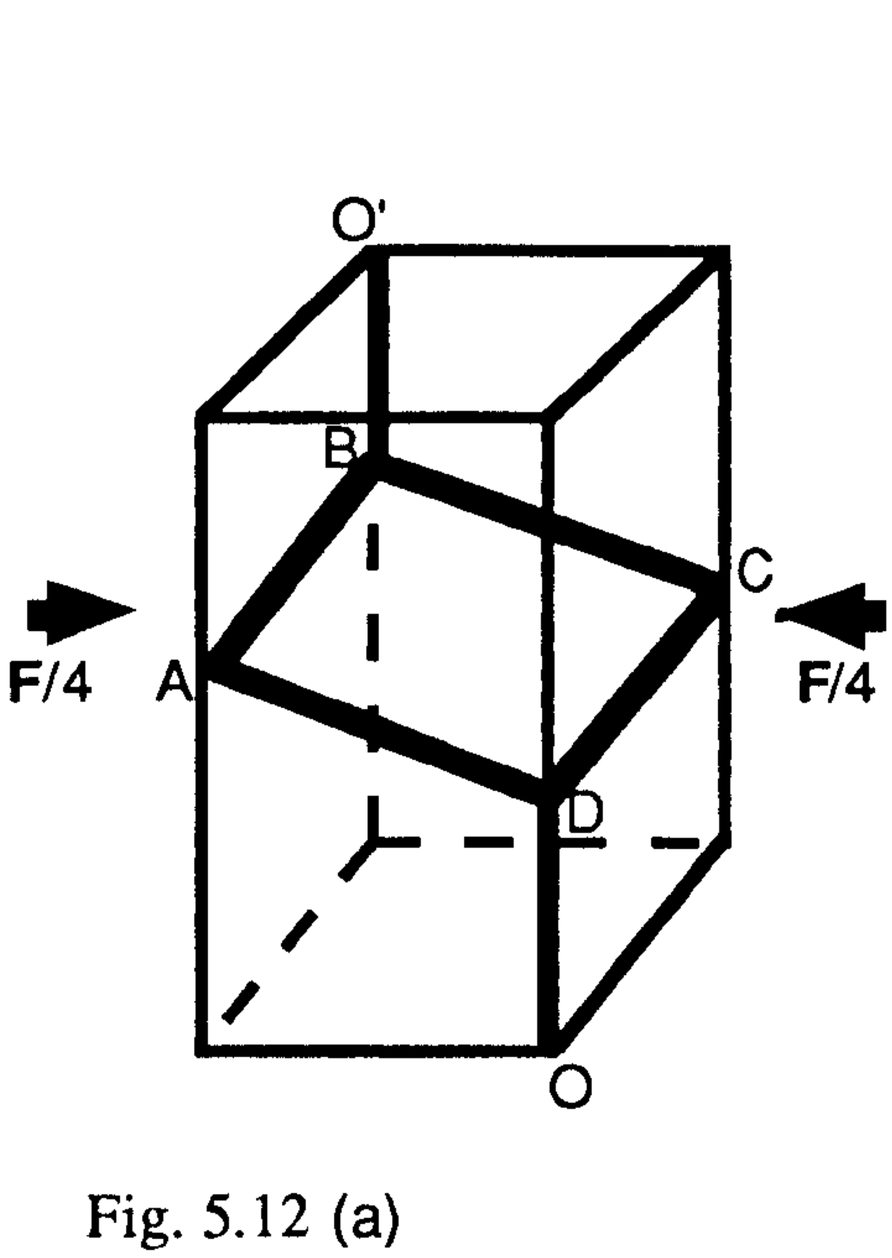

Fig. 5.12 (a)

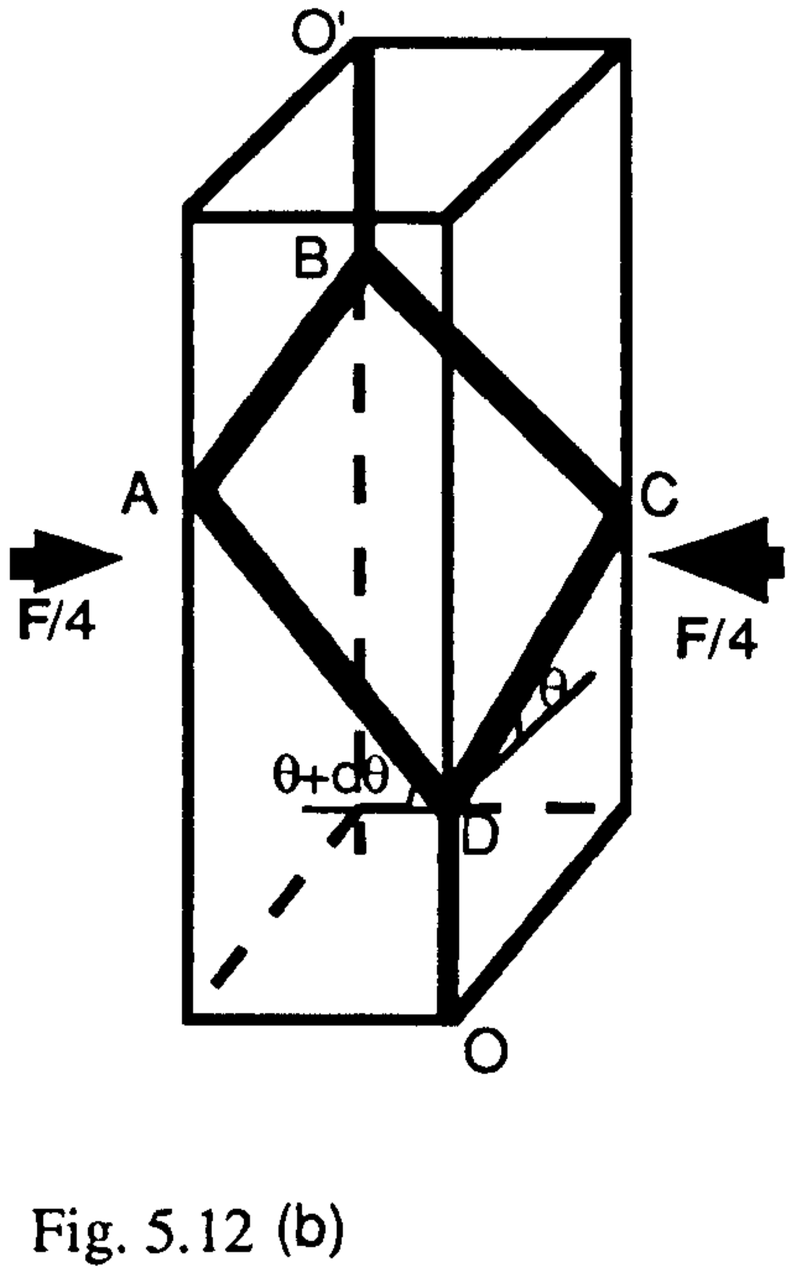

Fig. 5.12 (b)

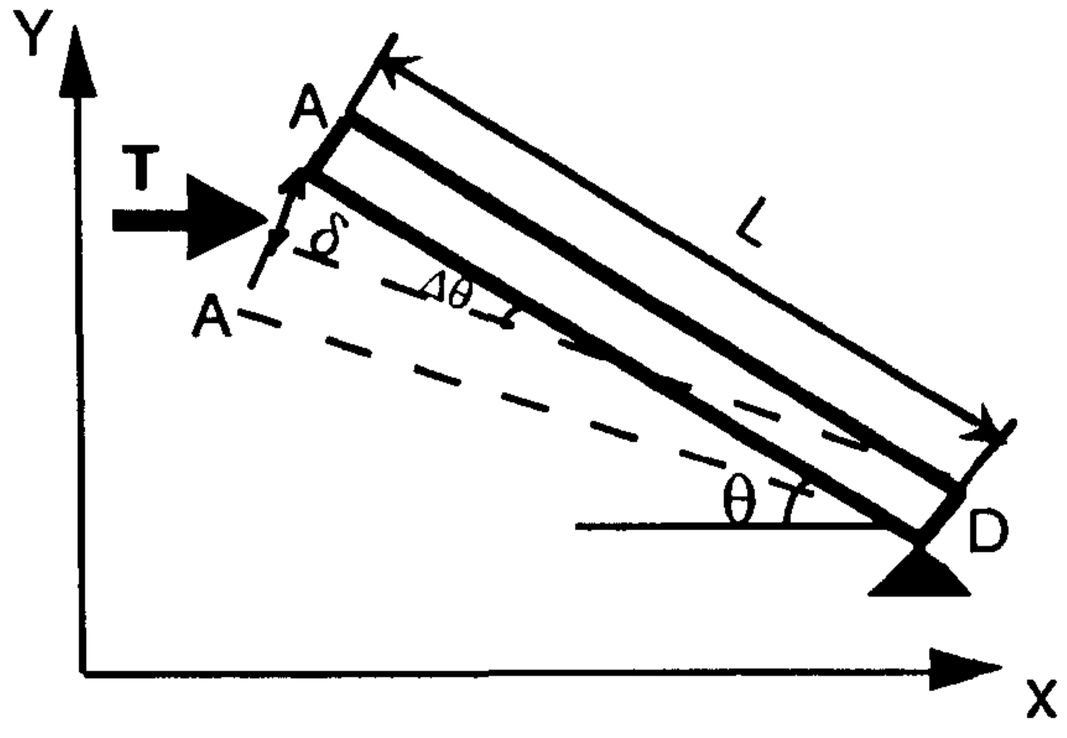

Fig.5.12 (c)

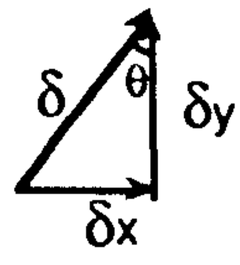

Fig.5.12 (d)

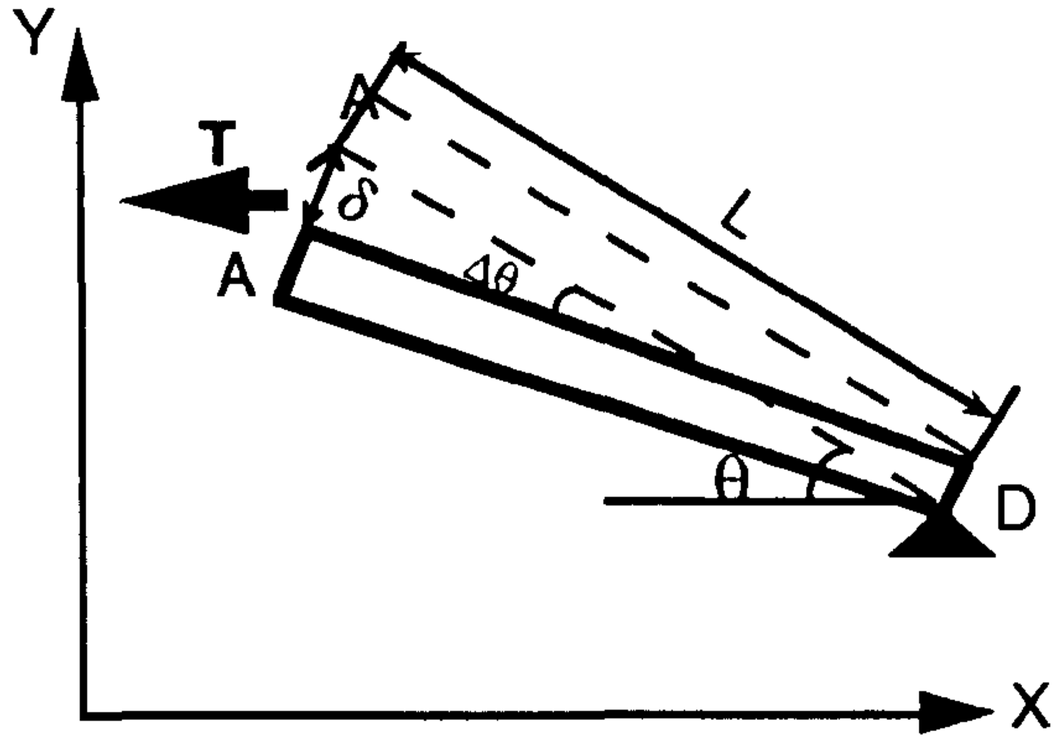

Fig.5.12 (e)

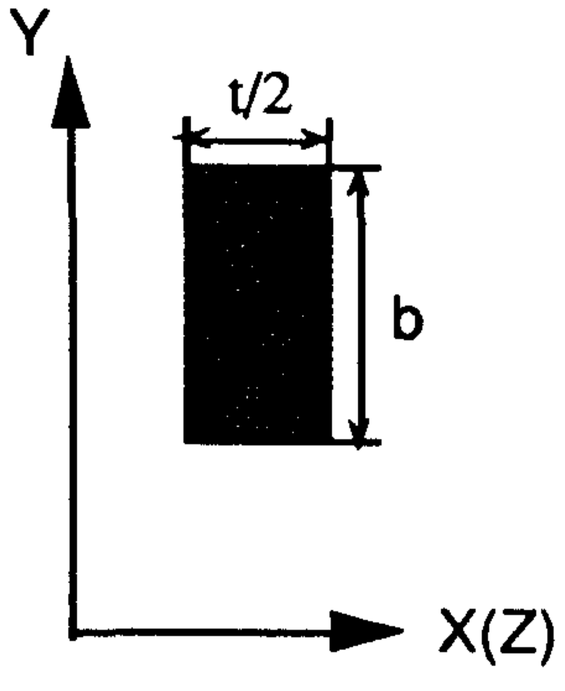

Fig.5.12 (f)

Fig. 5.12 Cell deformation by cell rib hinging, giving linear-elastic compression of the foam. (Loading in the x direction). (a) An in-deformed octant of the unit cell. (b) The deformation caused by loading in the x direction. (c) The hinging deflection of the cell rib caused by the compressive load in the x direction. (d) The deflection of the cell rib and its components along the x and y direction for compression along x. (e) The hinging deflection of the cell rib caused by the tensile force in the x direction. (f) The cross section area of one rib in an octant of the unit cell.

Figure 5.12 illustrates one octant of the unit cell for the conventional geometric unit loaded in the x direction. In this case ribs AD and BC are caused to hinge. The cell rib is assumed to act as a cantilever beam, fixed at the right end but guided and loaded at the left end thus ensuring a moment there. If the force in the x-direction applied to the whole unit cell is F, then that applied to the faces of one octant in the y-z plane will be F/4 which is defined here as T, so that

$$T = \frac{F}{4} = \frac{\sigma_x \times 2(h + 2L\sin\theta) \times 2L\cos\theta}{4} \qquad (5.53)$$

Where: σ_x, is negative for a compressive stress in the x direction.

The deflection, δ is,

$$\delta = L\sin\Delta\theta \approx L\Delta\theta \qquad (5.54)$$

Where: δ and $\Delta\theta$ are as defined in Figure 5.12.

and from the analysis in *Figure* 5.12(d), we know that,

$$\delta_x = -L\Delta\theta \sin\theta \qquad (5.55)$$

$$\delta_y = L\Delta\theta \cos\theta \qquad (5.56)$$

for compression loading in the x direction.

Since hinging only occurs in the x-y plane for a stress applied in the x-direction,

$$\delta_Z = 0. \qquad (5.57)$$

The engineering strain can be calculated as,

$$\varepsilon_x = \frac{\delta_x}{x} = \frac{\delta_x}{L\cos\theta} = -\frac{L\Delta\theta \sin\theta}{L\cos\theta} \qquad (5.58)$$

$$\varepsilon_y = \frac{\delta_y}{y} = \frac{\delta_y}{h + 2L\sin\theta} = \frac{L\Delta\theta \cos\theta}{h + 2L\sin\theta} \qquad (5.59)$$

and

$$\varepsilon_Z = 0. \qquad (5.60)$$

The Poisson's ratios can then be obtained as,

$$\upsilon_{xy} = \frac{-\varepsilon_y}{\varepsilon_x} = \frac{L\Delta\theta\cos\theta}{h + 2L\sin\theta} \times \frac{L\cos\theta}{L\Delta\theta\sin\theta}$$

$$= \frac{\cos^2\theta}{\sin\theta(\alpha + 2\sin\theta)} \qquad (5.61)$$

and

$$\nu_{xz} = \frac{-\varepsilon_Z}{\varepsilon_X} = 0. \qquad (5.62)$$

From *EQ* 5.53 and 5.58, the Young's modulus, E_X can also be easily calculated as,

$$E_x = \frac{\sigma_X}{\varepsilon_X} = \frac{T}{(h + 2L\sin\theta)L\cos\theta} \times \frac{L\cos\theta}{L\Delta\theta\sin\theta}. \qquad (5.63)$$

In this case, according to the usual definition, and resolving the force across the beam direction,

$$T\sin\theta = K_h L\Delta\theta \qquad (5.64)$$

Where: K_h, is the hinging force constant defined in the standard way (i.e. $F = K_h\delta$, and here $F = T\sin\theta$).

hence, $$T = \frac{K_h L\Delta\theta}{\sin\theta} \qquad (5.65)$$

therefore, $$E_x = \frac{K_h L\Delta\theta}{(h + 2L\sin\theta)L\cos\theta} \times \frac{L\cos\theta}{L\Delta\theta\sin^2\theta}$$

$$= \frac{K_h}{(h + 2L\sin\theta)\sin^2\theta}$$

$$= \frac{K_h}{L(\alpha + 2\sin\theta)\sin^2\theta}. \qquad (5.66)$$

5.4.3 Loading in the Z-Direction

Ribs AB and CD are caused to hinge. By symmetry,

$$\upsilon_{zy} = \frac{-\varepsilon_y}{\varepsilon_z} = \frac{\cos^2\theta}{\sin\theta(\alpha + 2\sin\theta)}. \qquad (5.67)$$

$$\nu_{zx} = \frac{-\varepsilon_X}{\varepsilon_Z} = 0. \qquad (5.68)$$

$$E_Z = \frac{\sigma_Z}{\varepsilon_Z} = \frac{K_h}{L(\alpha + 2\sin\theta)\sin^2\theta}. \qquad (5.69)$$

5.4.4 Loading in the Y-Direction

Figure 5.13 shows the vertical tensile loading of the foam. In this case ribs AB, BC, CD and AD all hinge. As for the previous case, the cell rib can be assumed to act as a cantilever beam, fixed at the right end but guided and loaded at the left end thus ensuring a moment there. If the force in the y-direction applied to the whole unit cell is F, then that applied to one octant of the unit cell will F/4.

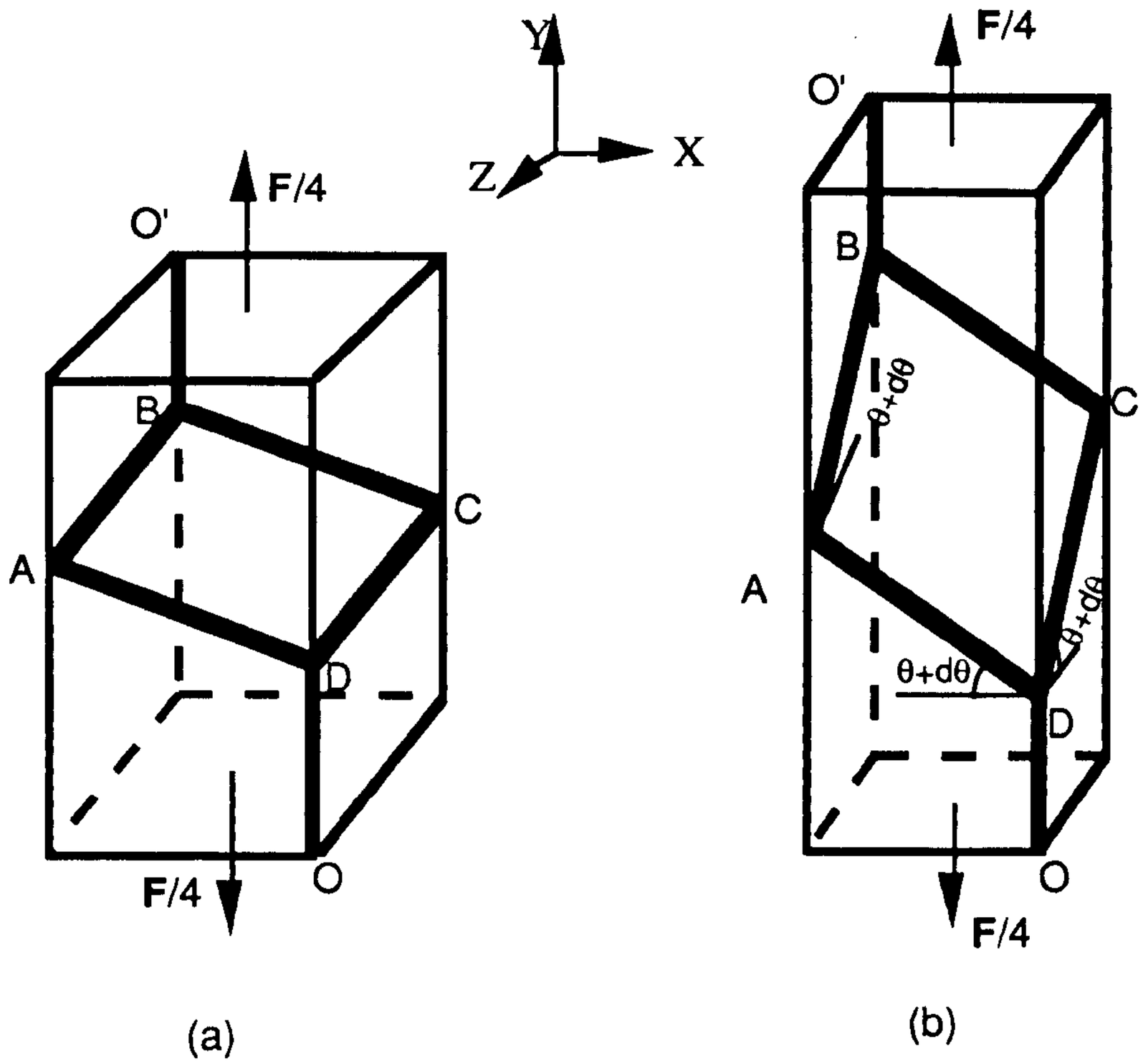

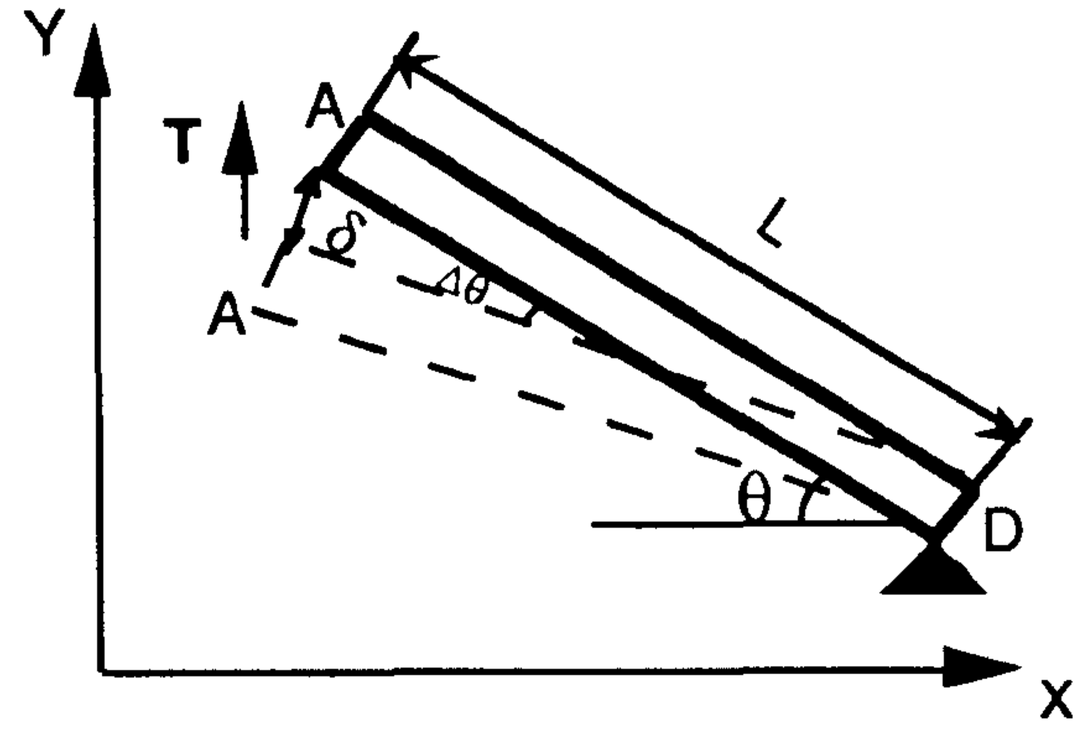

(c)

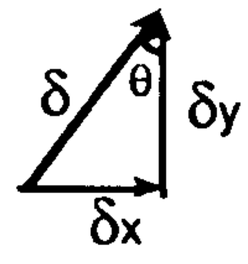

(d)

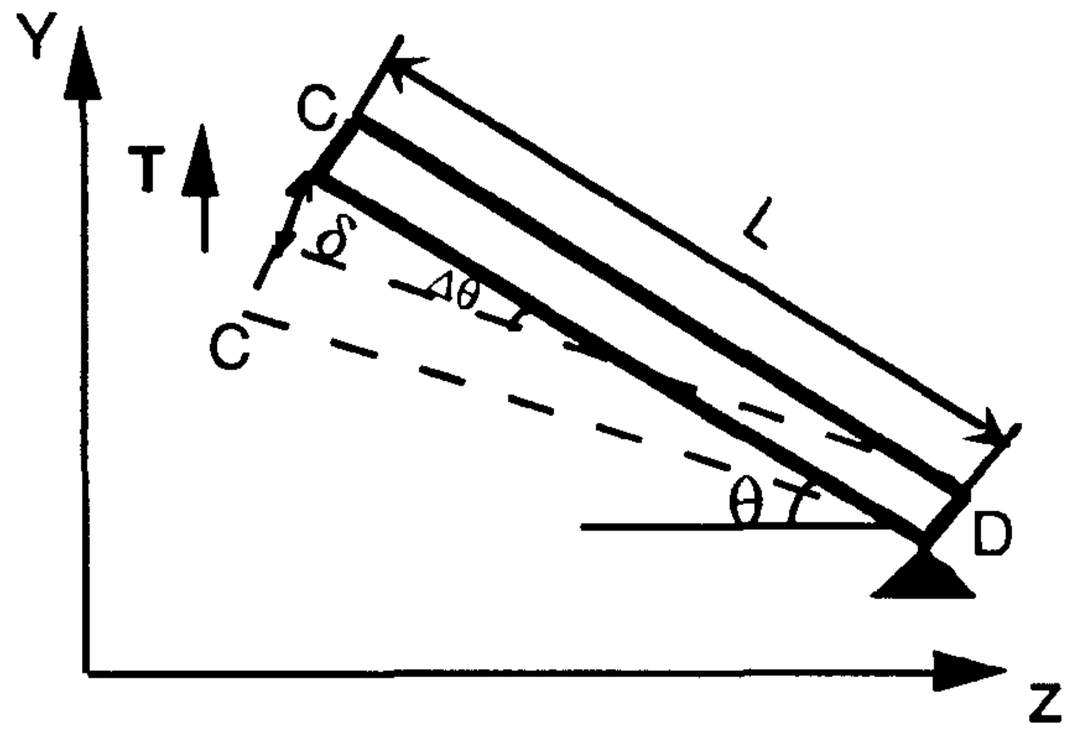

(e)

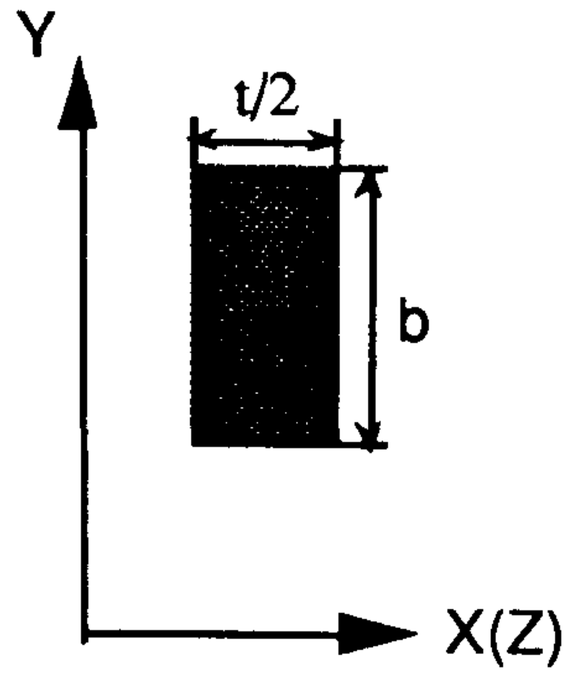

(f)

Fig. 5.13 Cell deformation by cell rib hinging, giving linear-elastic tension of the foam: (a) One octant of the in-deformed unit cell. (b) The deformation caused by a tensile force in the y direction. (c) The hinging deflection of the cell rib in the x-y plane caused by the tensile force in the y direction. (d) The deflection of the cell rib and its components along the x and y directions. (e) The hinging deflection of the cell rib in the y-z plane caused by the tensile force in the y direction. (f) The cross section area of one rib in an octant of the unit cell.

From beam theory, the deflection of each rib is,

$$\delta = L\sin\Delta\theta \approx L\Delta\theta .$$

Therefore, the total extensions of one octant under a tensile load in the y direction are given by:

$$\delta_x = -L\Delta\theta\sin\theta \qquad (5.70)$$

$$\delta_y = \delta_{yAD} + \delta_{yDC} = (L\Delta\theta\cos\theta) + (L\Delta\theta\cos\theta) \qquad (5.71)$$

Where: δ_{yAD} and δ_{yDC} are the components of the hinging deflection in the y direction for ribs AD and DC, respectively.

and $\delta_Z = -L\Delta\theta\sin\theta .$ (5.72)

Therefore,

$$\varepsilon_x = \frac{\delta_x}{x} = \frac{\delta_x}{L\cos\theta} = \frac{-L\Delta\theta\sin\theta}{L\cos\theta}. \qquad (5.73)$$

$$\varepsilon_y = \frac{\delta_y}{y} = \frac{\delta_y}{h+2L\sin\theta} = \frac{2L\Delta\theta\cos\theta}{h+2L\sin\theta}. \qquad (5.74)$$

$$\varepsilon_Z = \frac{\delta_z}{z} = \frac{\delta_Z}{L\cos\theta} = \frac{-L\Delta\theta\sin\theta}{L\cos\theta}. \qquad (5.75)$$

From *EQ* 5.73, 5.74 and 5.75, we can calculate the Poisson's ratio in the y direction,

$$\nu_{yx} = \frac{-\varepsilon_x}{\varepsilon_y} = \frac{\sin\theta(\alpha+2\sin\theta)}{(2\cos^2\theta)} \qquad (5.76)$$

and

$$\nu_{yz} = \frac{-\varepsilon_Z}{\varepsilon_y} = \frac{\sin\theta(\alpha+2\sin\theta)}{(2\cos^2\theta)}. \qquad (5.77)$$

Since the tensile force applied to one octant of the unit cell is T, then,

$$T = \sigma_y(L\cos\theta)(L\cos\theta) \qquad (5.78)$$

Where: σ_y, is the tensile stress in the y direction.

and from the usual definition,

$$T\cos\theta = K_h\delta = K_hL\Delta\theta, \qquad (5.79)$$

hence, $$E_y = \frac{\sigma_y}{\varepsilon_y} = \frac{T}{L^2\cos^2\theta}\times\frac{h+2L\sin\theta}{2L\Delta\theta\cos\theta}$$

$$= \frac{K_hL\Delta\theta}{L^2\cos^3\theta}\times\frac{h+2L\sin\theta}{2L\Delta\theta\cos\theta}$$

$$= \frac{K_h(\alpha+2\sin\theta)}{2L\cos^4\theta}. \qquad (5.80)$$

5.4.5 Shear Modulus of the Hinging Model

5.4.5.1 Shearing in the Z-Y Plane.

Consider a shear stress exerted on a half of the unit cell of the foam in the z direction on the faces with outward normal in the y direction, i.e. τ_{zy}. See Figure 5.11(a) and (b).

The cell deformation under the shear stress, τ_{zy} is illustrated by *Figure* 5.14. There is no relative motion of the points E, B and F. The shearing deflexion of the

structure is entirely due to hinging of beam BD and AB (and BC), and their rotation about the point B. The forces are shown in *Figure* 5.11(c). The shear displacement of unit cell in the z direction is:

$$u_z = 2(u_s + 2u_s'). \tag{5.81}$$

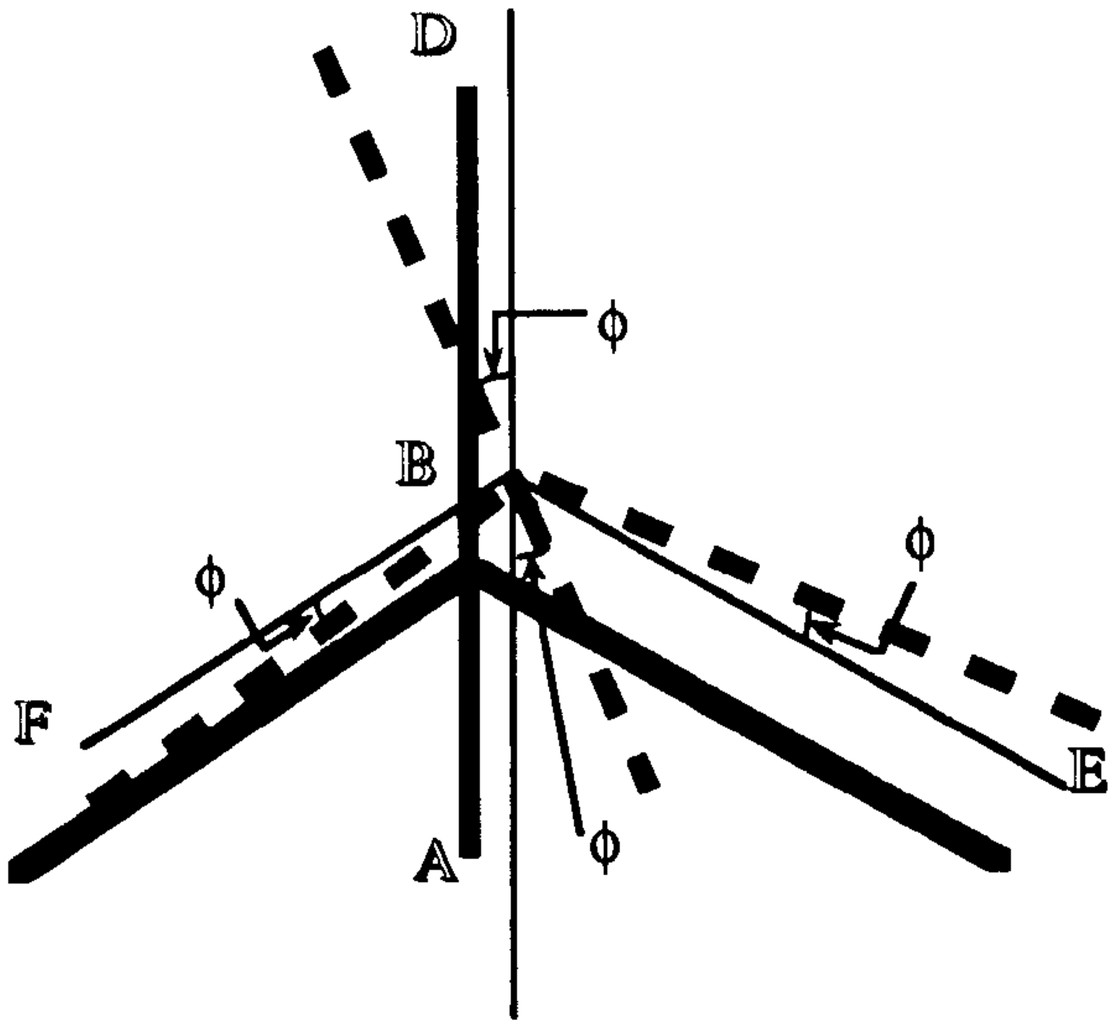

Fig. 5.14 Cell deformation (hinging and internal rotation) under shear stress, τ_{zy}.

All the joints rotate through an angle ϕ. The deflection of BE is:

$$\delta = \phi L. \tag{5.82}$$

According to the usual definition, in this case,

$$\frac{F}{4}\sin\theta = K_h\delta = K_h L\phi. \tag{5.83}$$

From EQ.5.44(a) and EQ. 5.46(c),

$$M^{BE} = \frac{F}{4}\sin\theta \times L = \frac{Fh}{4(1+\sin^2\theta)} = K_h L^2\phi, \tag{5.84a}$$

hence $$\phi = \frac{Fh}{4K_h(1+\sin^2\theta)L^2}. \tag{5.84b}$$

Shearing deflection of the point D with respect to B is:

$$u_s' = \frac{1}{2}\phi h. \tag{5.85a}$$

hence, $$u_s' = \frac{Fh^2}{8K_h(1+\sin^2\theta)L^2}. \tag{5.85b}$$

Shearing deflection of the point A with respect to B is,

$$u_s = \phi L. \tag{5.86}$$

$$u_z = 2 \times (2u_s + u_s')$$

$$= \frac{Fh}{2L^2 K_h} \times \frac{(2L + \frac{1}{2}h)}{(1 + sin^2\theta)}. \qquad (5.87)$$

The shear strain, γ_{zy}, is given by:

$$\gamma = \frac{u_z}{y} = \frac{u_z}{2(h + 2L\sin\theta)}. \qquad (5.88)$$

The shear stress, τ_{zy}, is,

$$\tau_{yx} = \frac{F}{xz} = \frac{F}{(2L\cos\theta)^2}, \qquad (5.89)$$

giving the shear modulus $G = \tau/\gamma$,

$$G_{zy} = \frac{F}{4L^2\cos^2\theta} \times \frac{2(h + 2L\sin\theta)}{u_z}$$

$$= \frac{K_h}{h cos^2\theta} \times \frac{(\alpha + 2sin\theta)(1 + sin^2\theta)}{(2 + \frac{\alpha}{2})} \qquad (5.90)$$

From the classical elasticity theory of anisotropic materials (e.g. Nye (1960)), we know that:

$$G_{yz} = G_{zy} \qquad (5.91)$$

therefore,

$$G_{yz} = \frac{K_h}{h cos^2\theta} \times \frac{(\alpha + 2sin\theta)(1 + sin^2\theta)}{(2 + \frac{\alpha}{2})}. \qquad (5.92)$$

5.4.5.2 Shearing in the X-Y Plane

In this case, the deformation caused by the shear stress which exerted on an octant of the unit cell in the x direction on the faces with outward normal in the y directional. i.e. τ_{xy}. By symmetry,

$$G_{xy} = G_{yx} = \frac{K_h}{h cos^2\theta} \times \frac{(\alpha + 2sin\theta)(1 + sin^2\theta)}{(2 + \frac{\alpha}{2})}. \qquad (5.93)$$

5.4.5.3 Shearing in the X-Z Plane

Consider a shear stress exerted on an octant of the unit cell of the foam in the x direction on the faces with outward normal in the z direction, i.e. τ_{xz}. The shear deflection is entirely due to hinging of the ribs AD and BC as shown in Figure 5.15.

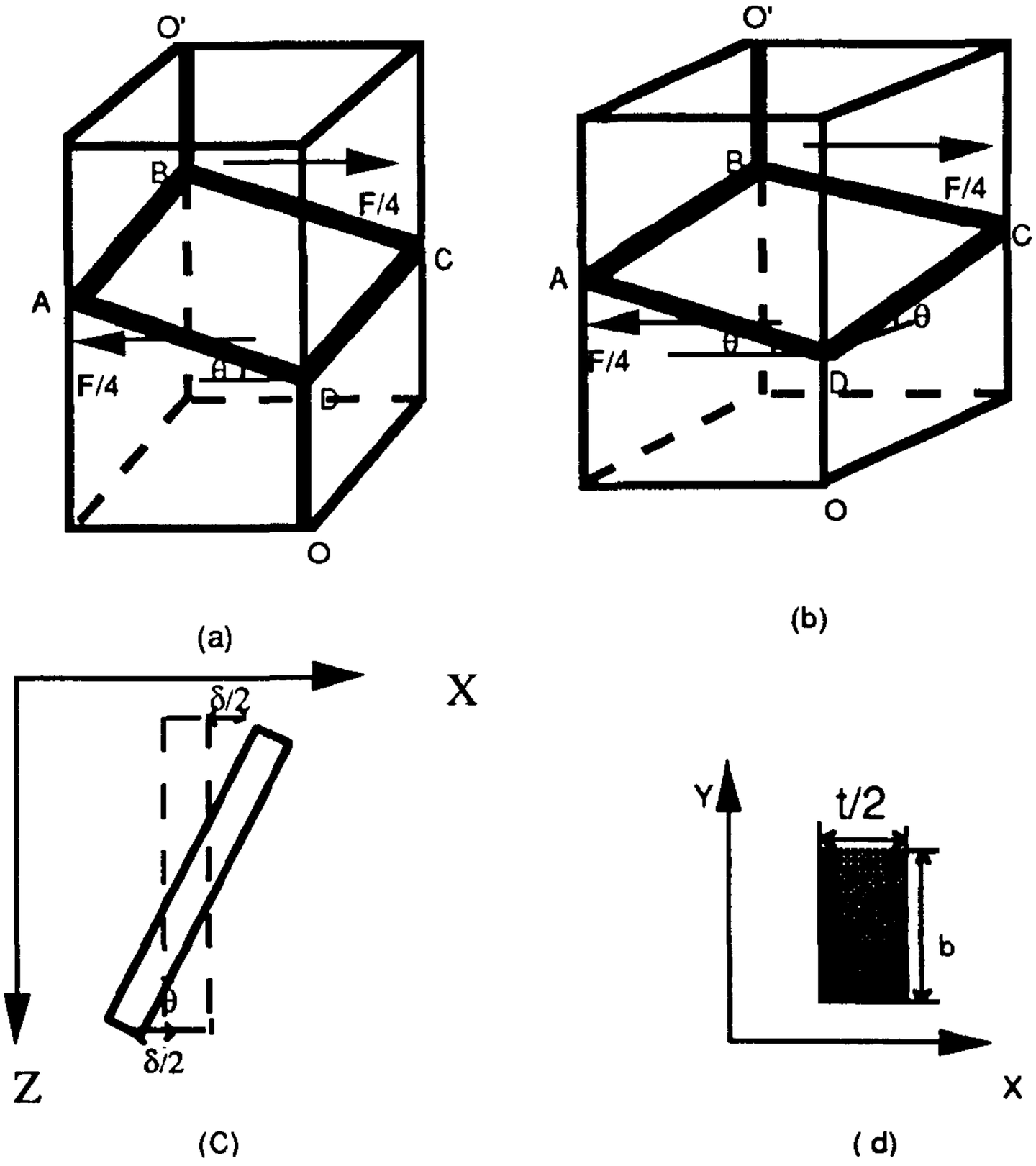

Fig. 5.15 The deformation due to τ_{xz} (Hinging model). (a) An in-deformed octant of the unit cell. (b) An deformed octant of the unit cell. (c) The hinging of the cell rib caused by the shear forces along the x direction. (Projection onto the x-y plane.) (d) The cross section area of one rib in an octant of the unit cell.

The deflection, δ, which caused by the shear force is,

$$\delta = L\cos\theta\sin\Delta\theta \approx (L\cos\theta)\Delta\theta . \qquad (5.94)$$

since here,

$$\delta_x = \delta = (L\cos\theta)\Delta\theta = u_s . \qquad (5.95)$$

therefore, the shear strain, γ, is given by

$$\gamma = \frac{u_s}{z} = \frac{u_s}{L\cos\theta} = \frac{(L\cos\theta)\Delta\theta}{L\cos\theta} . \qquad (5.96)$$

The shear stress, τ_{xz}, is

$$\tau_{xz} = \frac{T}{xy} = \frac{T}{L\cos\theta(h + 2L\sin\theta)} \qquad (5.97)$$

giving the shear modulus $G = \tau / \gamma$, hence

$$G_{xz} = \frac{T}{L\cos\theta(h + 2L\sin\theta)} \times \frac{L\cos\theta}{(L\cos\theta)\Delta\theta} \qquad (5.98)$$

and according to the usual definition,

$$T = K_h\delta = K_hL\Delta\theta \qquad (5.99)$$

therefore,

$$G_{xz} = \frac{K_hL\Delta\theta}{h+2L\sin\theta}\times\frac{1}{(L\cos\theta)\Delta\theta}$$

$$= \frac{K_h}{L\cos\theta(\alpha+2\sin\theta)}. \qquad (5.100)$$

By symmetry,

$$G_{zx} = \frac{K_h}{L\cos\theta(\alpha+2L\sin\theta)}. \qquad (5.101)$$

5.4.5.4 The Determination of K_h

From the micrographs of the foams, we know the two adjacent ribs are connected by a very small curved rib, q, and behave as one long bending beam (Figure 5.16). Under certain circumstances flexure was observed in the junction. This flexure is being interpreted as a hinging deformation mode. Assuming that a curved beam behaves in accordance with simple bending theory (Roark & Young 1975), then the change in angle due to an applied moment M is given by,

$$\Delta\theta = \int_0^q \frac{M}{E_sI}dq \qquad (5.102)$$

Where: q, is the length of the small curved beam DD'. $\Delta\theta$ is the change in cell angle.

Hence,

$$\Delta\theta = \frac{Mq}{E_sI}. \qquad (5.103)$$

Because q << L as shown in Figure 5.16, therefore, the applied moment acting on the hinge is approximately,

$$M \approx (T\cos\theta)\times\frac{L}{2}. \qquad (5.104)$$

Where: θ, is the cell angle.

Combining *EQ 5.103* and *EQ 5.104*, the deflection $\Delta\theta$ is derived as,

$$\Delta\theta = \frac{(T\cos\theta)Lq}{2E_sI}. \qquad (5.105)$$

Comparing *EQ.5.105* with *EQ. 5.79*, K_h can be obtained as:

$$K_h = \frac{2E_s I}{L^2 q}. \qquad (5.106)$$

The second moment of area of a rectangular beam of thickness, t, and width, b, is, $I = \frac{bt^3}{12}$, when b=t,

$$K_h = \frac{E_s t^4}{6L^2 q}. \qquad (5.107)$$

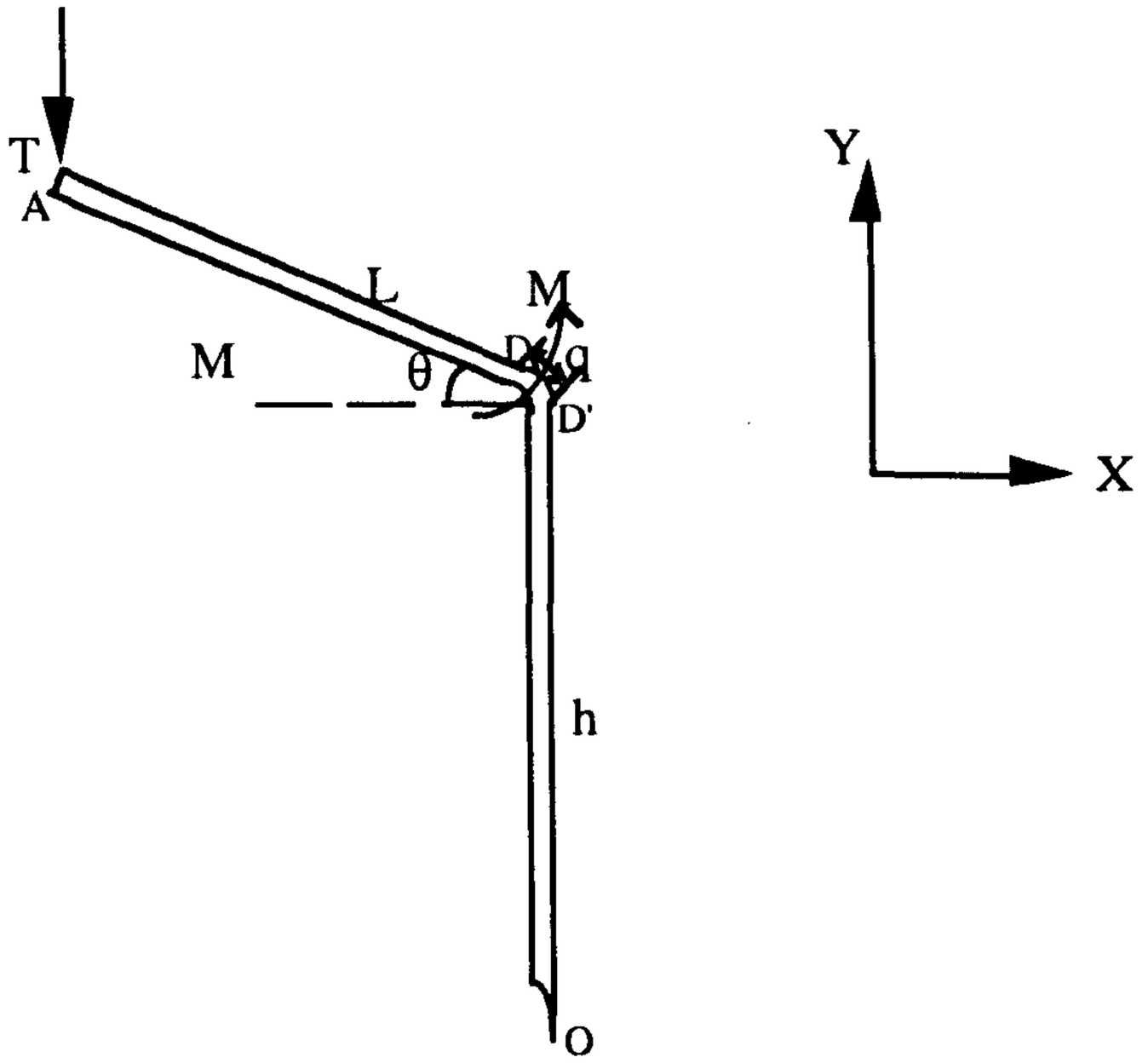

Fig. 5.16 The two adjacent ribs are jointed by a very small curved beam, q. (e.g. DD).

5.4.6 Summary of the Hinging Model

The elastic moduli due to hinging of the ribs are summarised in Table 5.2. As already noted, θ is positive for conventional foam and θ is negative for auxetic foam.

(Table 5.2)

	Expressions $(\theta_x = \theta_z = \theta, L_x = L_z = L)$	General Expressions $(L_x \neq L_z, \theta_x \neq \theta_z)$
Ex	$\frac{K_h}{L(\alpha + 2\sin\theta)\sin^2\theta}$	$\frac{K_h L_x \cos\theta_x}{L_z \cos\theta_z (h + L_x \sin\theta_x + L_z \sin\theta_z)\sin^2\theta_x}$
Ey	$\frac{K_h(\alpha + 2\sin\theta)}{2L\cos^4\theta}$	$\frac{K_h(L_x + L_z)(h + L_z \sin\theta_z + L_x \sin\theta_x)}{(\cos\theta_x + \cos\theta_z)(L_x \cos\theta_x)(L_z \cos\theta_z)(L_x \cos\theta_x + L_z \cos\theta_z)}$
Ez	$\frac{K_h}{L(\alpha + 2\sin\theta)\sin^2\theta}$	$\frac{K_h L_z \cos\theta_z}{L_x \cos\theta_x (h + L_x \sin\theta_x + L_z \sin\theta_z)\sin^2\theta_z}$
ν_{xy}	$\frac{\cos^2\theta}{(2\sin\theta + \alpha)\sin\theta}$	$\frac{L_x \cos^2\theta_x}{(h + L_x \sin\theta_x + L_z \sin\theta_z)\sin\theta_x}$
ν_{xz}	0	0
ν_{zx}	0	0
ν_{zy}	$\frac{\cos^2\theta}{(2\sin\theta + \alpha)\sin\theta}$	$\frac{L_z \cos^2\theta_z}{(h + L_x \sin\theta_x + L_z \sin\theta_z)\sin\theta_z}$

ν_{yx}	$\frac{\sin\theta(\alpha+2\sin\theta)}{(2\cos^2\theta)}$	$\frac{\sin\theta_x(h+L_x\sin\theta_x+L_z\sin\theta_z)}{\cos\theta_x(L_x\cos\theta_x+L_z\cos\theta_z)}$
ν_{yz}	$\frac{\sin\theta(\alpha+2\sin\theta)}{(2\cos^2\theta)}$	$\frac{\sin\theta_z(h+L_x\sin\theta_x+L_z\sin\theta_z)}{\cos\theta_z(L_x\cos\theta_x+L_z\cos\theta_z)}$
G_{zy}	$\frac{K_h}{h\cos^2\theta}\times\frac{(\alpha+2\sin\theta)(1+\sin^2\theta)}{(2+\frac{\alpha}{2})}$	$\frac{K_hL_z(1+\sin^2\theta_z)(h+L_x\sin\theta_x+L_z\sin\theta_z)}{L_xh\cos\theta_x\cos\theta_z(L_x+L_z+0.5h)}$
G_{yz}	$\frac{K_h}{h\cos^2\theta}\times\frac{(\alpha+2\sin\theta)(1+\sin^2\theta)}{(2+\frac{\alpha}{2})}$	$\frac{K_hL_z(1+\sin^2\theta_z)(h+L_x\sin\theta_x+L_z\sin\theta_z)}{L_xh\cos\theta_x\cos\theta_z(L_x+L_z+0.5h)}$
G_{yx}	$\frac{K_h}{h\cos^2\theta}\times\frac{(\alpha+2\sin\theta)(1+\sin^2\theta)}{(2+\frac{\alpha}{2})}$	$\frac{K_hL_z(1+\sin^2\theta_z)(h+L_x\sin\theta_x+L_z\sin\theta_z)}{L_xh\cos\theta_x\cos\theta_z(L_x+L_z+0.5h)}$
G_{xy}	$\frac{K_h}{h\cos^2\theta}\times\frac{(\alpha+2\sin\theta)(1+\sin^2\theta)}{(2+\frac{\alpha}{2})}$	$\frac{K_hL_z(1+\sin^2\theta_z)(h+L_x\sin\theta_x+L_z\sin\theta_z)}{L_xh\cos\theta_x\cos\theta_z(L_x+L_z+0.5h)}$
G_{xz}	$\frac{K_h}{L\cos\theta(\alpha+2\sin\theta)}$	$\frac{K_hL_z}{L_x\cos\theta_x(h+L_x\sin\theta_x+L_z\sin\theta_z)}$
G_{zx}	$\frac{K_h}{L\cos\theta(\alpha+2\sin\theta)}$	$\frac{K_hL_x}{L_z\cos\theta_z(h+L_x\sin\theta_x+L_z\sin\theta_z)}$

Table 5.2 The hinging model expressions of Young's modulus, Poisson's ratio and shear modulus of conventional and auxetic foams. θ is positive for conventional foam and θ is negative for auxetic foam.

Comparison of Table 5.1 and Table 5.2 reveals that the expressions for Poisson's ratio are identical for flexure and hinging. Furthermore, if we define the flexure force constant as:

$$K_f = \frac{E_s t^4}{L^3} = \frac{12E_sI}{L^3} \qquad (5.108)$$

then, for the special case: $\theta_x = \theta_z = \theta$, the expressions for Young's Modulus are seen to differ only by the ratio of the force constants involved.

i.e. $$\frac{E_i^{Hinging}}{E_i^{Flexure}} = \frac{K_h}{K_f}. \quad \text{(note: } i \text{ is x, y, or z).} \qquad (5.109)$$

5.5 The Stretching Model for the Foam Cell Structure

5.5.1 Loading in the X-Direction

This model assumes that the cell wall junctions are rigid so that the cell angles remain constant whilst the walls can only stretch along their axes. To develop the equations for the stretching model consider the force W applied to the yz faces of one octant of the unit cell:

$$W = \sigma_x(h+2L\sin\theta)L\cos\theta. \qquad (5.110)$$

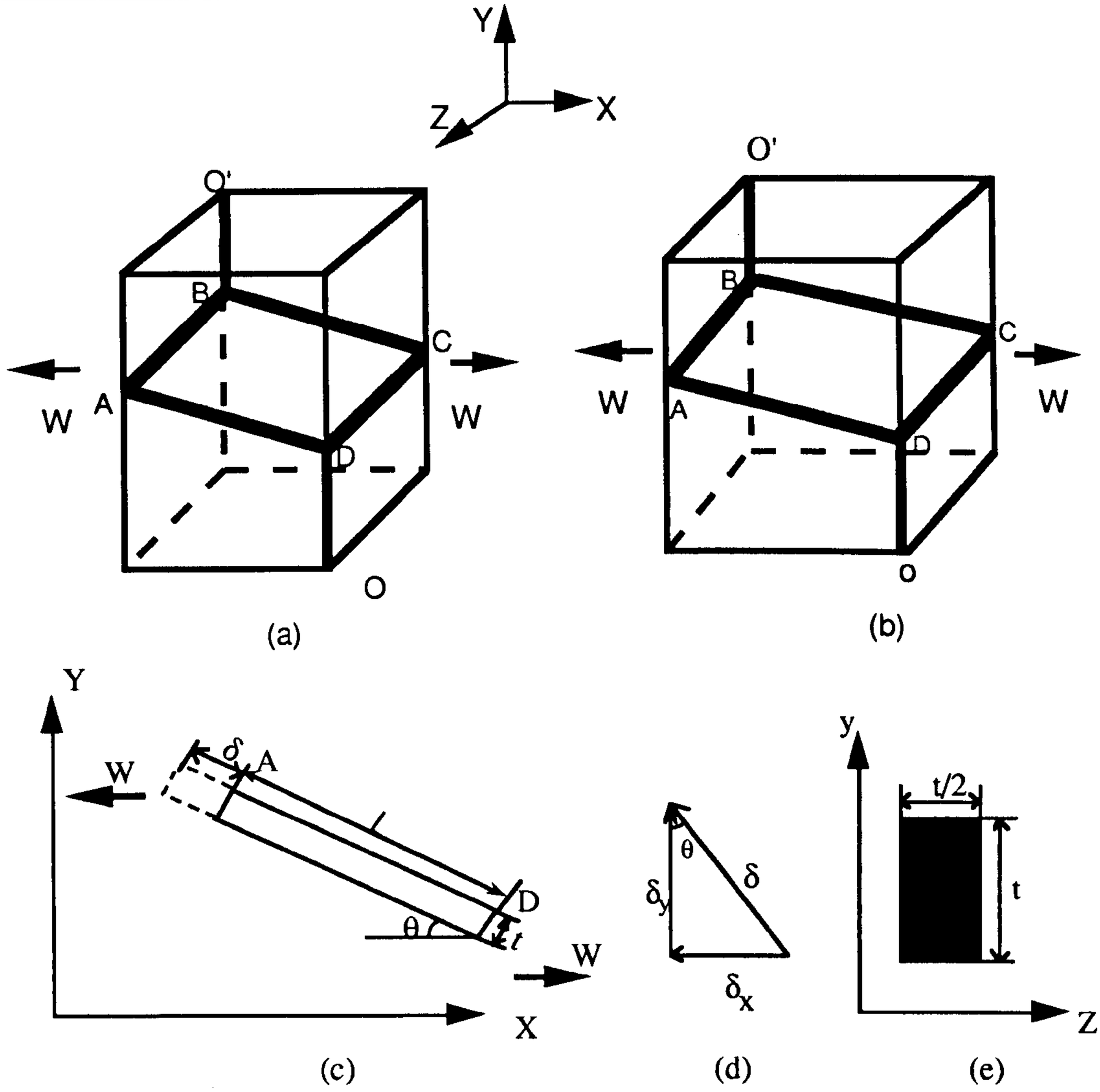

Fig. 5.17 Cell deformation by cell rib stretching, giving linear-elastic extension of the foam: (a) An undeformed octant of the unit cell. (b) The stretching deformation caused by loading in the x direction. (c) The extension of the cell rib AD caused by a tensile force in the x direction. (d) The extension of the cell rib and its components along the x and y directions. (e) The cross section area of one rib in an octant of the unit cell.

In this case, only ribs AD and BC stretch, and they are equivalent to one rib in the unit cell. When the force W is applied parallel to the x axis, ribs AD and BC extend by δ, and according to the usual definition:

$$W\cos\theta = K_s\delta \qquad (5.111)$$

Where: K_s, is the stretching force constant defined in the standard way.

$$\text{Since } E_s = \frac{\sigma_s}{\varepsilon_s} = \frac{W\cos\theta}{t^2} \times \frac{L}{\delta} \qquad (5.112)$$

Where: σ_s, is the tensile stress applied on one rib.

Therefore, the force constant for stretching, K_S, is

$$K_s = \frac{E_s t^2}{L}. \qquad (5.113)$$

From *Figure* 5.17 (d), the total deflection in the x-direction of the unit cell due to the extension of one rib is:

$$\delta_x = \delta cos\theta = \frac{W cos^2\theta}{K_s}. \qquad (5.114)$$

The total deflection in the y-direction of the unit cell is:

$$\delta_y = \delta sin\theta = \frac{W cos\theta sin\theta}{K_s}. \qquad (5.115)$$

Since there is no component of rib extension in the z-direction of the unit cell,

$$\delta_z = 0. \qquad (5.116)$$

The Poisson's ratios for the x direction can be calculated by using the following equations:

$$\nu_{xy} = \frac{-\varepsilon_y}{\varepsilon_x} = \frac{-\delta_y}{h + 2L sin\theta} \times \frac{L cos\theta}{\delta_x} = \frac{-sin\theta}{\alpha + 2 sin\theta} \qquad (5.117)$$

Where: $\alpha = \frac{h}{L}$.

and, $$\nu_{xz} = \frac{-\varepsilon_z}{\varepsilon_x} = \frac{-\delta_z}{L cos\theta} \times \frac{L cos\theta}{\delta_x} = 0. \qquad (5.118)$$

The engineering strain for one octant of the unit cell can be calculated by using:

$$\varepsilon_x = \frac{\delta_x}{x} = \frac{\delta_x}{L cos\theta} = \frac{W cos^2\theta}{K_s L cos\theta} = \frac{\sigma_x (h + 2L sin\theta) L cos^3\theta}{K_s L cos\theta}. \qquad (5.119)$$

Combining the strain and the stress, Young's modulus for the x-direction can be obtained as:

$$E_x = \frac{\sigma_x}{\varepsilon_x} = \frac{K_s}{(h + 2L sin\theta) cos^2\theta} = \frac{E_s}{(\alpha + 2 sin\theta) cos^2\theta} \left(\frac{t}{L}\right)^2. \qquad (5.120)$$

5.5.2 Loading in the Z-Direction

By symmetry: $\nu_{zy} = \frac{-sin\theta}{\alpha + 2 sin\theta}$ *(5.121)*

$$\nu_{zx} = 0 \qquad (5.122)$$

and

$$E_z = \frac{E_s}{(\alpha + 2\sin\theta)\cos^2\theta}\left(\frac{t}{L}\right)^2. \qquad (5.123)$$

5.5.3 Loading in the Y-Direction

The force W applied to the xz faces of one octant of the unit cell is:

$$W = \sigma_y \times L^2 \cos^2\theta. \qquad (5.124)$$

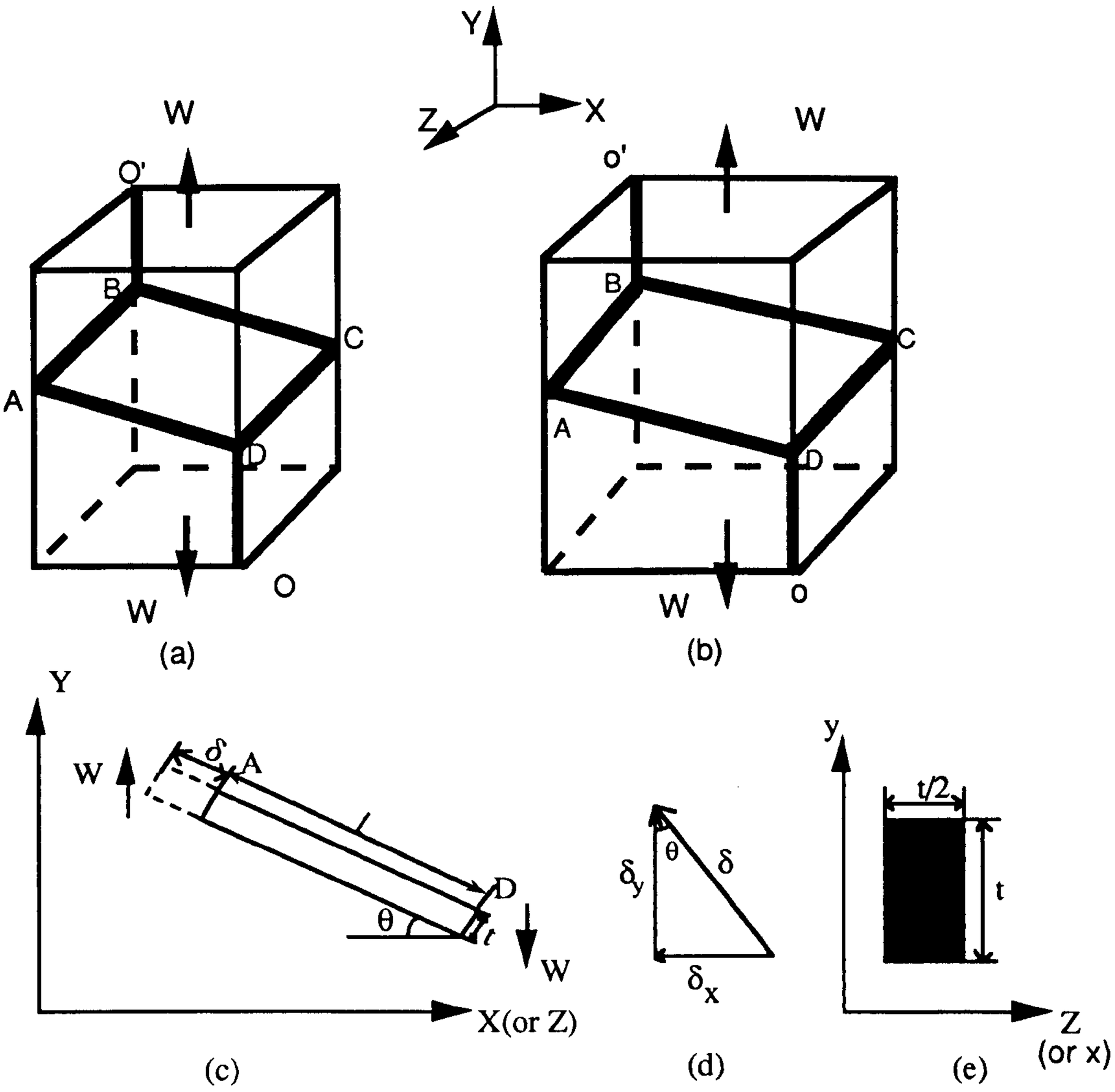

Fig. 5.18

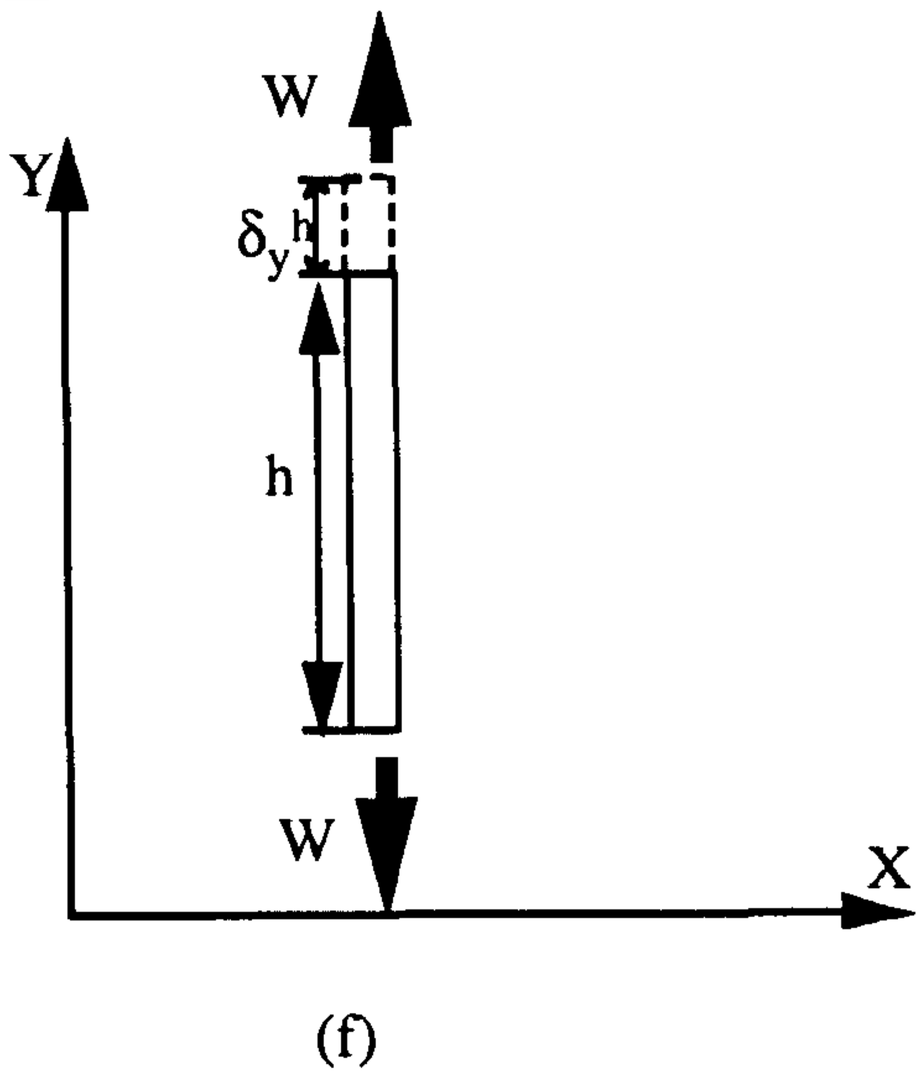

(f)

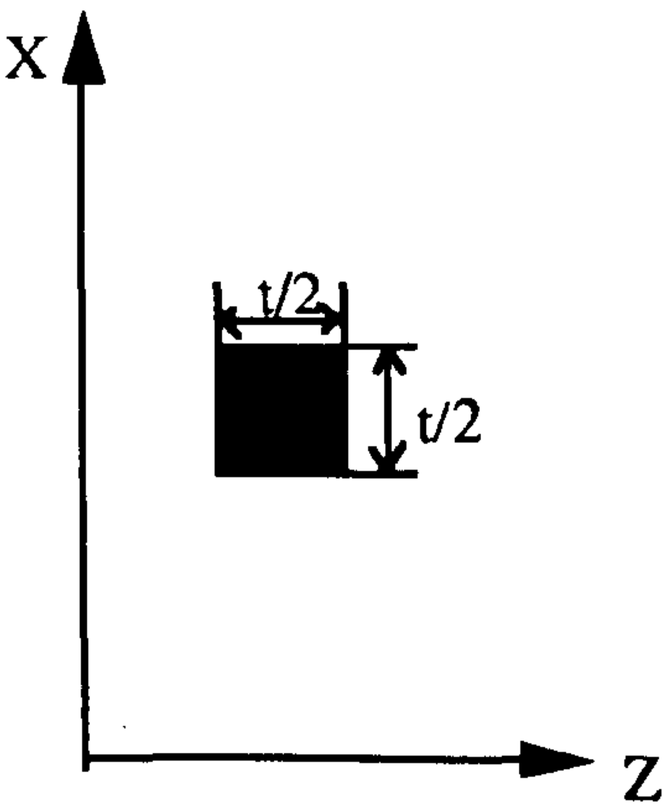

(g)

Fig. 5.18 Cell deformation by cell rib stretching, giving linear-elastic extension of the foam: (a) One in-deformed octant of the unit cell. (b) The stretching deformation caused by loading in the y direction. (c) The extension of the angled cell rib caused by the tensile force in the y direction. (d) The extension of the angled cell rib and its components along the x and y directions. (e) The cross section area of one angled rib in an octant of the unit cell. (f) The extension of the vertical cell rib caused by the tensile force in the y direction. (g) The cross section area of one vertical rib in an octant of the unit cell.

In this case, the vertical ribs O'B and OD equivalent to one rib of length h, depth t/2 and thickness t/2 in one octant of the unit cell, and

$$E_s = \frac{\sigma_s}{\varepsilon_s} = \frac{W}{\frac{t^2}{4}} \times \frac{h}{\delta_y{}^h} \qquad (5.125)$$

Where: σ_s, is the tensile stress applied along one vertical rib of length L (e.g. O'B+OD) in the y direction, and $\delta_y{}^h$ the extension of the vertical rib of length h in the y direction.

According to the usual definition,

$$W = K_s{}^h \delta_y{}^h. \qquad (5.126)$$

Where: $K_s{}^h$, is the stretching constant for the vertical rib of length h.

From EQ 5.125 and EQ 5.126,

$$E_s = \frac{4K_s{}^h h}{t^2} \qquad (5.127)$$

hence,

$$K_s{}^h = \frac{E_s t^2}{4h} = \frac{E_s \frac{t^2}{L}}{4\alpha} = \frac{K_s}{4\alpha}. \qquad (5.128)$$

and

$$\delta_y{}^h = \frac{W}{K_s{}^h} = \frac{W \times 4\alpha}{K_s}. \qquad (5.129)$$

The stretching deflection of the vertical rib in the other two directions is zero, i.e.

$$\delta_x{}^h = 0 \qquad (5.130)$$

$$\delta_z{}^h = 0. \qquad (5.131)$$

Where: $\delta_x{}^h$ and $\delta_z{}^h$ are the components of the extension of the vertical rib.

The angled ribs AD and BC in one octant of the unit cell are equivalent to one cell rib of length L, depth t and thickness t in the x-y plane of the unit cell, and the other two angled ribs AB and CD in the same octant of the unit cell are equivalent to one cell rib of length L, depth t and thickness t in the y-z plane of the unit cell. Therefore, The total stretching deflection of the two angled ribs in the unit cell is:

$$\delta_{total}{}^l = \delta^l + \delta^l = 2\delta^l. \qquad (5.132)$$

By definition,

$$W \sin\theta = K_s \delta^l \qquad (5.133)$$

Where: δ^l, is the extension of one angled rib of length L.

The total deflection of the two angled ribs in the y-direction is:

$$\delta_y{}^l = \delta^l \sin\theta + \delta^l \sin\theta = \frac{2W \sin^2\theta}{K_s}, \qquad (5.134)$$

the total deflection of the angled ribs in the x-direction is:

$$\delta_x{}^l = \delta^l \cos\theta + \delta^l \cos 90^0 = \frac{W \sin\theta \cos\theta}{K_s}, \qquad (5.135)$$

and the total deflection of the angled ribs in the z-direction is:

$$\delta_z{}^l = \delta^l \cos\theta + \delta^l \cos 90^0 = \frac{W \sin\theta \cos\theta}{K_s}. \qquad (5.136)$$

From EQ. 5.130 and EQ. 5.135, the total extension in the x-direction of one octant of the unit cell is:

$$\delta_x = \delta_x{}^h + \delta_x{}^l = 0 + \frac{W \sin\theta \cos\theta}{K_s} = \frac{W \sin\theta \cos\theta}{K_s}. \qquad (5.137)$$

From EQ. 5.131 and EQ. 5.136, the total extension in the z-direction of one octant of the unit cell is:

$$\delta_z = \delta_z{}^h + \delta_z{}^l = 0 + \frac{W \sin\theta \cos\theta}{K_s} = \frac{W \sin\theta \cos\theta}{K_s}. \qquad (5.138)$$

From EQ. 5.129 and EQ. 5.134 the total extension in the y-direction of one octant of the unit cell is:

$$\delta_y = \delta_y{}^h + \delta_y{}^l = \frac{W}{K_s}(4\alpha + 2\sin^2\theta). \qquad (5.139)$$

Poisson's ratios for the y direction are obtained as:

$$\nu_{yx} = -\frac{\varepsilon_x}{\varepsilon_y} = \frac{-\delta_x}{l\cos\theta} \times \frac{h + 2l\sin\theta}{\delta_y} = \frac{-\sin\theta(\alpha + 2\sin\theta)}{4\alpha + 2\sin^2\theta} \qquad (5.140)$$

and $$\nu_{yz} = -\frac{\varepsilon_z}{\varepsilon_y} = \frac{-\delta_z}{l\cos\theta} \times \frac{h + 2l\sin\theta}{\delta_y} = \frac{-\sin\theta(\alpha + 2\sin\theta)}{4\alpha + 2\sin^2\theta}. \qquad (5.141)$$

Since

$$\varepsilon_y = \frac{\delta_y}{y} = \frac{\delta_y}{h + 2l\sin\theta} = \frac{\sigma_y l^3 \cos^2\theta(4\alpha + 2\sin^2\theta)}{E_s t^2 (h + 2l\sin\theta)} \qquad (5.142)$$

the Young's modulus for the y direction is,

$$E_y = \frac{\sigma_y}{\varepsilon_y} = \frac{E_s(\alpha + 2\sin\theta)}{\cos^2\theta(4\alpha + 2\sin^2\theta)}\left(\frac{t}{l}\right)^2. \qquad (5.143)$$

5.5.4 Shearing in the X-Z Plane

Consider a shear stress exerted on an octant of the unit cell of the foam in the x-direction on the faces with outward normal in the z-direction, i.e. τ_{xz}. Since there are no ribs causing the stretching deflection, therefore $\gamma = 0$. The shear modulus, G_{xz} is:

$$G_{xz} = \frac{\tau_{xz}}{\gamma} = \frac{\tau_{xz}}{0} = \infty. \qquad (5.144)$$

By symmetry, $G_{zx} = \frac{\tau_{xz}}{\gamma} = \infty.$ (5.145)

5.5.5 Shearing in the Z-Y Plane

Consider a shear stress exerted on a half of the unit cell of the foam in the z direction on the faces with outward normal in the y direction, i.e. τ_{zy}. See Figure 5.11(a) and (b). Since the rib BF shortens as much as rib BE extents; and the other ribs DB, AB, BC do not cause any stretching deflection, therefore, $\gamma = 0$. The shear modulus, G_{zy} is,

$$G_{zy} = G_{yz} = \frac{\tau_{zy}}{\gamma} = \frac{\tau_{zy}}{0} = \infty. \qquad (5.146)$$

5.5.6 Shearing in the X-Y Plane

In this case, the deformation caused by the shear stress which applied in the x direction on the faces with outward normal in the y direction, i.e. τ_{xy}. Ribs DC and AB cause the deflection. By symmetry,

$$G_{xy} = G_{yx} = \frac{\tau_{xy}}{\gamma} = \infty. \qquad (5.147)$$

5.5.7 Summary of the Stretching Model

The elastic moduli due to stretching of the ribs are summarised in Table 5.3. As already noted, θ is positive for conventional foam and θ is negative for auxetic foam. Hence it is noted that for stretching auxetic behaviour is predicted to arise due to the conventional cell.

(Table 5.3)

Moduli	Expressions $(\theta_x = \theta_z = \theta, L_x = L_z = L)$	Expressions $(L_x \neq L_z and \theta_x \neq \theta_z)$
E_x	$\frac{E_s}{(\alpha + 2sin\theta)cos^2\theta}\left(\frac{t}{L}\right)^2$	$\frac{E_s A_{cross-section}}{(h + L_x \sin\theta_x + L_z \sin\theta_z)L_z \cos\theta_z \cos\theta_x}$
E_y	$\frac{E_s(\alpha + 2\sin\theta)}{\cos^2\theta(4\alpha + 2\sin^2\theta)}\left(\frac{t}{L}\right)^2$	$\frac{E_s A_{cross-section}(h + L_x \sin\theta_x + L_z \sin\theta_z)}{(4h + \sin^2\theta_x L_x + \sin^2\theta_z L_z)L_x \cos\theta_x L_z \cos\theta_z}$
E_z	$\frac{E_s}{(\alpha + 2sin\theta)cos^2\theta}\left(\frac{t}{L}\right)^2$	$\frac{E_s A_{cross-section}}{(h + L_x \sin\theta_x + L_z \sin\theta_z)L_z \cos\theta_z \cos\theta_x}$
ν_{xy}	$\frac{-\sin\theta}{\alpha + 2\sin\theta}$	$\frac{-L_x sin\theta_x}{h + L_x sin\theta_x + L_z sin\theta_z}$
ν_{xz}	0	0
ν_{zx}	0	0
ν_{zy}	$\frac{-\sin\theta}{\alpha + 2\sin\theta}$	$\frac{-L_z sin\theta_z}{h + L_x sin\theta_x + L_z sin\theta_z}$
ν_{yx}	$\frac{-\sin\theta(\alpha + 2\sin\theta)}{4\alpha + 2\sin^2\theta}$	$\frac{-sin\theta_x(h + L_x sin\theta_x + L_z sin\theta_z)}{4h + L_x sin^2\theta_x + L_z sin^2\theta_z}$
ν_{yz}	$\frac{-\sin\theta(\alpha + 2\sin\theta)}{4\alpha + 2\sin^2\theta}$	$\frac{-sin\theta_z(h + L_x sin\theta_x + L_z sin\theta_z)}{4h + L_x sin^2\theta_x + L_z sin^2\theta_z}$
G_{xy}	∞	∞
G_{zy}	∞	∞
G_{yz}	∞	∞
G_{yx}	∞	∞
G_{xz}	∞	∞
G_{zx}	∞	∞

Table 5.3 The stretching model expressions of Young's modulus, Poisson's ratio and the shear modulus of conventional and auxetic foams. θ is positive for conventional foam and θ is negative for auxetic foam. Note: $A_{cross-section}$ is the cross sectional area of the cell rib.

5.6 The Combined Model for the Foam Cell Structure

The deformation of a foam network due to the combination of flexure, hinging and stretching of the ribs is modelled in this section.

5.6.1 Loading in the X-Direction

Consider one octant of the unit cell, the total deflection in the x-direction, δ_x, due to a force, P, applied normal to the yz faces, is: -

$$\delta_x = \delta_x^{flexure} + \delta_x^{hinging} + \delta_x^{stretching}$$

$$= \frac{P\sin^2\theta}{K_f} + \frac{P\sin^2\theta}{K_h} + \frac{P\cos^2\theta}{K_s}. \qquad (5.148)$$

Where: $K_f = \frac{E_s t^4}{L^3} = \frac{12E_s I}{L^3}$, $K_h = \frac{E_s t^4}{6L^2 q} = \frac{2E_s I}{L^2 q}$ and $K_s = \frac{E_s t^2}{L}$ defined in EQs. 5.108, 5.107, and 5.113 respectively.

The total deflection in the y-direction, δ_y, is

$$\delta_y = \delta_y^{flexure} + \delta_y^{hinging} + \delta_y^{stretching}$$

$$= -\frac{P\sin\theta\cos\theta}{K_f} - \frac{P\sin\theta\cos\theta}{K_h} + \frac{P\sin\theta\cos\theta}{K_s}. \qquad (5.149)$$

The total deflection in the z-direction, δ_z, is zero.

The Poisson's ratio, ν_{xy}, can be calculated by using the following equations:

$$\nu_{xy} = \frac{-\varepsilon_y}{\varepsilon_x} = \frac{-\delta_y}{h + 2l\sin\theta} \times \frac{L\cos\theta}{\delta_x}$$

$$= \frac{\cos\theta\left(\frac{\sin\theta\cos\theta}{K_f} + \frac{\sin\theta\cos\theta}{K_h} - \frac{\sin\theta\cos\theta}{K_s}\right)}{(\alpha + 2\sin\theta)\left(\frac{\sin^2\theta}{K_f} + \frac{\sin^2\theta}{K_h} + \frac{\cos^2\theta}{K_s}\right)}. \qquad (5.150)$$

The Poisson's ratio, $\nu_{xz} = -\frac{\varepsilon_z}{\varepsilon_x} = \frac{-\delta_z}{L\cos\theta} \times \frac{l\cos\theta}{\delta_x} = 0.$ *(5.151)*

The engineering strain for one octant of the unit cell can be calculated by using:

$$\varepsilon_x = \frac{\delta_x}{x} = \frac{\delta_x}{l\cos\theta} = \frac{P\left(\dfrac{\sin^2\theta}{K_f} + \dfrac{\sin^2\theta}{K_h} + \dfrac{\cos^2}{K_s}\right)}{l\cos\theta}$$

$$= \sigma_x(h + 2l\sin\theta)\left(\frac{\sin^2\theta}{K_f} + \frac{\sin^2\theta}{K_h} + \frac{\cos^2\theta}{K_s}\right) \qquad (5.152)$$

Where σ_x, is the stress applied in the x-direction.

Combining the strain and the stress, the Young's modulus for the x-direction can be calculated from:

$$E_x = \frac{\sigma_x}{\varepsilon_x} = \frac{1}{(\alpha + 2\sin\theta)L\left(\dfrac{\sin^2\theta}{K_f} + \dfrac{\sin^2\theta}{K_h} + \dfrac{\cos^2\theta}{K_s}\right)}. \qquad (5.153)$$

5.6.2 Loading in the Z-Direction

By symmetry:

$$\nu_{zy} = \frac{\cos\theta\left(\dfrac{\sin\theta\cos\theta}{K_f} + \dfrac{\sin\theta\cos\theta}{K_h} - \dfrac{\sin\theta\cos\theta}{K_s}\right)}{(\alpha + 2\sin\theta)\left(\dfrac{\sin^2\theta}{K_f} + \dfrac{\sin^2\theta}{K_h} + \dfrac{\cos^2\theta}{K_s}\right)} \qquad (5.154)$$

$$\nu_{zx} = 0 \qquad (5.155)$$

and

$$E_z = \frac{\sigma_z}{\varepsilon_z} = \frac{1}{(\alpha + 2\sin\theta)L\left(\dfrac{\sin^2\theta}{K_f} + \dfrac{\sin^2\theta}{K_h} + \dfrac{\cos^2\theta}{K_s}\right)}. \qquad (5.156)$$

5.6.3 Loading in the Y-direction

Consider one octant of the unit cell, the total deflection in the x-direction, δ_x, due to a force, P, applied normal to the xz plane, is: -

$$\delta_x = \delta_x{}^{flexure} + \delta_x{}^{hinging} + \delta_x{}^{stretching}$$

$$= -\frac{P\sin\theta\cos\theta}{K_f} - \frac{P\sin\theta\cos\theta}{K_h} + \frac{P\sin\theta\cos\theta}{K_s}. \qquad (5.157)$$

The total deflection in the z-direction, δ_z, is

$$\delta_z = \delta_z{}^{flexure} + \delta_z{}^{hinging} + \delta_z{}^{stretching}$$

$$= -\frac{P\sin\theta\cos\theta}{K_f} - \frac{P\sin\theta\cos\theta}{K_h} + \frac{P\sin\theta\cos\theta}{K_s}. \qquad (5.158)$$

The total deflection in the y-direction, δ_y, is

$$\delta_y = \delta_y{}^{flexure} + \delta_y{}^{hinging} + \delta_y{}^{stretching}$$

$$= \frac{2P\cos^2\theta}{K_f} + \frac{2P\cos^2\theta}{K_h} + \frac{2P(2\alpha+\sin^2\theta)}{K_s}. \qquad (5.159)$$

Poisson's ratios are obtained as:

$$\nu_{yx} = -\frac{\varepsilon_x}{\varepsilon_y} = \frac{-\delta_x}{L\cos\theta} \times \frac{h+2L\sin\theta}{\delta_y}$$

$$= \frac{\left(\frac{\sin\theta\cos\theta}{K_f} + \frac{\sin\theta\cos\theta}{K_h} - \frac{\sin\theta\cos\theta}{K_s}\right)(\alpha+2\sin\theta)}{2\cos\theta\left(\frac{\cos^2\theta}{K_f} + \frac{\cos^2\theta}{K_h} + \frac{2\alpha+\sin^2\theta}{K_s}\right)} \qquad (5.160)$$

and $$\nu_{yz} = \frac{-\varepsilon_z}{\varepsilon_y} = \frac{-\delta_z}{L\cos\theta} \times \frac{h+2L\sin\theta}{\delta_y}$$

$$= \frac{\left(\frac{\sin\theta\cos\theta}{K_f} + \frac{\sin\theta\cos\theta}{K_h} - \frac{\sin\theta\cos\theta}{K_s}\right)(\alpha+2\sin\theta)}{2\cos\theta\left(\frac{\cos^2\theta}{K_f} + \frac{\cos^2\theta}{K_h} + \frac{2\alpha+\sin^2\theta}{K_s}\right)}. \qquad (5.161)$$

Since

$$\varepsilon_y = \frac{\delta_y}{y} = \frac{\delta_y}{h+2L\sin\theta} = \frac{2P\left(\frac{\cos^2\theta}{K_f} + \frac{\cos^2\theta}{K_h} + \frac{2\alpha+\sin^2\theta}{K_s}\right)}{h+2l\sin\theta}$$

$$= \frac{2\sigma_y L\cos^2\theta\left(\frac{\cos^2\theta}{K_f} + \frac{\cos^2\theta}{K_h} + \frac{2\alpha+\sin^2\theta}{K_s}\right)}{\alpha+2\sin\theta} \qquad (5.162)$$

Where: σ_y, is the stress applied in the y-direction.

Hence,

$$E_y = \frac{\sigma_y}{\varepsilon_y} = \frac{\alpha + 2\sin\theta}{2L\cos^2\theta\left(\frac{\cos^2\theta}{K_f} + \frac{\cos^2\theta}{K_h} + \frac{2\alpha + \sin^2\theta}{K_s}\right)}. \qquad (5.163)$$

5.6.4 Shearing in the Z-Y plane

Consider a shear stress exerted on an octant of the unit cell of the foam in the z-direction on the faces with outward normal in the y direction, i.e. τ_{zy}. The total deflection in the z-direction, u_z, is

$$u_z = \frac{2\alpha F}{K_f}\left(\alpha^2 + \frac{\alpha + 2\sin\theta}{2(1+\sin^2\theta)}\right) + \frac{2Fh(2L+0.5h)}{4K_h L^2(1+\sin^2\theta)}. \qquad (5.164)$$

The shear strain, γ_{zy}, is given by

$$\gamma = \frac{u_z}{y} = \frac{u_z}{2(h+2L\sin\theta)} \qquad (5.165)$$

The shear stress, τ_{zy}, is

$$\frac{F}{4L^2\cos^2\theta} \qquad (5.166)$$

giving the shear modulus, $G = \frac{\tau}{\gamma}$,

$$G_{zy} = \frac{F}{4L^2\cos^2\theta} \times \frac{2(h+2L\sin\theta)}{\frac{2\alpha F}{K_f}\left(\alpha^2 + \frac{\alpha+2\sin\theta}{2(1+\sin^2\theta)}\right) + \frac{Fh(2L+\frac{1}{2}h)}{2K_h L^2(1+\sin^2\theta)}}$$

$$= \frac{(\alpha+2\sin\theta)}{2L\cos^2\theta} \times \frac{1}{\frac{2\alpha}{K_f}(\alpha^2 + \frac{\alpha+2\sin\theta}{2(1+\sin^2\theta)}) + \frac{(2\alpha+0.5\alpha^2)}{2K_h(1+\sin^2\theta)}}. \qquad (5.167)$$

From the classical elasticity theory of anisotropic materials (e.g. Nye (1960)), we know that:

$$G_{zy} = G_{yz}$$

therefore,

$$G_{yz} = \frac{(\alpha+2\sin\theta)}{2L\cos^2\theta} \times \frac{1}{\frac{2\alpha}{K_f}(\alpha^2 + \frac{\alpha+2\sin\theta}{2(1+\sin^2\theta)}) + \frac{(2\alpha+0.5\alpha^2)}{2K_h(1+\sin^2\theta)}}. \qquad (5.168a)$$

5.6.5 Shearing in the X-Y Plane

By symmetry,

$$G_{xy} = G_{yx} = \frac{(\alpha + 2\sin\theta)}{2L\cos^2\theta} \times \frac{1}{\frac{2\alpha}{K_f}(\alpha^2 + \frac{\alpha + 2\sin\theta}{2(1+\sin^2\theta)}) + \frac{(2\alpha + 0.5\alpha^2)}{2K_h(1+\sin^2\theta)}}. \qquad (5.168b)$$

5.6.6 Shearing in the X-Z Plane

In this case, a shear stress exerted on an octant of the unit cell of the foam in the y-direction on the faces with outward normal in the z direction, i.e. τ_{xz}. Ribs AB and CD cause the deflection. The total deflection in the x direction, δ_x, is

$$\delta_x = \frac{P}{K_f} + \frac{P}{K_h} \qquad (5.169)$$

and in this case,

$$\delta_x = u_s. \qquad (5.170)$$

The shear strain, γ, is given by

$$\gamma = \frac{u_s}{L\cos\theta}. \qquad (5.171)$$

The shear stress, τ_{xz}, is

$$\frac{P}{L\cos\theta(h + 2L\sin\theta)} \qquad (5.172)$$

giving the shear modulus, $G = \frac{\tau}{\gamma}$,

$$G_{xz} = \frac{P}{L\cos\theta(h+2L\sin\theta)} \times \frac{L\cos\theta}{P\left(\frac{1}{K_f} + \frac{1}{K_h}\right)} \qquad (5.173)$$

$$= \frac{1}{L(\alpha + 2\sin\theta)\left(\frac{1}{K_f} + \frac{1}{K_h}\right)}. \qquad (5.174)$$

By symmetry,

$$G_{zx} = \frac{1}{L(\alpha + 2\sin\theta)\left(\frac{1}{K_f} + \frac{1}{K_h}\right)}. \qquad (5.175)$$

5.6.7 Summary of the Combined Analytical Model

The elastic moduli due to the combination of flexure, hinging and stretching of the ribs are summarised in Table 5.4. As already noted, θ is positive for conventional foam and θ is negative for an auxetic foam.

(Table 5.4)

Modulus	Expressions $(\theta_x = \theta_z = \theta, L_x = L_y = L)$
E_x	$\dfrac{1}{(\alpha + 2\sin\theta)L\left(\dfrac{\sin^2\theta}{K_f} + \dfrac{\sin^2\theta}{K_h} + \dfrac{\cos^2\theta}{K_s}\right)}$
E_y	$\dfrac{\alpha + 2\sin\theta}{2L\cos^2\theta\left(\dfrac{\cos^2\theta}{K_f} + \dfrac{\cos^2\theta}{K_h} + \dfrac{2\alpha + \sin^2\theta}{K_s}\right)}$
E_z	$\dfrac{1}{(\alpha + 2\sin\theta)L\left(\dfrac{\sin^2\theta}{K_f} + \dfrac{\sin^2\theta}{K_h} + \dfrac{\cos^2\theta}{K_s}\right)}$
ν_{xy}	$\dfrac{\cos\theta\left(\dfrac{\sin\theta\cos\theta}{K_f} + \dfrac{\sin\theta\cos\theta}{K_h} - \dfrac{\sin\theta\cos\theta}{K_s}\right)}{(\alpha + 2\sin\theta)\left(\dfrac{\sin^2\theta}{K_f} + \dfrac{\sin^2\theta}{K_h} + \dfrac{\cos^2\theta}{K_s}\right)}$
ν_{xz}	0
ν_{zx}	0
ν_{zy}	$\dfrac{\cos\theta\left(\dfrac{\sin\theta\cos\theta}{K_f} + \dfrac{\sin\theta\cos\theta}{K_h} - \dfrac{\sin\theta\cos\theta}{K_s}\right)}{(\alpha + 2\sin\theta)\left(\dfrac{\sin^2\theta}{K_f} + \dfrac{\sin^2\theta}{K_h} + \dfrac{\cos^2\theta}{K_s}\right)}$
ν_{yx}	$\dfrac{\left(\dfrac{\sin\theta\cos\theta}{K_f} + \dfrac{\sin\theta\cos\theta}{K_h} - \dfrac{\sin\theta\cos\theta}{K_s}\right)(\alpha + 2\sin\theta)}{2\cos\theta\left(\dfrac{\cos^2\theta}{K_f} + \dfrac{\cos^2\theta}{K_h} + \dfrac{2\alpha + \sin^2\theta}{K_s}\right)}$
ν_{yz}	$\dfrac{\left(\dfrac{\sin\theta\cos\theta}{K_f} + \dfrac{\sin\theta\cos\theta}{K_h} - \dfrac{\sin\theta\cos\theta}{K_s}\right)(\alpha + 2\sin\theta)}{2\cos\theta\left(\dfrac{\cos^2\theta}{K_f} + \dfrac{\cos^2\theta}{K_h} + \dfrac{2\alpha + \sin^2\theta}{K_s}\right)}$
G_{xy}	$\dfrac{(\alpha + 2\sin\theta)}{2L\cos^2\theta} \times \dfrac{1}{\dfrac{2\alpha}{K_f}(\alpha^2 + \dfrac{\alpha + 2\sin\theta}{2(1+\sin^2\theta)}) + \dfrac{(2\alpha + 0.5\alpha^2)}{2K_h(1+\sin^2\theta)}}$
G_{zy}	$\dfrac{(\alpha + 2\sin\theta)}{2L\cos^2\theta} \times \dfrac{1}{\dfrac{2\alpha}{K_f}(\alpha^2 + \dfrac{\alpha + 2\sin\theta}{2(1+\sin^2\theta)}) + \dfrac{(2\alpha + 0.5\alpha^2)}{2K_h(1+\sin^2\theta)}}$
G_{yz}	$\dfrac{(\alpha + 2\sin\theta)}{2L\cos^2\theta} \times \dfrac{1}{\dfrac{2\alpha}{K_f}(\alpha^2 + \dfrac{\alpha + 2\sin\theta}{2(1+\sin^2\theta)}) + \dfrac{(2\alpha + 0.5\alpha^2)}{2K_h(1+\sin^2\theta)}}$

G_{yx}	$\frac{(\alpha+2\sin\theta)}{2L\cos^2\theta}\times\frac{1}{\frac{2\alpha}{K_f}(\alpha^2+\frac{\alpha+2\sin\theta}{2(1+\sin^2\theta)})+\frac{(2\alpha+0.5\alpha^2)}{2K_h(1+\sin^2\theta)}}$
G_{xz}	$\frac{1}{L\cos\theta\times(\alpha+2\sin\theta)\left(\frac{1}{K_f}+\frac{1}{K_h}\right)}$
G_{zx}	$\frac{1}{L\cos\theta\times(\alpha+2\sin\theta)\left(\frac{1}{K_f}+\frac{1}{K_h}\right)}$

Table 5.4 The combination model expressions of Young's modulus, Poisson's ratio and shear modulus of conventional and auxetic foams. θ is positive for conventional foam and θ is negative for auxetic foam. K_f, K_h and K_s are the flexure, hinging and stretching force constant respectively. $K_f=\frac{E_s t^4}{L^3}=\frac{12E_sI}{L^3}$, $K_h=\frac{E_s t^4}{6L^2q}=\frac{2E_sI}{L^2q}$ and $K_s=\frac{E_s t^2}{L}$.

5.7 Summary

The linear elastic behaviour of a foam is characterized by a set of moduli, Young's moduli, E, Poisson ratio, ν, and the shear moduli, G. At first sight, one may think that stretching is the dominant deformation. But since only the struts which are aligned parallel to the principal axis of stress carry purely axial forces; the rest carry bending and hinging moments as well. Therefore, flexure and hinging may be the dominant deformations. However, because low density open-cell foams are made of long and thin struts, the bending deformation rather than the hinging deformation is the primary one under compression. It has been noted that Gibson and Ashby (1988) proposed the bending of the cell edges is the dominant mechanism and developed the flexure model (cubic box) for conventional foam. In this chapter, the flexure, hinging, stretching and the combined models (rhombic dodecahedron) for conventional and auxetic foam are developed.

Chapter 6 The Mechanical Properties of Foams (I)

6.1 Introduction

The mechanical properties of foams is divided into two parts: part one, *Chapter 6*, presents the basic, strain dependent elastic properties of the foams, in tension, compression, and shear, in each direction for each foam. In *Chapter 7*, emphasis is placed on the elastic resilience, energy absorption and time dependence of the foams which using ball indentation test, ball rebound, hysteresis loop, and DMTA tests.

6.2 Compression

6.2.1 Introduction

Most foams are anisotropic, although most previous work has assumed isotropy. In this chapter we present the results of obtaining full sets of elastic properties for both conventional and auxetic foams. As the polymer used for these foams is viscoelastic it is important, first, to characterise this effect to ensure the measurement of consistent elastic properties.

6. 2. 2 Compressive Creep

A material subjected to a constant load will deform over time. This phenomenon is known as creep. To determine how quickly readings have to be taken or tests done to ensure negligible effects due to creeps, we need to carry out an investigation on both conventional and auxetic foams. The apparatus used to investigate the creep behaviour is shown schematically in *Figure* 6.1. The foam was cut to dimensions, 50 x 50 x 50 mm, the average error was ±0.3 mm. To aid measurement, two pins were inserted into the foam specimens over a 10 mm gauge length in the central region of the gauge section. Care was taken to ensure that the pins were pushed straight through perpendicular to the specimen. The specimen was then loaded by a dead weight (e.g. 500±0.05g). Firstly, the specimen was photographed without a load, and then an external load was suspended from the end. Every minute a photograph was taken. After 10 minutes, the load was removed, and the foam began to recover from its deformation. Photographs were then taken every minute for a further 12 minutes, before the test was stopped. The photographs were then enlarged using a slide projector, and the distance between the pins measured for each case. This enabled the longitudinal strain and hence the creep behaviour of the specimens to be studied. Six conventional and auxetic specimens were tested for each type of the 10ppi polyether urethane foam (i.e. 10CO and 100AO). The strain-

time diagrams are shown in *Figures* 6.2 and 6.3. The Figures show that the foam creep response is dependent on the cell geometry. It can be seen that:

The creep behaviour of a foam depends on the cell geometry and the property of matrix polymer.

(1) Auxetic foam requires less time than conventional foam to restore to its original shape once the external load is removed.

(2) Within the same period of deformation time (e.g. 10 min.), the deformation of auxetic foam is less than that of conventional foam. This implies that auxetic foam may be a better load-bearing material than conventional foam. (Further investigation is shown in *Chapter* 7).

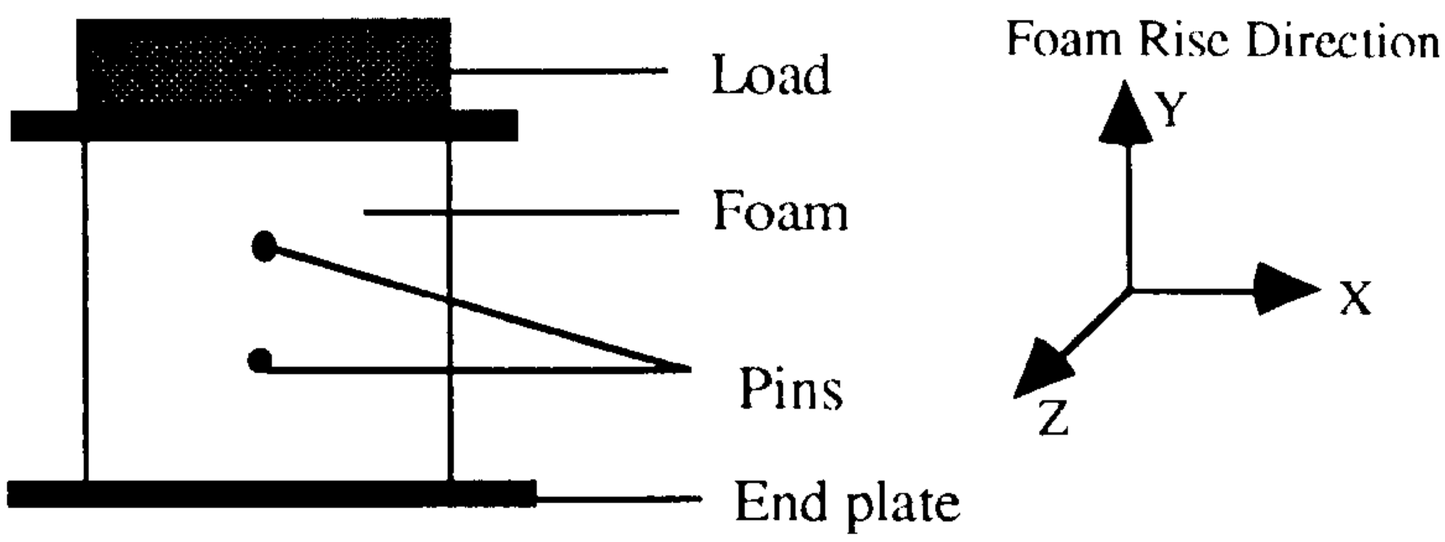

Fig. 6.1 Schematic diagram of compressive creep test.
(The pin dimensions: 0.2 x 0.2 x 50 mm).

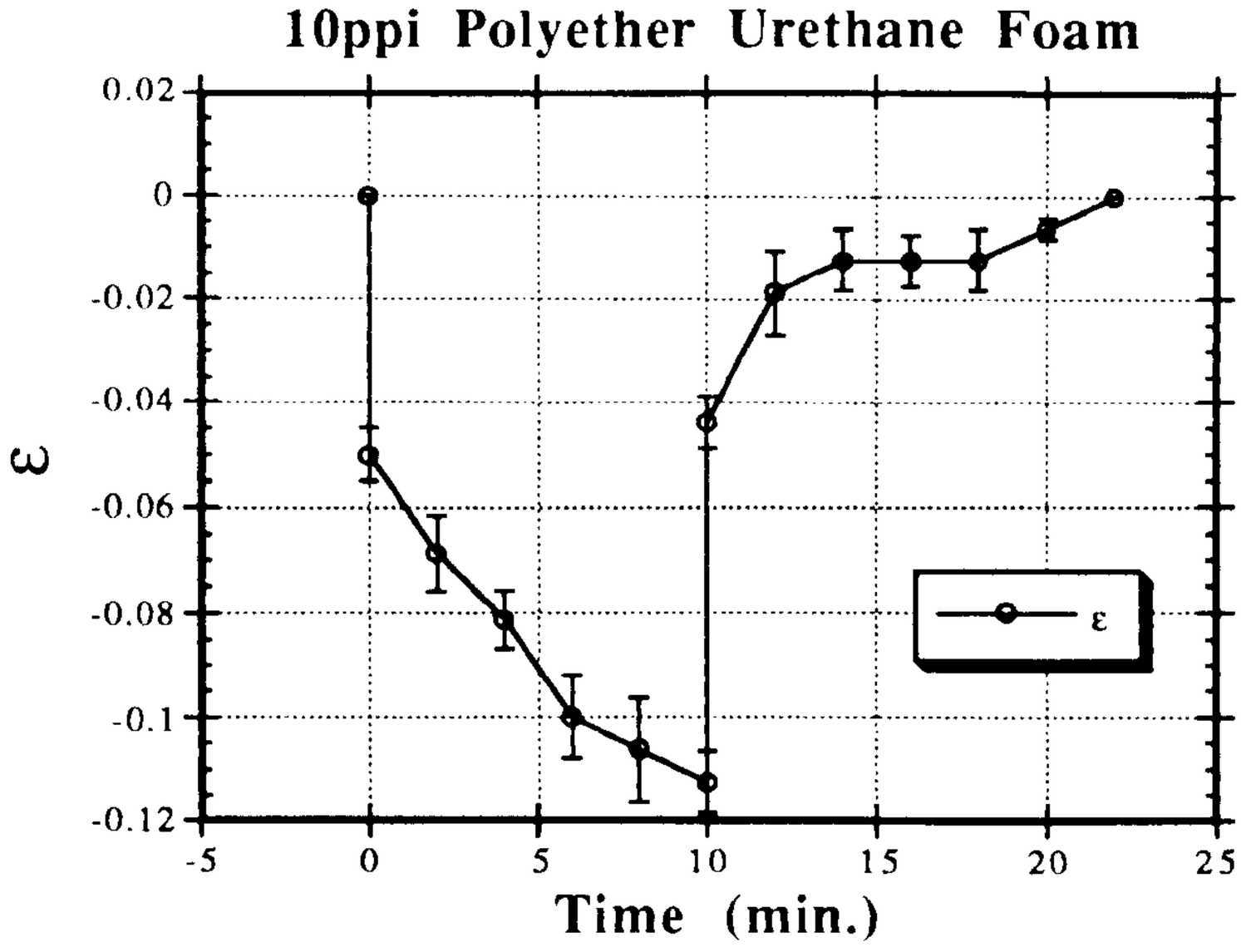

Fig. 6.2 Diagram of compressive strain versus time for the 10ppi conventional open-cell polyether urethane foam (10CO).

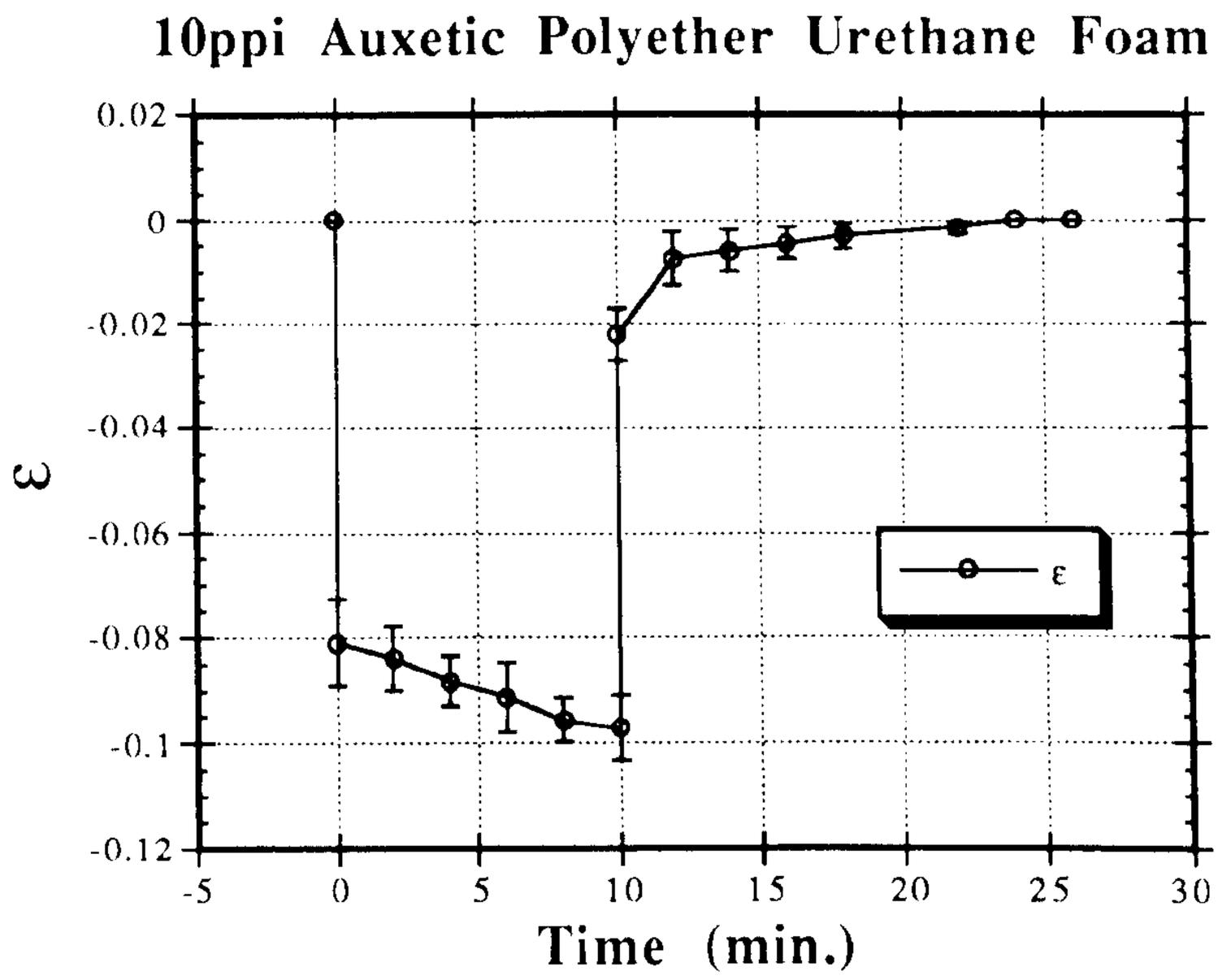

Fig. 6.3 Diagram of compressive strain versus time for the 10ppi auxetic open-cell polyether urethane foam (100AO).

6.2.3 Strain Rate Effect

Since the foam is a viscoelastic material, it is expected that it may be strain rate dependent. In order to investigate this, a series of compression tests at cross head speeds of 20, 10, 5 and 0.1 mm/min. were conducted on an Instron 4505 test machine.

Strain rate is defined as the rate of strain change with time, and it is calculated as follows:

Strain rate = Cross-head speed / Original gauge length, L_0. *(6.1)*

The 60ppi closed-cell conventional polyester urethane and the 60ppi open-cell auxetic polyether urethane foams had dimensions of 50 x 50 x 50 mm. For each foam, tests was carried out at 4 different cross-head speeds and, hence, at 4 different strain rates. Three specimens were tested for each type of foam and all errors were within 3%. The results are shown in *Figures* 6.4 and 6.5.

60ppi Closed-Cell conventional Polyester Urethane Foam

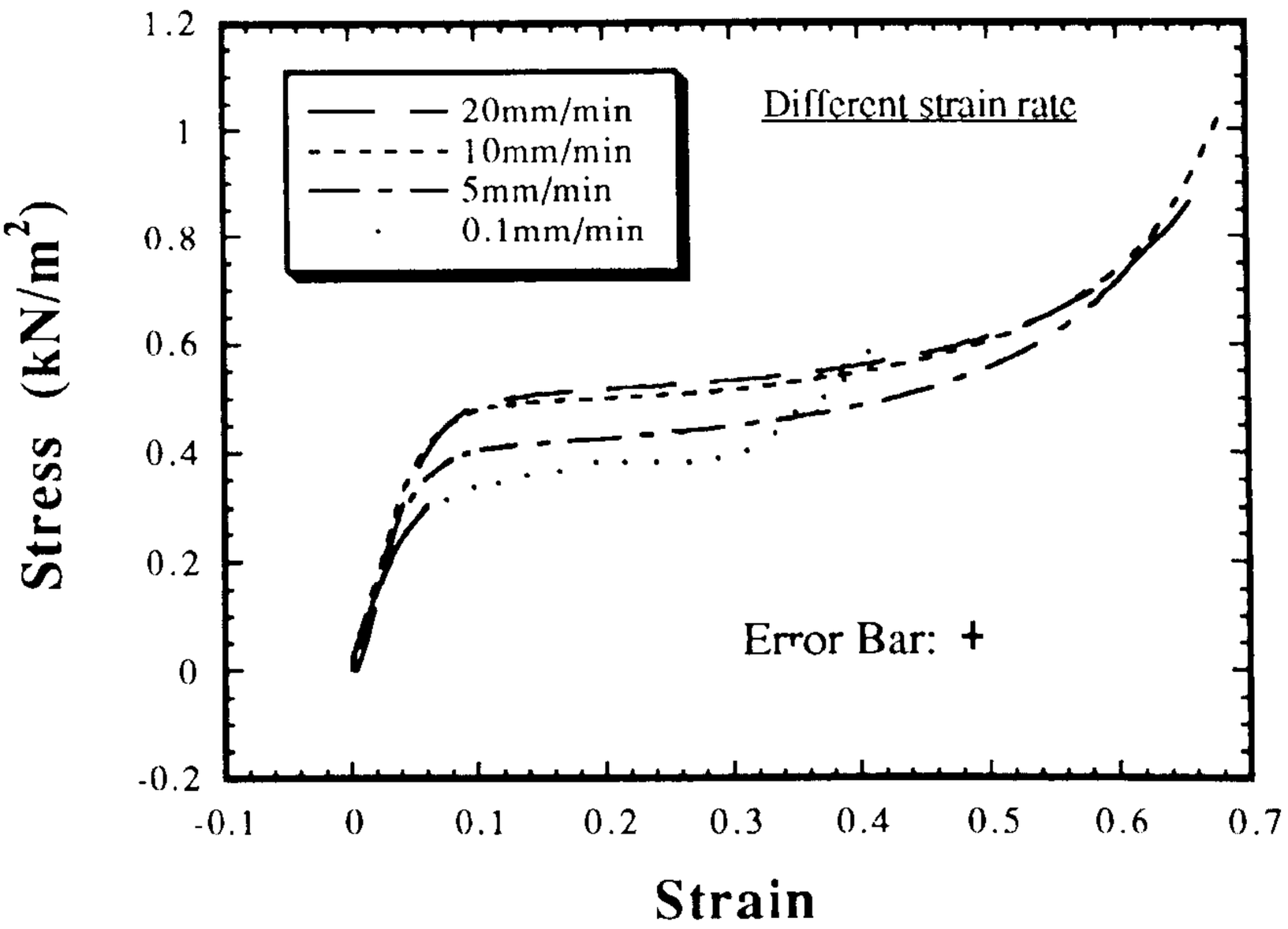

Fig. 6.4 Compressive stress-strain curves for the 60ppi conventional closed-cell polyester urethane foam (PECC) tested at 4 different cross-head speeds.

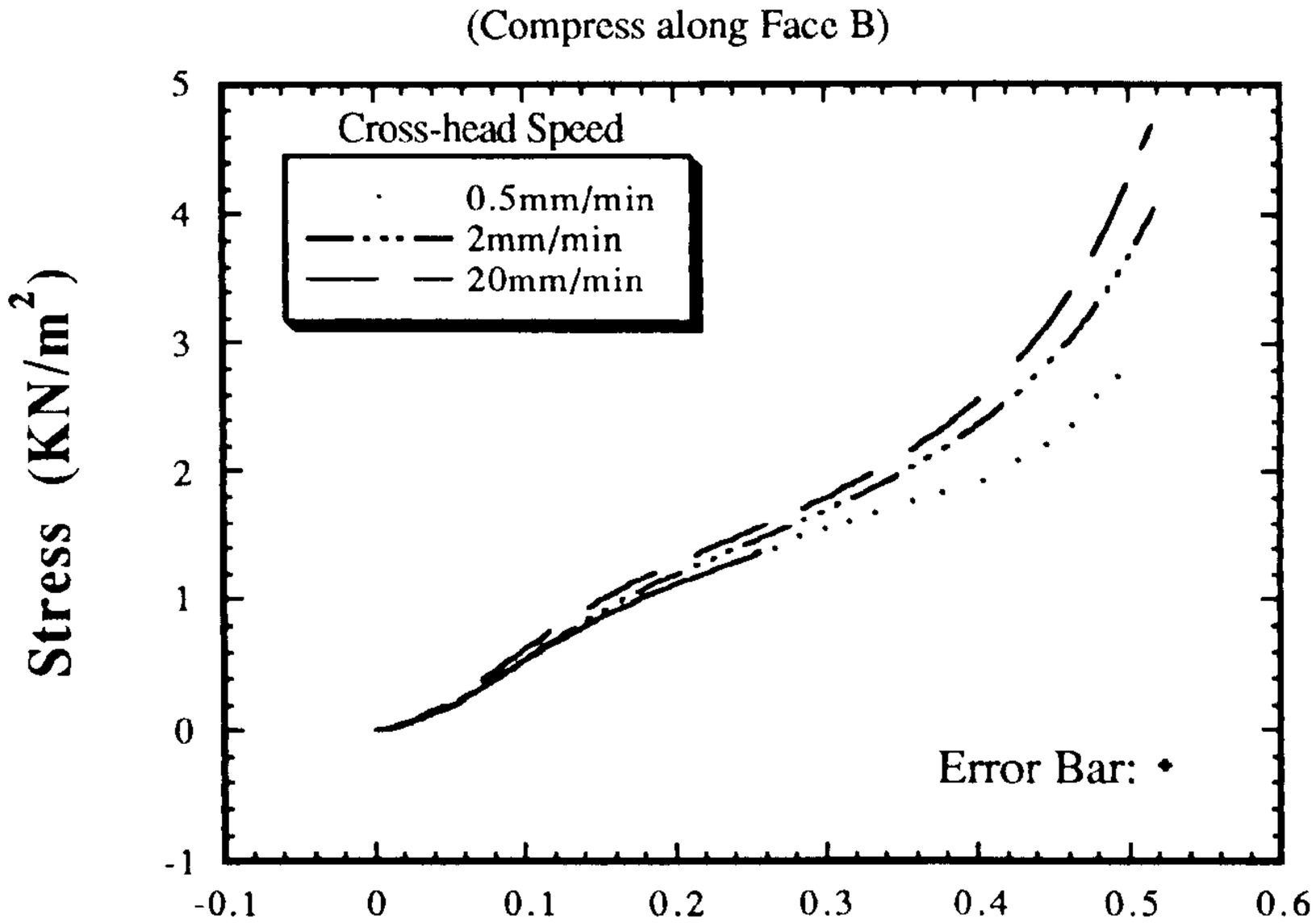

Fig. 6.5 Compressive stress-strain curves for the 30ppi auxetic open-cell polyether urethane foam (30ppi, 100AO) at 3 different cross-head speeds.

*Figure*s 6.4 and 6.5 show that the influence of strain rate at room temperature is small for both conventional and auxetic foams. Modulus values and the stress at 10% strain show only small variations. However, the stresses at higher strains and the elastic collapse stress do show substantial dependence on strain rate. It appears that when the strain rate is increased the stress-strain curve is shifted upwards. This is due to the viscoelastic behaviour of the foam.

6.2.4 Specimen Geometry Effect

An investigation into the effect of the specimen geometry was carried out. The base area of the 60ppi open-cell conventional polyether urethane foam samples, L x W, was varied from 620 mm^2 to 39600 mm^2, and the height h, of the samples was varied from 22 mm to 141 mm. The slenderness of the 30ppi auxetic open-cell polyether urethane foam, was varied from 13.34 to 146.32. The tests were carried out using an Instron 4505 at a cross head speed of 2 mm/min. Three specimens were tested for each foam type and the average errors were within 5%. The results of the tests are shown in *Figures* 6.7 to 6.9. It can be seen that the compression is dependent on the height and the base area of the specimen. Scatter of the test results decreases with increasing base area. This is because, for larger cross sections, random inhomogeneities have less effect. Also the compressive buckling strain, decreases with specimen height. On the other hand, the elastic modulus determined from these measurements increases with specimen height. Since the effect of the disturbed regions on the total deformation decreases with increasing specimen height, smaller characteristic compressive strain and hence higher modulus of elasticity, will be obtained for larger specimen heights. If the aspect ratio is too large (e.g. h = 141 mm), there is also the possibility of transverse displacement of the entire sample. If the height of the specimen is too small (e.g. h = 22 mm), there will be the end effects.

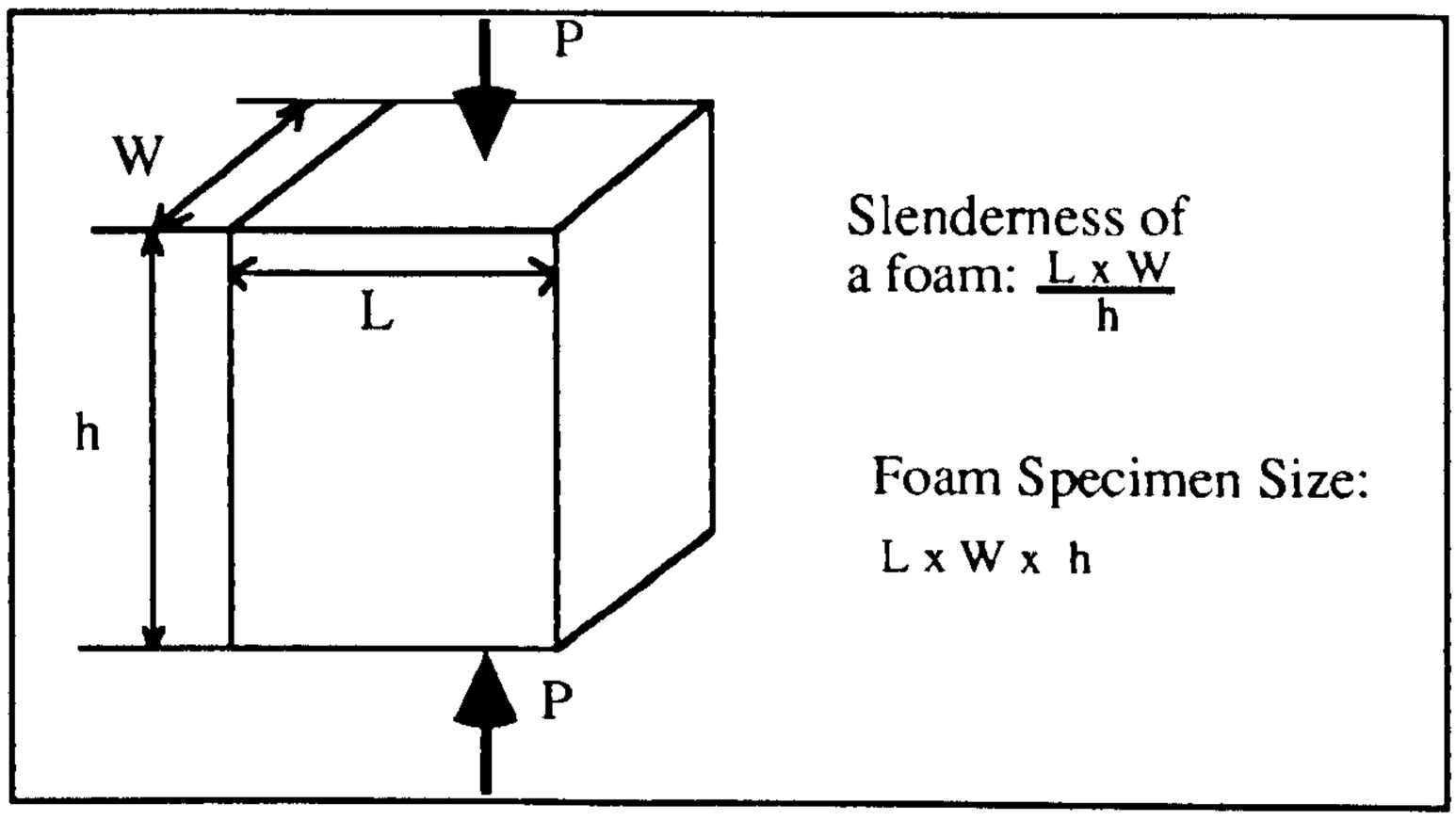

Fig. 6.6 Schematic diagram of the foam specimen aspect ratio.

60ppi Open-Cell Polyether Urethane Foam

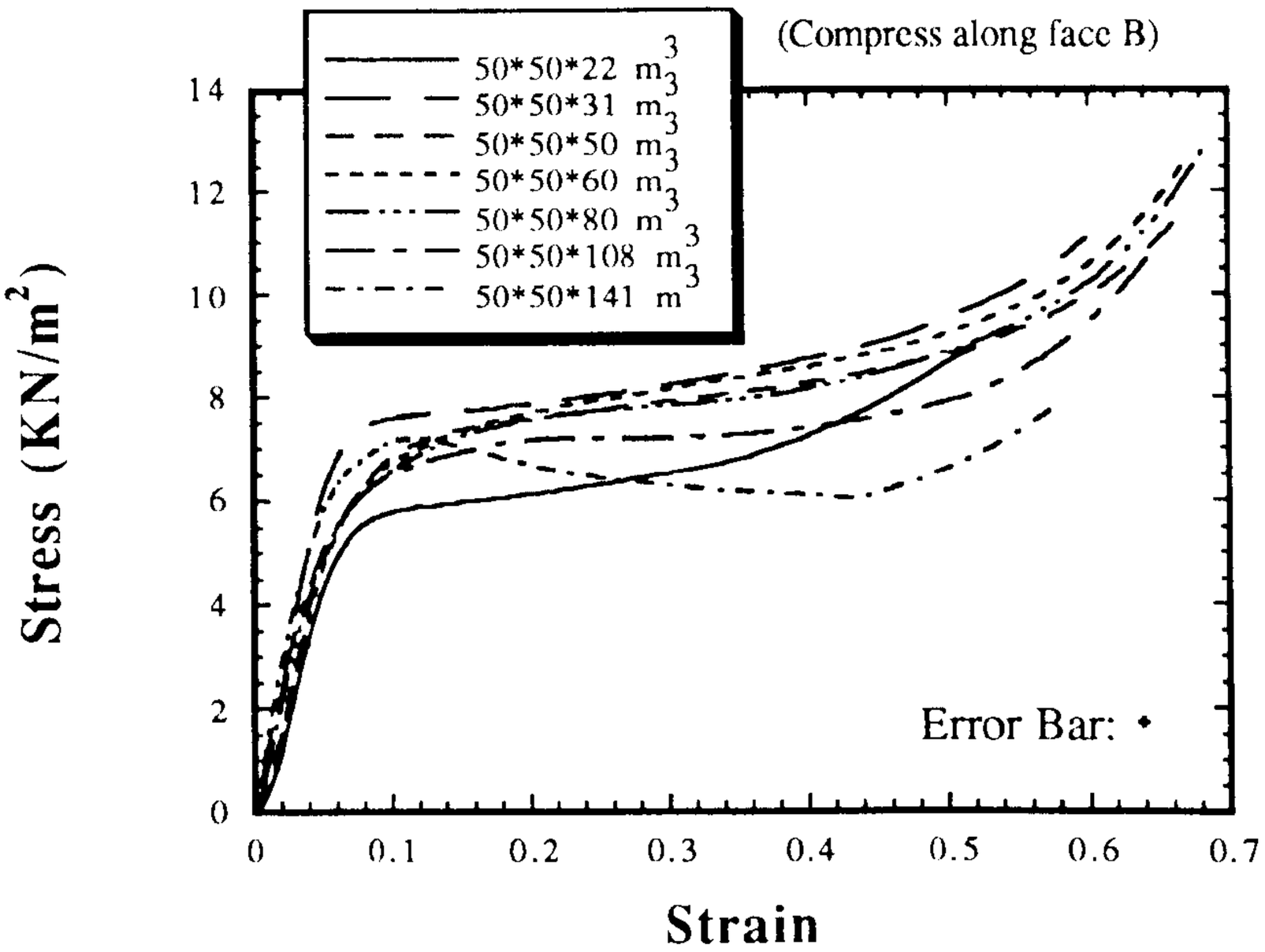

Fig. 6.7 Compressive stress-strain curves for the 60ppi conventional open-cell polyether urethane foam (60CO) tested with 7 different gauge lengths, h.

60ppi Conventional Polyether Urethane Foam

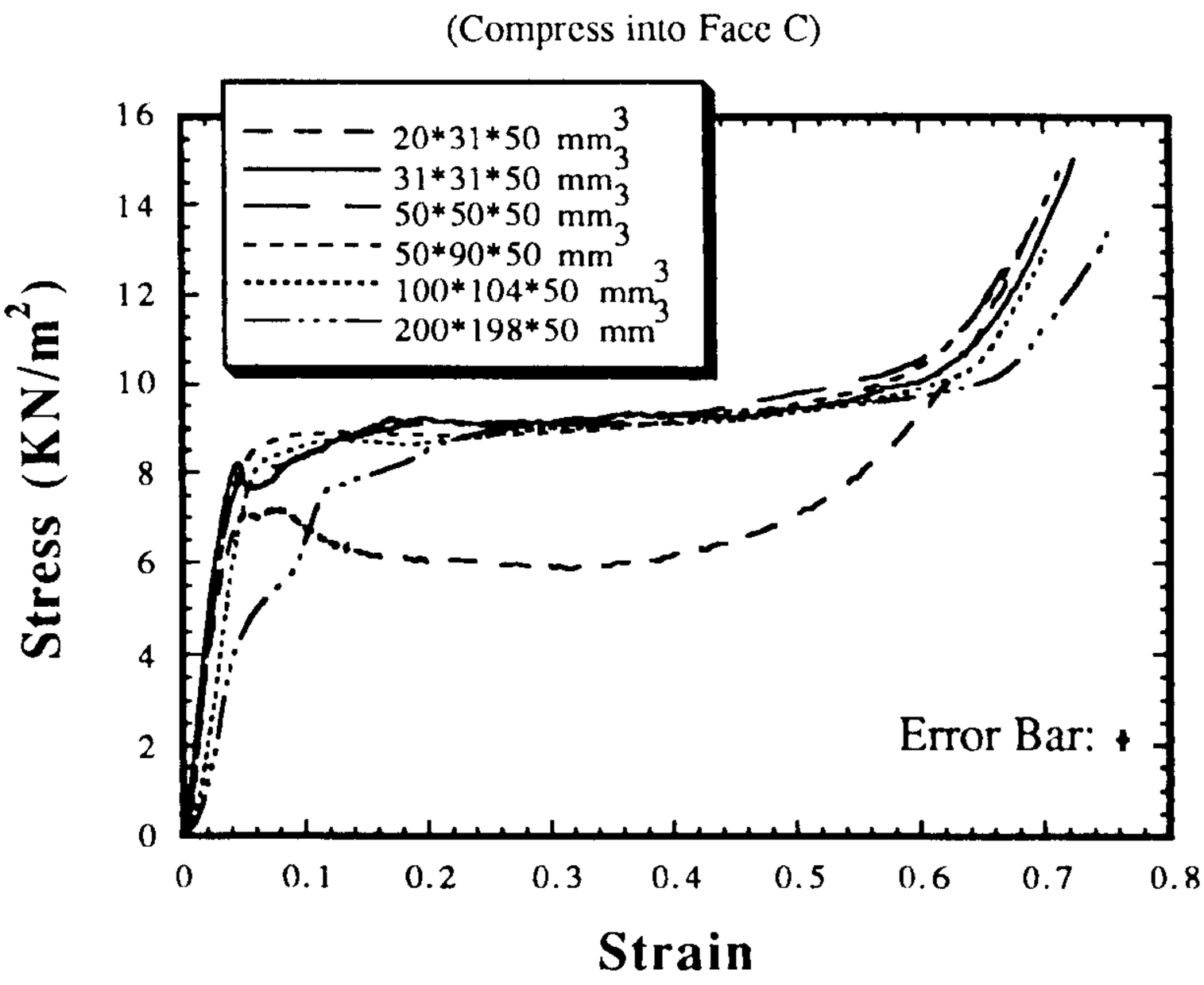

Fig. 6.8 Compressive stress-strain curves for the 60ppi conventional open-cell polyether urethane foam (60CO) tested with 6 different cross section areas, L x W. This figure shows that higher modulus of elasticity will be obtained for smaller specimen cross-sectional areas.

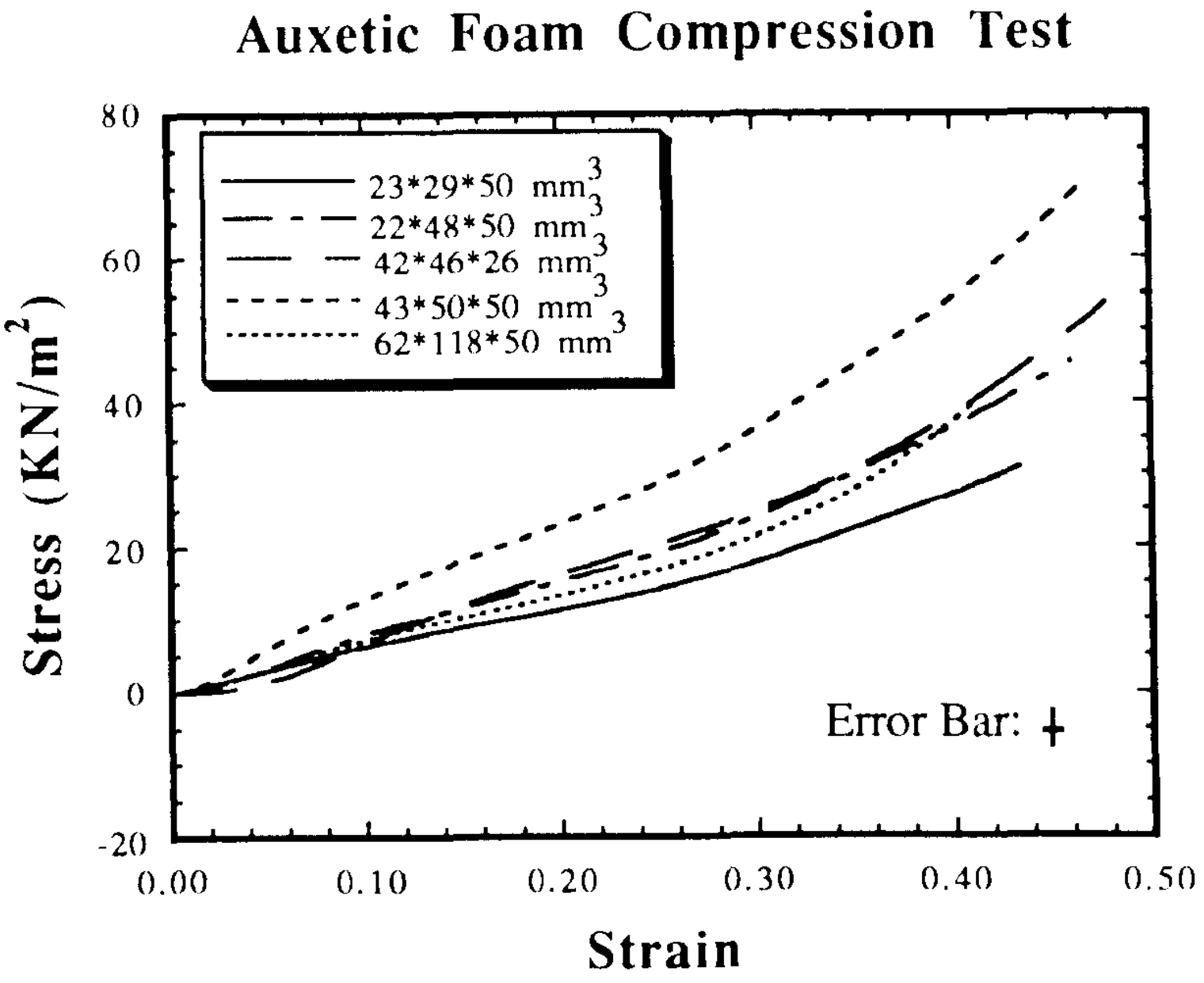

Fig. 6.9 Diagram of compressive stress-strain for the 30ppi auxetic open-cell polyether urethane foam (30ppi, 100AO) tested with 5 different slenderness, $\frac{L \times W}{h}$. This figure shows that the Young's modulus of auxetic foam is dependent on the specimen geometries.

It can be seen from *Figures* 6.7 to 6.9 that to obtain the highest possible accuracy in the measurements of the characteristic data, we need to use same dimensions for all samples.

6.2.5 The Compressive Stress-Strain Behaviour

A foam specimen, shown in *Figure 6.10,* was subjected to an axial compression force, P, using an Instron 4505 testing machine as shown schematically in *Figure 6.11.* The foam sample was placed between the parallel compression plates of the machine and compressed at a constant cross-head speed of 2 mm/min. At various increments of force, P, the change in length, ΔL, for the specimen with an initial gauge length, L_0, was recorded on the chart recorder, and the engineering stress is calculated by using:

$$\sigma = P/A_0 \qquad (6.2)$$

Where: the stress, σ, is measured in kN/m^2, since the force, P, is measured in kN and the initial cross-section area, A_0, in square meters.

The compression force, P, also produces an axial reduction of the specimen. For the initial gauge length, L_0, of the specimen, the stress is assumed to be uniformly distributed for all cross sections. It is also assumed that this uniform

stress will produce a uniform reduction, ΔL. With the uniform reduction assumed, the deformation is expressed by the engineering strain, ε.

$$\varepsilon = \Delta L / L_0 \qquad (6.3)$$

The engineering strain, ε , is measured in mm per mm since the change in length, ΔL, and the original gauge length, L_0, are both expressed in mm.

Within the linear elastic region Hooke's law can be considered valid, so that the average engineering stress is proportional to the average engineering strain,

$$\frac{\sigma}{\varepsilon} = E = \text{constant} \qquad (6.4)$$

The constant of proportionality, E, is known as the modulus of linear elasticity or the Young's modulus.

With PUR flexible foam, anisotropy in the cell structure (see *Figure* 4.4) may lead one to expect differences in the mechanical properties of foams when loaded in different directions. The studies will show the degree of scatter in the mechanical data that is likely to occur because of the variation in the cell structure of each dimension.

These compression tests on PUR foam conform to ASTM-D3574-91(C). The test specimens were 50 ± 0.5 mm cubes with all sides perpendicular to within ±0.5 mm and opposite sides parallel to within ±0.5 mm. End plates, which were 60 x 60 x 2.62 mm of stainless-steel stock parallel to within ±0.03 mm, were bonded onto the loaded surfaces. Apollo Adhesive A. 2874 (Apollo Chemicals Limited, Staffs.) was used between the specimen and the loading surface. All the tests were carried out using an Instron 4505 at a cross head speed of 2 mm/min. The test configuration is shown schematically in *Figures* 6.10 and 6.11. Five types of conventional foams were investigated, and their micrographs were shown in Figures 4.4 to 4.6. Three specimens were tested for each type of foam, some variation in the relative density of each specimen was observed but was considered negligible. The errors associated with the tests were within 10%. The effects of the orientations are shown in *Figures* 6.12 to 6.16. The primary effects of anisotropy are the decreasing value of the critical elastic collapse strain, ε_Q, and the increasing value of the Young's modulus in the foam rise direction. A decrease in the average cell size is accompanied by an increase in the Young's modulus and a decrease in the critical collapse strain, ε_Q, of the foam. It is evident that changing the cell structure has a pronounced effect.

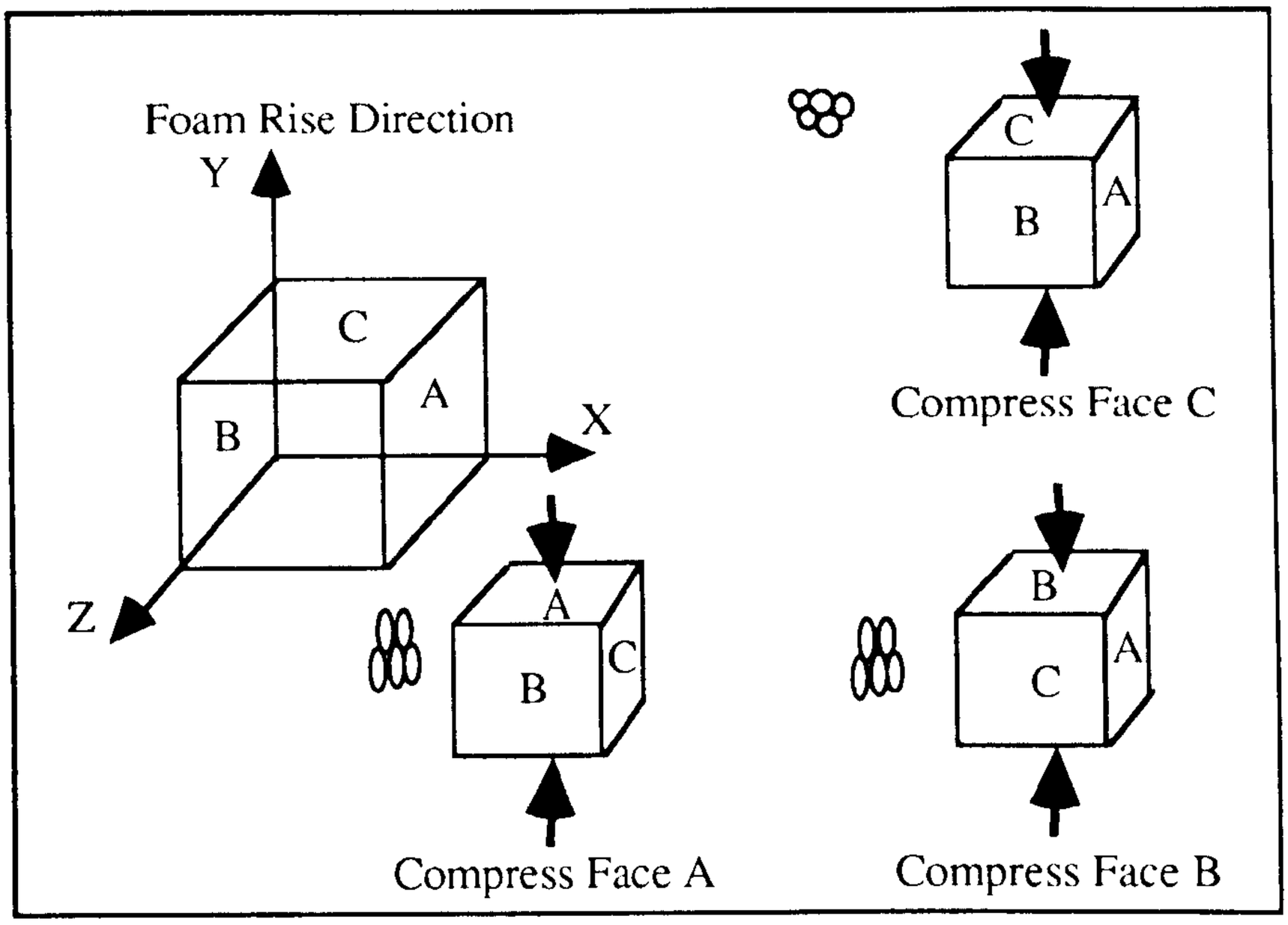

Fig. 6.10 Schematic diagram of a foam compression test specimen.

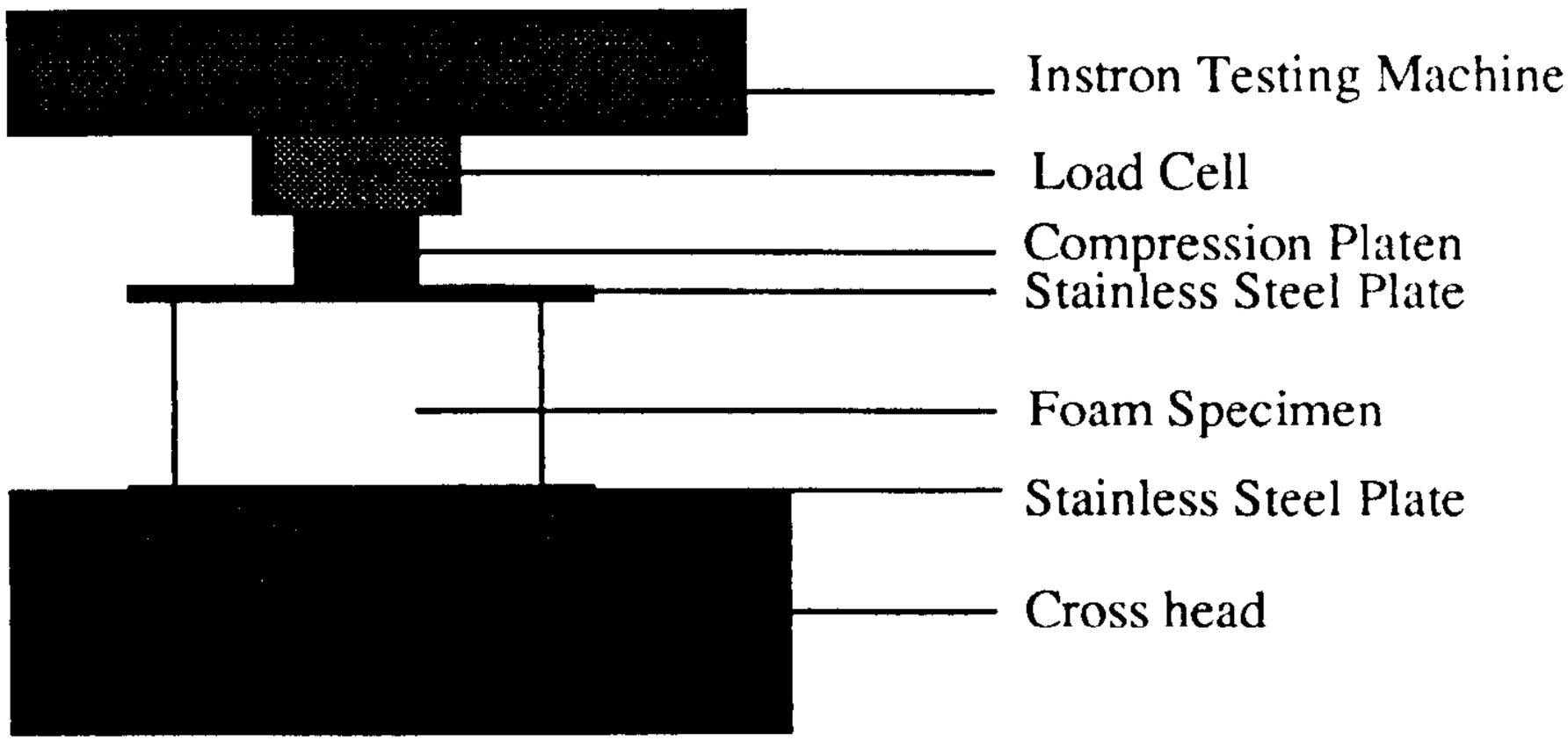

Fig. 6.11 Schematic diagram of the compression test configuration.

60ppi Reticulated Polyester Urethane Foam

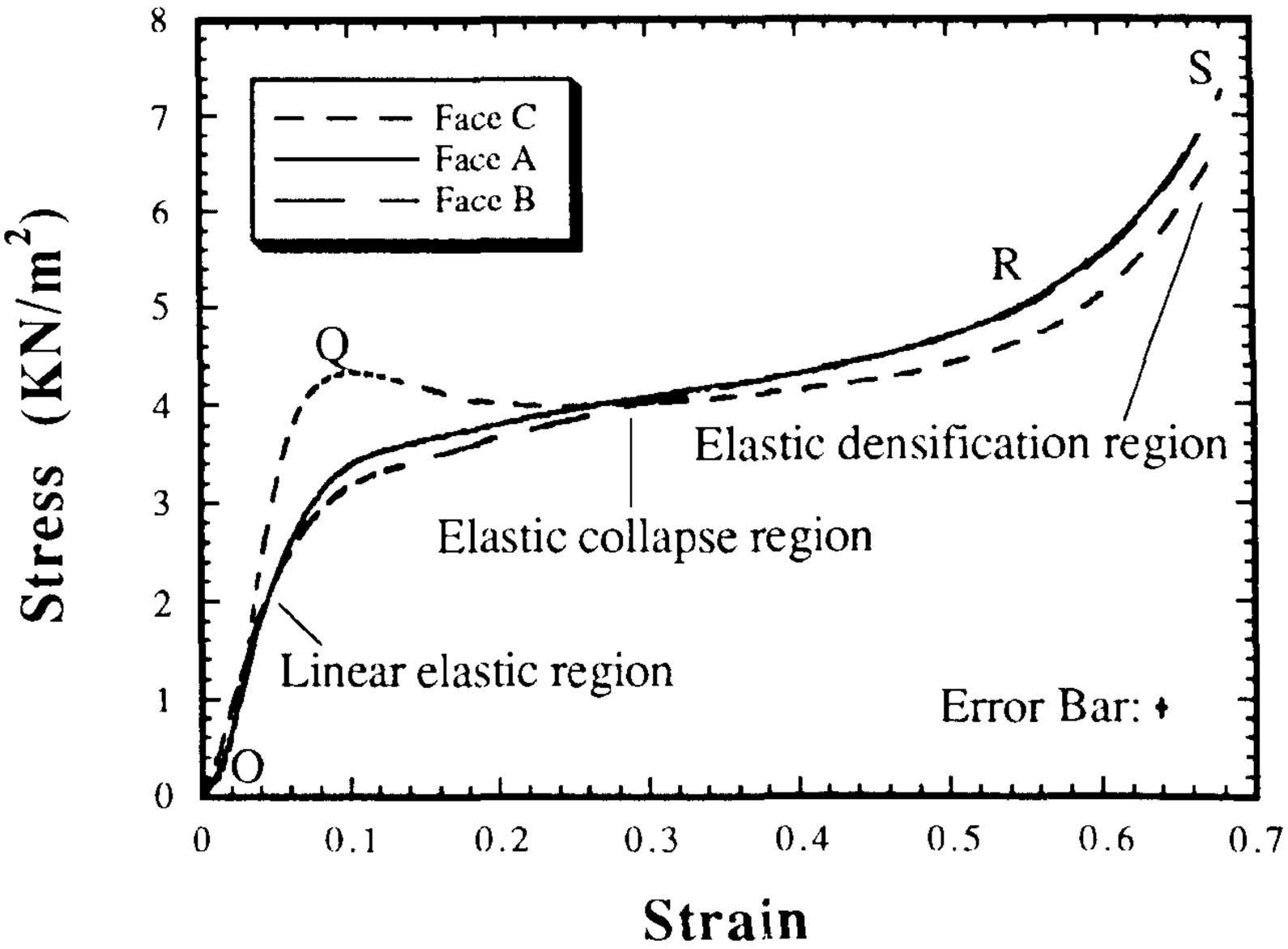

Fig. 6.12 Compressive stress-strain curves in two orthogonal directions in the planes normal to the rise direction (Face A and Face B) and in the rise direction (Face C) for the 60ppi conventional elastic reticulated polyester urethane foam (PECO).

60ppi Closed-Cell Polyester Urethane Foam

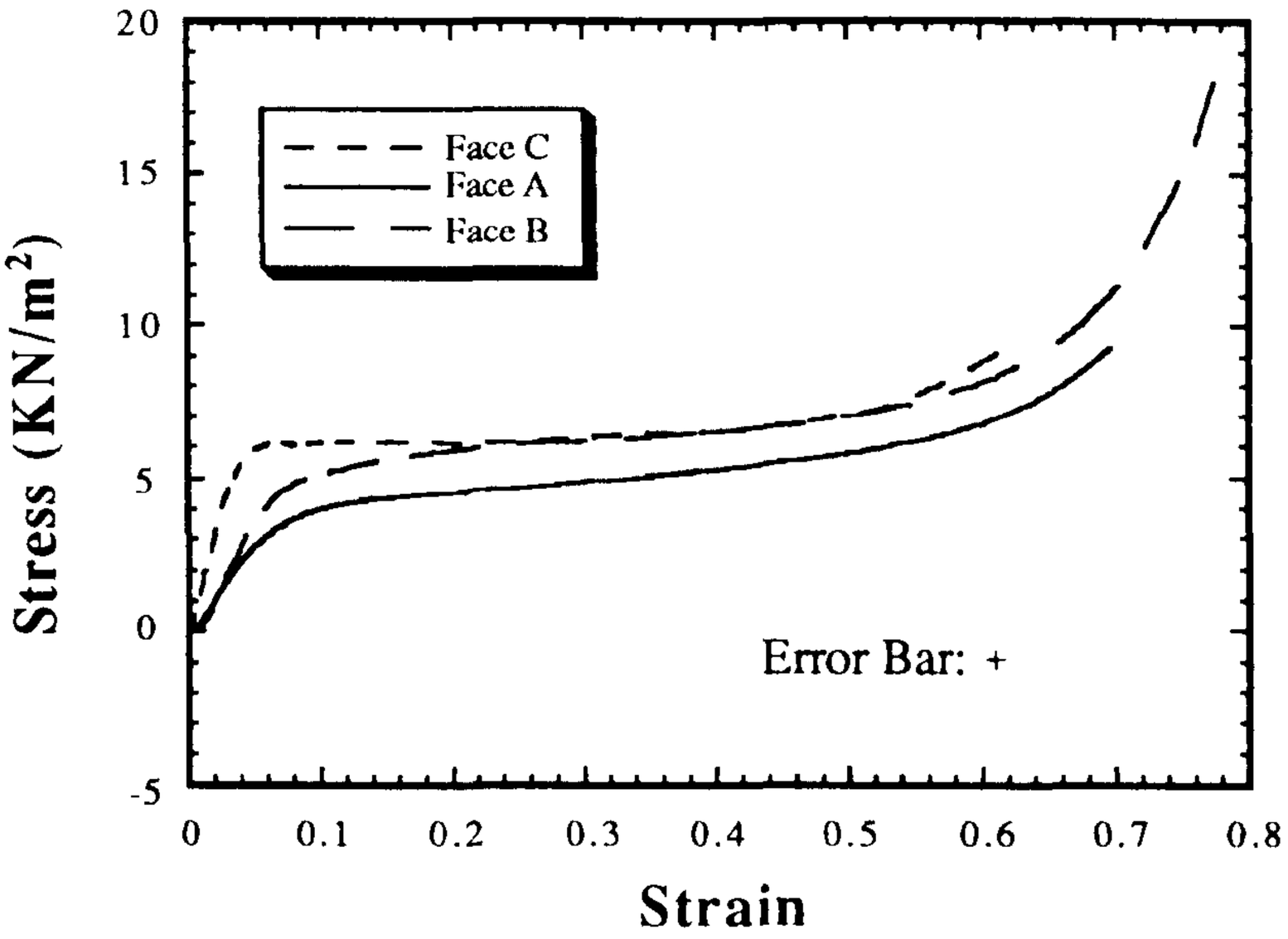

Fig. 6.13 Compressive stress-strain curves in two orthogonal directions in the planes normal to the rise direction (Face A and Face B) and in the rise direction (Face C) for the 60ppi conventional elastic closed-cell polyester urethane foam (PECC).

60ppi Open-Cell Polyether Urethane Foam

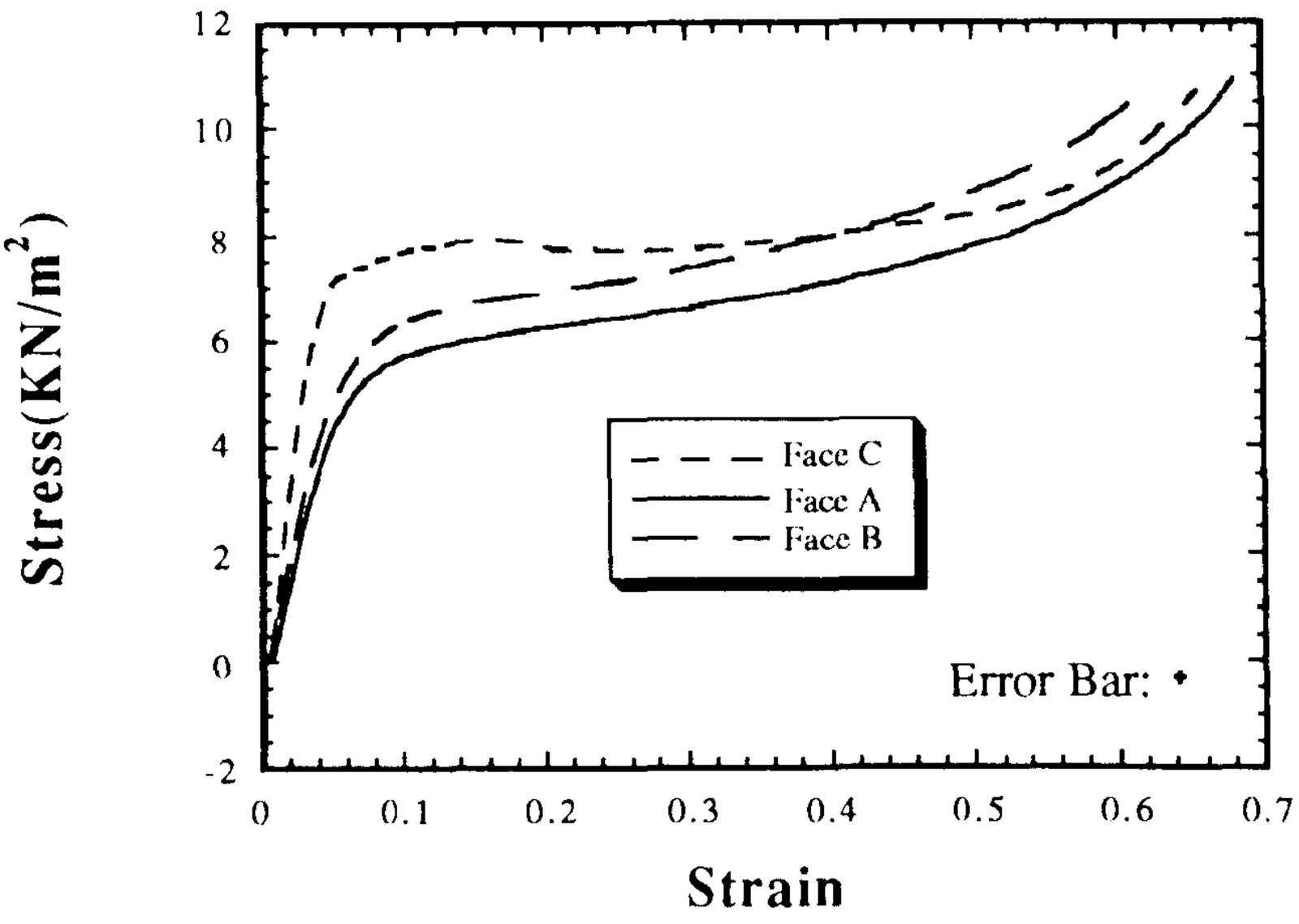

Fig. 6.14 Compressive stress-strain curves in two orthogonal directions in the planes normal to the rise direction (Face A and Face B) and in the rise direction (Face C) for the 60ppi conventional elastic open-cell polyether urethane foam (60CO).

10ppi Open-Cell Polyether Urethane Foam

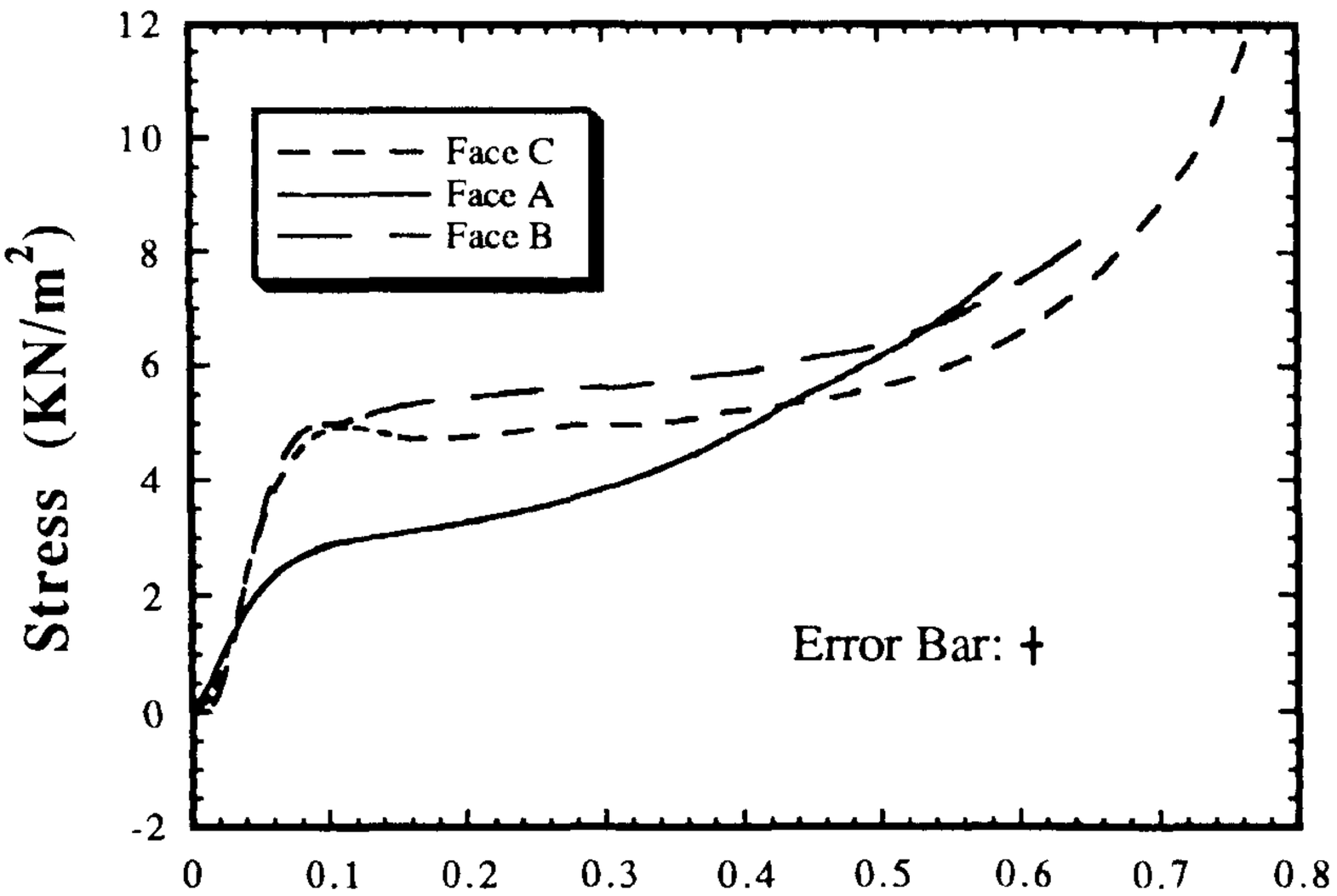

Fig. 6.15 Compressive stress-strain curves in two orthogonal directions in the planes normal to the rise direction (Face A and Face B) and in the rise direction (Face C) for the 10ppi conventional elastic open-cell polyether urethane foam (10CO).

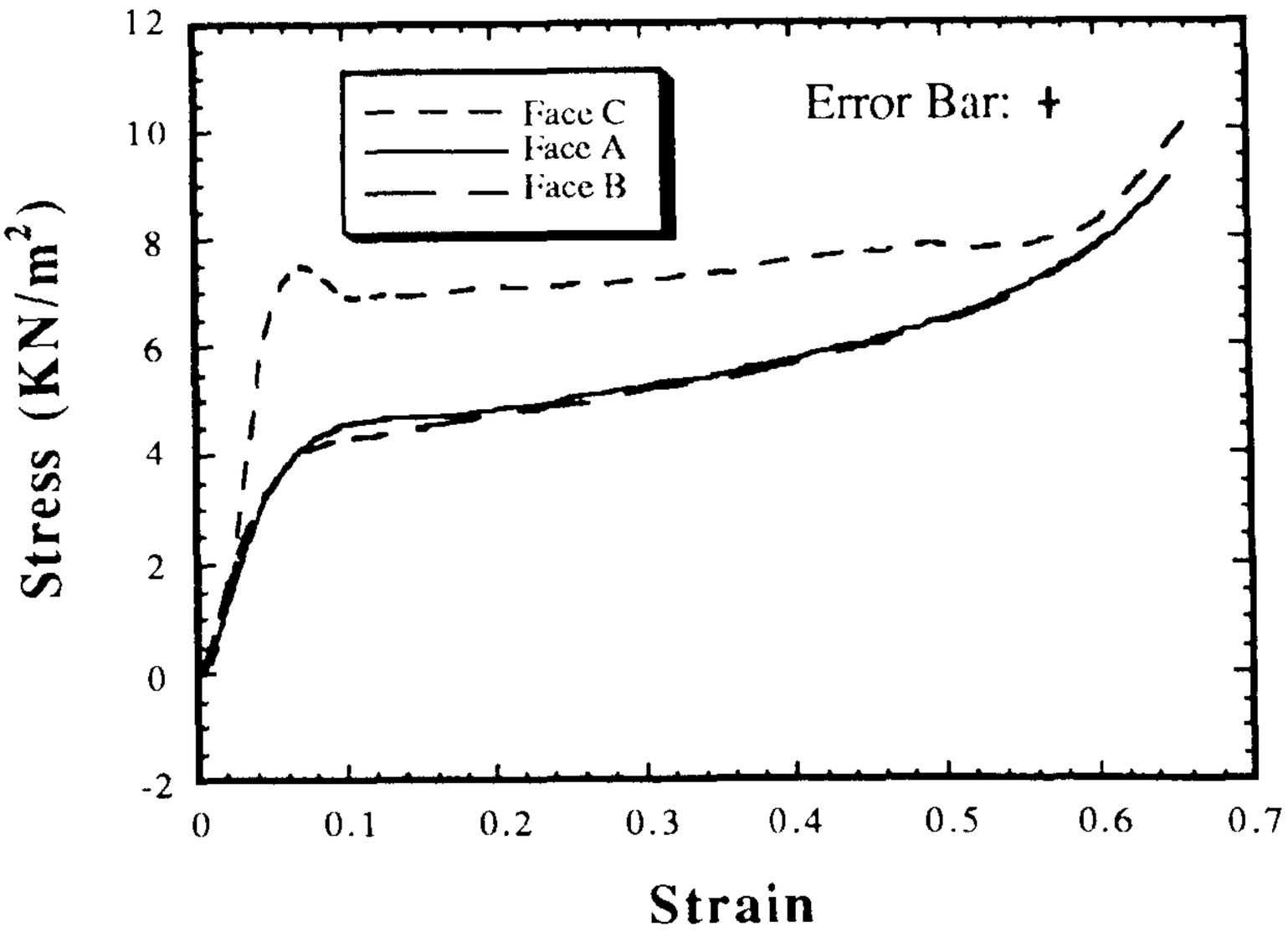

Fig. 6.16 Compressive stress-strain curves in two orthogonal directions in the planes normal to the rise direction (Face A and Face B) and in the rise direction (Face C) for the 30ppi conventional elastic open-cell polyether urethane foam (30CO).

It can be seen that there are three regions in the above conventional foam stress-strain diagrams (see *Figures* 6.12 to 6.16) and these are indicated in *Figure* 6.12. The initial linear portion of the curve, OQ, is the linear elastic region within which Hooke's law is obeyed. Point Q is the proportional limit, defined as the stress at which the stress-strain curve deviates from linearity. The slope of the stress-strain curve in this region (OQ) is the modulus of elasticity (the Young's modulus in compression). The second region, from Q to R, is described as the elastic collapse region. In this region, cells of the foam undergo an elastic collapse, the stress is almost keeping steady with the strain. The third region is the elastic densification region, RS. Elastic densification begins when the cell ribs of the foam are starting to touching each other and the foam density increases becoming more like a solid. As the densification increases, the foam becomes stronger (strain hardening) so that the load required to compress the specimen increases with further strain. Eventually, the load reaches a maximum value when the foam is fully deformed. For flexible polymer foams, such as the polyether urethane and polyester urethane foams used in this study, the specimen soon begins to recover once the load has been removed, as a result, the foam does not have any permanent deformation even after having been fully compressed.

Since cell geometry has a strong influence on the shape of the stress-strain curve, more markedly than any other variable, it is this parameter which should be changed if the strain function of a given foam is not desirable for a certain application. To vary the cell geometry, we can either change the cell shape or the slenderness of the cell rib (i.e. rib thickness (t) / rib length (L)). To investigate this, the stress-strain behaviour of auxetic foam were examined. The compressive stress-strain curves for auxetic foams which have a re-entrant cell shape are shown in *Figures 6.17 to 6.20*. The method used was the same as used for the conventional foam. All the tests were carried out at a cross head speed of 2 mm/min, and three specimens of each type were tested. The specimen dimensions were 50 x 50 x 50 mm, the average error was ±0.4 mm. The average errors of all the testing results were within 9%. As can be seen from these diagrams, the shape of the compressive stress-strain curve of auxetic foam is very different from that obtained from a conventional foam. The curves can be divided into two parts. The first region OM, having a relatively low modulus, is followed by a gradual transition MN to an increasingly larger modulus.

10ppi Polyether Urethane foam

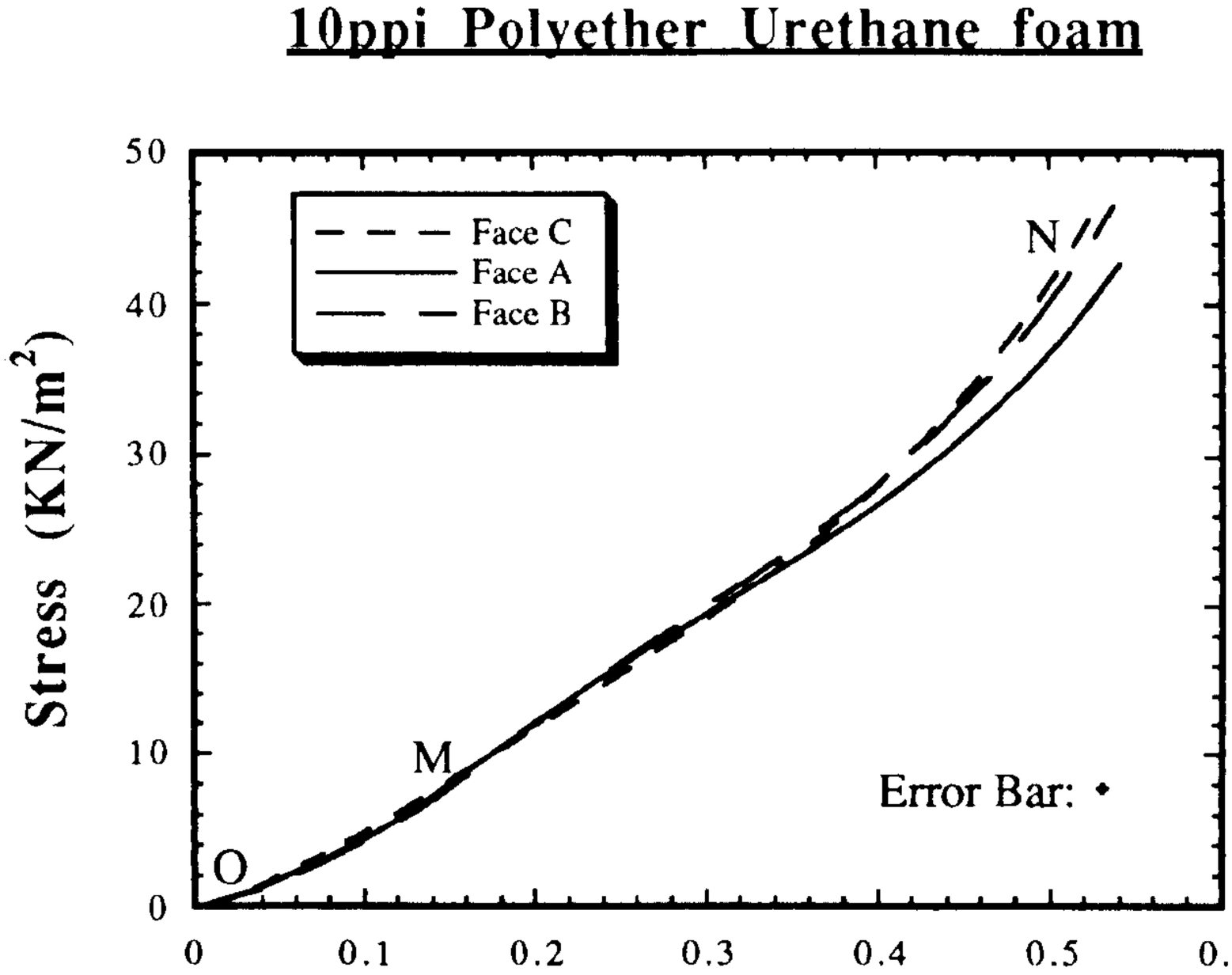

Fig. 6.17 Compressive stress-strain curves in two orthogonal directions in the planes normal to the rise direction (Face A and Face B) and in the rise direction (Face C) for the 10ppi auxetic open cell polyether urethane foam (100AO).

3D 10ppi Auxetic (90-50) Polyether Urethane Foam

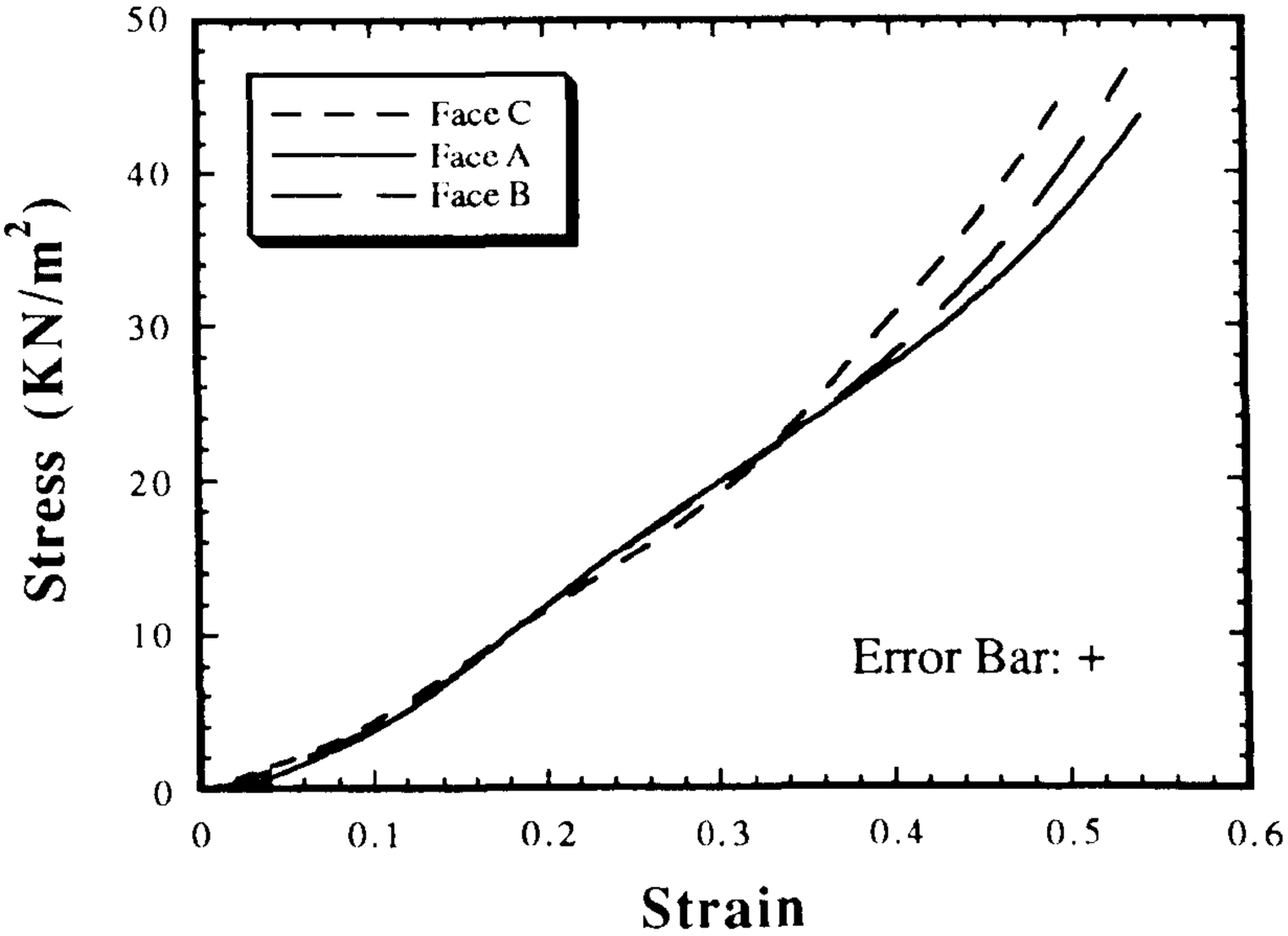

Fig. 6.18 Compressive stress-strain curves in two orthogonal directions in the planes normal to the rise direction (Face A and Face B) and in the rise direction (Face C) for the 10ppi auxetic elastic open-cell polyether urethane foam (90AO).

3D 10ppi Auxetic (80-50) Polyether Urethane Foam

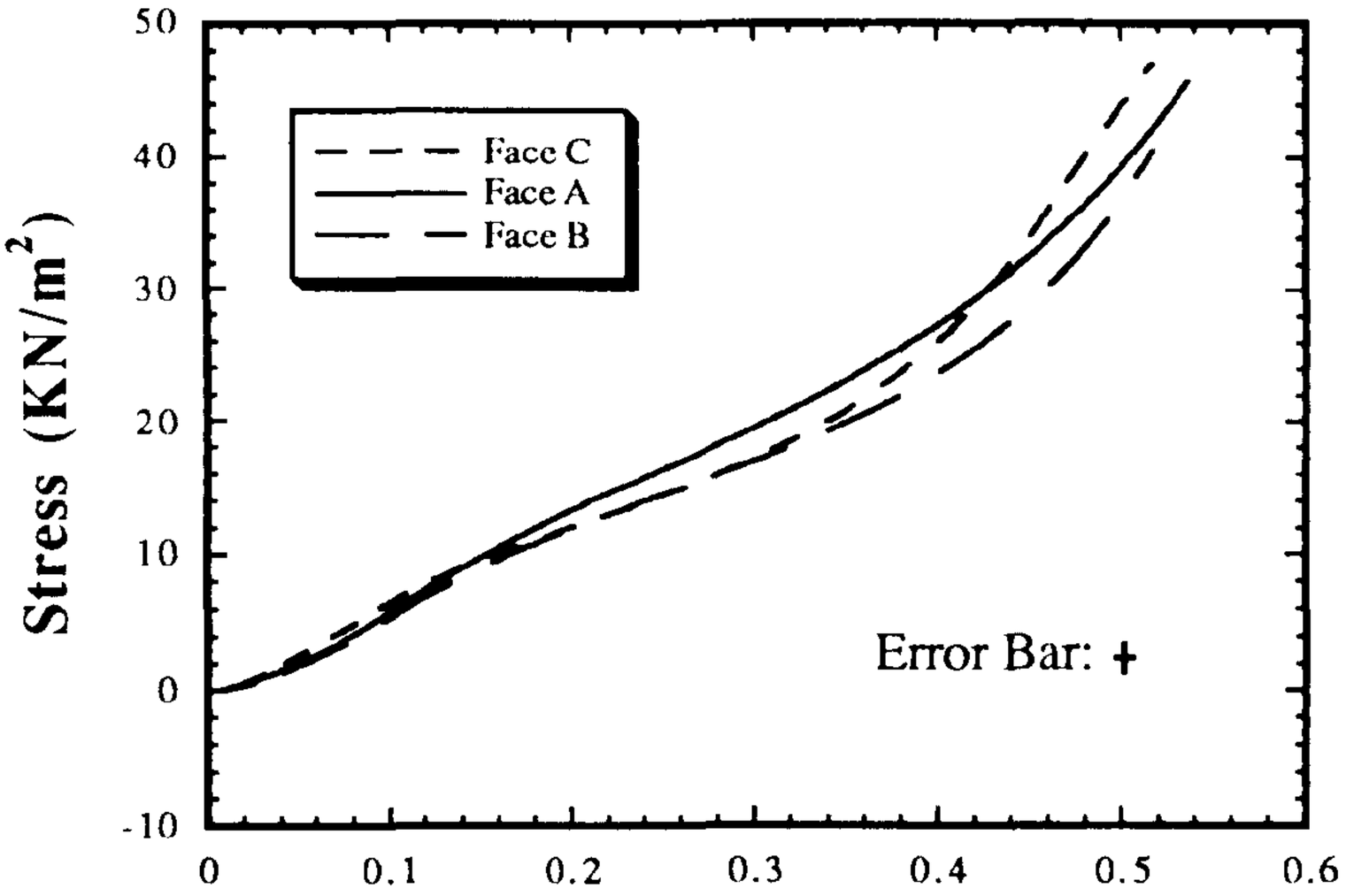

Fig. 6.19 Compressive stress-strain curves in two orthogonal directions in the planes normal to the rise direction (Face A and Face B) and in the rise direction (Face C) for the 10ppi auxetic elastic open-cell polyether urethane foam (80AO).

3D 10ppi Auxetic (70-50) Polyether Urethane Foam

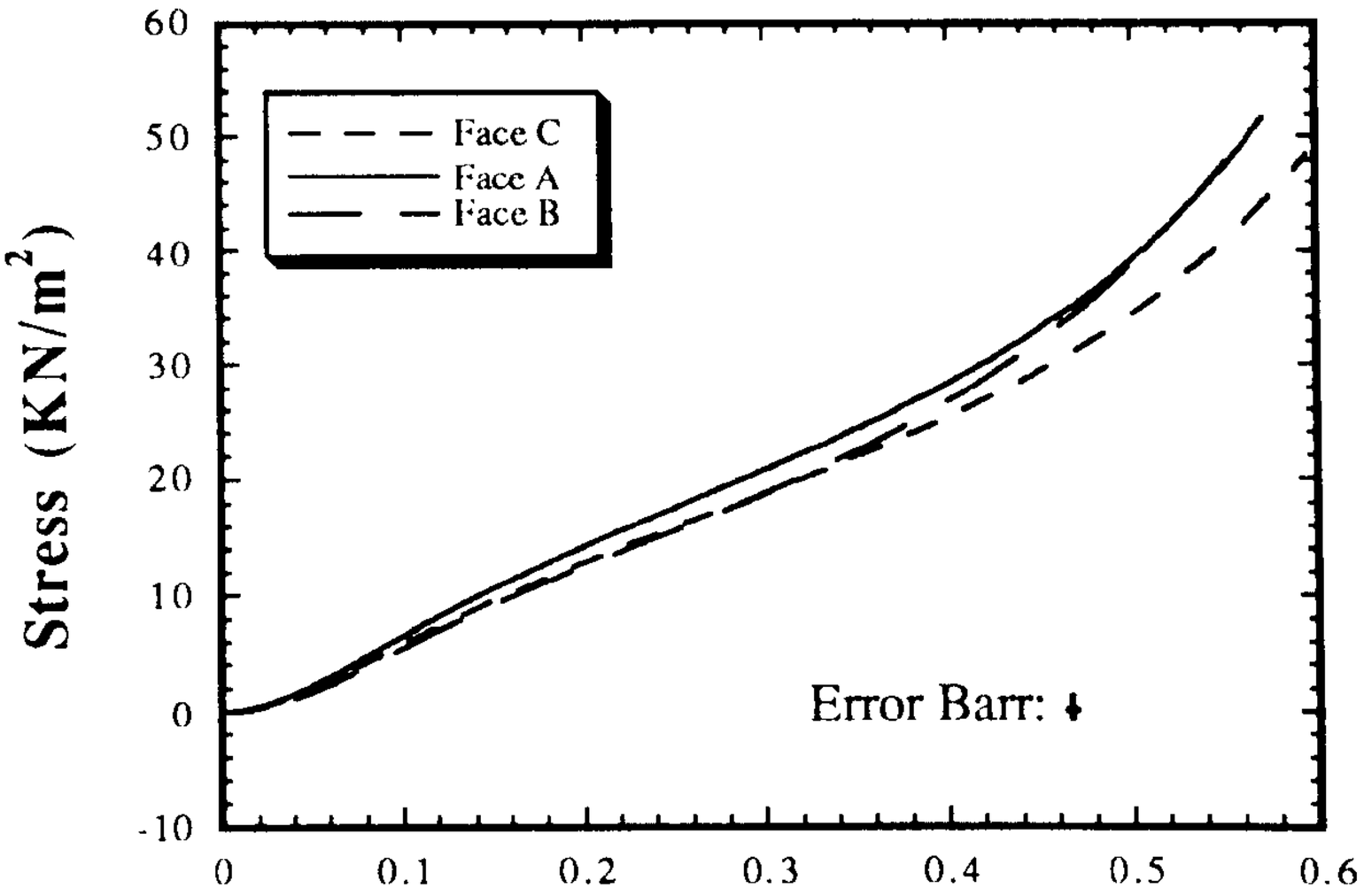

Fig. 6.20 Compressive stress-strain curves in two orthogonal directions in the planes normal to the rise direction (Face A and Face B) and in the rise direction (Face C) for the 10ppi auxetic elastic open-cell polyether urethane foam (70AO).

From the stress versus strain diagrams shown in *Figures* 6.17 to 6.20, it can be seen that the mechanical performance of conventional foam in compression is different from that of the auxetic foam. The mechanical properties of the conventional foam depend heavily on the directions of loading, whereas, the auxetic foam behaves more like an isotropic material (i.e. it is not strongly dependent on the loading direction). The compressive elastic modulus was measured by determining it from the linear elastic region (i.e. 0~5% strain for conventional foam and 0~8% strain for auxetic foam). The gradient of the load-displacement trace was obtained from the Instron 4505, then using the original cross-sectional area and original length to give the Young's modulus. The results are shown in *Table* 6.1. Loading in the rise direction of conventional foam deflects the shorter cell edges, of length, L. The stiffness in the rise direction is greater than that loading in the plane normal to it. However, for an auxetic foam, the orientation of the cell ribs is more random, and the re-entrant cell structure is similar in each dimension. Therefore, the mechanical behaviour in the three directions are similar.

Table 6.1

	PECC	PECO	60CO	30CO	10CO	100AO	90AO	80AO	70AO
ρ (kg/m^3)	37.9±2.1	33.7±1.3	21.7±1.2	24.5±2.2	24.1±1.4	79.1±2.2	76.9±1.8	76.3±2.8	74.7±2.5
E_x(kN/m^2)	58.3±3.3	44.7±1.7	91.1±3.4	71.3±2.4	39.2±1.8	35.1±1.5	42.4±2.3	47.8±2.7	49.4±1.2
E_y(kN/m^2)	150.3±4.5	68.2±2.3	170.4± 5	110.0±3	61.5±2.2	38.2±2.1	43.6±2.5	48.5±1.4	51.4±2.3
E_z(kN/m^2)	69.6±2.7	45.6±1.55	110.2±3	77.8±3.5	48.3±2.4	36.3±1.6	43.8±3.0	47.1±1.6	50.7±3.1

Table 6.1 The compressive modulus for the foams.

6.3 Tensile Test

6.3.1 Introduction

According to ASTM 3574-91(E), the tensile stress of a PUR foam, together with the corresponding tensile strain, is determined using rectangular specimens as shown in *Figure* 6.21. The force was applied using end-wise T profiles. These profiles were stuck onto the foam using Apollo Adhesion A. 2874 in such a way that an articulated suspension is effective in both directions as shown in *Figure* 6.22.

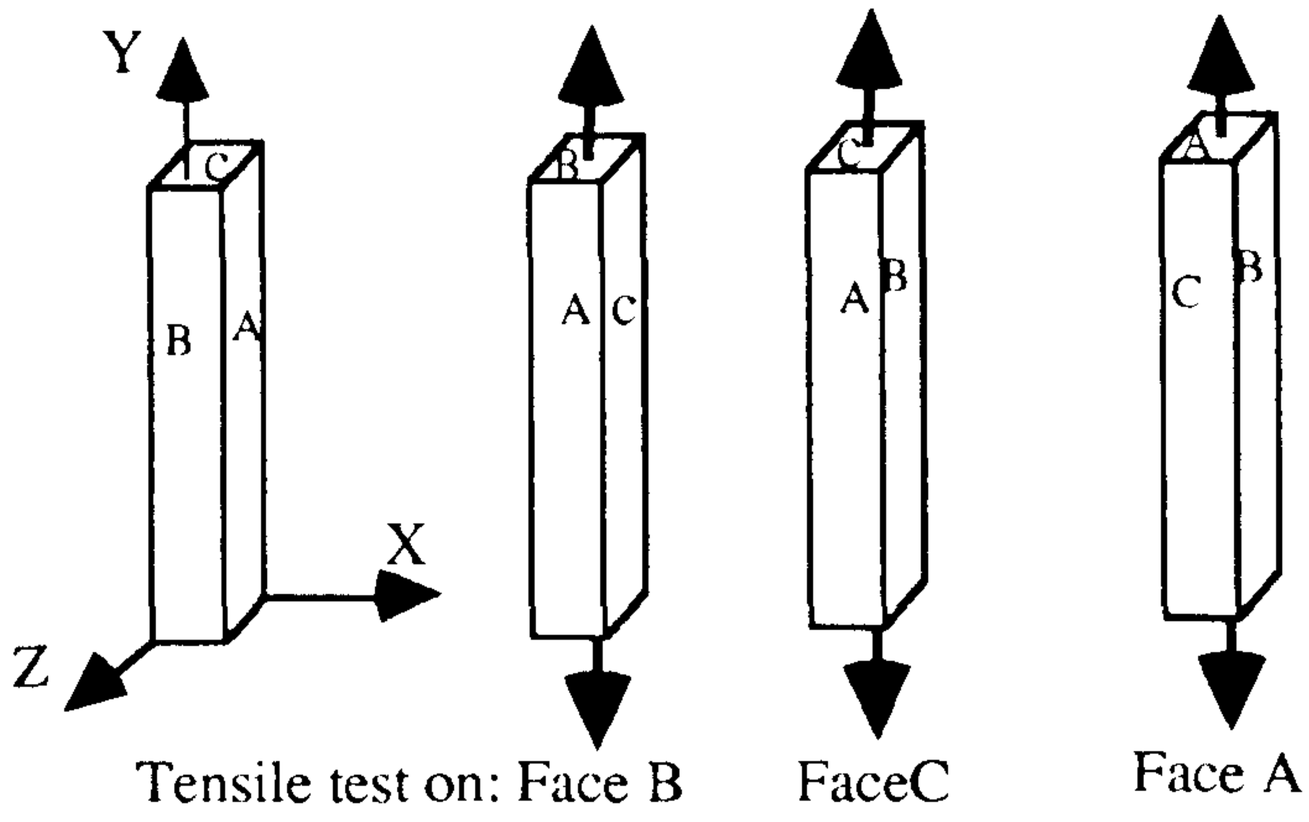

Fig. 6. 21 Schematic of the tensile test foam specimens.

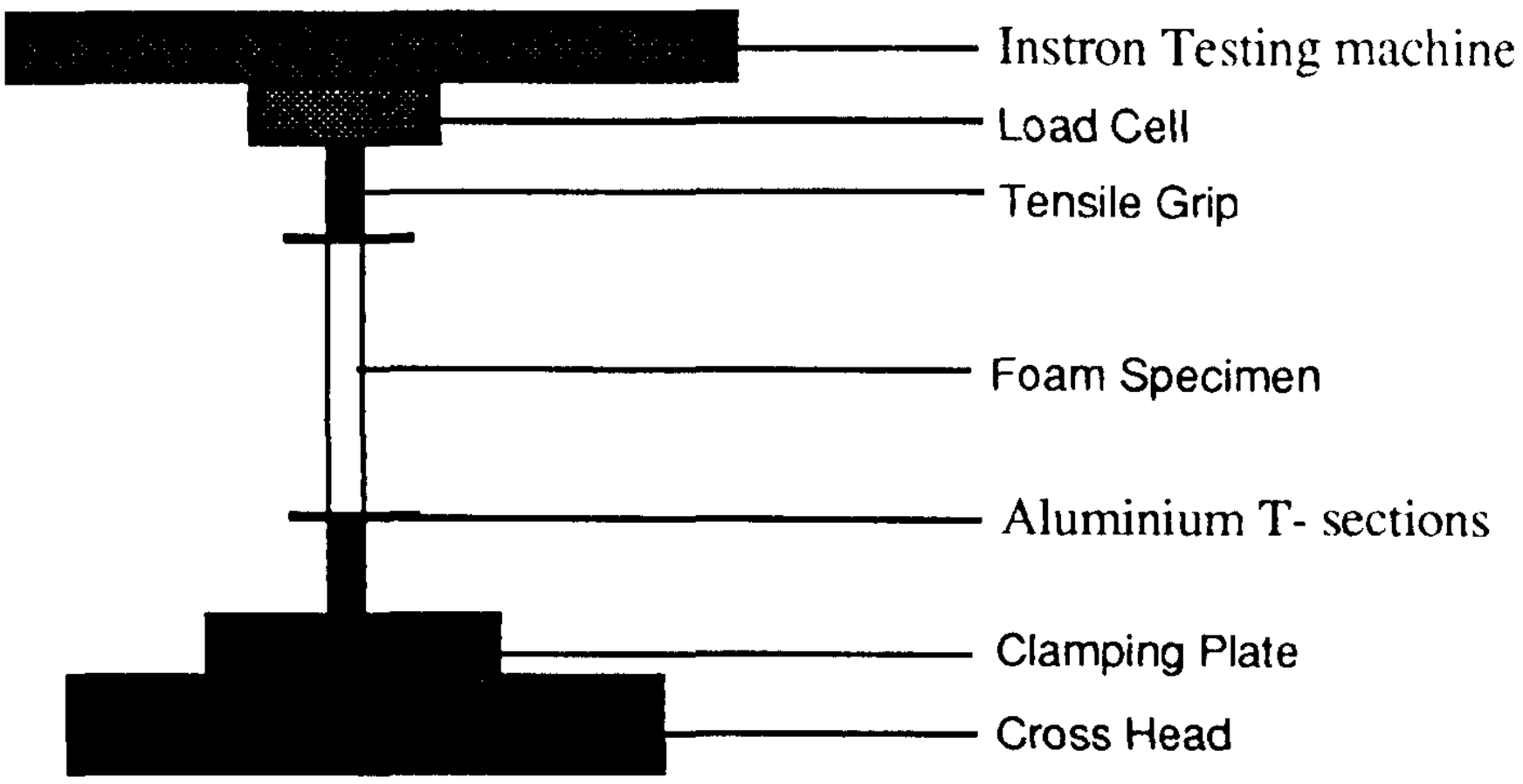

Fig. 6. 22 Schematic of the tensile test.

In a tensile test special consideration must be given to the application of the force. In order to obtain an unambiguous state of stress in the gauge length, the specimen was loaded along the central axis so that it was free of any bending moment. Properties of the foams depend upon the following effects as indicated in *Sections* 6.3.2 to 6.3.4.

6.3.2 Strain Rate Effect

The foams were cut to dimensions, 25 x 25 x 130 mm (the average error was ±0.5 mm). The tensile tests were carried out using an Instron 4505 at cross head speeds of 0.5, 2, 10 and 20 mm/min. At each cross-head speed, three specimens were tested and the errors were within 6%. (see *Figures* 6.23 and 6.24).

10ppi conventional Polyether Urethane Foam

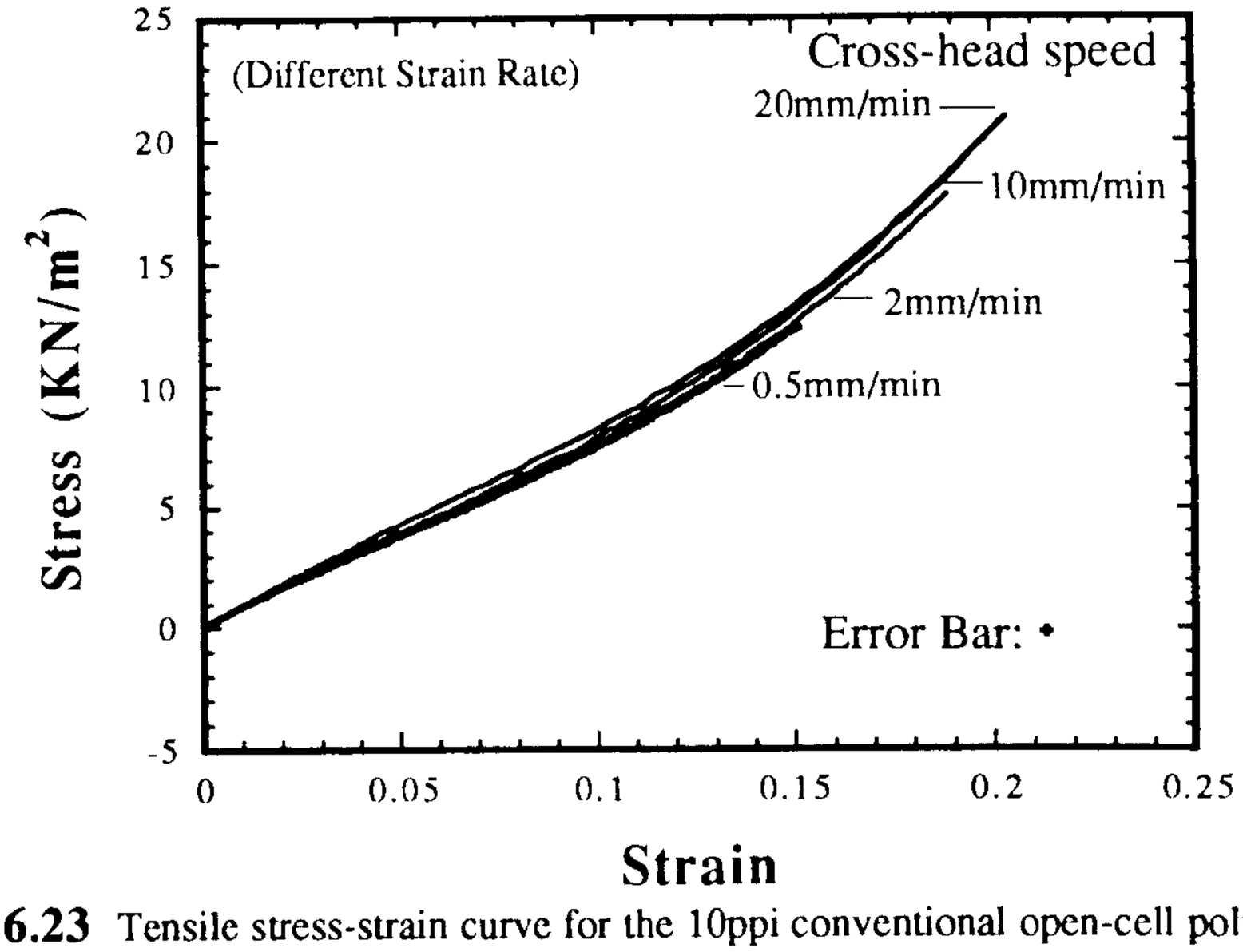

Fig. 6.23 Tensile stress-strain curve for the 10ppi conventional open-cell polyether urethane foam (10CO) tested of 4 different cross-head speeds .

10ppi Auxetic Polyether Urethane Foam

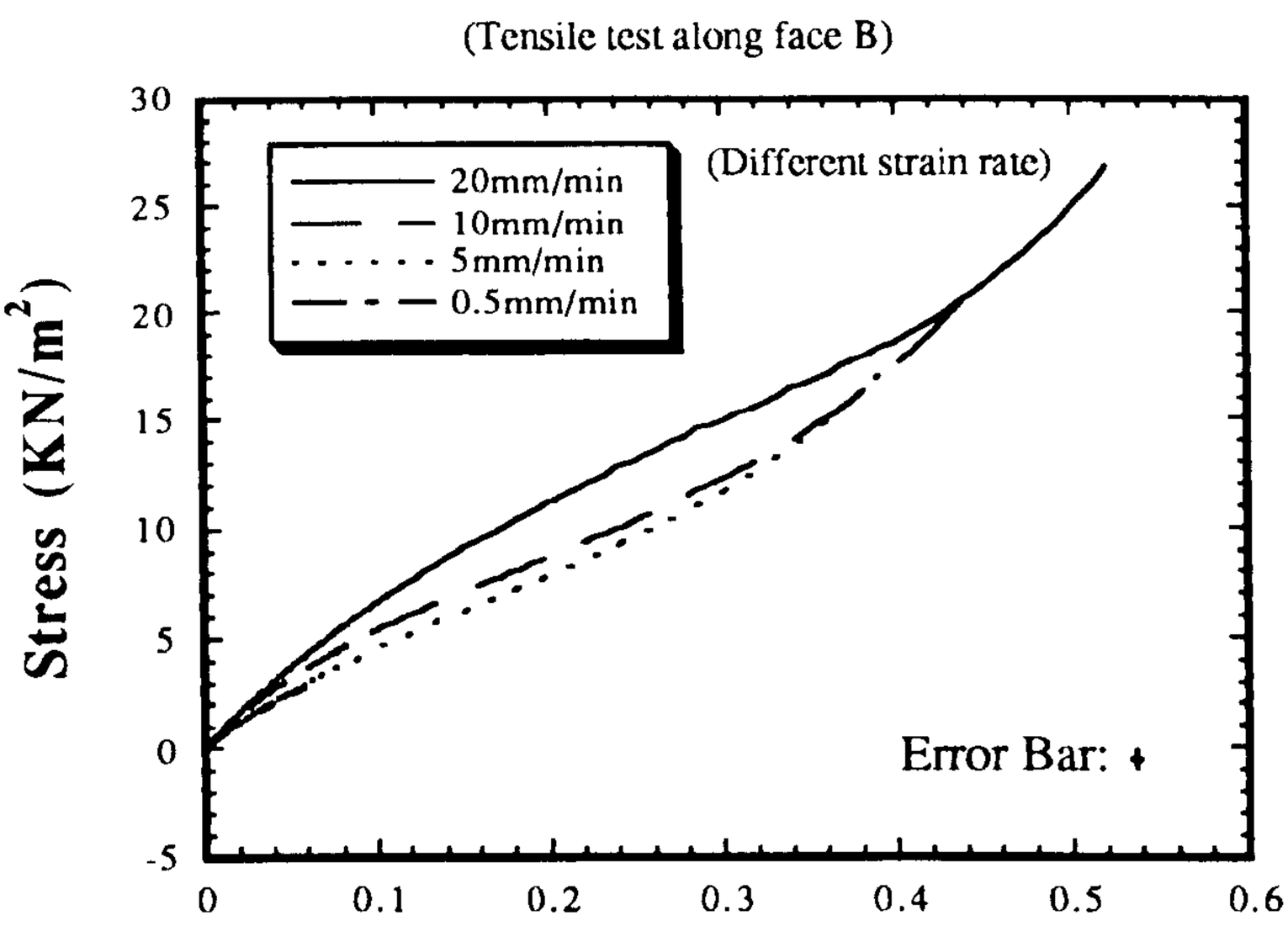

Fig. 6.24 Tensile stress-strain curve for the 10ppi auxetic open-cell polyether urethane foam (100AO) tested of 4 different cross-head speeds.

Once again, the tensile behaviour is similar to the compressive behaviour. The diagrams show that the influence of strain rate is small for both conventional and auxetic foams. It seems that when the strain rate is increased, the slope of the initial linear elastic region of the stress-strain curve also increases. This is due to the viscoelastic behaviour of the polymeric material. Comparing the tensile test results of this study with published data, it is found that Benjamin (1965) reported data on rigid polystyrene foam tested in tension at several strain rates which do not agree with the results presented here, as no change in failure strength was observed but an increase in modulus was. Since the type of foam used by Benjamin was a plastic rigid foam, this may account for the difference in the results. However, results obtained by Rinde and Hogg (1971) and by Green et. al. (1969) show that the failure stress is independent of rate, and the modulus increases with strain rate, which is agreement with the results of this study.

6.3.3 Specimen Geometry

An investigation on the 60ppi closed-cell conventional polyester urethane foam and the 30ppi auxetic open-cell polyether urethane foam was carried out. The sizes of the specimens tested are shown in *Figures 6.25 to 6.27*. The tensile tests were performed using an Instron 4505 at a cross head speed of 2 mm/min. Three specimens were tested for each case, and the errors were within 8%.

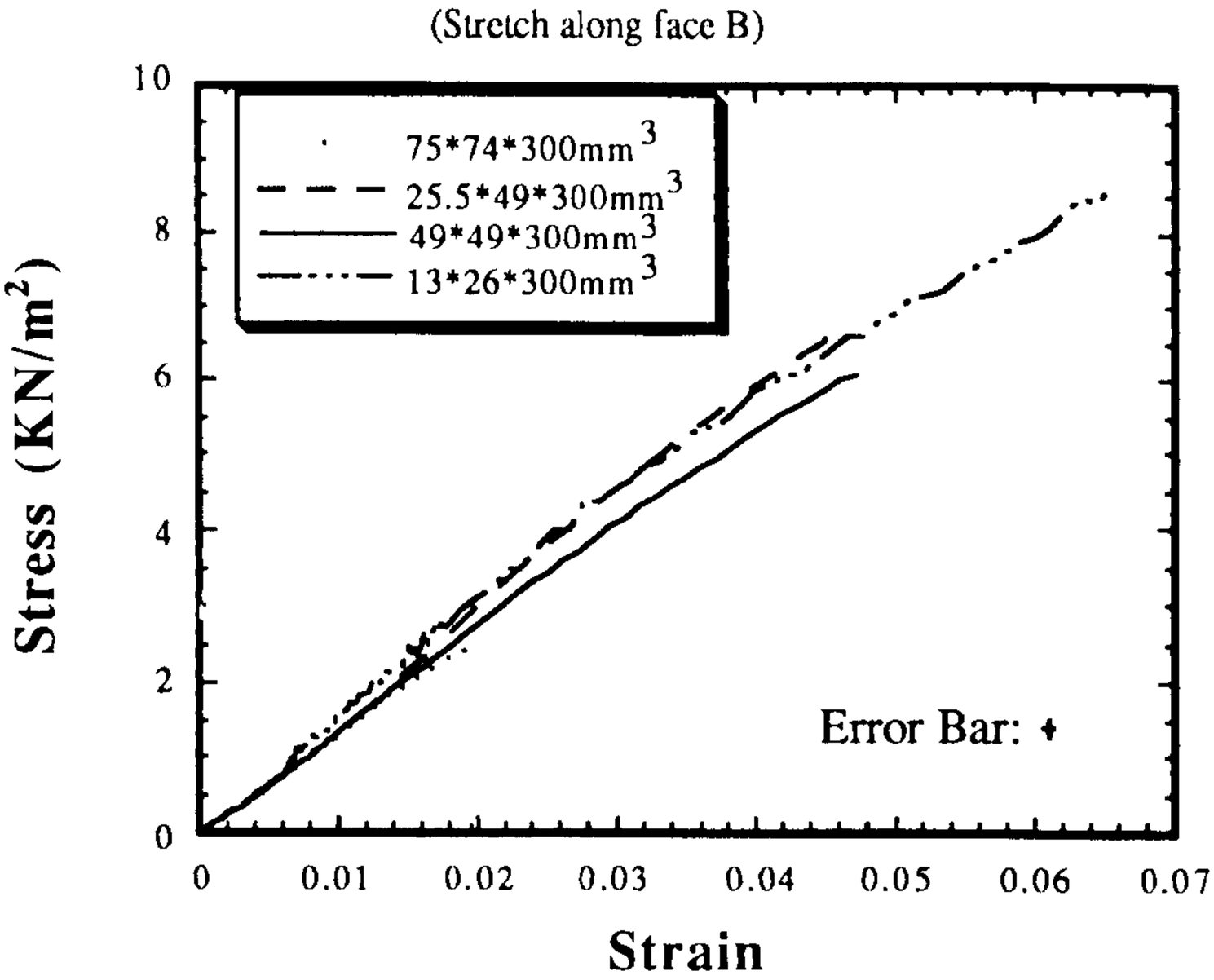

Fig. 6.25 Tensile stress-strain curve for the 60ppi conventional closed-cell polyester urethane foam (PECC) tested with 4 different cross section areas.

60ppi Closed-Cell Polyester Urethane Foam

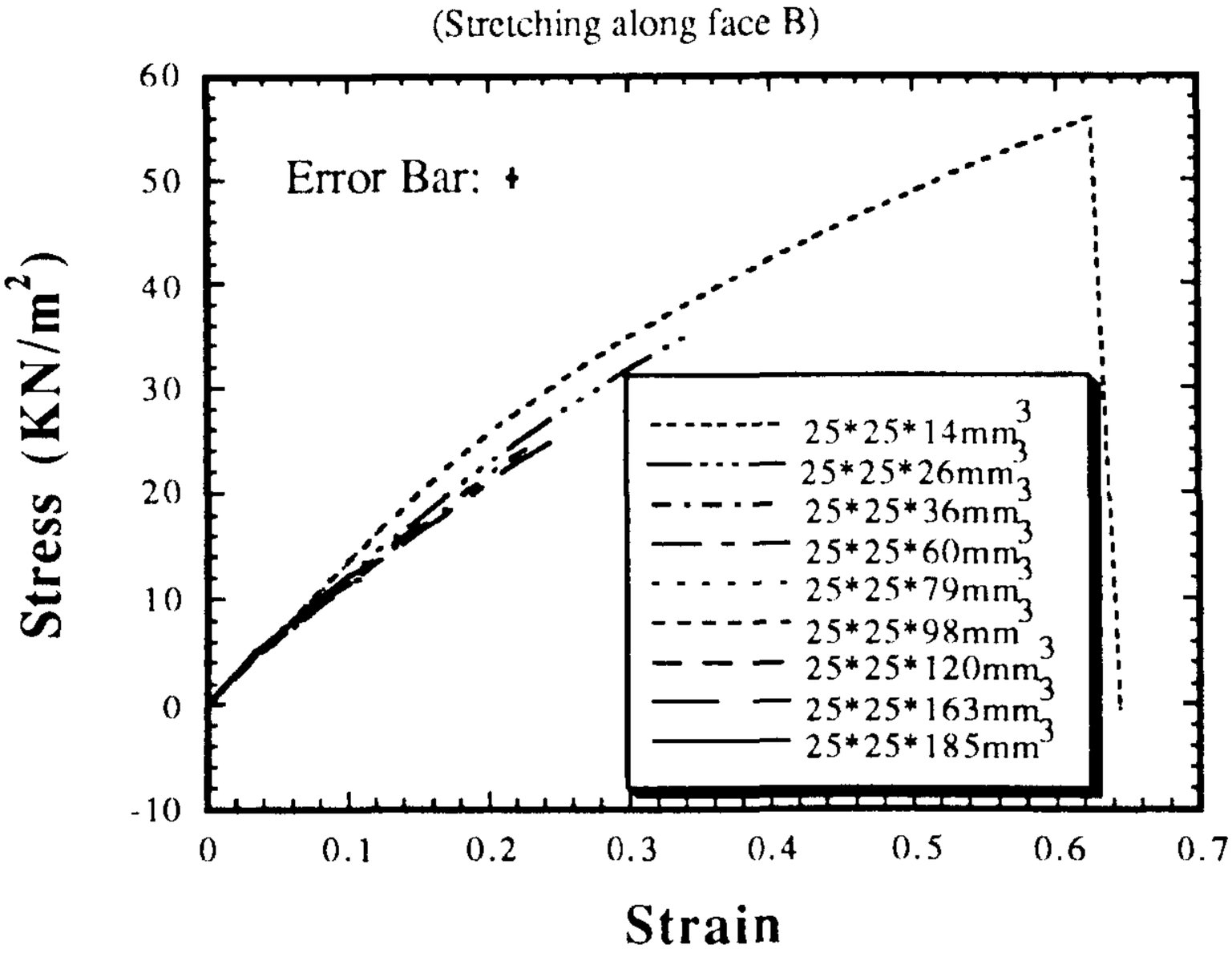

Fig. 6.26 Diagram of tensile stress versus tensile strain for the 60ppi conventional closed-cell polyester urethane foam (PECC) tested with 9 different gauge lengths.

Auxetic Foam Tensile Test

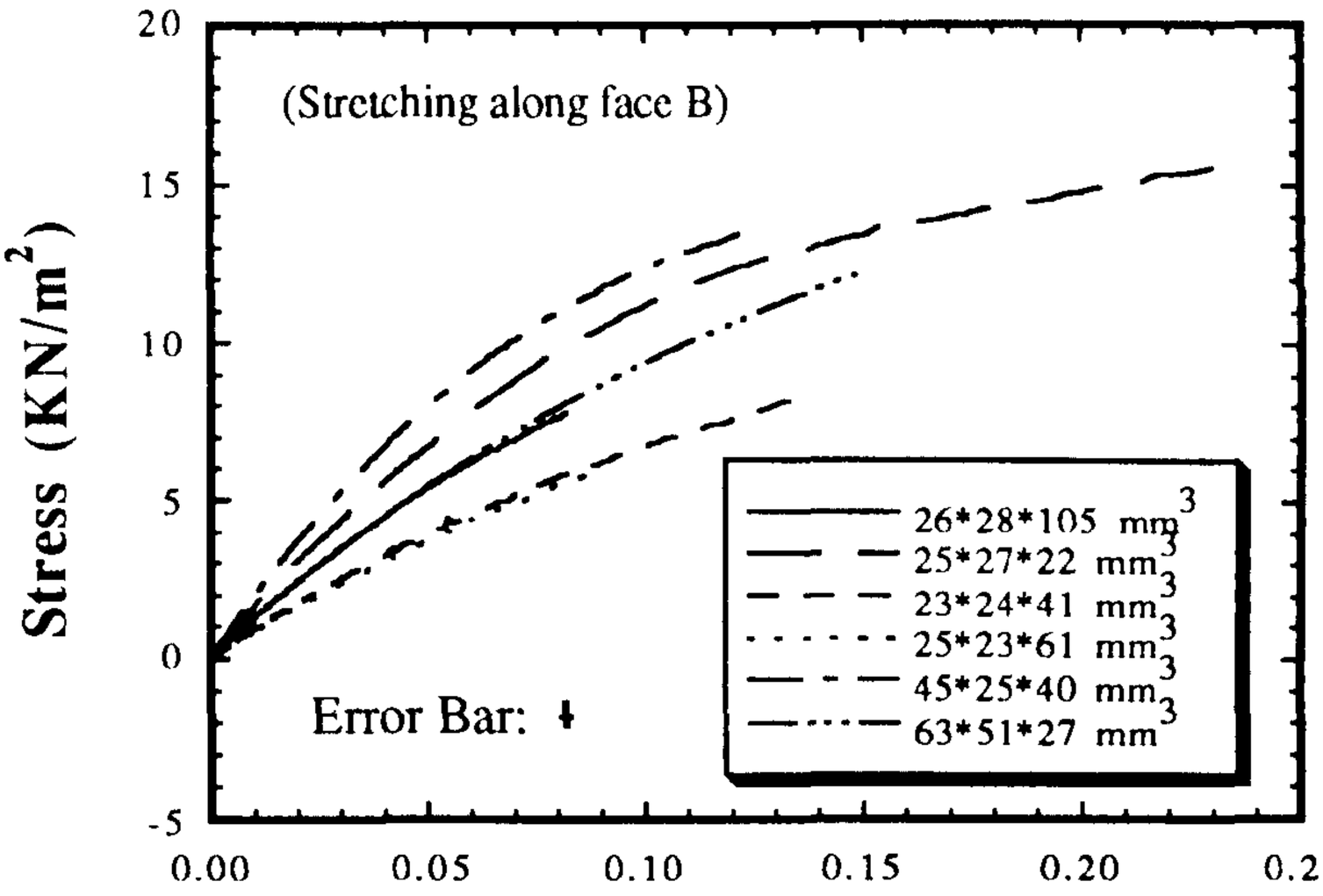

Fig. 6.27 Diagram of tensile stress versus tensile strain for the 30ppi auxetic open-cell polyether urethane foam (30ppi, 100AO) tested with 6 different slenderness.

Figures 6.25 to 6.27 show that the tensile stress-strain behaviour is also dependent on the length and the base area of the specimen. Increasing the base area, results in a reduction in the scatter of the test results; but increasing the length of the

specimen, causes an increase in the scatter of the test results. This is in agreement with the observation under compressive loading.

6. 3. 4 Tensile Creep

An investigation was carried out on rectangular specimens having dimensions of 25 x 25 x 130 mm, the average error was ±0.5 mm as shown schematically in *Figure* 6.28. The photographic measuring technique used in the compressive creep tests was used to give a point strain-time value for tensile creep. The results are shown in *Figures* 6.29 to 6.31.

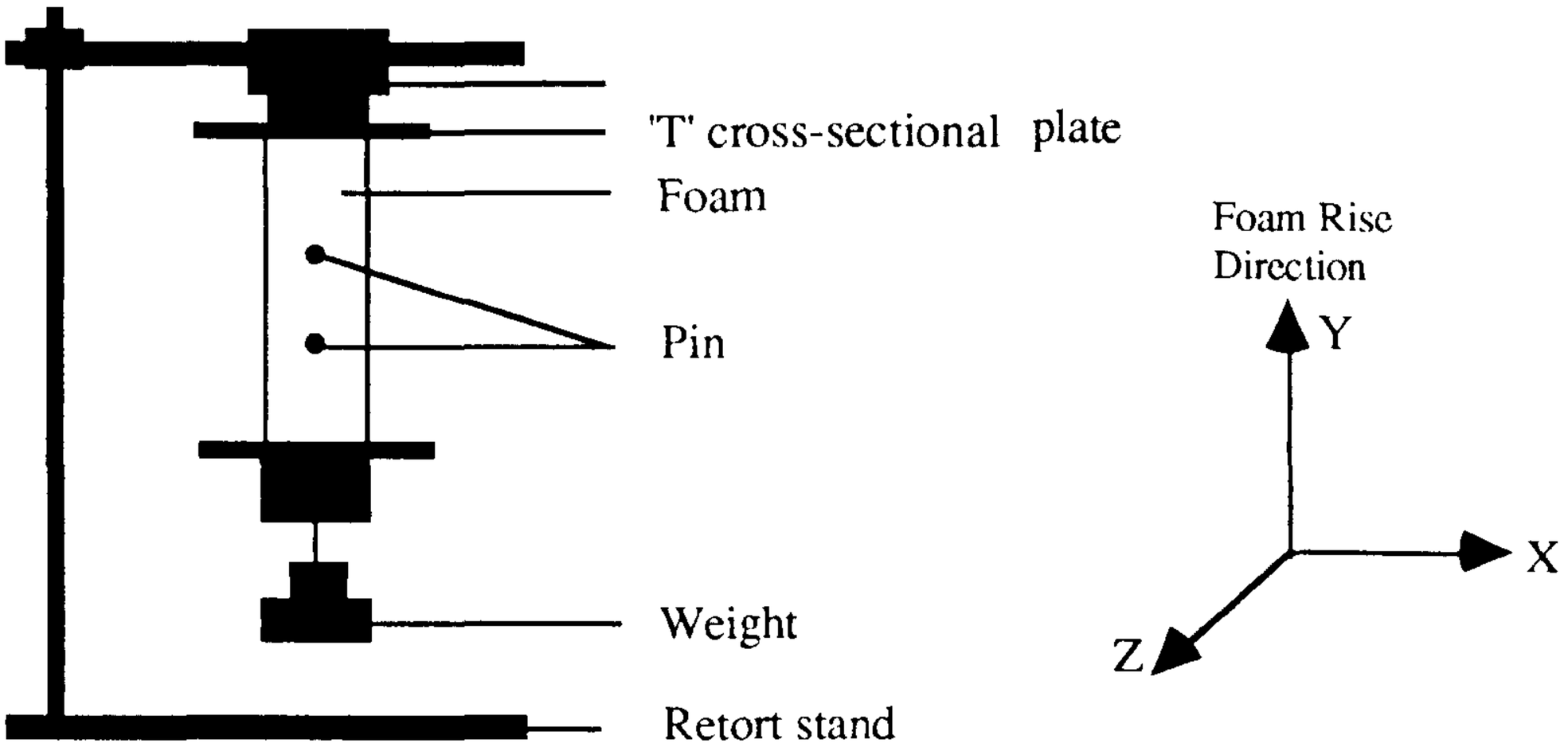

Fig. 6.28 Schematic diagram of the tensile creep test. (The pin dimensions: 0.2 x 0.2 x 25 mm).

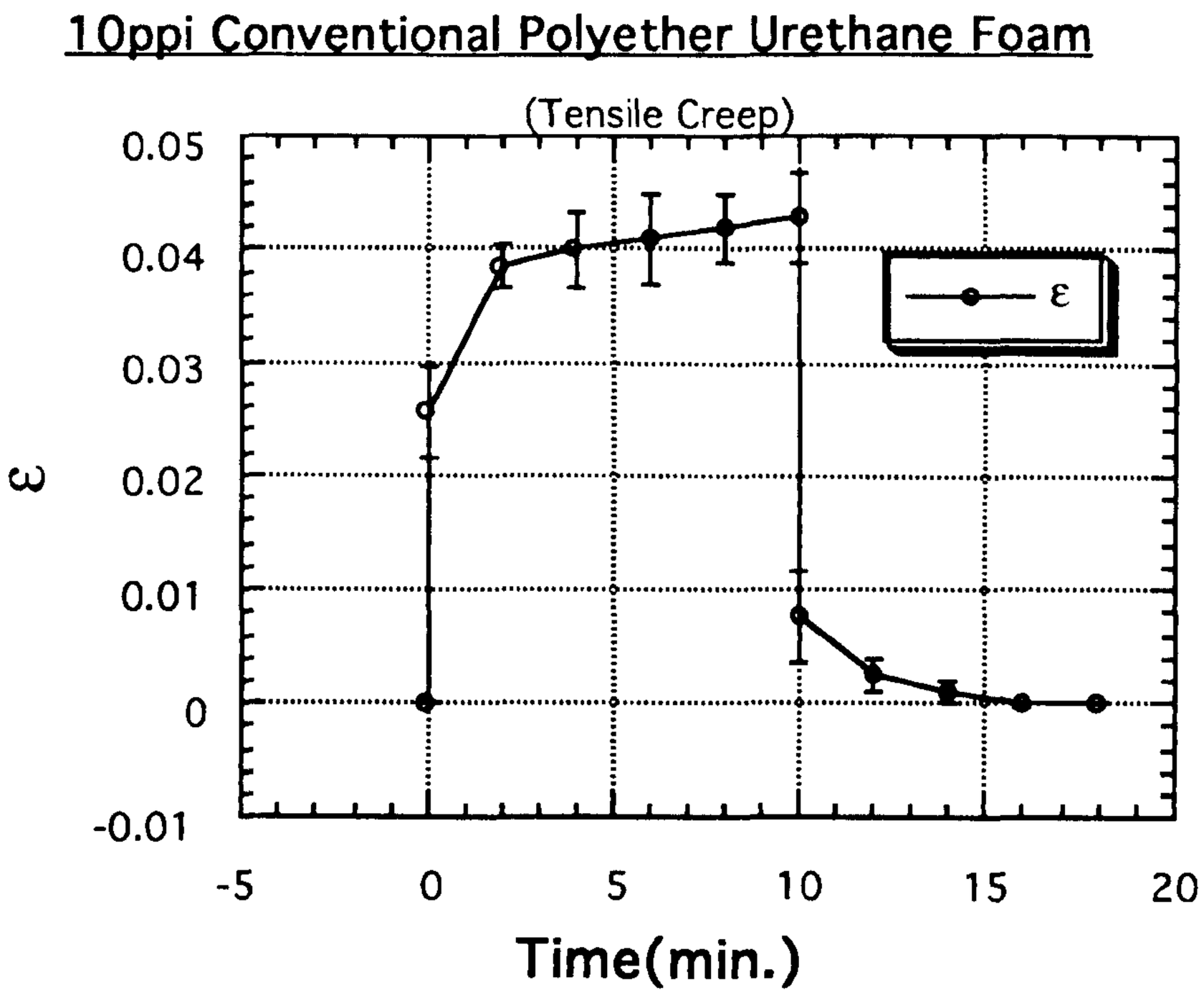

Fig. 6.29 Diagram of tensile strain versus time for the 10ppi open-cell conventional polyether urethane foam (10CO).

60ppi Conventional Reticulated Polyester Urethane Foam

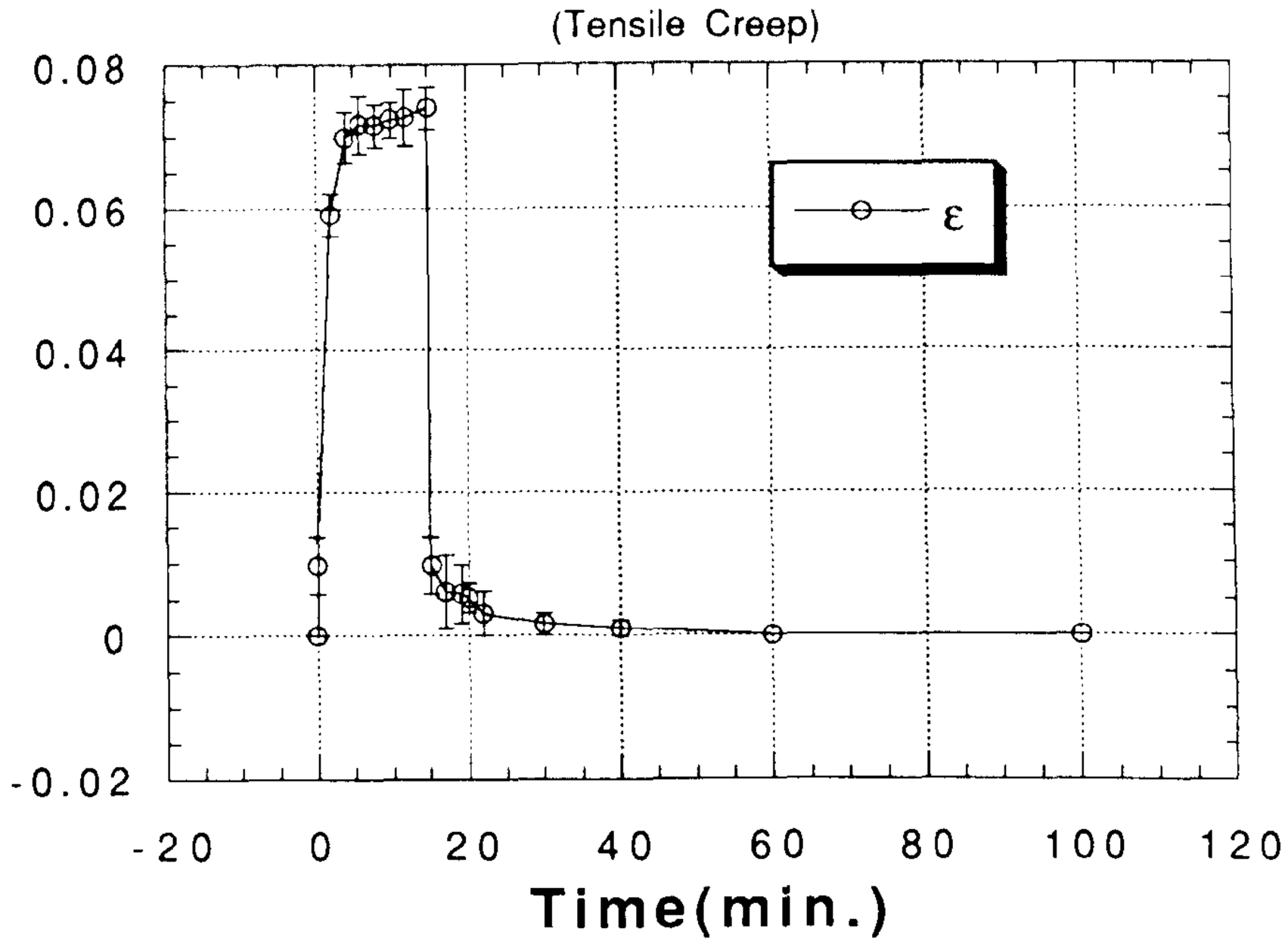

Fig. 6. 30 Diagram of tensile strain versus time for the 60ppi reticulated conventional polyester urethane foam (PECO).

10ppi Auxetic Polyether Urethane Foam (100A0)

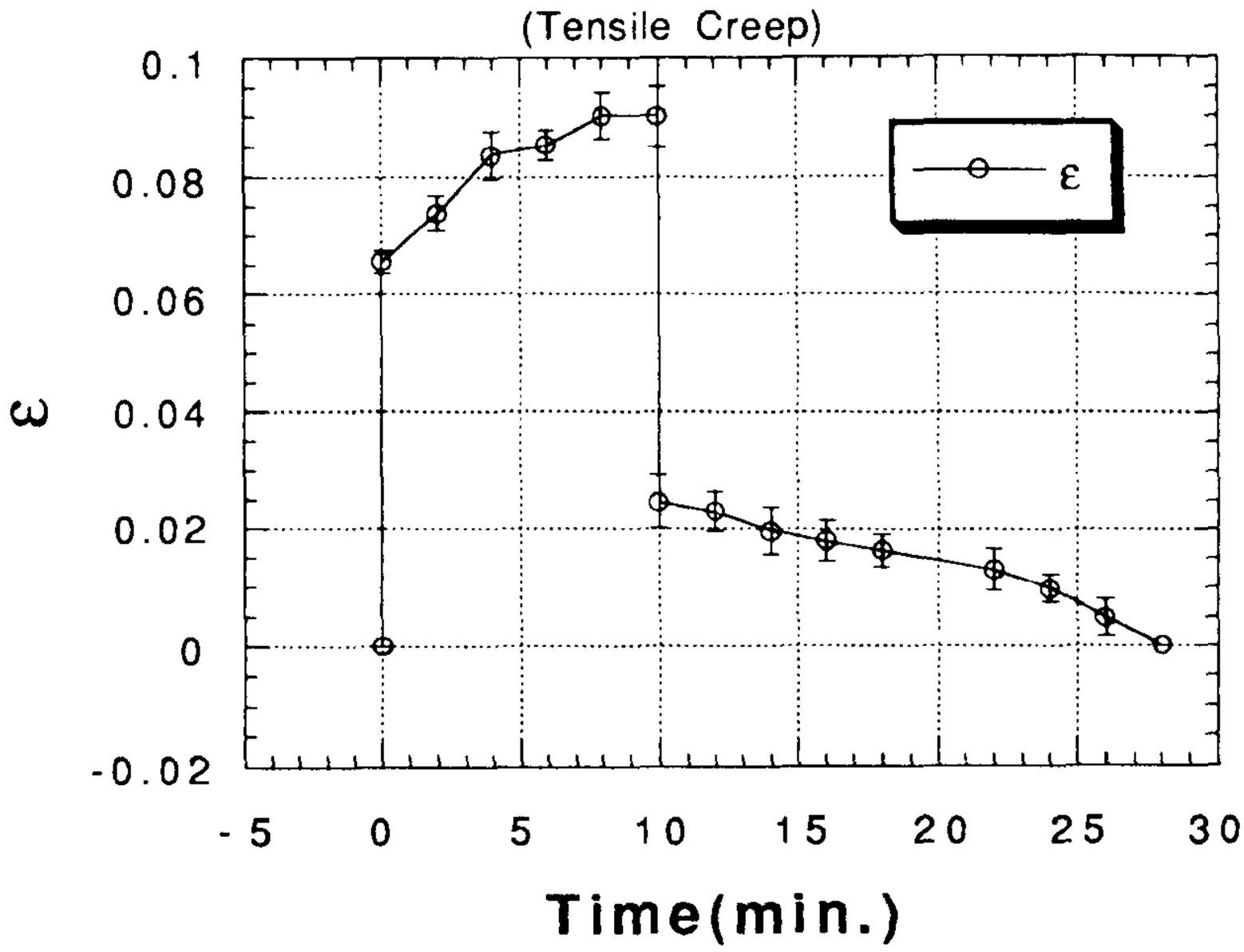

Fig. 6.31 Diagram of tensile strain versus time for the 10ppi open-cell auxetic polyether urethane foam (100AO).

From *Figures* 6.29 to 6.31, it can be seen that conventional foam requires less time to restore to its original length once the external tensile load is removed.

The strain-time curve shape is similar to that of the compression test. The foams are non-linear viscoelastic materials.

6.3.5 The Tensile Stress-Strain Behaviour

An Instron 4505 was used to conduct the tests and the modulus was calculated from the load-displacement traces, and by substituting the original cross-sectional area and the original length of the foam specimens. The dimensions of all the PUR tensile specimens were, 25 x 25 x 130 mm (the average error was ±0.3 mm). All the tests were carried out at a speed of 2 mm/min. Three specimens were tested for each type of foam in the three directions and the average errors were within 10%. The experimental results are shown in *Figures* 6.32 to 6.39.

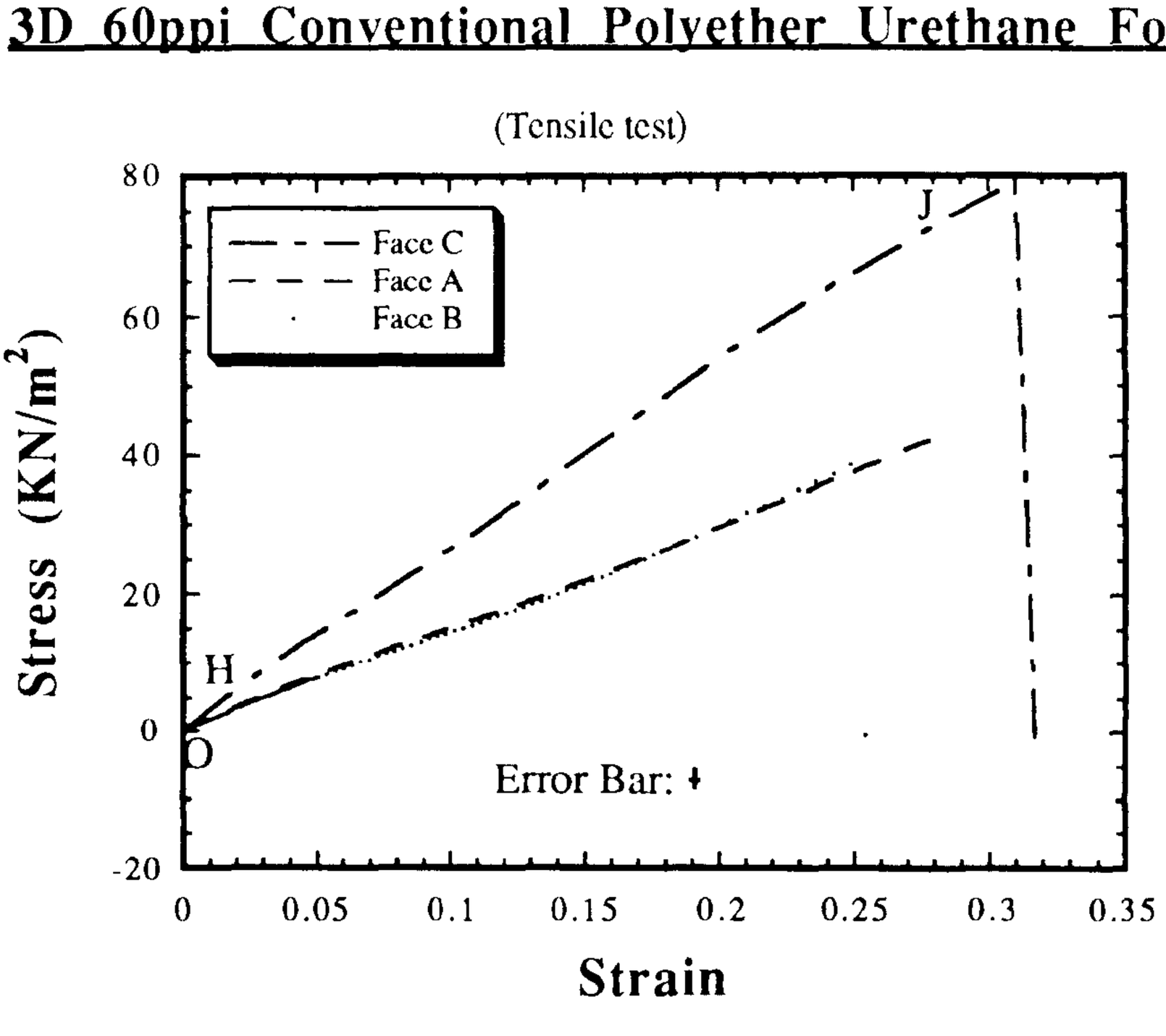

Fig. 6. 32 Tensile stress-strain curve for the 60ppi conventional open-cell polyether urethane foam (60CO). The graphical end-points represent fracture of the foam at the glue joint.

3D 30ppi Conventional Polyether Urethane Foam

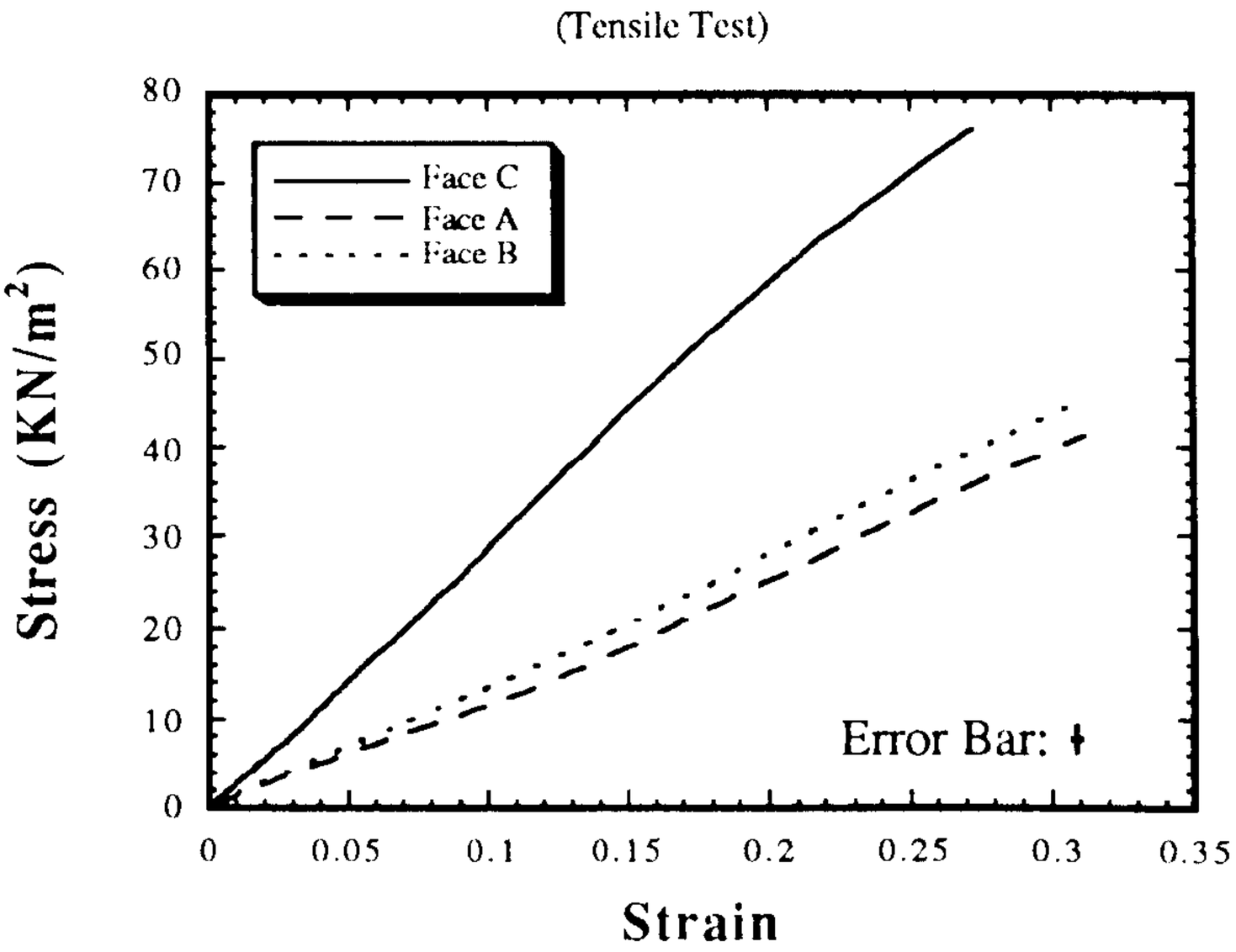

Fig. 6.33 Tensile stress-strain curve for the 30ppi conventional elastic open-cell polyether urethane foam (30CO).

3D 10ppi Conventional Polyether Urethane foam

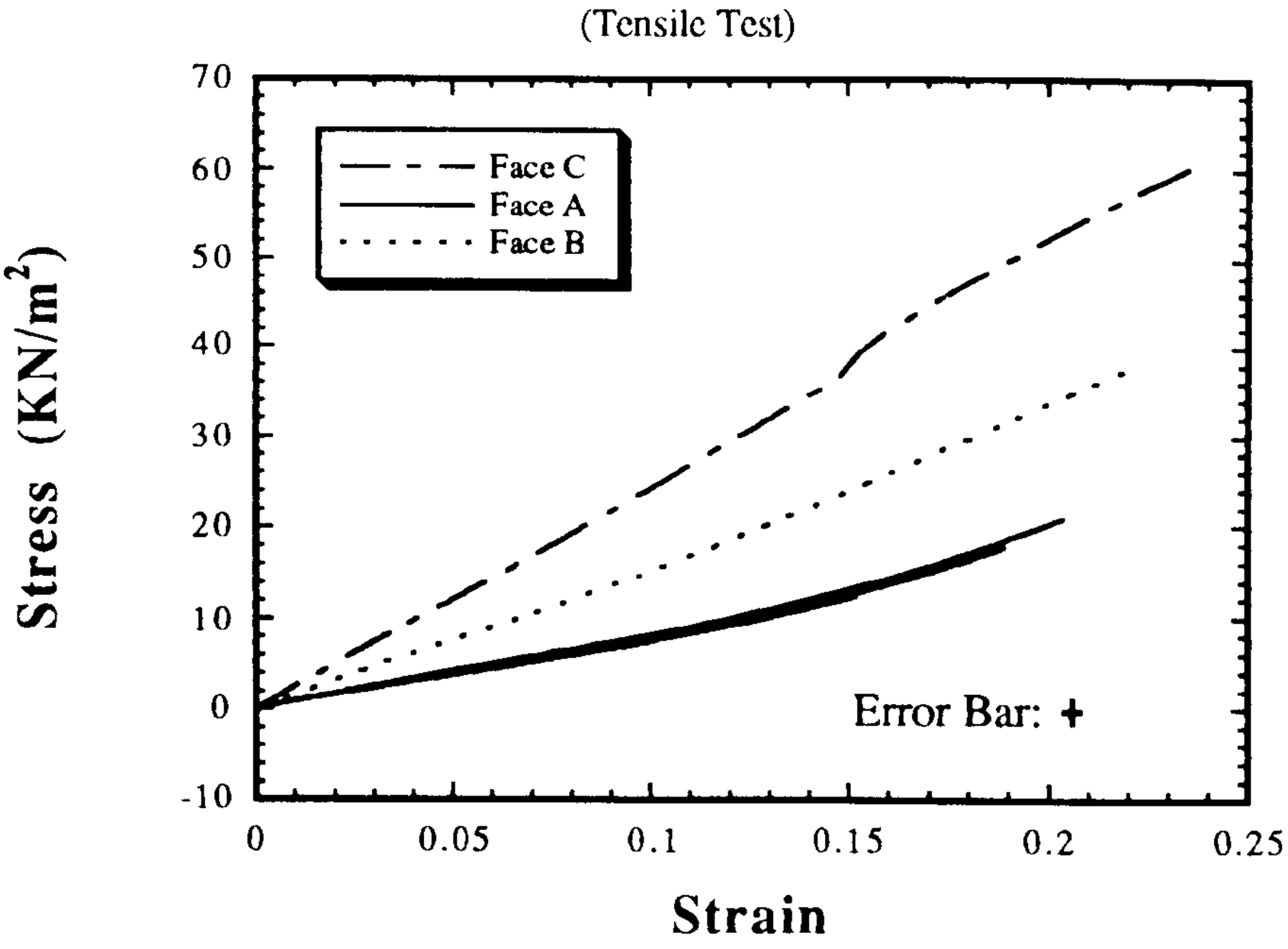

Fig. 6.34 Tensile stress-strain curve for the 10ppi conventional elastic open-cell polyether urethane foam (10CO).

3D 60ppi Closed-Cell Polyester Urethane Foam

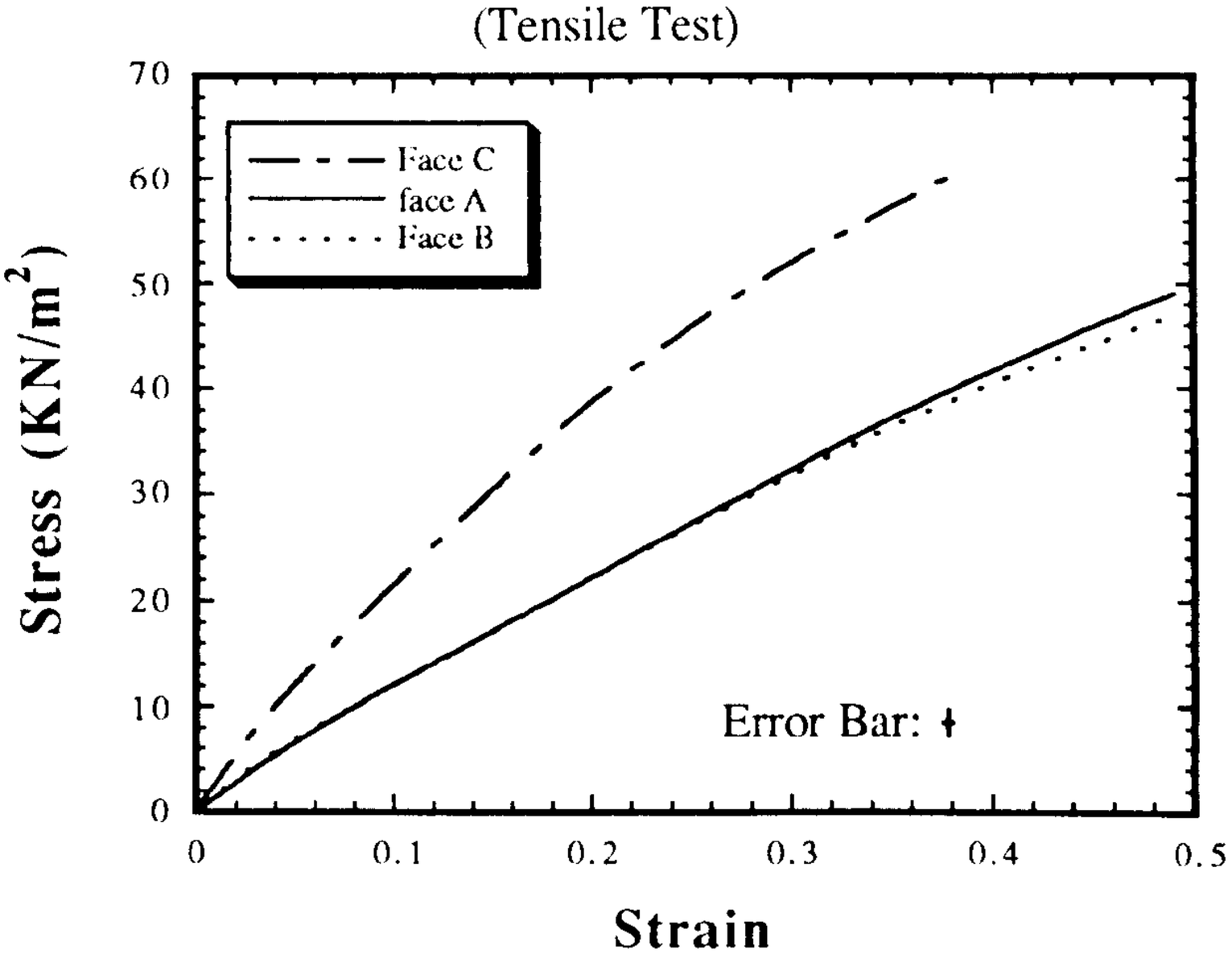

Fig. 6.35 Tensile stress-strain curve for the 60ppi conventional elastic closed-cell polyester urethane foam (PECC).

3D 10ppi Auxetic (70-50) Polyether Urethane Foam

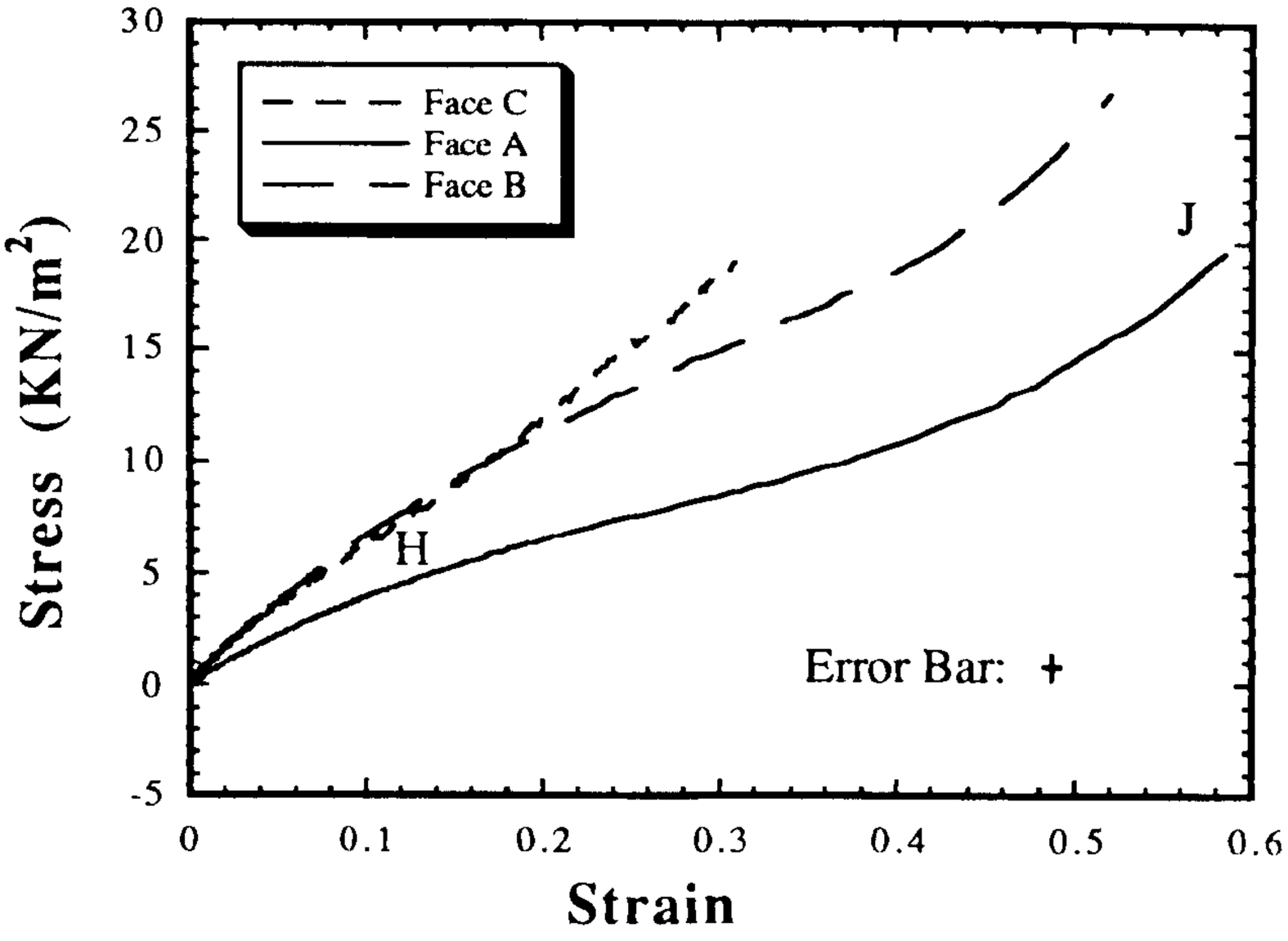

Fig. 6.36 Tensile stress-strain curve for the 10ppi auxetic open-cell polyether urethane foam (70AO).

3D 10ppi Auxetic (80-50) Polyether Urethane Foam

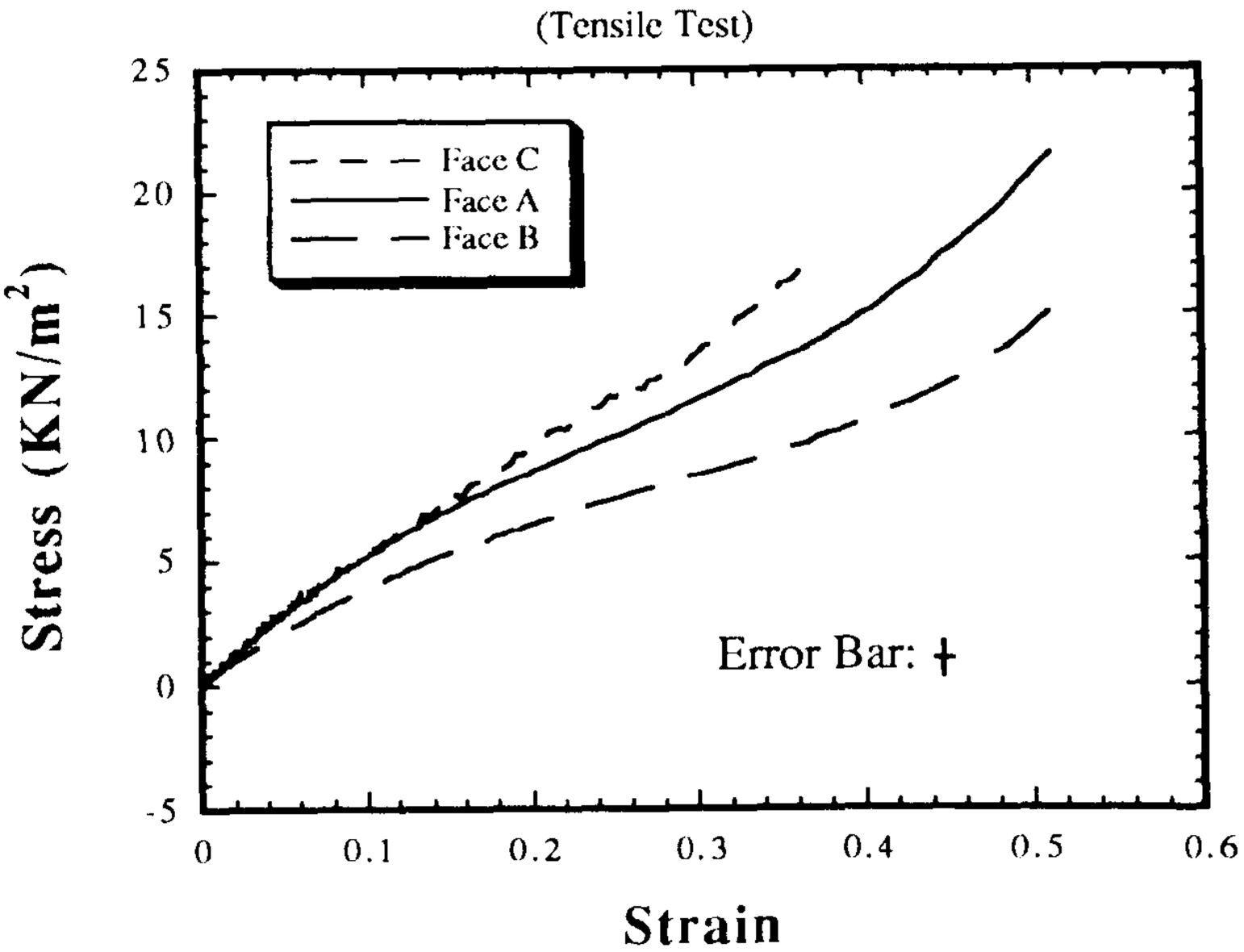

Fig 6.37 Tensile stress-strain curve for the 10ppi auxetic open-cell polyether urethane foam (80AO).

3D 10ppi Auxetic (90-50) Polyether Urethane Foam

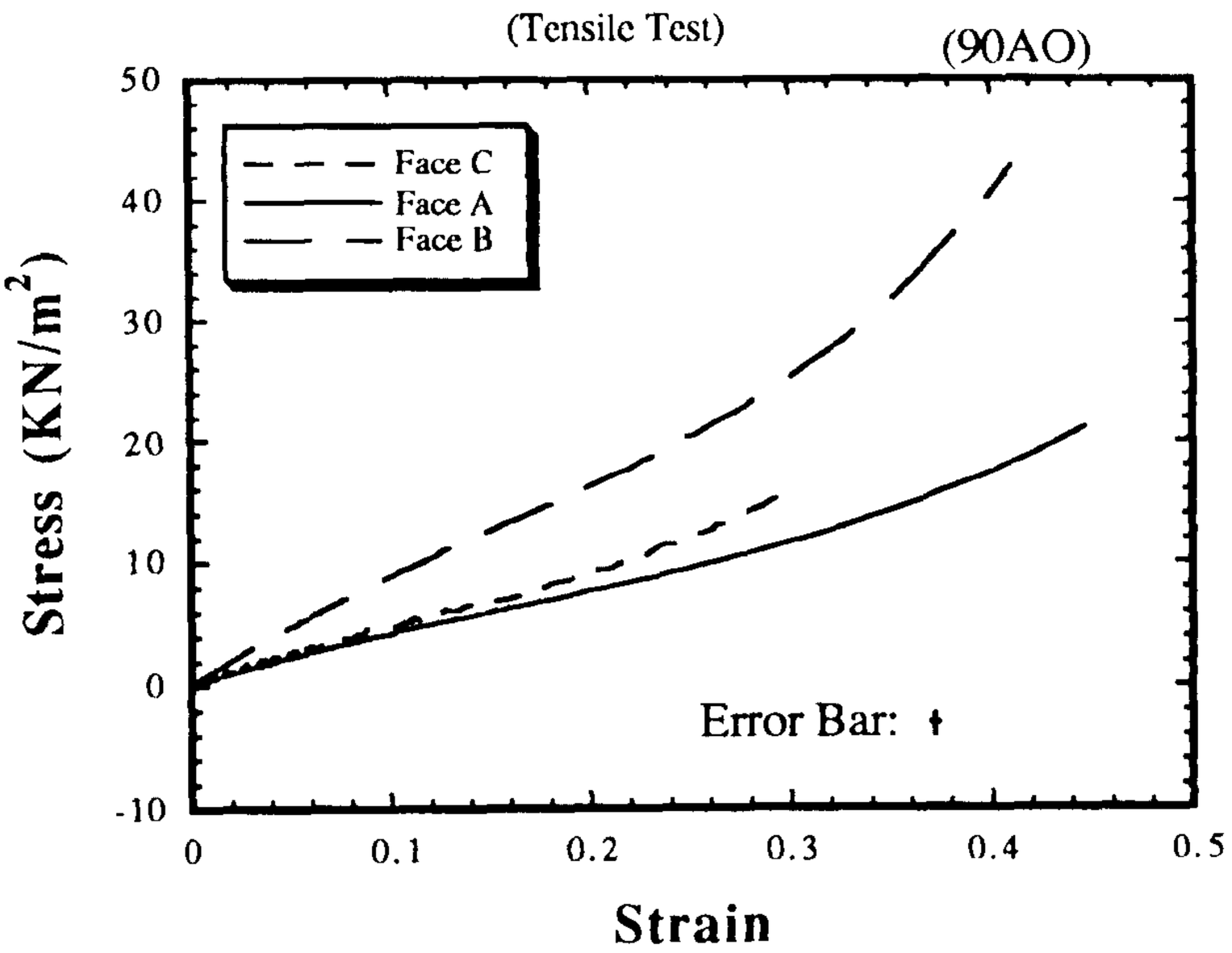

Fig. 6.38 Tensile stress-strain curve for the 10ppi auxetic open-cell polyether urethane foam (90AO).

3D 10ppi Auxetic (100-50) Polyether Urethane foam

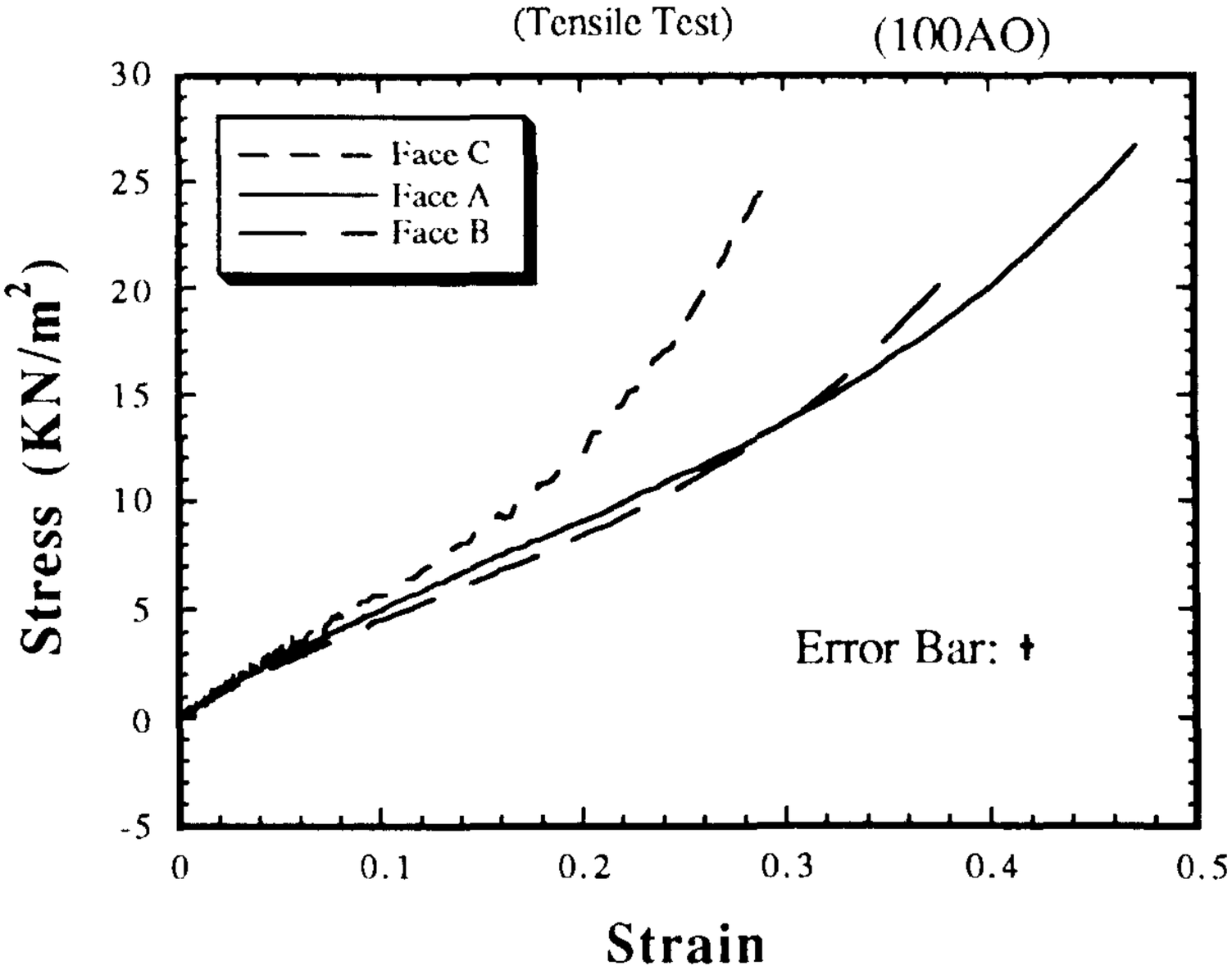

Fig. 6.39 Tensile stress-strain curve for the 10ppi auxetic open-cell polyether urethane foam (100AO).

With the flexible conventional and auxetic foams under tensile loading, the stress initially increases approximately in proportion to the strain so that it is possible to determine a tensile modulus with reasonable accuracy. (see *Figures* 6.25 to 6.32) as in the case of compression, the proportional limit depends upon the detailed cell structure and the properties of the cell ribs. For conventional foams, the tensile proportional limit is approximately 2.5% (strain) this is the case for the data shown in *Figures* 6.32 to 6.35. For auxetic foams, the tensile proportional limit is about 6% (strain) as shown in *Figures* 6.36 to 6.39. This small Hooken region (e.g. OH for both conventional and auxetic foams) is followed by a region in which the stress does not increase linearly with increasing strain (e.g. HJ).

However, the Young's modulus of conventional foam is about twice that of auxetic foam in the linear elastic region. The results are shown in Table 6.2.

Table 6.2

	PECC	PECO	60CO	30CO	10CO	100AO	90AO	80AO	70AO
ρ (kg/m^3)	37.9±2.1	33.7±1.3	21.7±1.2	24.5±2.2	24.1±1.4	79.1±2.2	76.9±1.8	76.3±2.8	74.7±2.5
E_x(kN/m^2)	79.1±4.5	56.7±3.2	91.1±2.1	89.6±3.4	60.5±3.5	41.8±3.1	43.2±2.3	50.3±2.8	58.2±2.5
E_y(kN/m^2)	161.5±5.3	93.9±2.5	170.4±5	131.3±2	74.7±2.4	42.4±2.3	45.3±3.0	53.6±2.1	63.1±2.2
E_z(kN/m^2)	82.4±4.7	61.1±2.8	110.2±4	97.2±3.3	62.3±3.8	42.3±2.2	44.8±2.1	51.1±2.3	61.8±1.9

Table 6.2 Tensile moduli of the foams.

6.3.6 The Effect of Cell Rib Thickness

Specimens with different rib thickness were prepared as described in *Chapter 4*. The dimensions of the rectangular specimens were 25 x 25 x 130 mm and the average error was ±1 mm. The tensile tests were carried out using an Instron 4505 at a cross head speed of 2 mm/min. Four specimens were tested in each case. The average values were used to plot *Figure* 6.40.

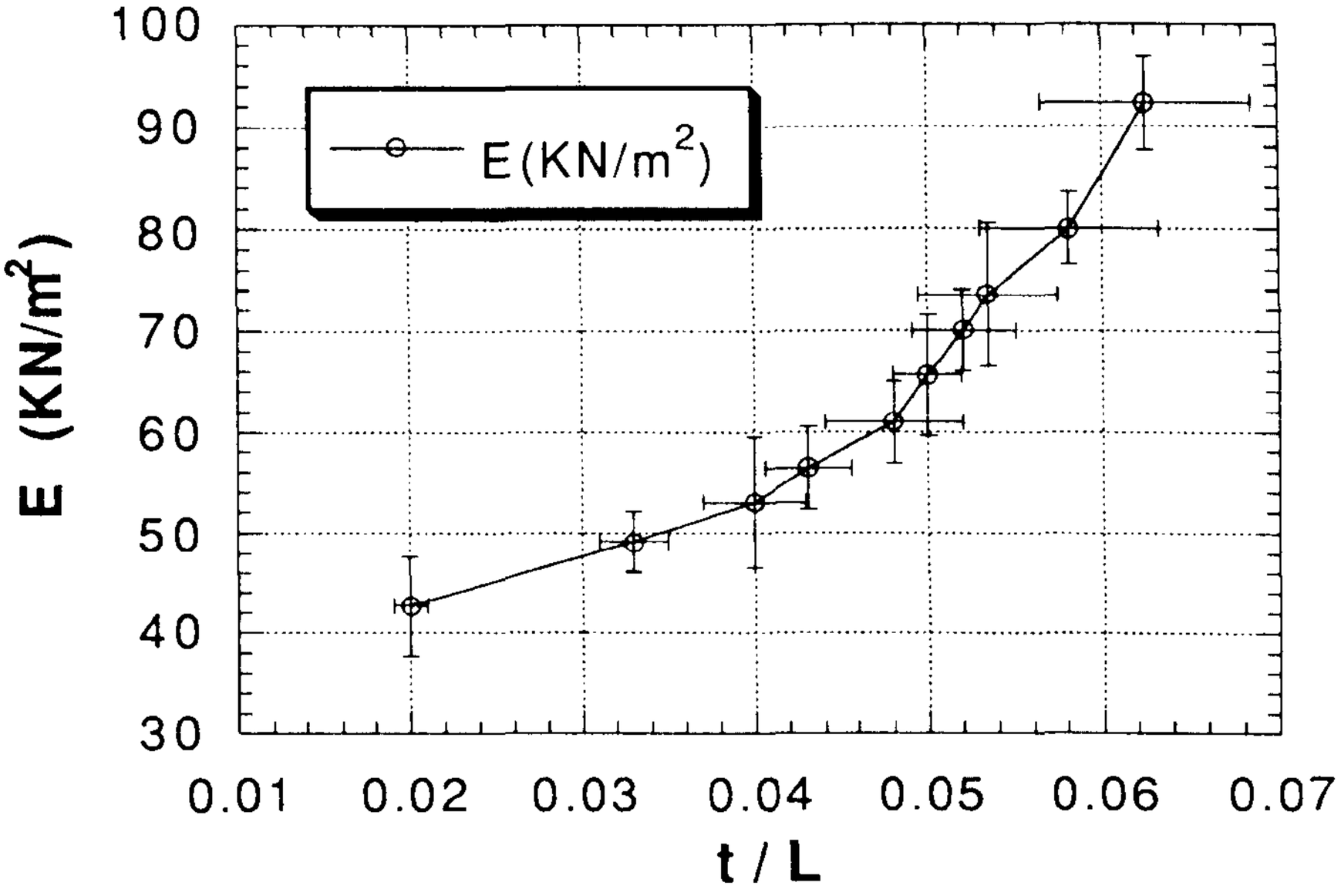

Fig. 6.40 Diagram of the tensile modulus versus cell rib thickness/cell rib length for the 60ppi conventional closed-cell polyester urethane foam.

6.4 Poisson's Ratio

6. 4. 1 The Tensile Poisson's Ratio

The samples were sectioned to the dimensions shown in *Figure 6. 41*. Nine pins were inserted into the foam in a three by three arrangement in the central region of the gauge section. They were spaced at equal distances apart and care was taken to ensure that the pins were pushed straight through the foam. One end of the foam was suspended from a retort stand. First, it was photographed without any weight hanging from it and then weights of varying size were suspended from the end. To minimise creep effects, the weights were left for a maximum of one minute before photographing. The weight was then removed, and the foam left to recover for five minutes before another weight was suspended. This procedure was repeated for six different weights. Three specimens were tested in each case. The photographs were enlarged using a slide projector, and the distance between the pins measured for each

case. This enable the longitudinal and the transverse strains to be determined, and hence the Poisson's ratio to be calculated. This pin method has the additional advantage of measuring a through-thickness average property of the foam.

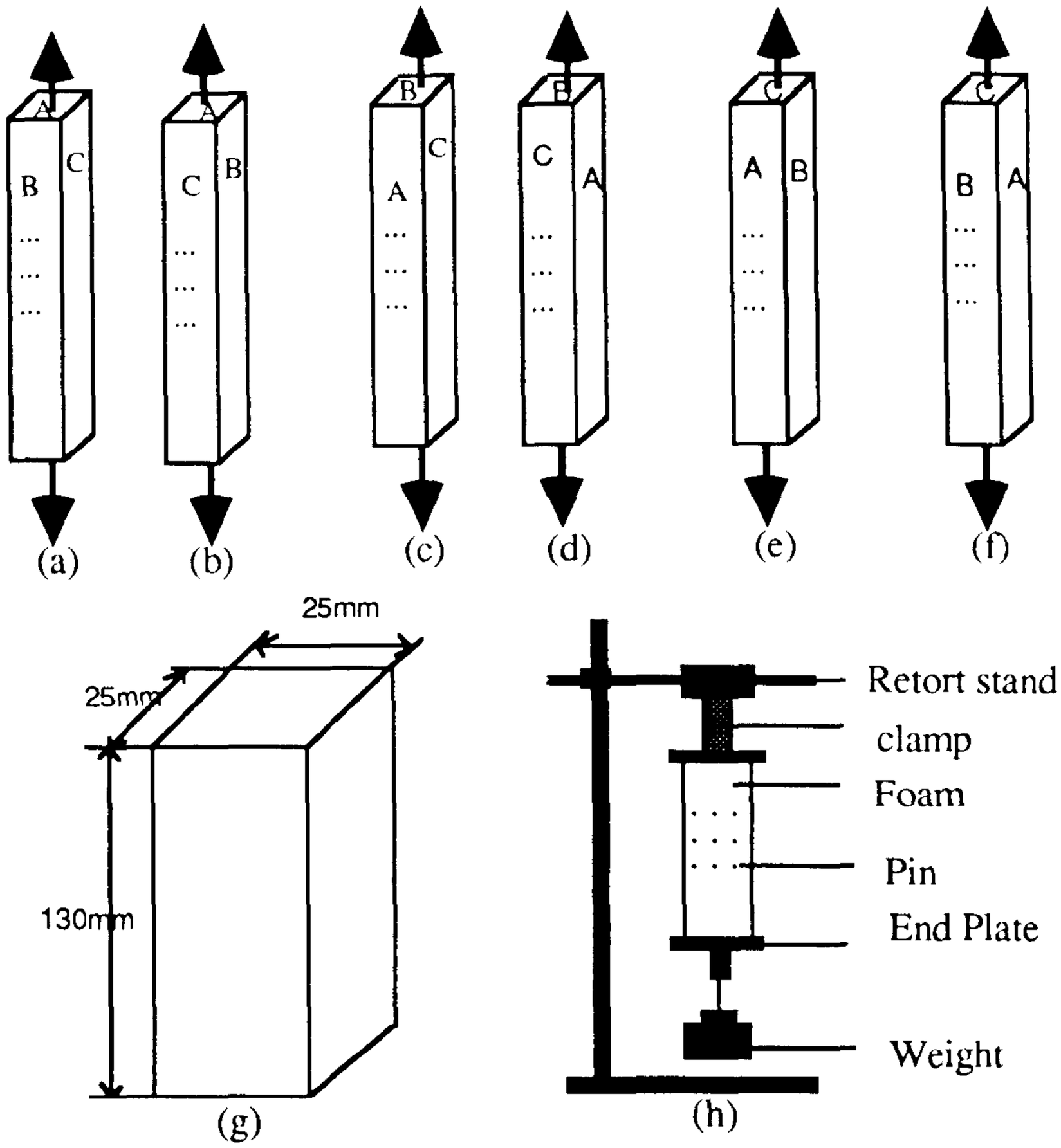

Fig. 6.41 Schematic diagram of the preparation of the tensile Poisson's ratio test specimens. Measure: $(a)\nu_{xy}, (b)\nu_{xz}, (c)\nu_{zy}, (d)\nu_{zx}, (e)\nu_{yz}, (f)\nu_{yx}$.(g) The dimensions of the foam specimen. (h) Schematic diagram of the apparatus used to measure the tensile Poisson's ratio of foam. (The pin dimensions: 0.2 x 0.2 x 25 mm).

Calculation of Poisson's Ratio

The distance between the pins was measured and plotted against the weight in both directions. The graphs were then extrapolated to zero weight to obtain values for X_0 and y_0; the original lengths and widths respectively. The distances between the centre set of pins in both directions were used and the values of X_0 and y_0 as shown in *Figure* 6.42 to calculate the longitudinal and the transverse strains,

$$\varepsilon_x = \frac{X' - X_0}{X_0} \qquad (6.5)$$

and
$$\varepsilon_y = \frac{y' - y_0}{y_0}. \qquad (6.6)$$

The transverse strain versus the longitudinal strain was plotted and the best linear fit to the small strain data found. The gradient was the Poisson's ratio, ν_{yx},

$$\nu_{yx} = -\frac{\varepsilon_x}{\varepsilon_y} \qquad (6.7)$$

Note that the graph should pass through the origin. For example, *Figures* 6.43 and 6.44 are typical of tensile strain plots of conventional foam and auxetic foam respectively.

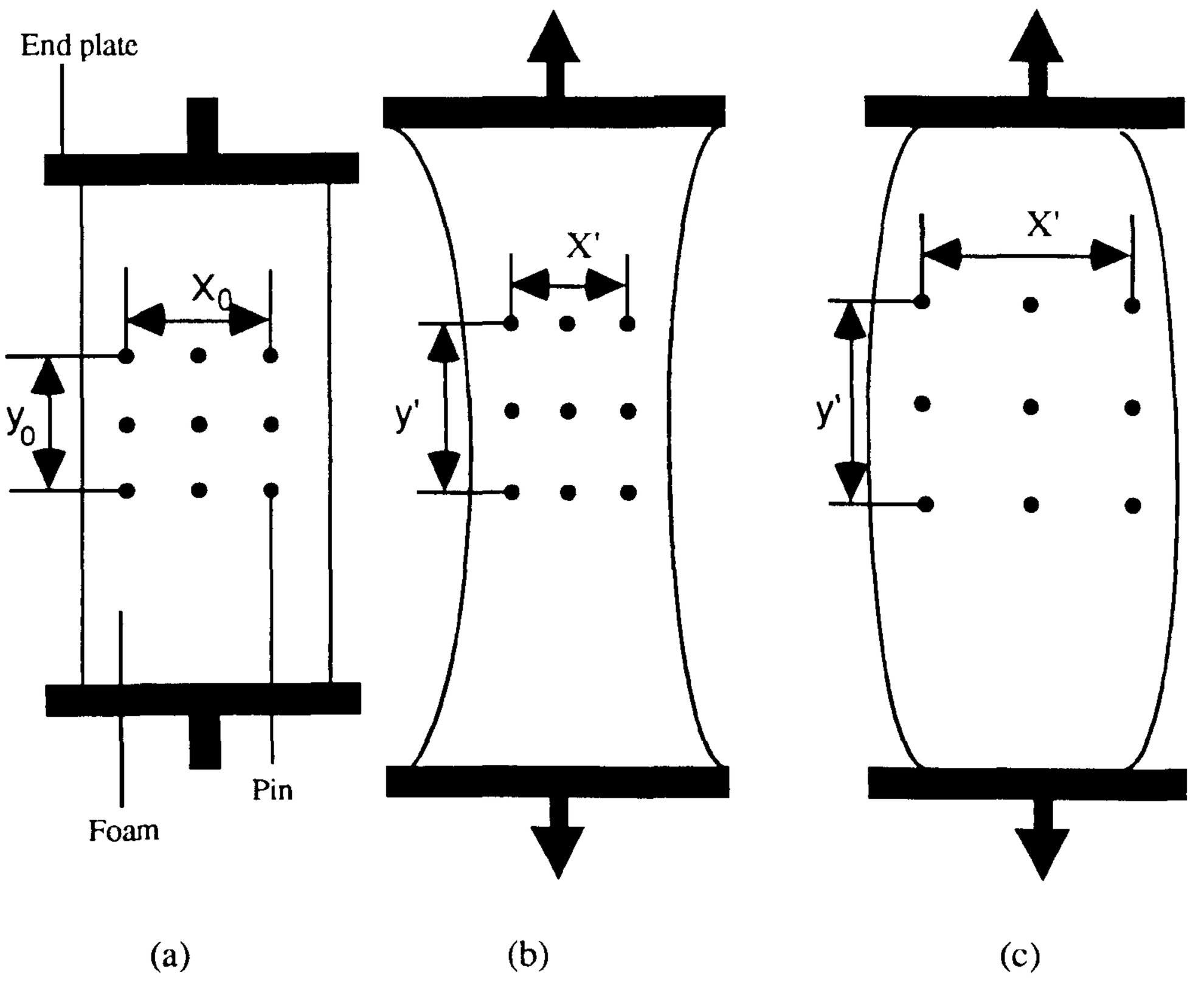

Fig. 6. 42 Schematic diagram of the tensile Poisson's ratio measurements. (a) unstressed foam specimen (b) conventional foam under tension. (c) auxetic foam under tension.

Figures 6.43 and 6.44 show that the longitudinal strain is not always proportional to the transverse strain, hence the Poisson's ratio is non-linearly dependent on the axial strain. This is because the cell ribs become aligned at large strains, inducing stretching as well as hinging and bending. The Poisson's ratio presented in Table 6.3 is for the linear region indicated by the thick line.

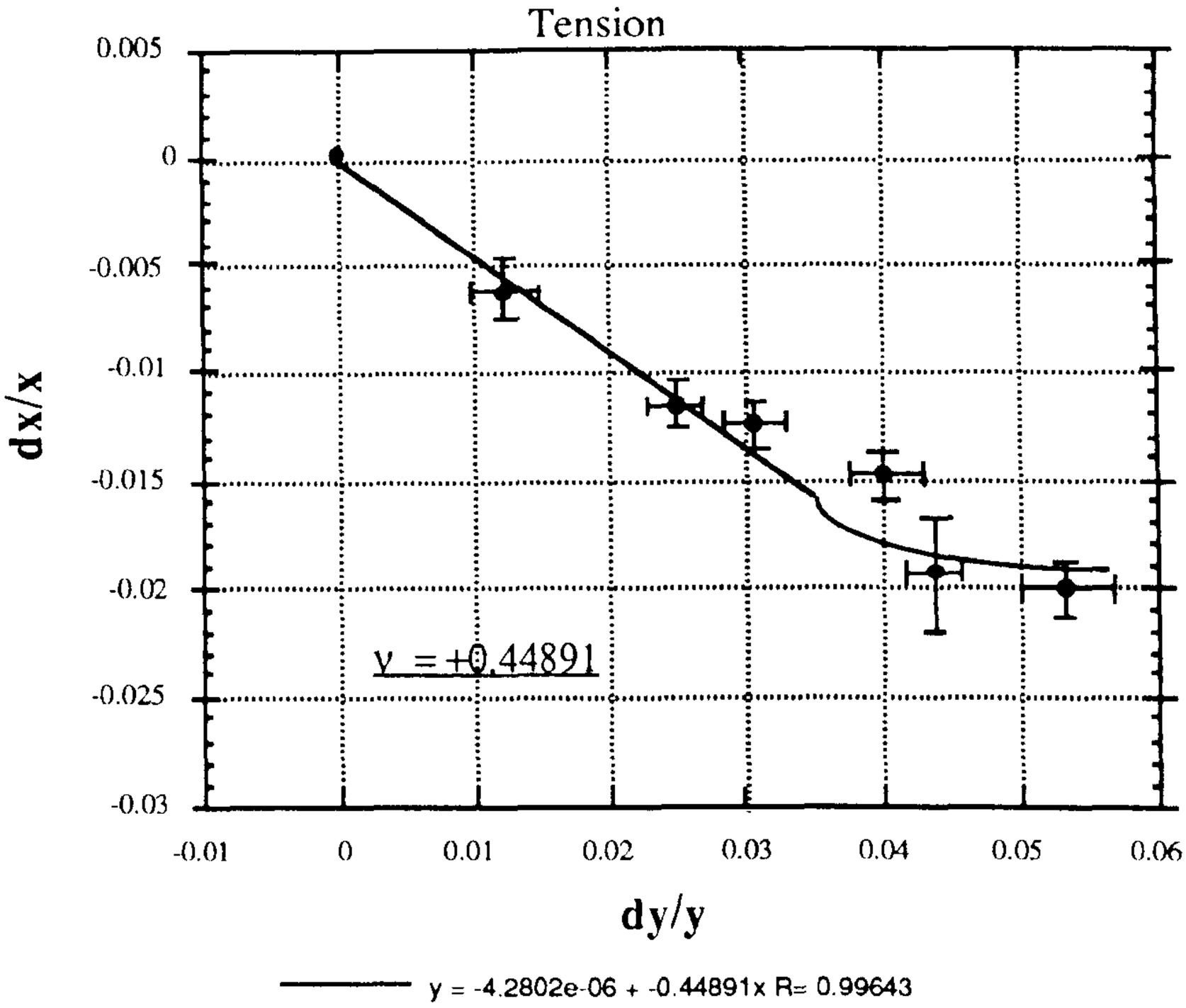

Fig. 6.43 Diagram of the tensile transverse strain versus the tensile longitudinal strain for the 60ppi open-cell polyether urethane conventional foam (60CO).

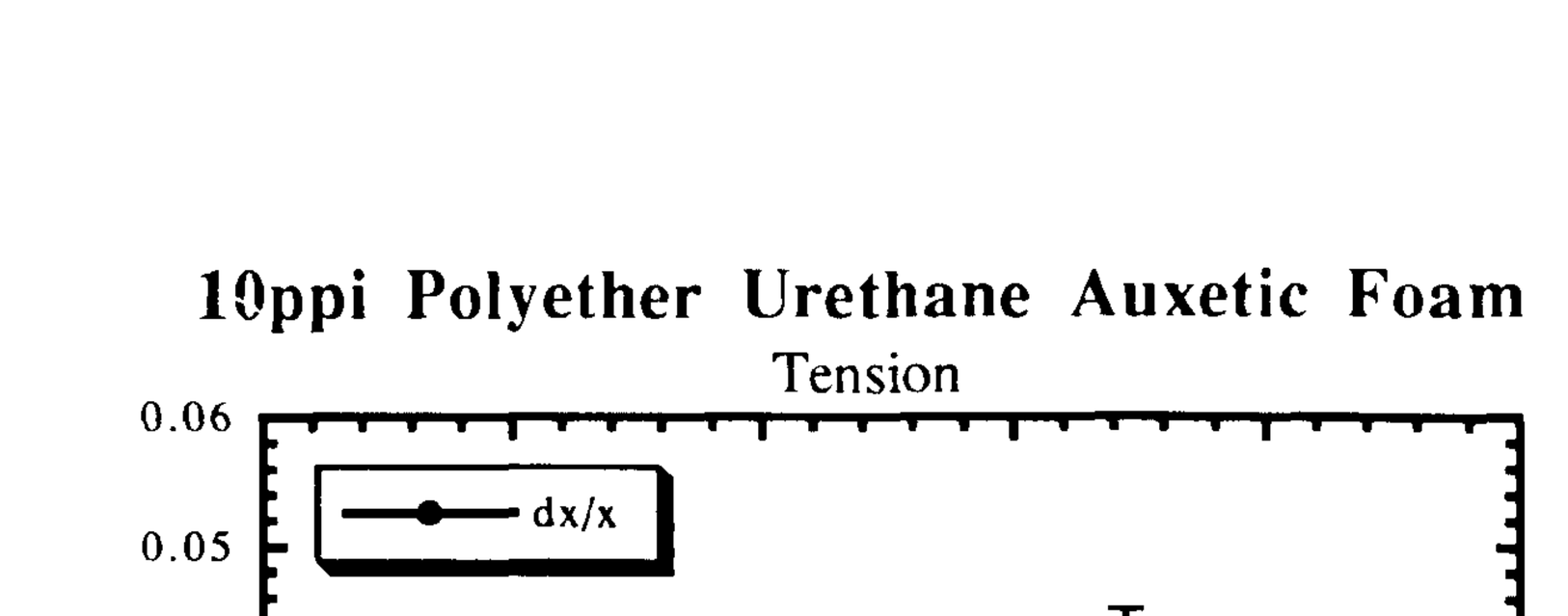

Fig. 6.44 Diagram of the tensile transverse strain versus the tensile longitudinal strain for the 10ppi blue open-cell polyether urethane auxetic foam (90AO).

Three specimens were tested in each case and an average was taken. The results are shown in *Table 6.3*. The Poisson's ratios greater than 0.5 do not violate any physical law since the foam is an anisotropic material.

Table 6.3

Poisson's Ratio	PECC	30CO	10CO	100AO	90AO	80AO	70AO
ν_{xy}	0.42±0.03	0.37±0.02	0.21± 0.033	-0.79±0.02	-0.64±0.03	-0.59±0.01	-0.52±0.013
ν_{zy}	0.38±0.04	0.32±0.01	0.25±0.022	-0.76±0.03	-0.61±0.04	-0.66±0.02	-0.54±0.022
ν_{xz}	0.15±0.02	0.18±0.01	0.12±0.018	-0.38±0.01	-0.36±0.02	-0.22±0.02	-0.18±0.005
ν_{zx}	0.13±0.01	0.11±0.01	0.07±0.008	-0.43±0.01	-0.43±0.04	-0.28±0.01	-0.21±0.004
ν_{yx}	0.62±0.03	0.48±0.02	0.407±0.05	-0.82±0.05	-0.78±0.05	-0.68±0.02	-0.53±0.011
ν_{yz}	0.58±0.02	0.44±0.03	0.38±0.045	-0.88±0.03	-0.75±0.03	-0.62±0.04	-0.54±0.015

Table 6.3 Tensile Poisson's ratio of conventional and auxetic foams.

6. 4. 2 The Compressive Poisson's Ratio

The specimens were sectioned to the dimensions shown in Figure 6.46. All the compression tests were carried out using an Instron 1185 at a cross head speed of 2 mm/min. The test arrangement is shown schematically in Figures 6.45.

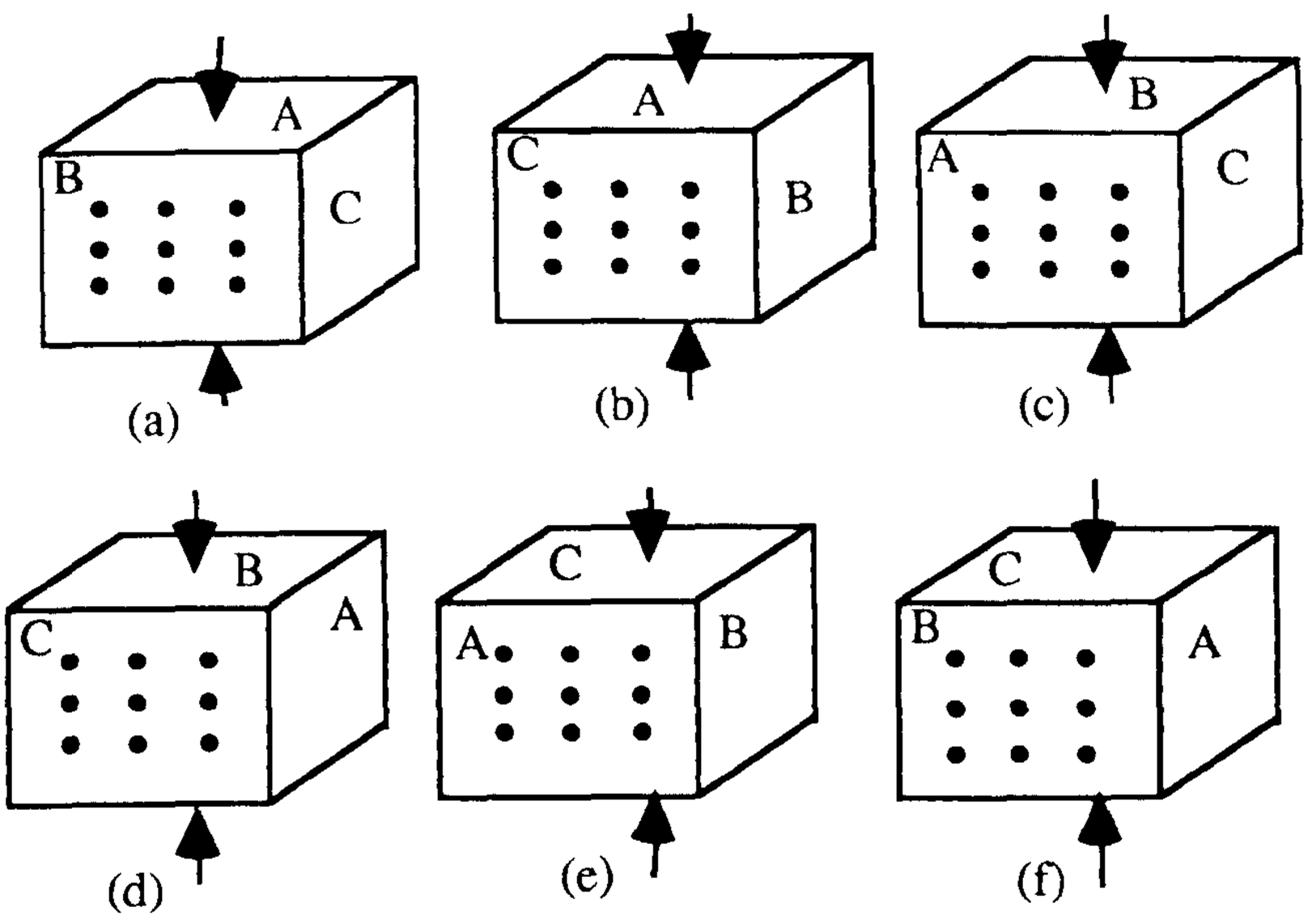

Fig. 6.45 Schematic diagram of the compressive Poisson's ratio specimens. Measure: *(a)*ν_{xy}, *(b)*ν_{xz}, *(c)*ν_{zy}, *(d)*ν_{zx}, *(e)*ν_{yz}, *(f)*ν_{yx}.

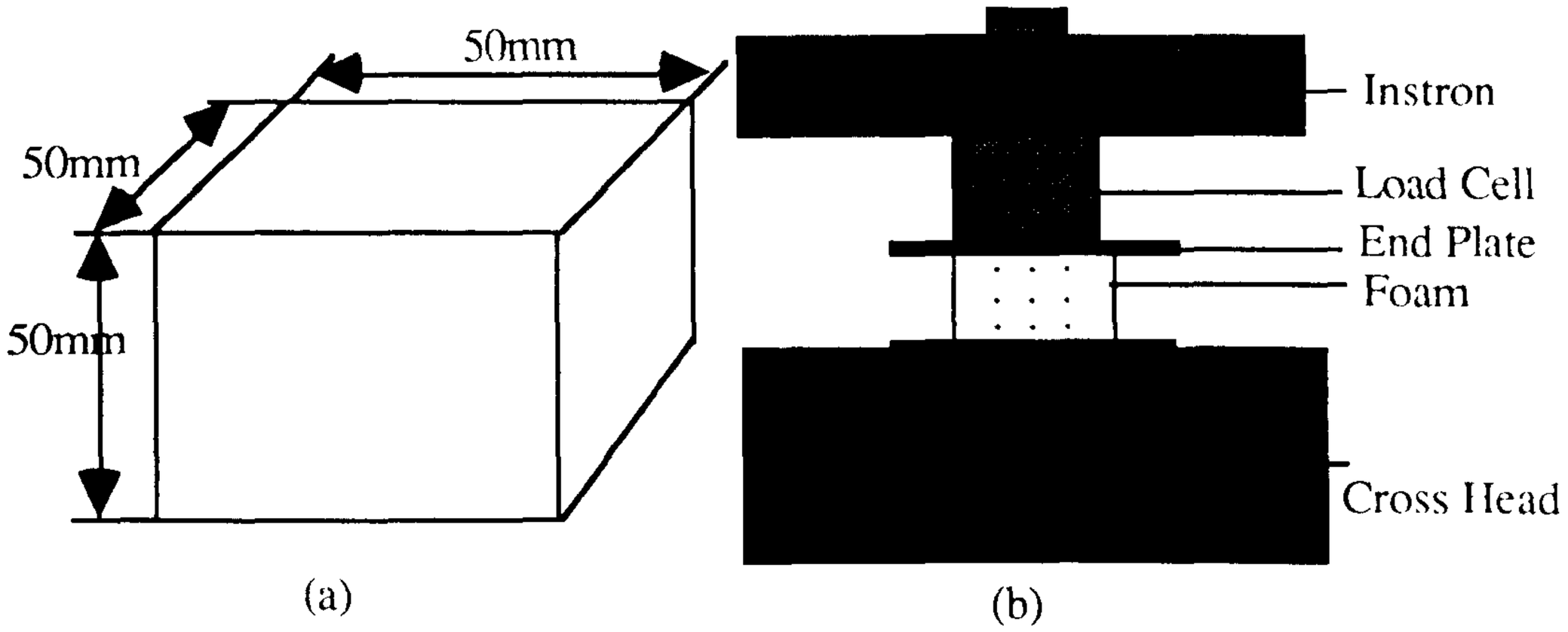

Fig. 6.46 (a) Diagram showing the sample dimensions. (b) Schematic diagram of the apparatus used to measure the compressive Poisson's ratio of foams.

A schematic diagram of the deformations of the foam samples is shown in *Figure* 6.47. The photographic measuring technique and method of calculation are the same as for the tensile test.

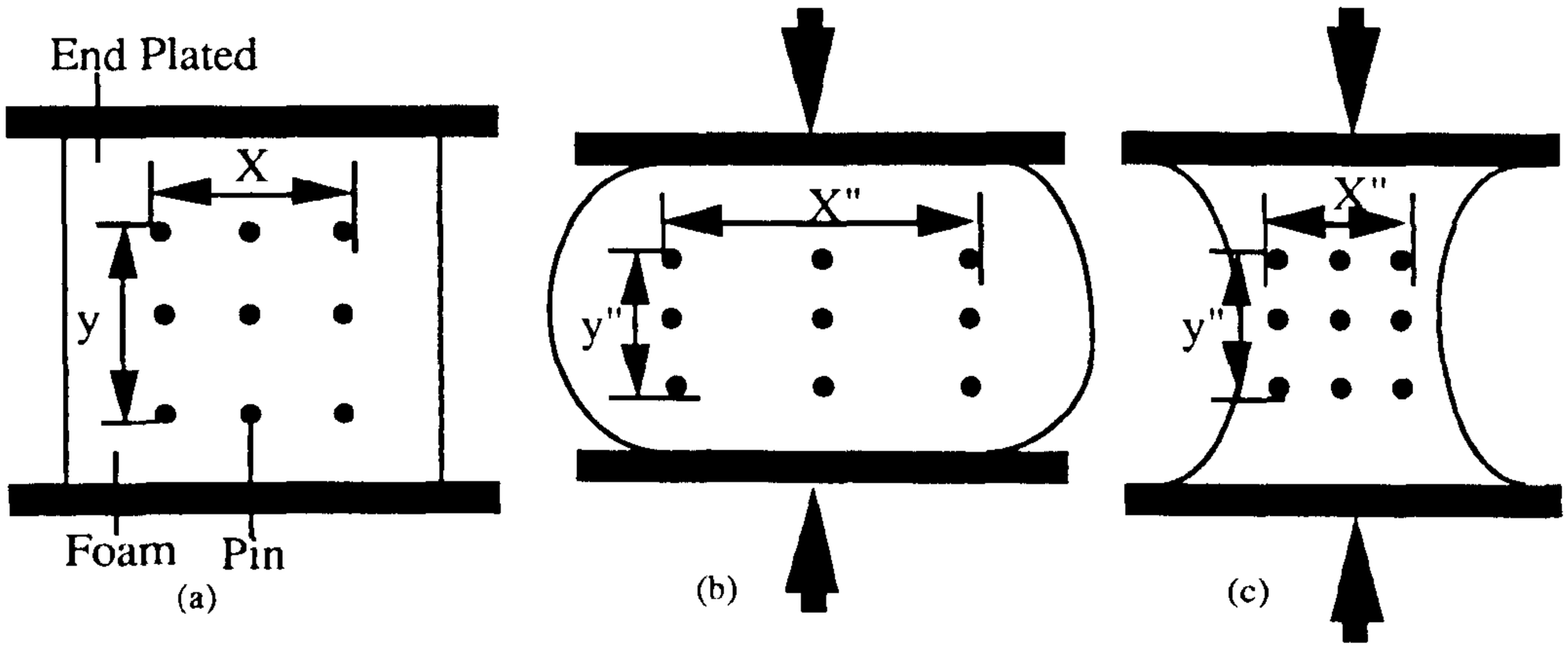

Fig. 6. 47 Schematic diagram of the compressive Poisson's ratio measurements. (a) An unloaded foam specimen (b) Conventional foam under compression. (c) Auxetic foam under compression.

The transverse strain, ε_x, versus the longitudinal strain, ε_y, is plotted in which the gradient of the initial linear region is the compressive Poisson's ratio for foam. A typical ε_x versus ε_y plot for a conventional and an auxetic foam loaded under compression is shown in Figures 6.48 and 6.49, respectively.

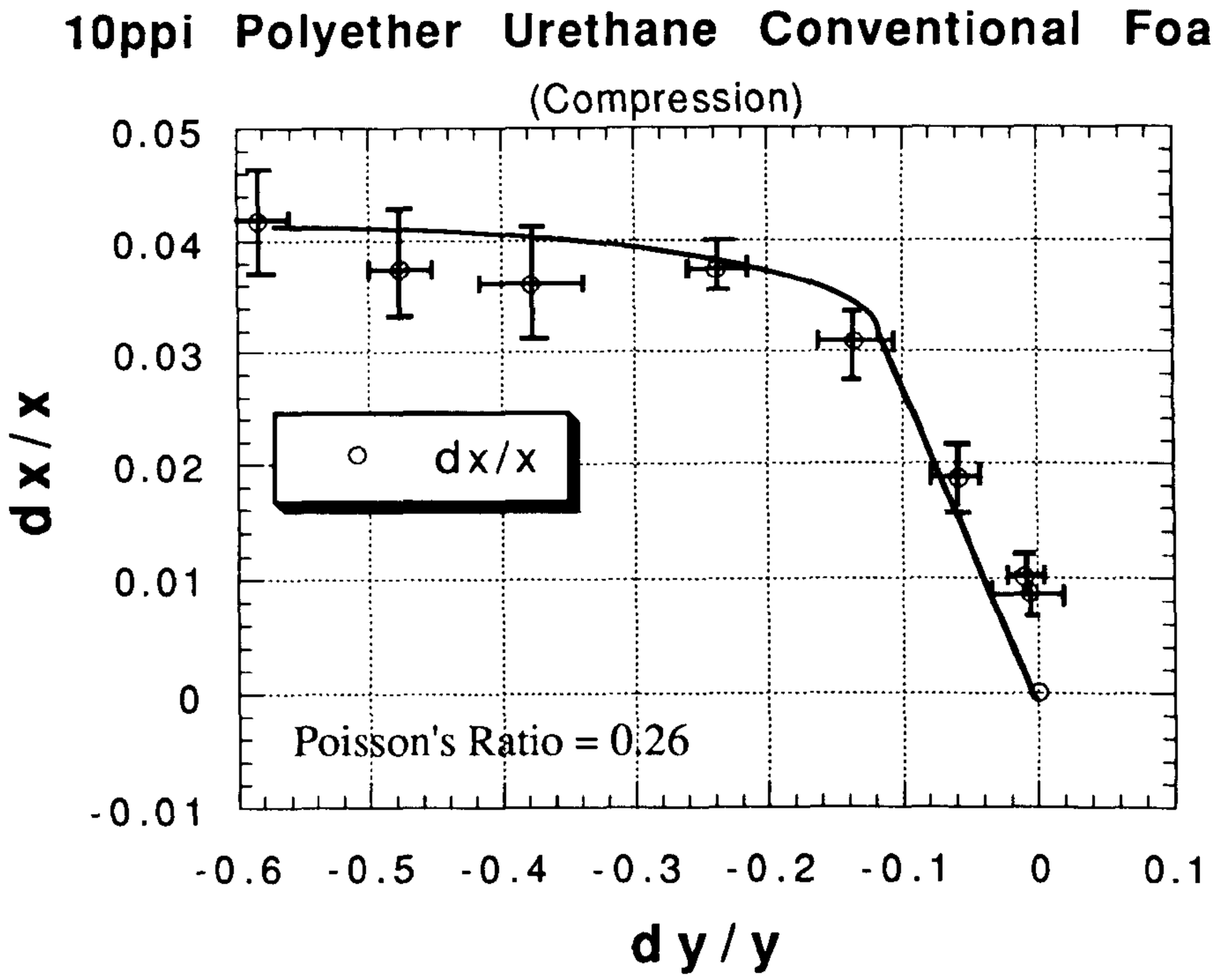

Fig. 6.48 Graph of compressive transverse strain versus longitudinal strain for the 10ppi conventional foam (10CO).

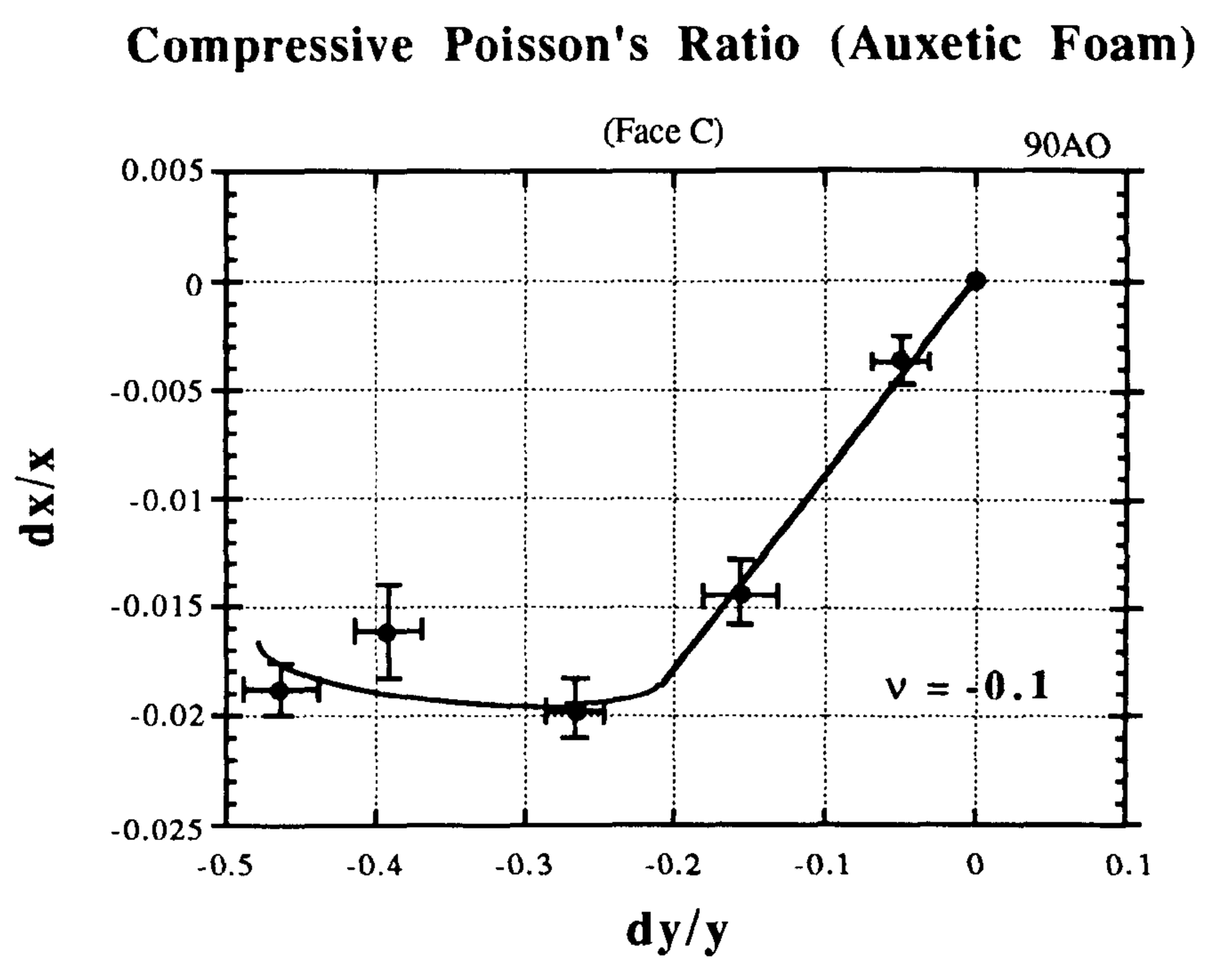

Fig. 6.49 Graph of compressive transverse strain versus longitudinal strain for the 10ppi auxetic foam (90AO).

Figures 6.48 and 6.49 show that the Poisson's ratio in compression is non-linearly dependent on the axial strain, implying that some cell rib buckling or contact occurs before the yield strain is reached. This behaviour is similar to the results

obtained by Rinde (1970), Choi and Lakes (1992), and Evans and Caddock (1989), even though Evans and Caddock used a dense polymer. The experimentally determined values for Poisson's ratio in compression are presented in *Table* 6.4. Values shown are average values obtained from four or five determinations. Note: the Poisson's ratio is given in the sense of a strain range for linear behaviour, within 12% deviation from a tangent line through the origin.

Table 6.4

Poisson's Ratio	PECC	30CO	10CO	100AO	90AO	80AO	70AO
ν_{xy}	0.22±0.06	0.22±0.04	0.14± 0.03	-0.76±0.02	-0.63±0.04	-0.55±0.01	-0.48±0.01
ν_{zy}	0.17±0.04	0.20±0.03	0.12±0.03	-0.73±0.021	-0.64±0.03	-0.51±0.02	-0.42±0.02
ν_{xz}	0.08±0.01	0.11±0.03	0.05±0.01	-0.26±0.012	-0.10±0.02	-0.08±0.02	-0.06±0.004
ν_{zx}	0.04±0.01	0.08±0.02	0.02±0.005	-0.21±0.011	-0.15±0.02	-0.08±0.01	-0.07±0.003
ν_{yx}	0.26±0.05	0.24±0.05	0.20±0.08	-0.66±0.06	-0.60±0.05	-0.54±0.02	-0.43±0.03
ν_{yz}	0.25±0.08	0.20±0.06	0.26±0.04	-0.7±0.06	-0.59±0.05	-0.52±0.04	-0.41±0.01

Table 6.4 The compressive Poisson's ratio of conventional and auxetic foams.

Poisson's ratio for conventional and auxetic foams has been determined in both tension and compression. For flexible PUR foam, Poisson's ratio is greater in tension than in compression, and is not linear in either tension or compression, showing a larger value below the elastic collapse strain and a value near zero for high strains.

6. 5 Shear Test

6.5.1 Introduction

In isotropic materials the Young's modulus, E, the Poisson's ratio, ν, and the shear modulus, G, are related by:

$$G = \frac{E}{2(1+\nu)} \qquad (6.8)$$

However, no single relationship exists in an anisotropic material. Therefore, the shear moduli, G_{ij}, were measured to look for their independence.

6. 5. 2 Static Shear Modulus Measurement

Two equal samples from the same foam were cut to the dimensions as shown in *Figure 6.51 (a)*. A direct shear stress is applied to the specimen as represented schematically in *Figure 6.50*. Double shear was used to test the foams.

Six straight lines were marked onto the surfaces of the foam in a two by three arrangement in the central region of the gauge section. They were spaced an equal distance apart and care was taken to ensure that the lines were marked straight. The sides of the foam were fixed to aluminium plates using *Apollo A. 2874 Adhesive* and the end of the middle plate was suspended from a retort stand. First, it was photographed without any weight hanging from it, and then weights of varying size were suspended from the end of the middle plate. To minimise creep effects, the weight was left for a maximum one minute before photographing. The weight was then removed and the foam was left to recover for five minutes before another weight was suspended. This procedure was repeated for six different weights. Three specimens were tested in each case. The photographs were enlarged using a Ilford Multigrade 500 enlarger and the angle of deformation, γ, and hence, the shear strain was measured using a protractor for each case. Using EQ. 6.9 the shear stress together with the shear strain enable the shear modulus to be calculated.

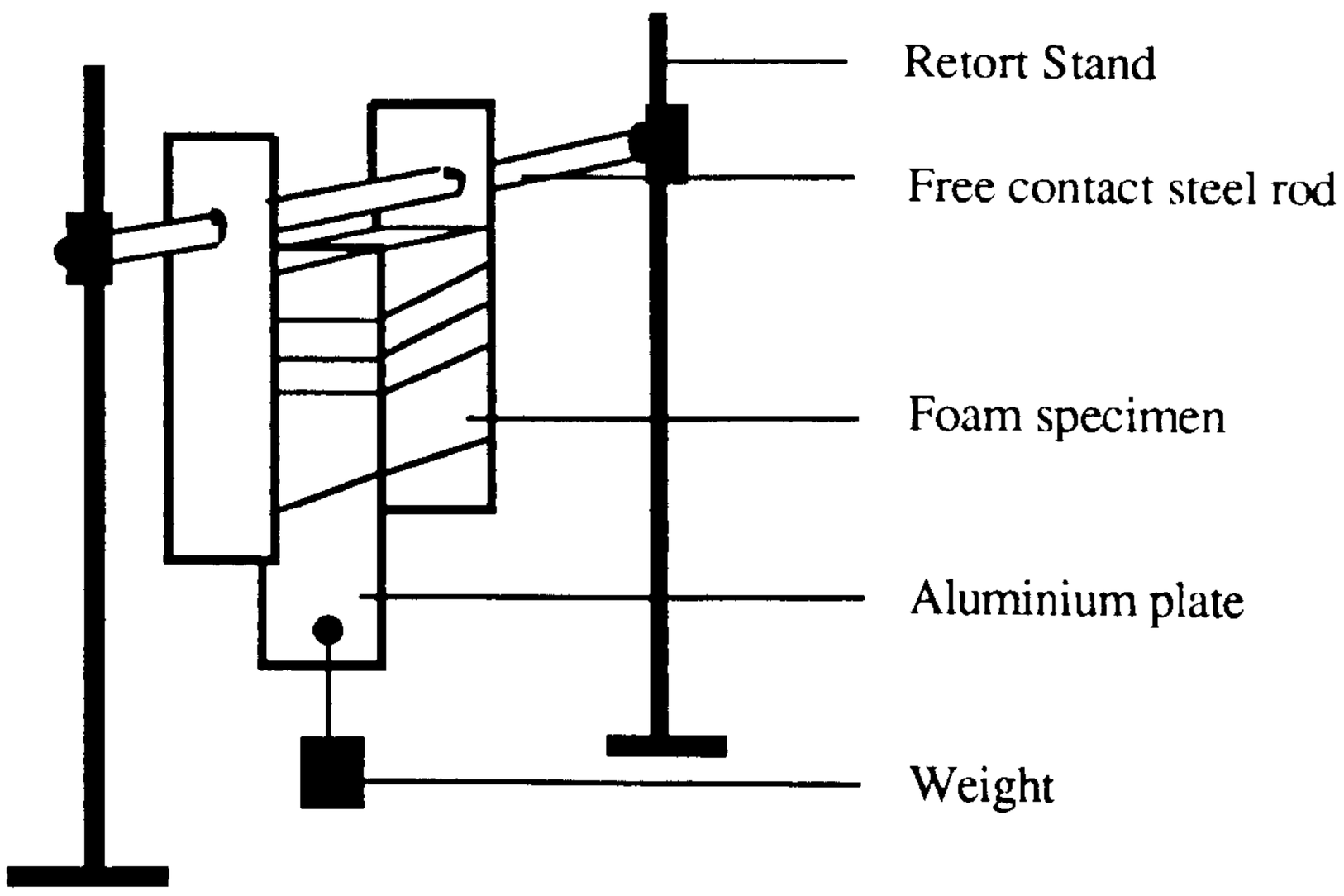

Fig. 6.50 Schematic diagram of the shear test.

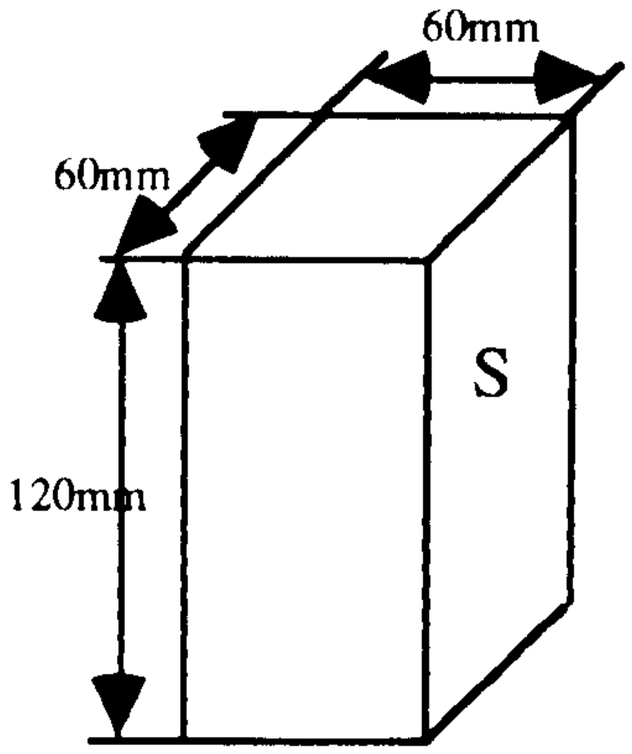

Fig. 6.51 (a)

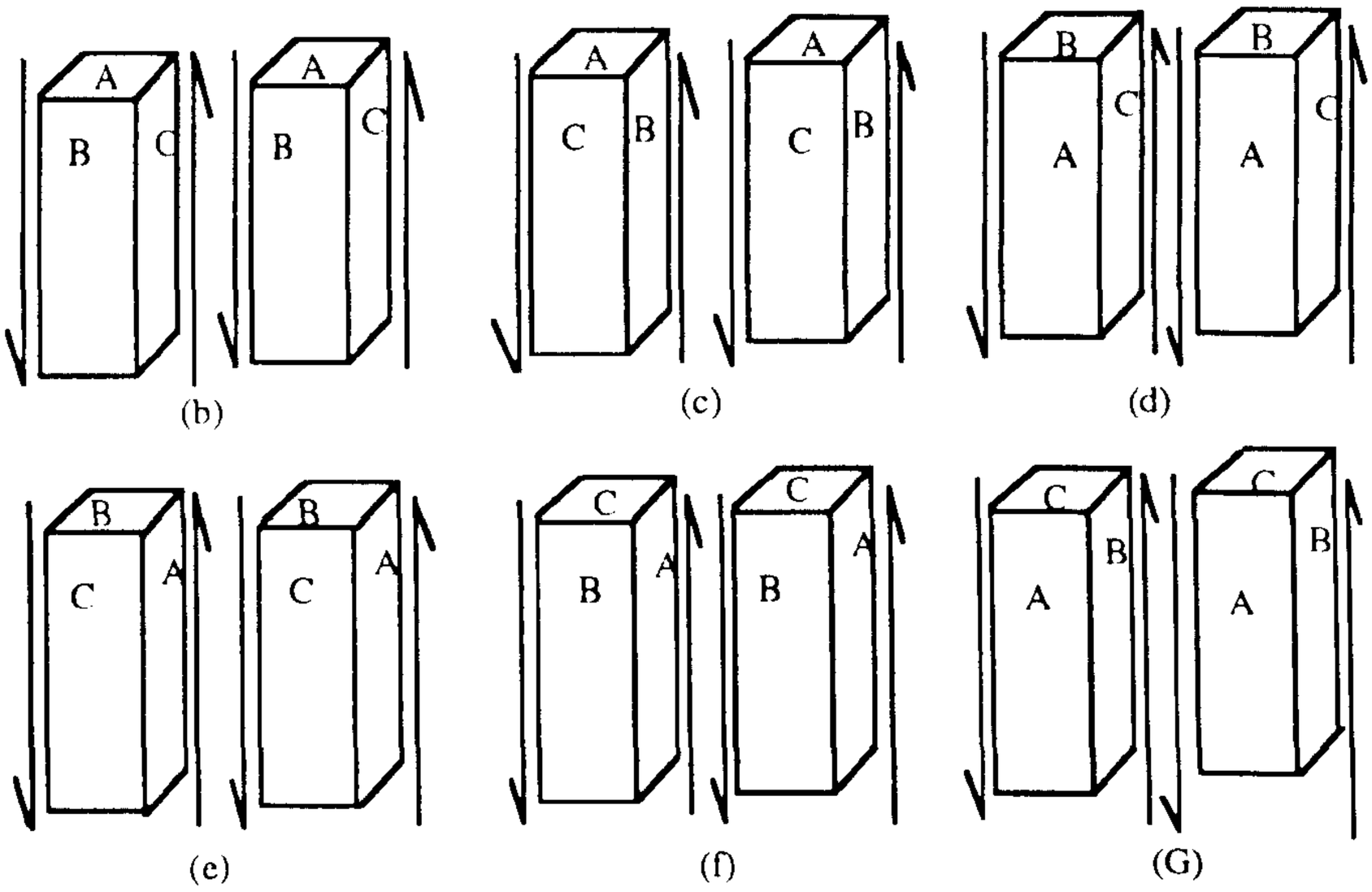

Fig. 6. 51 Schematic diagram of the preparation of the shear test specimens. (a) The dimensions of the foam sample. Measure: (b) G_{xy} (c) G_{xz} (d) G_{zy} (e) G_{zx} (f) G_{yx} (g) G_{yz}.

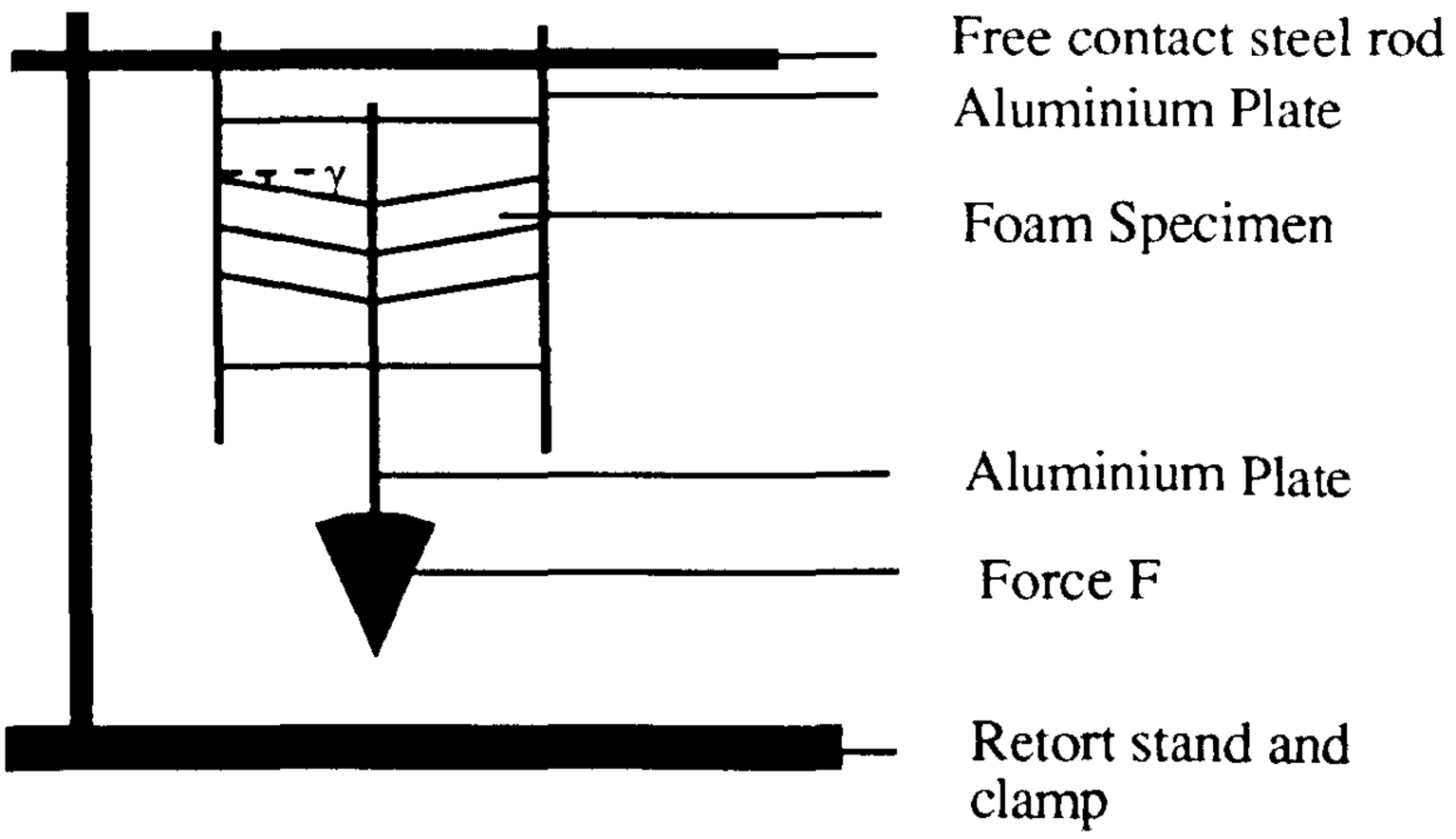

Fig. 6. 52 Schematic diagram of the photographic measuring technique for the shear test.

6. 5. 3 Calculation of the Shear Modulus

The double shear method shown in *Figures 6.50 to 6.52* was used to determine the shear modulus. In such a case twice the area of the foam is resisting the applied force so that the shear stress is calculated by using:

$$\text{Shear stress } \tau = F / 2S \qquad (6.9)$$

Where F is the applied force as shown in *Figure* 6.52, and S is the shear area of one side of the foam as shown in *Figure* 6.51(a).

The shear strain, and the angle of deformation, γ, were measured using enlarged photographs. The shear stress versus shear strain was plotted and the shear

modulus calculated from the gradient of the linear portion of the curve. Note: the graph should pass through the origin. *Figures* 6.53 to 6.55 are the typical shear stress-strain diagrams of conventional and auxetic foams.

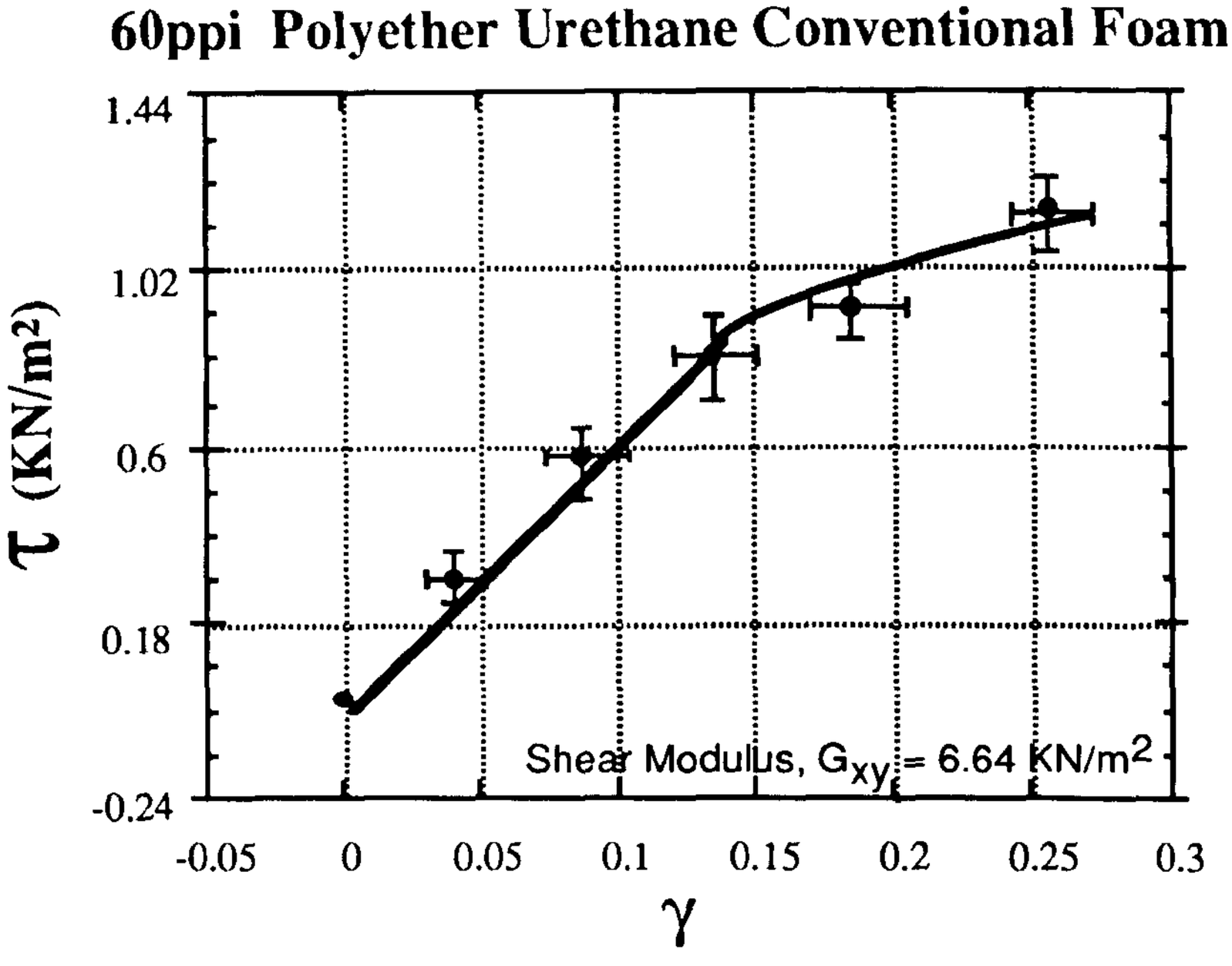

Fig. 6. 53 Graph of the shear stress versus the shear strain for the 60ppi conventional foam (60CO).

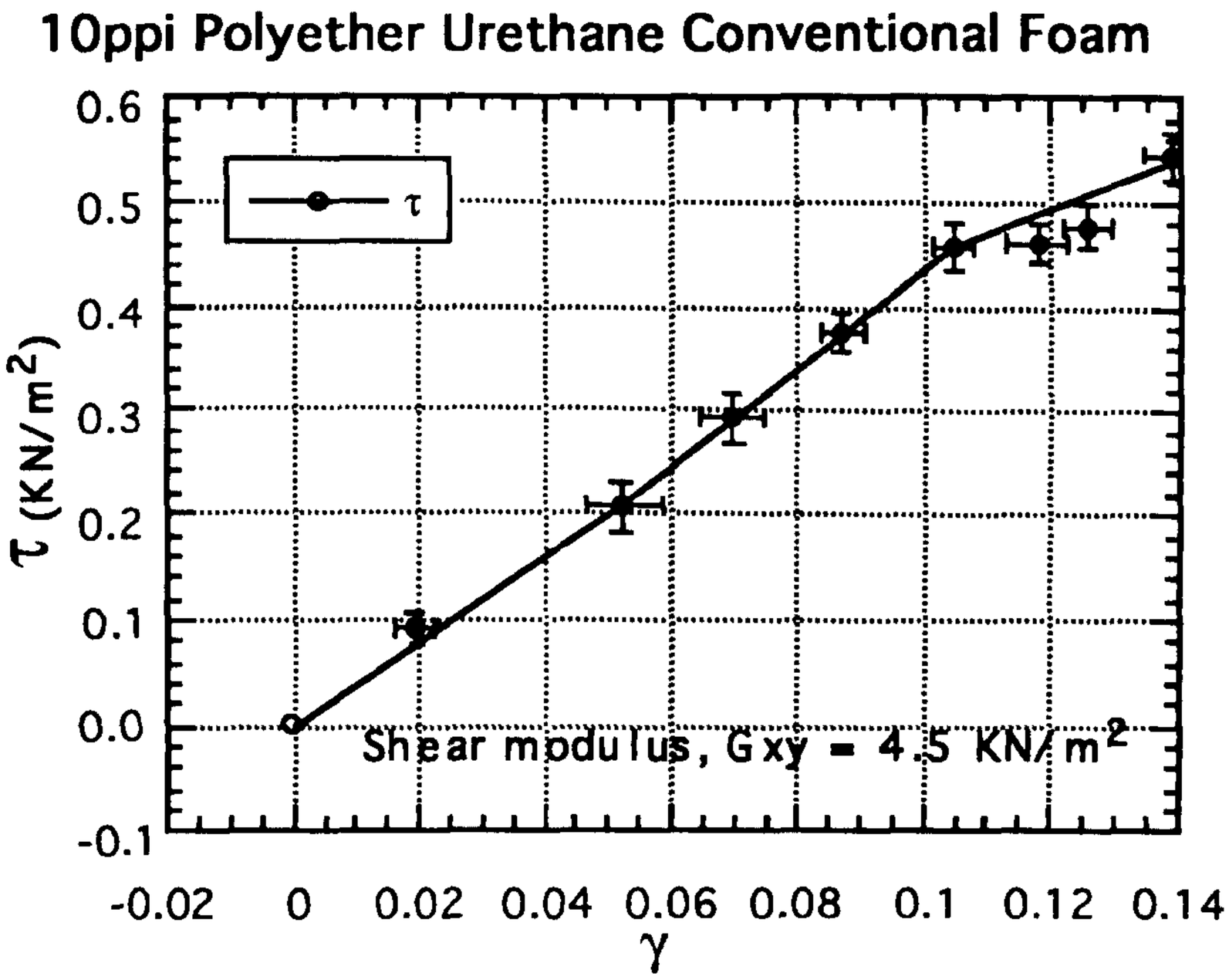

Fig. 6. 54 Graph of the shear stress versus the shear strain for the 10ppi conventional foam (10CO).

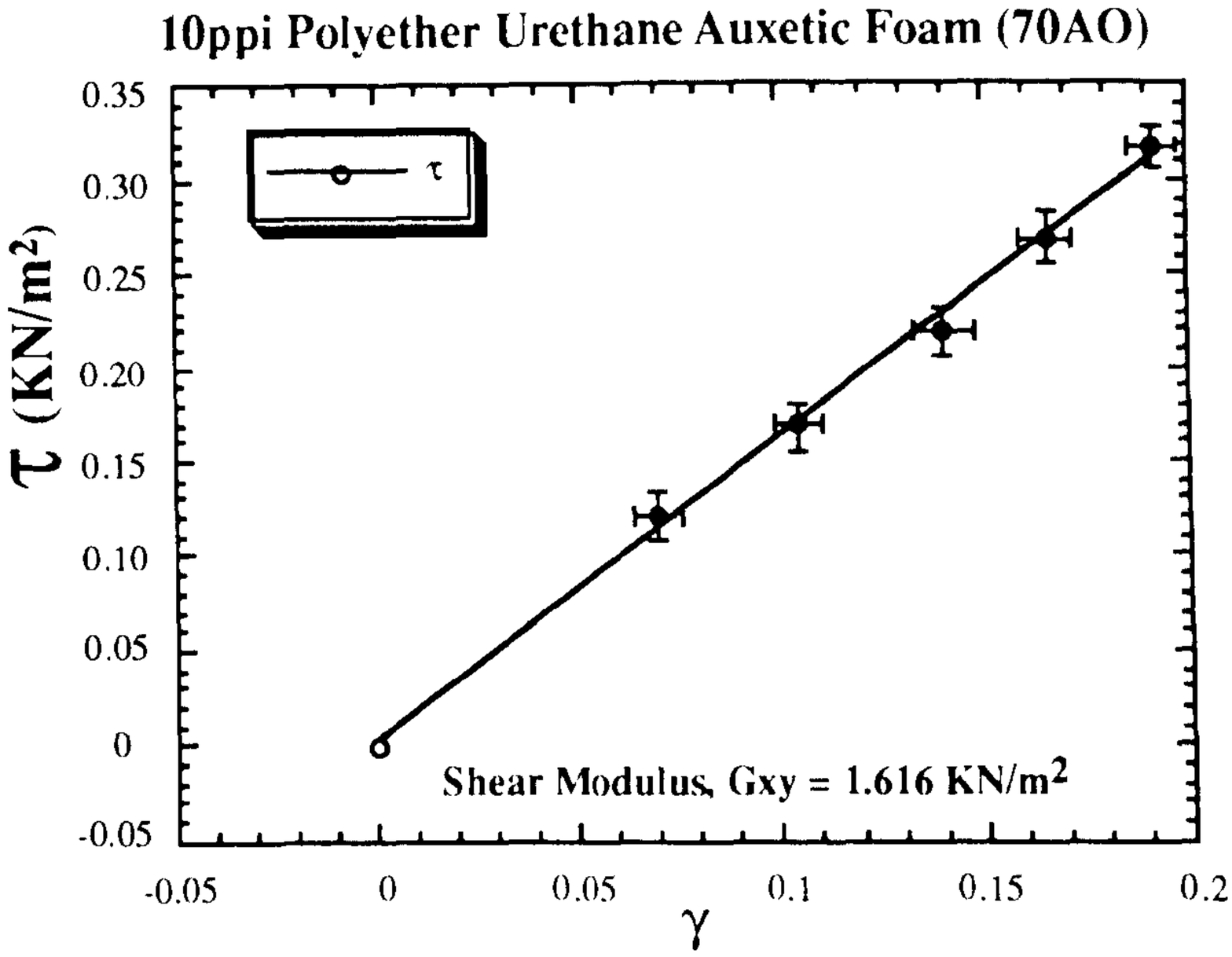

Fig 6. 55 Graph of shear stress vs. shear strain for the 10ppi auxetic foam (70AO).

From *Figures* 6.53 to 6.55, it can be seen that, for a conventional foam, the shear stress-strain diagram can be divided into two parts exhibiting significantly different stress-strain behaviours. The first region, having a relatively high modulus, is followed by a region where there is a large increase in strain for a small increase in stress. The transition between the two regions can be specified quite accurately. For an auxetic foam, the behaviour is different, an almost linear relationship between the shear stress and strain is observed throughout. These differences were detected with all of the types of foam investigated. Furthermore, the shear modulus depends heavily on cell size as well as cell shape. The effect of cell size is still not fully understood.

To get an accurate value of the shear modulus, three or four specimens were tested in each case and an average was taken. The results are shown in *Table 6.5*.

Table 6.5

Shear Moduli kN/m^2	PECC	PECO	30CO	10CO	100AO	90AO	80AO	70AO	PEAO-4
G_{zy}	2.42±1.6	1.97±0.8	2.24±1.9	2.8±1.2	2.4±0.1	2.2±0.1	1.8±0.1	1.7±0.1	2.3±0.2
G_{xy}	3.03±2.2	1.93±1.0	2.79±1.2	4.5±1.9	1.5±0.1	2.1±0.1	1.9±0.1	1.6±0.1	2.0±0.1
G_{xz}	2.8±0.5	1.24±0.5	2.3±0.5	2.9±0.3	10.4±1.2	18.6±1.8	35.2±2.0	26.2±2.3	9.1±0.5
G_{zx}	2.2±0.4	1.36±0.5	2.1±0.4	2.6±0.3	13.7±1.0	17.5±1.6	26.0±2.0	17.9±1.9	8.3±0.8
G_{yz}	2.69±2.8	1.85±1.3	2.54±2.9	3.0±1.6	2.6±0.7	2.3±0.5	2.0±0.3	1.9±0.4	2.5±0.6
G_{yx}	2.84±2.2	2.16±1.9	2.53±2.6	4.6±1.9	1.7±0.6	2.2±0.5	1.9±0.3	1.7±0.3	2.6±0.8

Table. 6.5 The shear moduli of foams.

Table 6.5 shows that the shear modulus of a foam depends upon the physical properties of the solid material making up the cell ribs, the cell shape, the cell size and the loading directions. In some directions, the shear modulus of a conventional foam is lower than that of an auxetic foam and in the other directions, the reverse is true. The volumetric compression ratio changes in an auxetic foam is accompanied by a cell shape change as well as a cell size change. The high value of the shear modulus of an auxetic foam is not always due to the high value of the volumetric compression ratio. The shear modulus depends upon the Poisson's ratio of the foam. The results show that a better way to improve the shear stiffness may be to use a conventional foam of higher density.

6. 5. 4 Dynamic Shear Modulus Measurement

An investigation of the dynamic behaviour of foams was carried out using a DMTA (Dynamic Mechanical Thermal Analyser), shown in *Figure* 6.56 to measure the dynamic shear modulus. The shear sandwich arrangement is shown in *Figure* 6.57(a). Two identical disc shaped samples were fixed between the drive shaft plate and the supporting studs using *Apollo A. 2874 Adhesive* . The sample radius was 4.0±0.05 mm. The dimensions of the foam sample is shown in *Figure* 6.57(b) and the Z-X planes were sheared. The thickness of the adhesion layer was approximately 0.003 mm. Three pairs of samples were tested for each case, the average error of the LogG' and the loss $\tan\delta$ was within 8% and 10% respectively. The testing results of the LogG' and $\tan\delta$ are shown in *Figures* 6.58 to 6.63, and 7. 31 to 7.36 respectively. Here G_{xz} was measured and the storage moduli are presented for comparison with the static data.

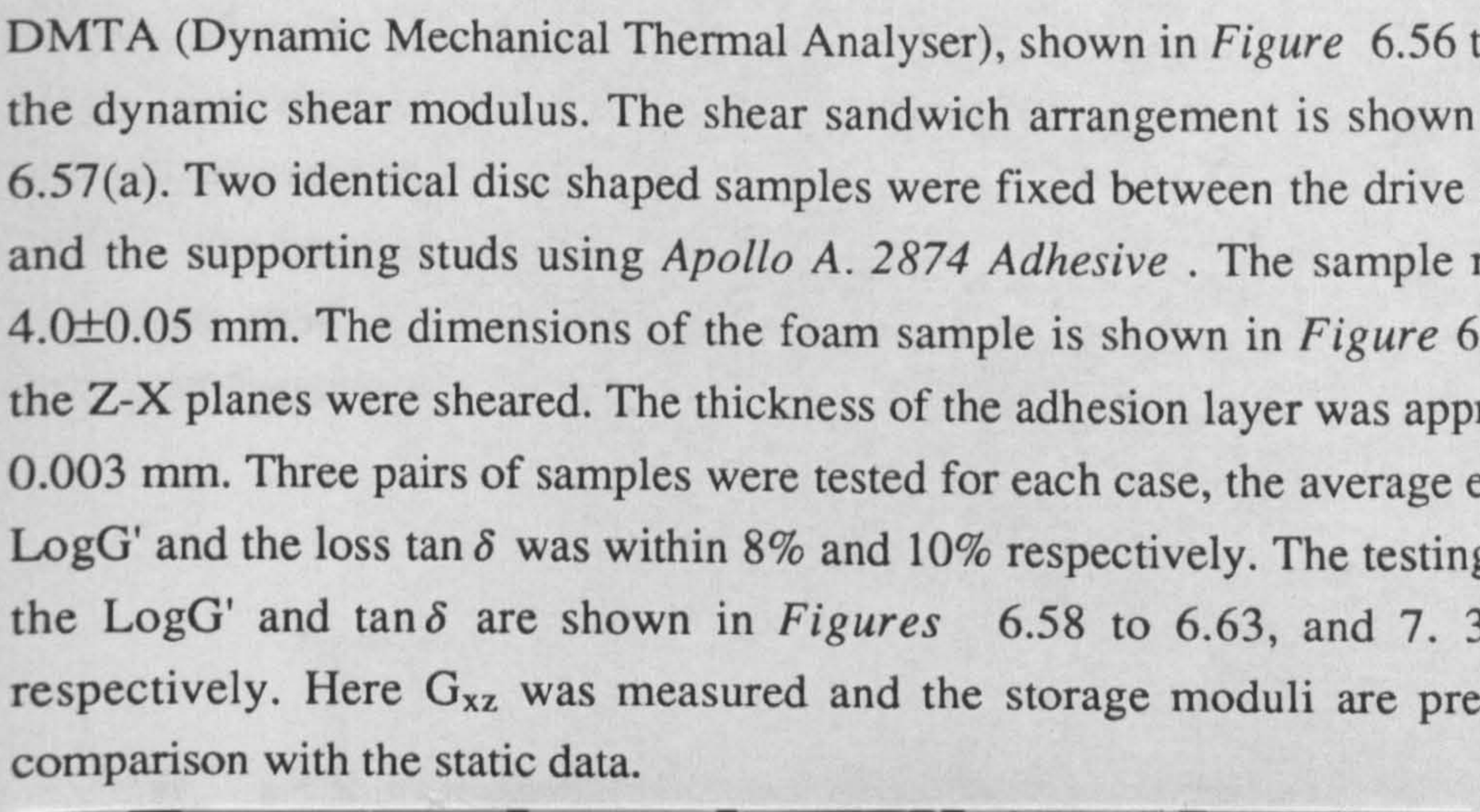

Fig. 6.56 The DMTA, Dynamic Mechanical Testing Analyser.

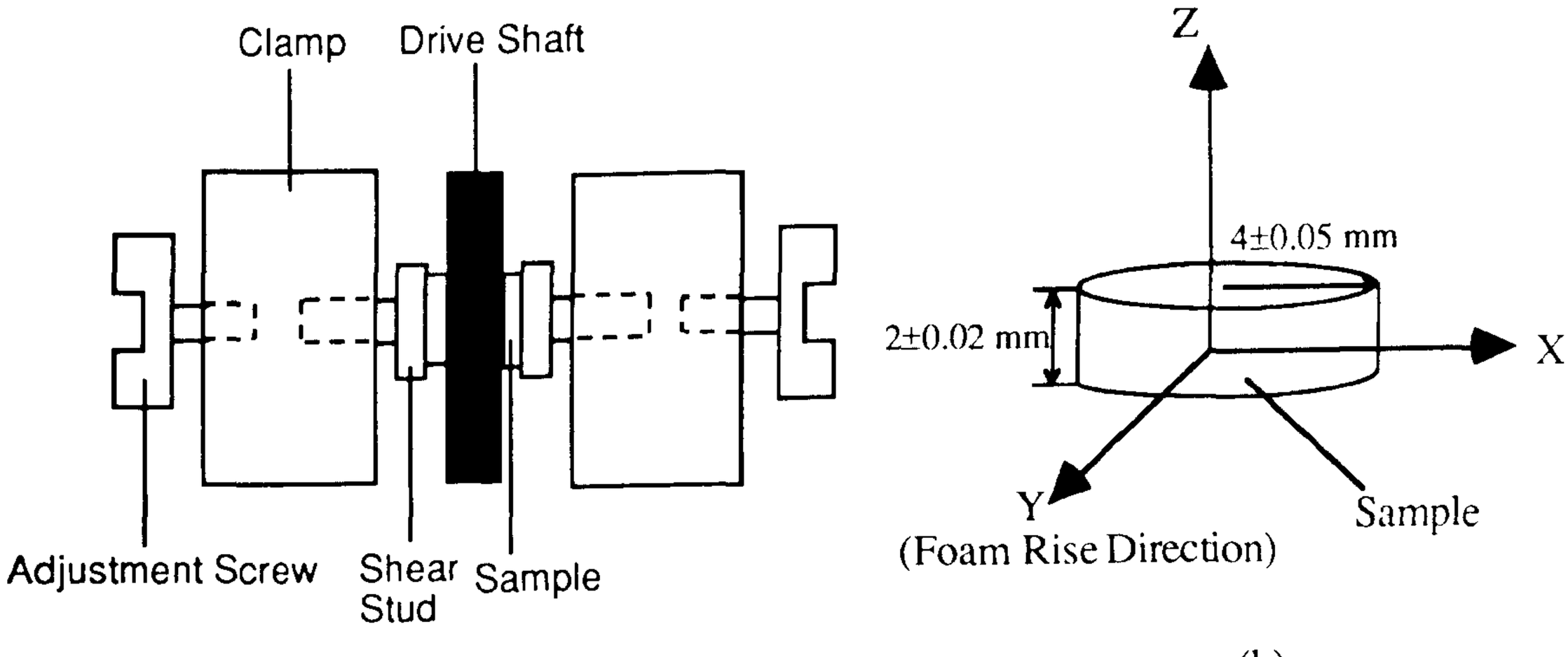

Fig. 6.57 (a) Shear sandwich arrangement. (b) The dimensions of the foam sample.

The properties of the prepared PUR foam samples were measured using the DMTA. The temperature, the storage modulus (G') and the loss tan δ were recorded. LogG' was used to measure the change of stiffness with temperature. DMTA analysis was carried out at a frequency of 10 Hz over the temperature range -70^{0}C to 100^{0}C. The heating rate used was 2^{0}C/min. Liquid nitrogen was used to achieve maximum cooling. The DMTA graphs are illustrated in *Figures* 6.58 to 6.60. The effects of frequency on the dynamic modulus are shown in *Figures* 6.61 to 6.63.

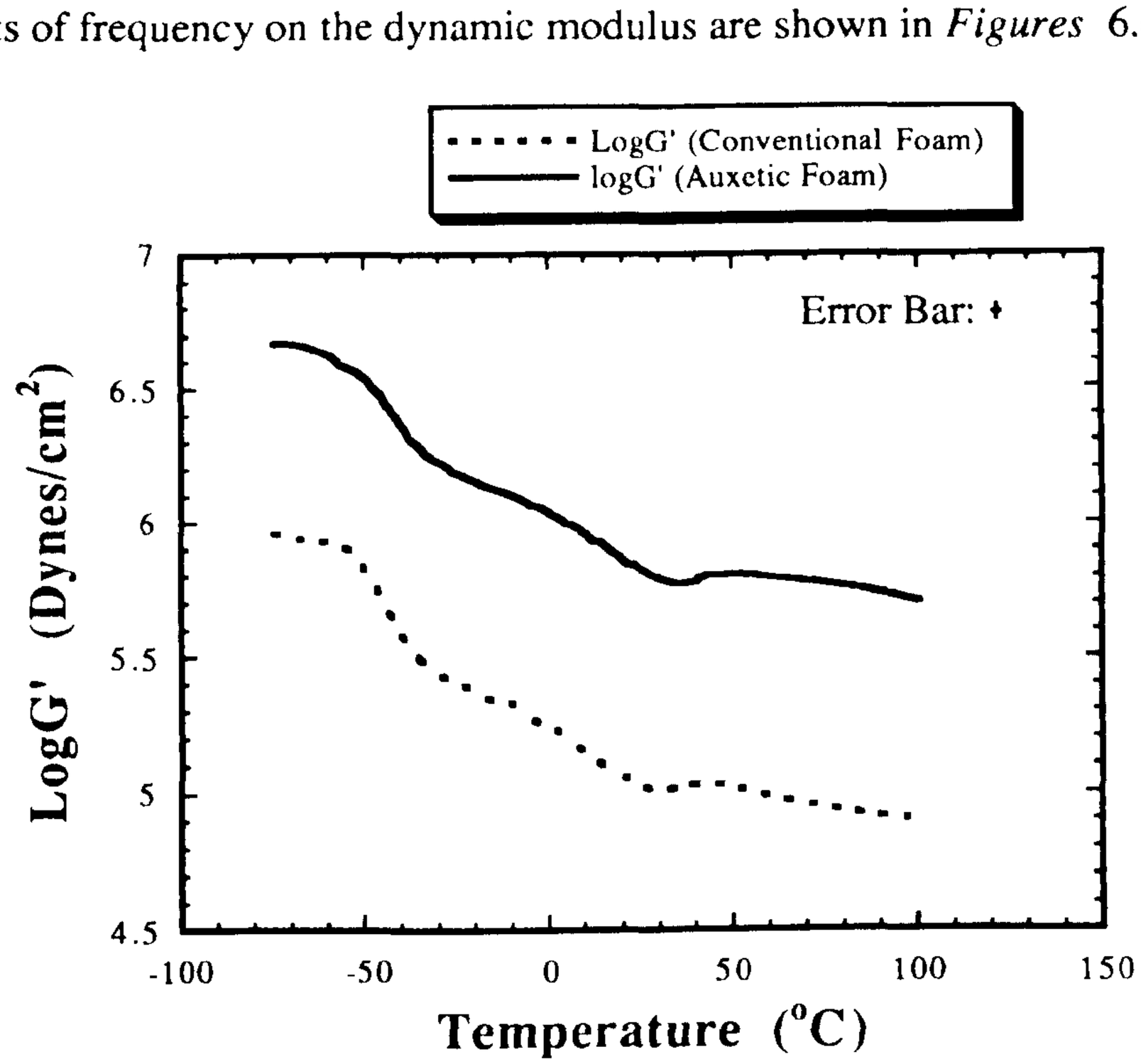

Fig. 6.58 DMTA results of the open-cell polyether urethane foams. Comparison of the storage shear modulus of an auxetic foam (90AO) with its parent conventional foam (10CO). (The testing frequency was 10Hz).

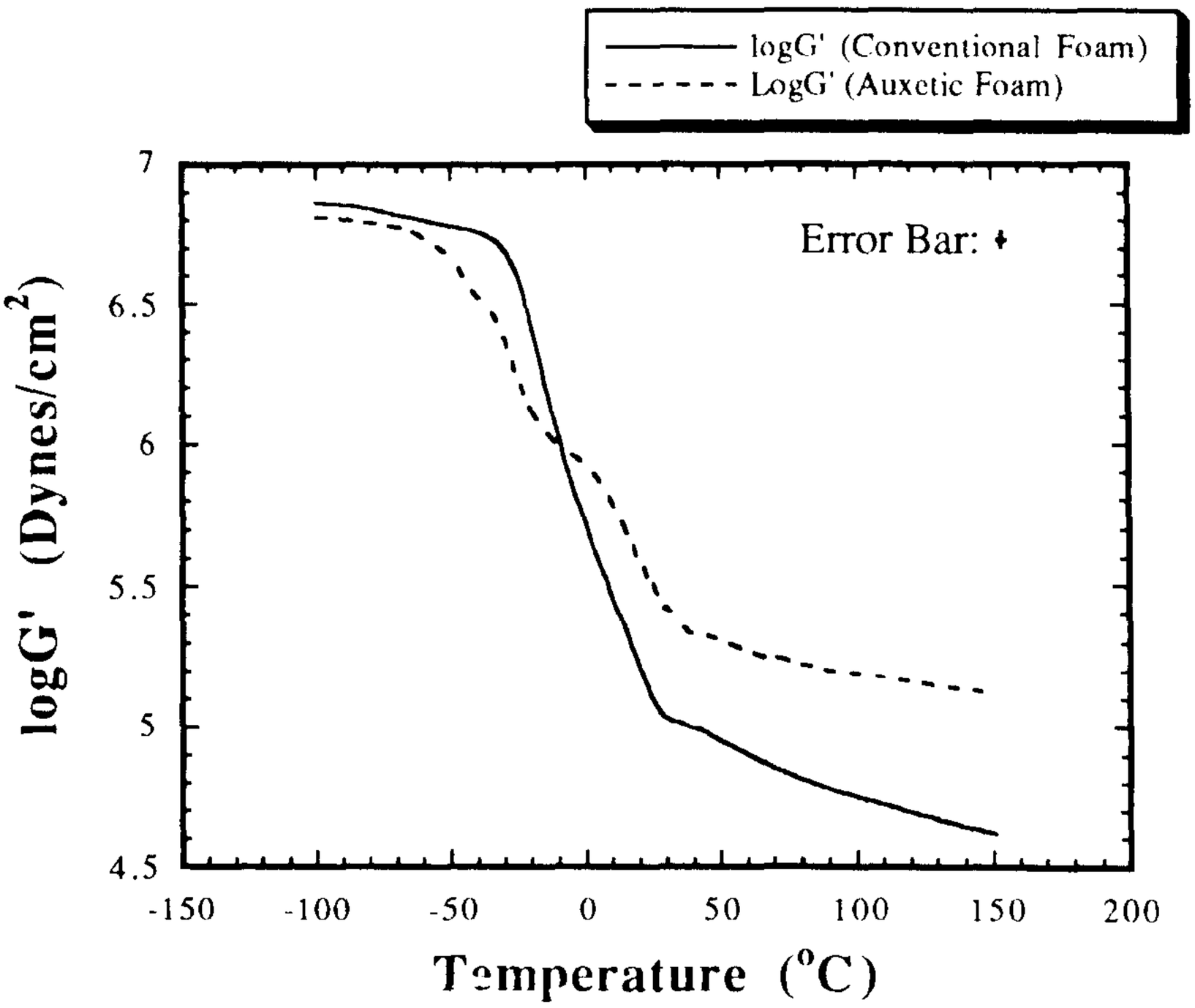

Fig. 6.59 DMTA results of the 60ppi reticulated polyester urethane foam. Comparison of the dynamic behaviour of auxetic foam (PEAO-4) with its parent conventional foam (PECO). (The testing frequency was 10Hz).

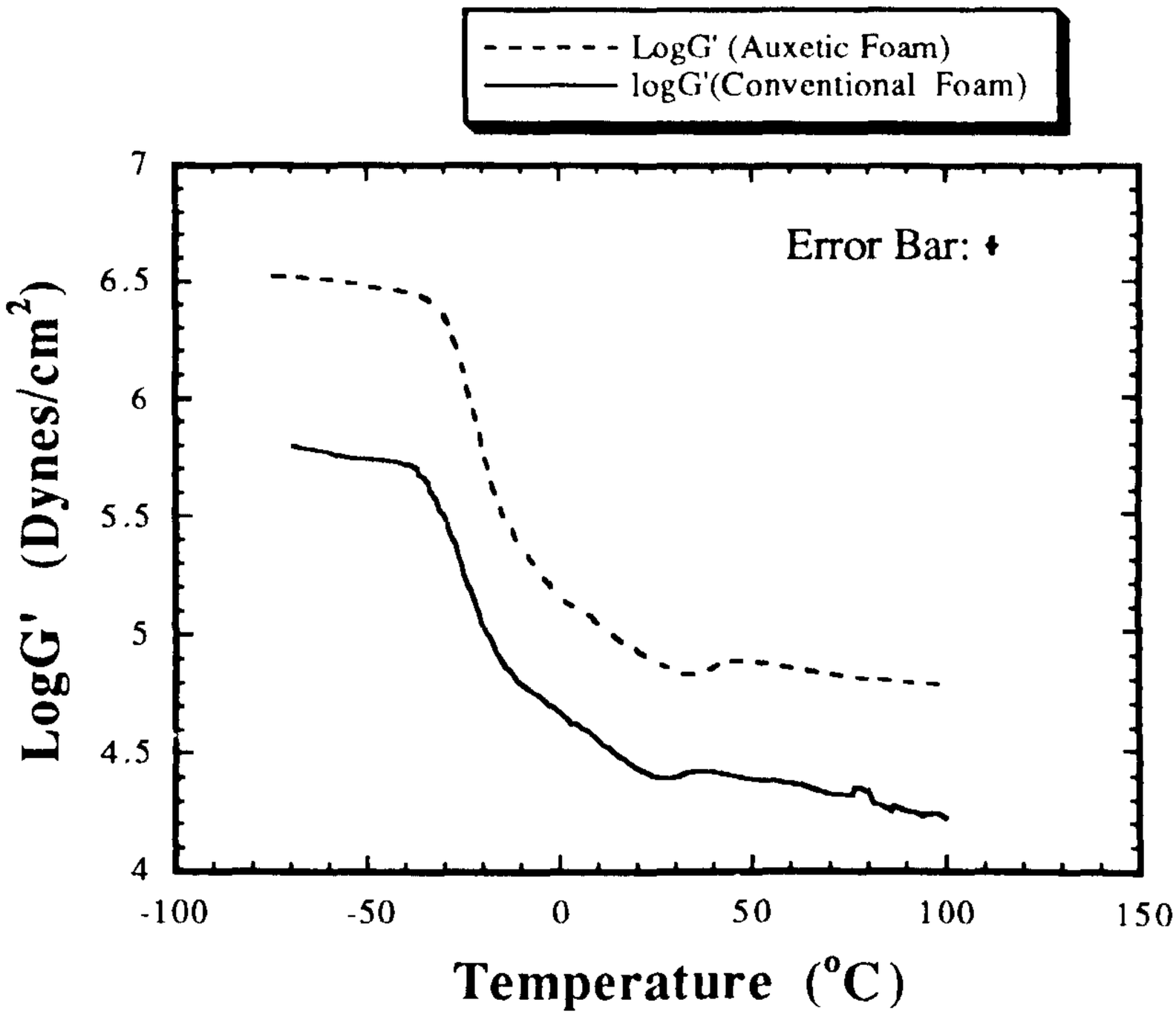

Fig. 6.60 DMTA results of the 60ppi closed-cell polyester urethane foam. Comparison of the storage shear modulus of an auxetic foam (PEAC-1) with its parent conventional foam (PECC). (The testing frequency was 10 Hz).

Typical dynamic mechanical properties of foams as a function of temperature are illustrated in Figures 6.58 to 6.60. The storage shear modulus LogG' is plotted versus temperature in the range from -75 to 100^0C at a constant frequency of 10 Hz. Two changes of gradient of modulus are discernible in the case of reticulated and open-cell foams: one corresponding to the glass transition at around -30^0C, and a secondary peak at around 25^0C. A sharp decrease in modulus of approximately one and half orders of magnitude is seen to occur as the temperature increases through the glass transition region over a temperature range of about 60^0C after which the sample enters the rubbery region (above the glass transition temperature, T_g) where a slight decrease in modulus is observed to occur with temperature rise, over the range 30^0C to 100^0C. All the PUR foam samples prepared showed similar thermal relaxation trends. However, the DMTA results show that the storage shear modulus, G_{xz} of auxetic foam is higher than that of conventional foam over a large temperature range (e.g. $0^o < Temp. < 100^o$) at the normal dynamic testing frequency of 10 Hz. For clarity and brevity, the DMTA data have been shown for only a single frequency. However, when other frequencies were used, the trends of the curves were observed to be the same, the curve shifted upwards as the frequency was increased, and shifted downwards as the frequency was reduced as shown in *Figures* 6.61 and 6.62.

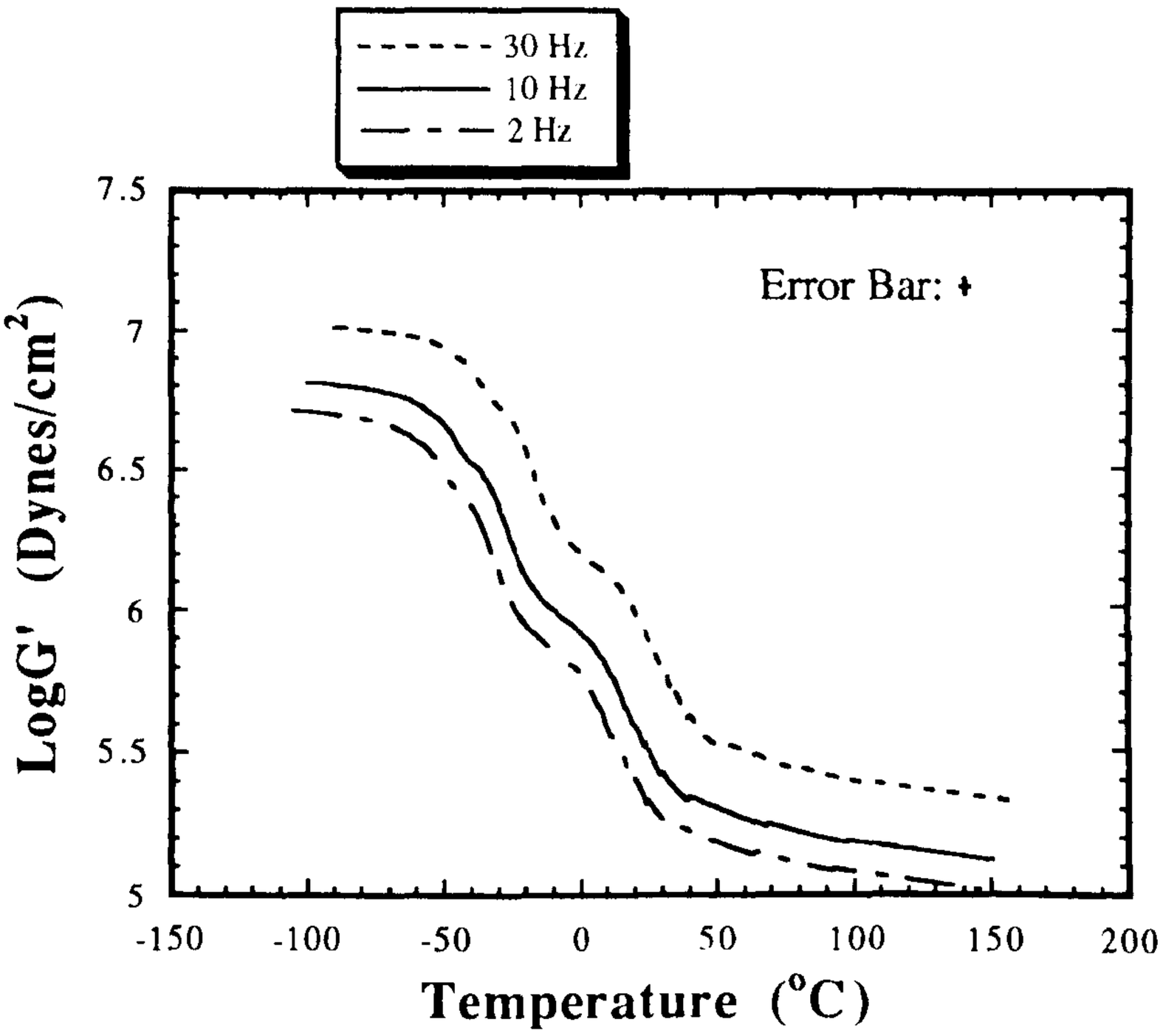

Fig. 6.61 DMTA results of the 60ppi reticulated auxetic polyester urethane foam (PEAO-4). Illustration on effect of frequency on the storage shear modulus, Log G_{xz}'.

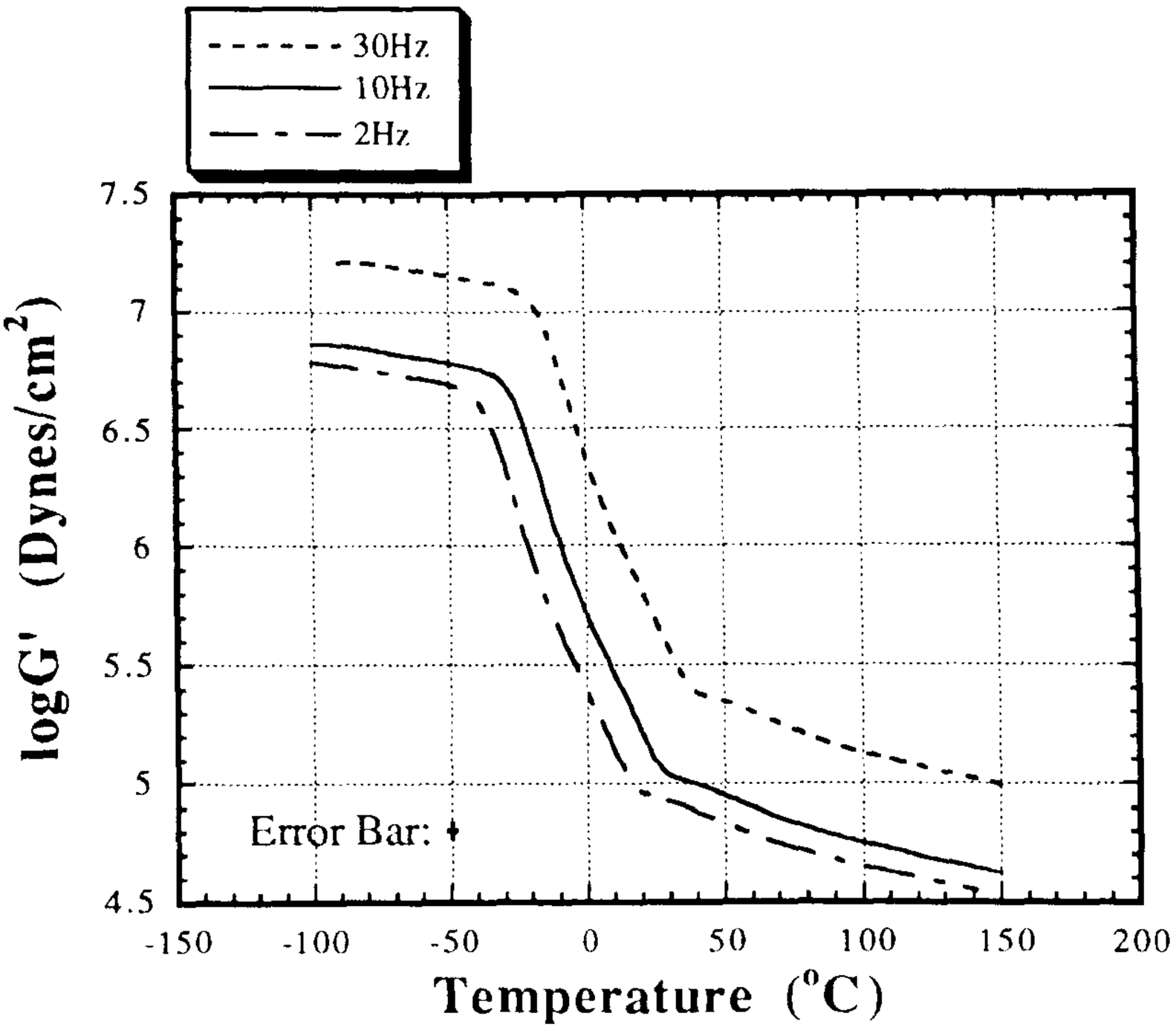

Fig. 6.62 DMTA results of the 60ppi reticulated conventional polyester urethane foam (PECO). Illustration on effect of frequency on the storage shear modulus.

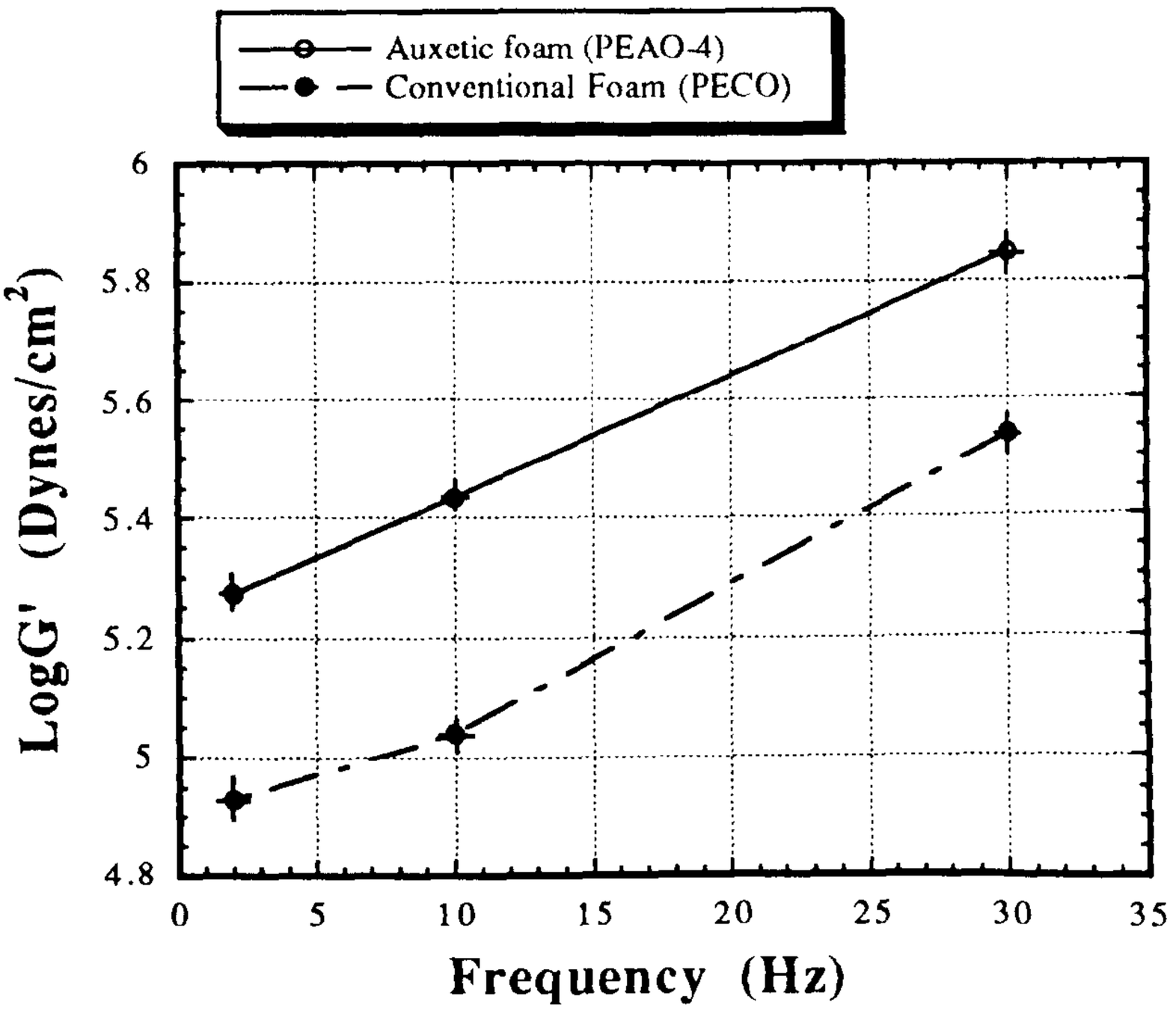

Fig. 6.63 Effect of variable frequencies on the storage shear modulus logG'.

Figure 6.63 shows that decreasing the frequency decreases the shear modulus of both conventional and auxetic foams. When the frequency is 10Hz, LogG' is approximate 5.45 dynes/cm^2 for the conventional foam (PECO) and is approximate 5.05 dynes/cm^2 for the auxetic foam (PEAO-4). (Note: One kN/m^2 is equal to 10^4 dyne/cm^2). If we compare these dynamic experimental results with the static experimental results (Table 6.4), we can see that the dynamic shear modulus (G_{xz} or G_{zx}) of both conventional and auxetic foams is of the same order of magnitude as the static shear modulus. Both static and dynamic shear moduli of the auxetic foam PEAO-4 are higher than that of its parent conventional foam PECO.

Chapter 7 The Mechanical Properties of Foams (II)

7.1 Introduction

The behaviour of polymeric foams in energy absorption applications, such as automotive seating, where static and dynamic indentation resilience are the main functional attributes, is governed by two material properties: the effective stiffness; and energy loss through hysteresis. In most applications the foam is subject to combined stresses (tension, shear and compression) and in some characterization procedures, such as ball indentation and ball rebound, these conditions prevail. In this chapter we present the results of ball indentation, hysteresis, ball rebound and DMTA tests for both conventional and auxetic foams.

7.2 The Ball Indentation Test (Static Indentation Resilience)

In engineering terms the indentation resilience or the hardness of a material is a measure of its resistance to local indentation. The Ball Indentation Test has been used for many years to measure the hardness of metals. Foams are widely used for packaging, and usually the packaged object has corners. Therefore the local indentation resistance is an important mechanical property of foams.

The indentation resilience of the 10ppi and 30ppi open-cell polyether urethane foams, consisting of conventional and auxetic foams with a range of densities, were examined. The relevant properties are summarised in Table 7.2. Both spherical and cylindrical indenters (Table 7.1) were compressed into the rectangular foam samples in the foam rise direction using an Inston 1185 mechanical testing machine, with a full scale deflection of 0.1 kN, at a cross head speed of 2 mm/min. as shown schematically in *Figure* 7.1. The load-deflection response was recorded by the Instron chart recorder. The shapes of indentation profiles of the cylinder and the indentation depths were recorded by a camera (see *Figure* 7.3, 7.4, and 7.5). Although the indentation profile of a ball cannot be recorded directly by the camera, we know that the diameter of the ball indentation profile is qualitatively similar to that of the cylinder indentation profile (see Wilsea, Johnson and Ashby (1974)).

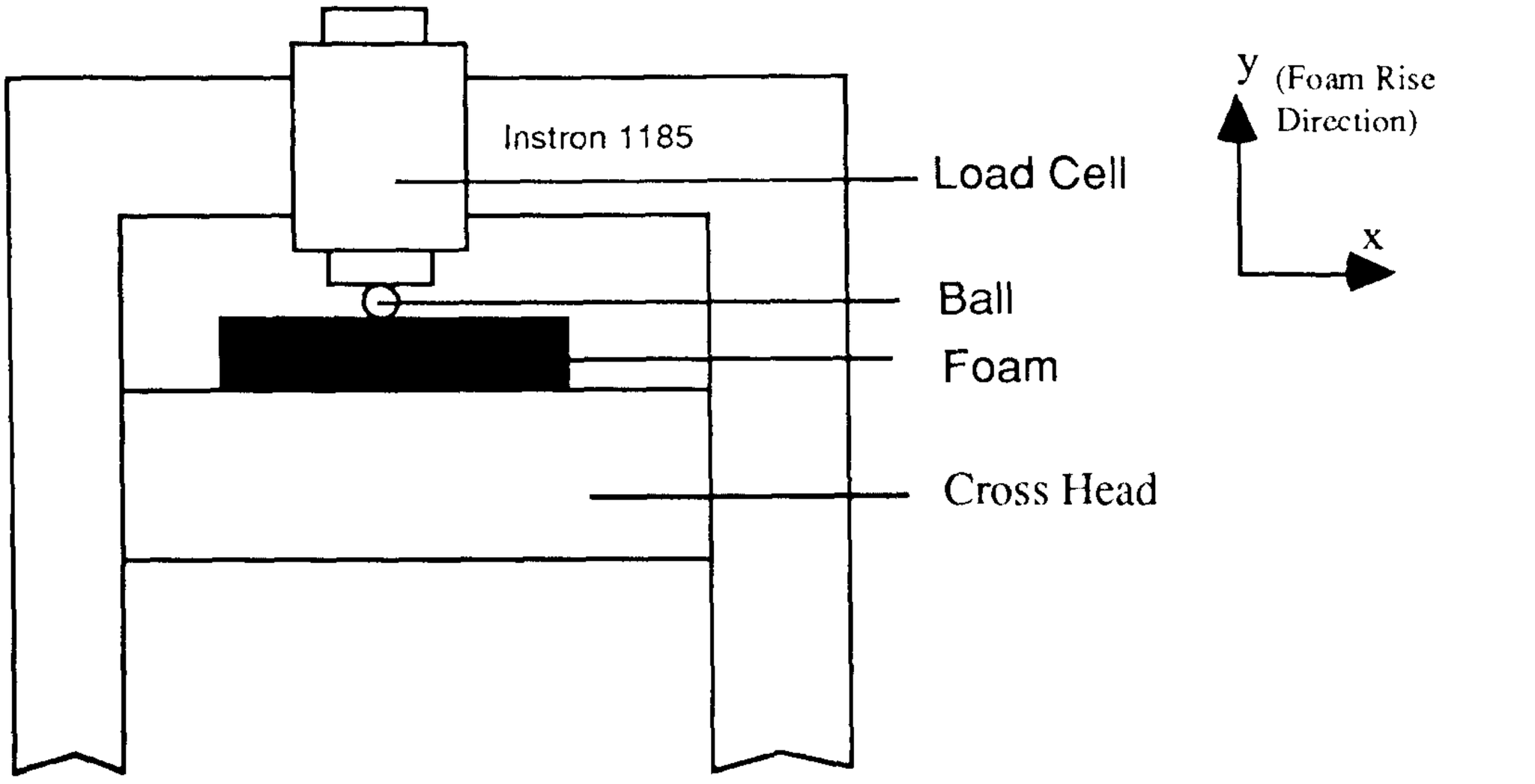

Fig. 7.1 Schematic diagram of the Ball Indentation Test, looking along the z direction.

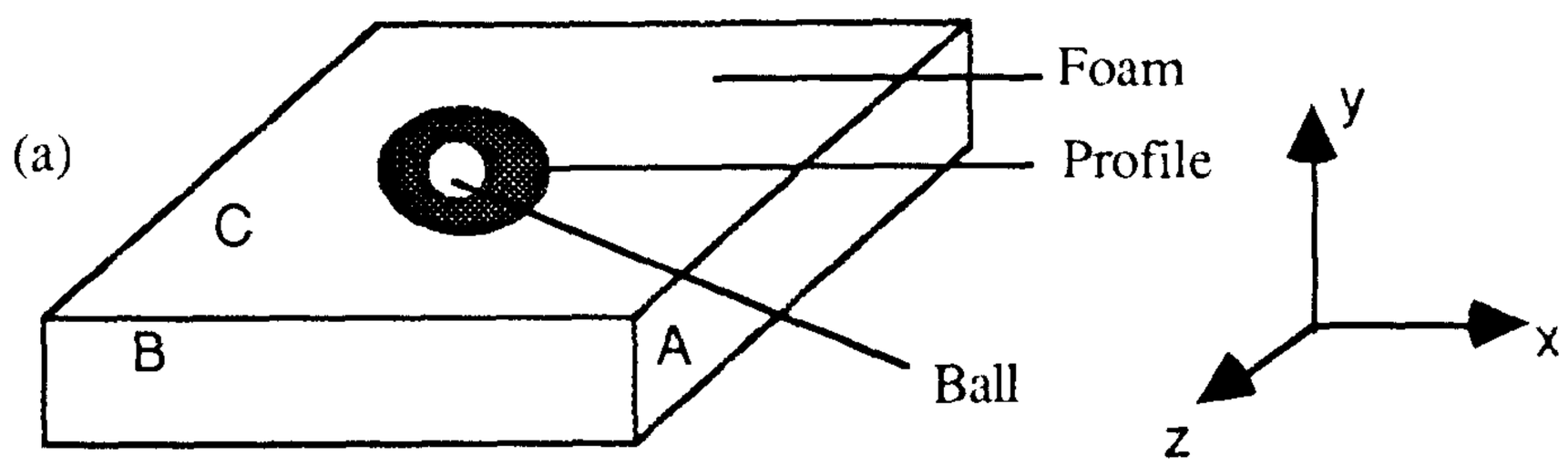

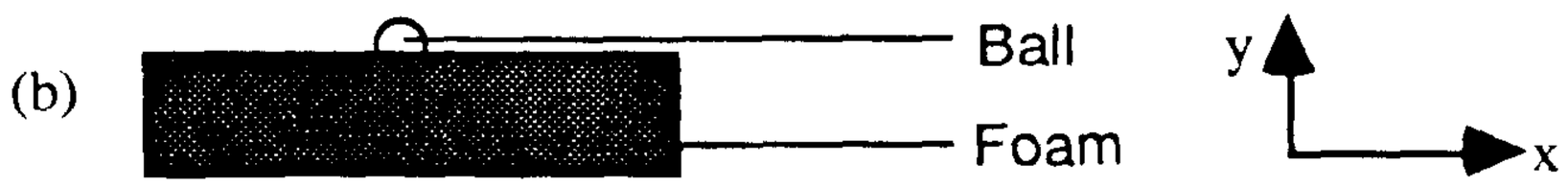

Fig. 7.2 (a) View of the ball at 45° above the horizontal level. (b) View of the ball along the z direction.

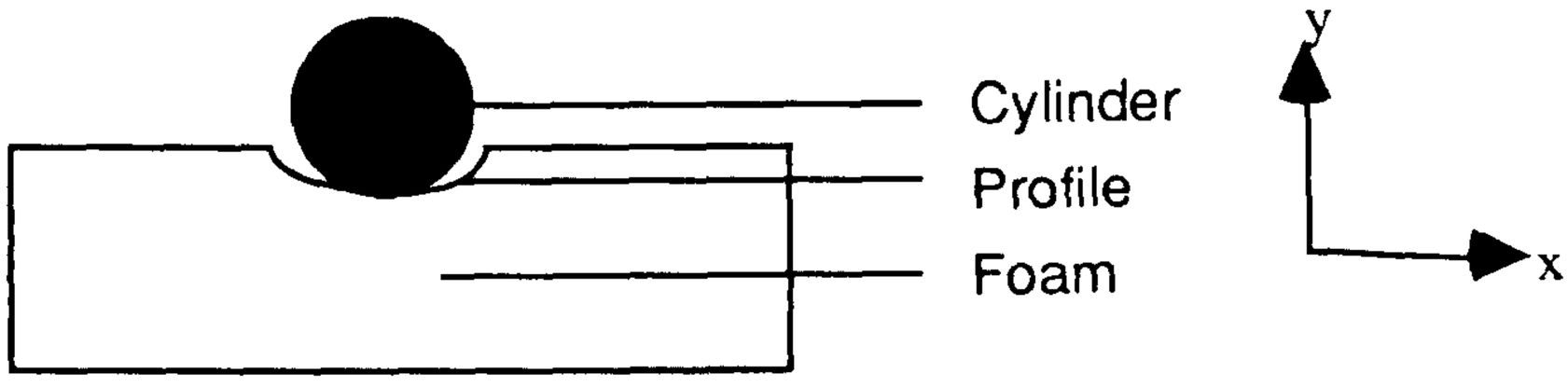

Fig. 7.3 Schematic diagram of the Cylinder Indentation Test, looking along the z direction.

Examples of the photographs taken of the indentation profiles are given in Figures 7.3 and 7.4.

(a)

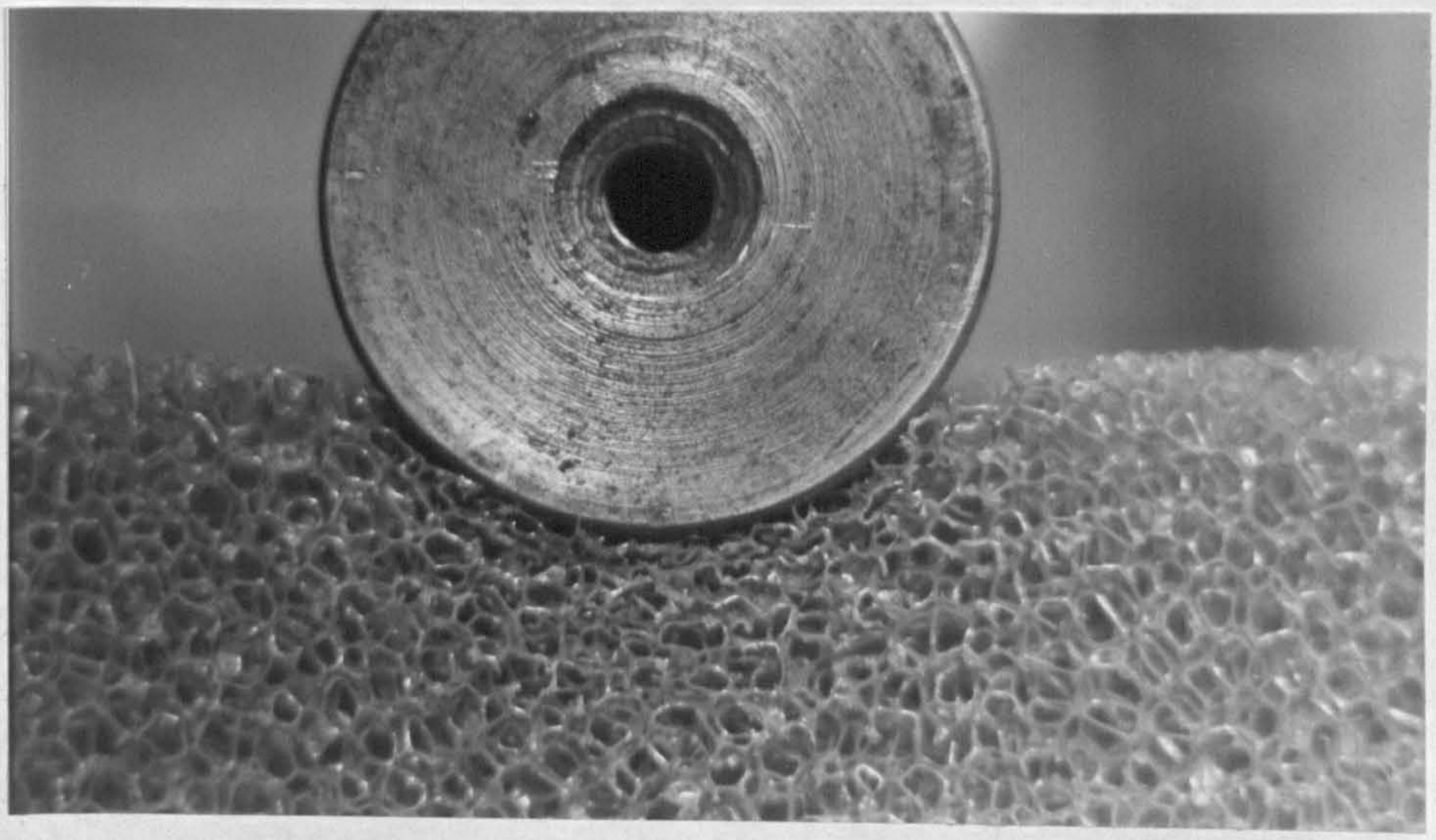

(b)

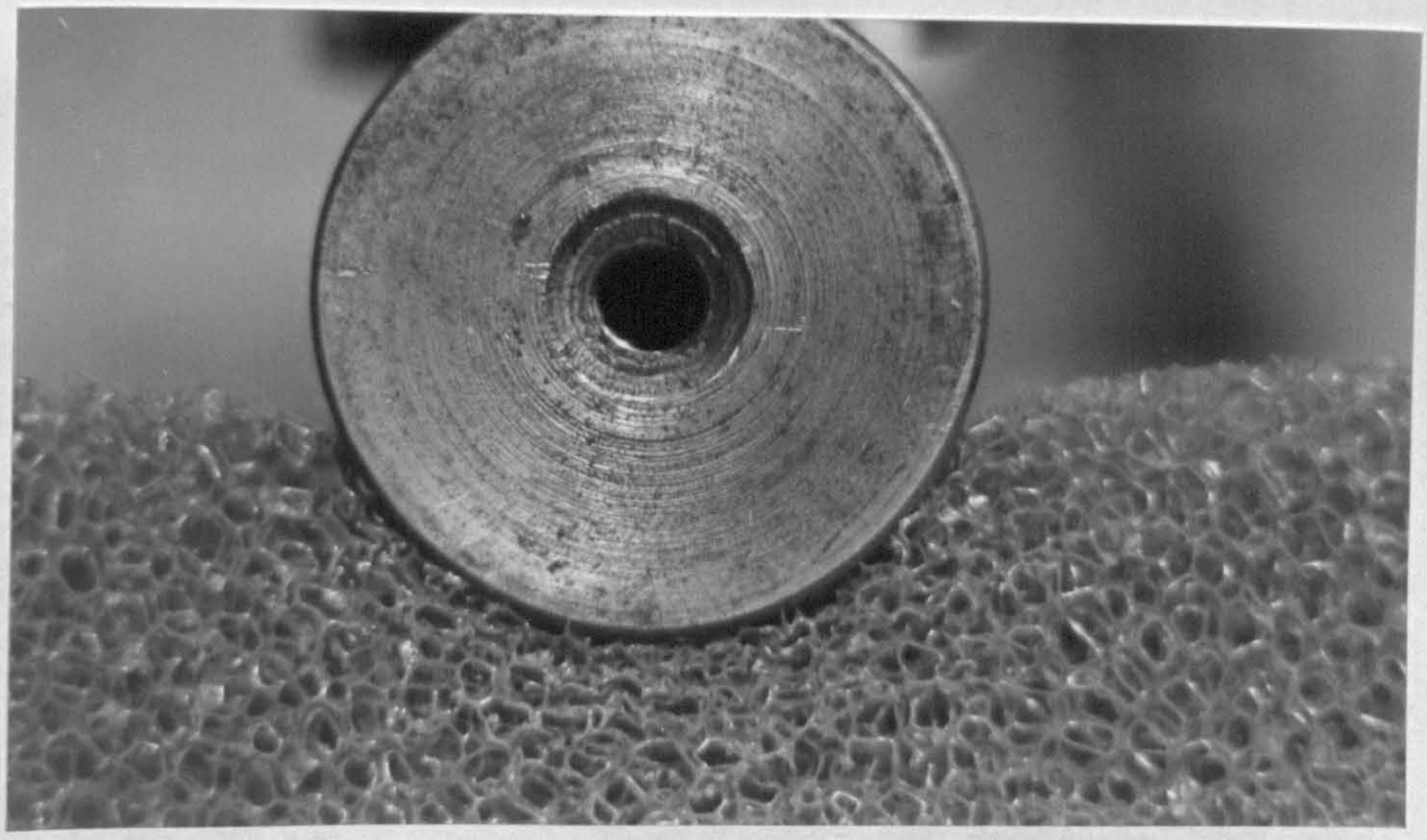

(c)

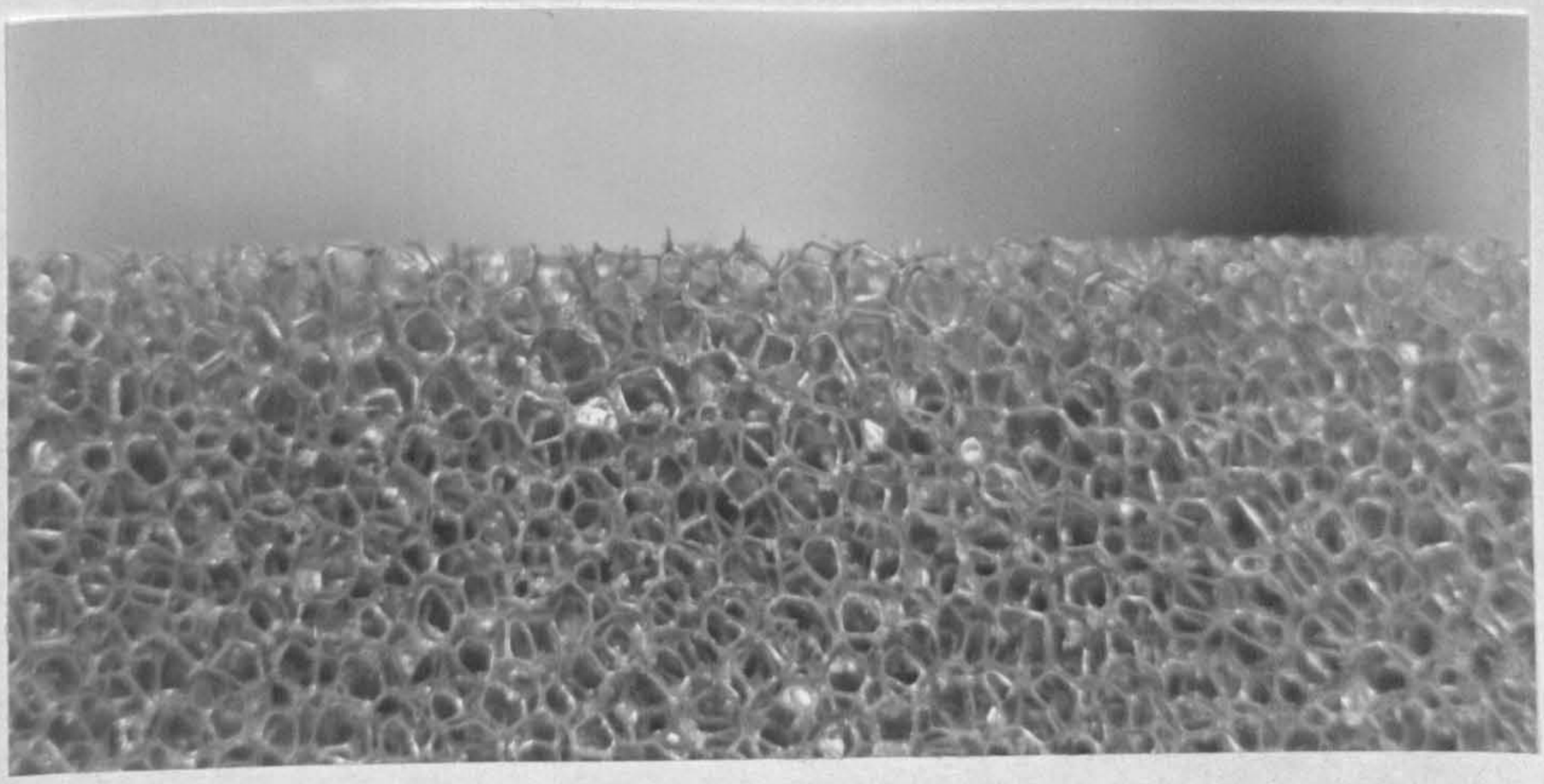

Fig. 7.4 Compressive displacement of the 10ppi conventional foam (10CO) produced by a cylindrical indenter. The displacement is (a). 4mm. (b) 8mm. (c) 0mm (Restore to its original height).

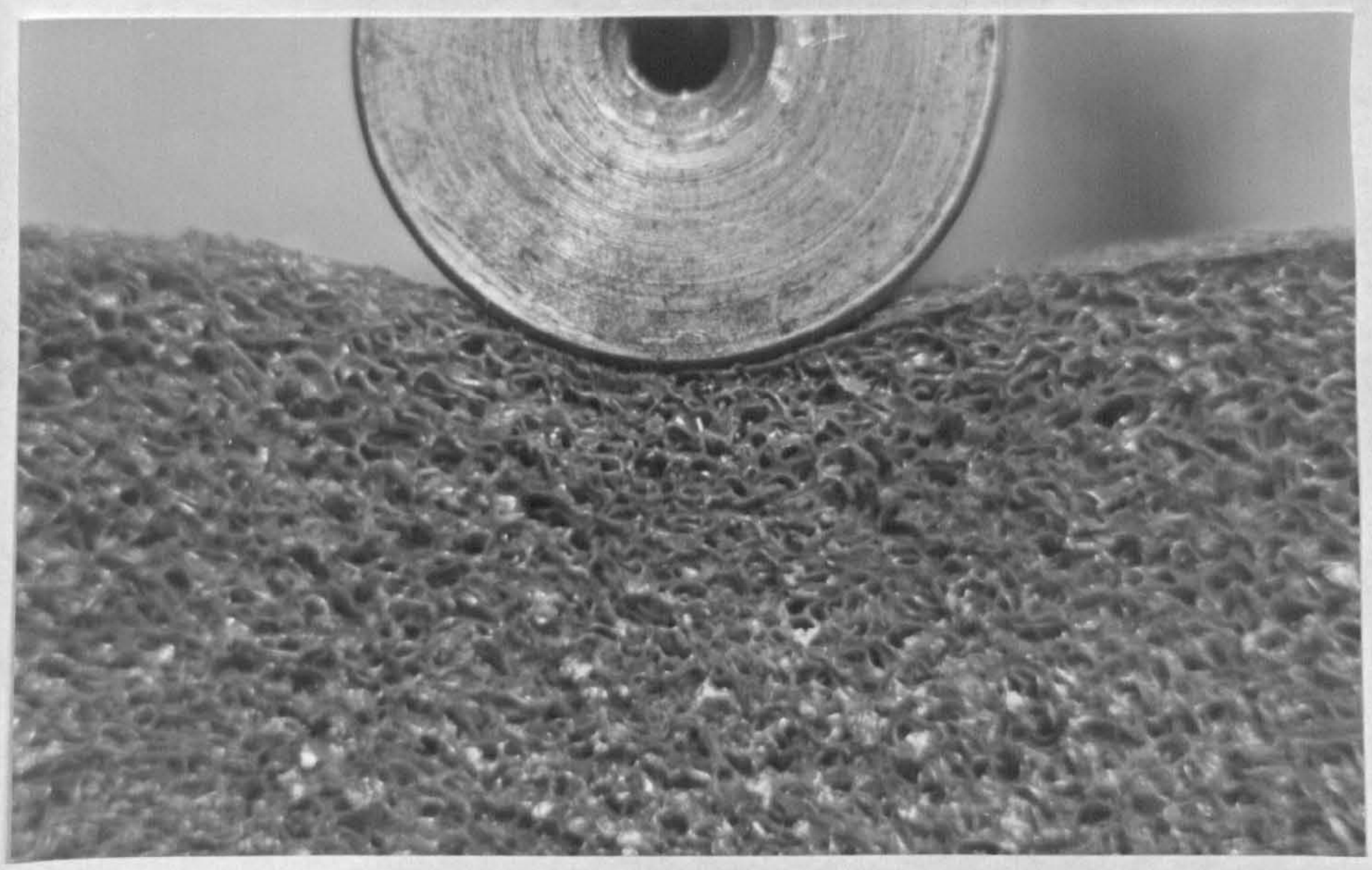

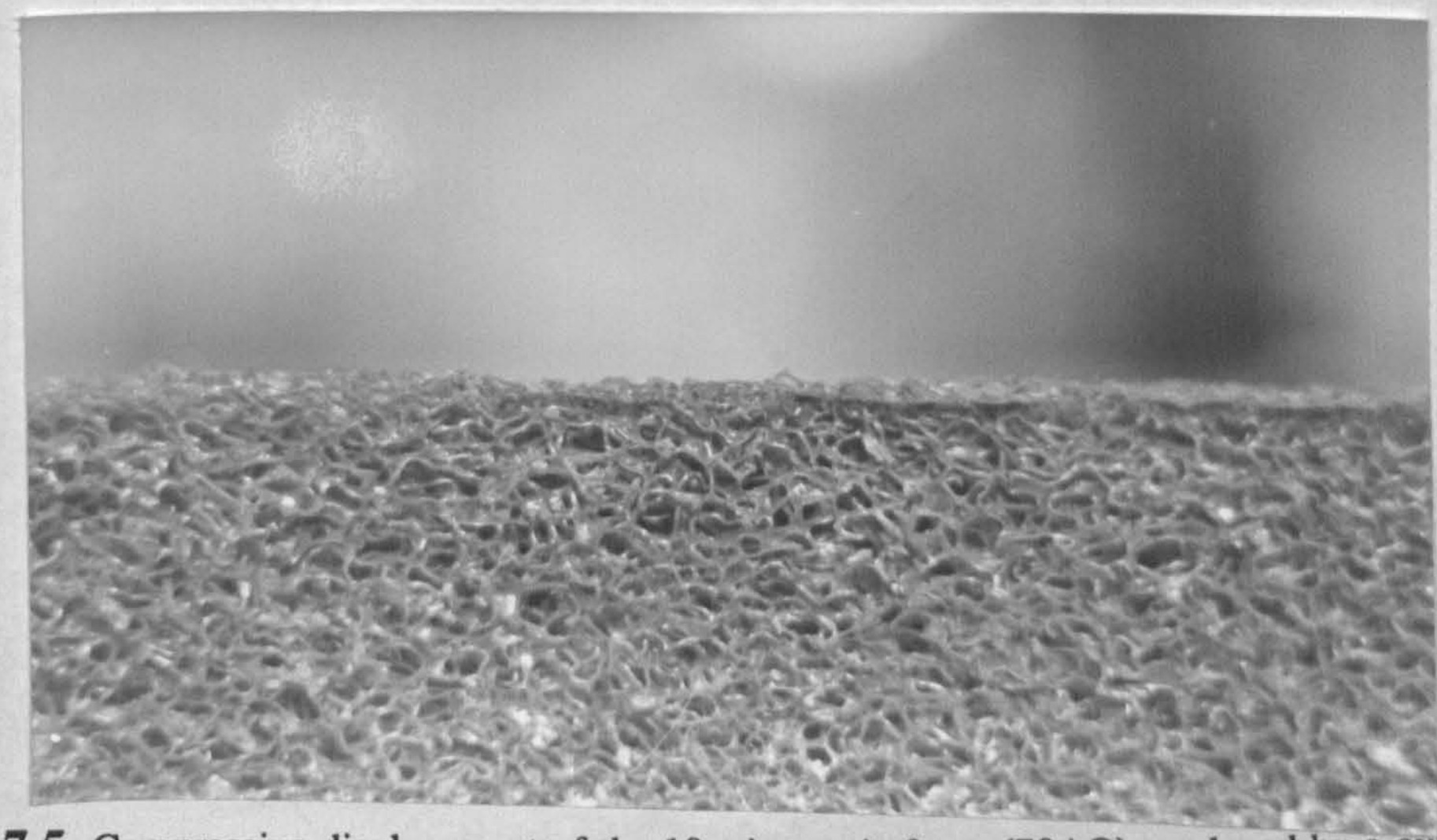

Fig. 7.5 Compressive displacement of the 10ppi auxetic foam (70AO) produced by a cylindrical indenter. The displacement is (a). 4mm. (b) 8mm. (c) 0mm (Restore to its original height).

Figure 7.4 and 7.5 show typical photos of the deformation below a cylindrical indenter. The circular cap of elastically deformed foam is clearly visible, and it is evidence of shear banding. In all cases, the indented area was much larger than the area of any individual cell, and the diameter of the indentation profile is larger than that of the indenter.

Table 7.1

Indenter	Steel Ball 1	Steel Ball 2	Steel Cylinder 1	Steel Cylinder 2
Diameter, D (mm)	50±0.002	22±0.001	50±0.002	22±0.0013
Length, L (mm)	-	-	200±0.5	200±0.3

Table 7.1 The sizes of the indenter.

Table 7.2

Sample	Dimensions (mm)			Density (kg/m^3)	Compression Poisson's Ratio, V_{yx}
	X	Y	Z		
10ppi-100AO	203±2.8	53±0.5	204±2.5	79±3.0	-0.66±0.06
10ppi-90AO	205±2.5	51±0.3	202±2.7	77±2.1	-0.6±0.05
10ppi-80AO	202±2.2	50±0.5	203±2.5	76±2.2	-0.54±0.02
10ppi-70AO	198±2.0	49±0.3	200±1.7	75±2.5	-0.43±0.01
10CO	200±1.5	50±0.5	199±1.2	24±3.1	+0.2±0.08
30ppi-100AO	203±3.2	52±0.8	200±2.5	95±1.8	-0.62±0.05
30ppi-90AO	202±2.6	52±0.3	204±3.1	84±2.3	-0.56±0.04
30ppi-80AO	201±3.0	53±0.3	202±2.6	73±2.5	-0.50±0.04
30ppi-70AO	200±2.1	50±0.5	200±2.7	69±1.6	-0.38±0.02
30CO	198±2.3	50±0.4	200±1.8	24.5±2.7	+0.24±0.05

Table 7.2 The Dimensions, Poisson's ratios and densities of the testing samples.

The test were performed by allowing a steel ball (i.e. Steel Ball 1) to penetrate into the test specimen and the ball indentation load-displacement curve recorded on the Instron chart recorder. The specimen restored to its original dimensions once the load was removed. Then, a steel cylinder of identical diameter (i.e. Steel Cylinder 1) was forced into the same specimen and the cylinder indentation load-displacement curve was also recorded on the Instron chart recorder. It was photographed right from the beginning of the Cylinder Indentation Test. An average 25 photos were taken for each test. The photographs were enlarged and the diameter of the indentation profile, d, and the depth of the impression, h, were measured as shown in Figure 7.6.

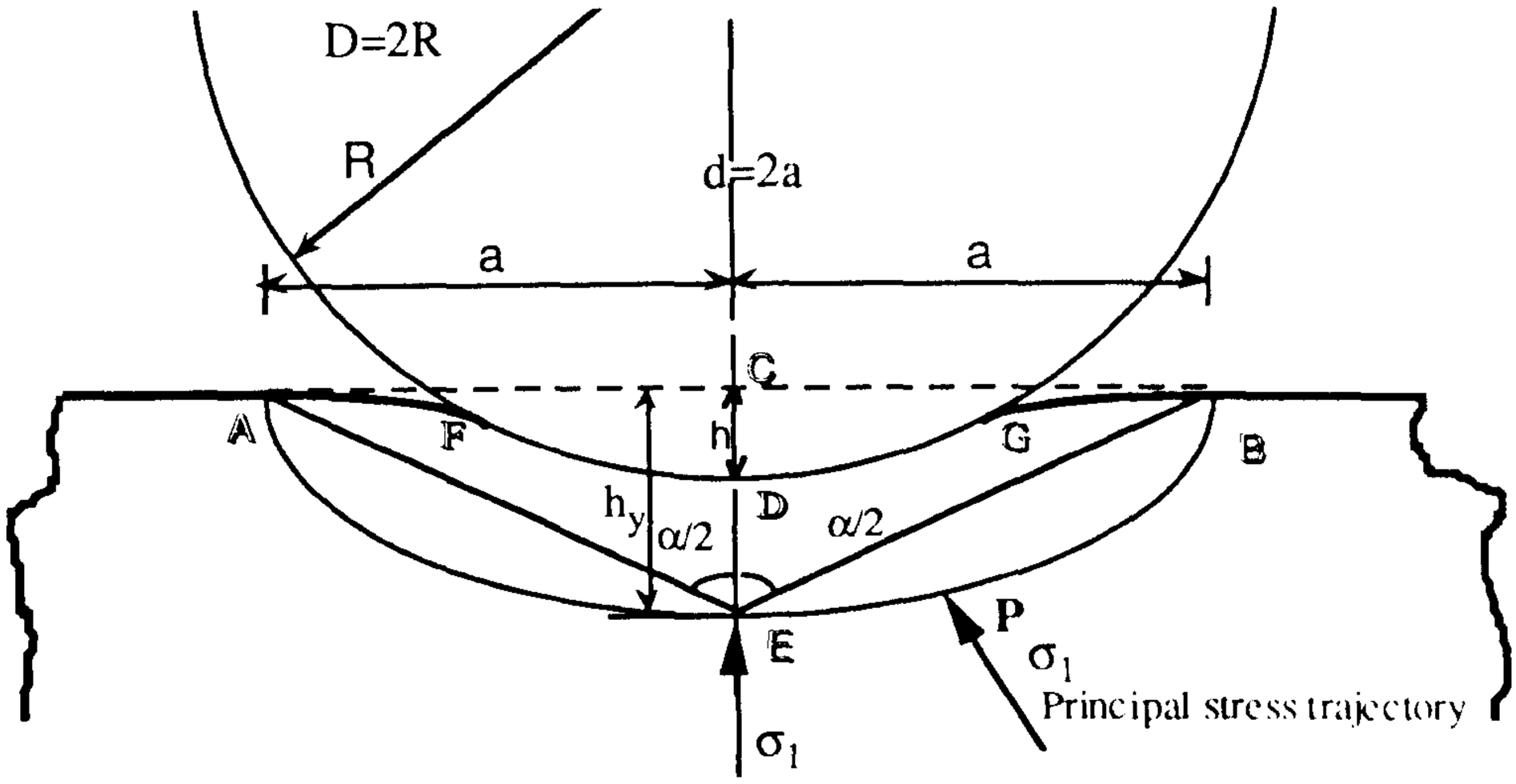

Fig. 7.6 The stress system beneath a cylindrical indenter having a uniform indentation pressure. d, h are the diameter and the height of the profile respectively. D= 2R, d= 2a, d/D= a/R.

Figure 7.6 shows the indentation of a flexible foam by a smooth steel cylindrical indenter of radius R and length L under the action of a load P. Suppose, in the first instance, that the indentation pressure is uniform and the foam remains elastic; Timoshenko and Goodier (1934) show that contours of principal stress are circles passing through A and B (e.g. $\overline{AEB}$). The maximum (compressive) principal stress is given by:

$$\sigma_1 = -\frac{P}{2\pi aL}(\alpha + \sin\alpha) \qquad (7.1)$$

Where: $AB = d = 2a$, and α is the angle subtended by $\overline{AEB}$. The trajectories of principal stress bisect the angle α.

The static indentation resilience (or the Meyer's hardness) of the foams, H, was obtained from the force applied to produce a given indentation depth, h, divided by the projected area of the indentation profile (Tabor, 1951),

$$H = P/\pi a^2 . \qquad (7.2)$$

The indentation strain (or Ball Indentation Size), ε, experienced by the foam during the indentation test was calculated according to an empirical formula proposed by Wilsea et al. (1974):

$$\varepsilon = d/D \qquad (7.3)$$

Where: D, is the diameter of the indenter, and d, is the chordal diameter of the ball indentation profile.

Both the Ball Indentation and the Cylinder Indentation Tests were carried out on the ten 10ppi and 30ppi open-cell polyether urethane foams with a range of compression ratios and, hence, with a range of Poisson's ratios (Table 7.2). In total,

20 separate tests were carried out to ensure accuracy. Approximately two hundred and fifty photos were taken. Two repeat tests were made for each type of foam. Average load-displacement data was taken to plot the *Figures* 7.7 to 7.14. The average errors were within 8%.

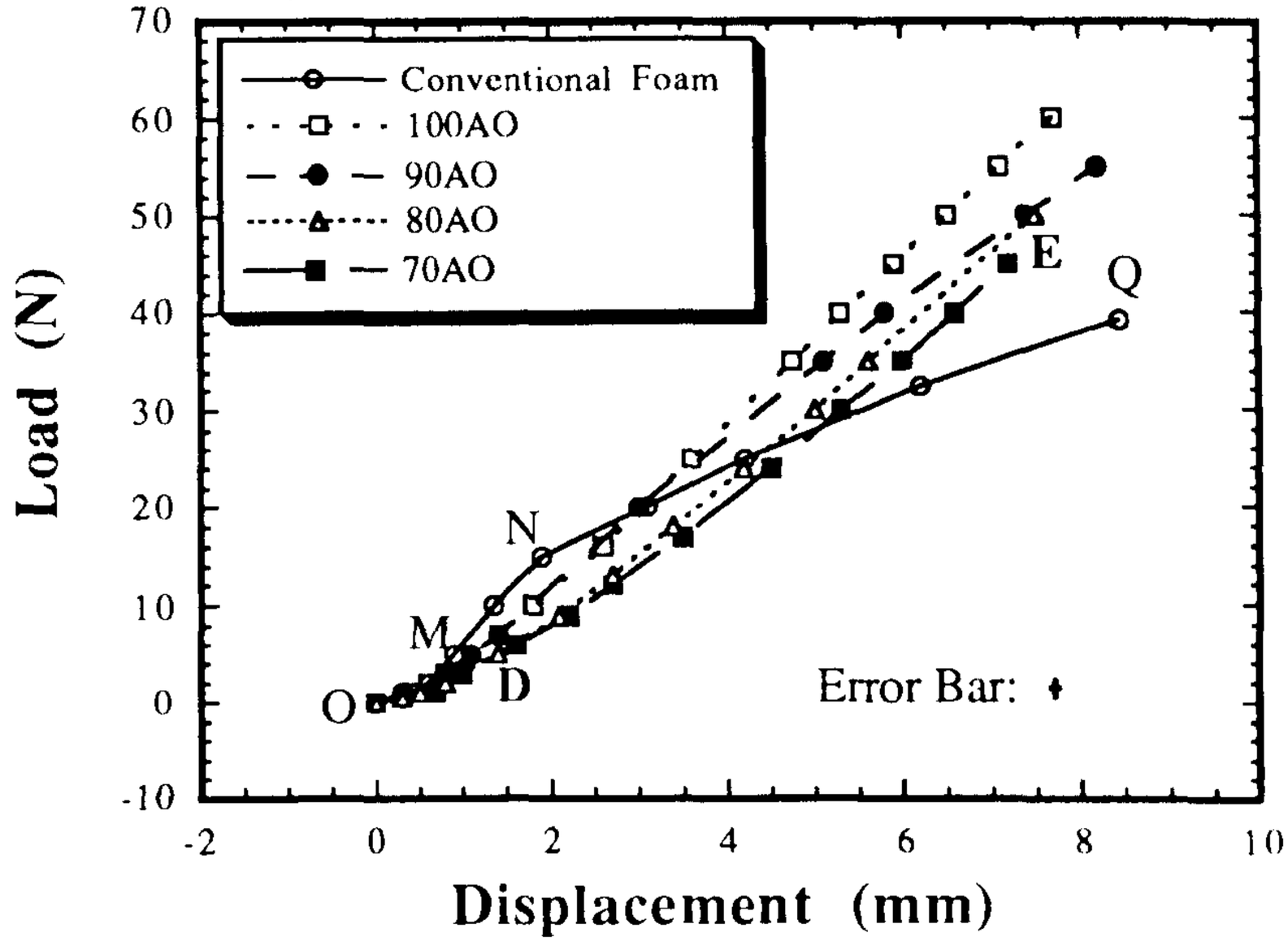

Fig. 7.7 Cylinder indentation load-displacement curves in the foam rise direction for the 10ppi polyether urethane foams. The diameter of the cylindrical indenter is: 22 mm.

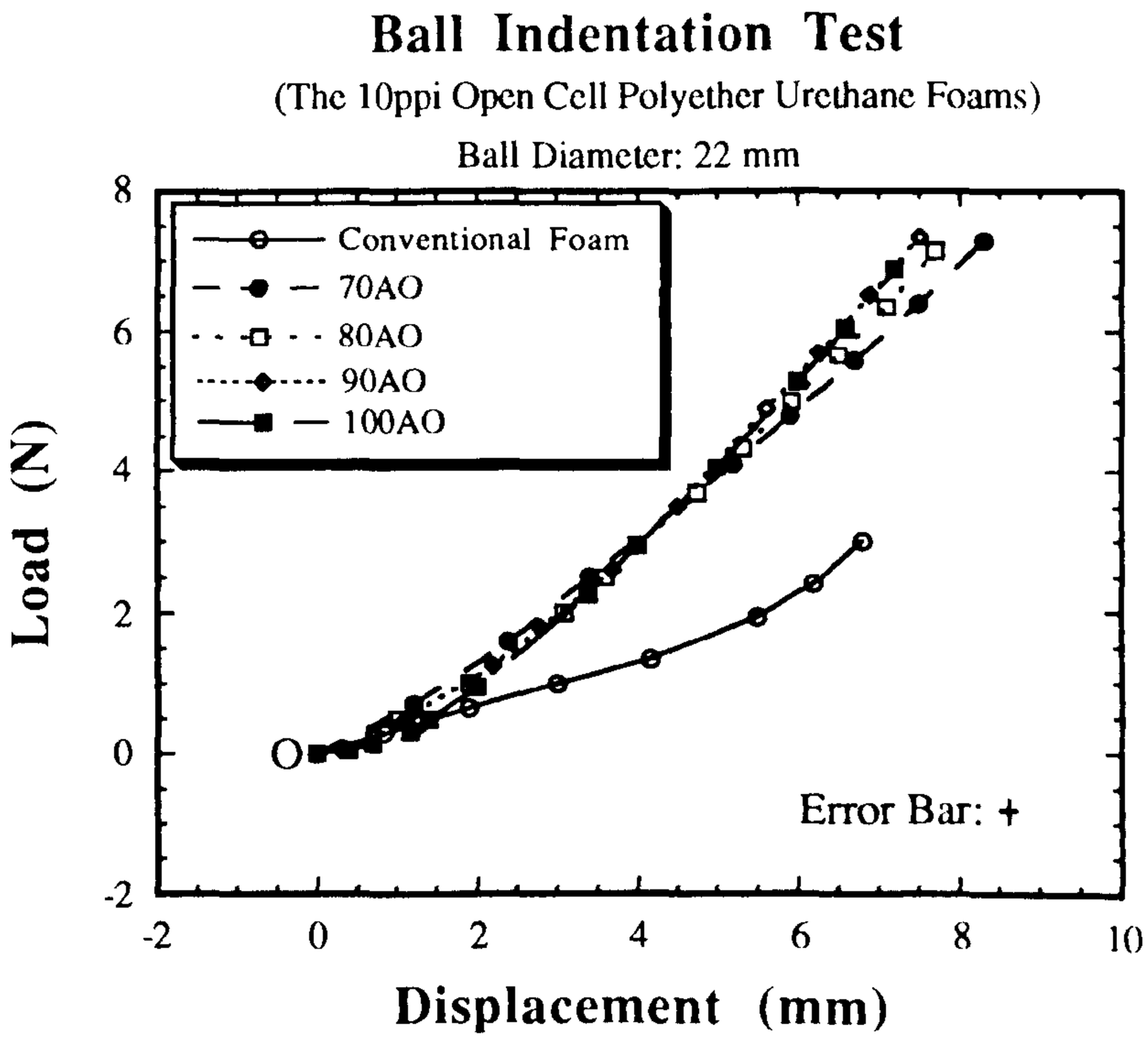

Fig. 7.8 Ball indentation load-displacement curves in the foam rise direction for the 10ppi polyether urethane foams. The diameter of the spherical indenter is: 22 mm.

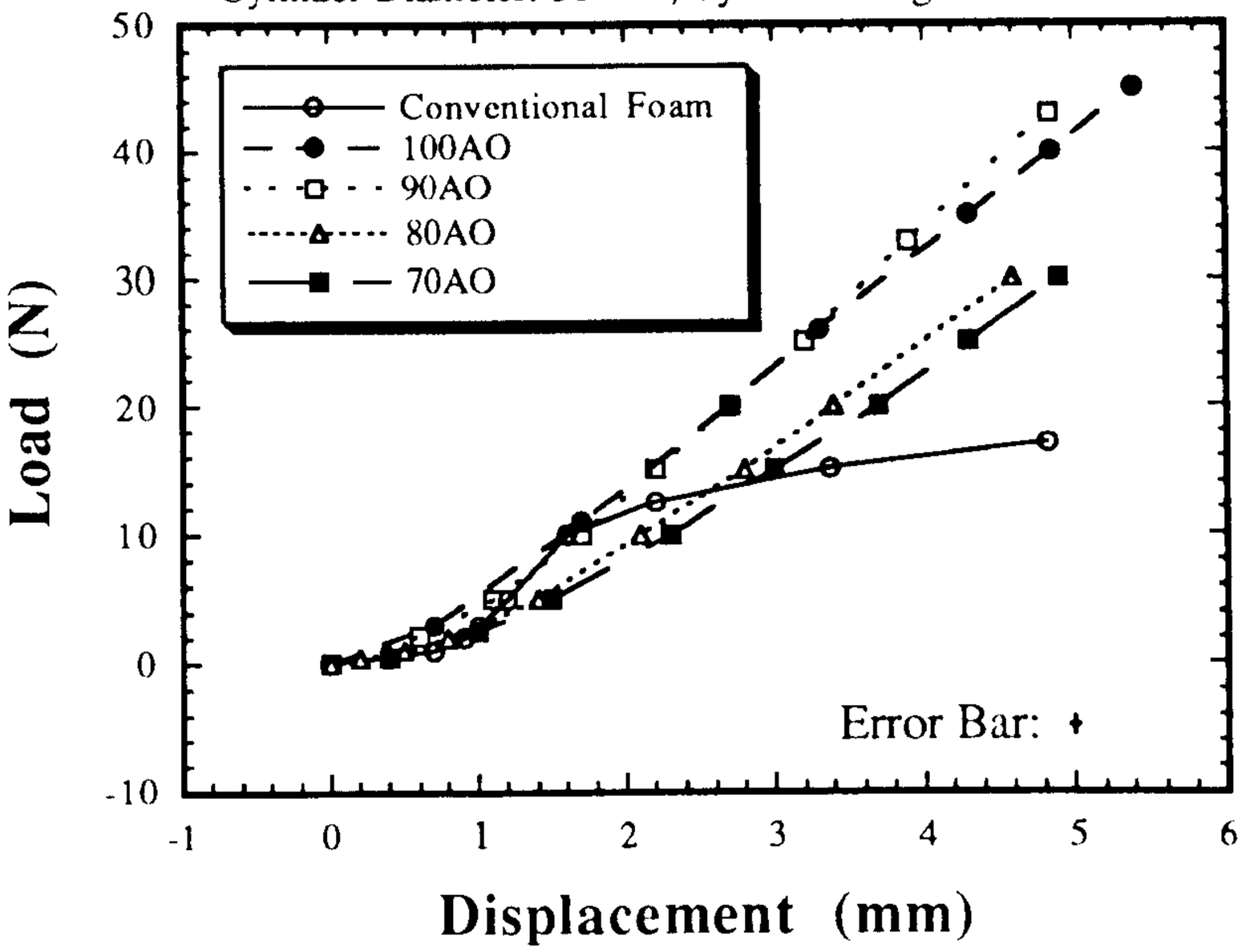

Fig. 7.9 Cylinder indentation load-displacement curves in the foam rise direction for the 10ppi polyether urethane foams. The diameter of the cylindrical indenter is: 50 mm.

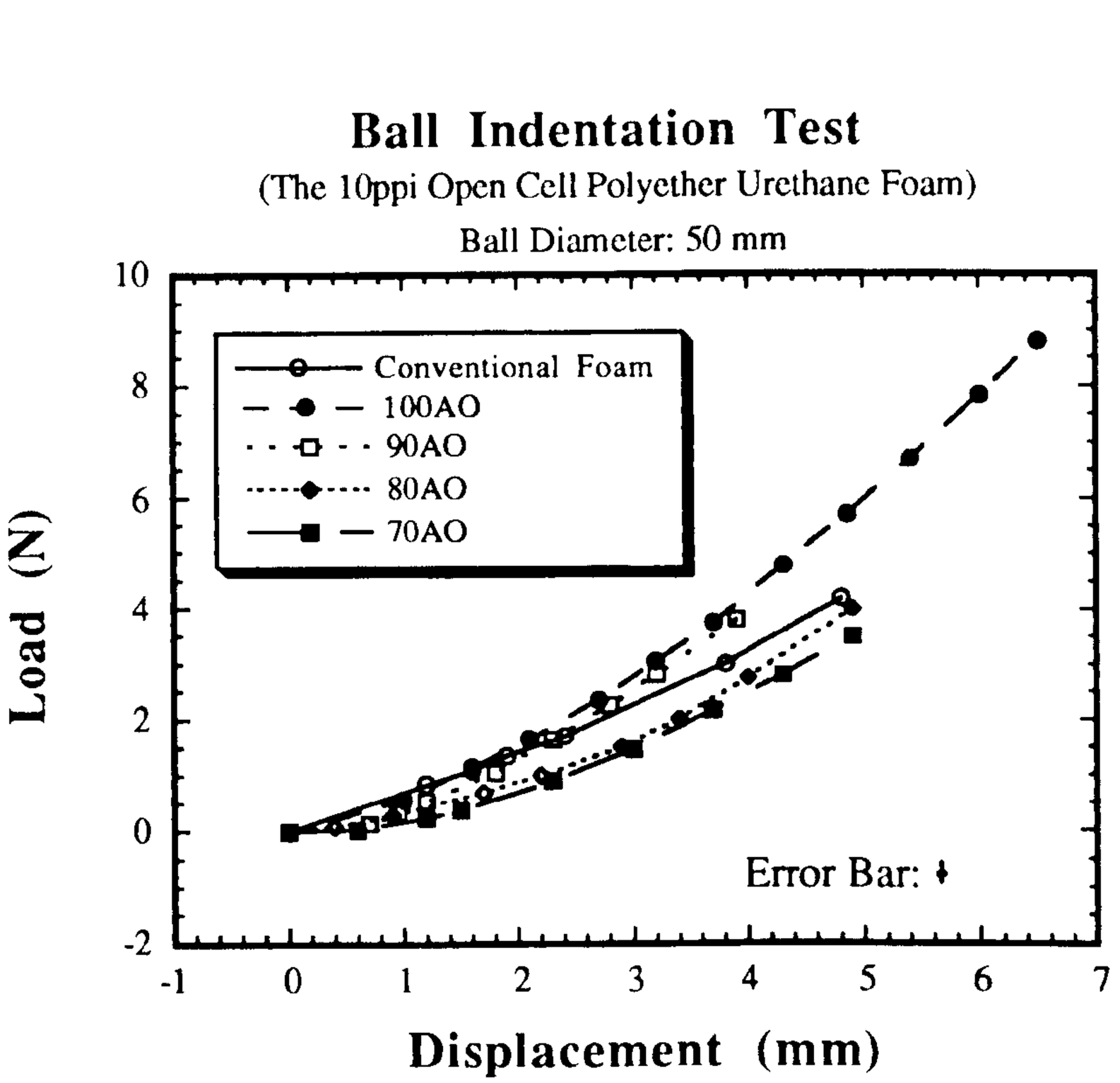

Fig. 7.10 Ball indentation load-displacement curves in the foam rise direction for the 10ppi polyether urethane foams. The diameter of the spherical indenter is: 50 mm.

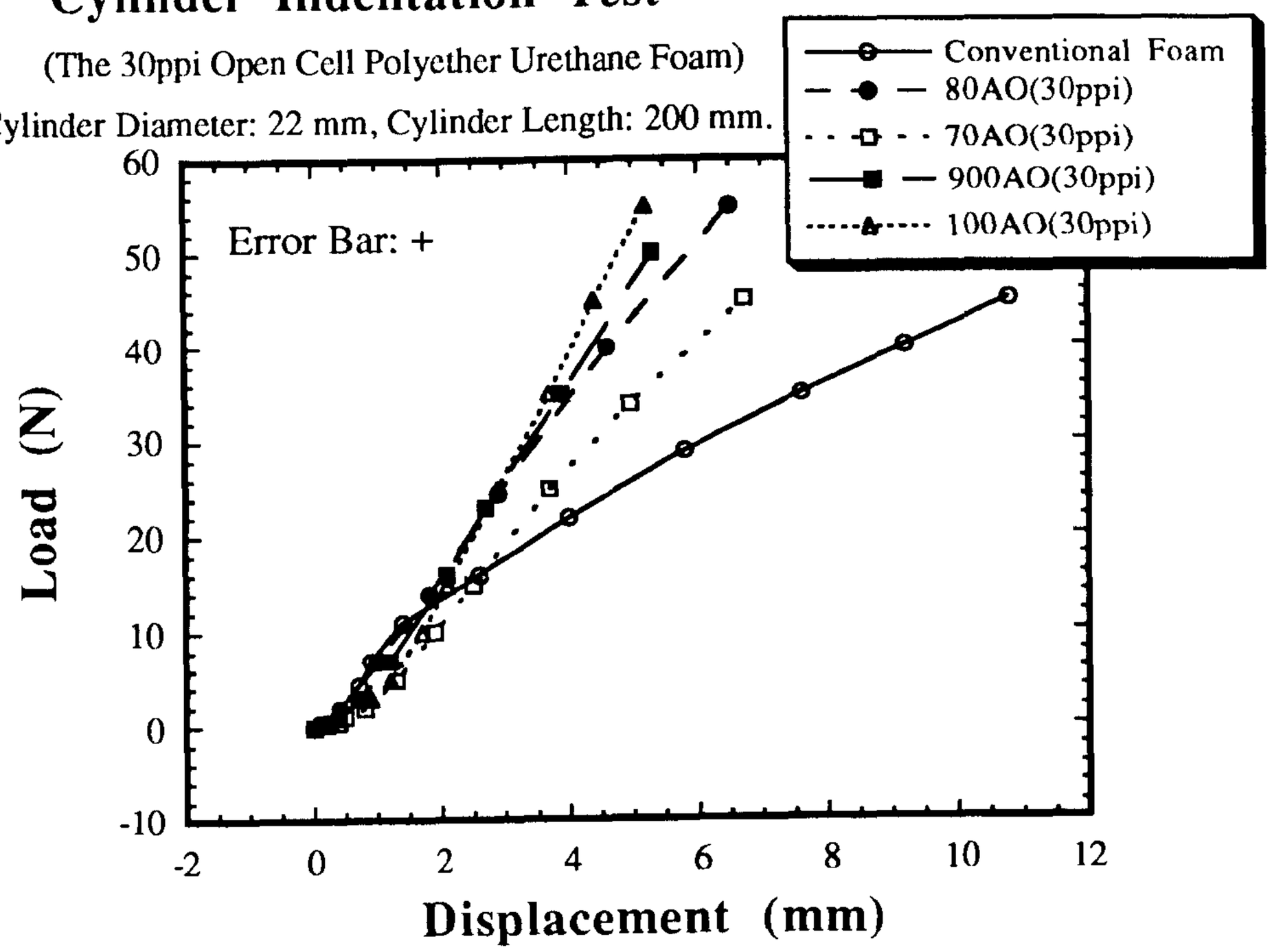

Fig. 7.11 Cylinder indentation load-displacement curves in the foam rise direction for the 30ppi polyether urethane foams. The diameter of the cylindrical indenter is: 22 mm.

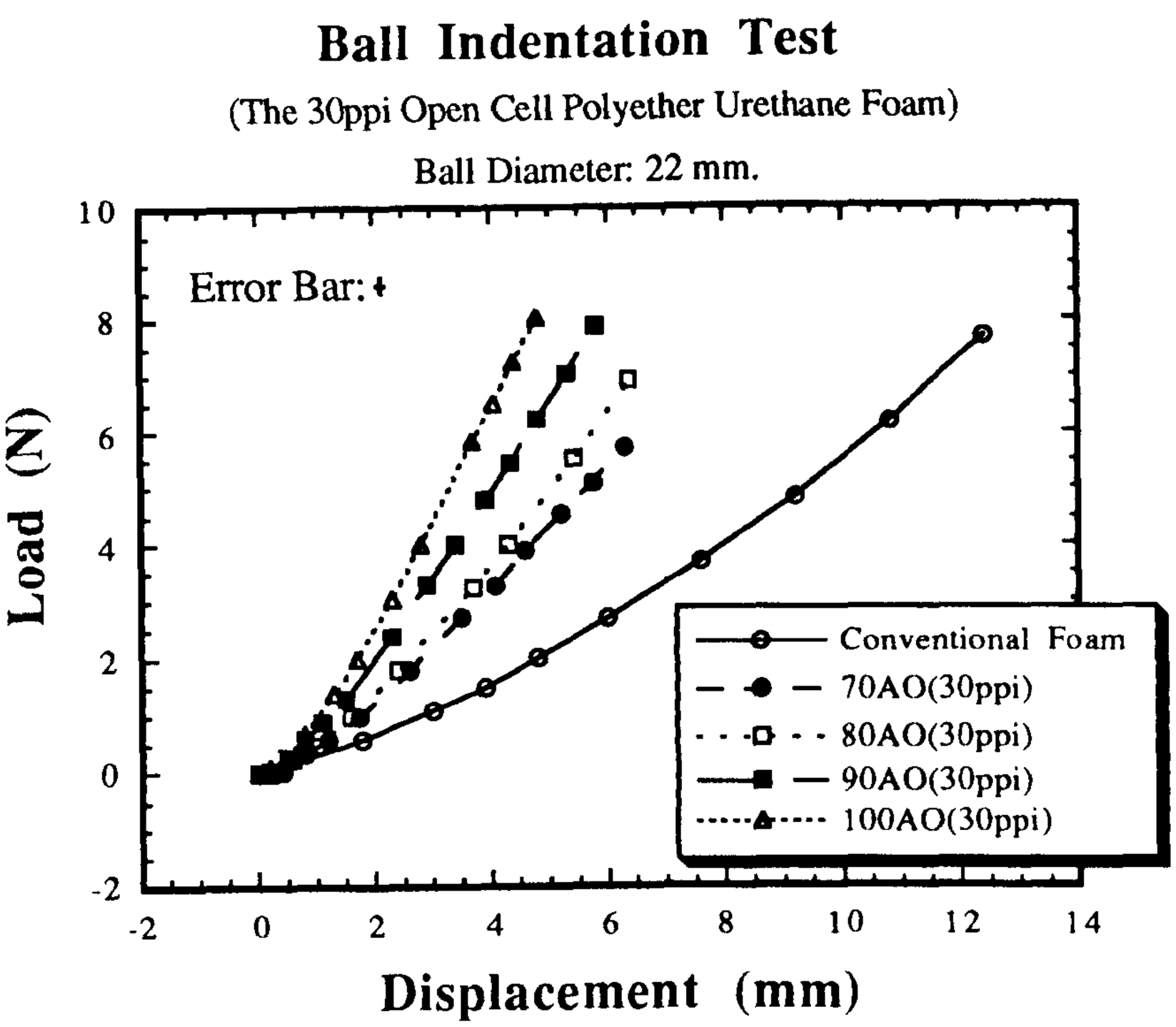

Fig. 7.12 Ball indentation load-displacement curves in the foam rise direction for the 30ppi polyether urethane foams. The diameter of the spherical indenter is: 22 mm.

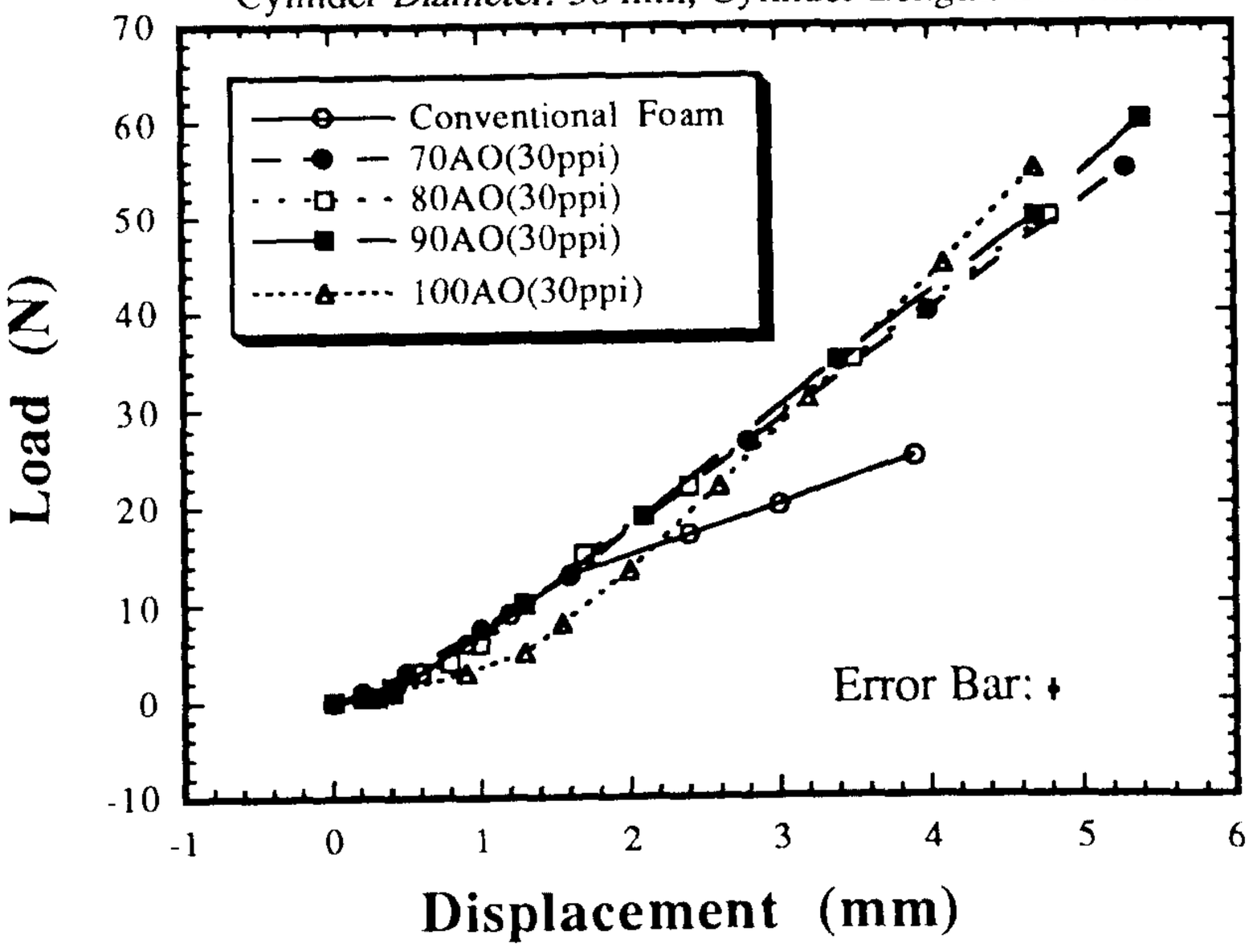

Fig. 7.13 Cylinder indentation load-displacement curves in the foam rise direction for the 30ppi polyether urethane foams. The diameter of the cylindrical indenter is: 50 mm.

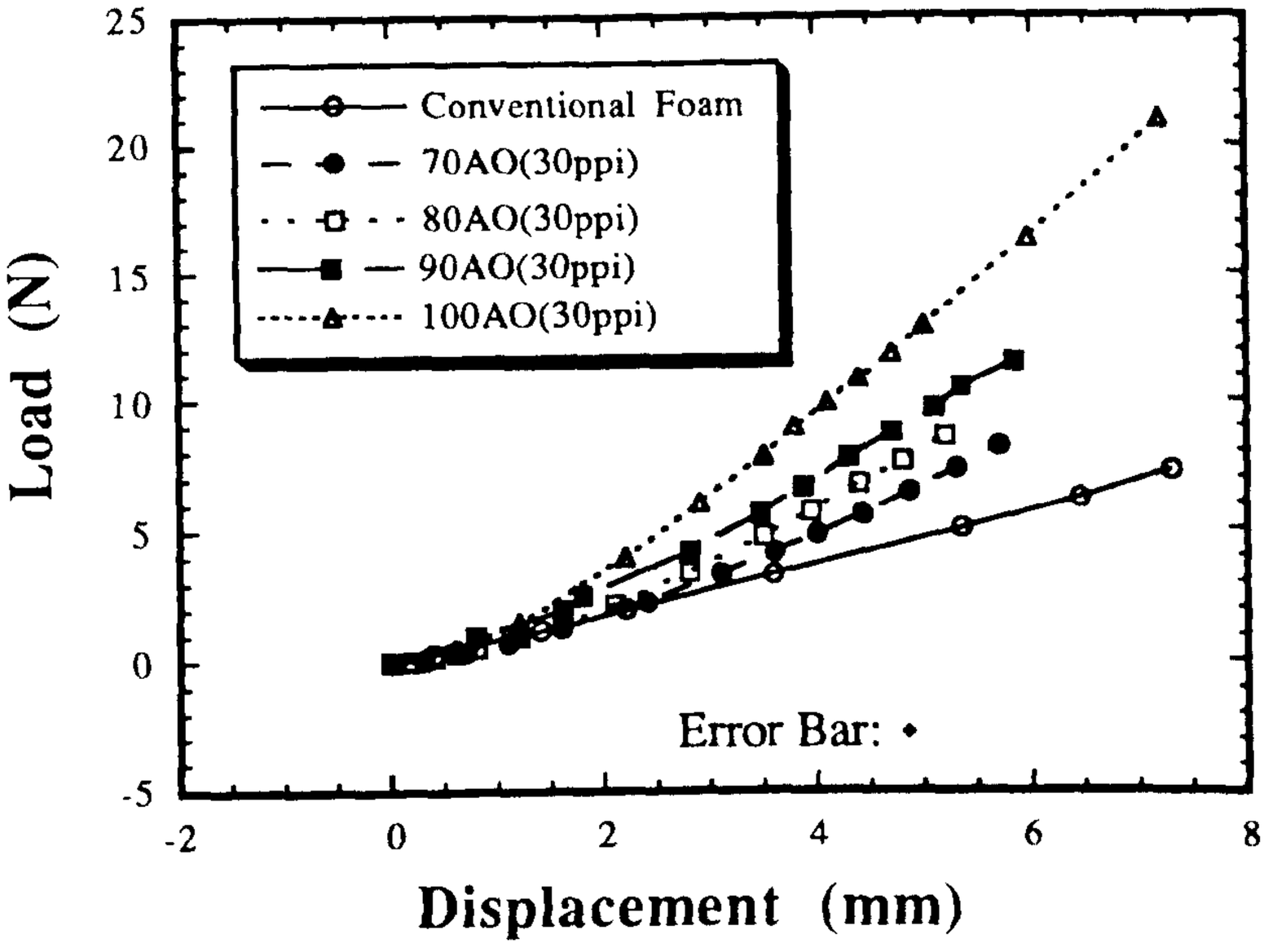

Fig. 7.14 Ball indentation load-displacement curves in the foam rise direction for the 30ppi polyether urethane foams. The diameter of the spherical indenter is: 50 mm.

Figures 7.7 to 7.14 show that the shape of the load-displacement curve for the cylinder and ball indentation of conventional foam is different from that of an auxetic foam. There are three regions in the conventional foam load-displacement curve. The first very short linear elastic region, OM, is followed by a rapid elastic strain hardening region, MN. The gradient of the third region, NQ, is higher than that of the first region, OM, but is much smaller than that of the second region MN. Whereas, the load-displacement curve of auxetic foam can only be divided into two parts (see Figure 7.7). The first region, OD, having a relatively low slope, is followed by a region, DE, where there is a increase in displacement for a large increase in load. The mechanical behaviour of the ball and cylinder indentation is not only dependent on the properties of the cell ribs and the diameter of the indenter, but also on the cell geometry of the foams. In order to show the latter clearly, I have to put in some photographs of the cylinder indentation of honeycombs, see Figures 7.15 and 7.16. Since honeycombs are actually two dimensional foams, and usually have a much bigger cell size, we may be able to use them as an example to show the mechanisms involved in the local indentation.

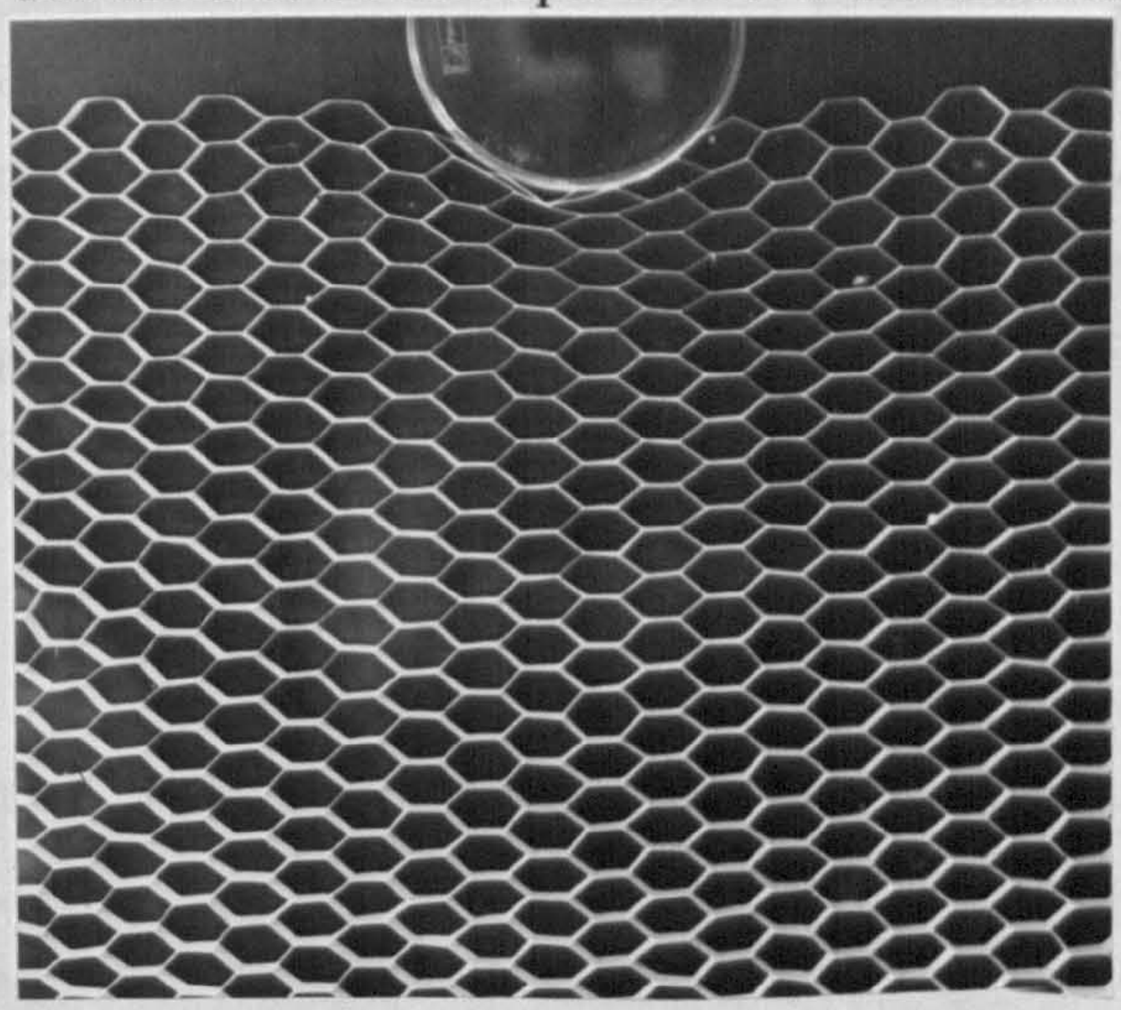

Fig. 7.15 Compressive deformation of the conventional honeycomb produced by a cylindrical indenter.

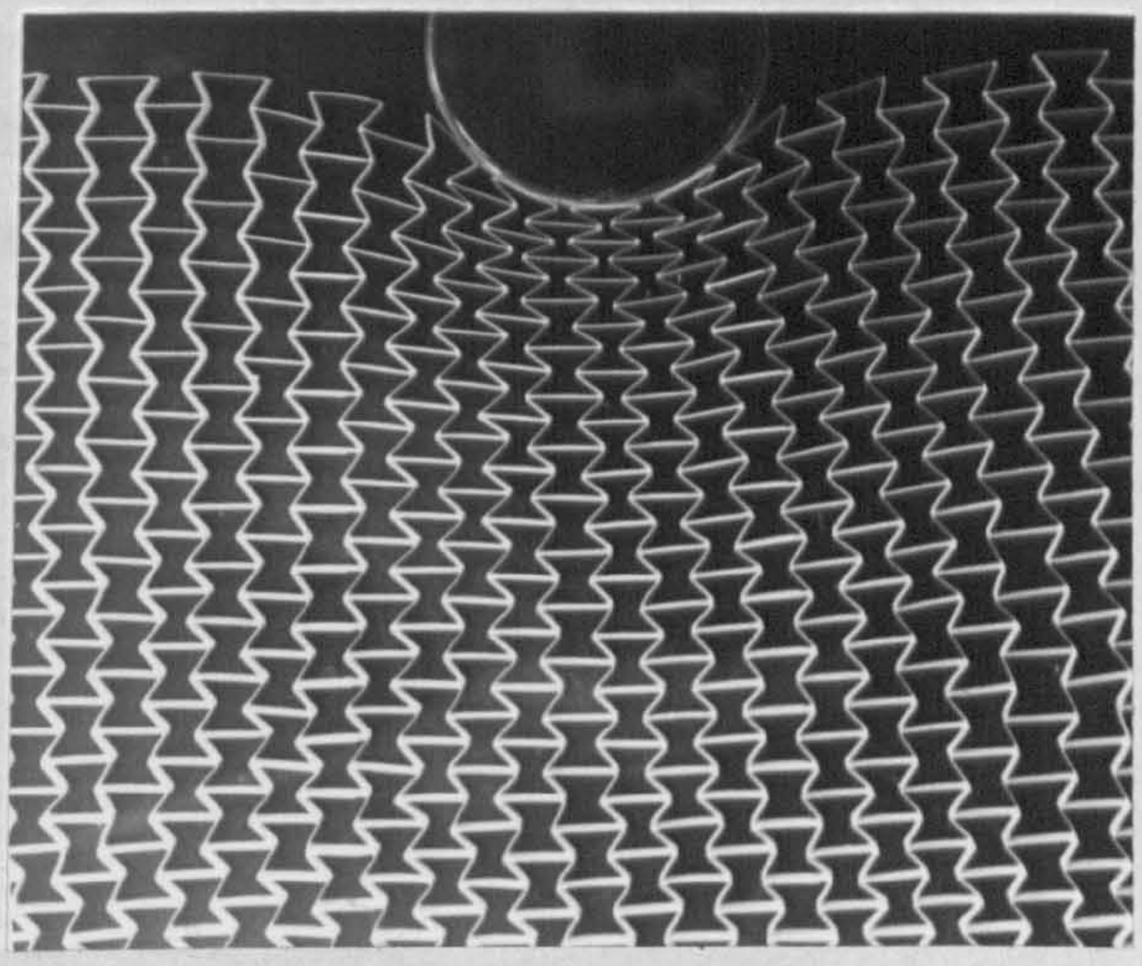

Fig. 7.16 Compressive deformation of the auxetic honeycomb produced by a cylindrical indenter.

Figures 7.15 and 7.16 show that, only the local area has deformed when a cylindrical indenter was indented into the conventional honeycomb, and that the cell ribs next to the indenter have failed (collapsed) due to flexure. Whereas, the large area deformed when a cylindrical indenter was indented into the auxetic honeycomb, none of the cell ribs failed. Hinging is the dominant deformation mode. This may suggest that auxetic material may be a better packaging material.

7.2 The Indentation Stress-Strain Curves

The average compressive stress, P, in the cylinder indentation was calculated by

$$P = \frac{F}{L \times d} \qquad (7.4)$$

Where: F, is the compressive load, L, is the length of the cylinder and d, is the chordal diameter of the indentation profile (see Figure 7.6) which were measured from the photographs (For example, see Figures 7.4 and 7.5). The cylinder indention strain was calculated by using EQ. 7.3. The results are shown in Figures 7.17 to 7.20.

The compression stress in the ball indentation is not simple to calculate. The approach used was as follows. Firstly, the ball indentation sizes (e.g. d, the chordal diameter of the indentation profile, and h, the height of the indentation profile) were measured from the cylinder indentation test using the photographic method. Then, the corresponding value of the compressive load, F, for each displacement, h, was obtained from the ball indentation load-displacement curve. The value of the ball indentation area, A, associated with each value of the displacement, h, was calculated by, $\frac{\pi d^2}{4}$. The ball indentation stresses and strains for all the tests were calculated by using EQ. 7.2 and EQ. 7.3 respectively. The results are shown in *Figures* 7.21 to 7.24. The average errors were within 12%.

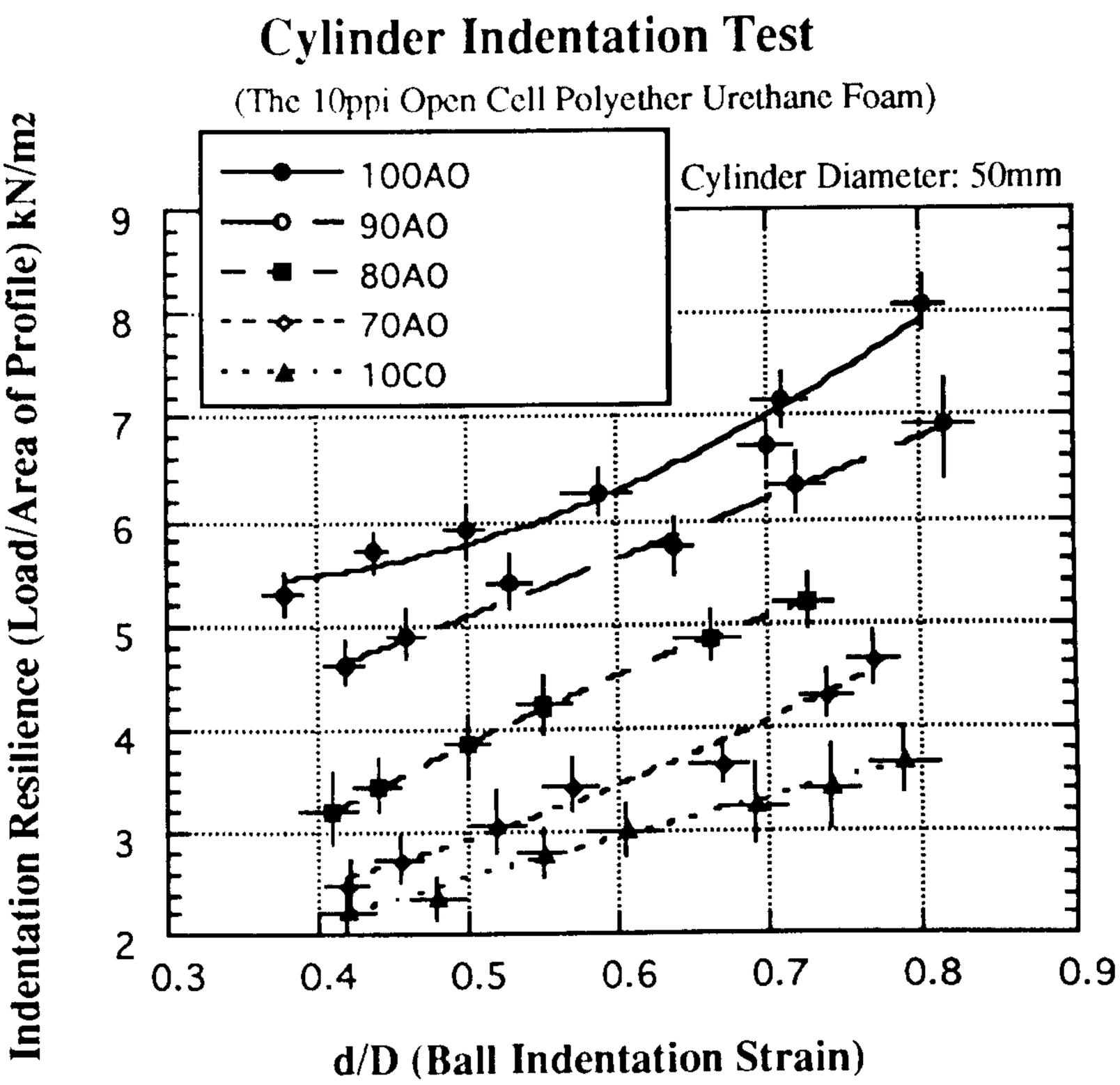

Fig. 7.17 Cylinder Indentation stress-strain curves in the foam rise direction for the 10ppi open cell polyether urethane foams. The diameter of the spherical indenter is: 50 mm.

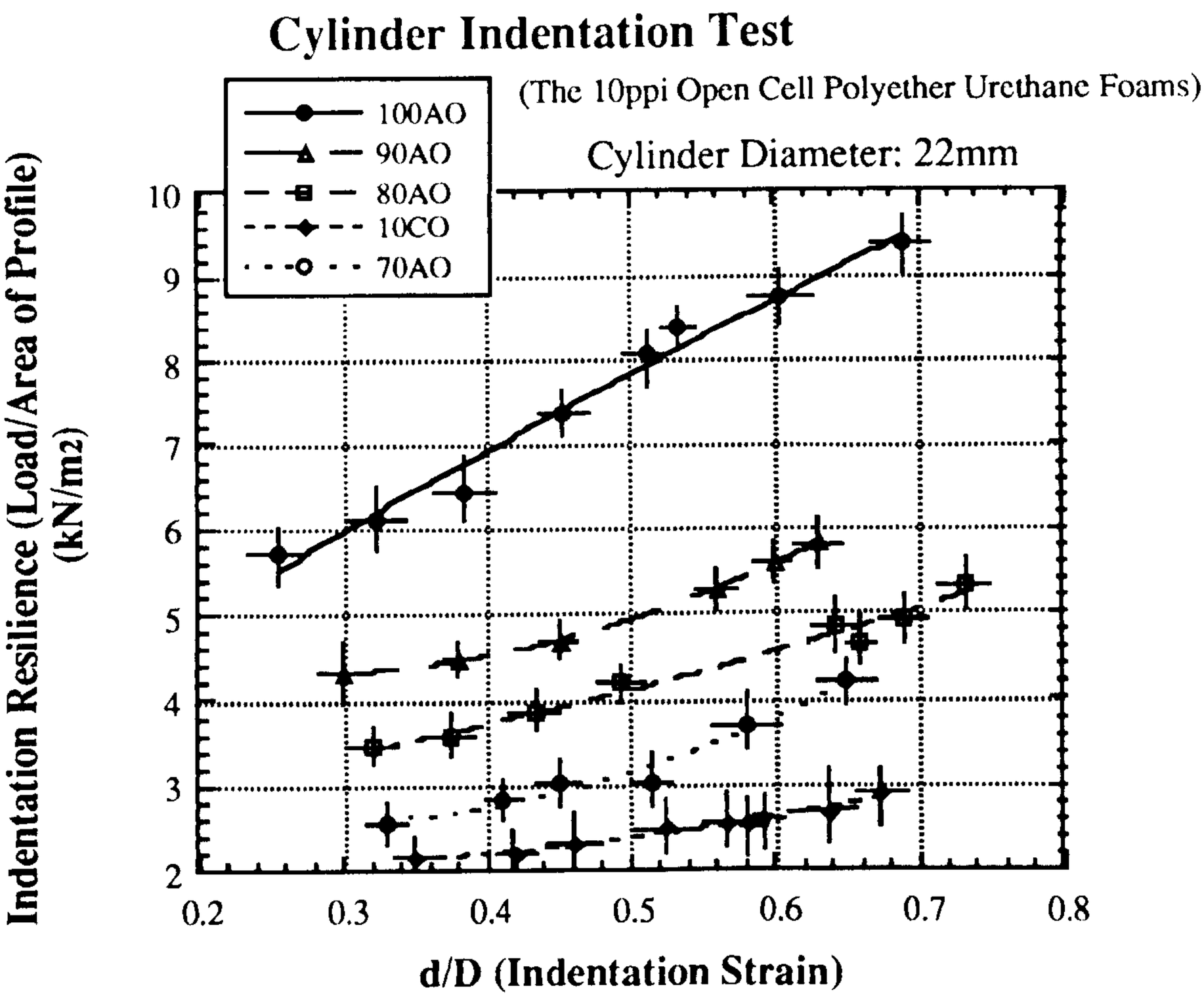

Fig. 7.18 Cylinder Indentation stress-strain curves in the foam rise direction for the 10ppi open cell polyether urethane foams. The diameter of the spherical indenter is: 22 mm.

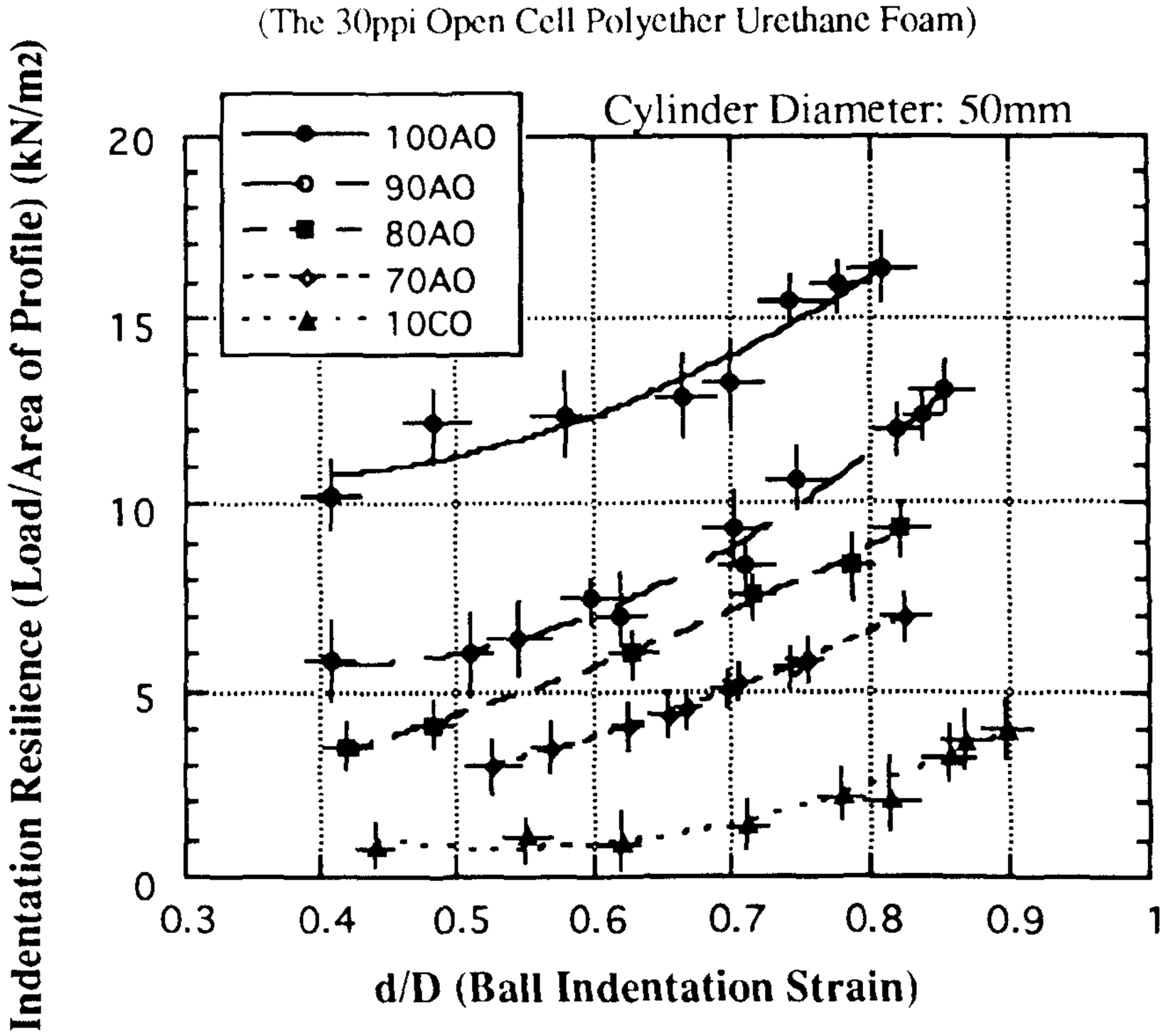

Fig. 7.19 Cylinder Indentation stress-strain curves in the foam rise direction for the 30ppi open cell polyether urethane foams. The diameter of the spherical indenter is: 50 mm.

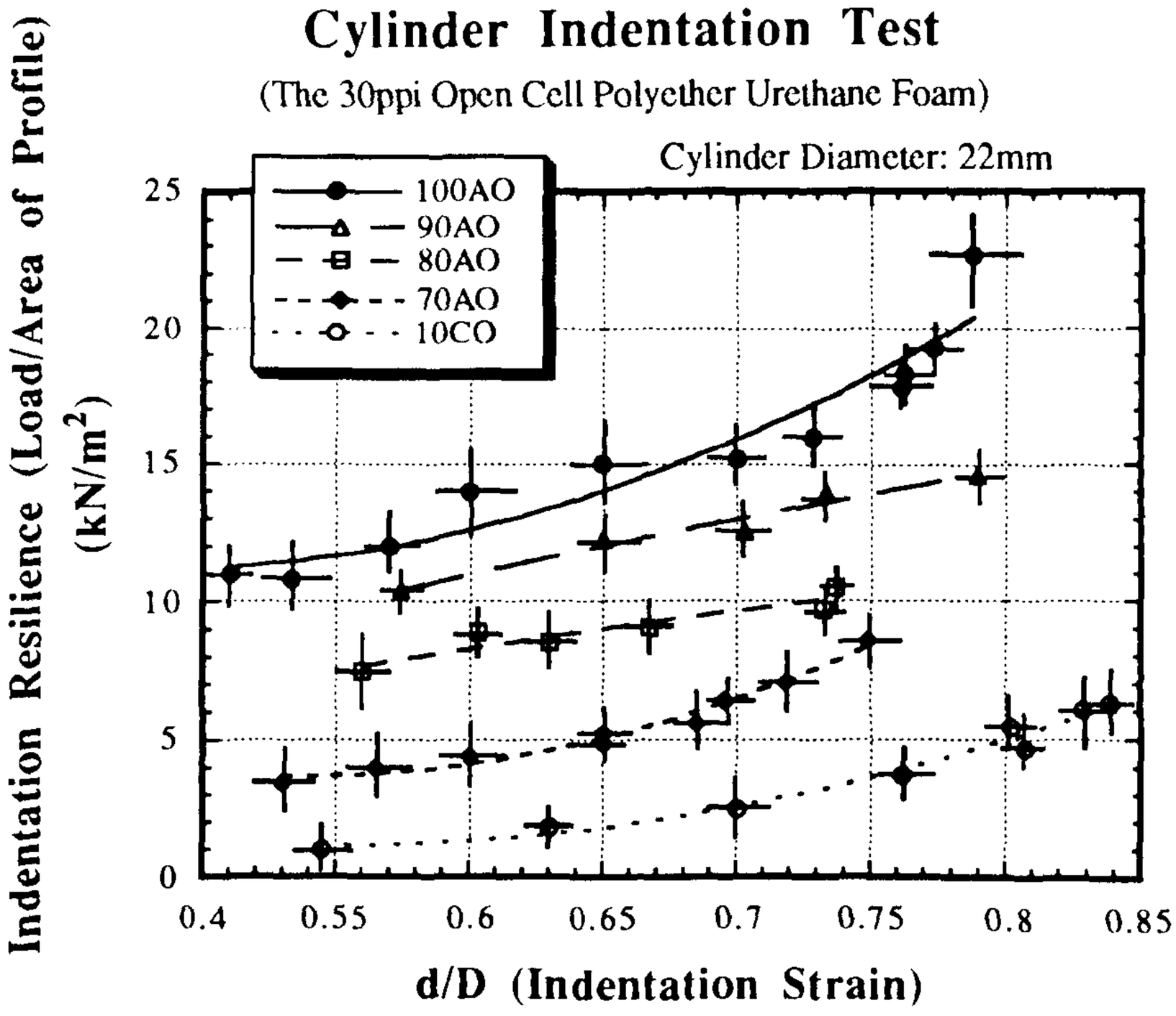

Fig. 7.20 Cylinder Indentation stress-strain curves in the foam rise direction for the 30ppi open cell polyether urethane foams. The diameter of the spherical indenter is: 22 mm.

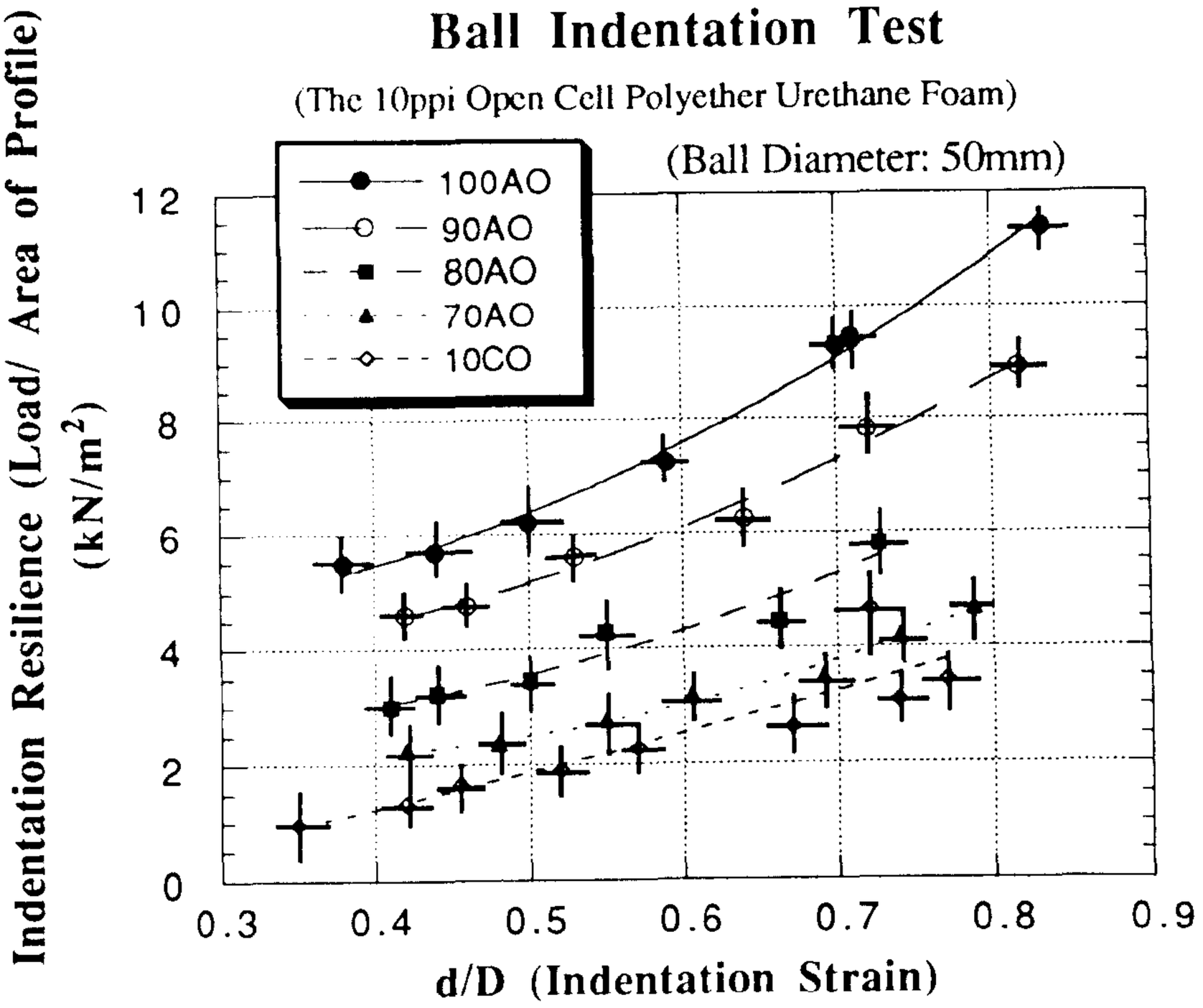

Fig. 7.21 Ball Indentation stress-strain curves in the foam rise direction for the 10ppi open cell polyether urethane foams. The diameter of the spherical indenter is: 50 mm.

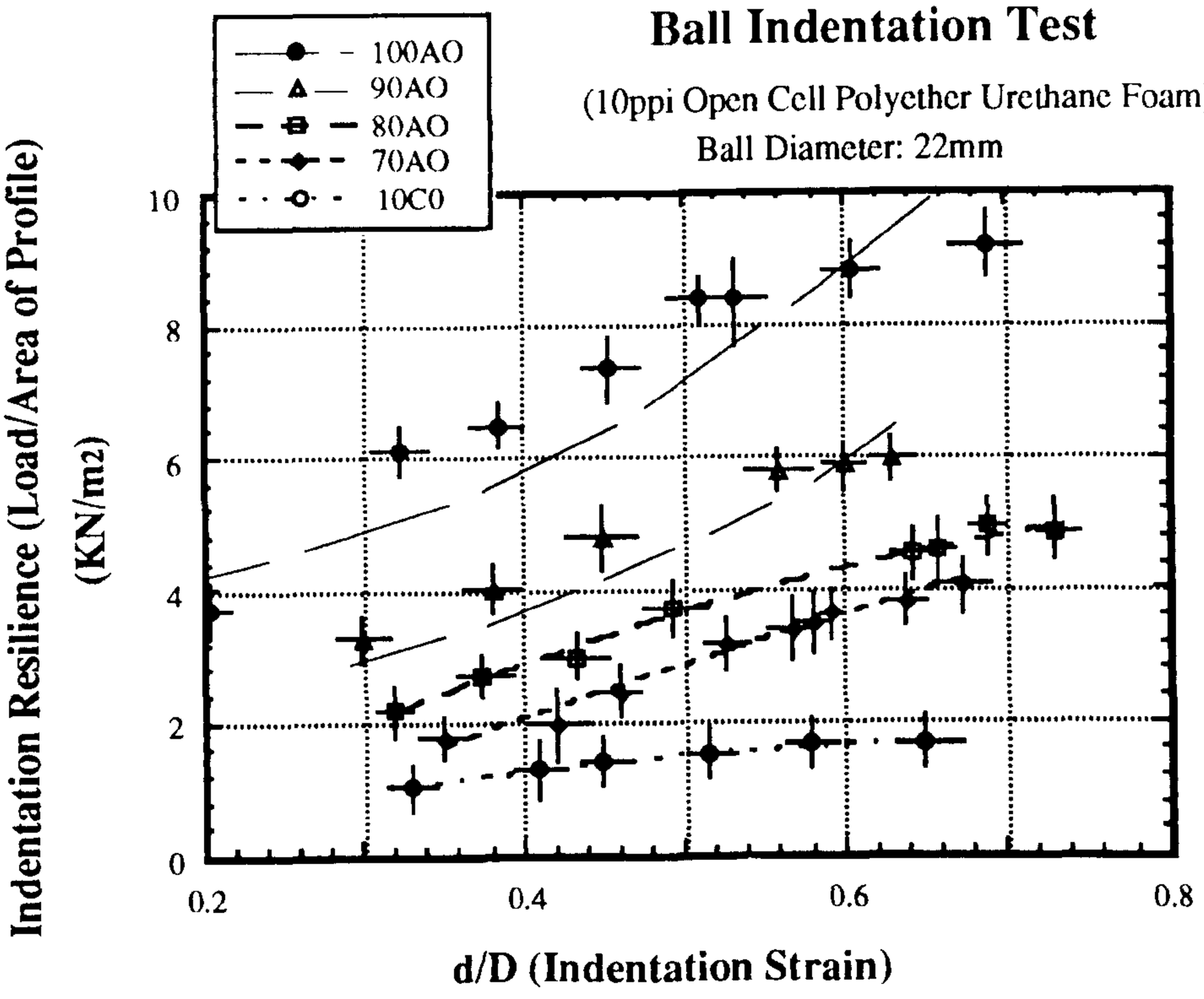

Fig. 7.22 Ball Indentation stress-strain curves in the foam rise direction for the 10ppi open cell polyether urethane foams. The diameter of the spherical indenter is: 22 mm.

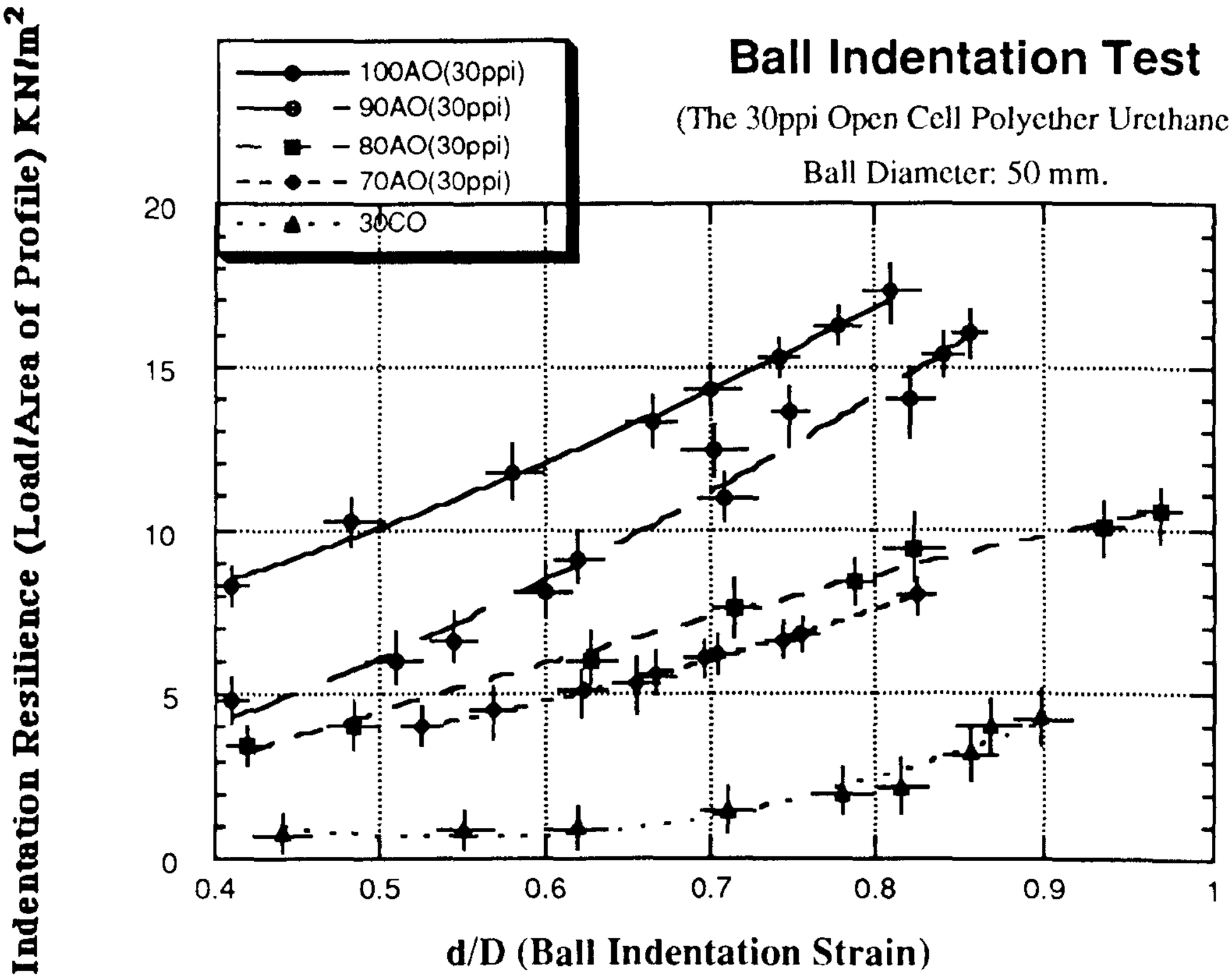

Fig. 7.23 Ball Indentation stress-strain curves in the foam rise direction for the 30ppi open cell polyether urethane foams. The diameter of the spherical indenter is: 50 mm.

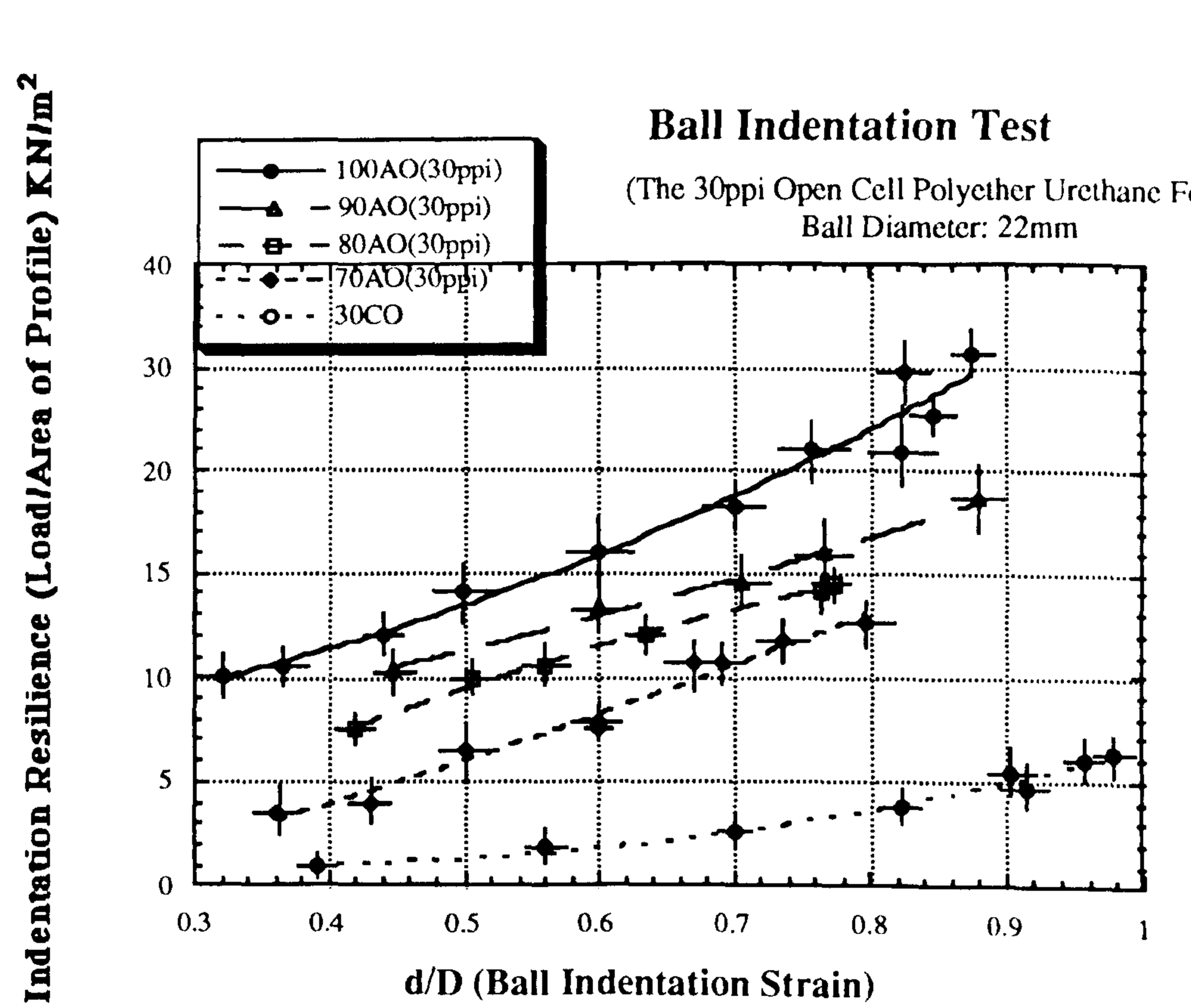

Fig. 7.24 Ball Indentation stress-strain curves in the foam rise direction for the 30ppi open cell polyether urethane foams. The diameter of the spherical indenter is: 22 mm.

Figures 7.17 to 7.24 show that, in each case there is a substantial gain in indentation resilience for the auxetic foam specimens compared with the conventional foams. In addition the following features are apparent:

1. The indentation resilience of a foam increases slowly with the ball (or cylinder) indentation strain.
2. The incompressibility of the foam increases more rapidly with the strain when the indentation material is auxetic.
3. The indentation stress-strain curves are not strongly dependent on the diameter of the indenter. They depend on the cell structure and the cell rib property of the foam.

7.3 Hysteresis Loop

As part of the investigation of the non-linear elastic mechanical properties of foams the hysteresis loops were examined. The hysteresis loops of the 10ppi polyether foams (10CO, 70AO and 80AO) are shown in Figures 7.25 (a), (b) and (c). All of these examples of hysteresis loss were measured by applying a force to a foam (dimensions: 200 x 200 x 50 mm, and the average error is ±0.5 mm) using a Instron 1185 at a cross head speed of 2 mm/min. over the same deflection of 2.8 mm and then allowing the foam to relax back to zero deflection by reversing the movement of the cross-head at a fixed rate of 2 mm/min. The areas within the loop reflect the loss of energy per cycle. In general the lost energy is dissipated as heat.

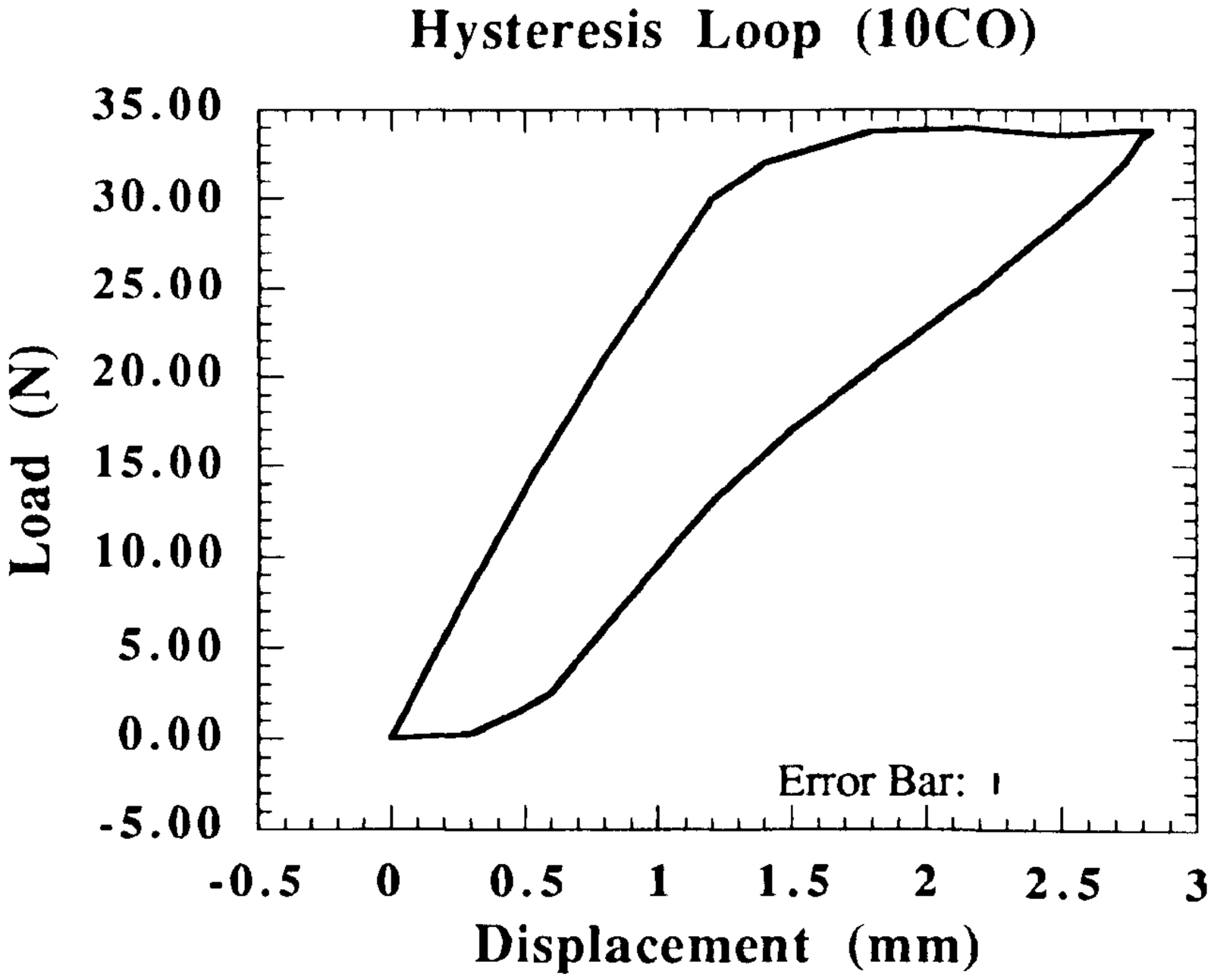

Fig. 7.25(a) The hysteresis loop for the 10ppi open-cell conventional polyether urethane foam (10CO). *Note: The foam was tested along the foam rise direction.*

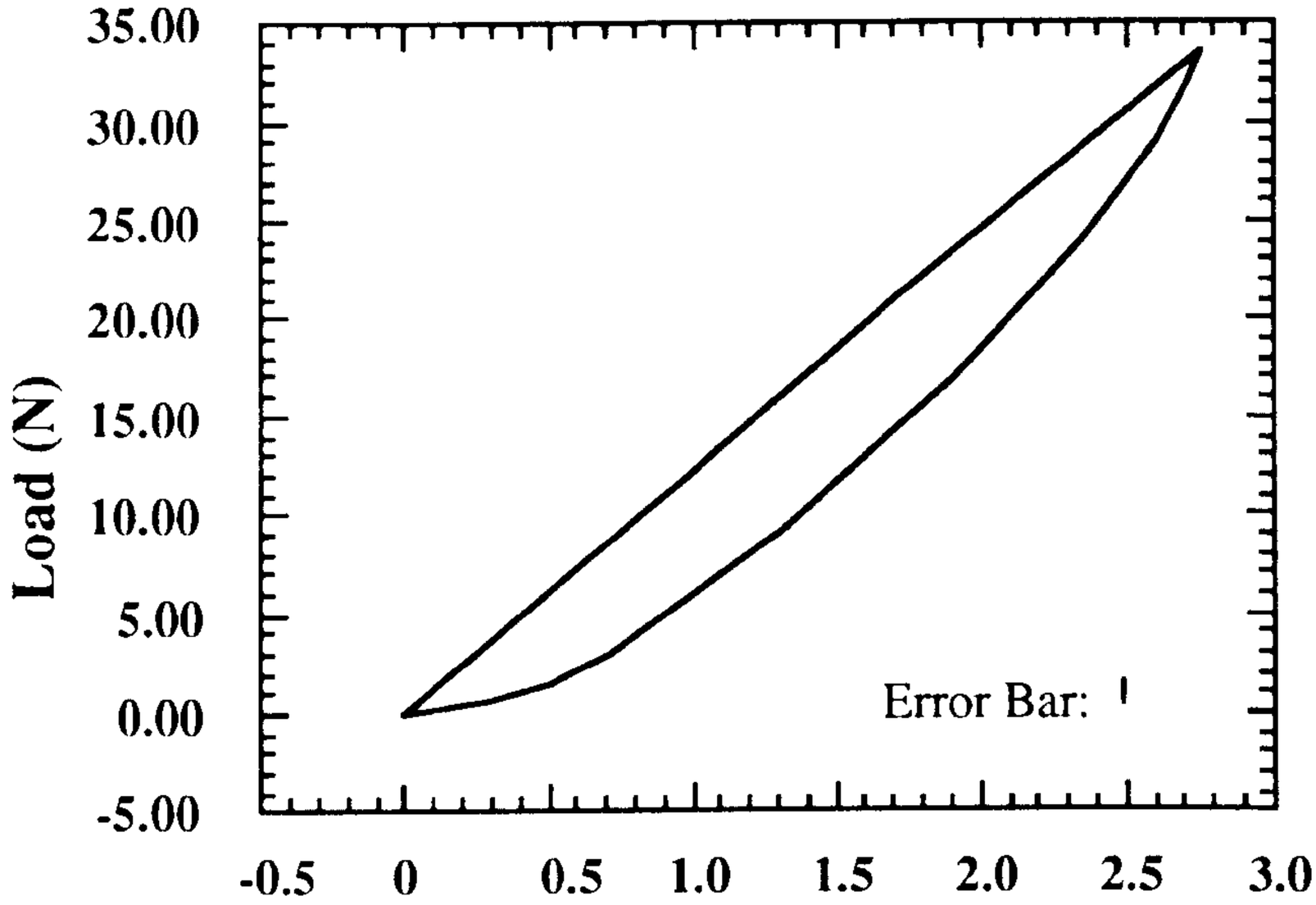

Fig. 7.25(b) The hysteresis loop for the 10ppi open-cell auxetic polyether urethane foam (70AO). Note: The foam was tested along the foam rise direction.

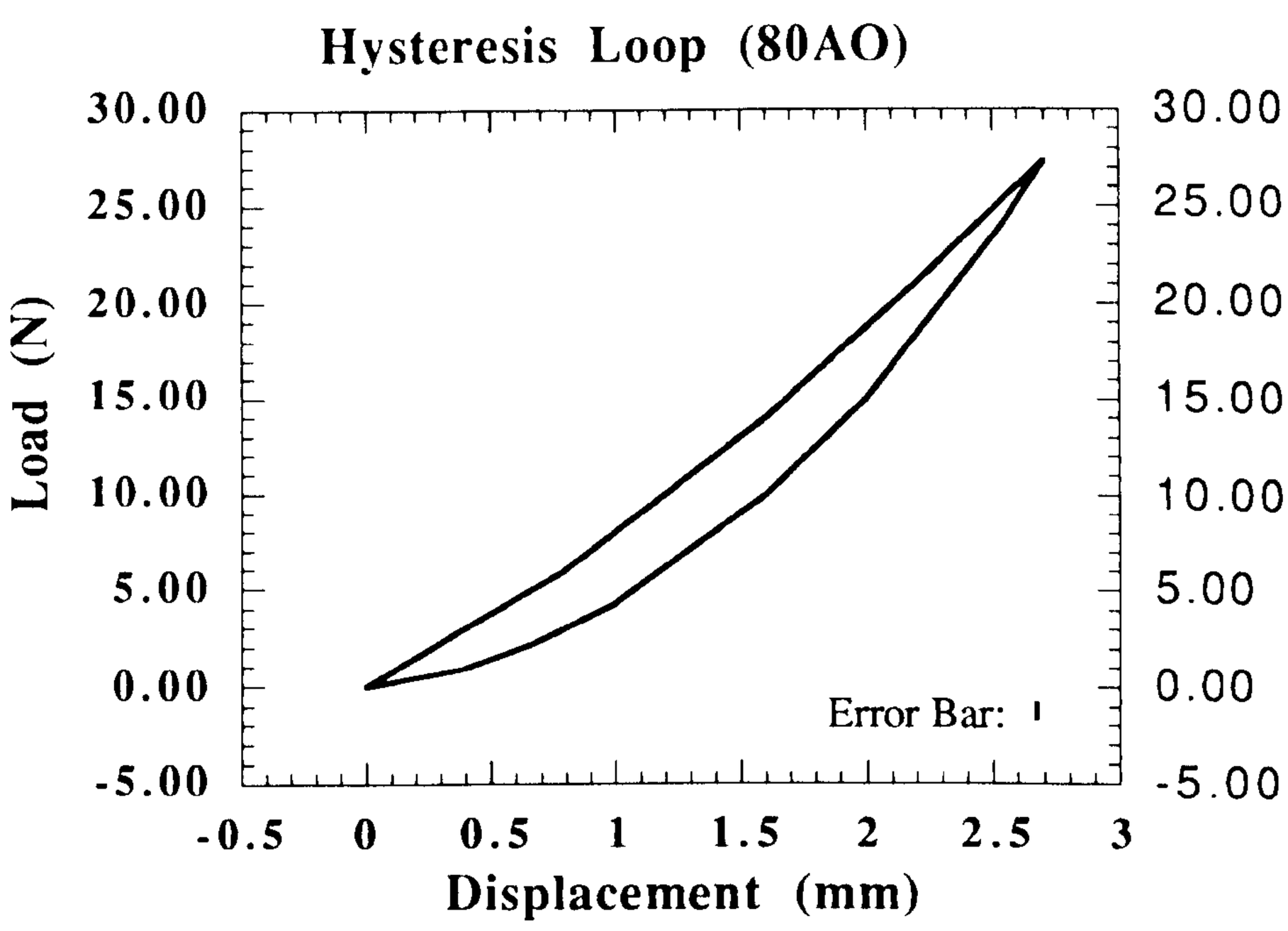

Fig. 7.25(C) The hysteresis loop for the 10ppi open-cell auxetic polyether urethane foam (80AO). Note: The foam was tested along the foam rise direction.

Figures 7.25(a), (b) and (c) show that the area within the hysteresis loop of auxetic foam is much smaller than that of the conventional foam. Hysteresis is a

measure of the energy lost by a foam when subjected to a deformation cycle. Therefore, at small strain and low strain rate the energy lost by an auxetic foam is less than that of conventional foam, and an auxetic foam with a higher negative Poisson's ratio (e.g. 80AO) has a smaller energy loss than auxetic foam with a lower negative Poisson's ratio (e.g. 70AO).

Energy loss is also strain rate dependent as shown in *Figure* 7.26. High strain rates may cause the foam to lose more energy.

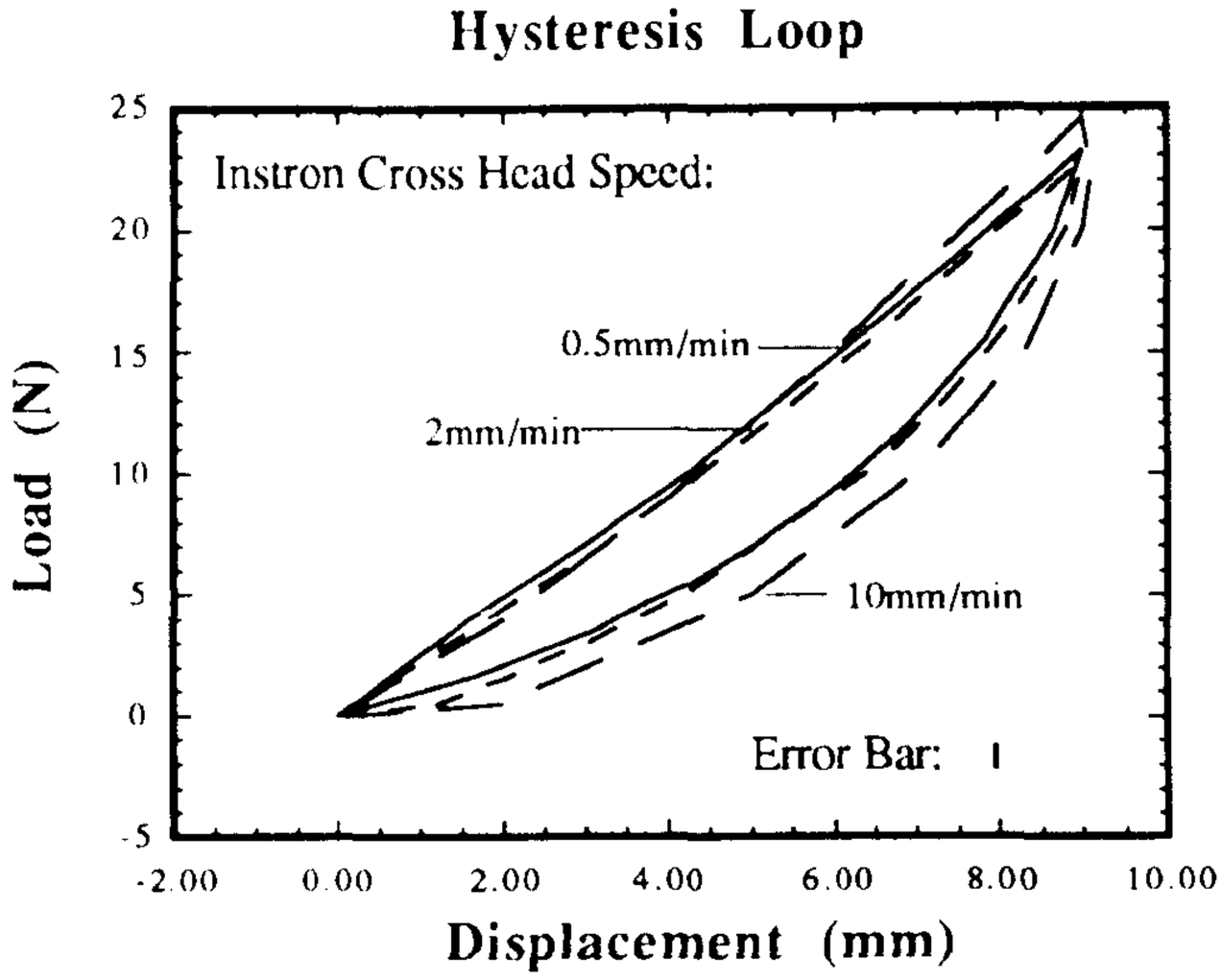

Fig. 7.26 Diagram of the hysteresis loop for the 30ppi open-cell auxetic polyether urethane foam (30ppi, 100AO), showing strain rate dependence. Note: The foams were tested along the foam rise direction.

Foams with a high level of hysteresis show poor energy absorption, since the energy lost in the loading and unloading cycle is not able to do work. The net result of this may be either: deformation of the original shape of the foam, or the foam may be slow in regaining its original configuration. A ball or some other light object when dropped into the foam surface may show a low rebound. In contrast to a conventional foam, an auxetic foam has low hysteresis and will have a high rebound for the same object dropped from an identical height.

7.4 The Ball Rebound Test (Dynamic Indentation Resilience)

An alternative measure of energy absorption by a foam is the ball rebound test. This explores a higher frequency range than does the hysteresis loop measurement.

In cushioning and packaging, the aim is to absorb any kinetic energy imparted to the packaged object, to keep the item being protected from damaged. An

investigation using the ball rebound test was carried out to compare the capacity of auxetic foam with conventional foam to dissipate energy.

According to ASTM D 3574-91(H), the Ball Rebound Test apparatus consists of a vertical clear plastic tube, such as acrylic, with an inside diameter of 38 mm. Into this tube a steel ball with a diameter of 16 mm (mass: 16.68g) is held and released by an electromagnet as shown in *Figure* 7.27 from a drop height of 500mm.

The steel ball was allowed to fall under gravity onto the foam surface without rotating. Centring of the ball was assured by a recess at the base of the electromagnet. The height of the drop was 500 mm. Since it is more convenient from a practical point of view to note the position of the top of the ball on rebound, the top of the ball when held by the electromagnet was positioned 516 mm above the surface of the foam. The scale on the back of the tube was marked as follows: at intervals of every 1 cm, a complete circle was scribed and at every 0.5 cm a 120^0 arc was scribed. The test specimens were sectioned to dimensions: 100 x 100 x 50 mm. Care was taken to make sure the specimens had parallel top and bottom surfaces. At the beginning of each test, The specimen was centred at the base of the tube and the height of the tube adjusted so that zero rebound was 16 mm above the surface of the foam specimen. Then the ball was released and drppped onto the foam, and the maximum rebound height noted. If the ball struck the tube on the drop or rebound, the value obtained was invalid. This condition is usually due to the tube not being vertical or to irregularities on the specimen surface. Triplicate tests were made on each specimen. Four specimens per sample were tested. The median of the four specimen medians was reported as the ball rebound resilience value of the sample in *Tables* 7.3 and 7.4.

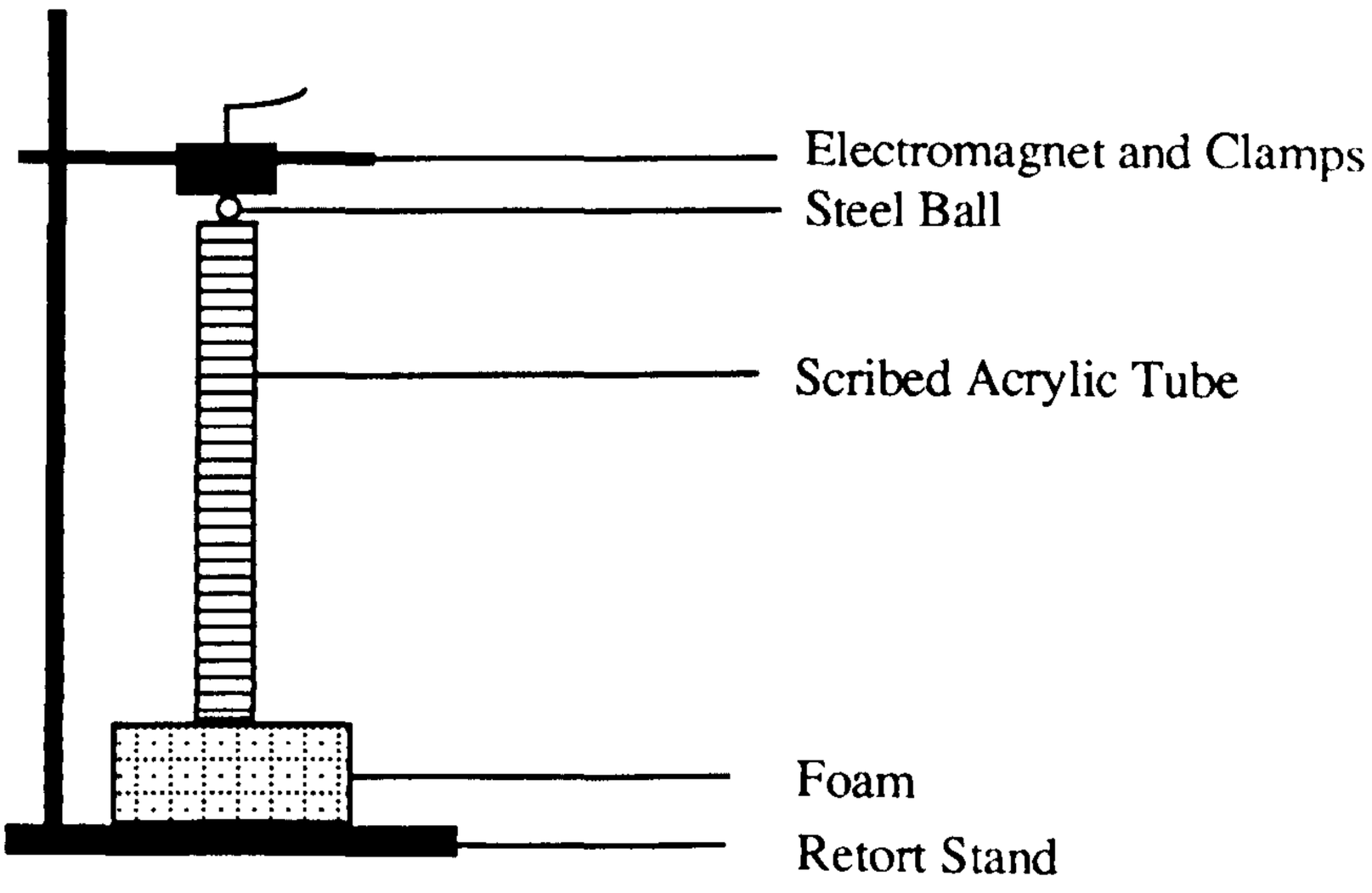

Fig. 7.27 Schematic of the ball rebound test.

Table 7.3

	PECO	PEAO-4	PECC	PEAC-1
Density (kg/m^3)	33.7±1.3	81±2.0	37.9±2.1	89±1.6
Compressive Young's Modulus (KN/m^2)	68.2±2.3	-	150.3±4.5	-
Rebound Height (cm)	11.86±0.15	17.85±0.2	14.49±0.38	26.6±0.15
Compressive Poisson's Ratio, ν_{yx}	-	-	0.25±0.08	-

Table. 7.3 Table of the ball rebound test for PECO, PEAO-4, PECC, and PEAC. Note: The foam was tested along the foam rise direction.

Table 7.4

	10CO	70AO	80AO	90AO	100AO
Density (kg/m^3)	24±3.1	74±2.5	76±2.2	77±2.1	79±3.0
Compressive Young's Modulus (KN/m^2)	61.5±3.44	51.4±2.51	48.5±2.43	43.6±1.20	38.2±0.82
Compressive Poisson's Ratio, ν_{yx}	0.20±0.08	-0.43±0.03	-0.54±0.02	-0.60±0.05	-0.66±0.06
Ball Rebound Height (cm)	14.7±0.34	21.3±0.48	24.6±0.35	25.2±0.3	25.4±0.5

Table. 7.4 Table of the ball rebound test for the 10ppi foams, i.e. 10CO, 70AO, 80AO, 90AO, and 100AO. Note: the Young's moduli and the Poisson's ratios were obtained from the compression tests (Table 6.1 and 6.4). The foam was tested along the foam rise direction.

Table 7.3 and 7.4 shows that the ball rebound height of auxetic foam is larger than that of its parent conventional foam.

7.5 DMTA - Loss Tangent

An alternative measure of energy absorption by a foam is the loss tangent, $tan\delta$ which can be obtained from the DMTA test.

The loss tangent, $tan\delta$ is called internal friction or damping, and is the ratio of energy dissipated per cycle to the maximum potential energy stored during a cycle.

$$tan\delta = G''/G' \qquad (7.11)$$

where G' is the storage modulus, G'' is the loss modulus. The detail of the DMTA test was explained in Chapter 6. Here the DMTA results related to the loss $tan\delta$ are presented in Figures 7.28 to 7.33.

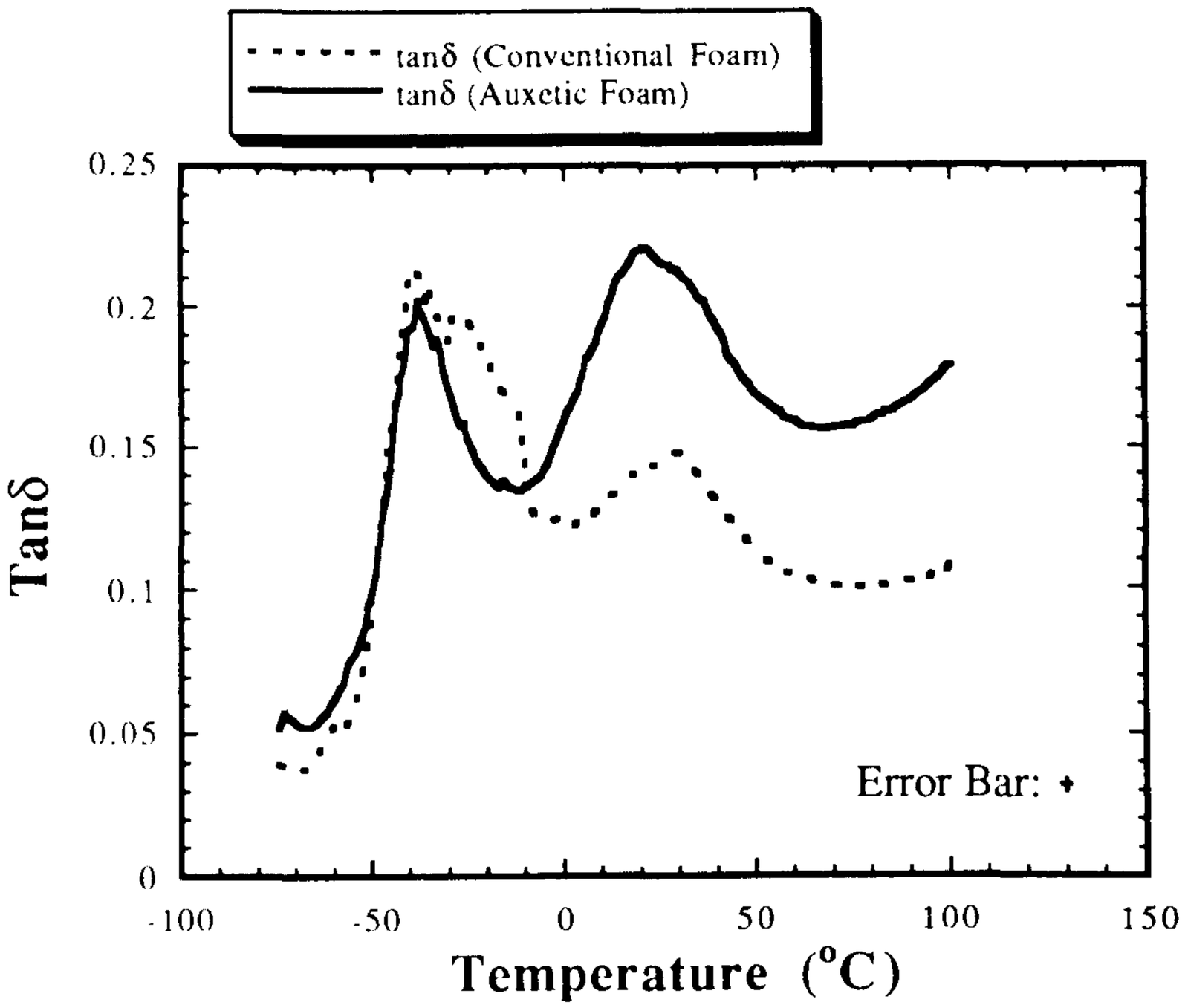

Fig. 7.28 DMTA results of the open-cell polyether urethane foams. Comparison of the loss tangent, *tan*δ of an auxetic foam (100AO) with its parent conventional foam (10CO). (The testing frequency was 10Hz).

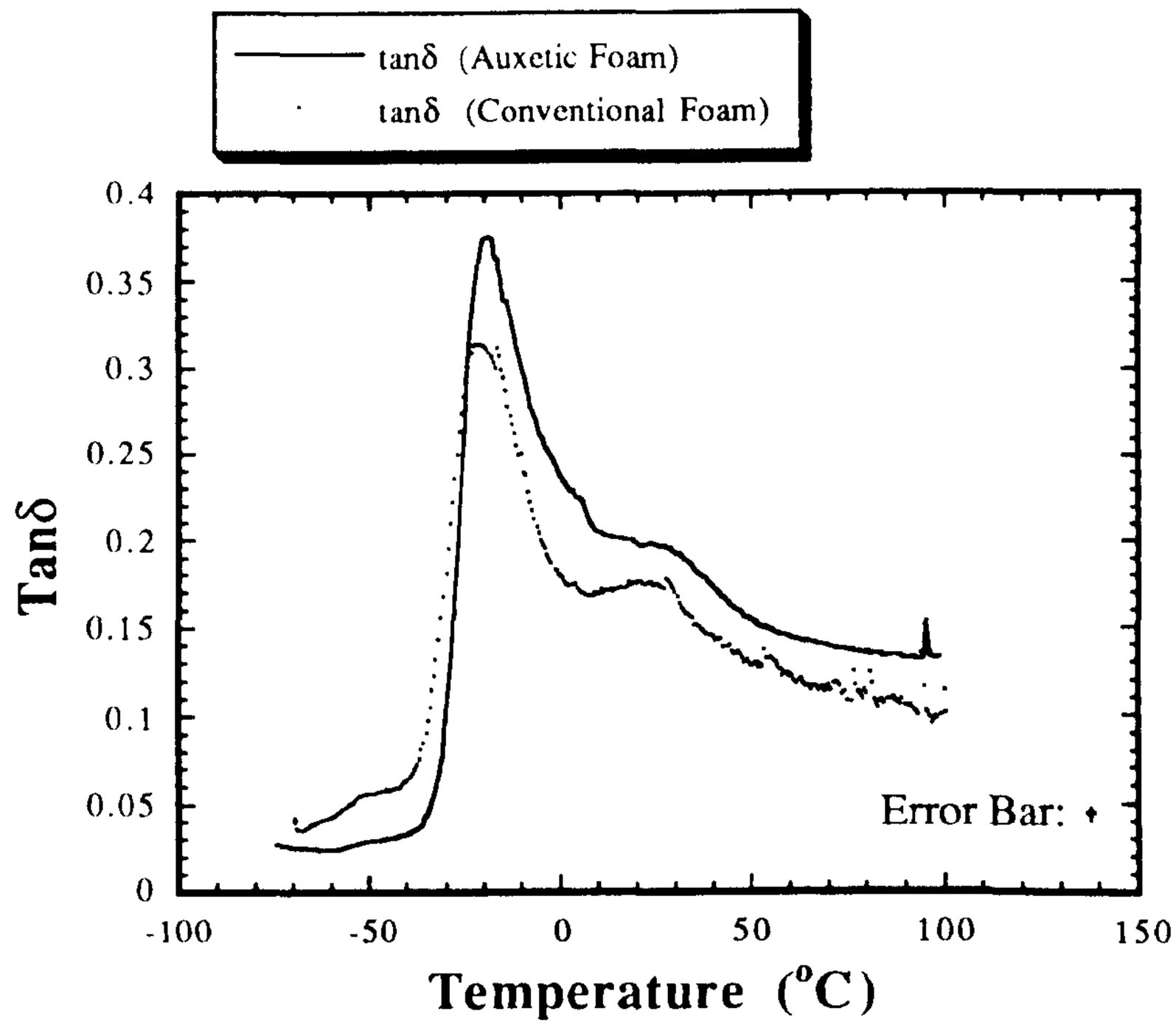

Fig. 7.29 DMTA results of the 60ppi closed-cell polyester urethane foam. Comparison of the loss tangent, *tan*δ of an auxetic foam (PEAC-1) with its parent conventional foam (PECC). (The testing frequency was 10Hz).

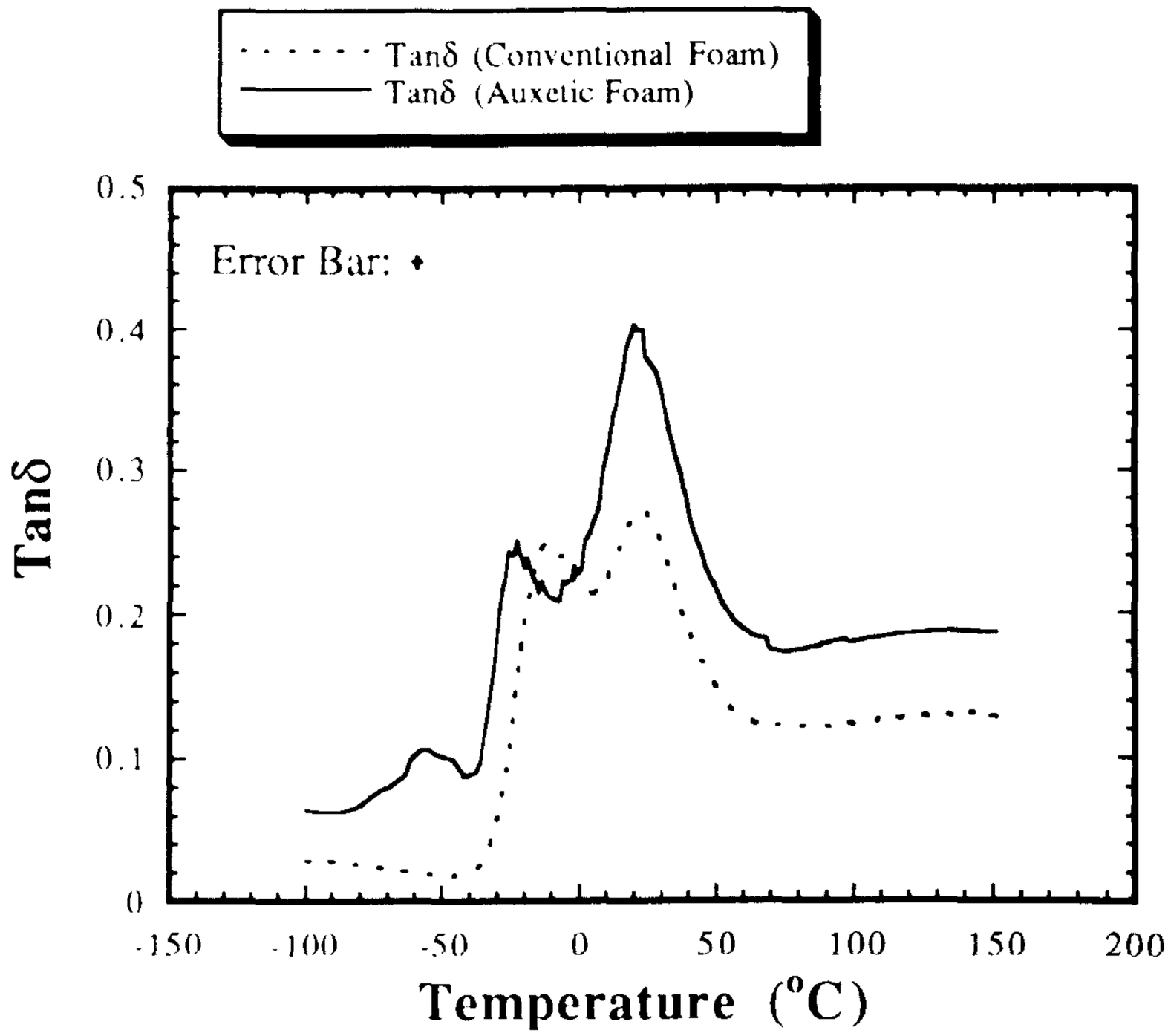

Fig. 7.30 DMTA results of the 60ppi reticulated polyester urethane foam. Comparison of the loss tangent, *tan* δ of auxetic foam (PEAO-4) with its parent conventional foam (PECO). (The testing frequency was 10Hz).

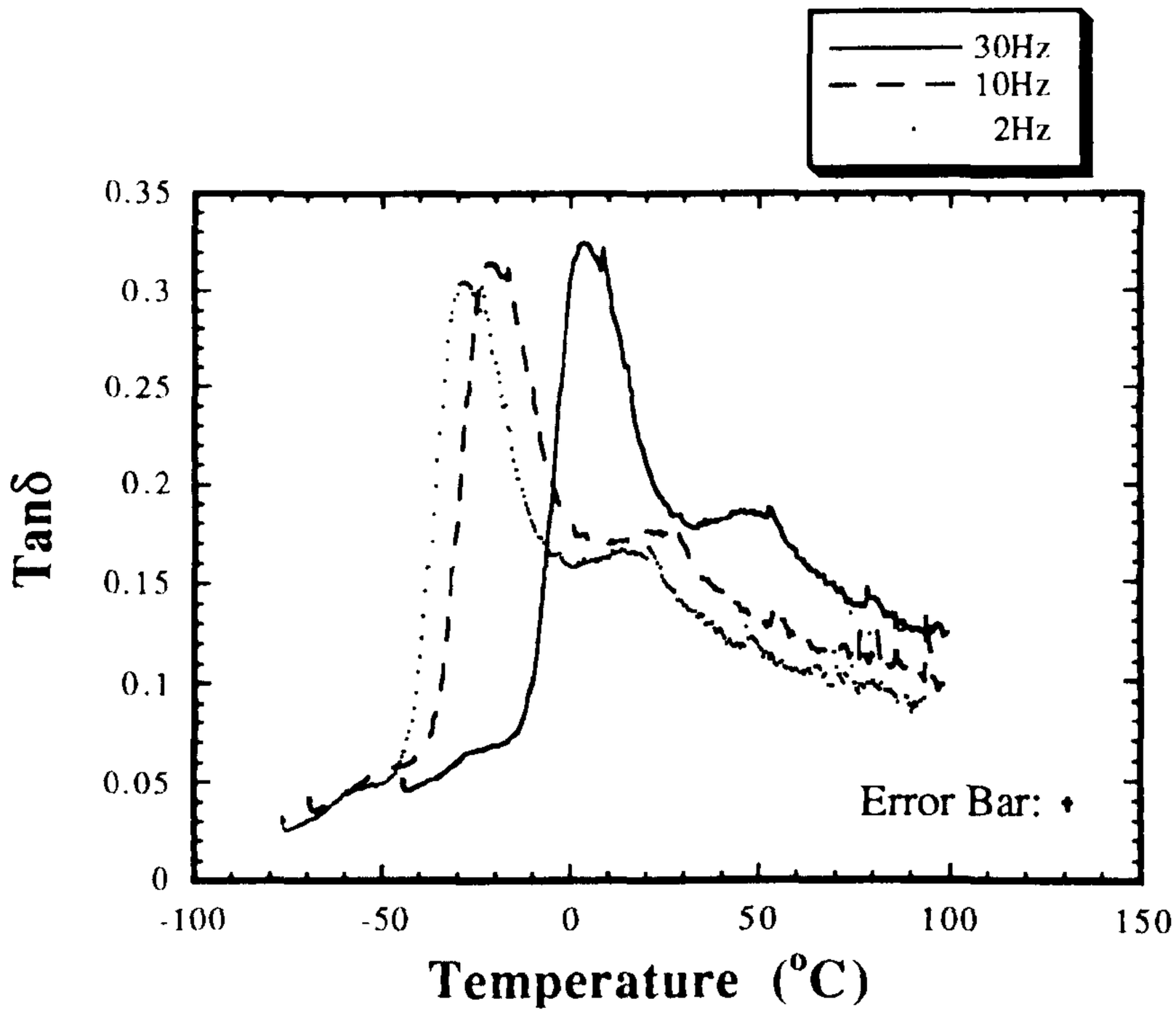

Fig. 7.31 DMTA results of the 60ppi closed-cell conventional polyester urethane foam (PECC). Illustration on effect of frequency on the loss tangent, *tan* δ.

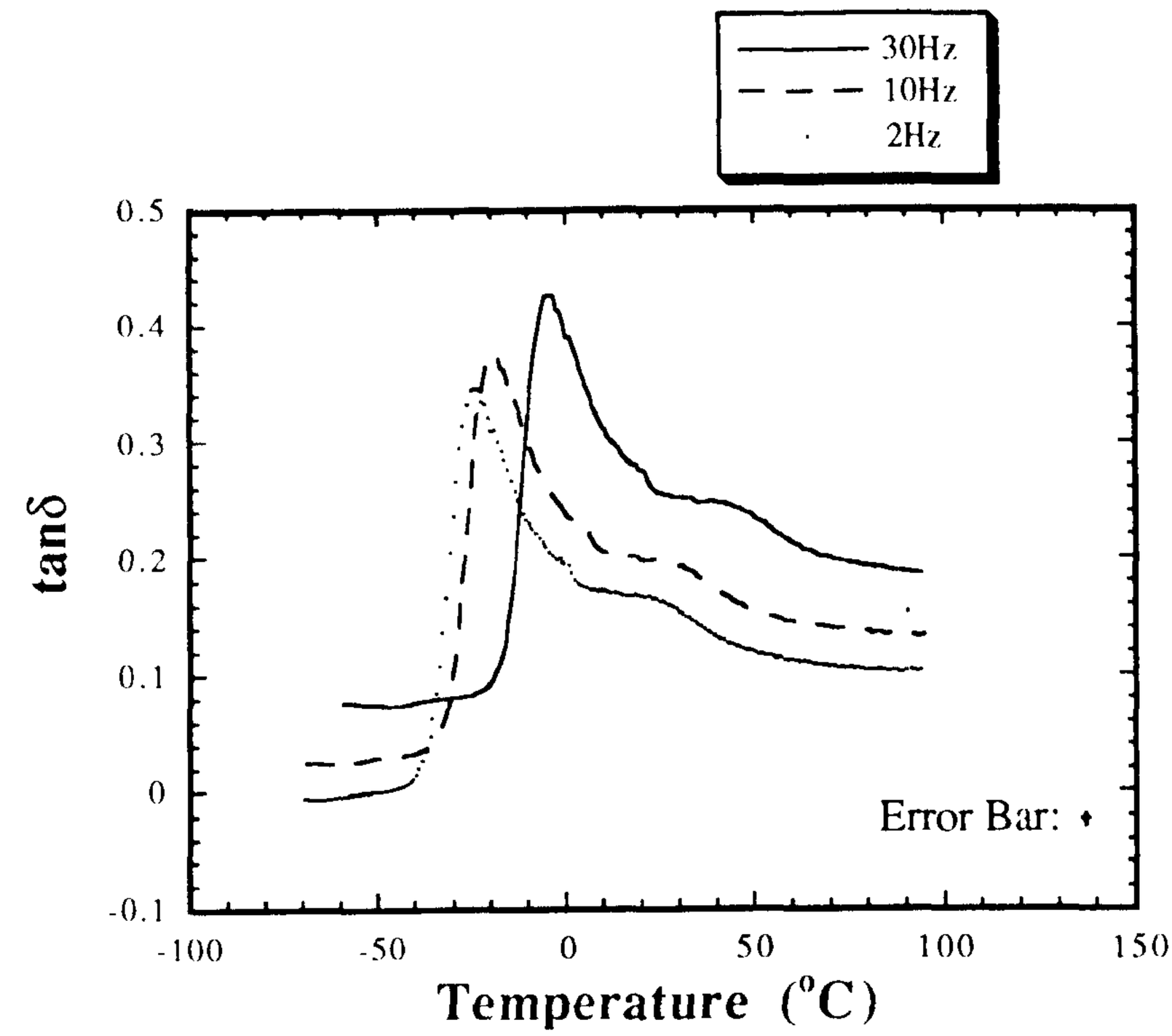

Fig. 7.32 DMTA results of the 60ppi closed-cell Auxetic polyester urethane foam (PEAC-1). Illustration on effect of frequency on the loss tangent, *tan* δ at a large range temperature.

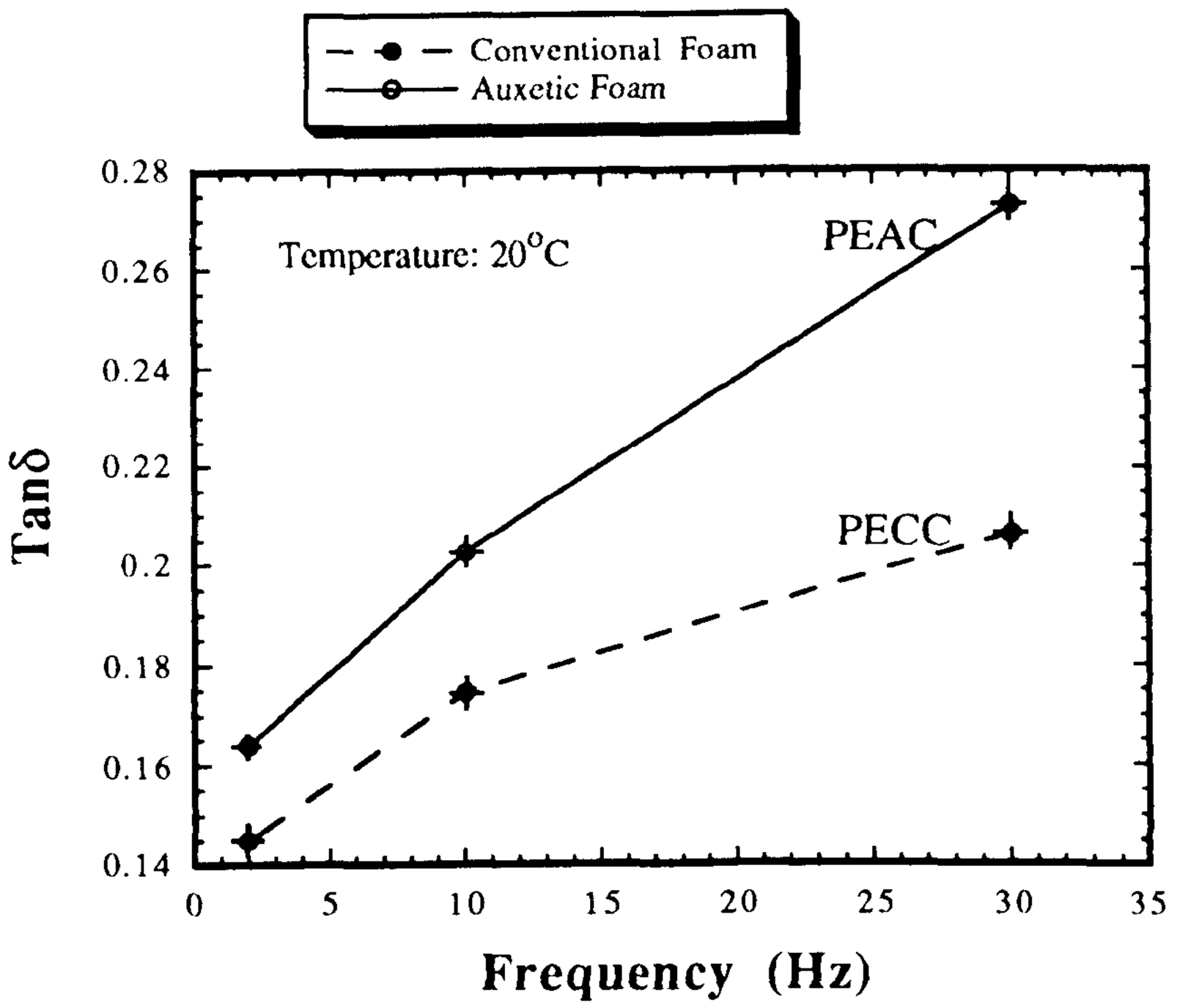

Fig. 7.33 *Tanδ* is a function of frequency for both auxetic and conventional foams.

Figures 7.28 to 7.33 show that at a relatively high frequency (i.e. 10Hz)

$tan\delta$ of auxetic foam is higher than that of conventional foam in a large region. Therefore, auxetic foam may be a good damping material. Figure 7.31 to 7.33 show that $tan\delta$ is a function of the frequency. Increasing the test frequency increases the value of $tan\delta$.

Chapter 8 Discussion

8.1 Introduction

In *Chapter* 5, a new theoretical model was developed for the deformation of foams. In the first part of this chapter, the aim is to investigate the effects of variations in the cell geometry for each of the three models developed. First, plots are made of the moduli E_x (or E_z), E_y, G_{xy} (or G_{zy}, G_{yz}, G_{yx}), and G_{xz} (or G_{zx}), and the Poisson's ratios ν_{xy}(or,ν_{zy}), ν_{xz}(or,ν_{zx}),and ν_{yx}(or,ν_{yz}), against the cell angle θ for various values of h/L and t/L. Next, the work on the elastic properties is brought together with the work on the ball indentation. According to Gibson and Ashby (1988), the Young's modulus of solid flexible PUR, E_s=45000 kN/m^2. In order to simplify the calculations the plots have been drawn for the cases h = 2L, for various values of t/L; t = 0.1L, for various h/L values, and q = t, for the hinging model.

In the second part of this chapter, the experimental results are discussed together with the theoretical models.

8.2 Comparison of the 3D Model with the 2D Model

In order to view the 3D foam modelling in a broader context, It is necessary to examine the model by considering whether it reduces to the known answers developed by Gibson and Ashby (1987) and Masters (1994) on a similar, but not identical 2D cell structure (see *Figure* 8.1).

When $\theta_z = 90^o$, and L_z=0 the rhombic dodecahedron cells (*Figure* 5.1) are reduced to the conventional 2D hexagonal cells. Following the same method used in *Chapter* 5, and by putting the thickness of the unit cell in the z direction=t for the 2D foam model, the formulas for the Young's modulus and Poisson's ratio in *Table* 5.1, 5.2, 5.3 can be reduced to the 2D results, as shown in *Tables* 8.1, 8.2, and 8.3 respectively, of Gibson and Ashby (1987) and Masters (1994). The calculations for the shear modulus of the 3D model is completely different from that of the 2D case. As a result of the more complicated nature of the 3D model it is necessary to consider the 3D internal rotation in the unit cell and for this reason, it can't simply be reduced to the 2D model. However, the 3D shear moduli expressions can be reduced to the cubic box model which is given by Huber and Gibson (1988). The comparisons were made in Table 8.4.

Table 8.1

	General Expressions (Chan, 1994)	Expressions (Gibson and Ashby, 1988)
E_x	$\frac{E_s \cos\theta_x}{(h/L_x + \sin\theta_x)\sin^2\theta_x}\left(\frac{t}{L_x}\right)^3$	$\frac{E_s \cos\theta}{(h/L + \sin\theta)\sin^2\theta}\left(\frac{t}{L}\right)^3$
E_y	$\frac{E_s(h/L_x + \cos\theta_x)}{\cos^3\theta_x}\left(\frac{t}{L_x}\right)^3$	$\frac{E_s(h/L + \cos\theta)}{\cos^3\theta}\left(\frac{t}{L}\right)^3$
ν_{xy}	$\frac{\cos^2\theta_x}{(h/L_x + \sin\theta_x)\sin\theta_x}$	$\frac{\cos^2\theta}{(h/L + \sin\theta)\sin\theta}$
ν_{yx}	$\frac{\sin\theta_x(h/L_x + \sin\theta_x)}{\cos^2\theta_x}$	$\frac{\sin\theta(h/L + \sin\theta)}{\cos^2\theta}$

Table 8.1 The flexure model expressions of the Young's moduli, and Poisson's ratios of the 2D conventional and auxetic foams. θ is positive for conventional foam and θ is negative for auxetic foam.

Table 8.2

	General Expressions (Chan, 1994)	Expressions (Masters, 1994)
E_x	$\frac{K_h \cos\theta_x}{(h/L_x + \sin\theta_x)t\sin^2\theta_x}$	$\frac{K_h \cos\theta}{(h/L + \sin\theta)t\sin^2\theta}$
E_y	$\frac{K_h(h/L_x + \sin\theta_x)}{t\cos^3\theta_x}$	$\frac{K_h(h/L + \sin\theta)}{t\cos^3\theta}$
ν_{xy}	$\frac{\cos^2\theta_x}{(h/L_x + \sin\theta_x)\sin\theta_x}$	$\frac{\cos^2\theta}{(h/L + \sin\theta)\sin\theta}$
ν_{yx}	$\frac{\sin\theta_x(h/L_x + \sin\theta_x)}{\cos^2\theta_x}$	$\frac{\sin\theta(h/L + \sin\theta)}{\cos^2\theta}$

Table 8.2 The hingeing model expressions of the Young's modulus, and Poisson's ratio of the 2D conventional and auxetic foams. θ is positive for conventional foam and θ is negative for auxetic foam.

Table 8.3

	General Expressions (Chan, 1994)	Expressions (Masters, 1994)
E_x	$\frac{K_s}{(h/L_x + \sin\theta_x)t\cos\theta_x}$	$\frac{K_s}{(h/L + \sin\theta)t\cos\theta}$
E_y	$\frac{K_s(h/L_x + \sin\theta_x)}{t\cos\theta_x(2h/L_x + \sin^2\theta_x)}$	$\frac{K_s(h/L + \sin\theta)}{t\cos\theta(2h/L + \sin^2\theta)}$
ν_{xy}	$\frac{-\sin\theta_x}{h/L_x + \sin\theta_x}$	$\frac{-\sin\theta}{h/L + \sin\theta}$
ν_{yx}	$\frac{-\sin\theta_x(h/L_x + \sin\theta_x)}{2h/L_x + \sin^2\theta_x}$	$\frac{-\sin\theta(h/L + \sin\theta)}{2h/L + \sin^2\theta}$

Table 8.3 The stretching model expressions of the Young's modulus, and Poisson's ratio of the 2D conventional and auxetic foams. θ is positive for conventional foam and θ is negative for auxetic foam.

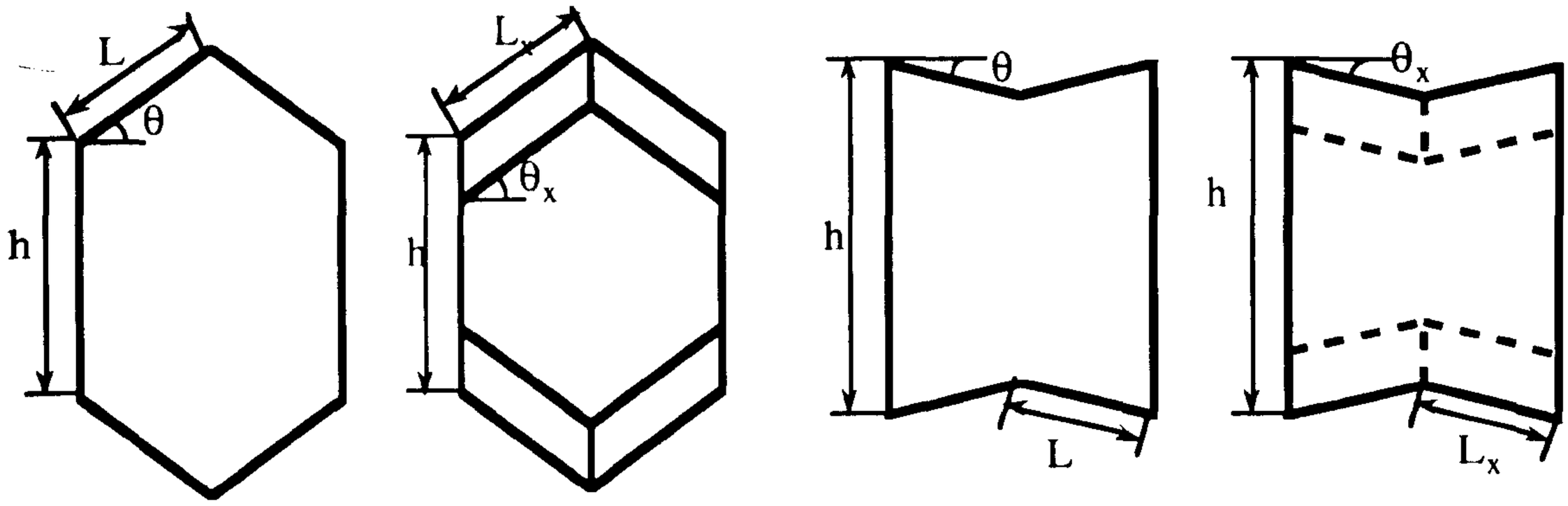

Fig. 8.1 Schematic of the 2D honeycomb models. (a) and (c) Gibson and Ashby (1988), and Masters (1994) model. (b) and (d) Chan (1994) model.

8.3 Examination of the Special Cases

When $\theta_x = 0^o$, $\theta_z = 0^o$, and $L_x = L_z \neq 0$, the rhombic dodecahedron cell (*Figure* 5.1) is reduced to a cubic box (*Figure* 8.2). This box-like structure is similar, but not identical to the model of Huber and Gibson (1988) (see *Figure* 2.2). The results reduced from *Table* 5.1 together with Gibson and Ashby model are shown in *Table* 8.4.

When $\theta_x = \theta_z = 90^o$, and $L_x = L_z = 0$, the rhombic dodecahedron cell (see *Figure* 5.1) is reduced to a rectangular beam along the y direction and the foam becomes a solid polymer beam.

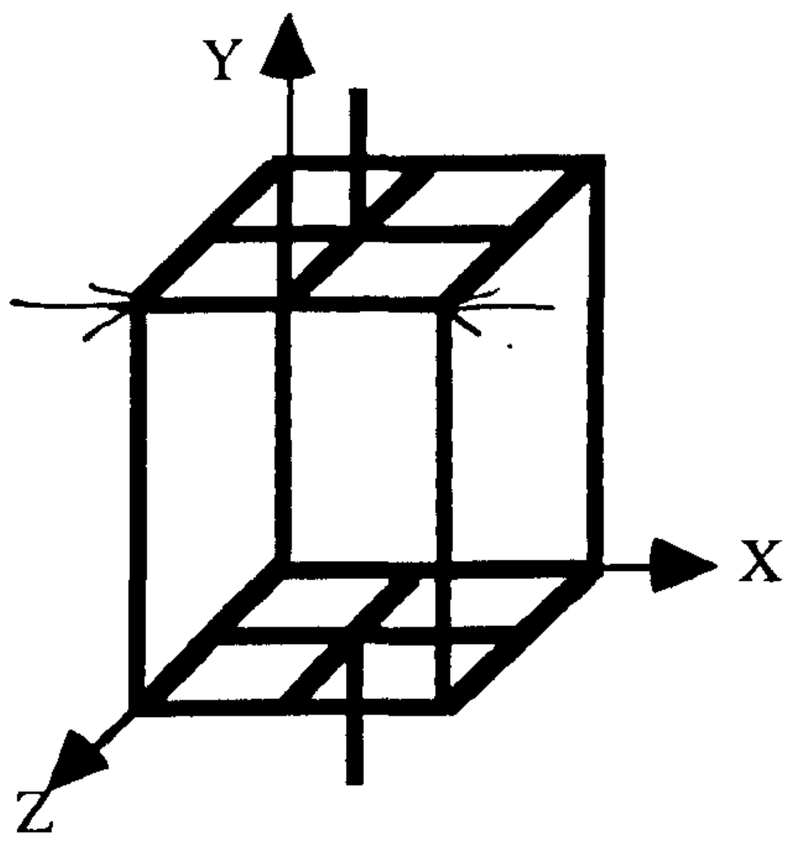

Fig. 8.2 One single box-like cell model which is reduced from a rhombic dodecahedron cell model shown in Fig. 5.1.

Table 8.4

	Expression for the Box-like Model Chan (1994)	The Model of Huber and Gibson (1988)	Expression for the solid polymer beam
E_x	∞	$\frac{CE_s}{2}\left(\frac{t}{L}\right)^4\left(\frac{L}{h}\right)\left(1+\left(\frac{L}{h}\right)^3\right)$	E_s
E_y	$\frac{1}{2}E_s\left(\frac{t}{L}\right)^4\left(\frac{h}{L}\right)$	$CE_s\left(\frac{t}{L}\right)^4\left(\frac{h}{L}\right)$	E_s
E_z	∞	$\frac{CE_s}{2}\left(\frac{t}{L}\right)^4\left(\frac{L}{h}\right)\left(1+\left(\frac{L}{h}\right)^3\right)$	E_s
ν_{xy}	∞	-	$\frac{E_s}{2G_s}-1$
ν_{xz}	0	-	$\frac{E_s}{2G_s}-1$
ν_{zx}	0	-	$\frac{E_s}{2G_s}-1$
ν_{zy}	∞	-	$\frac{E_s}{2G_s}-1$
ν_{yx}	0	-	$\frac{E_s}{2G_s}-1$
ν_{yz}	0	-	$\frac{E_s}{2G_s}-1$
G_{xy}	$\frac{E_s}{4}\left(\frac{t}{L}\right)^4\left(\frac{L}{h}\right)\frac{1}{\left(\frac{h}{L}\right)+\frac{1}{2}}$	$2CE_s\left(\frac{t}{L}\right)^4\left(\frac{L}{h}\right)\frac{1}{\left(\frac{h}{L}\right)+1}$	G_s
G_{zy}	$\frac{E_s}{4}\left(\frac{t}{L}\right)^4\left(\frac{L}{h}\right)\frac{1}{\left(\frac{h}{L}\right)+\frac{1}{2}}$	$2CE_s\left(\frac{t}{L}\right)^4\left(\frac{L}{h}\right)\frac{1}{\left(\frac{h}{L}\right)+1}$	G_s
G_{yz}	$\frac{E_s}{4}\left(\frac{t}{L}\right)^4\left(\frac{L}{h}\right)\frac{1}{\left(\frac{h}{L}\right)+\frac{1}{2}}$	$2CE_s\left(\frac{t}{L}\right)^4\left(\frac{L}{h}\right)\frac{1}{\left(\frac{h}{L}\right)+1}$	G_s
G_{yx}	$\frac{E_s}{4}\left(\frac{t}{L}\right)^4\left(\frac{L}{h}\right)\frac{1}{\left(\frac{h}{L}\right)+\frac{1}{2}}$	$2CE_s\left(\frac{t}{L}\right)^4\left(\frac{L}{h}\right)\frac{1}{\left(\frac{h}{L}\right)+1}$	G_s
G_{xz}	$E_s\left(\frac{t}{L}\right)^4\left(\frac{L}{h}\right)$	$CE_s\left(\frac{t}{L}\right)^4\left(\frac{L}{h}\right)$	G_s
G_{zx}	$E_s\left(\frac{t}{L}\right)^4\left(\frac{L}{h}\right)$	$CE_s\left(\frac{t}{L}\right)^4\left(\frac{L}{h}\right)$	G_s

Table 8.4 The flexure model expressions of the Young's modulus, Poisson's ratio and the shear modulus of the box-like structure, and solid polymer block. Note: E_s and G_s are the Young's modulus and the shear modulus of the solid polymer respectively. We assume that the solid polymer is an isotropic material.

8.4 Examination of the Combined Model

In order to check the final expressions (Table 5.4) for the combined model, it is necessary to reduce the combined model to the individual model expressions by

putting Ki (i= f, h, s) $\rightarrow \infty$.

Firstly, when K_h, and $K_f \rightarrow \infty$, EQ. 5.153 is reduced to $E_x = \frac{K_f}{(\alpha + 2\sin\theta)L\sin^2\theta}$, EQ. 5.163 is reduced to $E_y = \frac{K_f(\alpha + 2\sin\theta)}{2L\cos^4\theta}$, EQ. 5.150 is reduced to $\nu_{xy} = \frac{\cos^2\theta}{\sin\theta(\alpha + 2\sin\theta)}$, EQ. 5.160 is reduced to $\nu_{yx} = \frac{\sin\theta(\alpha + 2\sin\theta)}{2\cos^2\theta}$, EQ. 5.151 is $\nu_{xz} = 0$, EQ. 5.167 is reduced to $G_{zy} = \frac{(\alpha + 2\sin\theta)}{2L\cos^2\theta} \times \frac{1}{\frac{2\alpha}{K_f}(\alpha^2 + \frac{\alpha + 2\sin\theta}{2(1+\sin^2\theta)})}$, and EQ. 5.173 is reduced to $G_{xz} = \frac{K_f}{L\cos\theta(\alpha + 2\sin\theta)}$ which are identical to the flexure model expressions for Ex (EQ. 5.13), Ey (EQ. 5.32), ν_{xy} (EQ. 5.12), ν_{yx} (EQ. 5.30), ν_{xz} (EQ. 5.11), Gzy (EQ. 5.52a), and Gxz (EQ. 5.41b) respectively.

Secondly, when K_f, and $K_s \rightarrow \infty$, EQ. 5.153 is reduced to $E_x = \frac{K_h}{(\alpha + 2\sin\theta)L\sin^2\theta}$, EQ. 5.163 is reduced to $E_y = \frac{K_h(\alpha + 2\sin\theta)}{2L\cos^4\theta}$, EQ. 5.150 is reduced to $\nu_{xy} = \frac{\cos^2\theta}{\sin\theta(\alpha + 2\sin\theta)}$, EQ. 5.160 is reduced to $\nu_{yx} = \frac{\sin\theta(\alpha + 2\sin\theta)}{2\cos^2\theta}$, EQ. 5.151 is $\nu_{xz} = 0$, EQ. 5.167 is reduced to $G_{yz} = \frac{(\alpha + 2\sin\theta)}{L\cos^2\theta} \times \frac{K_h(1+\sin^2\theta)}{(2\alpha + 0.5\alpha^2)}$, and EQ. 5.173 is reduced to $G_{xz} = \frac{K_h}{L\cos\theta(\alpha + 2\sin\theta)}$ which are identical to the hinging model expressions for Ex (EQ. 5.66), Ey (EQ. 5.80), ν_{xy} (EQ. 5.61), ν_{yx} (EQ. 5.76), ν_{xz} (EQ. 5.62), G_{zy} (EQ. 5.90), and G_{xz} (EQ. 5.100) respectively.

Thirdly, when K_f, and $K_h \rightarrow \infty$, EQ. 5.153 is reduced to $E_x = \frac{K_s}{(\alpha + 2\sin\theta)L\cos^2\theta}$, EQ. 5.163 is reduced to $E_y = \frac{K_s(\alpha + 2\sin\theta)}{2L\cos^2\theta(2\alpha + \sin^2\theta)}$, EQ. 5.150 is reduced to $\nu_{xy} = \frac{-\sin\theta}{\alpha + 2\sin\theta}$, EQ. 5.160 is reduced to $\nu_{yx} = \frac{-\sin\theta(\alpha + 2\sin\theta)}{2(2\alpha + \sin^2\theta)}$, EQ. 5.151 is $\nu_{xz} = 0$ which are identical to the stretching model expressions for Ex (EQ. 5.120), Ey (EQ. 5.143), ν_{xy} (EQ. 5.117), ν_{yx} (EQ. 5.140), and ν_{xz} (EQ. 5.118) respectively.

8.5 Effects of Cell Geometry on the Flexure Model

Figure 8.3 shows the modulus E_x (or E_z) plotted against the cell angle, θ using EQ. 5.14 and 5. 20. The maximum values of E_x occur when the cell angles are small and the walls of length L are orientated along the direction of loading. Because we are dealing with a flexure model, then when $\theta=0^0$, E_x (or E_z) becomes infinity since no flexure can occur at this angle. Increasing the h/L ratio reduces the values E_x for a given cell angle. As can be seen from the graph of E_x versus θ, the curve is not quite symmetrical around $\theta=0^0$. This results in a re-entrant cell of geometry h/L=2 and $\theta=-30^0$, having a modulus E_x of 18kN/m^2; whereas, to achieve the same modulus in a conventional foam cell using the same h/L values requires a cell angle of 18^0 (see *Figure* 8.3(a)). For a conventional foam the modulus E_x for a given h/L value within the range, $0^o < \theta < 90^o$, increased as the angle becomes less positive. For a re-entrant cell of the geometry h/L=2, very high moduli are achieved when the cell angle is numerically large and small i.e. $-90^o < \theta < -80^o$ and $-10^o < \theta < 0^o$ respectively. This 'U'-shaped curve of E_x versus θ shows a high degree of symmetry around $\theta=-45^0$. From *Figure* 8.3(b), it can be seen that, for a given t/L ratio, to obtain the same value of E_x in a re-entrant cell as in a hexagonal cell, it is necessary to increase the size of the re-entrant angle. For example, for a hexagonal cell of the geometry t/L=0.1 and $\theta=10^0$, the modulus E_x is 63.5 kN/m^2. To achieve an equivalent modulus in a re-entrant cell of the same aspect ratio requires a cell angle of -12^0 or -74^0. It is noted that all the curves of E_x versus θ for re-entrant cells in *Figure* 8.3(b) are 'U'-shaped, and they are very nearly symmetrical around $\theta=45^0$. The trends of the curves are the same: the curves shift upwards as the value of t/L is increased. For most foam structures t<<L so small variations in t/L have little effect on the value of E_x.

Figure 8.4 shows the modulus E_y plotted against the cell angle, θ using EQ.5.33. Very high moduli are achieved when the cell angle is numerically large (i.e. $60^o < \theta < 90^o$, $-70^o < \theta < -90^o$) the cell ribs of length L become oriented parallel to the load direction as shown in *Figure* 8.4(a). For conventional foam cells, it is clear that as the ratio of h/L is increased there is a increase in the value of E_y. The curves are all skewed to the left so that the minimum value of E_y occurs at $\theta=-12^0$ and $\theta=-28^0$ when the values of h/L are 0.5 and 1 respectively. The modulus E_y of a foam for a given h/L ratio is thus reduced as the angle becomes negative. *Figure* 8.4(b) shows that as t/L ratio is increased there is a significant increase in the value of E_y particularly when the cell angle is large. The graph of E_y versus θ is not truly symmetrical around 0^0, with the result that a re-entrant cell of geometry t/L=0.1, $\theta=30^0$ has a lower

are independent of t. *Figures* 8.5 and 8.6 show the effects of h/L on Poisson's ratio ν_{yx} and ν_{xy} respectively. A significant feature of both of these graphs is that ratios of much less than -1 and much greater than +1 are achieved. It can be seen from *Figure* 8.5 that increasing the value of h/L increases the numerical value of the effective Poisson's ratio for both hexagonal and re-entrant cells. ν_{xy} is correspondingly reduced as shown in *Figure* 8.6. It should also be noted that the graphs are not symmetrical. For example, in *Figure* 8.5, a hexagonal cell of geometry h/L=2, $\theta=20^0$ has a Poisson's ratio $\nu_{yx}=0.52$ whereas the re-entrant cell of h/L=2, $\theta=-20^0$ has a Poisson's ratio $\nu_{yx}=-0.255$. A limitation of the model is that at large angles approaching $+90^0$ and -90^0 very high Poisson's ratios are achieved. This is clearly unrealistic as $\theta=+90^0$ or -90^0 the cell has completely collapsed and all the cell walls are aligned in the direction of the applied force, in which case ν_{yx} must be the same as the Poisson's ratio of the cell wall material.

The maximum shear modulus, G_{xy} (*Figure* 8.7(a)) is achieved at $\theta=+90^0$ or -90^0. Increasing the value of h/L reduces the value of G_{xy} over the majority of the cell angle range, and increasing the value of t/L significantly increases the shear moduli, G_{xy} (*Figure* 8.7(b)). EQ. 5.52c is used for these plots.

For a given h/L ratio, the minimum shear modulus, G_{xz}, of a hexagonal cell (Figure 8.8(a)) is achieved at around $\theta=+45^0$. The 'n'-shaped curves of G_{xz} versus θ of re-entrant cells are almost symmetrical around $\theta=-47^0$ so that a re-entrant cell with cell geometry h/L=2, $\theta=-45^0$ has a higher modulus, G_{xz}, than the corresponding hexagonal cell with the same geometry. *Figure* 8.8(b) shows the effect of t/L ratio on the moduli, G_{xz}. For these plots h=2L. Again, the value of G_{xz} greatly increases as the ratio of t/L increases. EQ. 5.41b is used for these plots.

Notes: There are limits on the possible range of negative angle, θ values due to the geometric constraints of the cell. i.e. the cell ribs overlap, , isn't possible. The maximum negative angle, θ_{max} is depending on h/L ratio. i.e.

θ_{max} is -14.5^0 for h/L= 0.5.

θ_{max} is -30^0 for h/L=1.

θ_{max} is -90^0 for h/L≥2.

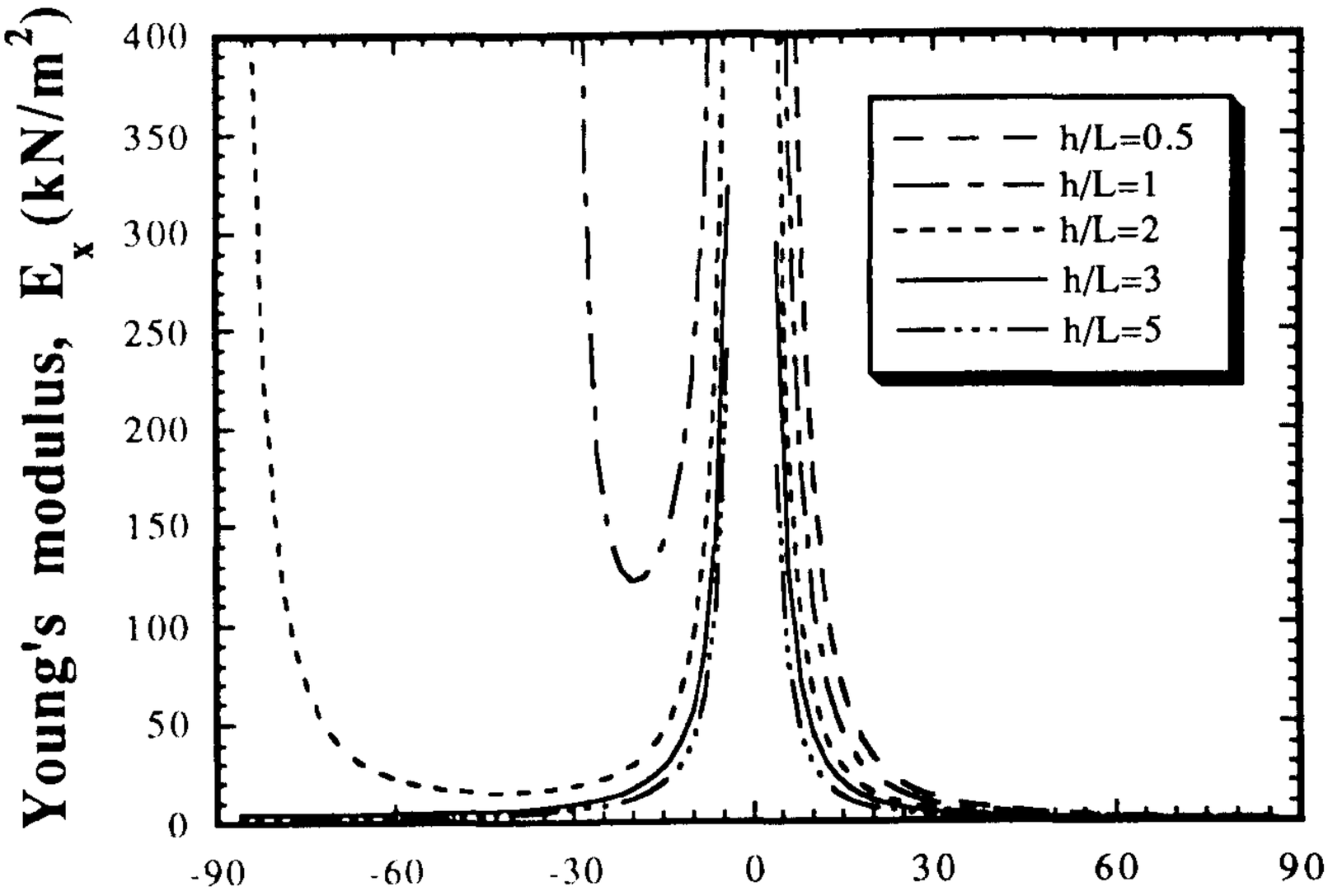

Fig. 8.3(a)

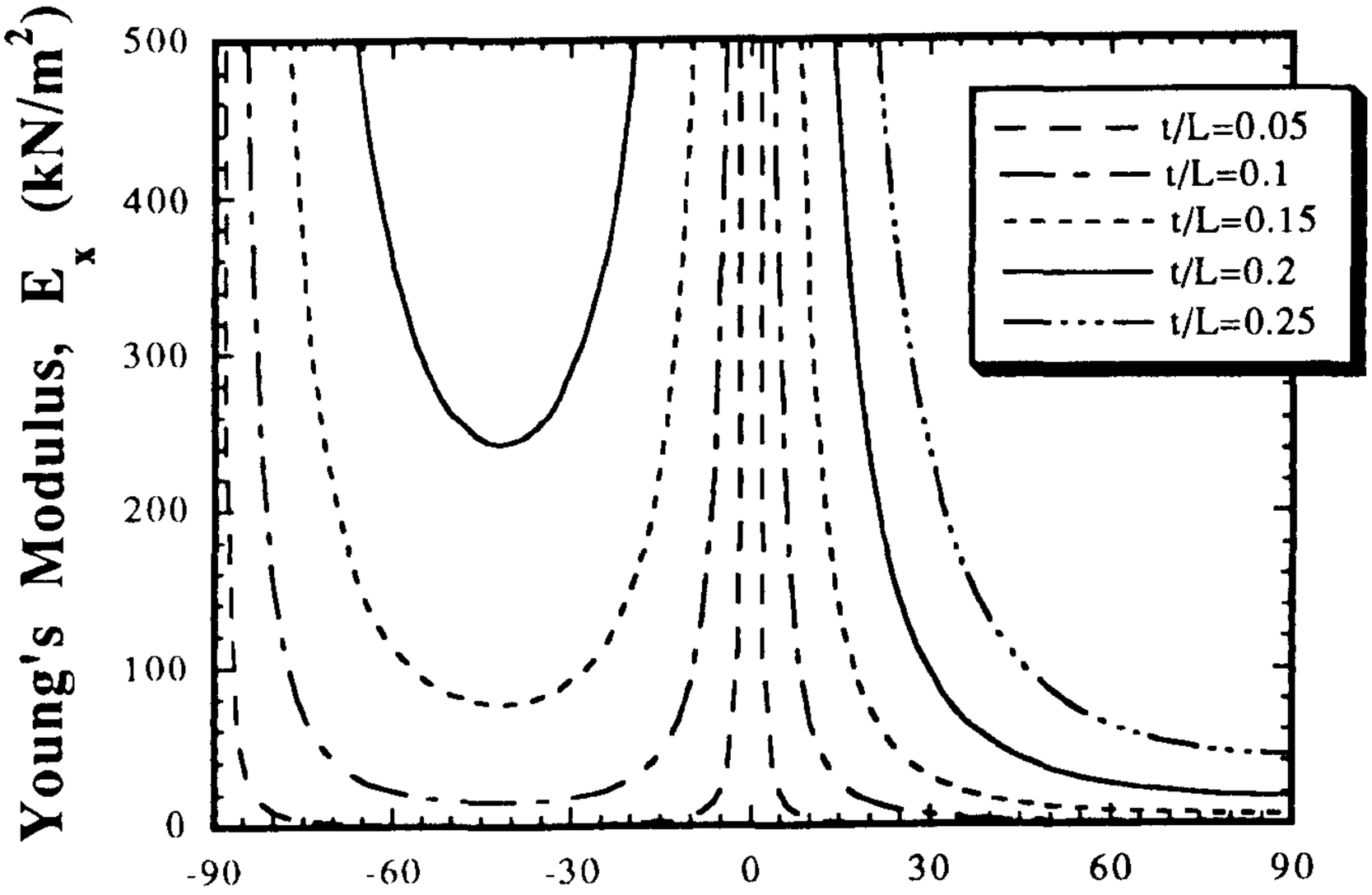

Fig. 8.3(b)

Fig. 8.3 Plots of E_x vs. θ for the flexure model of conventional foam showing the effects of varying cell geometry (θ, α and t/L). (a) Varying θ and α for t=0.1L. (b) Varying θ and t/L for h=2L.

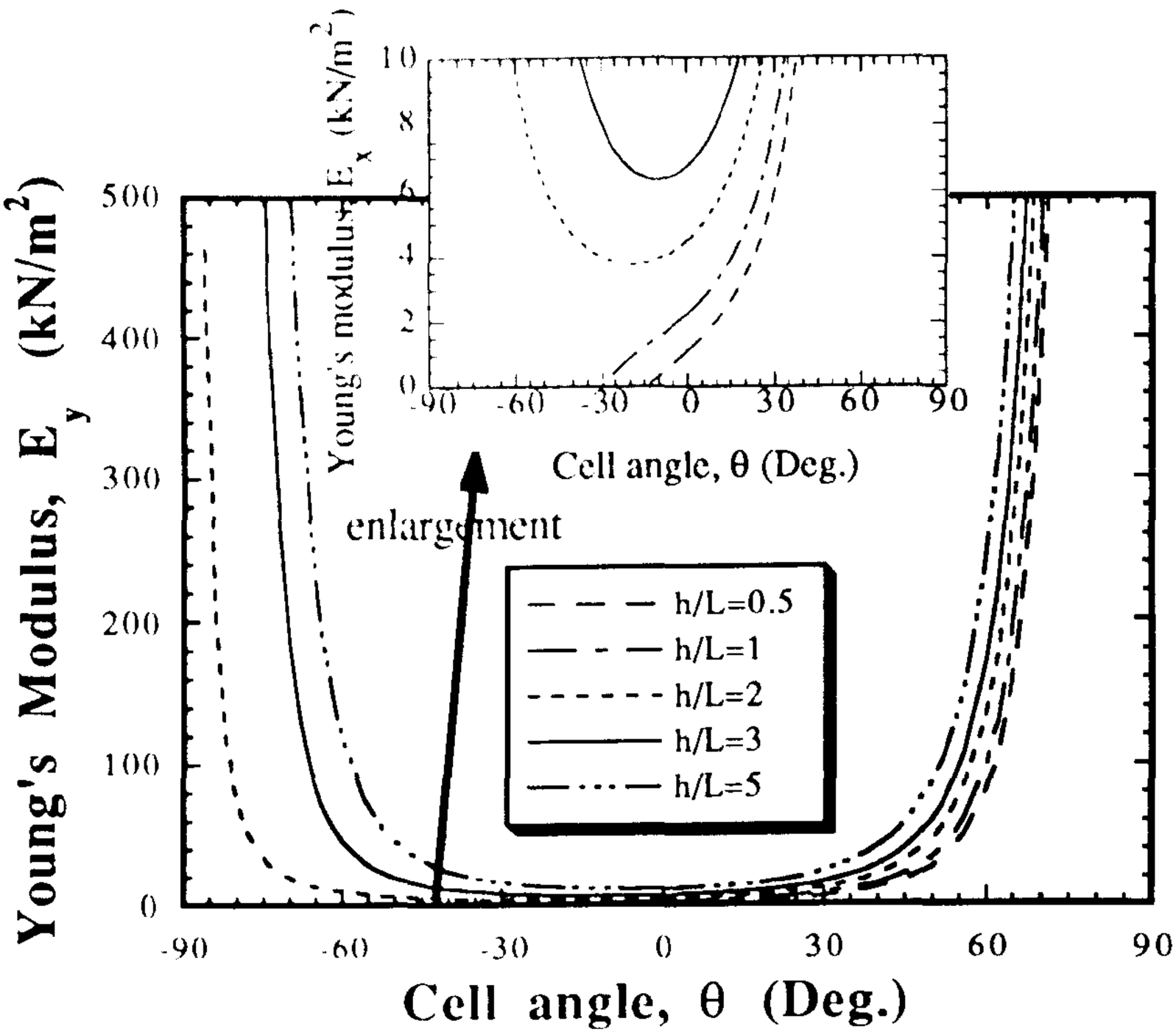

Fig. 8.4(a)

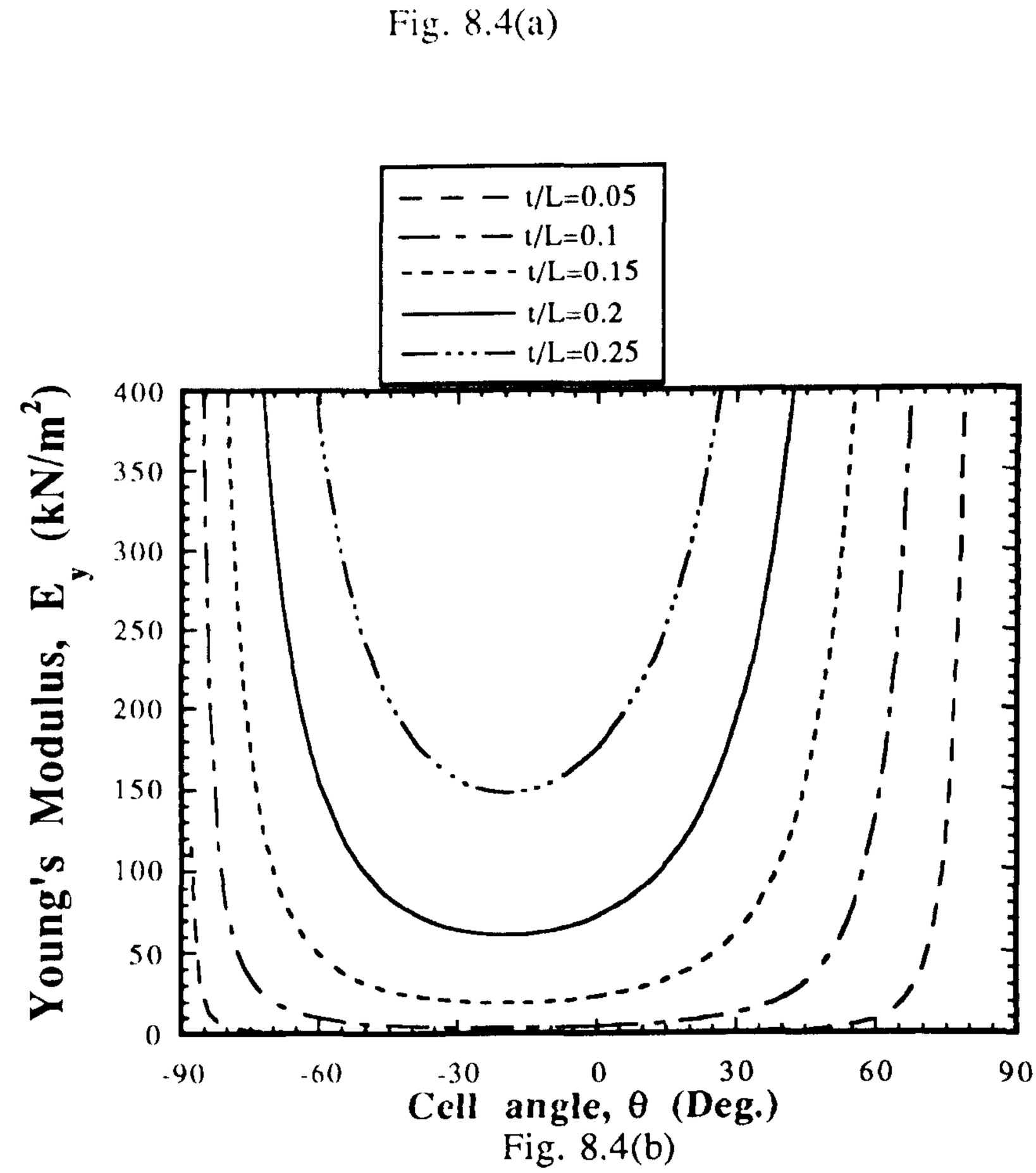

Fig. 8.4(b)

Fig. 8.4 Plots of E_y vs. θ for the flexure model of conventional foam showing the effects of varying cell geometry (θ, α and t/L). (a) Varying θ and α for t=0.1L. (b) Varying θ and t/L for h=2L.

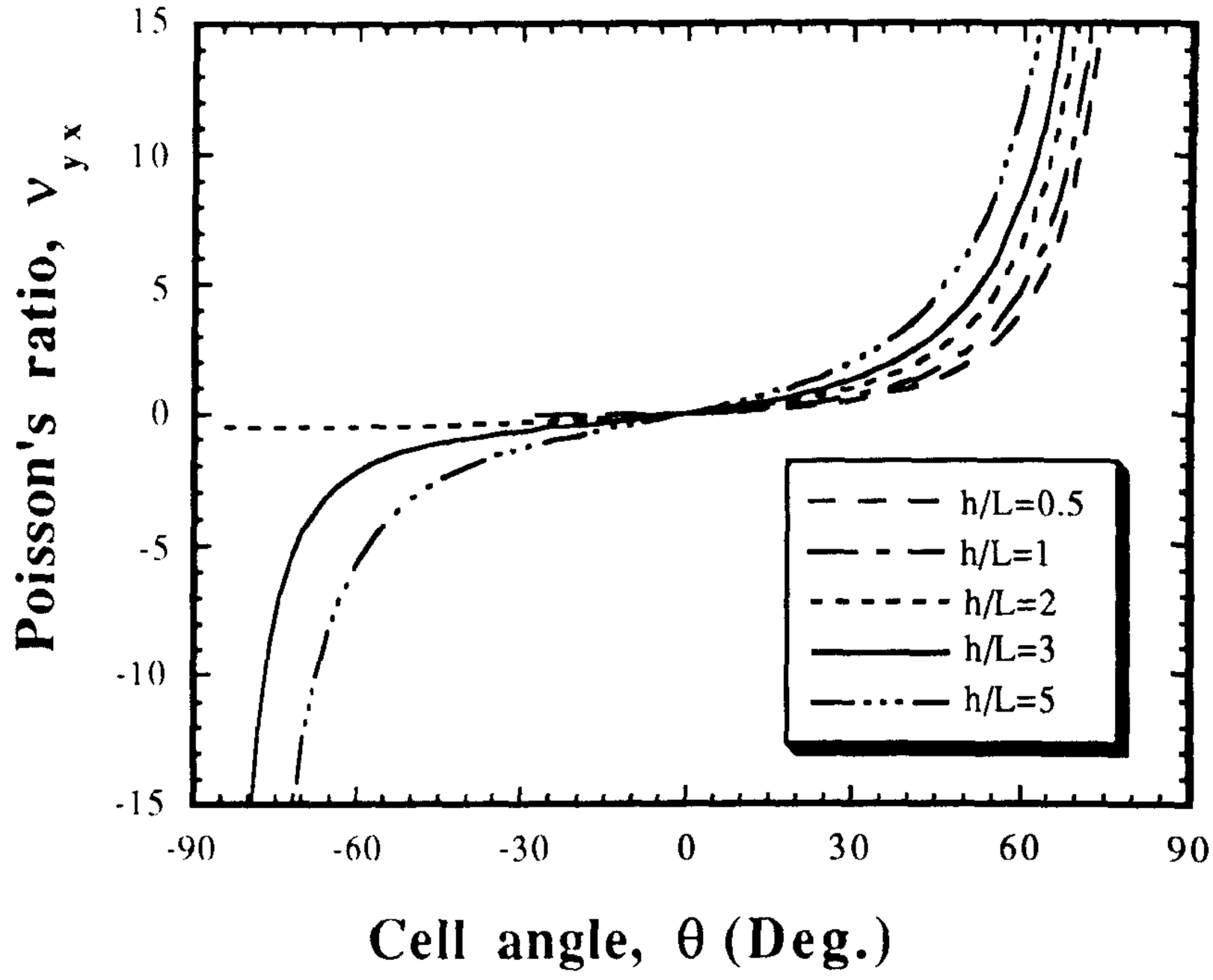

Fig. 8.5 Plots of υ_{yx} vs. θ for both the flexure model and the hinging model showing the effects of varying cell geometry, θ and h/L for t=0.1L.

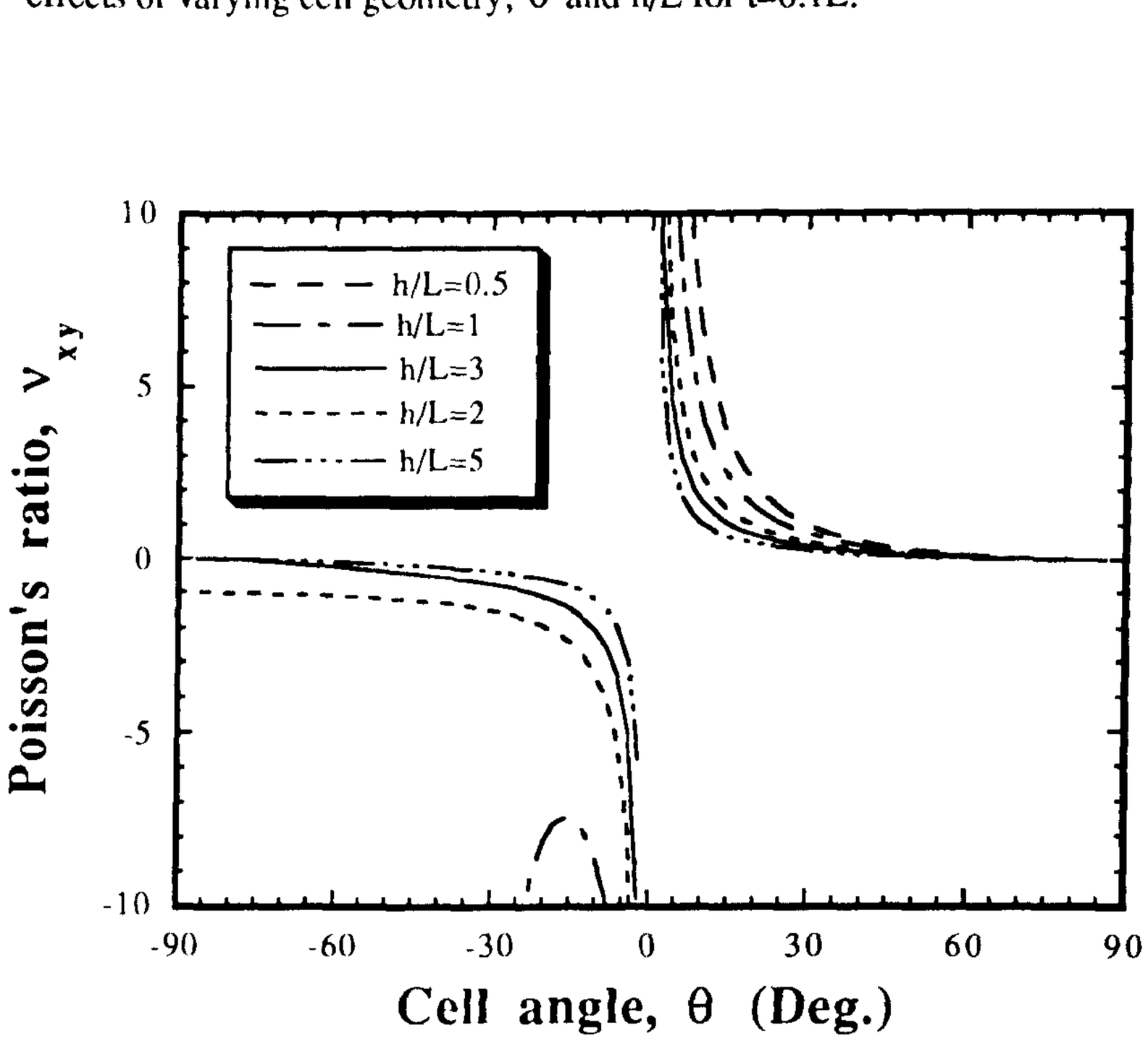

Fig. 8.6 Plots of υ_{xy} vs. θ for both the flexure model and the hinging model showing the effects of varying cell geometry, θ and h/L for t=0.1L.

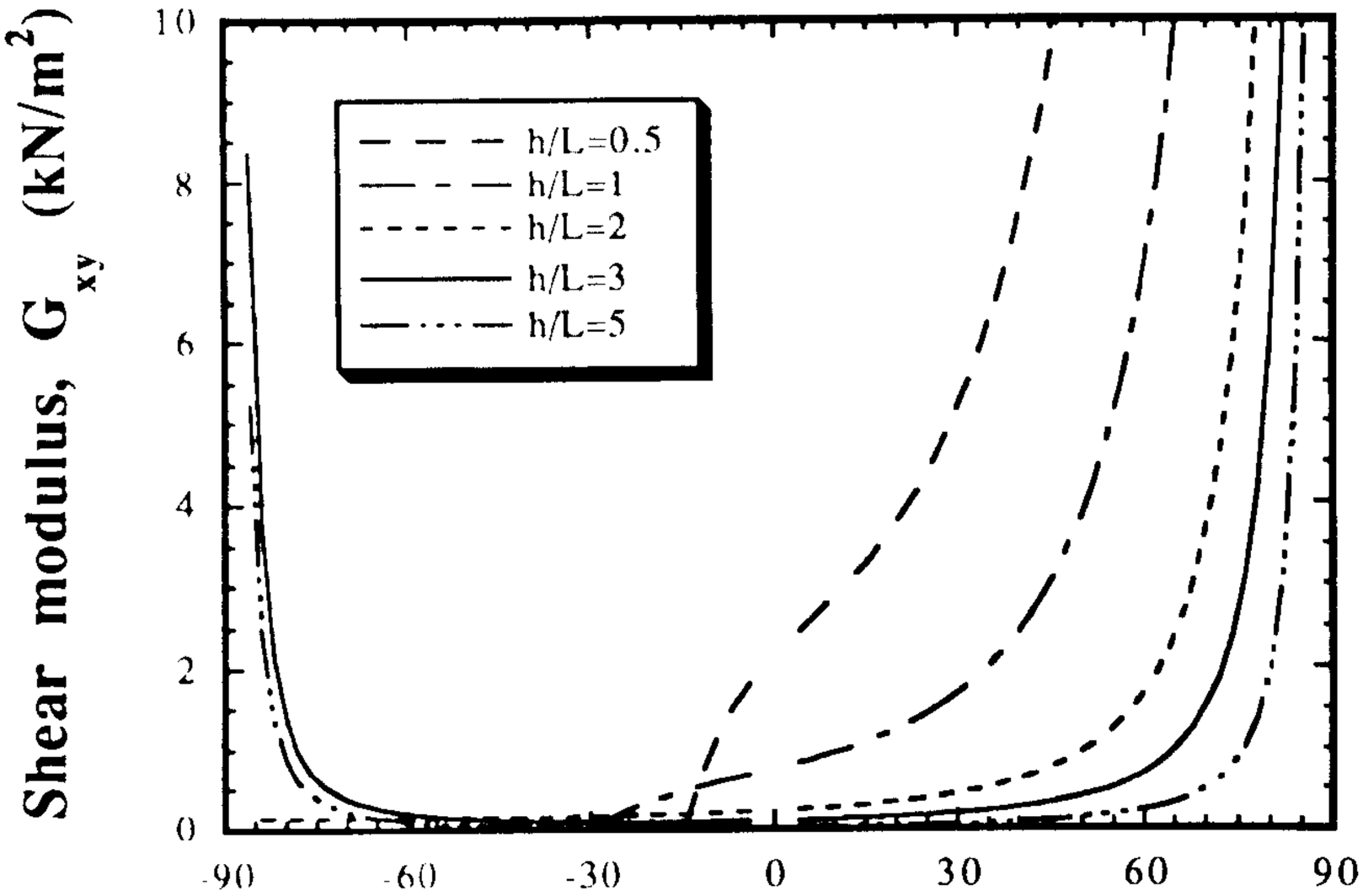

Fig. 8.7(a)

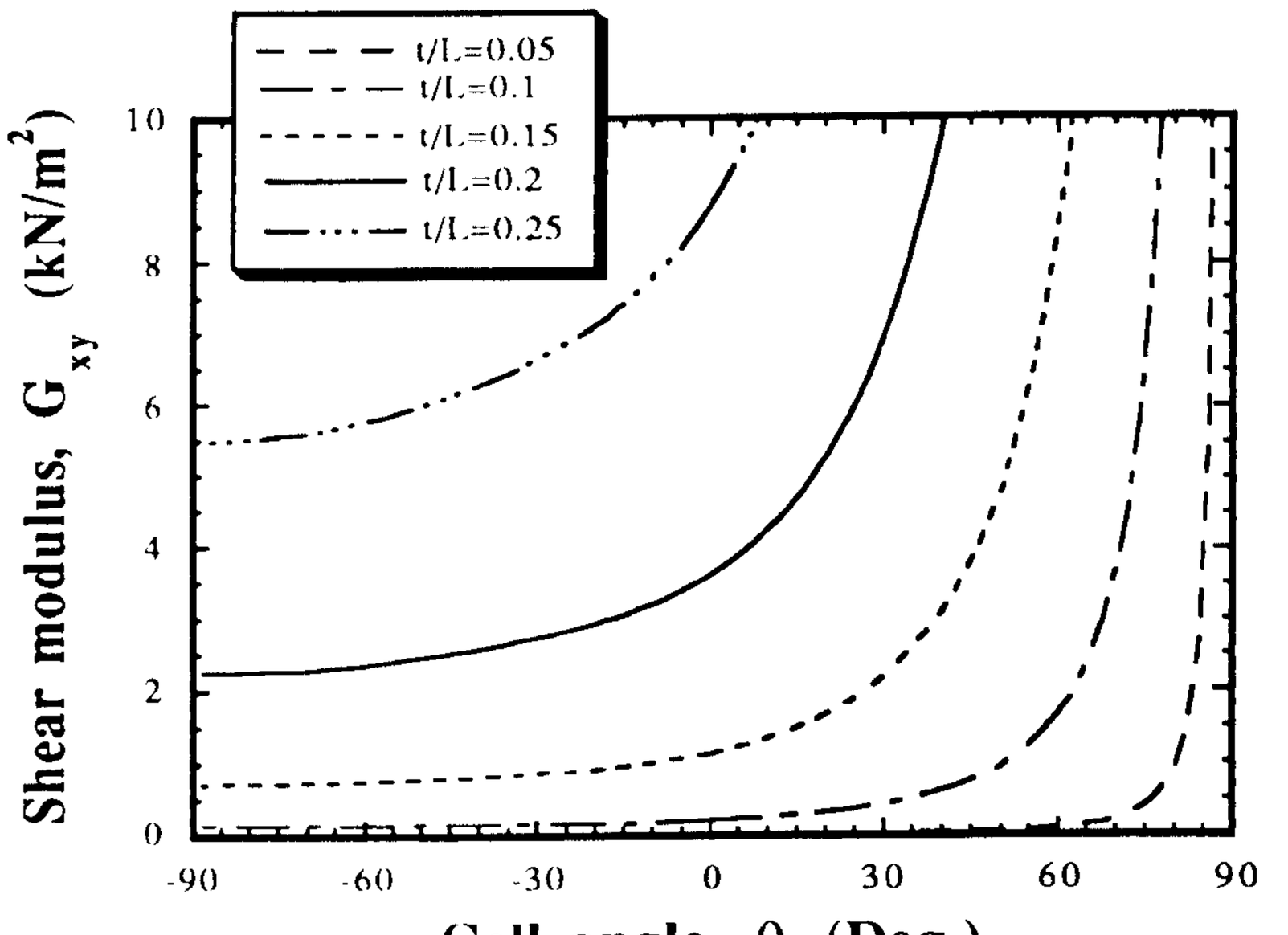

Fig. 8.7(b)

Fig. 8.7 Plots of G_{xy} vs. θ for the flexure model of conventional foam showing the effects of varying cell geometry (θ, α and t/L). (a) Varying θ and α for t=0.1L. (b) Varying θ and t/L for h=2L.

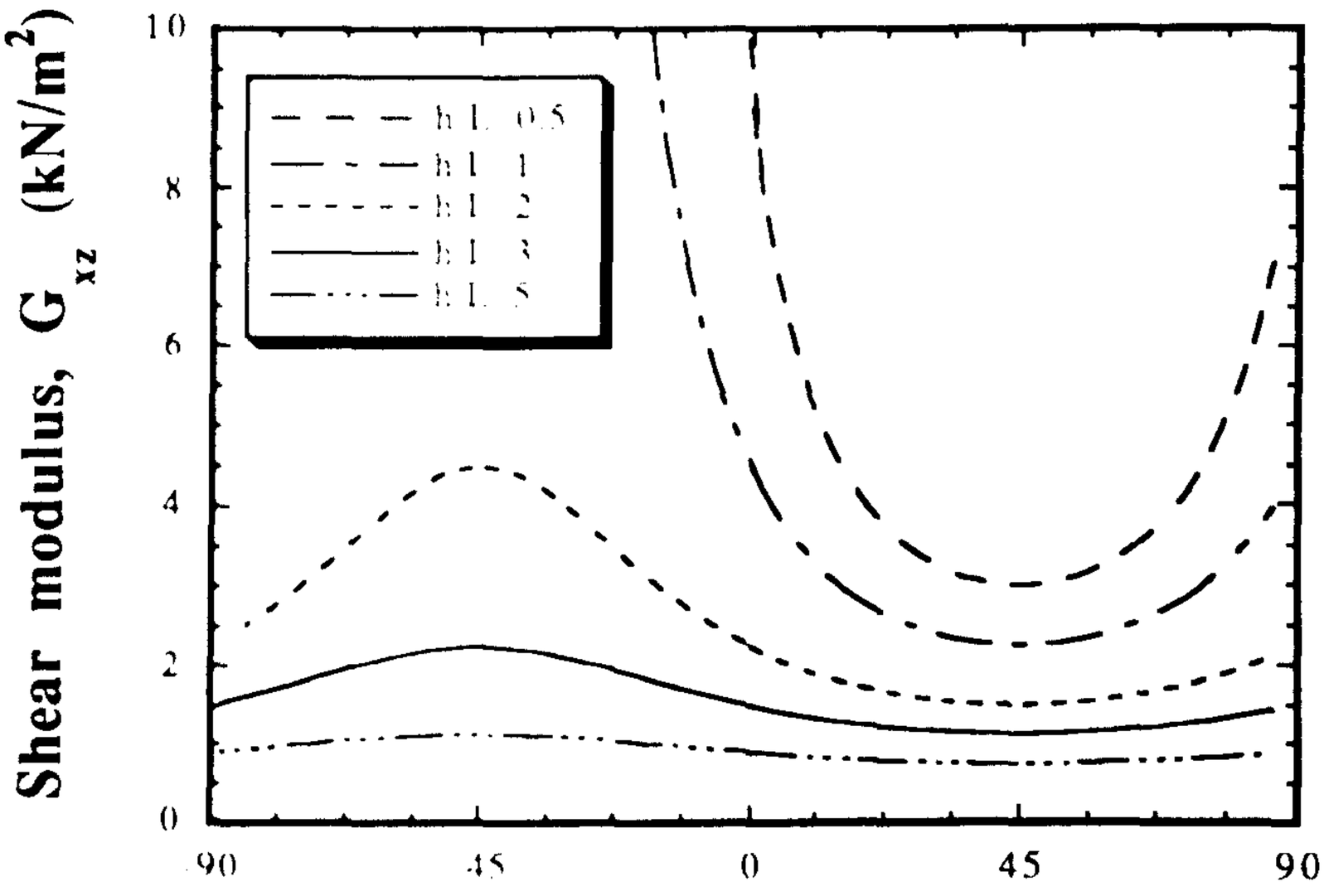

Fig. 8.8(a)

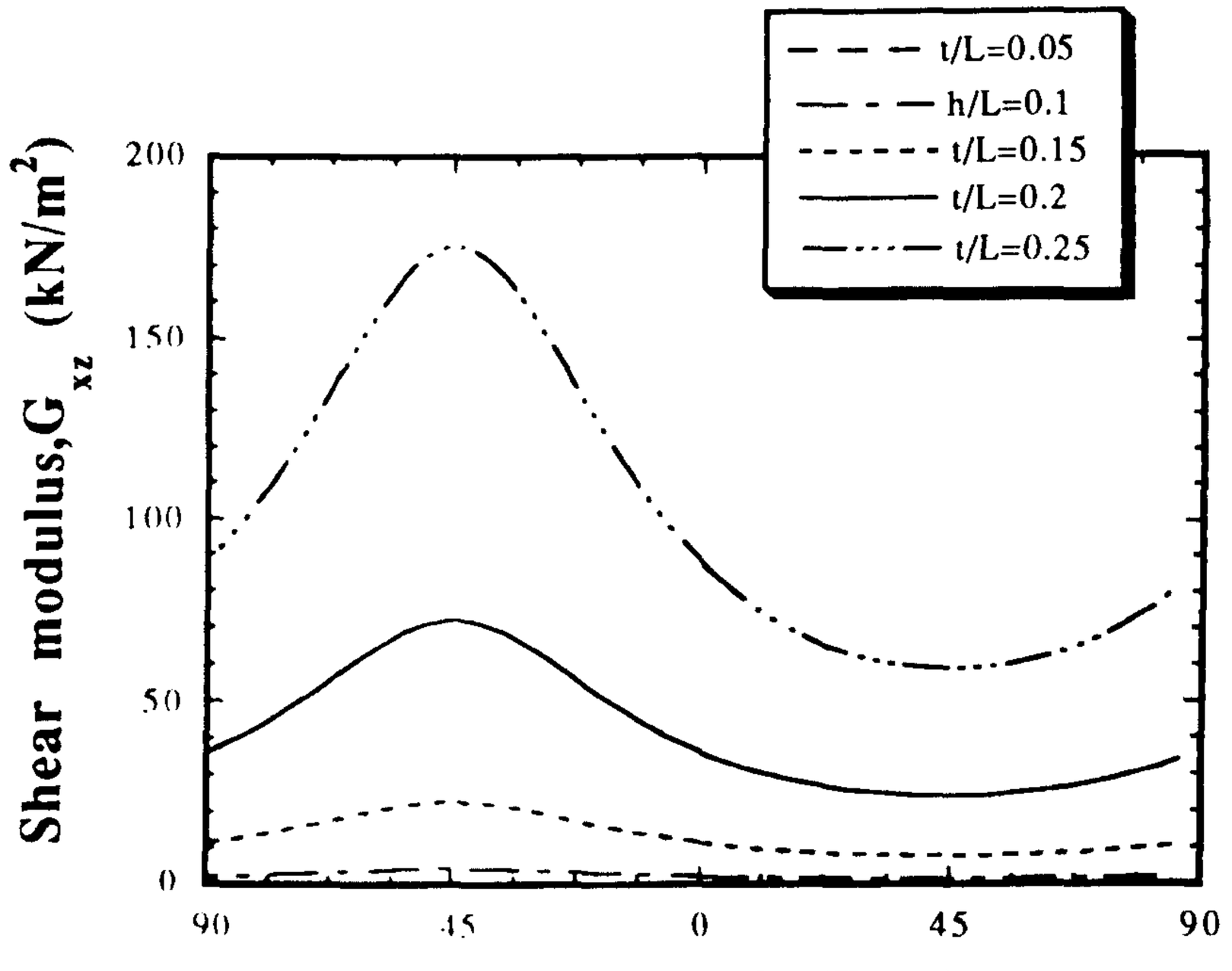

Fig. 8.8(b)

Fig. 8.8 Plots of G_{xz} vs. θ for the flexure model of conventional foam showing the effects of varying cell geometry (θ, α and t/L). (a) Varying θ and α for t=0.1L. (b) Varying θ and t/L for h=2L.

8.6 Effects of Cell Geometry on the Hinging Model

The graph of E_x versus θ plotting EQ. 5.66 (*Figure* 8.9(a) and (b)) and E_y versus θ plotting EQ. 5. 80 (Figure 8.10(a) and (b)) are identical in shape to those for the flexure model, differing only in the value of the force constant K_i as shown in EQ. 5.109. For a given t/L ratio, the hinging mechanism is operative at much larger forces than those required for flexure. As a result, the effects of h/L on the moduli E_x and E_y are significantly increased. In contrast to this, for a given h/L ratio, the hinging mechanism is operative at much lower forces than those required for flexure. The effects of t/L on the modulus E_x and E_y are significantly reduced as a result.

Comparison of EQ. 5.11 with 5.62, EQ. 5.12 with 5.61, and EQ. 5.30 with 5.76 shows that the effect of h/L on the Poisson's ratio ν_{xz}, ν_{xy} and ν_{yx} is identical to those for the flexure model and is shown in *Figures* 8.5 and 8.6.

Figures 8.11(a) and (b) show the reduction in the shear modulus, G_{xy} caused by increasing the h/L ratio, or reducing the t/L ratio for a conventional hexagonal cell. EQ. 5.93 is used for these plots.

Figures 8.12(a) and (b) show the shear modulus, Gxz, plotted against the cell angle, θ using EQ. 5.98. The curves are all skewed to the right so that for a given h/L or t/L ratio and θ a re-entrant cell has a higher modulus, Gxz, than the corresponding hexagonal cell of the same geometry.

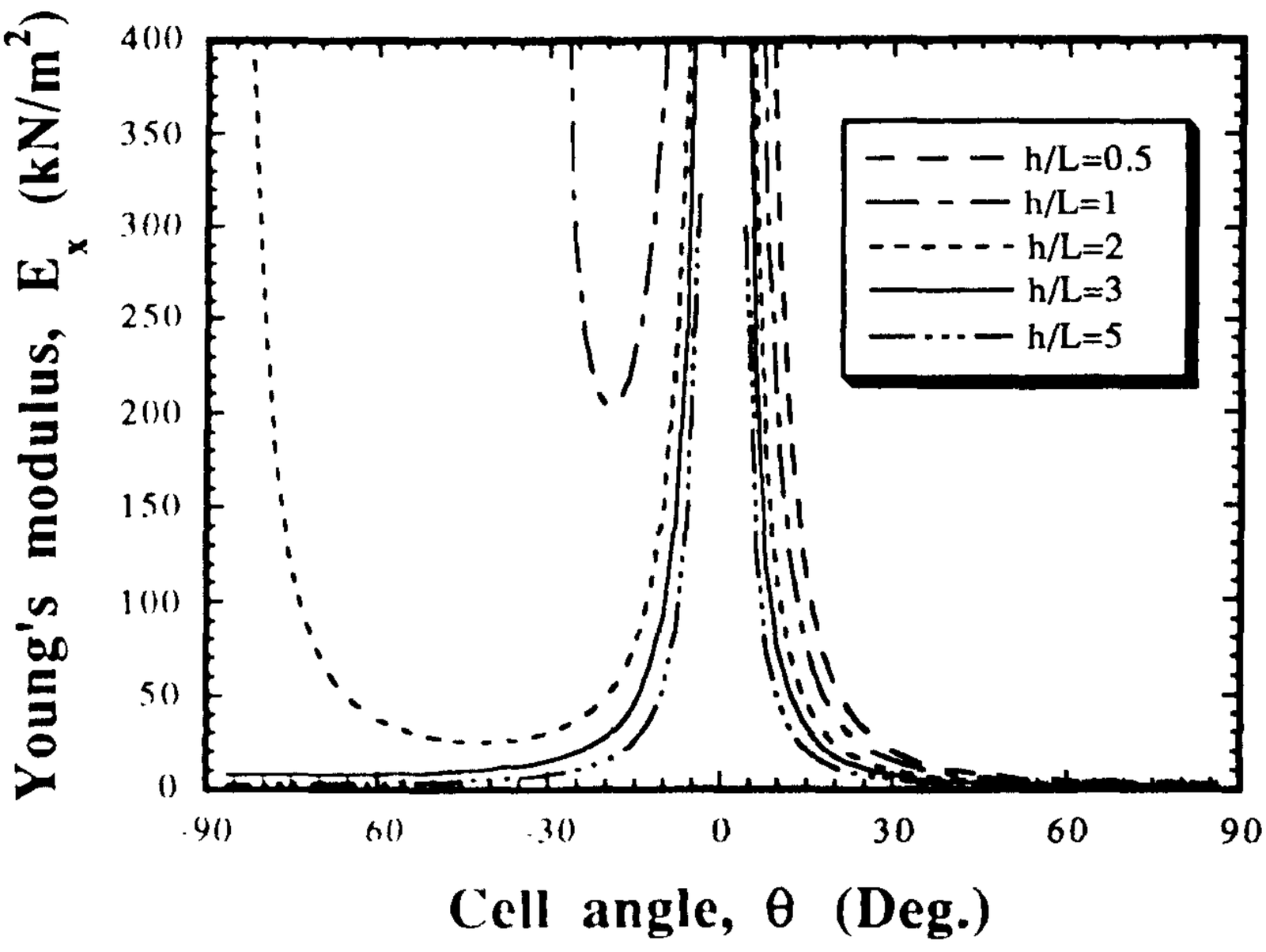

Fig. 8.9(a)

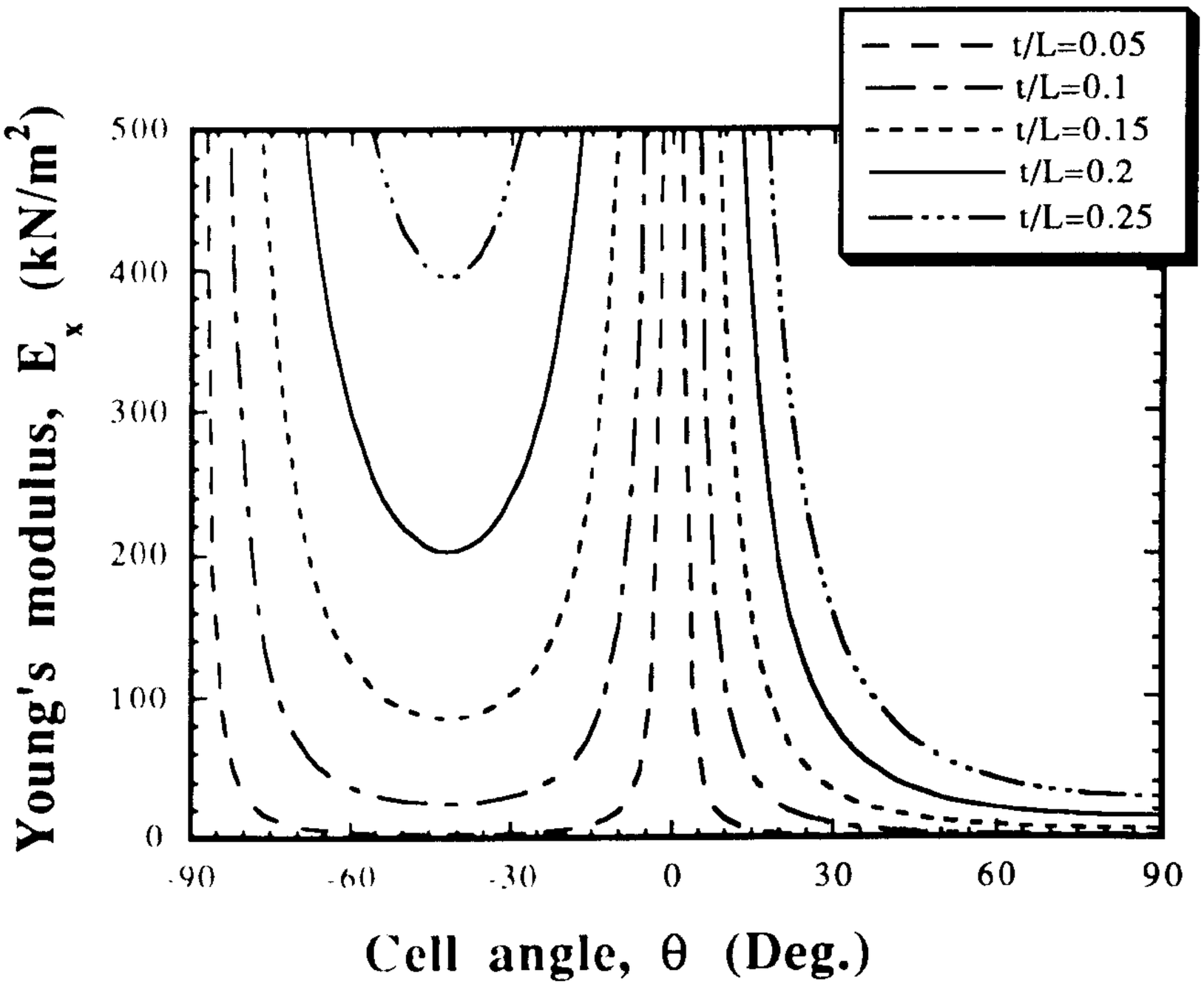

Fig. 8.9(b)

Fig. 8.9 Plots of E_x vs. θ for the hinging model of conventional foam showing the effects of varying cell geometry (θ, α and t/L). (a) Varying θ and α for t=0.1L. (b) Varying θ and t/L for h=2L.

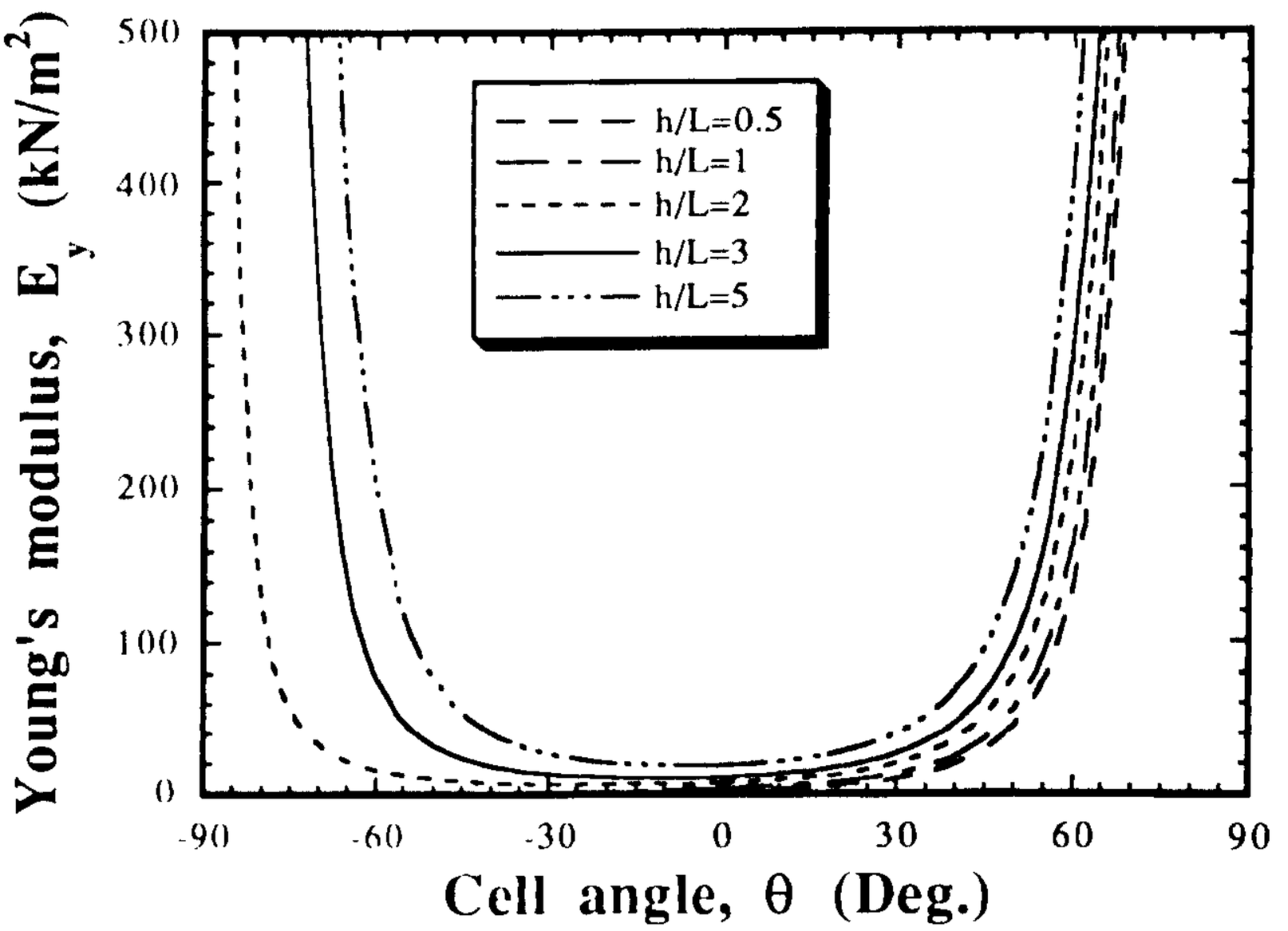

Fig. 8.10(a)

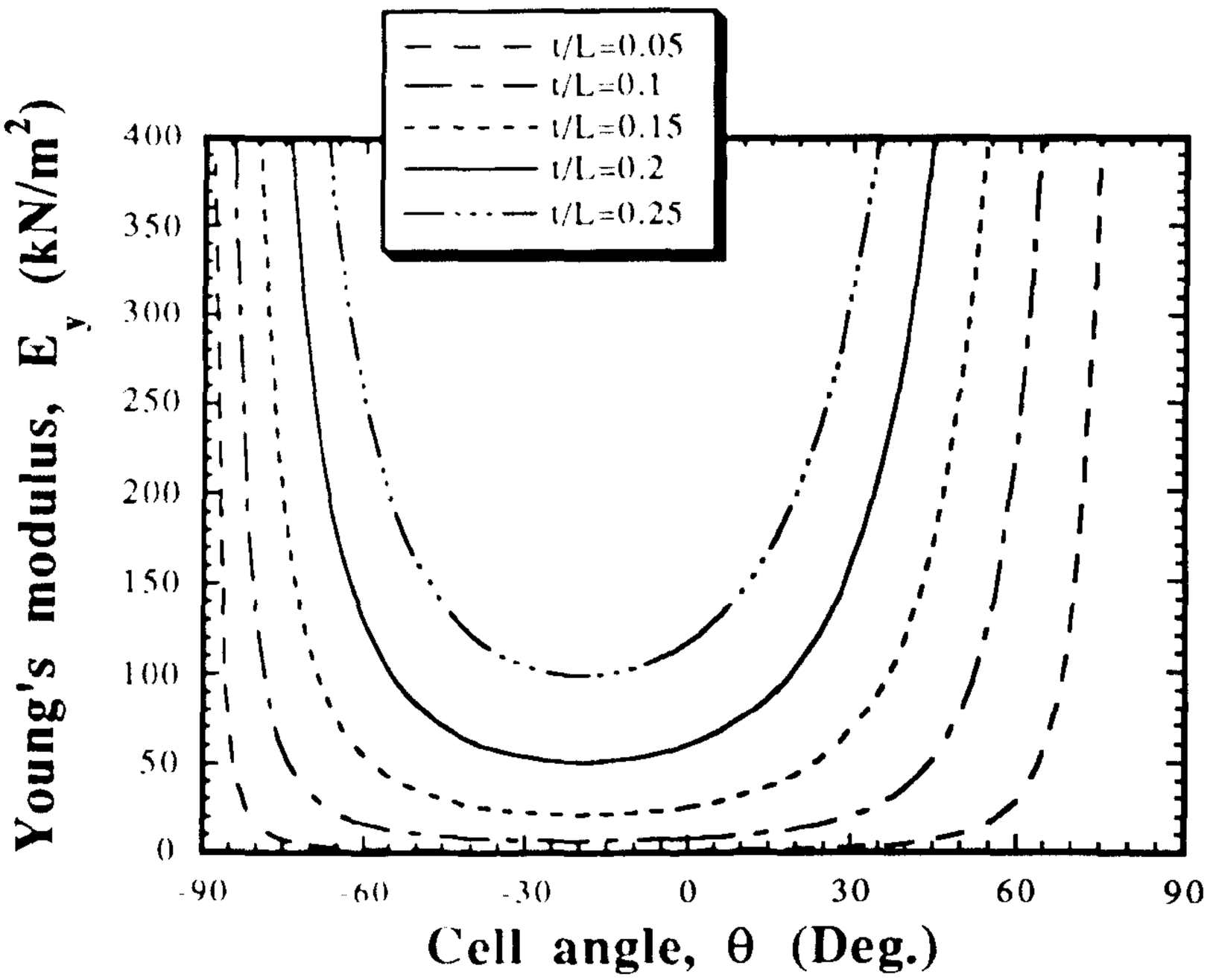

Fig. 8.10(b)

Fig. 8.10 Plots of E_y vs. θ for the hinging model of conventional foam showing the effects of varying cell geometry (θ, α and t/L). (a) Varying θ and α for t=0.1L. (b) Varying θ and t/L for h=2L.

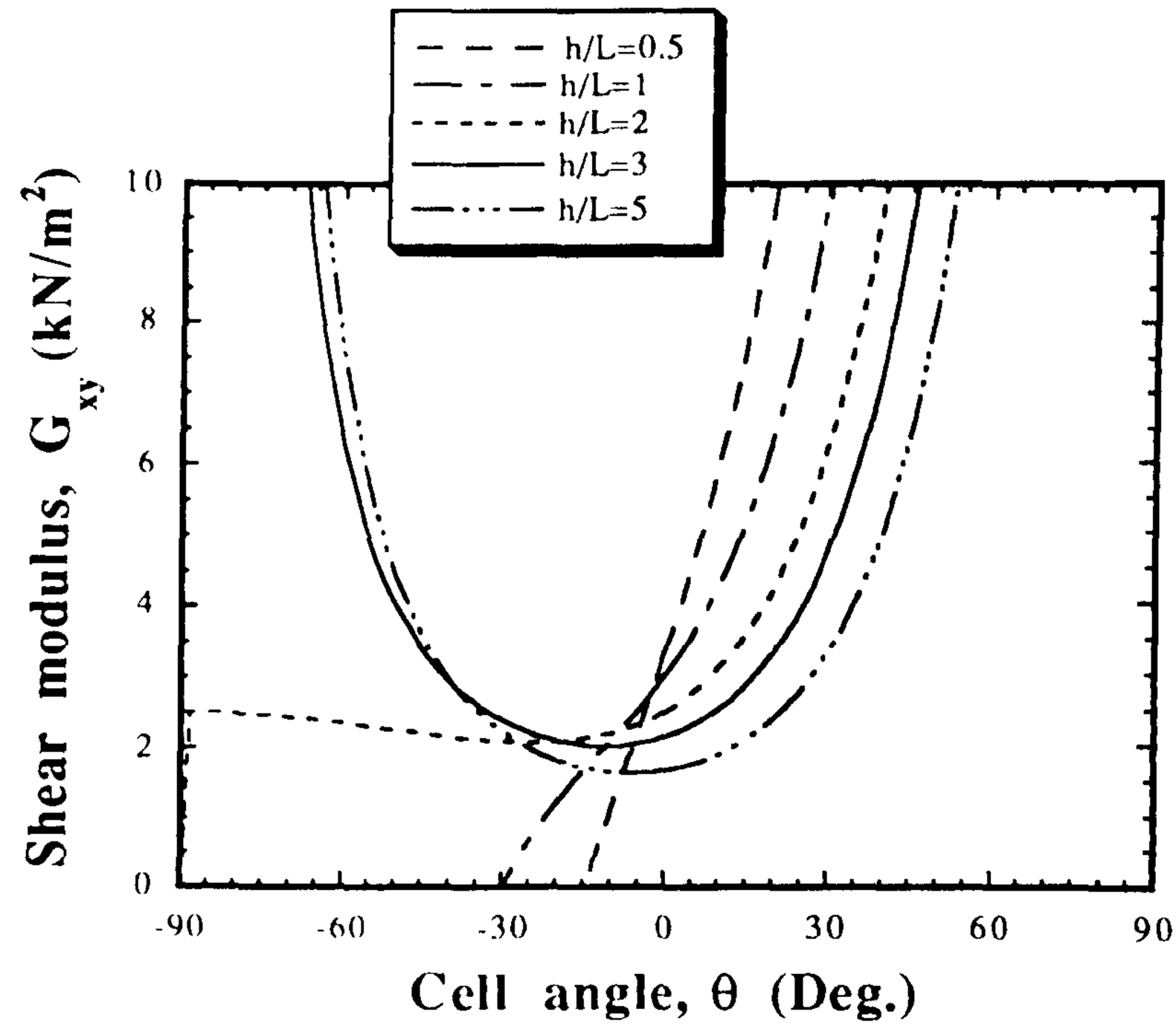

Fig. 8.11(a)

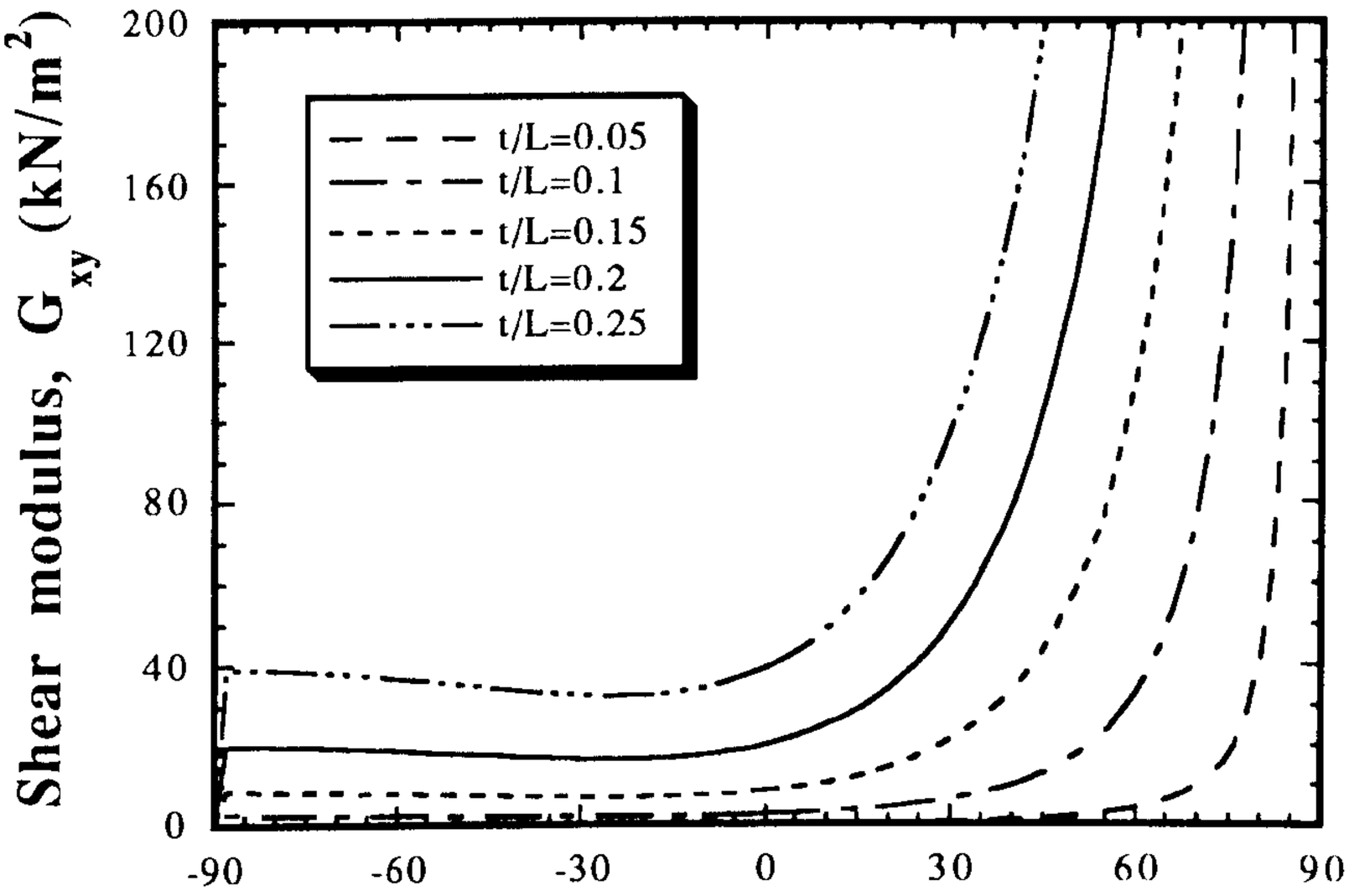

Fig. 8.11(b)

Fig. 8.11 Plots of G_{xy} vs. θ for the hinging model of conventional foam showing the effects of varying cell geometry (θ, α and t/L). (a) Varying θ and α for t=0.1L. (b) Varying θ and t/L for h=2L.

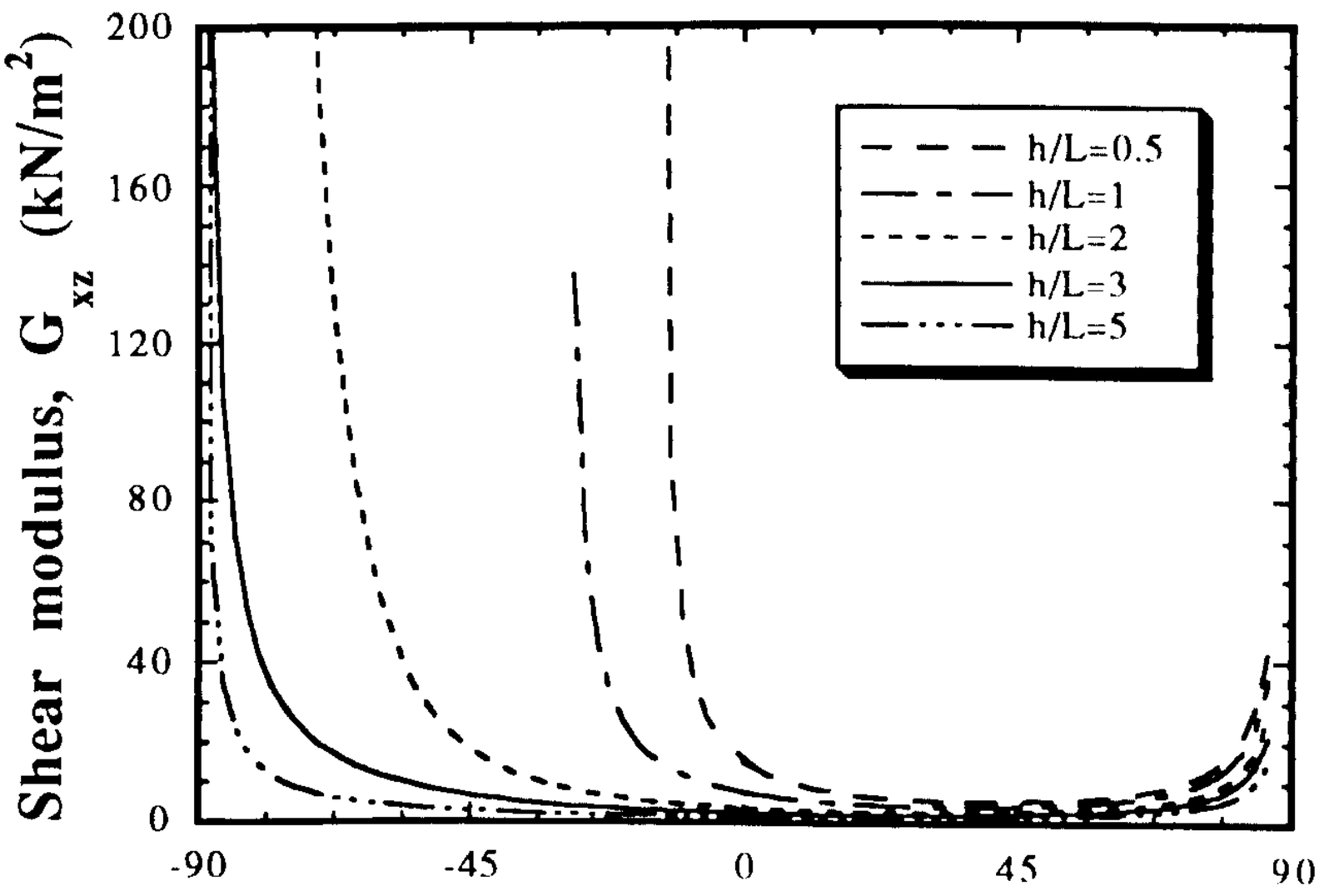

Fig. 8.12(a)

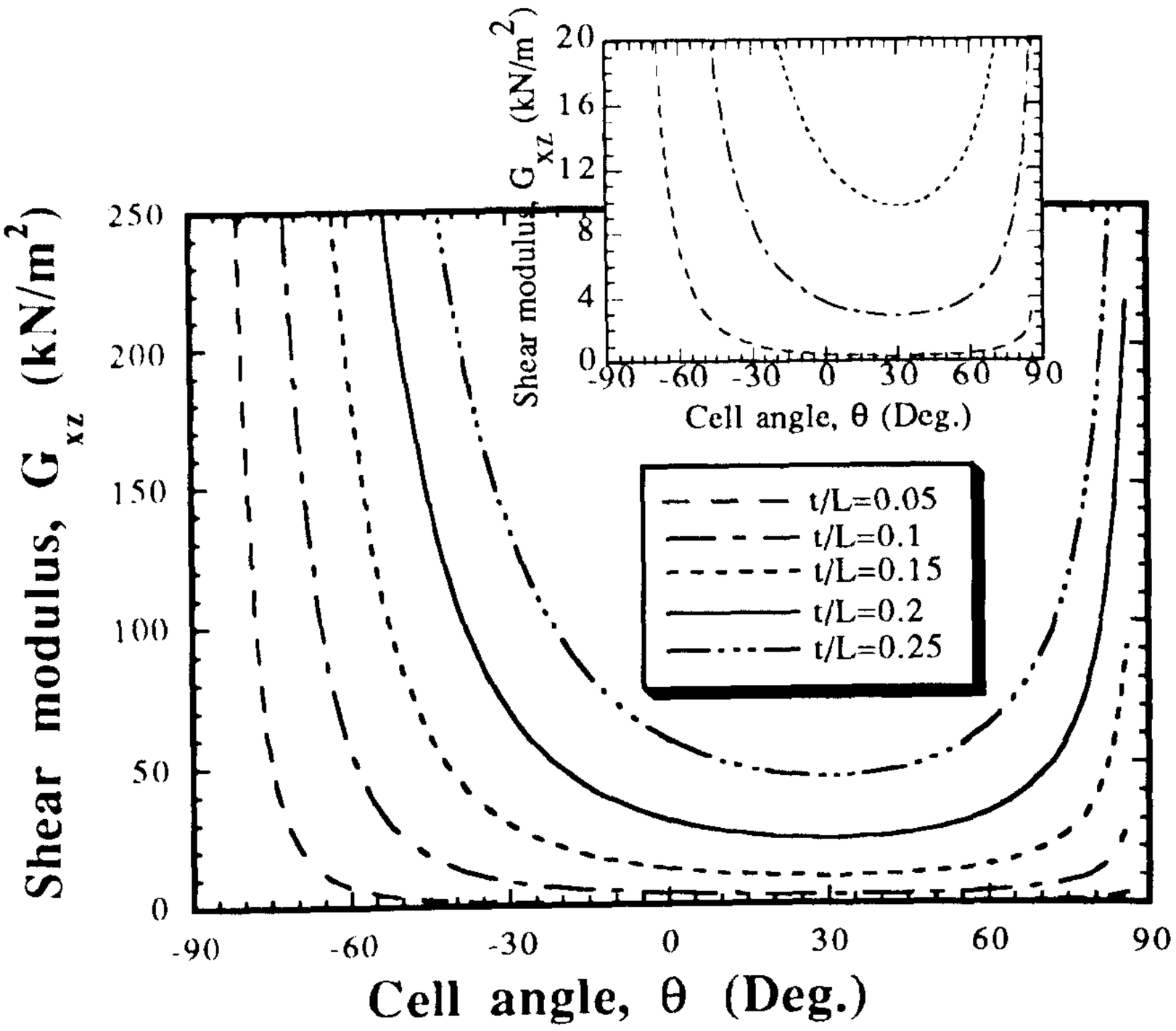

Fig. 8.12(b)

Fig. 8.12 Plots of G_{xz} vs. θ for the hinging model of conventional foam showing the effects of varying cell geometry (θ, α and t/L). (a) Varying θ and α for t=0.1L. (b) Varying θ and t/L for h=2L.

8.7 Effects of Cell Geometry on the Stretching Model

Unlike the moduli graphs for the flexure and hinging models, the moduli E_x, and E_y, for the stretching model, both reach their maxima at $+90^0$ and -90^0. *Figure* 8.13(a) shows that the plot of E_x is skewed to the right with the minimum value of E_x moving further to the right as t/L is increased. The value of E_x rapidly rises when the cell angle lies in the ranges $-30^o < \theta < -60^o$ and $60^o < \theta < 90^o$ and increasing the value of t/L causes an increases in E_x for a given angle. As expected, the t/L ratio is important to the moduli in stretching since the latter is directly proportional to the cross-sectional area of the cell walls. *Figure* 8.13(b) shows that the plot of E_x is skewed to the right with the minimum values of E_x moving further to the right as h/L is reduced. As h/L decreases E_x increases. *Figure* 8.14(a) shows the reduction in the Young's modulus, E_y caused by increasing the h/L ratio for a conventional hexagonal cell. For a given h/L ratio, i.e. 2, the graph of E_y versus θ (*Figure* 8.14(b)) shows the reduction in the Young's modulus, Ey, caused by decreasing the t/L ratio, and that the value of E_y of a conventional hexagonal cell is always larger than that of the corresponding re-entrant cell of the same geometry.

The plots for Poisson's ratio are shown in *Figures* 8.15 and 8.16. The most

important feature is that both ν_{xy} and ν_{yx} are positive for re-entrant cells and negative for hexagonal cells. The plots are not symmetrical. Decreasing h/L ratio increases the numerical value of ν_{xy} for both hexagonal and re-entrant cells (*Figure* 8.15). *Figure* 8.16 shows that increasing h/L ratio increases the value of ν_{yx} of the re-entrant cell, and decreases the numerical value of ν_{yx} of the hexagonal cell.

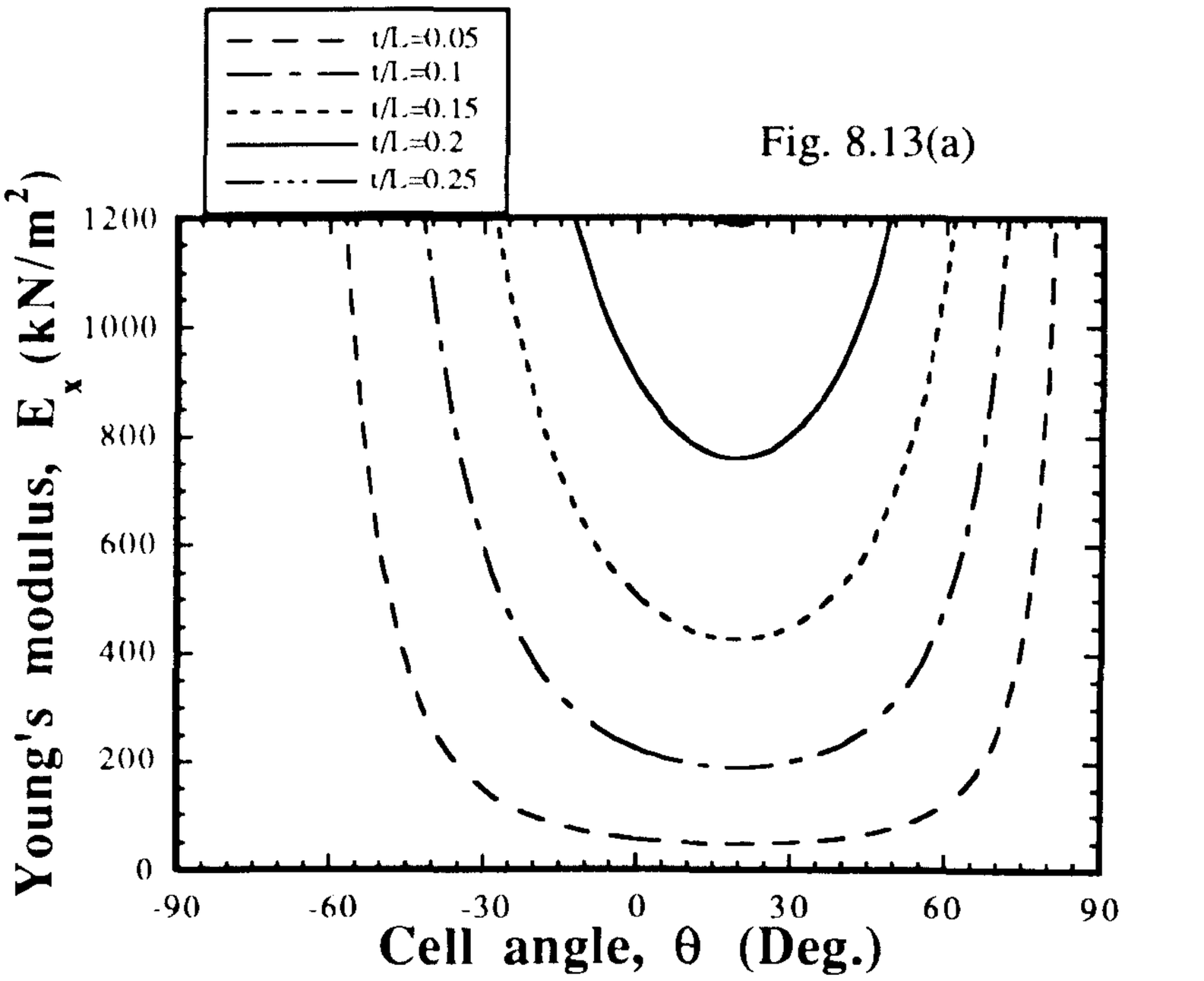

Fig. 8.13(a)

Fig. 8.13(b)

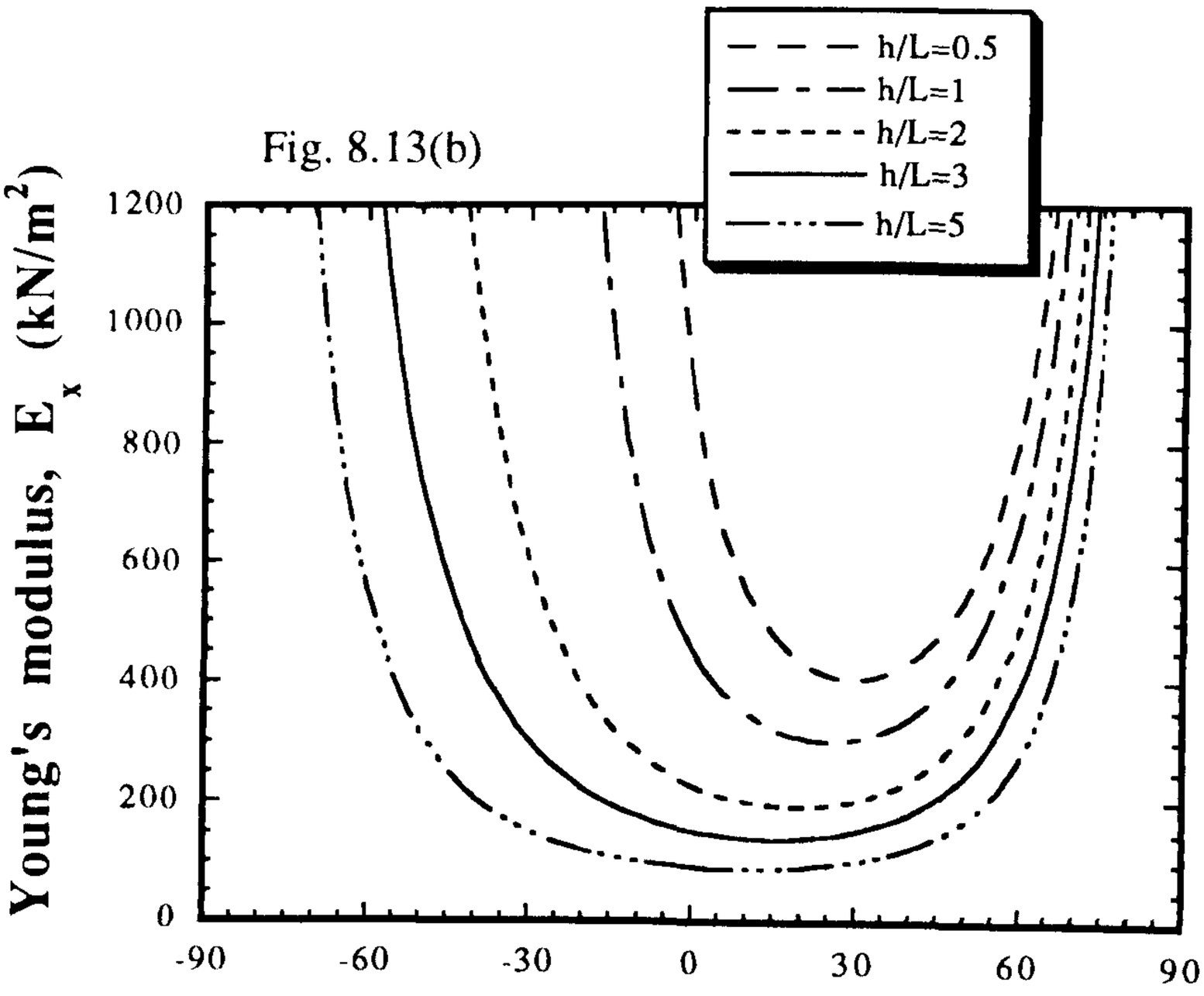

Fig. 8.13 Plots of E_x vs. θ for the stretching model of conventional foam showing the effects of varying cell geometry (θ, α and t/L). (a) Varying θ and t/L for h=2L. (b) Varying θ and α for t=0.1L.

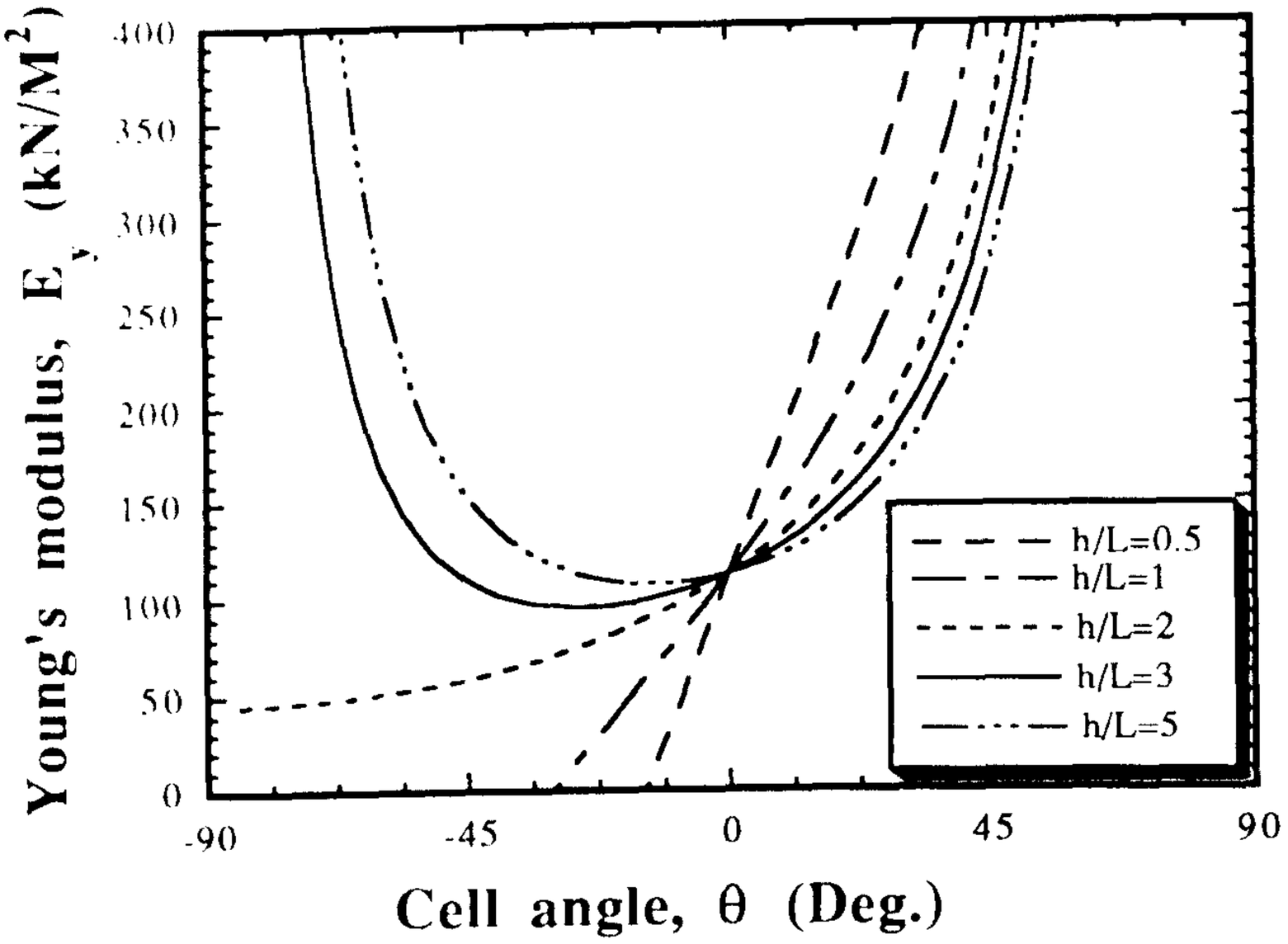

Fig.8.14(a)

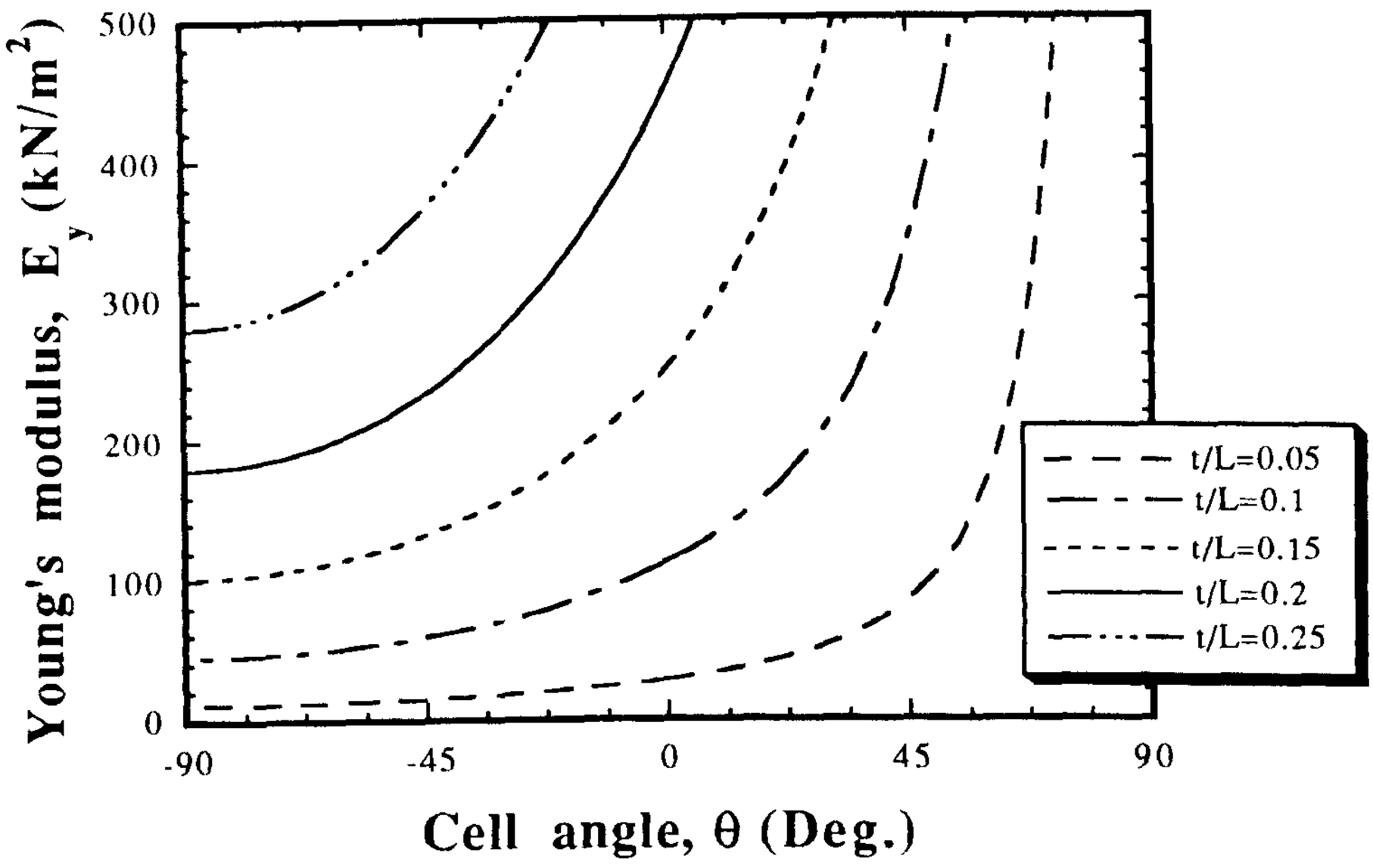

Fig. 8.14(b)

Fig. 8.14 Plots of E_y vs. θ for the stretching model of conventional foam showing the effects of varying cell geometry (θ, α and t/L). (a) Varying θ and α for t=0.1L. (b) Varying θ and t/L for h=2L.

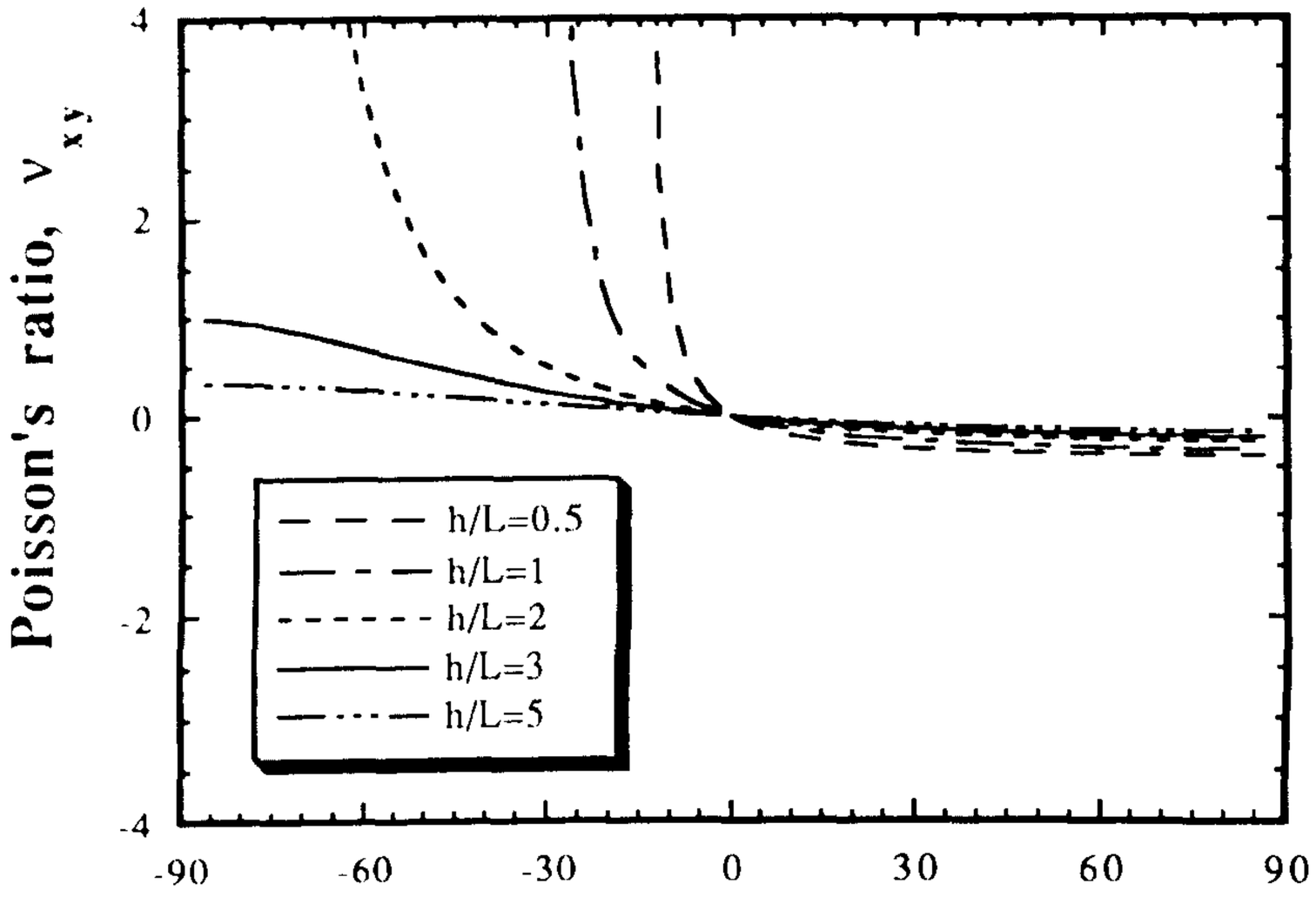

Fig. 8.15 Plots of υ_{xy} vs. θ for both the stretching model and the hinging model showing the effects of varying cell geometry, θ and h/L for t=0.1L.

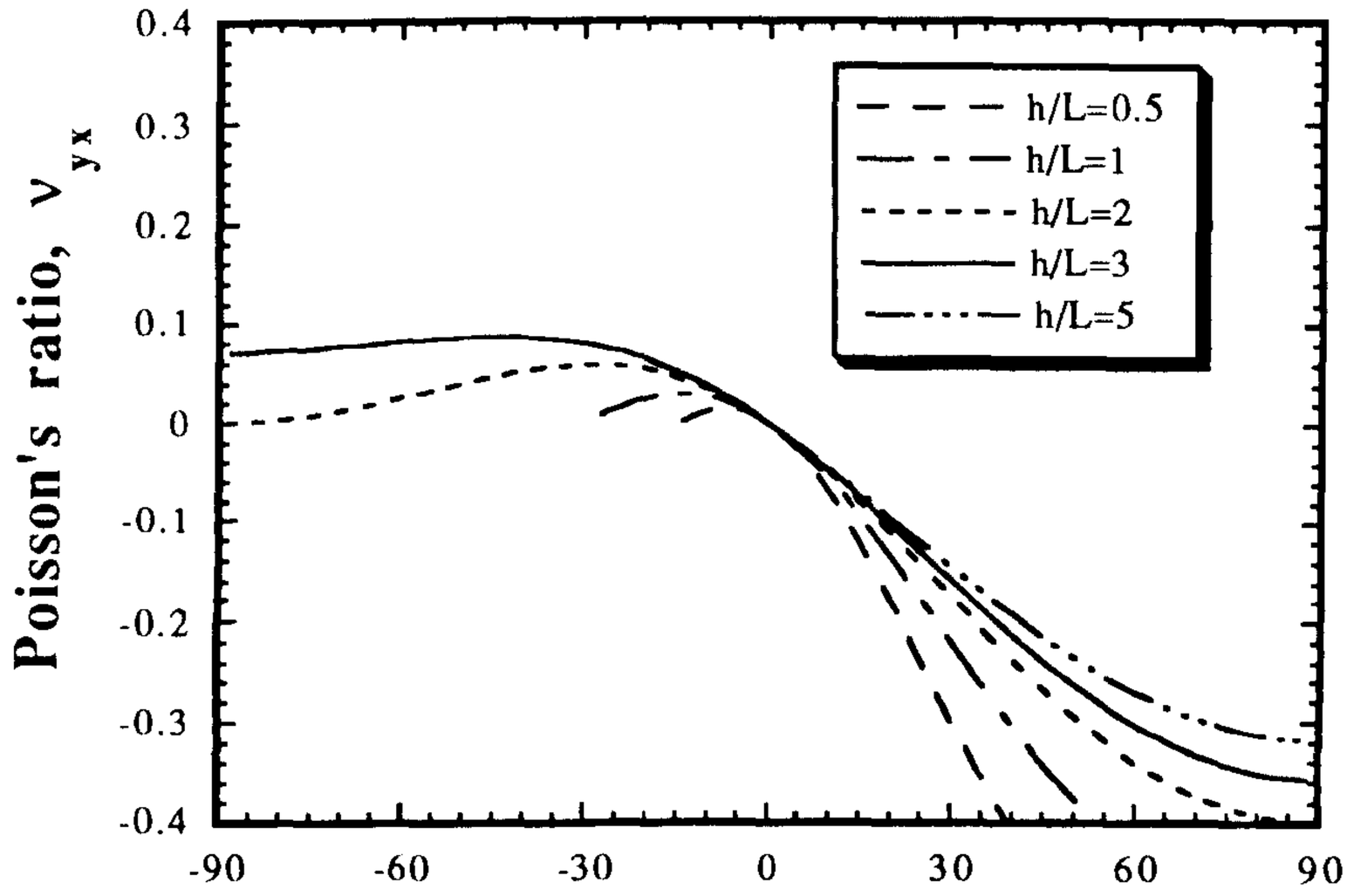

Fig. 8.16 Plots of υ_{yx} vs. θ for both the stretching model and the hinging model showing the effects of varying cell geometry, θ and h/L for t=0.1L.

8.8 Effects of Cell Geometry on the Combined Model

The graphs of E_x versus θ (*Figure* 8.17(a) and (b)) and E_y versus θ (*Figures* 8.18(a) and (b)) are almost identical in shape to those for the flexure and hinging models described earlier. As expected, flexure and hinging are more important to the moduli than the stretching mechanism since the value of the force constant, $K_f<K_h<K_s$. This is obvious when EQs. 5.107, 5.108 and 5.113 are compared. Similarly, the effects of t/L on the moduli E_x (*Figure* 8.17) and E_y (*Figure* 8.18) are identical to those for the flexure and the hinging model only differing in the value of the moduli. EQs. 5.153 and 5.163 are used for Figures 8.17 and 8.18 respectively.

Figure 8.19(a) and (b) show the effects of h/L and t/L on Poisson's ratio ν_{xy}. EQ. 5.150 is used for these plots. A limitation of the model is that for small angles, i.e. 0^0 the highest Poisson's ratios are achieved. Decreasing h/L or t/L ratio increases the numerical value of the effective Poisson's ratio of both hexagonal and re-entrant cells. It should also be noted that the graphs are not symmetrical. Very low Poisson's ratio are achieved when the cell angle is numerically large (i.e. $-70^\circ < \theta < -90^\circ$, and $60^\circ < \theta < 90^\circ$).

Figure 8.20(a) and (b) show the effects of h/L and t/L on the Poisson's ratio ν_{yx} respectively. EQ. 5.160 is used for these plots. The lowest value of ν_{yx} is achieved when the cell angle is extremely small, i.e. 0^0. Increasing the value of h/L increases the numerical value of the Poisson's ratio of both hexagonal an re-entrant cells (Figure 8.20(a)). However, increasing the value of t/L decreases the numerical value of the Poisson's ratio of both hexagonal and re-entrant cells (Figure 8.20(b)). Again, it should also be noted that the graphs are not symmetrical.

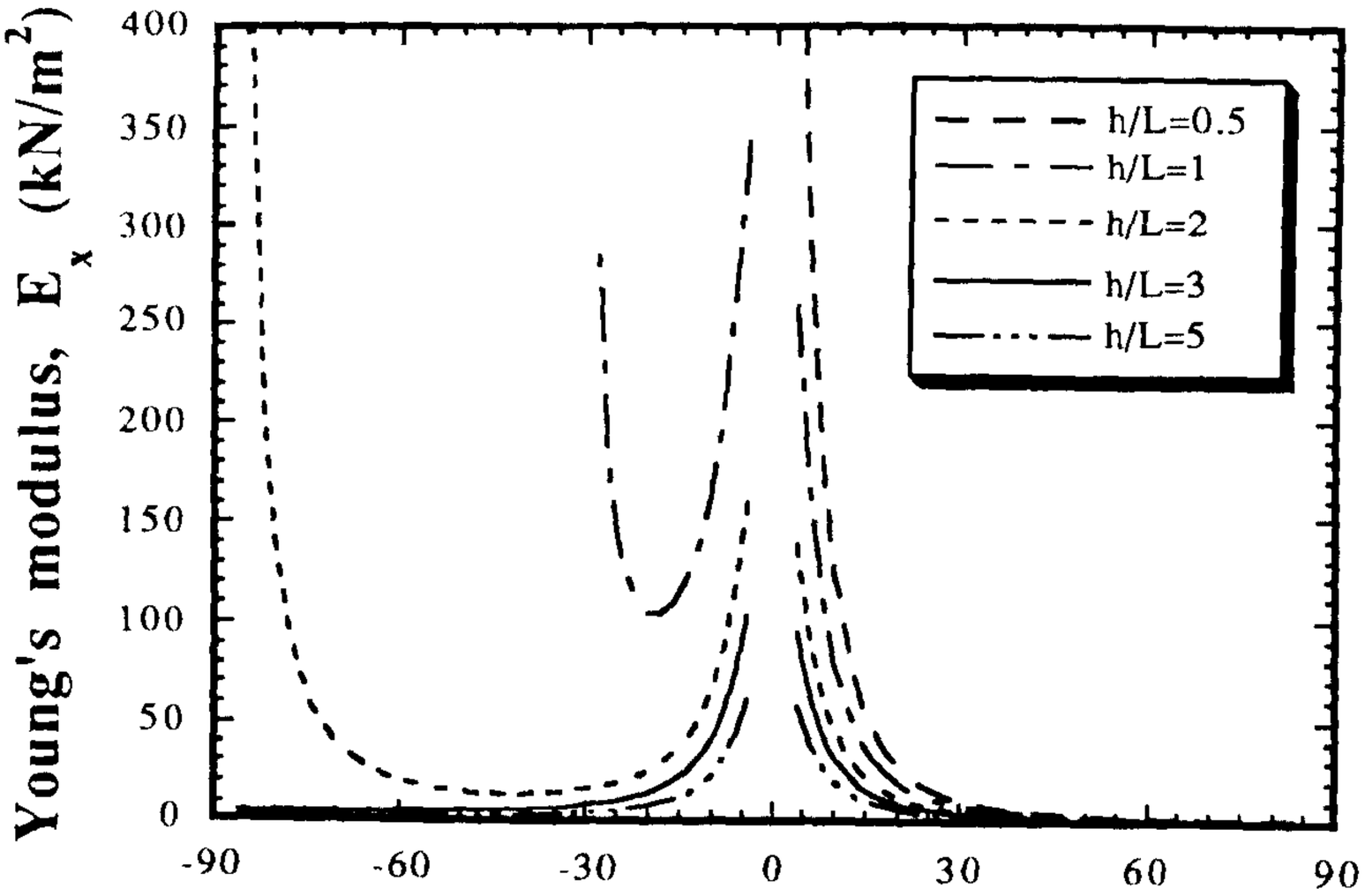

Fig. 8.17(a)

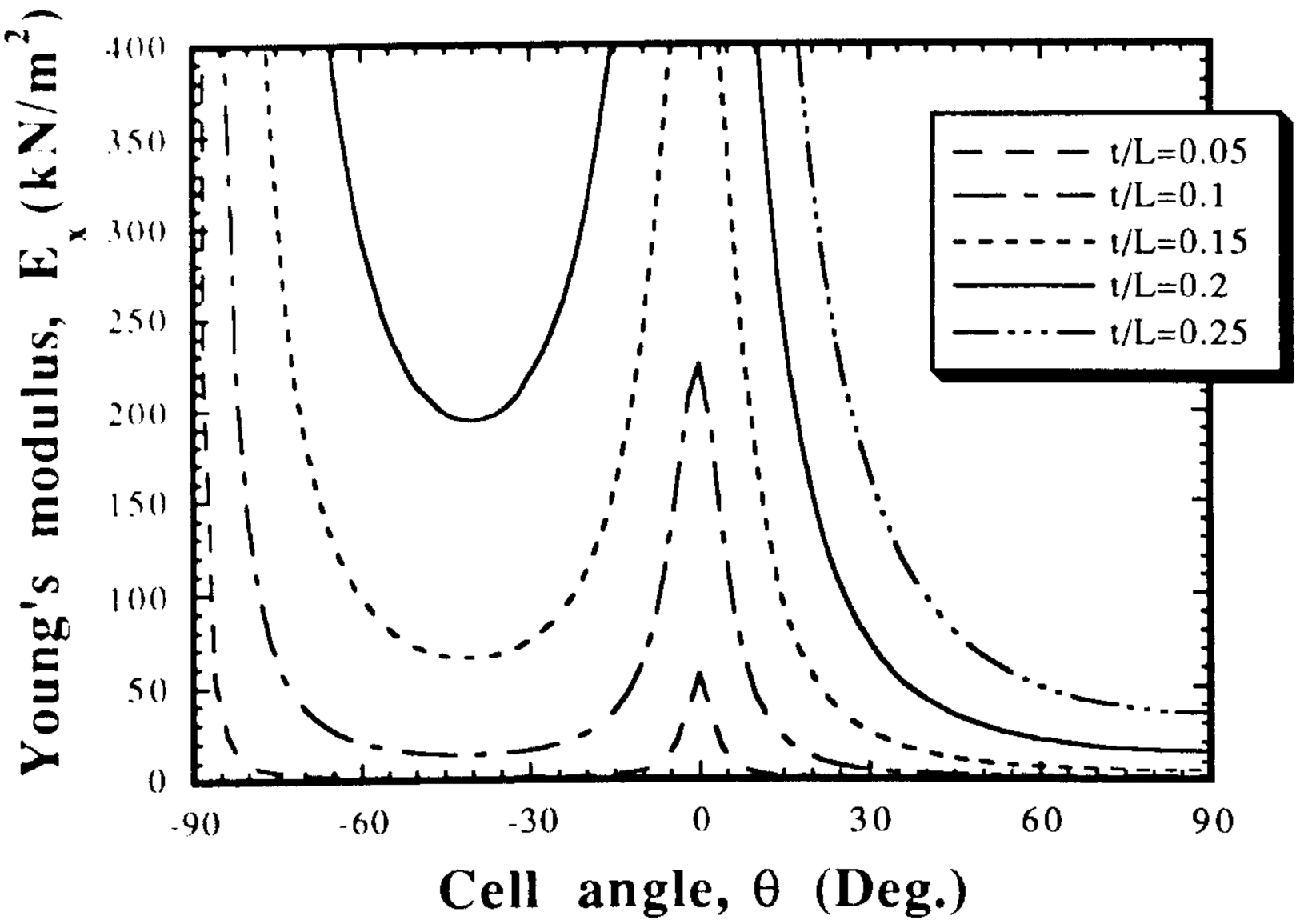

Fig. 8.17(b)

Fig. 8.17 Plots of E_X vs. θ for the combined model of conventional foam showing the effects of varying cell geometry (θ, α and t/L). (a) Varying θ and α for t=0.1L. (b) Varying θ and t/L for h=2L.

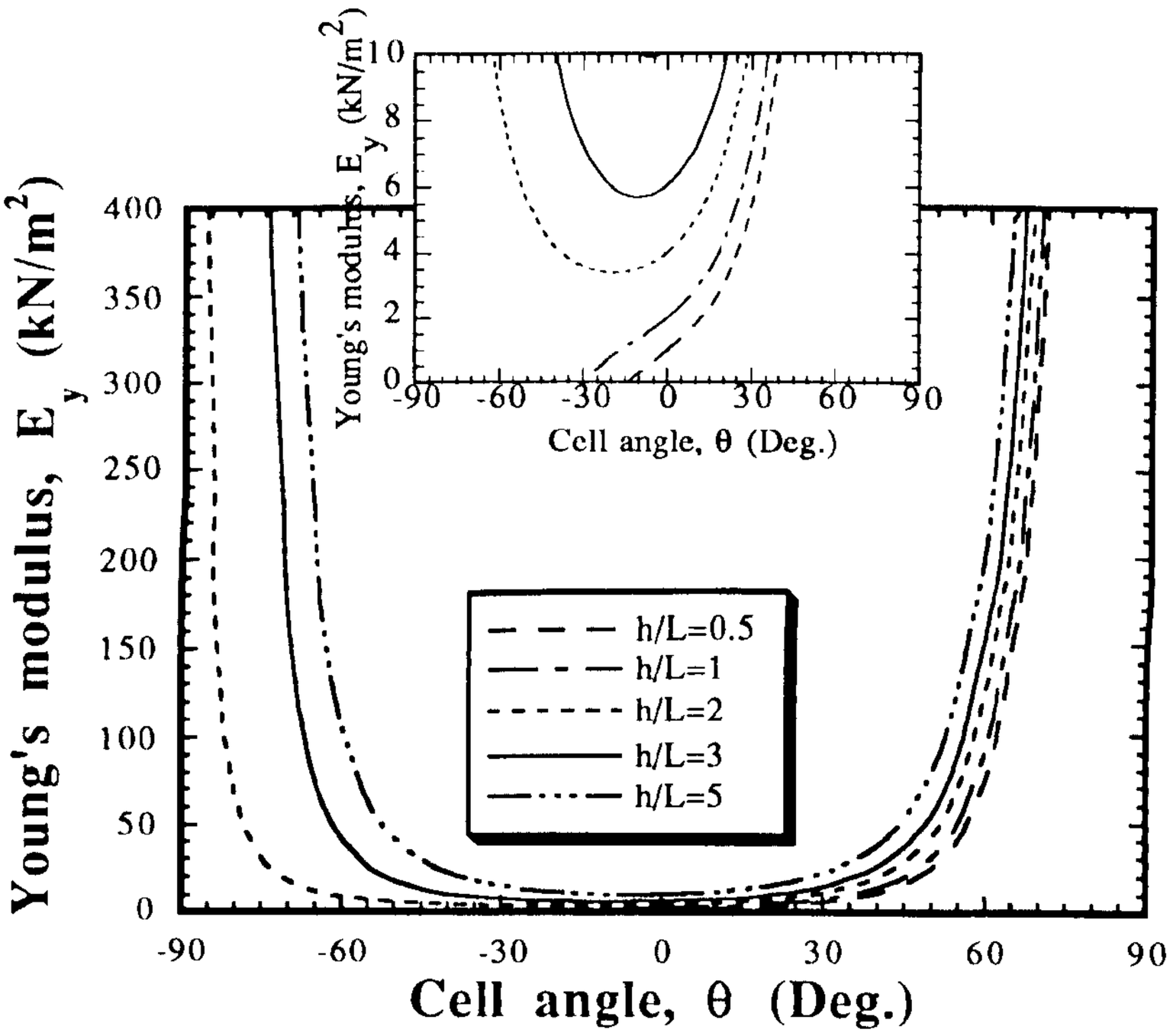

Fig. 8.18(a)

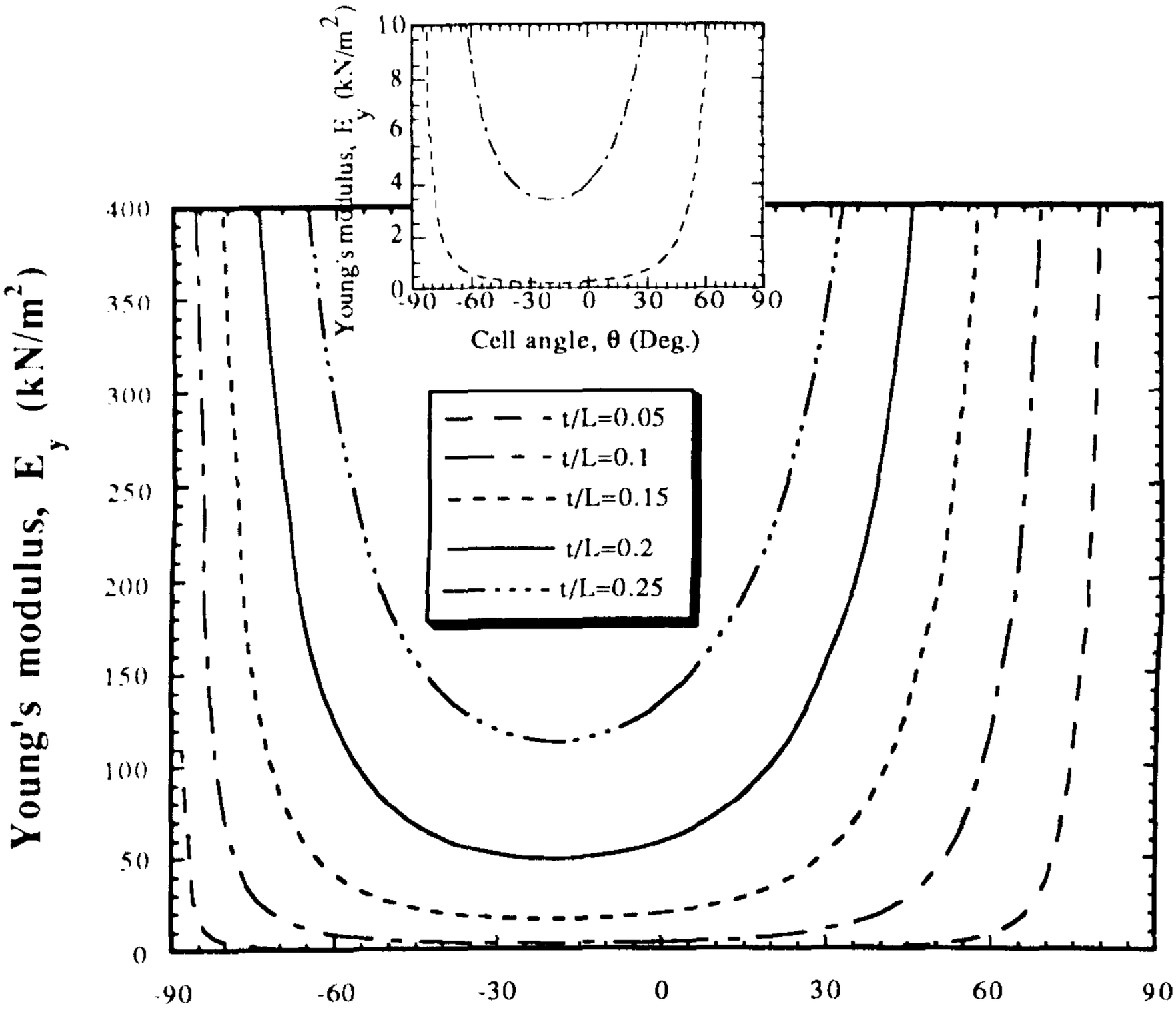

Fig. 8.18(b)

Fig. 8.18 Plots of E_y vs. θ for the combined model of conventional foam showing the effects of varying cell geometry (θ, α and t/L). (a) Varying θ and α for t=0.1L. (b) Varying θ and t/L for h=2L.

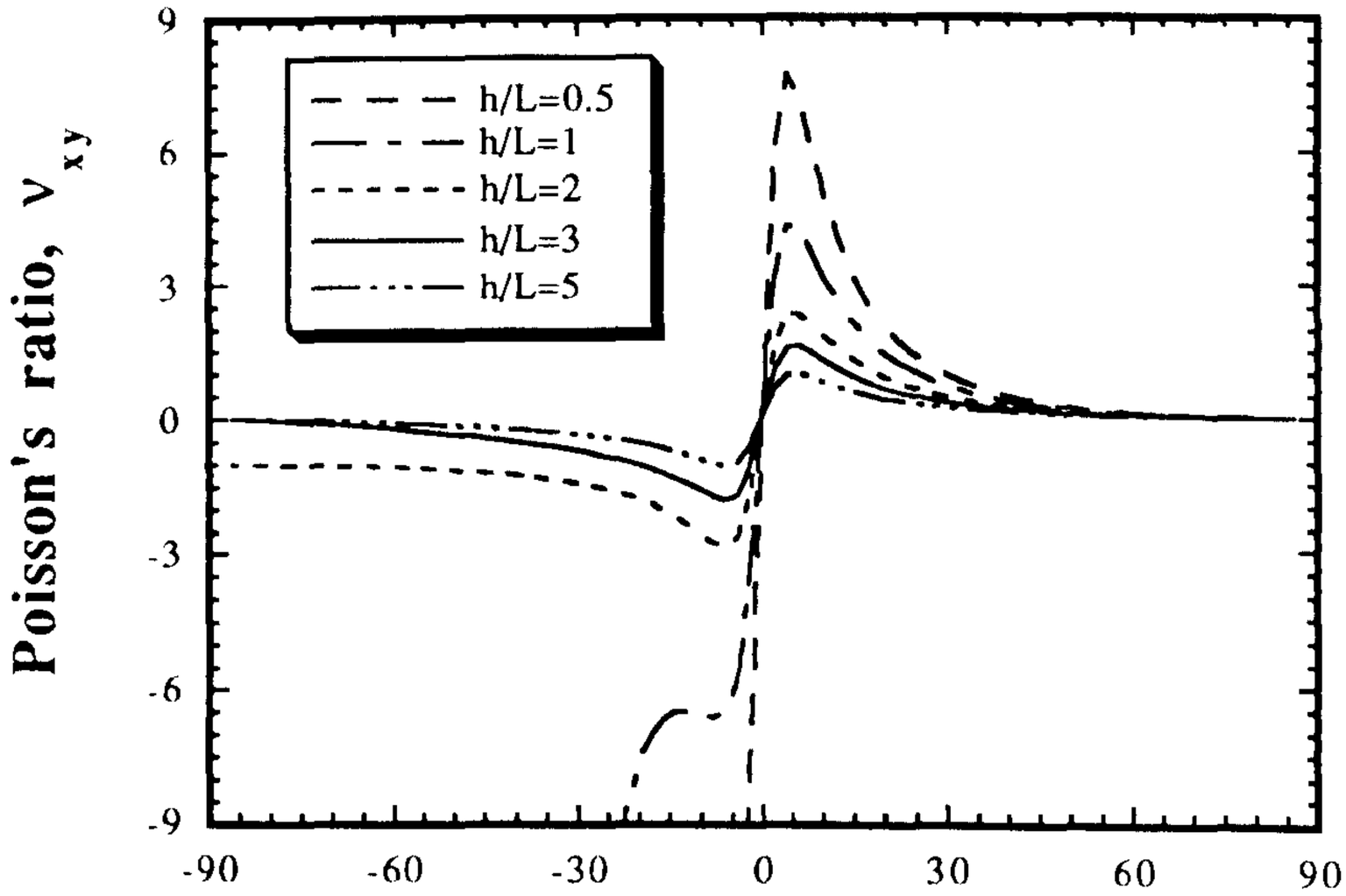

Fig. 8.19(a)

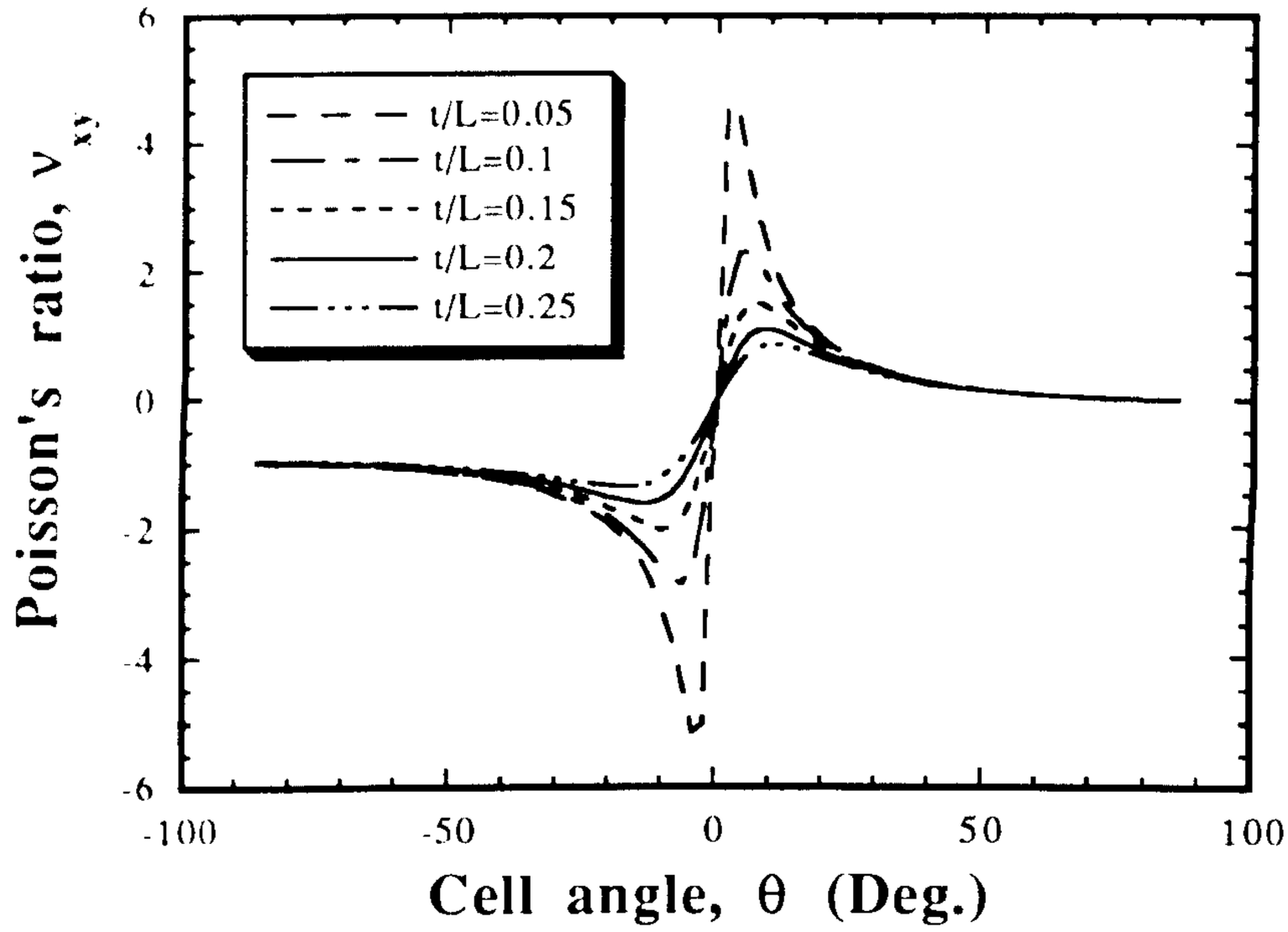

Fig. 8.19(b)

Fig. 8.19 Plots of υ_{xy} vs. θ for both the combined model and the combined model showing the effects of varying cell geometry, θ, t/L and h/L.(a) Varying θ and α for t=0.1L. (b) Varying θ and t/L for h=2L.

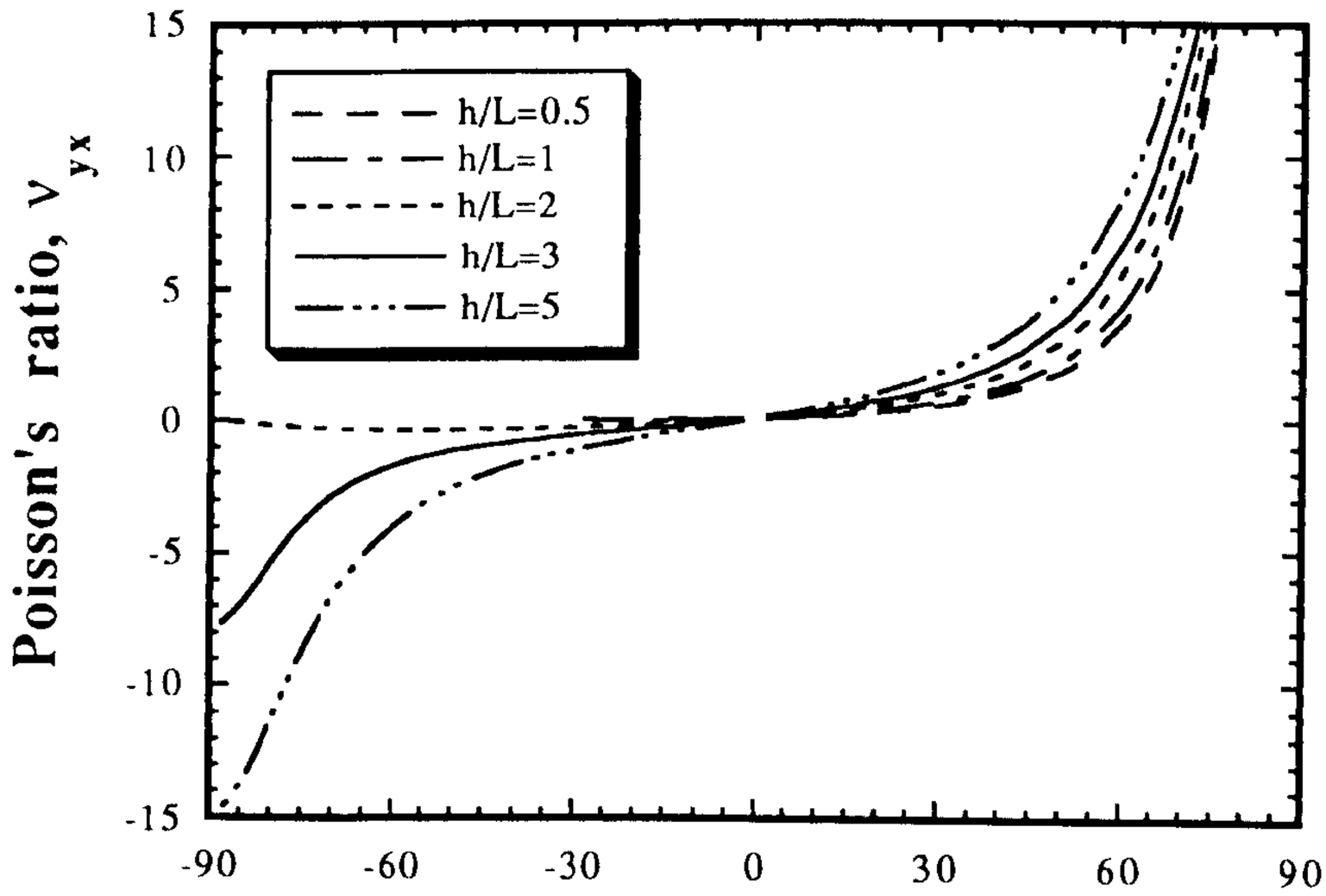

Fig. 8.20(a)

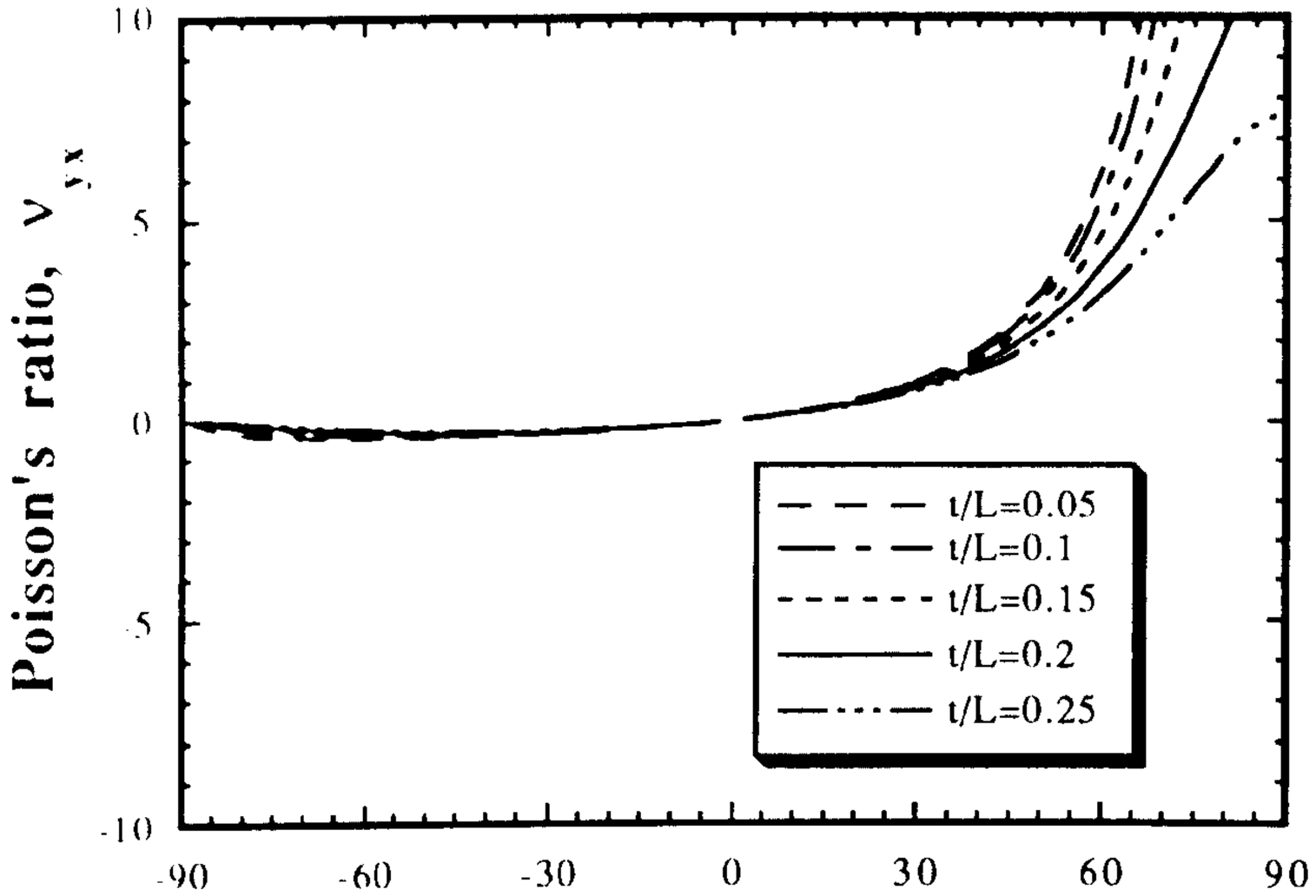

Fig. 8.20(b)

Fig. 8.20 Plots of υ_{yx} vs. θ for both the flexure model and the combined model showing the effects of varying cell geometry, θ, t/L and h/L. (a) Varying θ and α for t=0.1L. (b) Varying θ and t/L for h=2L.

Figure 8.21(a) shows the reduction in the shear modulus, G_{xy}, caused by decreasing the t/L ratio for both the hexagonal and re-entrant cells. The value of G_{xy} for a re-entrant cell is always lower than the corresponding hexagonal cell of the same geometry. As the value of h/L is increased, the shear modulus, G_{xy}, of a re-entrant cell is also increased, but G_{xy} of a hexagonal cell is reduced (*Figure* 8.21(b)).

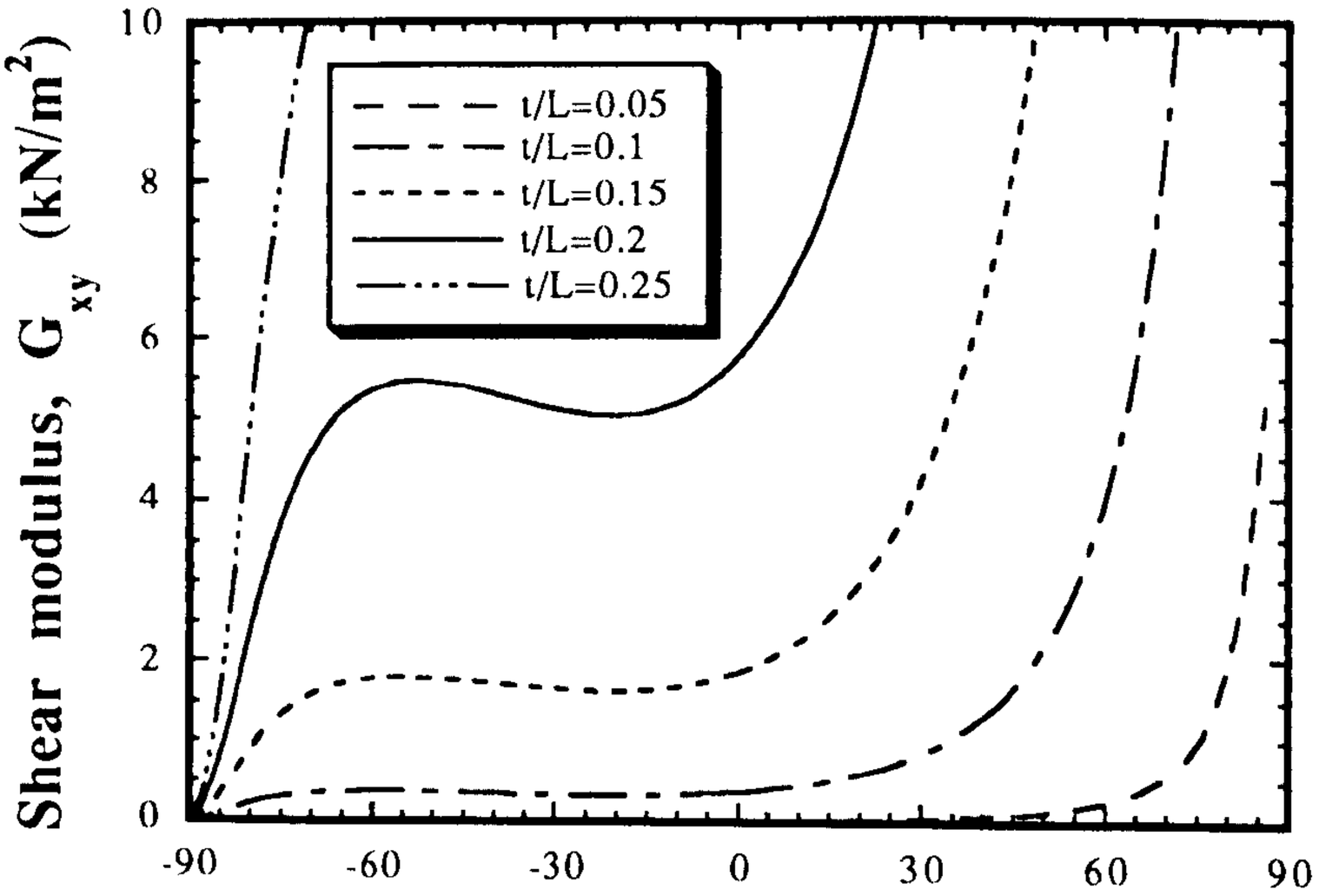

Fig. 8.21(a)

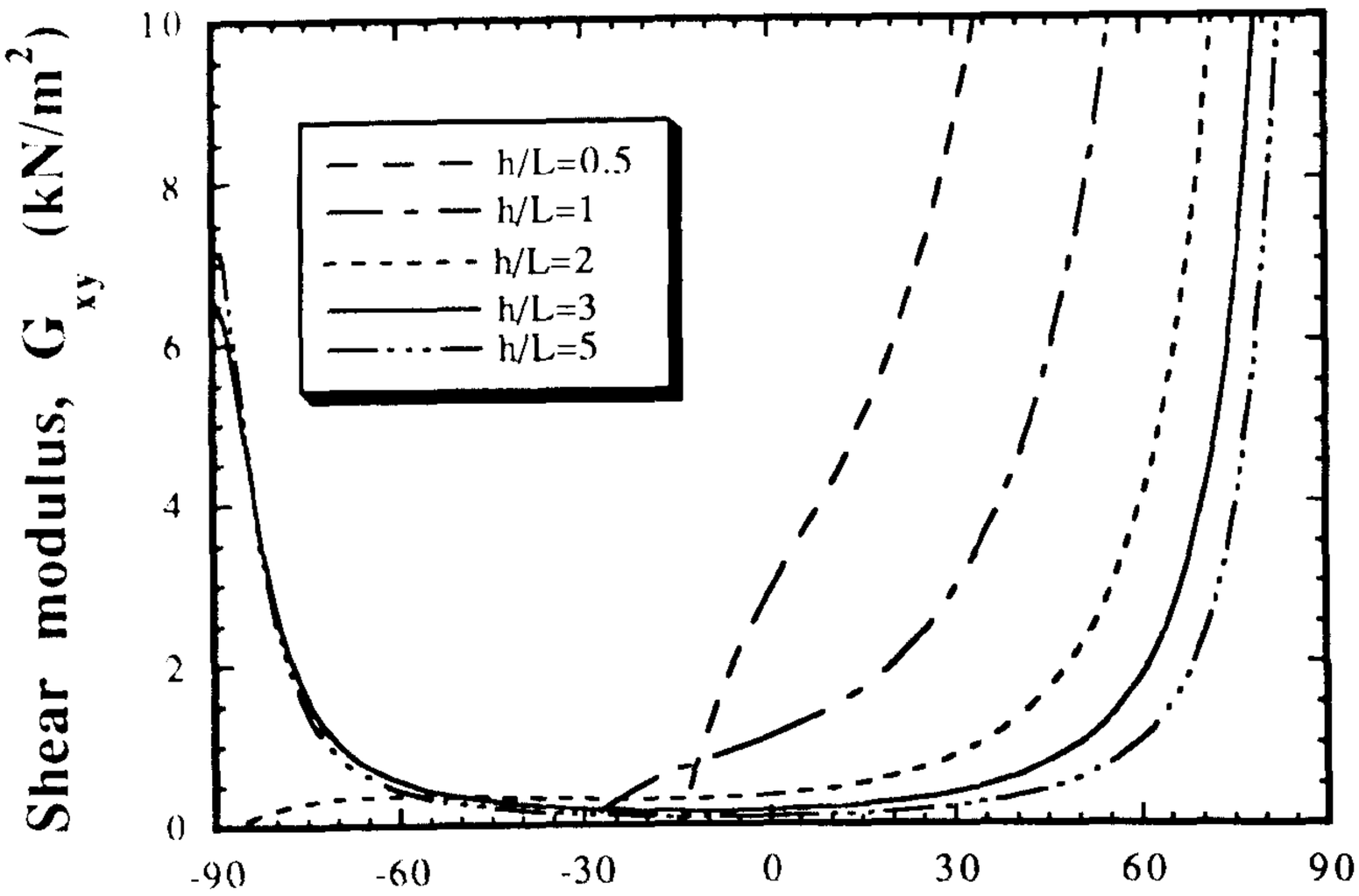

Fig. 8.21(b)

Fig. 8.21 Plots of G_{xy} vs. θ for both the flexure model and the combined model showing the effects of varying cell geometry, θ, t/L and h/L. EQ. 5. 168 is used for these plots. (a) Varying θ and t/L for h=2L. (b) Varying θ and α for t=0.1L.

Figures 8.22(a) and (b) show the reduction in the shear modulus, G_{xz}, caused by increasing the h/L or decreasing t/L ratio for both the hexagonal and re-entrant cells. The value of G_{xz} of a re-entrant cell is always higher than the corresponding hexagonal cell of the same geometry. EQ. 5.174 is used for these plots.

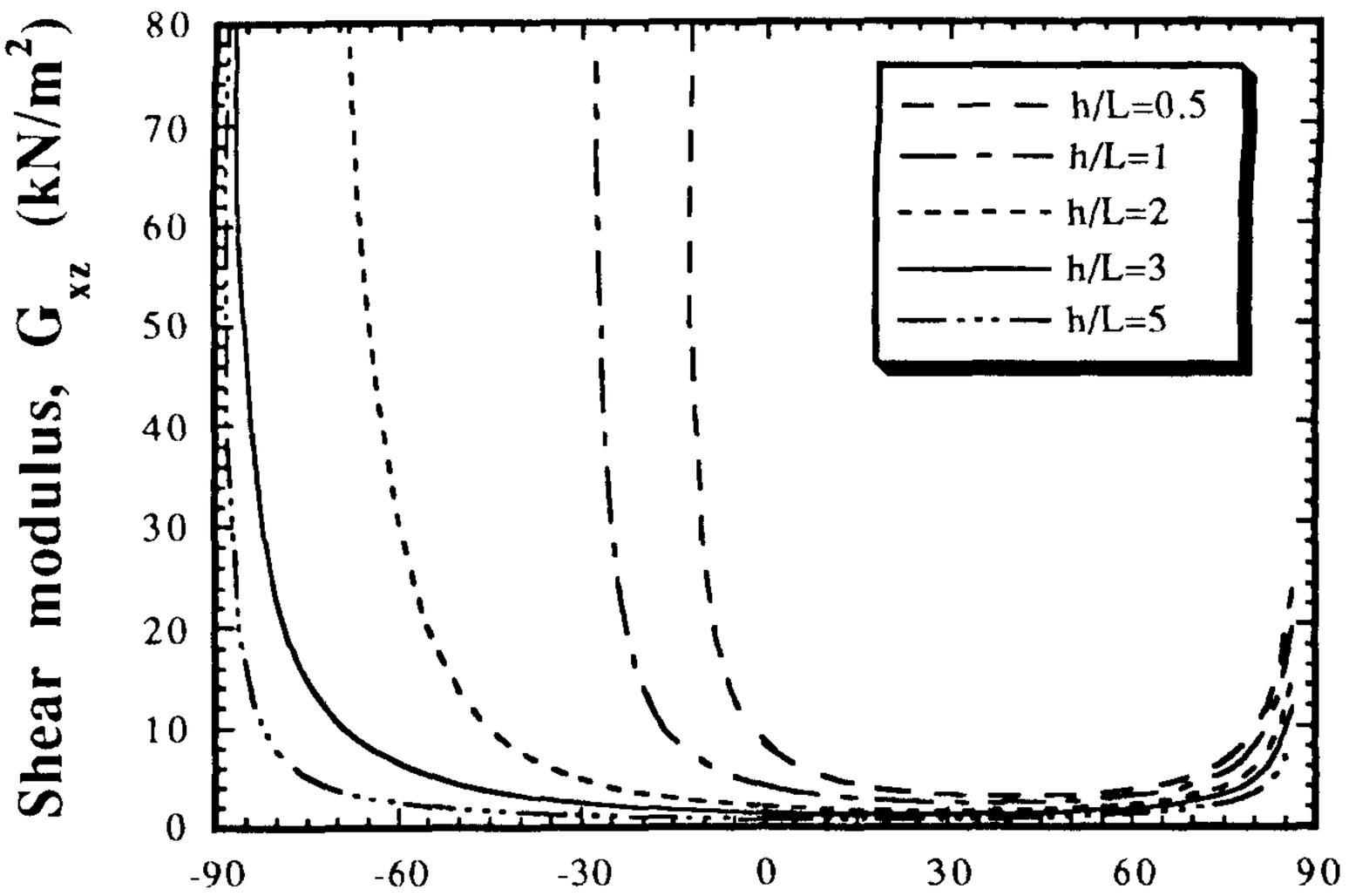

Fig. 8.22(a)

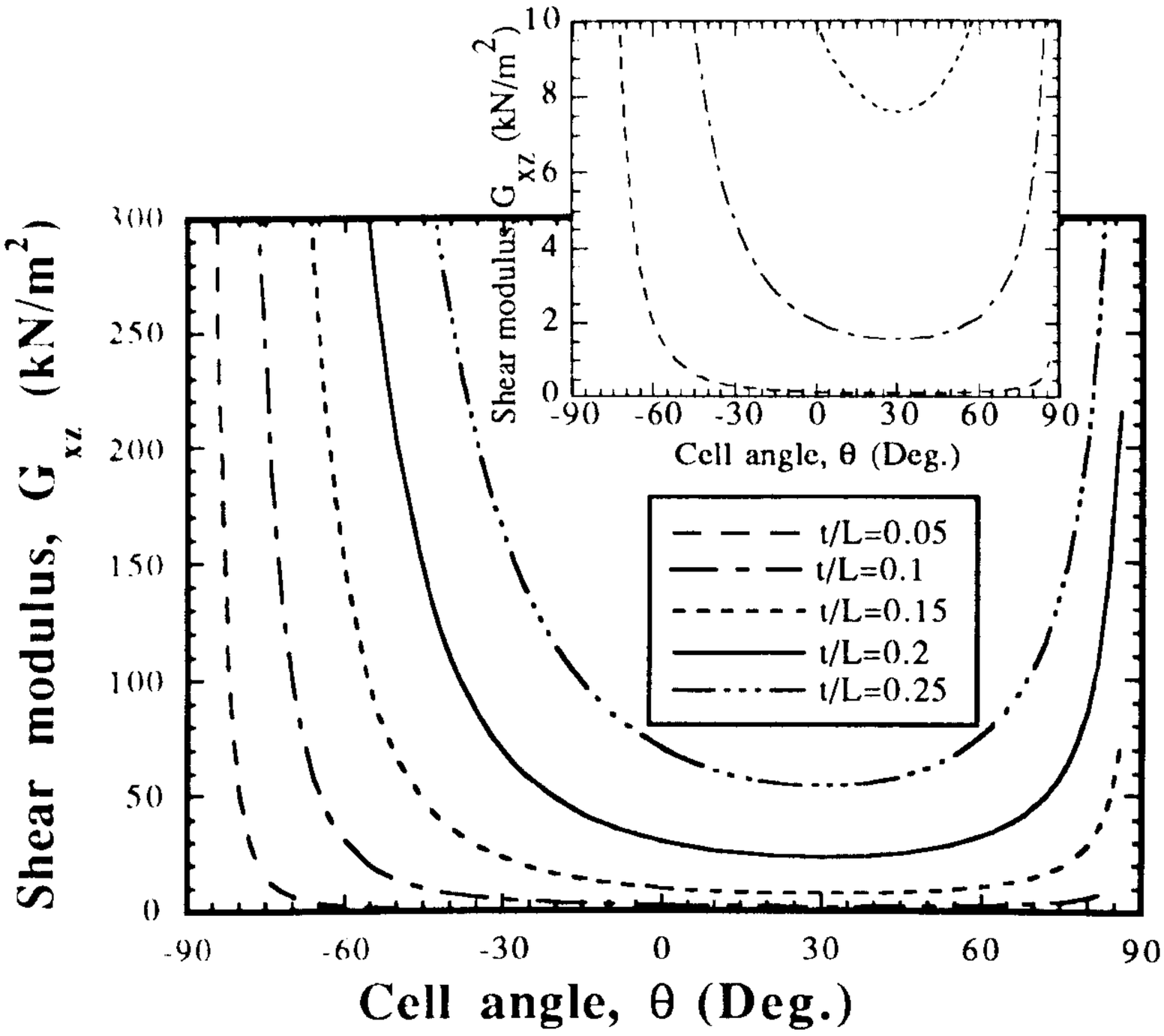

Fig. 8.22(b)

Fig. 8.22 Plots of G_{xz} vs. θ for both the flexure model and the combined model showing the effects of varying cell geometry, θ, t/L and h/L. (a) Varying θ and α for t=0.1L. (b) Varying θ and t/L for h=2L.

Plots of the equations for the models show that if the cell angle is kept constant then the elastic properties are governed by the ratio of the cell rib lengths (i.e. h/L). Specific values of E_i , ν_{ij} and G_{ij} can be obtained for any required density of foam. The limiting factor governing the density is the cell size for a given rib thickness.

8.9 The Stress-Strain Behaviour of Foams under Small Strain

The typical compressive and tensile stress-strain curves for both conventional and auxetic foams obtained using EQ. 5.28, 5.80, 5.143, and 5.162 are shown in *Figures* 8.23, 8.24, 8.25, and 8.26. As a result of the different cell geometry of the foams, in order to simplify the calculations, the plots have been obtained by putting E_s=45000 kN/m^2, h/L=2, t/L=0.2, q=t, and $\theta = \pm 30^o$.(note: θ is positive for conventional foam and negative for auxetic foam).

From *Chapter* 5, it is known that $K_f = \frac{E_s t^4}{L^3} = \frac{12 E_s I}{L^3}$, $K_h = \frac{E_s t^4}{6 L^2 q} = \frac{2 E_s I}{L^2 q}$

and $K_s = \frac{E_s t^2}{L}$. K_f and K_h are much more sensitive to small deviations in the values of t and L than is K_s. The flexure and hinging model are the dominant mechanisms for the deformation of foams. For the combined model, because it is internally consistent, it should prove to be a valid model to test against experiments. However, there are some small discrepancies between the theory and the experimental results. There are two possible sources for this variation: (a) the complicated cell geometry of foams i.e. h, L, t, q and θ vary between cells; or, (b) the value used for the solid Young's modulus, E_s, could be incorrect. E_s is rarely known accurately- it being dependant on the degree of polymer chain alignment, on chemical changes brought about by the foaming agent, on the gradual ageing and oxidation of the polymer and on other such uncontrolled factors. These errors can cause the apparent variation between the theory and the experimental results.

The compressive stresses in the foam rise direction are plotted against the compressive strain for conventional foams shown in *Figure* 8.23. For comparison with the experimental results the theoretical stress-strain curves are also plotted in the same figure. *Figure* 8.23 shows that for the low strains (< 5%) used in these experiments, the linear behaviour is a reasonable assumption. As was presented in Chapter 6, there are three regimes of behaviour: at small strains (< 5%) the material can be modelled as a network of bending ribs while at high strain it behaves like a solid containing spherical holes. Mackenzie (1950) has derived expressions for the shear and bulk moduli of such materials. It can be seen from Figure 8.23 that the experimental results follow the theoretical curves although the combined model appear to over estimate the values of E_y of the open cell foams and under estimate the values of E_y of the closed cell foams.

Figure 8.24 shows the tensile stress-strain for a conventional foam in the foam rise direction. The experimental results from this study predominantly lie between the upper and the lower theoretical values showing good agreement with the model. *Figure* 8.25 and 8.26 show the equivalent plots for an auxetic foam. For both of the compression and tension, the experiment data fit the model very well.

There is considerably more scatter in the experimental data measured by other researchers. The degree of scatter can be accounted for by the variety of the cell geometry of the foams (i.e. the cell size and the cell rib thickness). It is clear that the gross foam geometry is unlikely to be constant for different foams. Therefore, for comparison with others experimental results the theoretical equations (i.e. EQ. 5.28, 5.80, 5.143, and 5.162) might need to be evaluated for new values of K_f, K_h, and K_s to achieve the best fit.

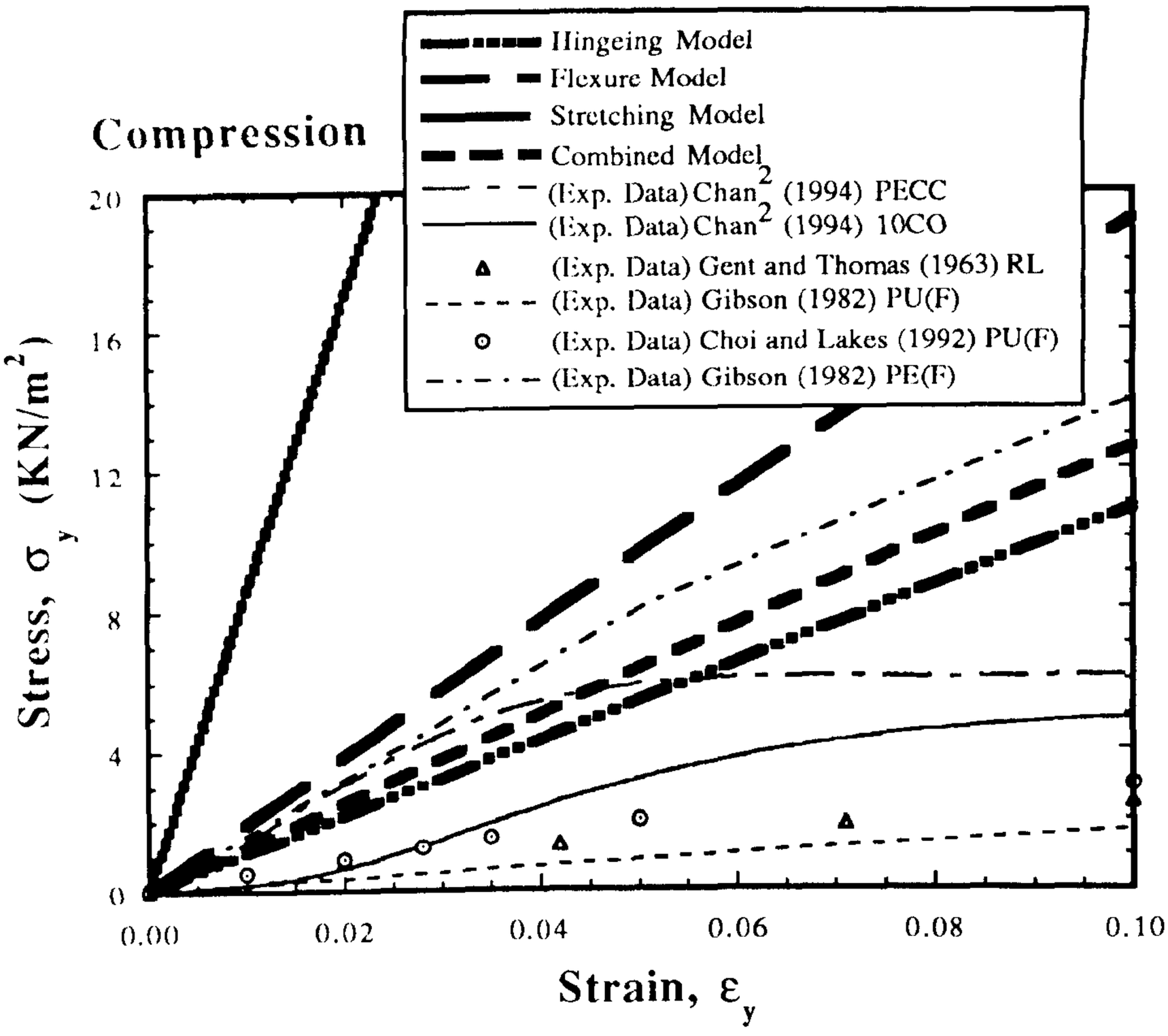

Fig. 8.23 Experimental and theoretical stresses plotted against strains for conventional foam loaded along the foam rise direction.

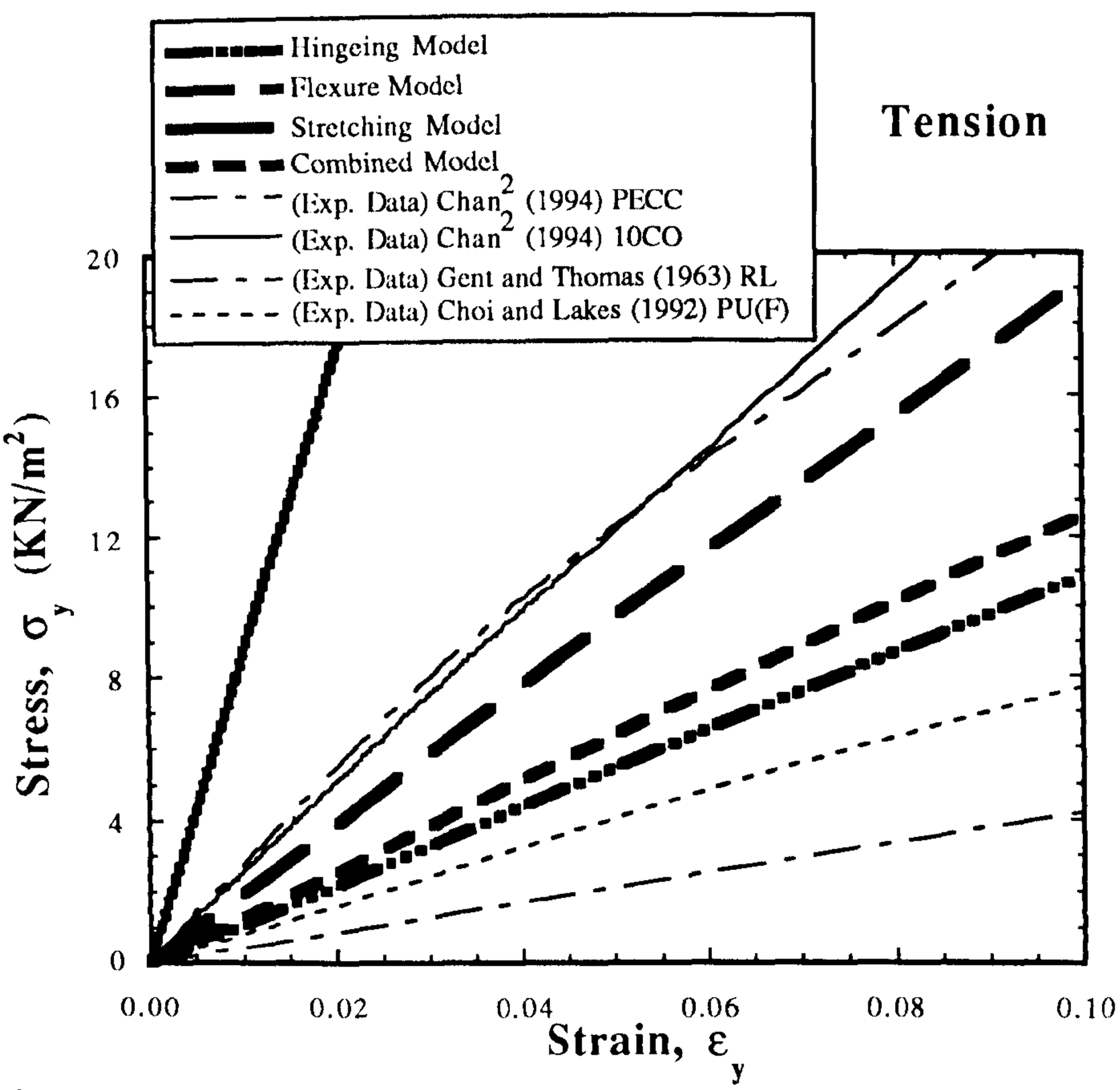

Fig. 8.24 Experimental and theoretical stresses plotted against strains for conventional foam pulled along the foam rise direction.

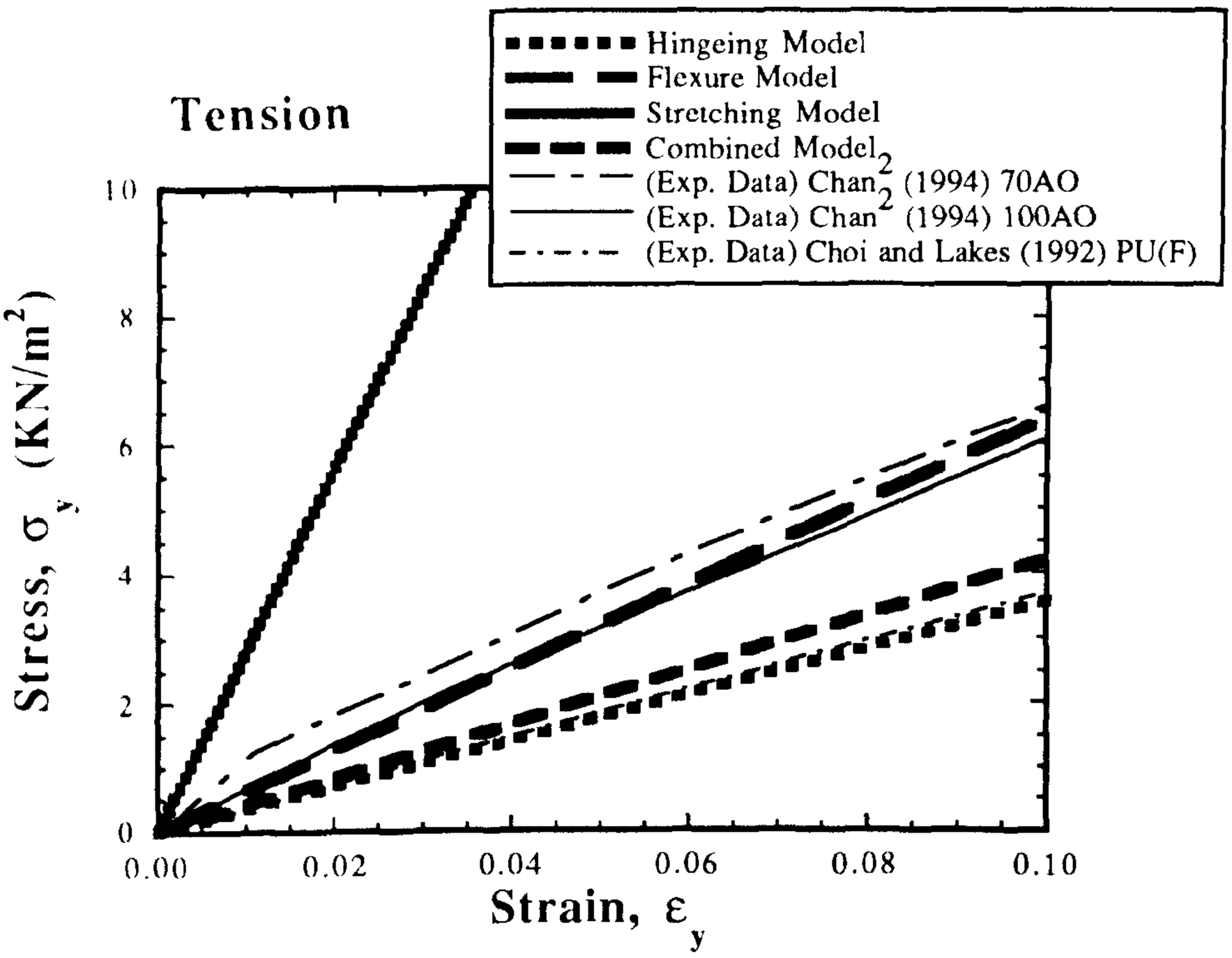

Fig. 8.25 Experimental and theoretical stresses plotted against strains for auxetic foam pulled along the foam rise direction.

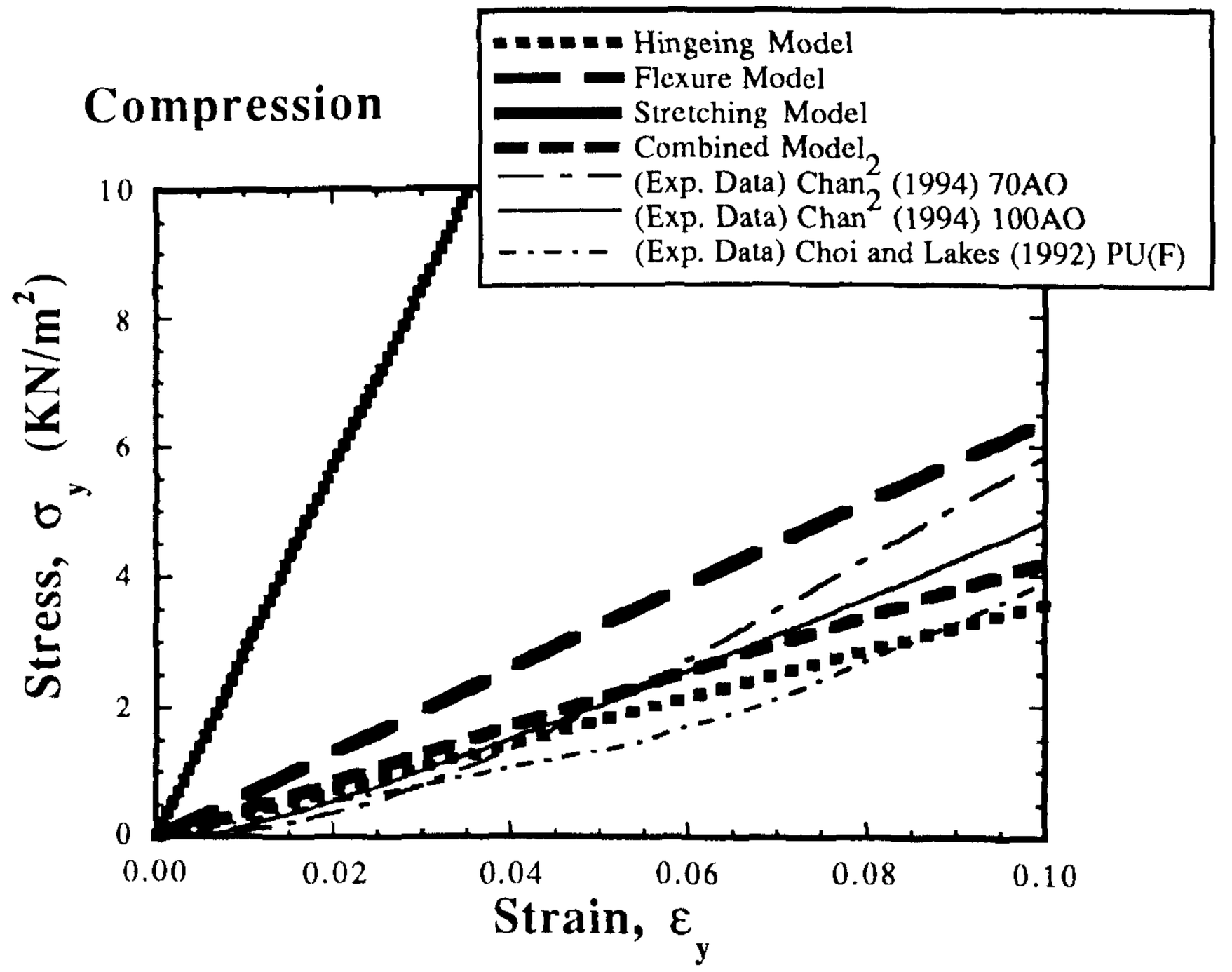

Fig. 8.26 Experimental and theoretical stresses plotted against strains for auxetic foam loaded along the foam rise direction.

8.10 Comparison of Experimental and Theoretical Results

The foam usually deforms by one or a combination of three mechanisms (see chapter 4). As a result, the equations (Table 5.4) used to draw the theoretical curves (Figure 8.27 to 8.42) for describing the different deformation modes needed to be modified with the loading conditions. The geometrical parameters for conventional and auxetic foams were determined in Chapter 4. For a comparison, the experimental data for Young's modulus (Table 6.1 and 6.2), shear modulus, (Table 6.5), and Poisson's ratio (Table 6.3, 6.4) are also shown in the same figures. Note: α is h/L, and β is t/L.

Figure 8.27 to 8.42 include data from Chapter 4 for PECC (Table 4.2), PECO (Table 4.1), 60CO (Table 4.5), 30CO (Table 4.4), 10CO(Table 4.3), 100AO (Table 4.8), 90AO (Table 4.8), 80AO (Table 4.8), and 70AO (Table 4.8). The curves on each figure show the theoretical prediction for open-cell foams. Since the surface of closed-cell foam is about 20 times thinner than the cell edges, it may be possible for it to be described using a microstructural model for open-cell microstructure. The data (except Poisson's ratio) for closed-cell foams generally lie above the theoretical prediction for open-cell foams. Probably because the contribution of the cell fluid in the case of closed-cell foams is not taken into account in the theory for open-cell foams. An auxetic foam with many broken ribs may also cause scatter of the results. However, if we take the irregular and very complicated cell structure into account, we can see that the experimental results agree reasonably well with the theoretical model.

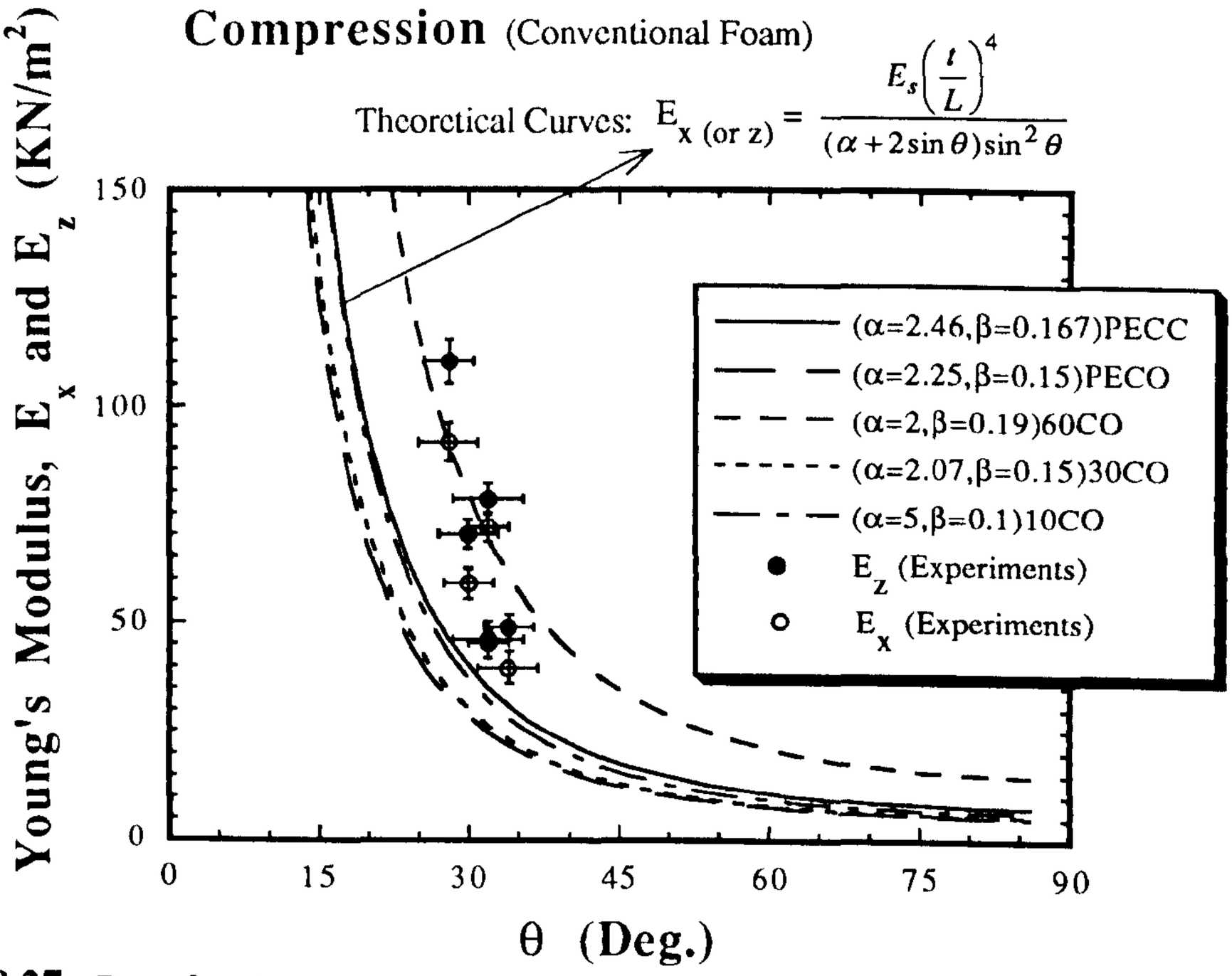

Fig. 8.27 Data for the compressive Young's modulus, E_x and E_z of PECC, PECO, 10CO, 30CO, and 60CO plotted against the cell angle θ. The curves represent the flexure model for these conventional foams.

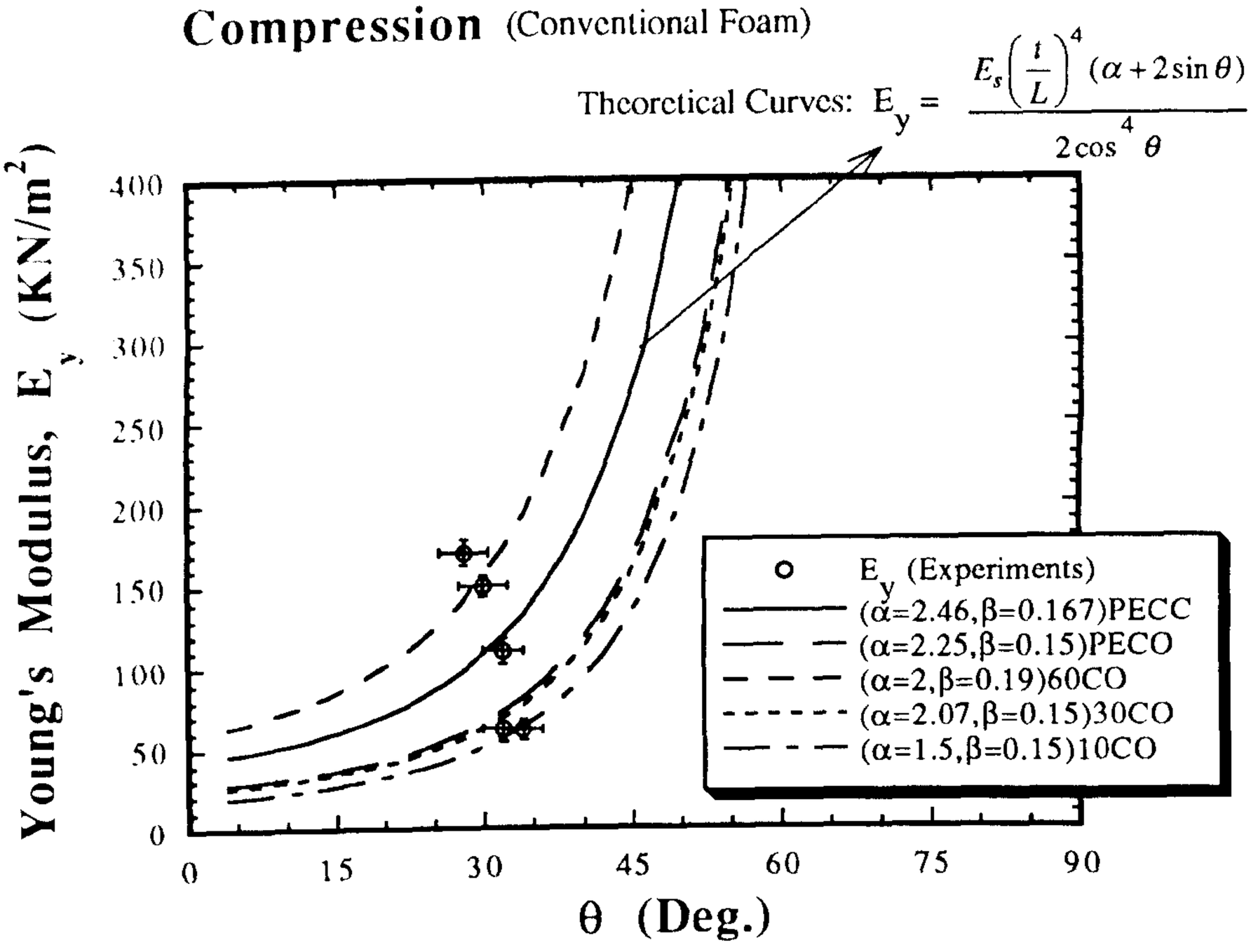

Fig. 8.28 Data for the compressive Young's modulus, E_y of PECC, PECO, 10CO, 30CO, and 60CO plotted against the cell angle θ. The curves represent the flexure model for these conventional foams.

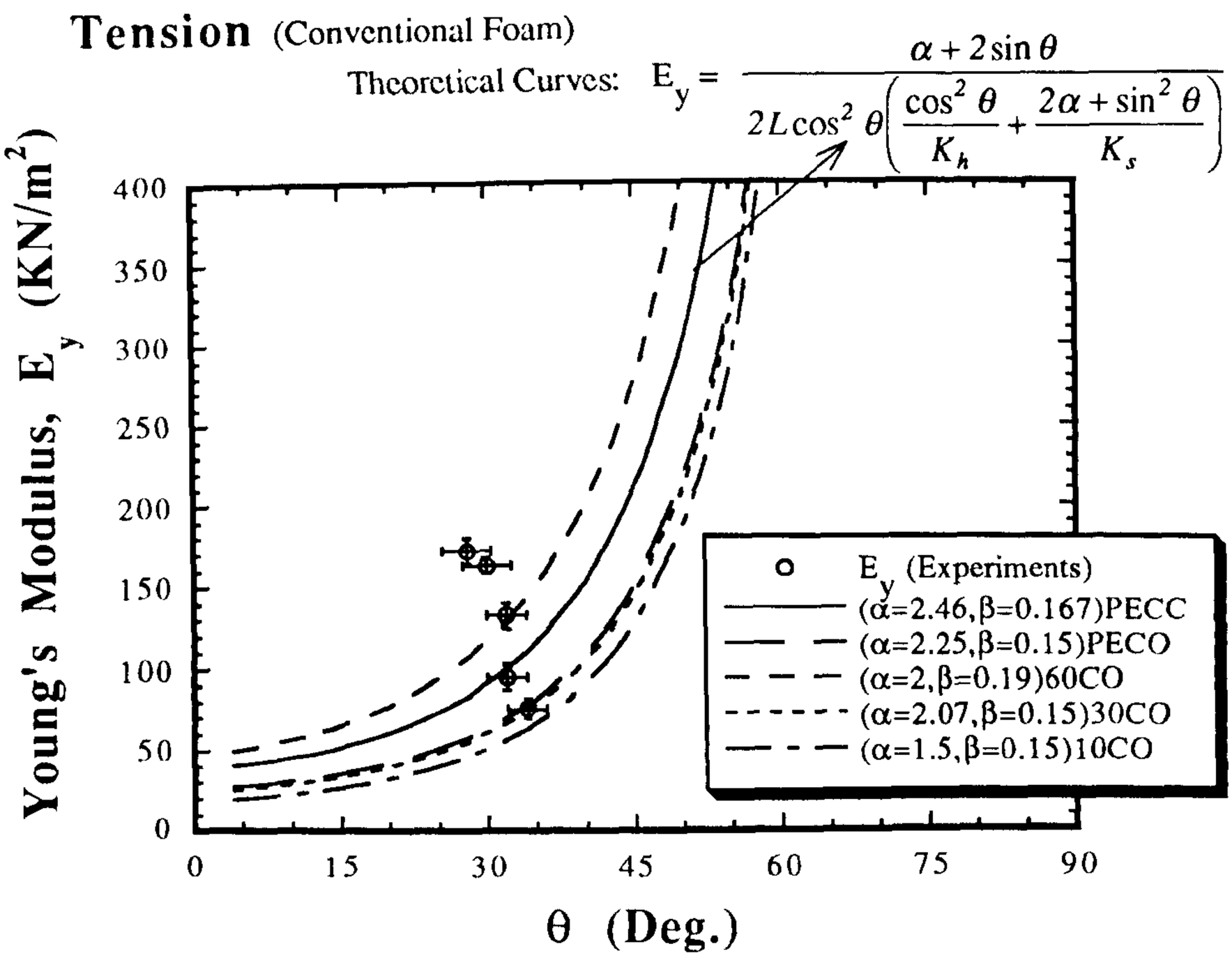

Fig. 8.29 Data for the tensile Young's modulus, E_y of PECC, PECO, 10CO, 30CO, and 60CO plotted against the cell angle θ. The curves represent the combination of the hinging and stretching model for these conventional foams.

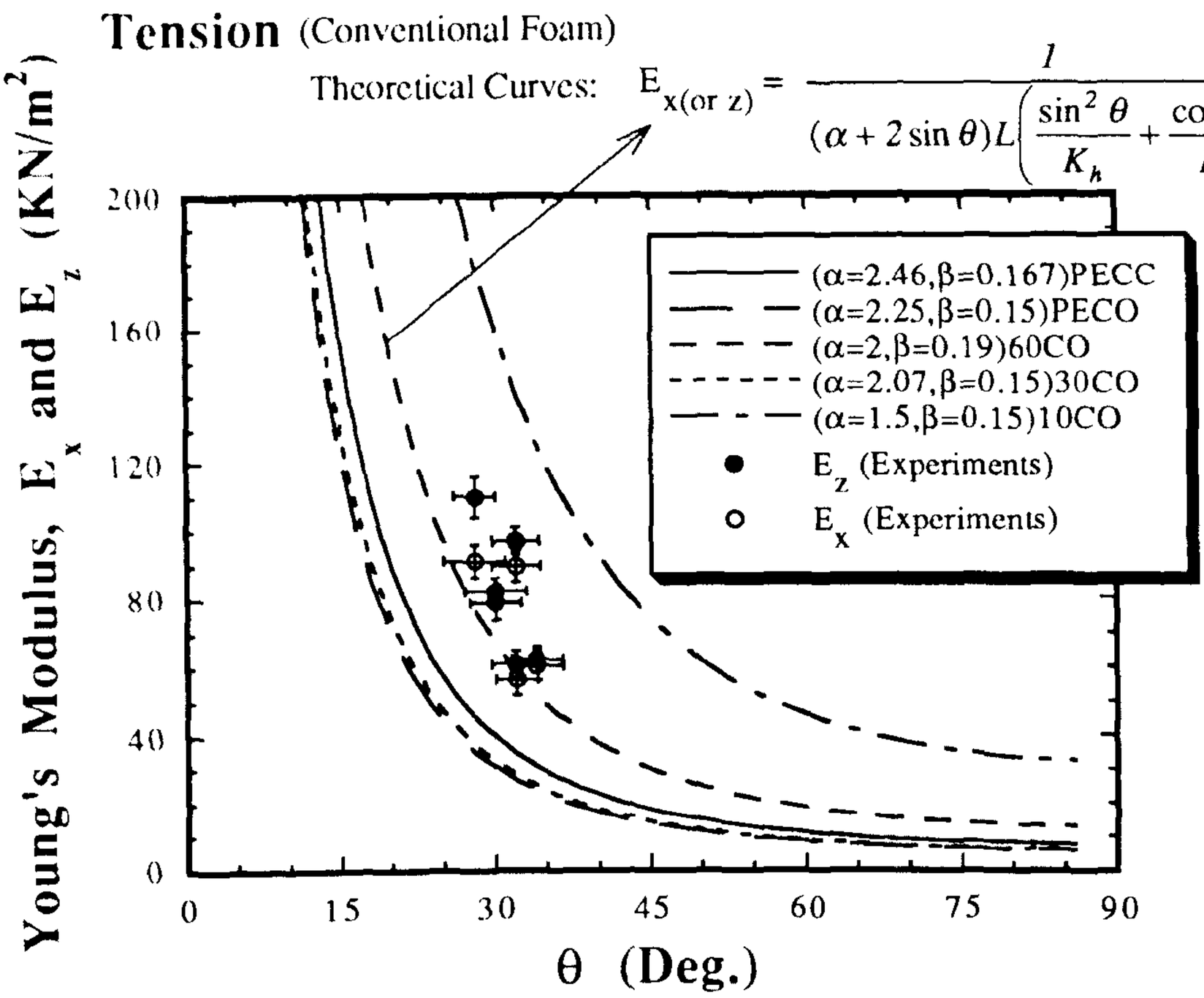

Fig. 8.30 Data for the tensile Young's modulus, E_x and E_z of PECC, PECO, 10CO, 30CO, and 60CO plotted against the cell angle θ. The curves represent the combination of the hinging and stretching model for these conventional foams.

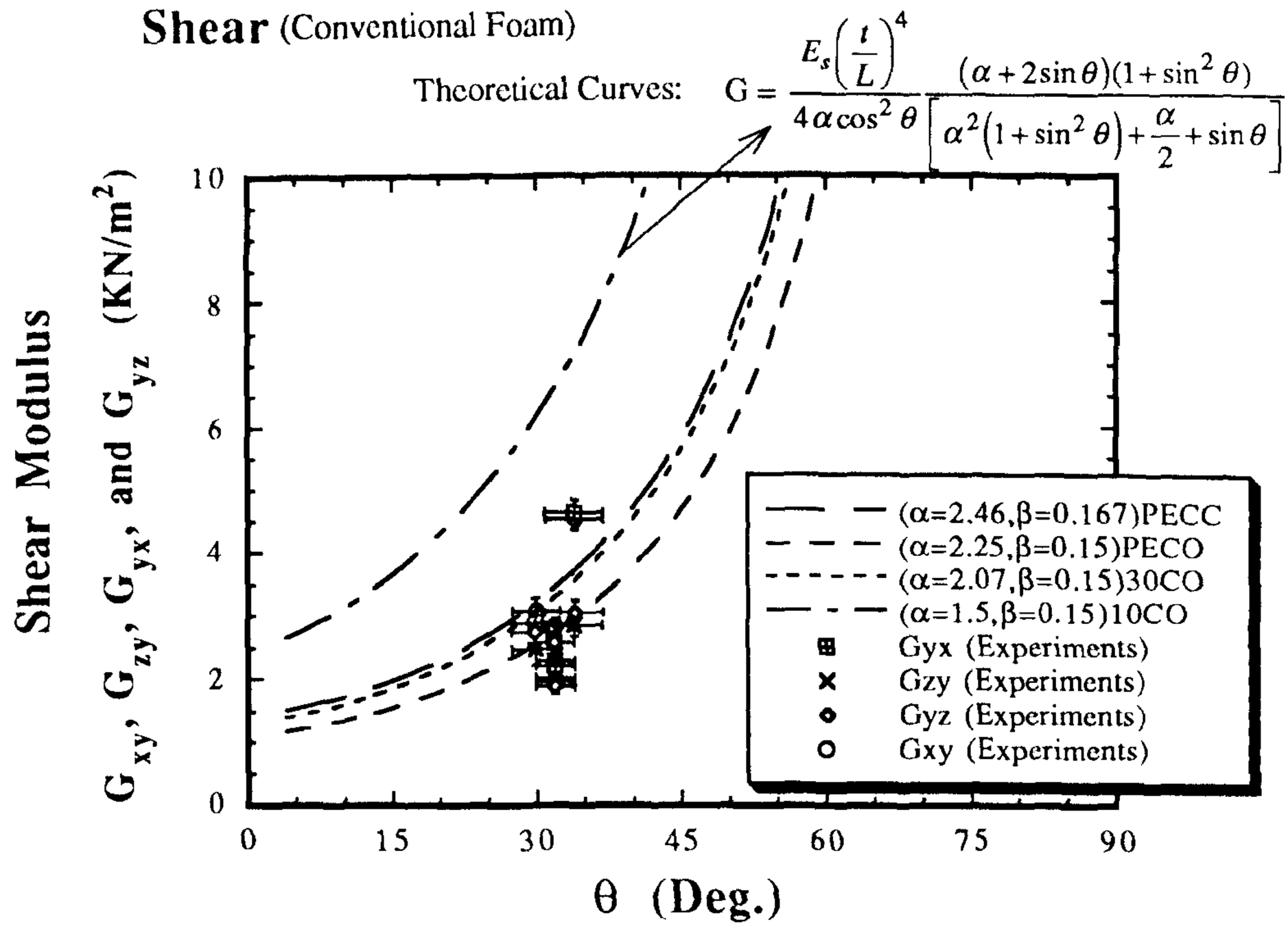

Fig. 8.31 Data for the shear modulus, G_{xy}, G_{zy}, G_{yx}, and G_{yz} of PECC, PECO, 10CO, 30CO, and 60CO plotted against the cell angle θ. The curves represent the flexure model for these conventional foams.

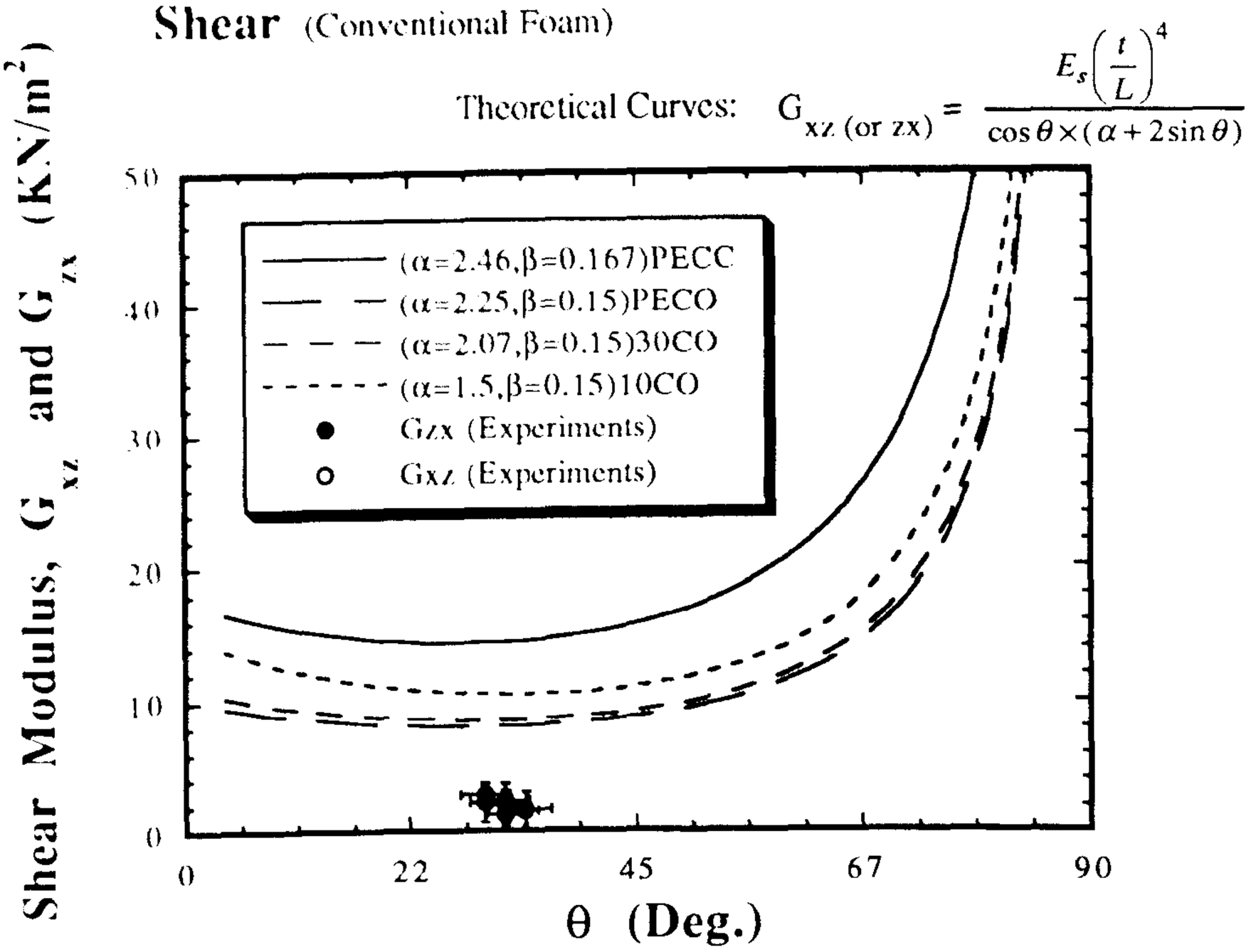

Fig. 8.32 Data for the shear modulus, G_{xz} and G_{zx} of PECC, PECO, 10CO, 30CO, and 60CO plotted against the cell angle θ. The curves represent the flexure model for these conventional foams.

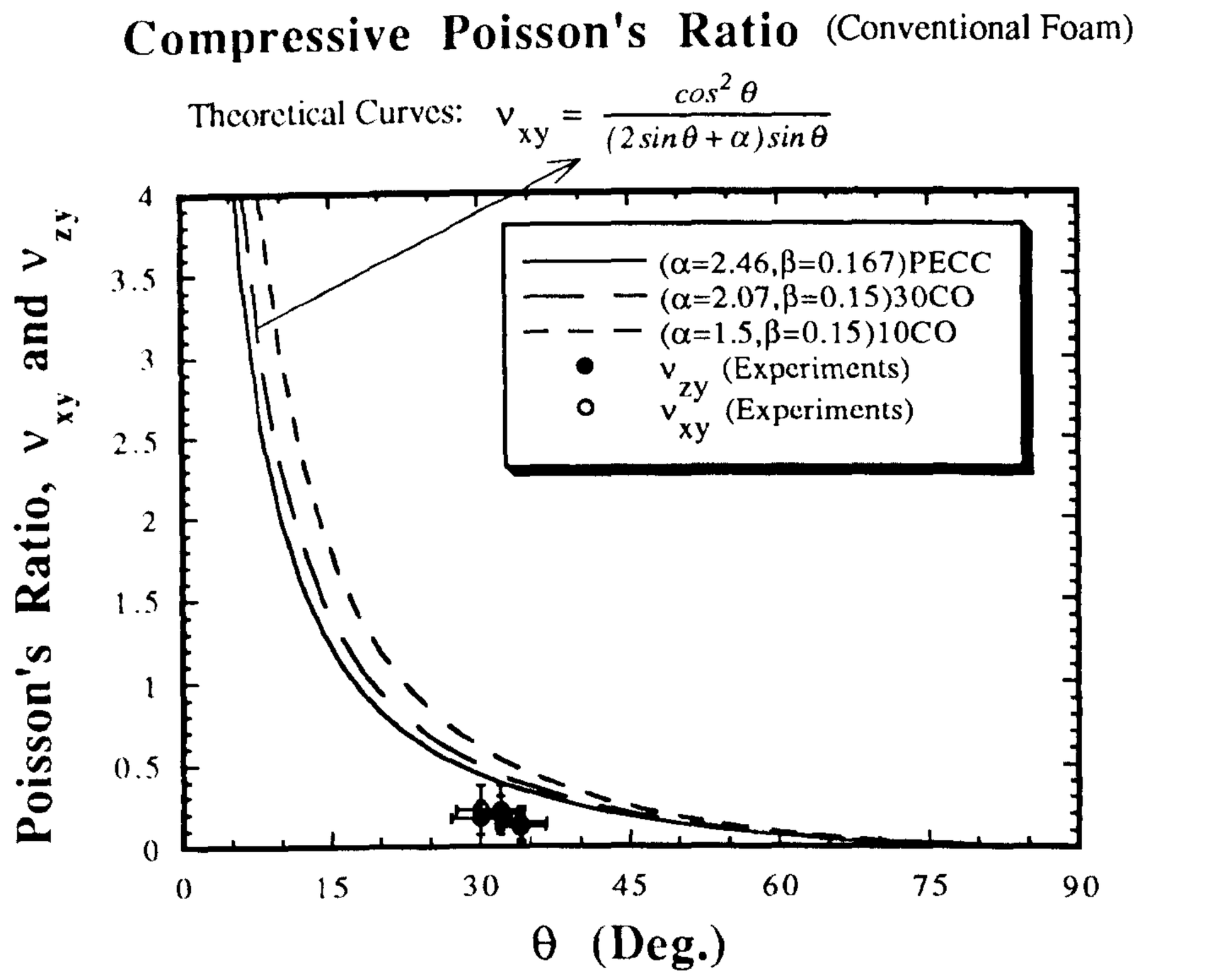

Fig. 8.33 Data for the compressive Poisson's ratio, ν_{xy} and ν_{zy} of PECC, PECO, 10CO, 30CO, and 60CO plotted against the cell angle θ. The curves represent the flexure model for these conventional foams.

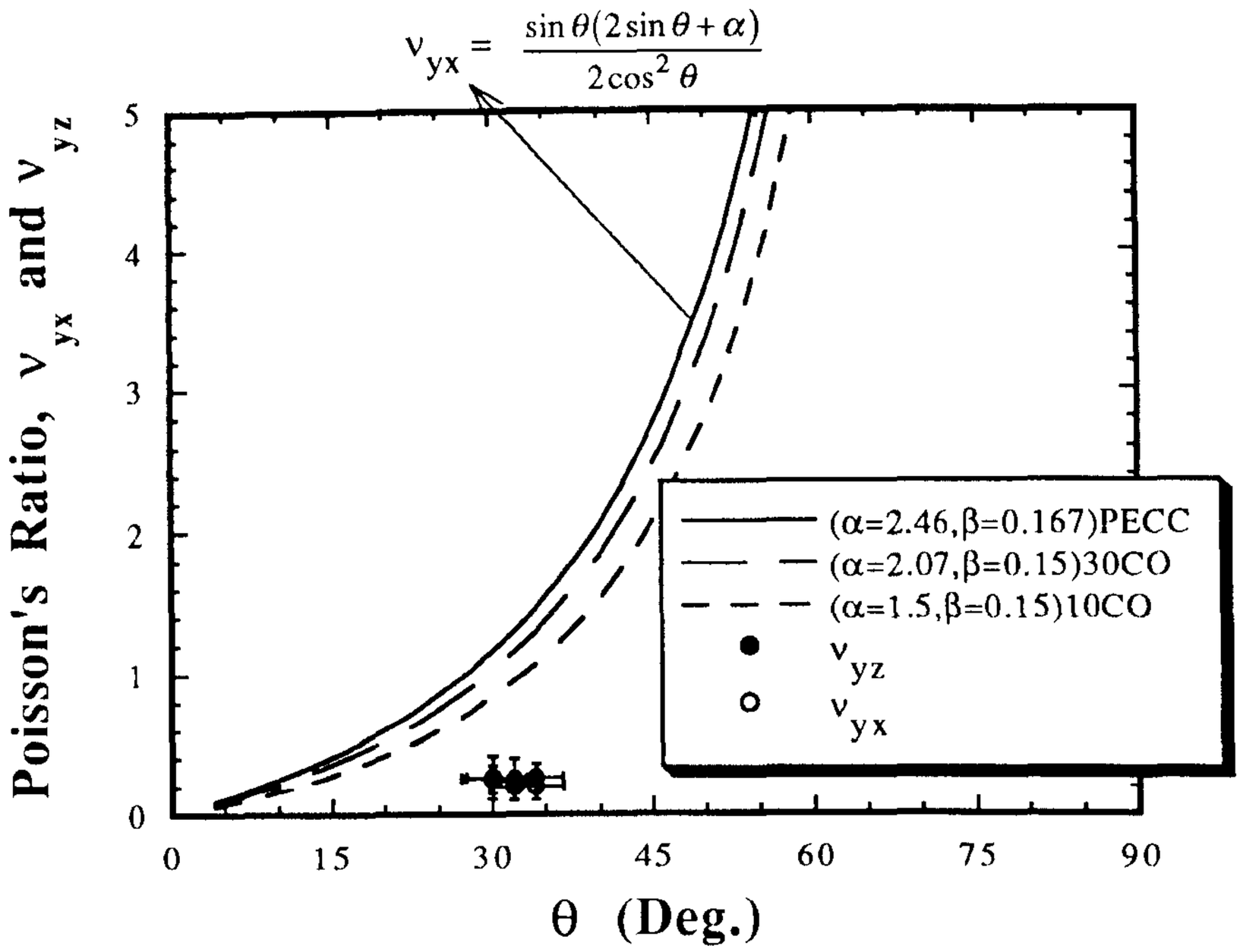

Fig. 8.34 Data for the compressive Poisson's ratio, ν_{yx} and ν_{yz} of PECC, PECO, 10CO, 30CO, and 60CO plotted against the cell angle θ. The curves represent the flexure model for these conventional foams.

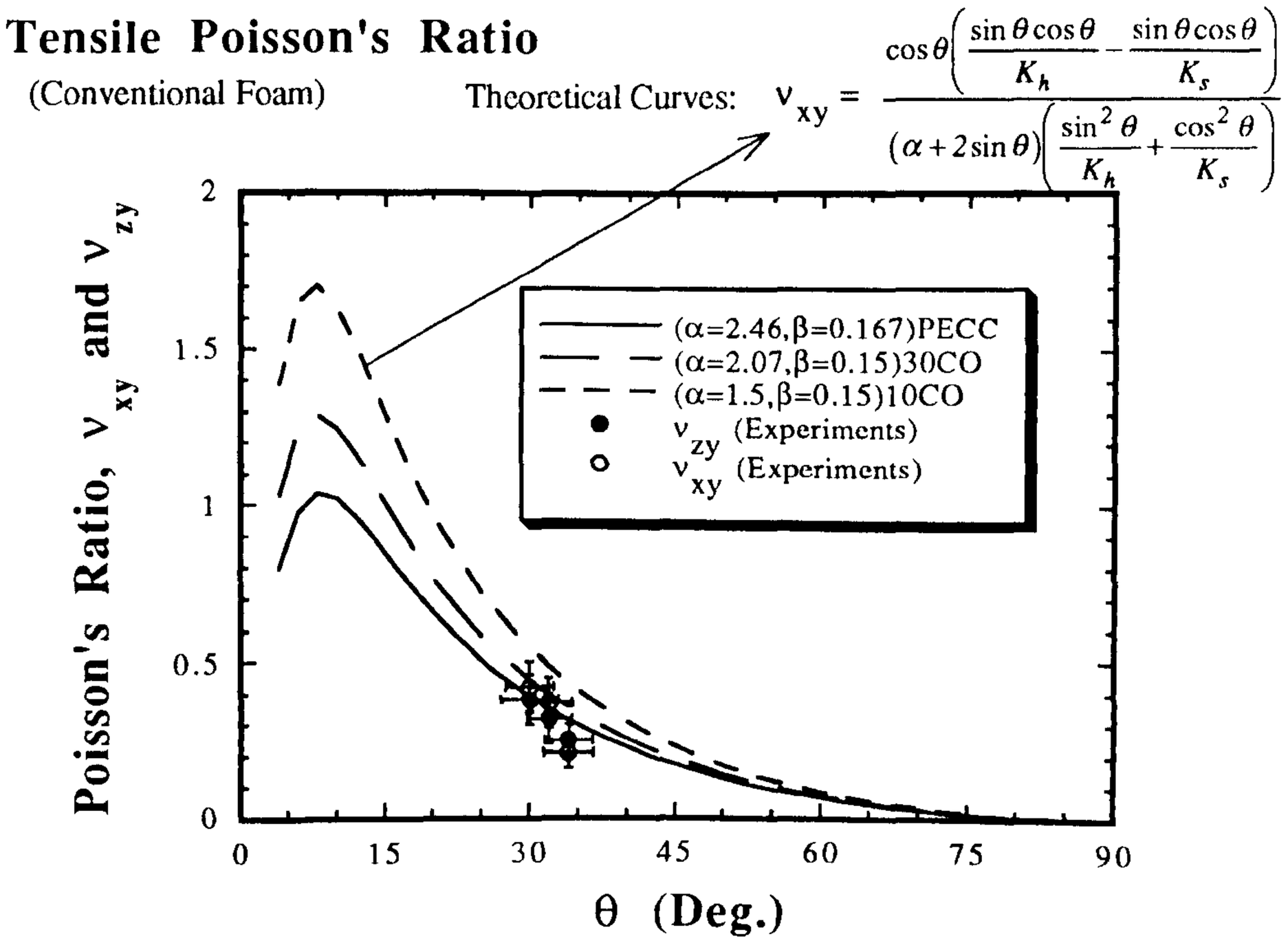

Fig. 8.35 Data for the tensile Poisson's ratio, ν_{xy} and ν_{zy} of PECC, PECO, 10CO, 30CO, and 60CO plotted against the cell angle θ. The curves represent the combination of the hinging and stretching model for these conventional foams.

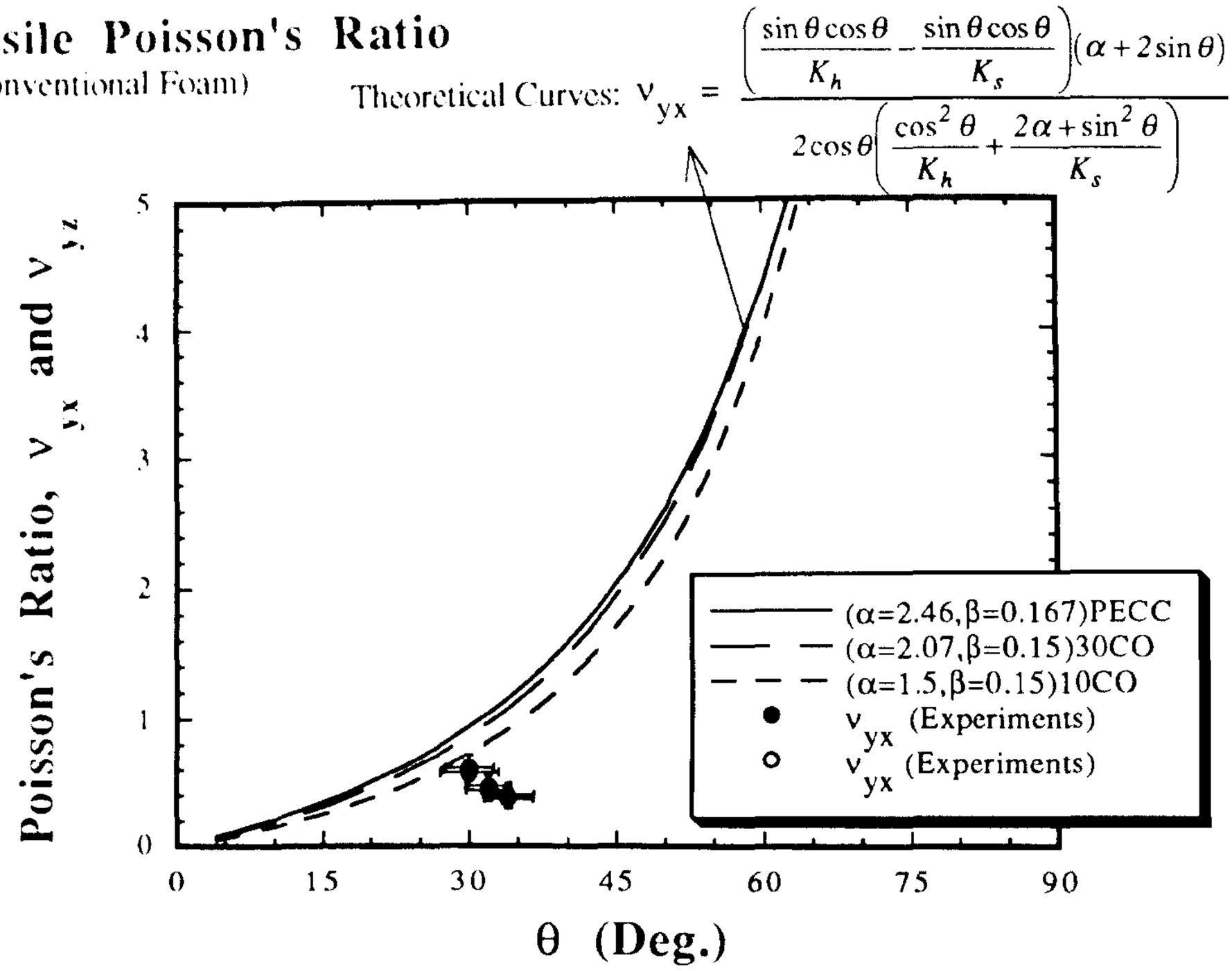

Fig. 8.36 Data for the tensile Poisson's ratio, ν_{yx} and ν_{yz} of PECC, PECO, 10CO, 30CO, and 60CO plotted against the cell angle θ. The curves represent the combination of the hinging and stretching model for these conventional foams.

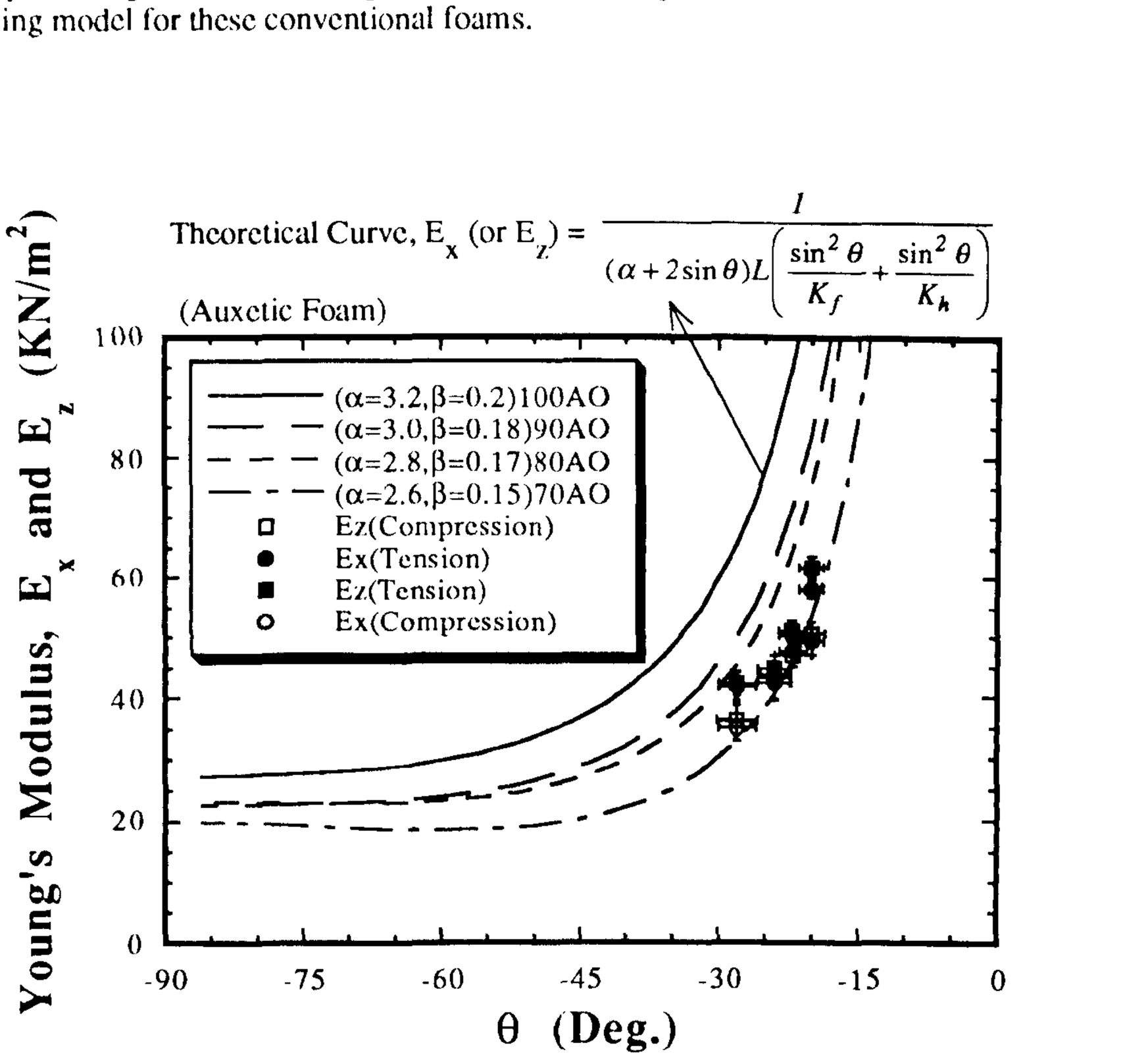

Fig. 8.37 Data for the Young's modulus, E_x and E_z of 100AO, 90AO, 80AO, and 70CO plotted against the cell angle θ. The curves represent the combination of the hinging and flexure model for these auxetic foams.

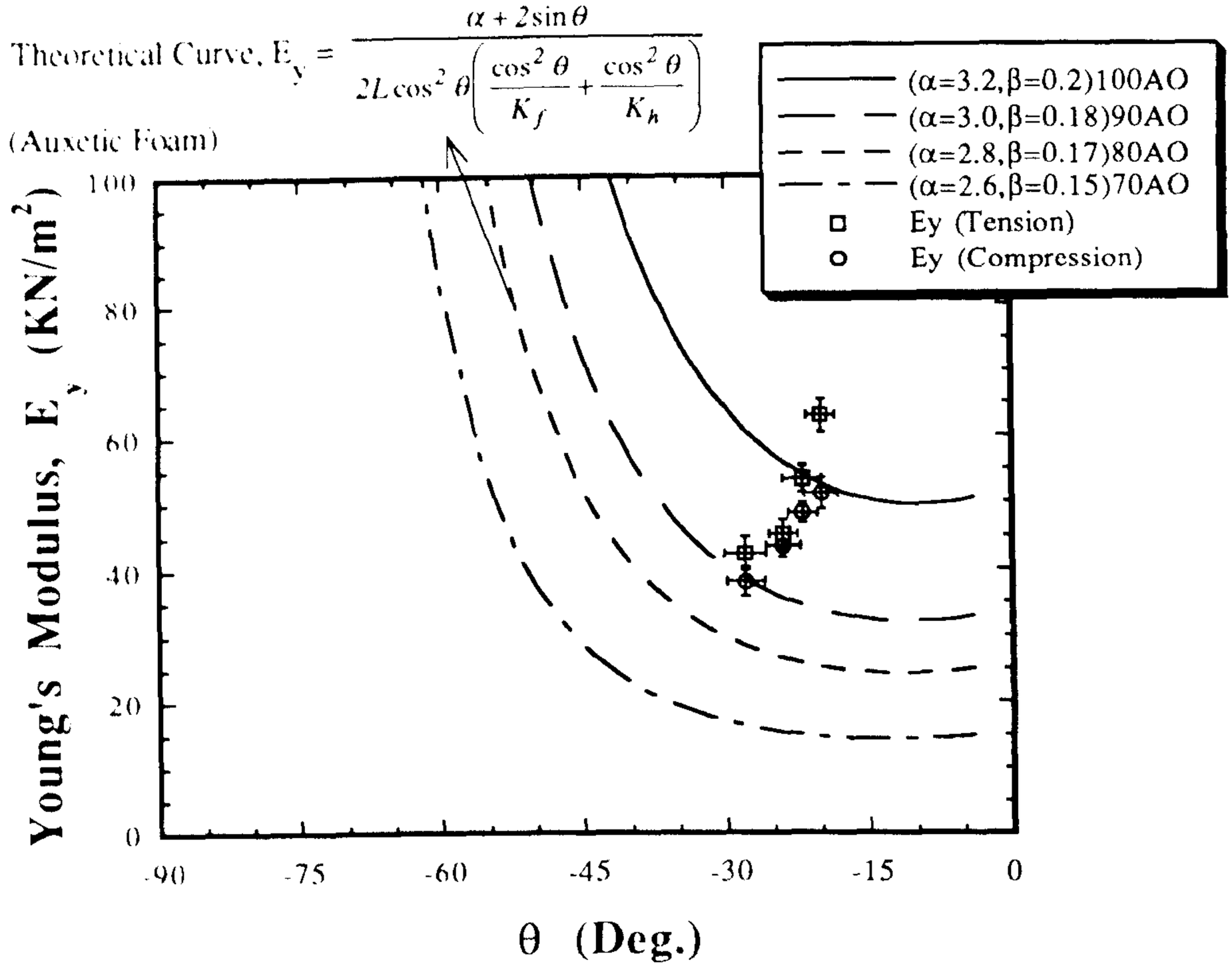

Fig. 8.38 Data for the Young's modulus, E_y of 100AO, 90AO, 80AO, and 70AO plotted against the cell angle θ. The curves represent the combination of the hinging and flexure model for these auxetic foams.

Poisson's Ratio (Auxetic Foam)

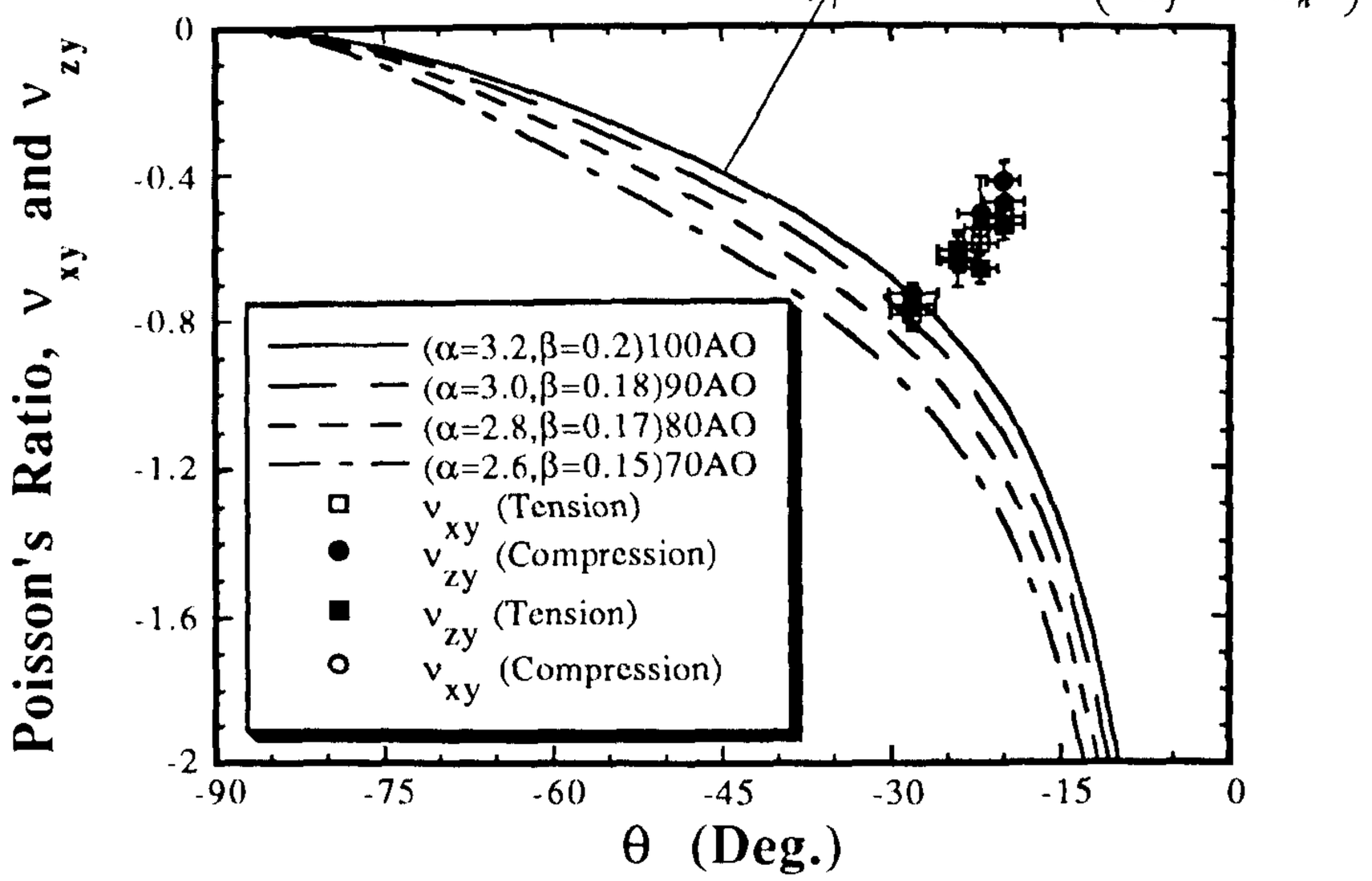

Fig. 8.39 Data for the Poisson's ratio, ν_{xy} and ν_{zy} of 100AO, 90AO, 80AO, and 70AO plotted against the cell angle θ. The curves represent the combination of the hinging and flexure model for these auxetic foams.

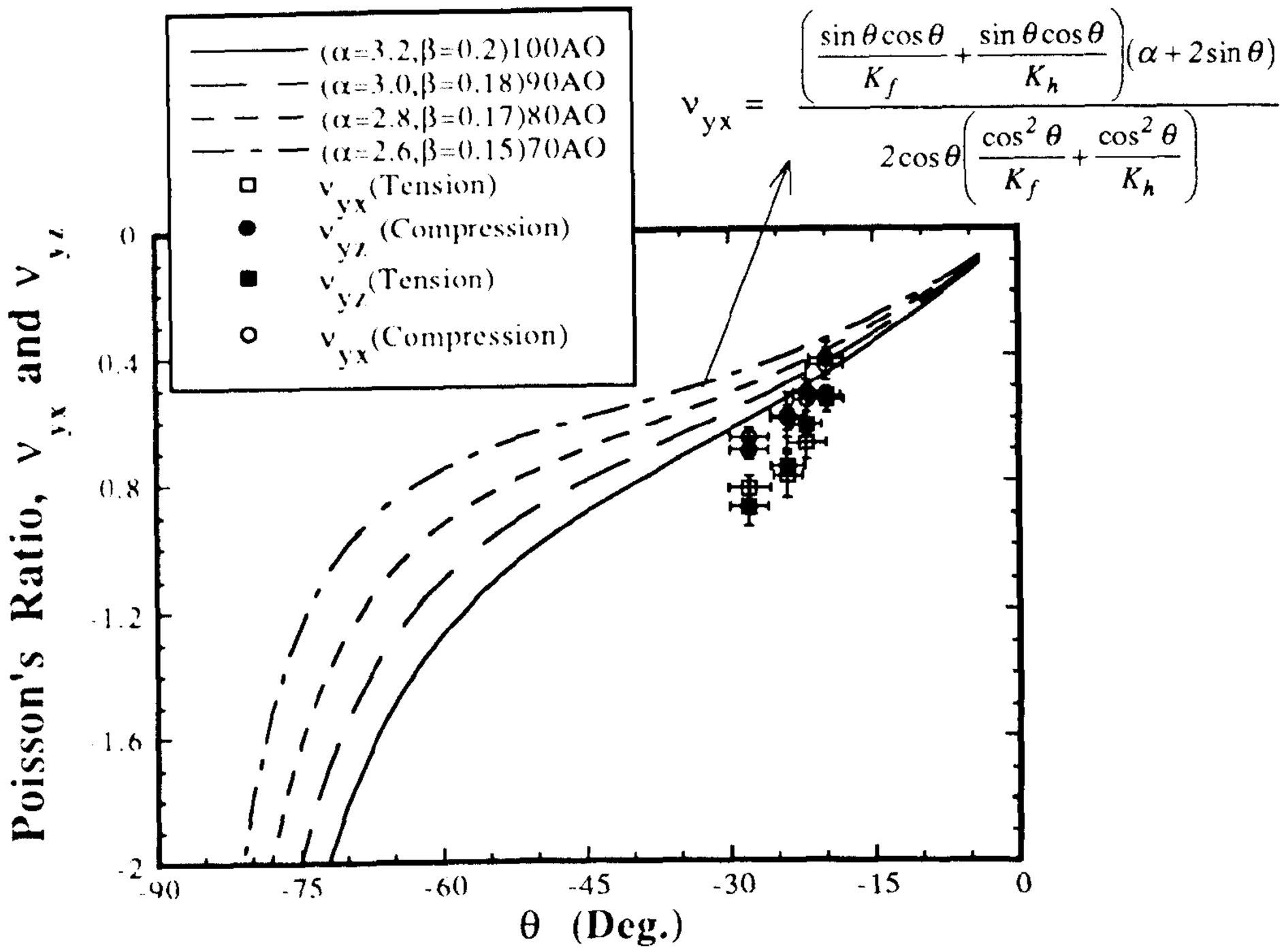

Fig. 8.40 Data for the Poisson's ratio, ν_{yx} and ν_{yz} of 100AO, 90AO, 80AO, and 70AO plotted against the cell angle θ. The curves represent the combination of the hinging and flexure model for these auxetic foams.

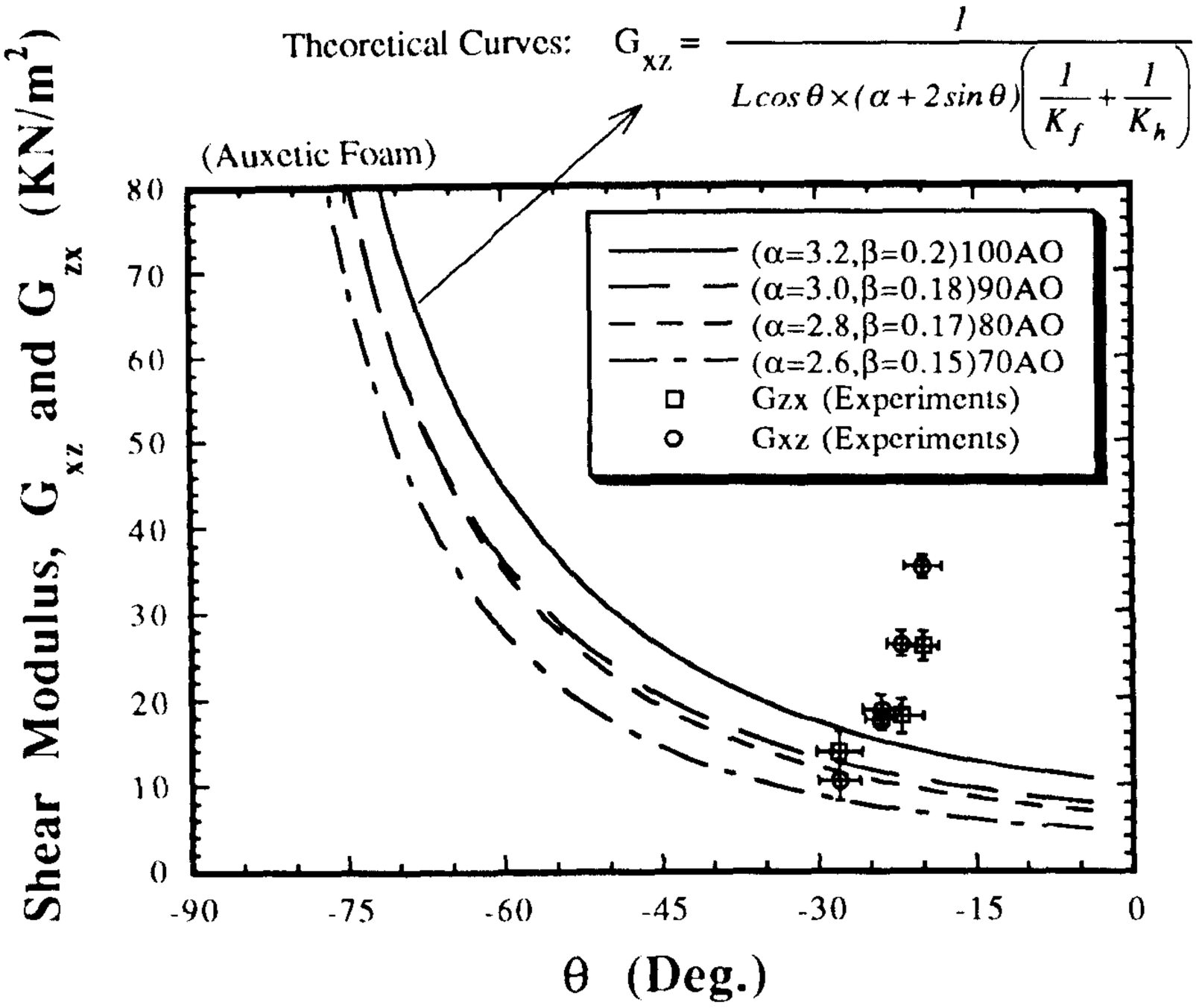

Fig. 8.41 Data for the shear modulus, G_{xz} and G_{zx} of 100AO, 90AO, 80AO, and 70AO plotted against the cell angle θ. The curves represent the combination of the hinging and flexure model for these auxetic foams.

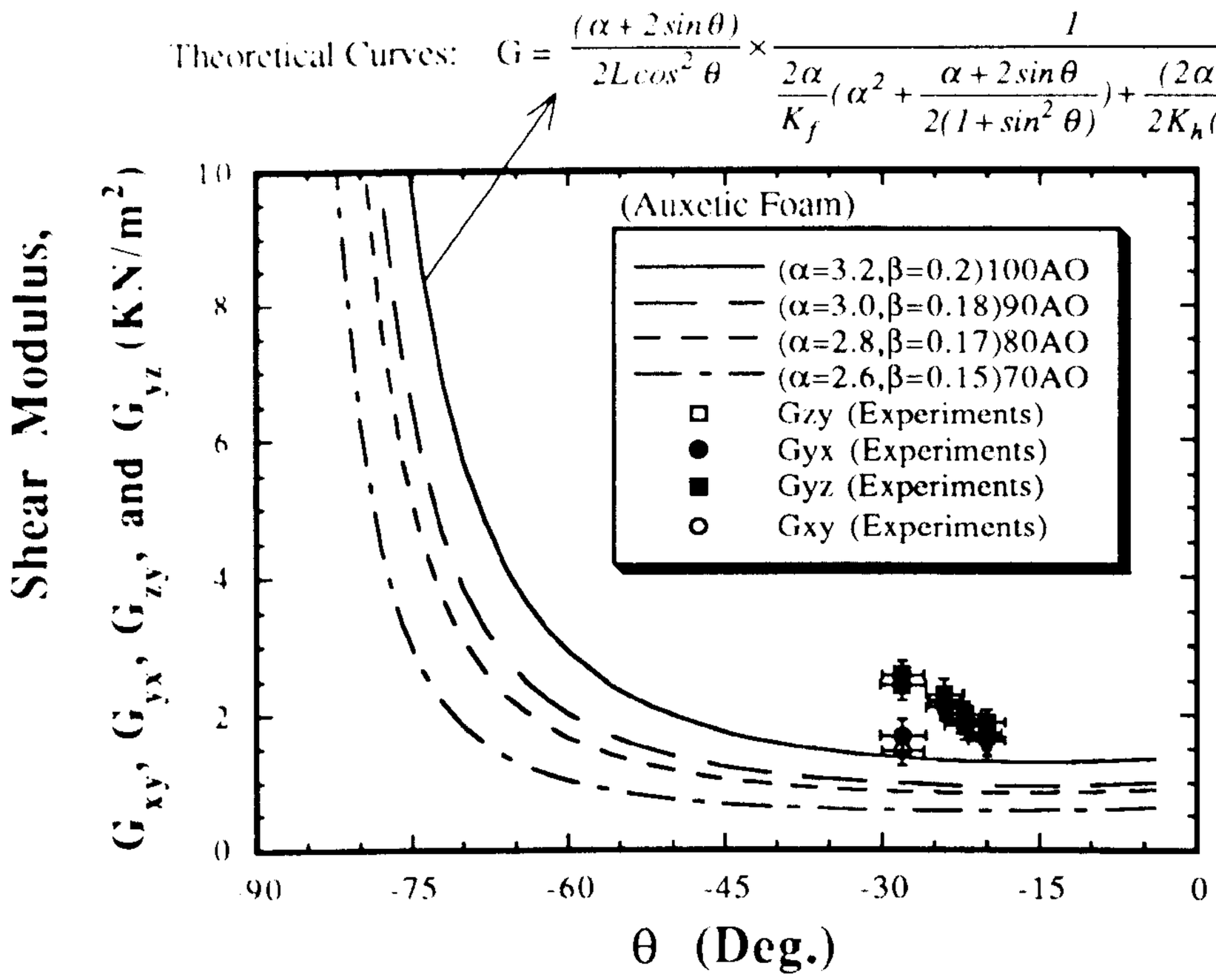

Fig. 8.42 Data for the shear modulus, G_{zy}, G_{yx}, G_{yz} and G_{xy} of 100AO, 90AO, 80AO, and 70AO plotted against the cell angle θ. The curves represent the combination of the hinging and flexure model for these auxetic foams.

8.11 The Mechanical Properties in Terms of Relative Density

From *Figure* 5.5, when $\theta_x = \theta_z$, and $L_X=L_Z$ the relative density of a foam can be calculated as:

$$\frac{\rho}{\rho_s} = \frac{t^2(2L + \frac{h}{4})}{(h + 2L\sin\theta)L^2\cos^2\theta} = \left(\frac{t}{L}\right)^2 \frac{2 + \frac{\alpha}{4}}{(\alpha + 2\sin\theta)\cos^2\theta} \qquad (8.1)$$

Ey (EQ. 5.32) in terms of the relative density is:

$$\frac{E_y}{E_s} = \frac{(\alpha + 2\sin\theta)^3}{2\left(\frac{\alpha}{4} + 2\right)^2\cos^2\theta}\left(\frac{\rho}{\rho_s}\right)^2 \qquad (8.2)$$

When $\frac{(\alpha + 2\sin\theta)^3}{2\left(\frac{\alpha}{4} + 2\right)^2\cos^2\theta} = 1$, EQ. 8.2 can be rewritten as $\frac{E_y}{E_s} = \left(\frac{\rho}{\rho_s}\right)^2$ which is what Gibson and Ashby (1988) got for a cubic box-like model (see *Figure* 2.2).

G_{zy} (EQ. 5.52a) in terms of the relative density is:

$$\frac{G_{xy}}{E_s} = \frac{(\alpha + 2\sin\theta)^3\left(1 + \sin^2\theta\right)}{4\alpha^2\left(2 + \frac{\alpha}{4}\right)^2\left[\alpha^2\left(1 + \sin^2\theta\right) + \frac{\alpha}{2} + \sin\theta\right]}\left(\frac{\rho}{\rho_s}\right)^2 \qquad (8.3)$$

When $\frac{(\alpha + 2\sin\theta)^3\left(1 + \sin^2\theta\right)}{4\alpha^2\left(2 + \frac{\alpha}{4}\right)^2\left[\alpha^2\left(1 + \sin^2\theta\right) + \frac{\alpha}{2} + \sin\theta\right]} = \frac{3}{8}$, EQ. 8.3 can be rewritten as

$\frac{G_{xy}}{E_s} = \frac{3}{8}\left(\frac{\rho}{\rho_s}\right)^2$ which is what Gibson and Ashby got (1988) for a cubic box-like model (*Figure* 2.2).

Poisson's ratios, $\nu_{xy} = \frac{\cos^2\theta}{(2\sin\theta + \alpha)\sin\theta}$ (EQ. 5.12), $\nu_{xz} = 0$ (EQ. 5.11), and $\nu_{yx} = \frac{\sin\theta(2\sin\theta + \alpha)}{2\cos^2\theta}$ are solely the functions of cell geometry and are independent of density. Gibson and Ashby (1987) proposed that the Poisson's ratio of a foam is approximately a constant, $\nu \approx 0.33$.

Data for Young's modulus, shear modulus and Poisson's ratio, for foams with a wide range of densities are taken from this study (Table 6.1 to 6.5) and from literature. These are shown in *Figures* 8.43, 8.44, 8.45, and 8.46. The figures include data for rigid polymers, elastomers, metals and glasses. The normalizing properties $\rho_s = 1.2$ Mg/m^3 and $E_s = 45000$ kN/m^2 for the flexible polyurethane foams are chosen from Gibson and Ashby (1988). In these figures, the experimental data are plotted as symbols. The solid and dashed line on each figure shows the equation for open-cell foams developed in this thesis (EQ. 5.32) and by Gibson and Ashby (1988) respectively.

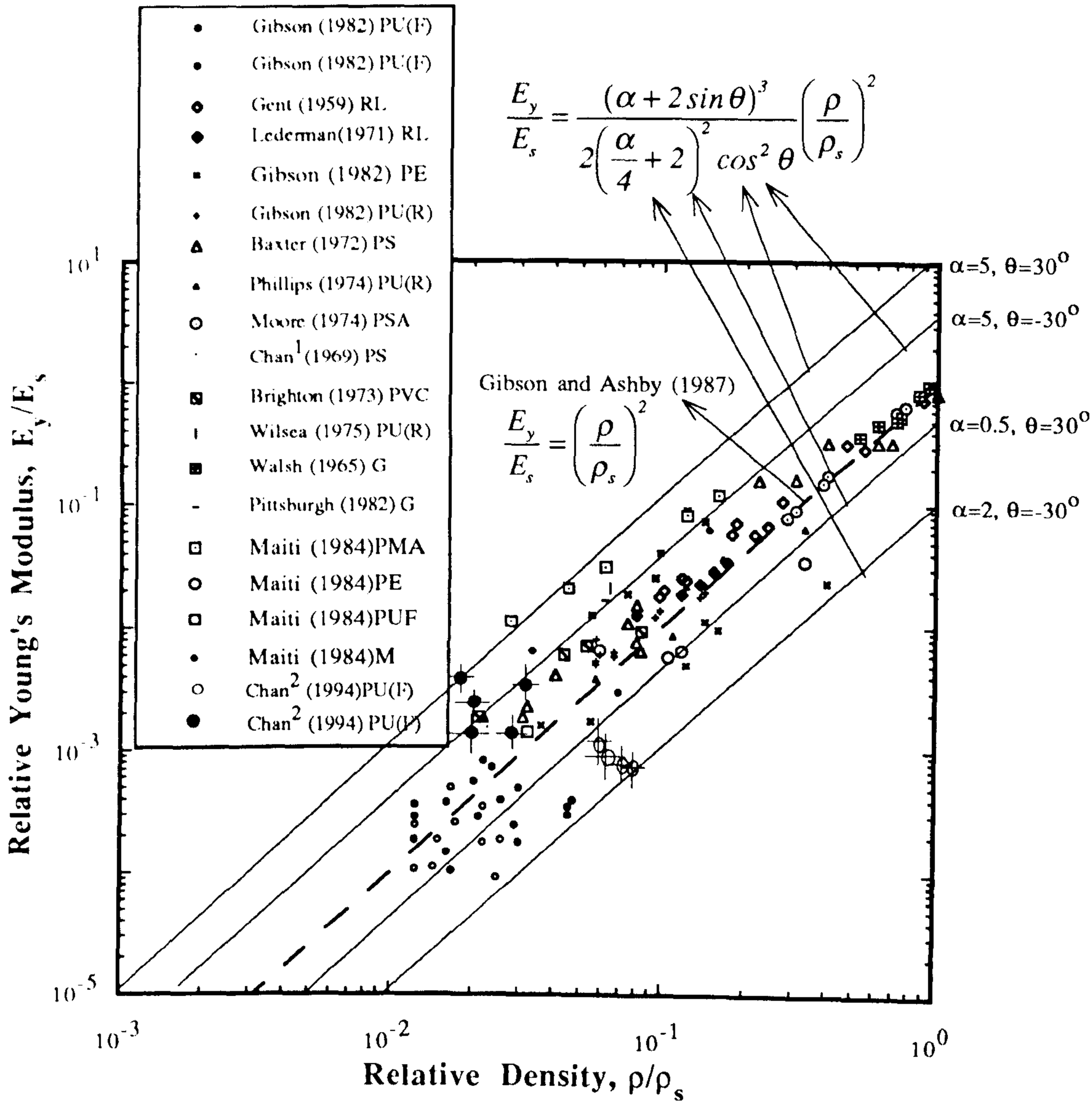

Fig. 8.43 Data for the relative Young's modulus of foams, Ey/Es, plotted against relative density, ρ^*/ρ_s. The four solid lines represent the theory for both conventional and auxetic foams. The dashed line represents the theory of Gibson and Ashby (1988).

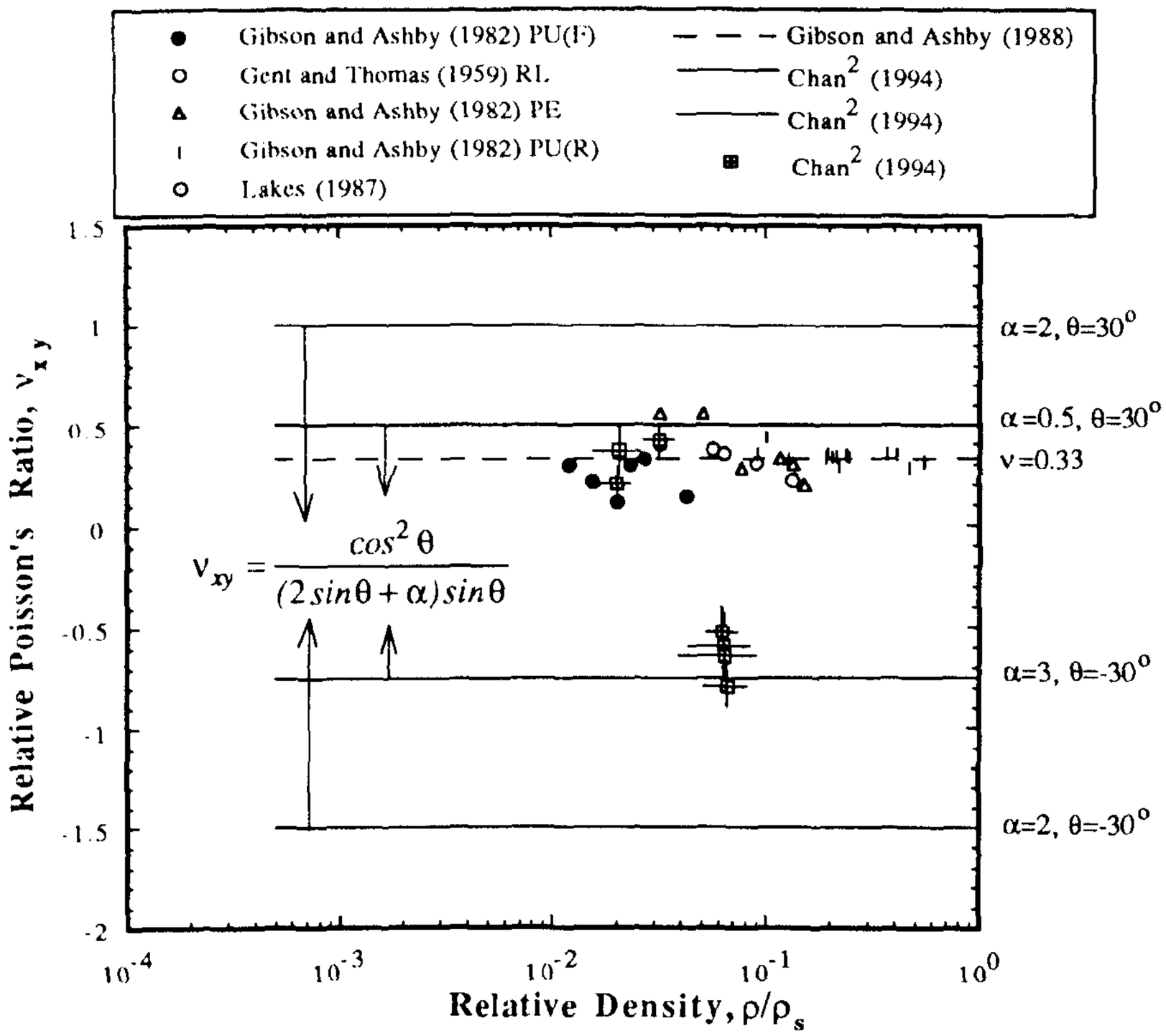

Fig. 8.44 Data for Poisson's ratio of foams, ν_{xy}, plotted against relative density, ρ^*/ρ_s. The four solid lines represent the theory for both conventional and auxetic foams. The dashed line represents the theoretical value of Gibson and Ashby (1988).

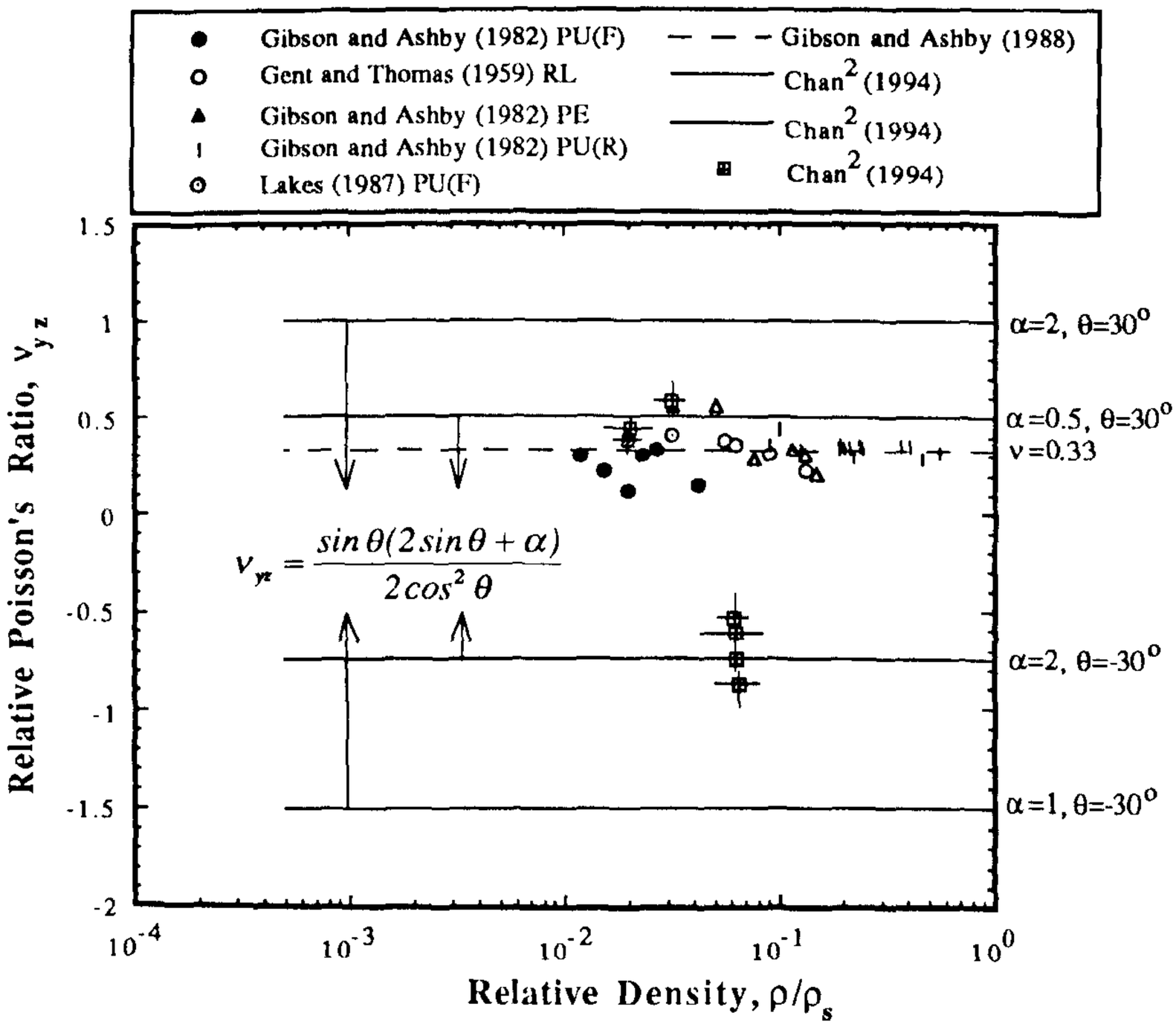

Fig. 8.45 Data for Poisson's ratio of foams, ν_{yz}, plotted against relative density, ρ^*/ρ_s. The four solid lines represent the theory for both conventional and auxetic foams. The dashed line represents the theoretical value of Gibson and Ashby (1988).

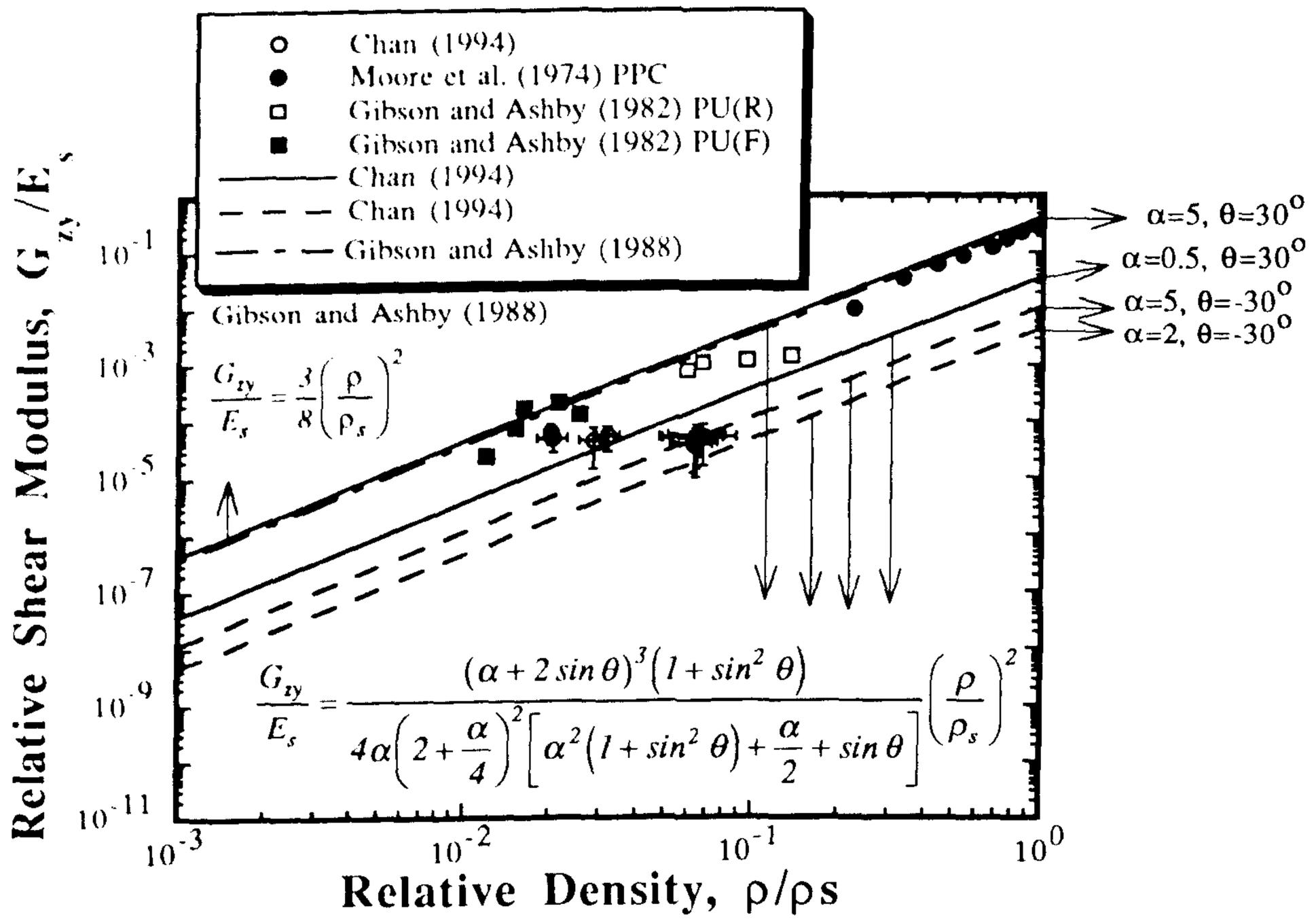

Fig. 8.46 Data for the relative shear modulus of foams, Gzy/Es, plotted against relative density, ρ^*/ρ_s. The two solid lines represent the theory for both conventional and auxetic foams. The dashed line represents the theory of Gibson and Ashby (1988).

Figures 8. 43 and 8.46 show that the experimental data for the foams fit well with the theoretical curves. The large scatter in the data for Poisson's ratio (Figures 8.44 and 8.45) reflects, in part, the variability in ν for foams of different cell geometry (cell shape, as discussed above) and, in part, the inherent difficulty in measuring this property.

8.12 The Cross Sectional Area of the Cell Ribs

The loading on a component can generally be broken down into some combination of axial tension or compression, bending, hinging, and torsion. Almost always, one mode dominates. The effect on the shape of the cross sectional area depends upon the mode of loading. In axial tension, the area of cross-section is important but its shape is not: all sections with the same area will carry the same load. On the other hand, in bending and hinging it is the shape that matters. This is because the second moment of area is dependent on the shape of the cross-section as shown in *Table* 8.5.

Section Shape	A (m^2)	I (m^4)
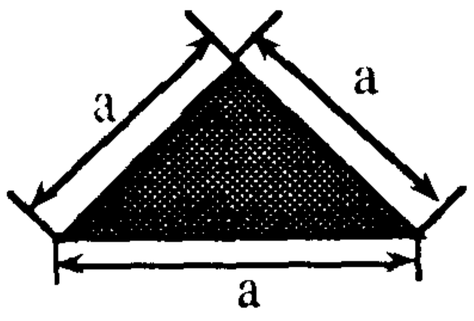	$\frac{\sqrt{3}}{4}a^2$	$\frac{a^4}{32\sqrt{3}}$
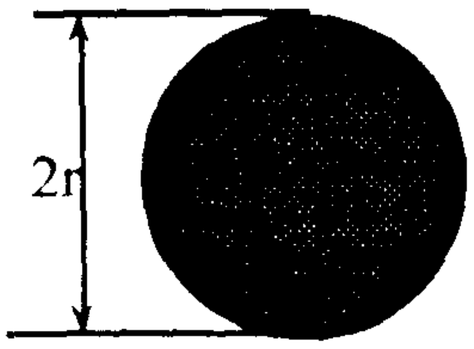	πr^2	$\pi r^4/4$
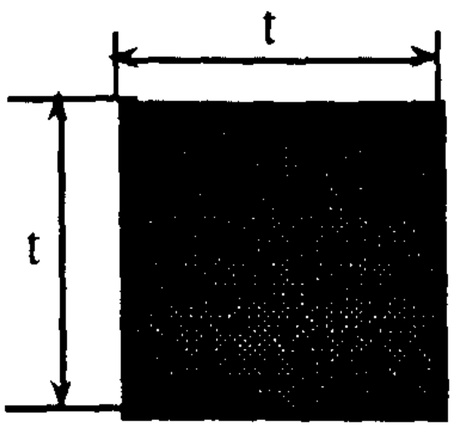	t^2	$t^4/12$
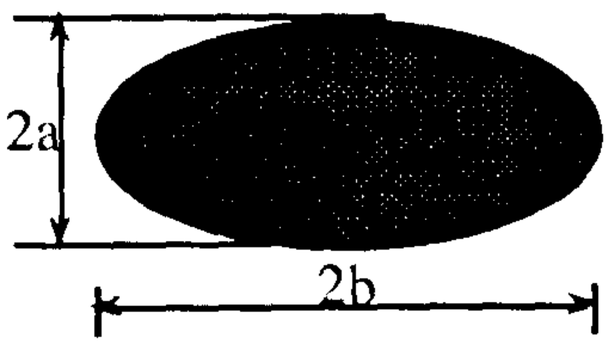	πab	$\pi a^3 b/4$

Table. 8.5 The second moments of sections.

The best material-and-shape combination depends upon the mode of loading. The cross-section area of a foams is normally triangular in shape. If we assume a=t, then the moduli of foam having triangular ribs are $\frac{12}{32\sqrt{3}}$ times that of foam having square ribs. Although the shapes of the moduli-cell angle curves are the same for the two cases, the curve for the foam having triangular shape will shift upwards. The reason a rectangular rib was used instead of a triangular rib in the foam model is because each vertical rib, h, is equally sheared between 4 identical cells. In order to divide the vertical rib into four identical ribs, it was necessary to choose the rectangular rib instead of the triangular rib. However, the results should be the same for both of the cases, the only difference being that the values of the moduli of the foam having the ribs triangular in shape are $\frac{12}{32\sqrt{3}}$ times that of the foam having the ribs square in shape.

It should be noted that the theoretical models can also be used for molecular design. Several types of the cross-sections, and therefore, second moment of area can be chosen according to the mode of loading.

8.13 Elastic Theory of the Ball Indentation Test

The theory of plastic hardness of the foams were developed by Wilsea et. al. (1974) and Shaw and Sata (1966). Since the foams used in this study are elastic materials and have no yield stresses they are therefore different from plastic foams. As a result the approach of Wilsea et al. (1974) and Shaw (1966) cannot be used here to analyse my experimental results. However, the theoretical treatment of elastic hardness of metal is well developed. Both static and dynamic indentation resistance to elastic deformation have a dependence on Poisson's ratio that is predicted from the classical Hertz equation (Tabor, 1951). This equation was originally derived to describe the penetration of an elastic surface by an elastic ball (see Figure 8.47).

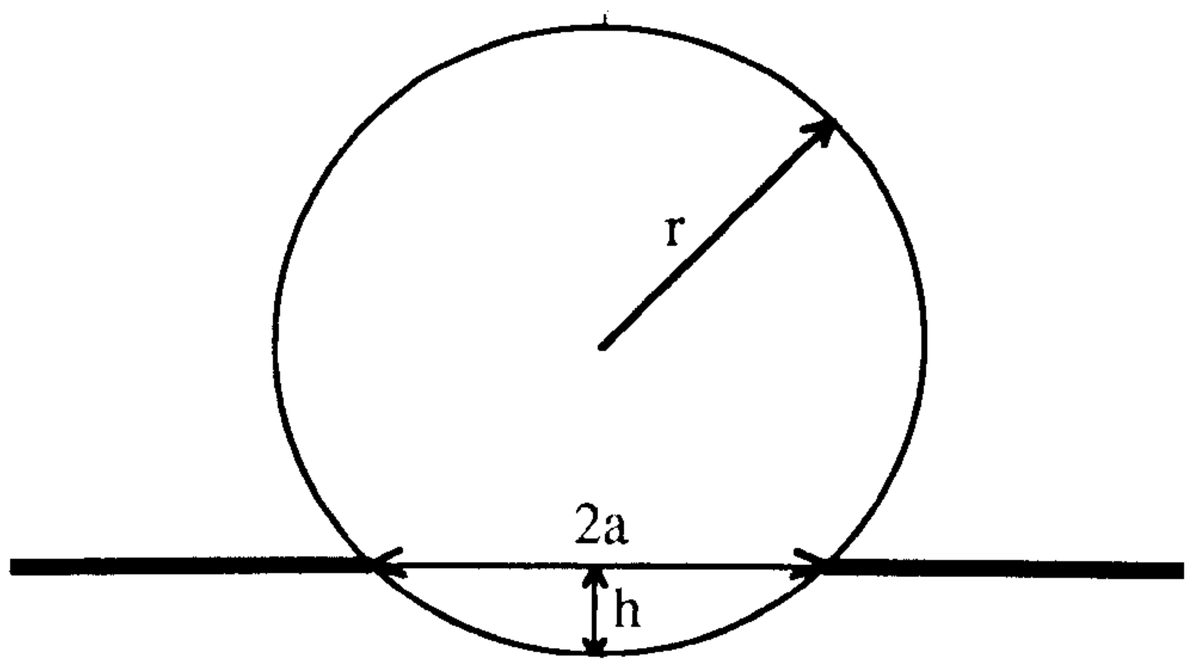

Fig. 8.47 Schematic diagram showing the indentation of an ideal elastic surface by a steel ball.

$$a = \left(\frac{3}{4} Fr \left(\frac{1 - \nu_B^{\,2}}{E_B} + \frac{1 - \nu_M^{\,2}}{E_M} \right) \right)^{1/3} \qquad (8.4)$$

Where: a = radius of indentation

F = applied load

r = radius of ball

ν_B = Poisson's ratio of ball

ν_M = Poisson's ratio of material

E_B = Modulus of ball

E_M = Modulus of Material

The steel ball is much harder than the foams, therefore the ball is considered to be infinitely stiff and then the equation can be rewritten as:

$$a = \left(\frac{3}{4} Fr \left(\frac{1 - \nu_M{}^2}{E_M} \right) \right)^{1/3} \qquad (8.5)$$

Relate the radius of the indentation, a to the depth, h, we know that

$$(r-h)^2 = r^2 - a^2 \qquad (8.6)$$

$$a = \left(r^2 - (r-h)^2 \right)^{1/2} \qquad (8.7)$$

Therefore,

$$\left(r^2 - (r-h)^2 \right)^{1/2} = F^{1/3} \left(\frac{3r}{4} \times \frac{1 - \nu_M{}^2}{E_M} \right)^{1/3} \qquad (8.8)$$

$$F^{1/3} = \frac{\left(r^2 - (r-h)^2 \right)^{1/2}}{\left(\frac{3r}{4} \times \frac{1 - \nu_M{}^2}{E_M} \right)^{1/3}} \qquad (8.9)$$

So, for a given radius of indenter and applied force, the indentation resistance of the material in this case is proportional to $\left(1 - \nu_M{}^2\right)^{-2/3}$. It can clearly be seen that, as ν_M approaches ±1, the material will become much more difficult to indent. Since the compressive Poisson's ratio for the conventional polymeric foams is normally around 0.33 (Gibson and Ashby, 1988), and that for the auxetic foams can be as large as -0.76. Therefore, the indentation resistance of auxetic foam maybe higher than that of conventional foam.

The equation 8.9 was used to plot the *Figure* 8.48. The value of E_m and ν_m were listed in Table 6.1 and 6.4. *Figure* 8.48 shows the load/deflection curves expected for the 10ppi conventional and auxetic polyether urethane foams under the indentation of the two different sizes spherical indenters, Ball 1 and Ball 2. In both cases there is an initial linear region, and the indentation resistance is dependent on the indenter size. However, Despite having low in-plain shear moduli and Young's moduli auxetic foams can offer greater resistance to indentation.

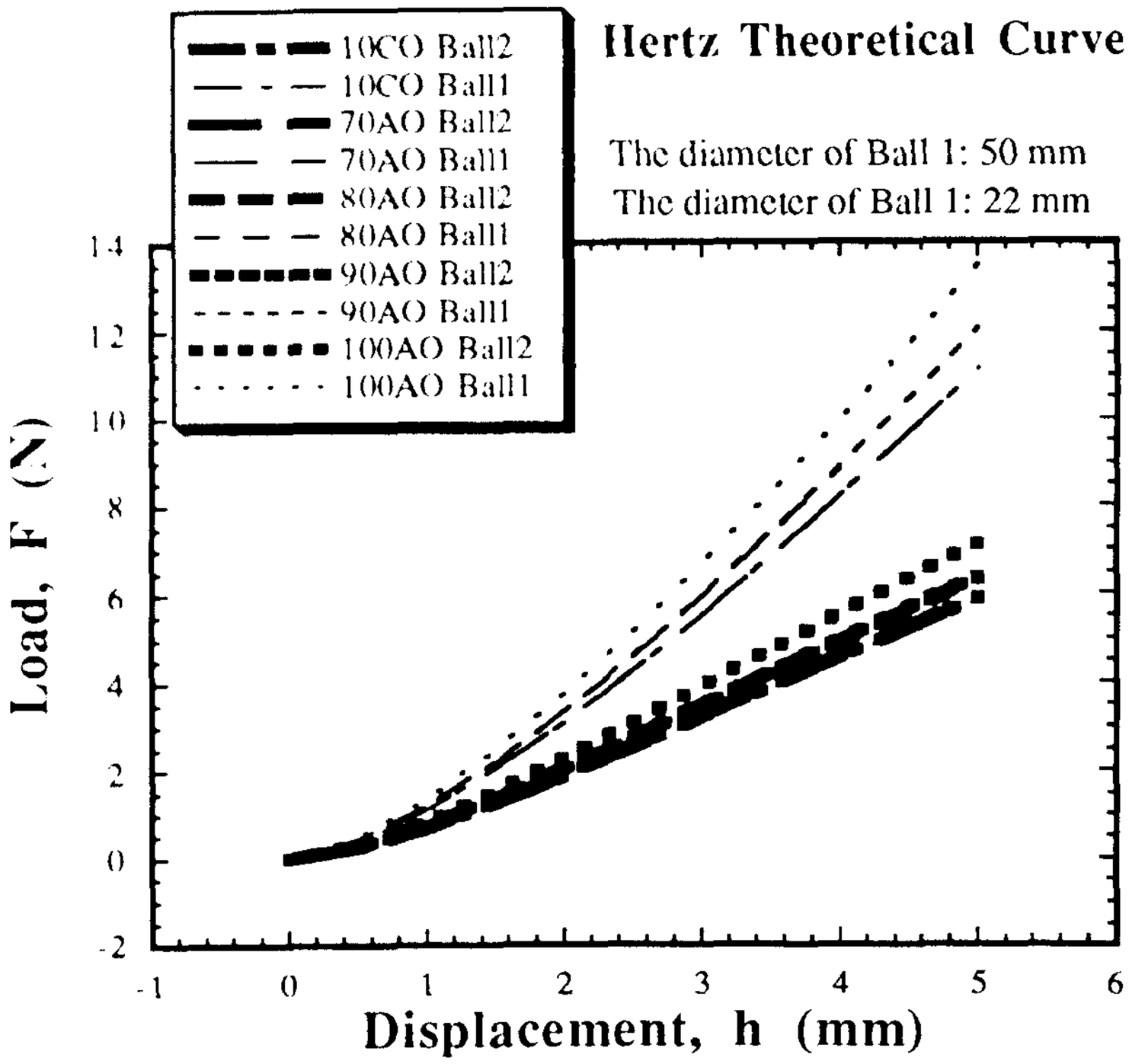

Fig. 8.48 Plot of the Hertz equation for the two sizes spherical indenters, Ball 1 and Ball 2 indenting the 10ppi conventional and auxetic polyether urethane foams in the foam rise, y direction.

Figure 8.49 shows the experimental load-deflection curve of the 10ppi conventional polyether urethane foam (10CO) together with the theoretical plots under indentation of the Ball 1 and Ball 2. For very low strains there is reasonable agreement between theory and experiment, but the equation breaks down at larger strains.

An equivalent plot for an auxetic foam (70AO) is shown in Figure 8.50. The theory predict that Ball 1 has higher benefit for auxetic foam in the entire strain range, The experiment shows this prediction is true only when the strain is greater than 12%. Since the experimental data for Ball 1 and Ball 2 are close, so if we take the measuring errors into account the experimental results may agree well with the theory.

Figures 8.51 and 8.52 show the load-deflection of the 10ppi polyether urethane foams (10CO and 70AO) under the indentation of Ball 1 and Ball 2 with those obtained from the theory. The initial gradient shows good agreement with the theory. Again, the theory overestimates the resistance to indentation and the deviation from linearity in the experimental data arises from the change of the effective area of foam supporting the load. Unlike dense solids, which can be considered to be incompressible when deformed plastically to large strains, foams change their volume when compressed. This is because the cells of the foam collapse as the foam is squeezed, so much so that, for low density foams, axial compression produces almost no lateral spreading. However, it can be seen that caution must be used in applying the

results of the Hertz theory to low modulus foams where it is easy to produce deformations which exceed the restriction to small strains.

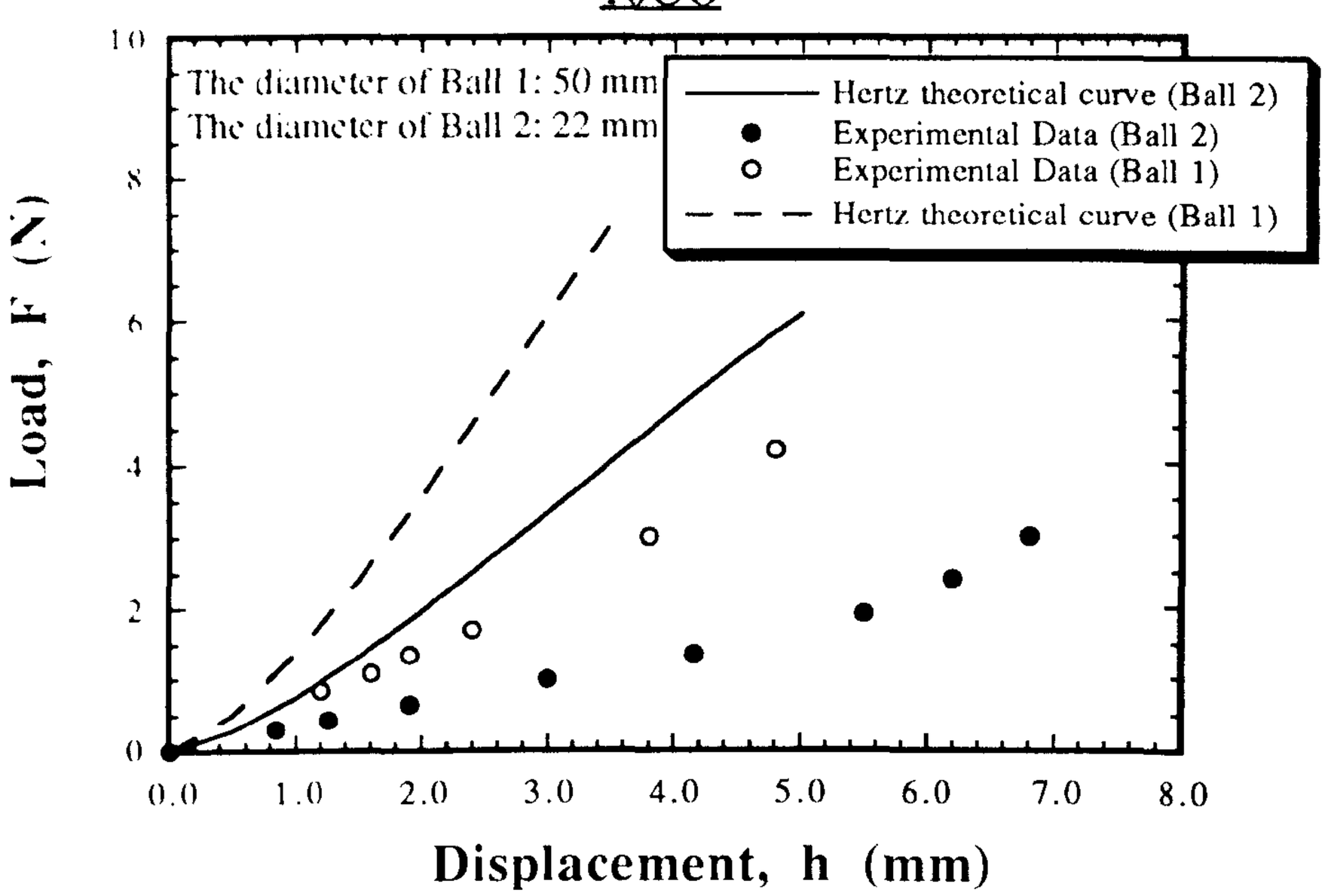

Fig. 8.49 Load versus displacement plot for the two sizes spherical indenters, Ball 1 and Ball 2 indenting the 10ppi conventional polyether urethane foam in the foam rise, y direction.

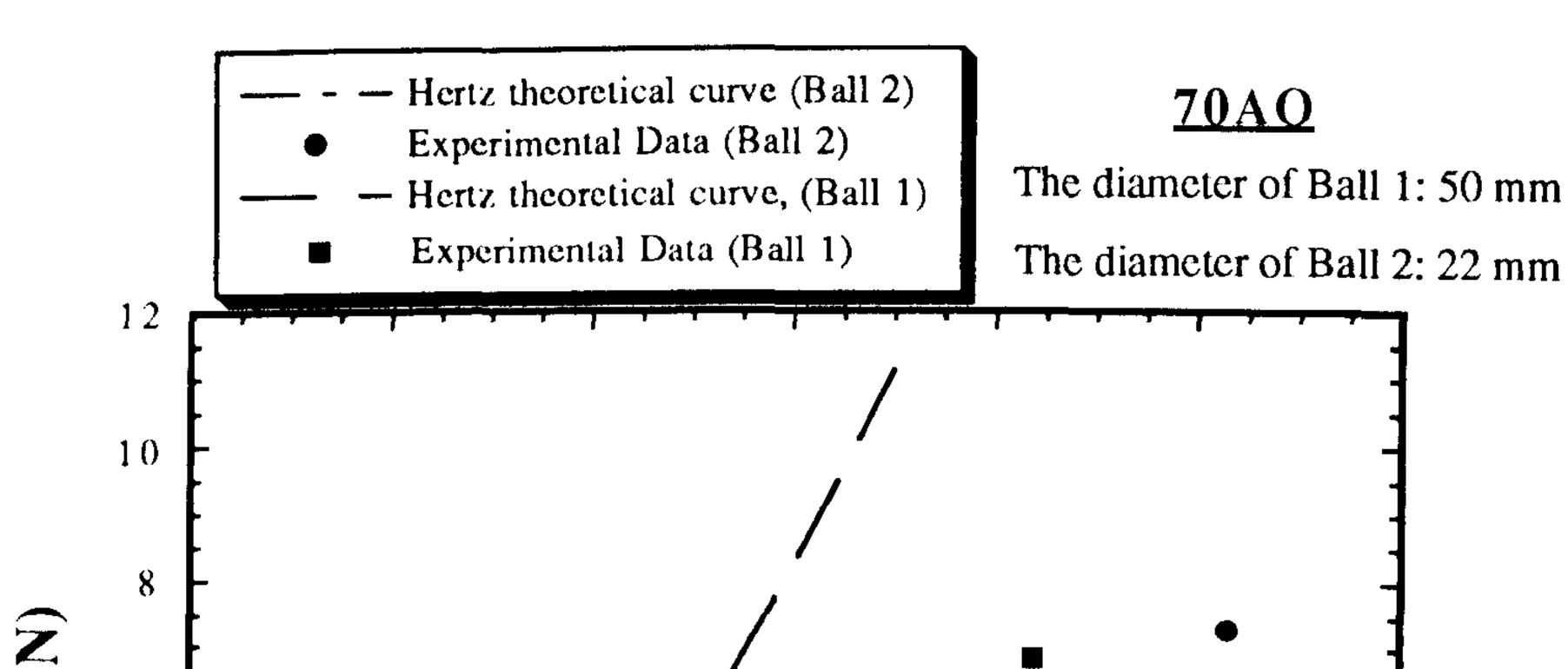

Fig. 8.50 Load versus displacement plot for the two sizes spherical indenters, Ball 1 and Ball 2 indenting the 10ppi auxetic polyether urethane foam in the foam rise, y direction.

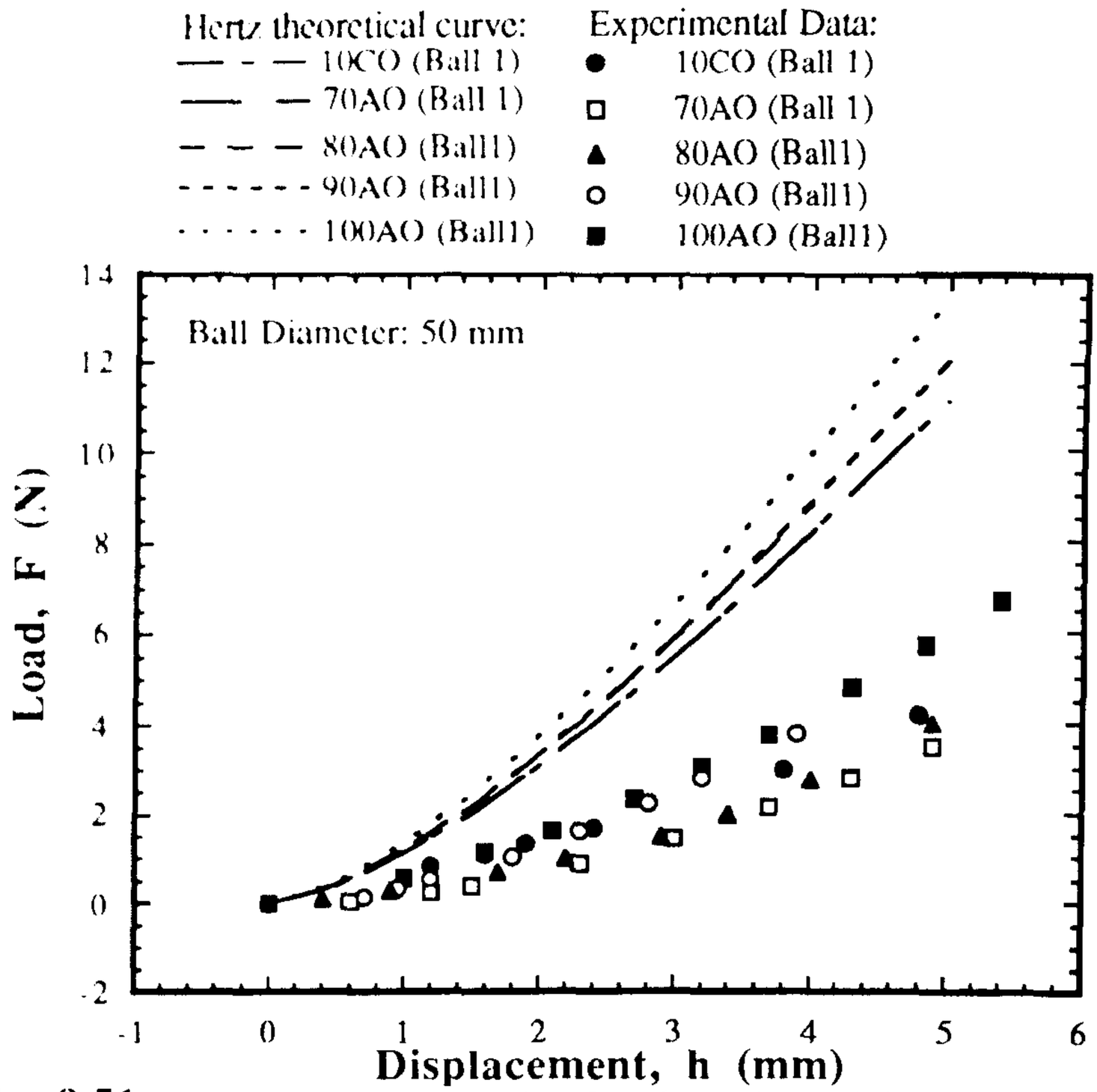

Fig. 8.51 Load-displacement plot for the spherical indenter, Ball 1 indenting the 10ppi conventional and auxetic polyether urethane foams in the foam rise, y direction.

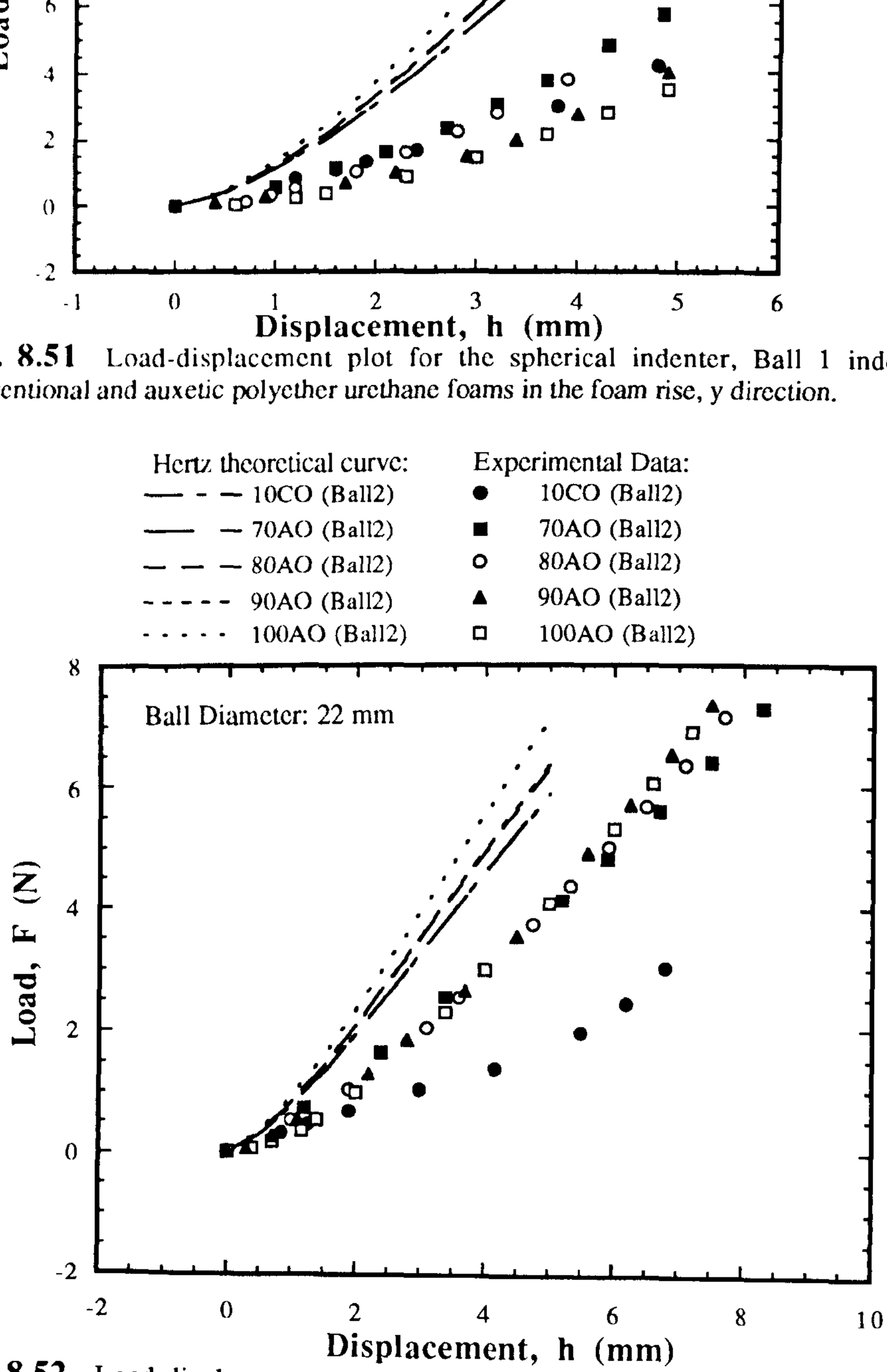

Fig. 8.52 Load-displacement plot for the spherical indenter, Ball 2 indenting the 10ppi conventional and auxetic polyether urethane foams in the foam rise, y direction.

In every case it is evident that auxetic foam is more resistant to indentation than its parent conventional foam. It could be argued that this is to be expected considering that it is three times as dense. However, this is not the most important consideration. Experimental examination of the uniaxial stress-strain curves in *Figures* 7.7 to 7.14 show that in the initial part of the load-deflection curve for the auxetic foam is less stiff than its parent conventional foam. This weakness can be attributed firstly to a difference in the initial deformation modes of conventional and auxetic foams (see Figure 7.7 and 7.8). With the conventional foam, the applied load must overcome the inherent stiffness of the straight ribs that make up the hexagonal cells. At a relatively low load this mode changes as the ribs start to buckle and the progressive collapse of the structure into a buckled form generates the elastic collapse, the plateau region of the load-deflection curve. The microstructure of auxetic foam is different from that of conventional foam. Since the ribs of auxetic foam are already buckled inwards, and the increased density of the foam plus the additional densification that occurs as a consequence of the negative Poisson's ratio enables the material to sustain a constant modulus that is comparable with but smaller than that of the initial modulus of the parent conventional foam as shown in *Figures* 8.51 and 8.52. From EQ. 8.9, we know that increasing the diameter of the inderter reduces the gradient of the load-displacement curve. It is noted that when we try to interpret the results obtained with a spherical indenter we should consider the effective contact area of the indenter-indentation profile as shown in *Figure* 7.6. Therefore, a more accurate elastic indentation theory for the low modulus material requires further development in the future research.

Looking at honeycomb indentation (Figure 7.15 and 7.16) we can see a much more local indentaion in the conventional honeycomb whereas the auxetic honeycomb has a wider indentation. Exactly the same effect is seen in the photographs of foams (Figure 7.4 and 7.5). A possible explaination for this effect is: (see Figure 8.53)

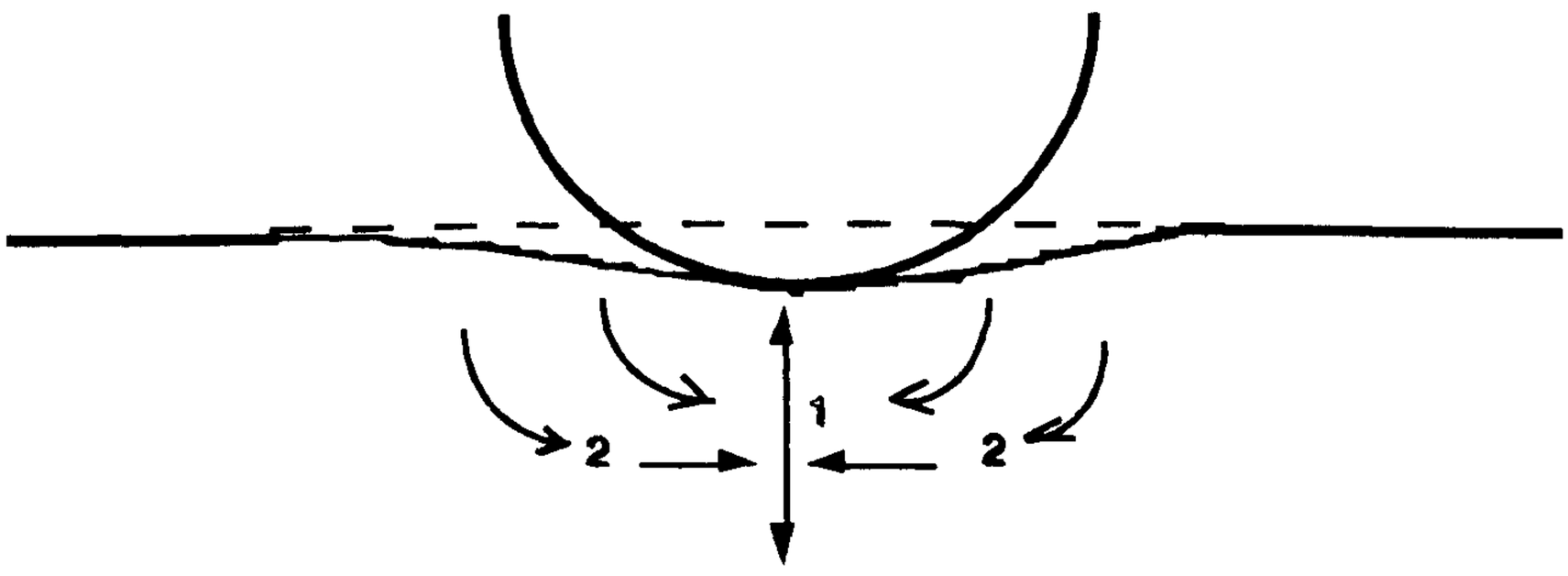

Fig. 8.53 Schematic diagram for the ball indentaion test on an auxetic foam.

Region 1: Material is squashed. This because region 2: material to be drawn in from sides. This movement of material increases width of indentation.

Compare the ball indentation profile of auxetic foam with that of conventional foam (Figure 8.54), we can see that the auxetic foam has a much smaller shear strain than the conventional foam. For a given h, the diameter of the indentation profile, d, is smaller for the conventional foam. This means that the shear bending of auxetic foam is less than that of conventional foam.

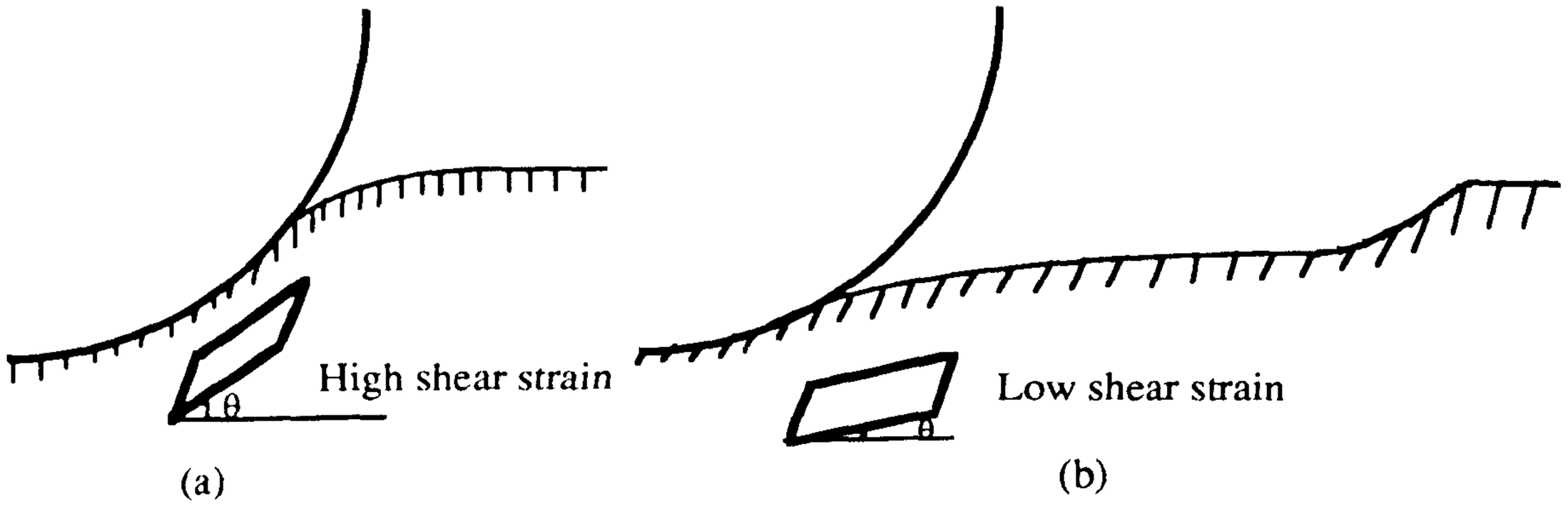

Fig. 8.54 Schematic diagram for the ball indentaion test on (a) convetional foam, and (b) auxetic foam.

8.14 Elasticity Theory of the Ball Rebound Test

The energy expended during the rebound test is very difficult to quantify if we attempt to measure it directly by the indentation produced. This is because, as we shall see, as a result of elastic recovery there is no indentation remaining in the surface when rebound occurs. The approach used here is that adopted by Shore (1918) and by Roudie (1930). In their methods, the height of rebound itself was used as a measure of the dynamic resilience. It was found that if the height of fall is constant, the height of rebound is roughly proportional to the static indentation resilience of the material concerned. The result for the foams (Tables 6.4, 7.3 and 7.4) is shown in Figure 8.55.

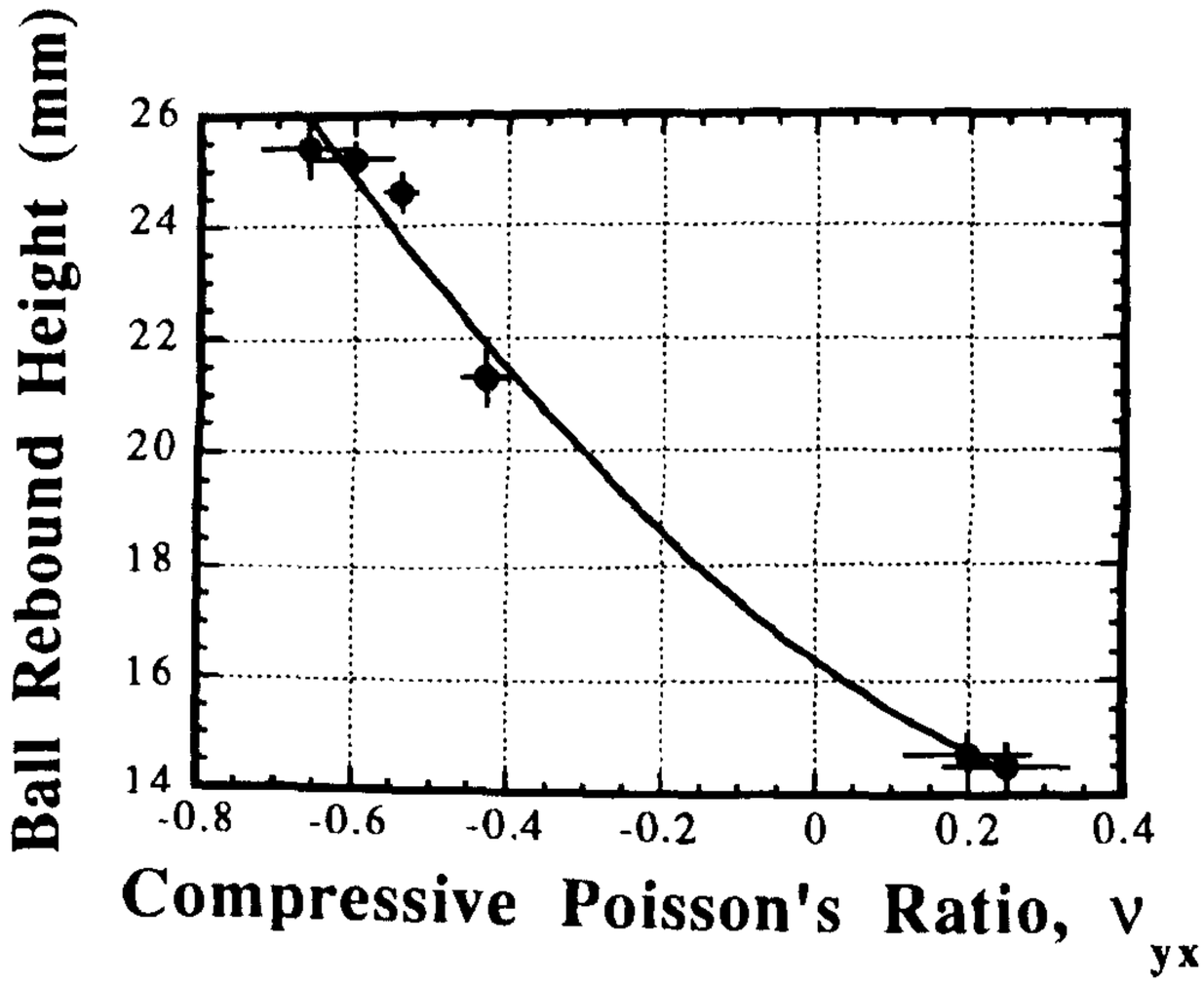

Fig. 8.55 The ball rebound height vs. the compressive Poisson's ratio for the 10ppi open cell polyether urethane foams (10CO, 100AO, 90AO, 80AO, 70AO) and the 60ppi closed cell conventional polyester urethane foam (PECC).

The experiments show that the region of contact deformed elastically. Although the foam may be slow in regaining its original configuration because of its viscoelastic behaviour, the surface recovered elastically and separate without residual deformation after the impact. Suppose the indenter has a mass m, and a radius r_B, and that it falls from a height h_1, onto a flat foam surface. After the collision, the indenter rebounds to a height h_2, and leaves a indentation profile in the foam surface of diameter d=2a (Figure 8.56). We assume that (1) the mechanism involved in the dynamic indentation is essentially the same as that which occurs under static conditions. That is to say, when the elastic deformation has been completed there is a release of elastic stresses in the indenter and in the indentation. (2) The energy involved in the release of these elastic stresses is equal to the energy of rebound of the indenter. (3) The Young's moduli for the indenter and the foam are essentially the same as for static conditions. Consider the indentation after the impact has occured. Since there has been a release of elastic stresses in the indentation, its radius of curvature will not be r_B but will be somewhat greater, say r_m. If the indenter apply a mean pressure, P, at the end of the deforming process, and it deforms the foam (and itself) elastically, according to Tabor's equation (1951):

$$P^{5} = \frac{h_2^{4}}{\left(h_1 - \frac{3}{8}h_2\right)^{3}} \times \frac{mg}{109 r_B^{3}} \left(\frac{1 - \nu_B^{2}}{E_B} + \frac{1 - \nu_m^{2}}{E_m} \right)^{-1/4} \qquad (8.10)$$

Where: m and r_B are the mass and the radius of the spherical indenter respectively. g, is the acceleration due to gravity (approx. 9.81 m/s^2), h_1, is the height of the ball free fall, and h_2 is the height of the ball rebound. E_B and E_m are Young's moduli for the indenter and the foam respectively, and ν_B, ν_m are Poisson's ratios.

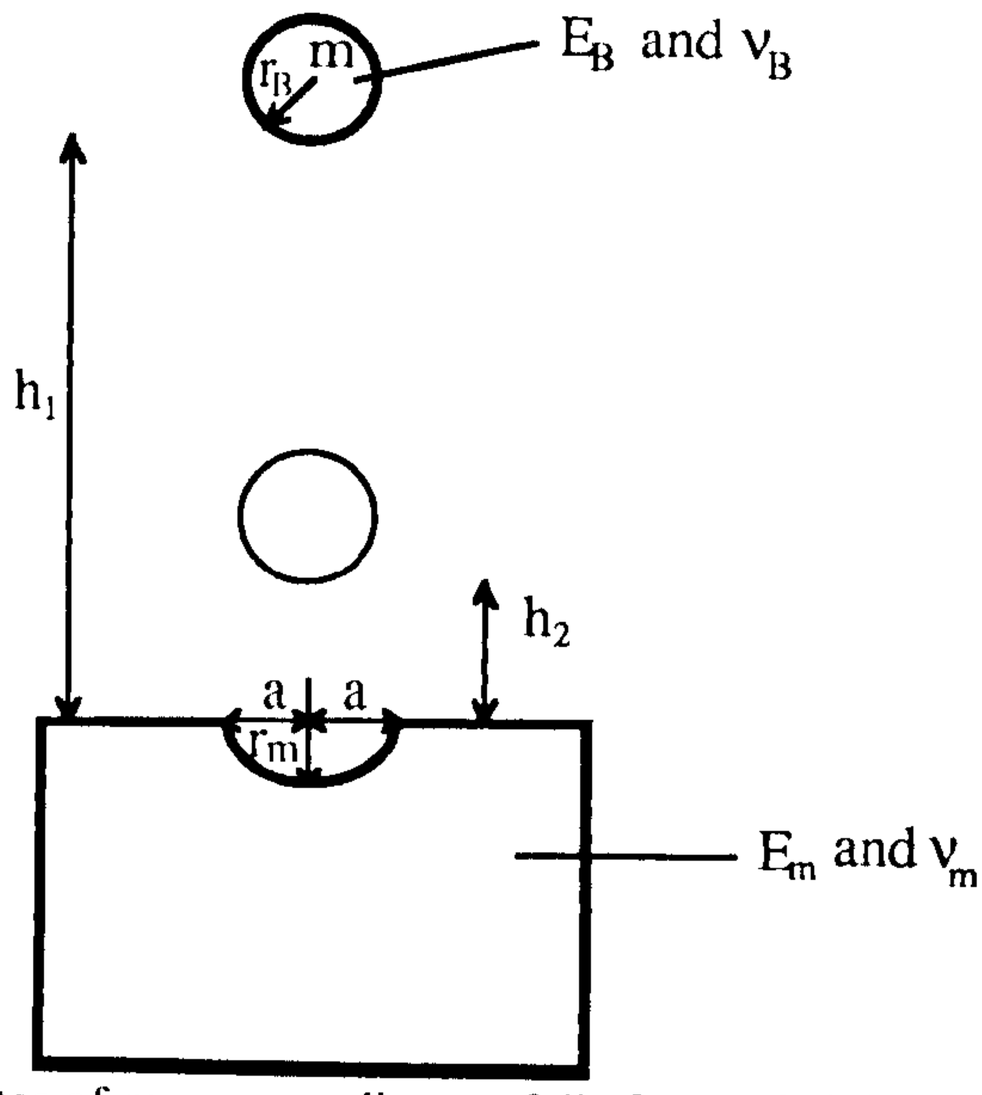

Fig. 8.56 A hard spherical indenter of mass m, radius r_1, falls from a height h_1 on to a massive anvil, rebounds to a height h_2 and creates an indentation of chordal diameter. (Tabor, 1951)

Since the steel ball is much harder than the foam under test it is therefore the ball is considered to be infinitely stiff, and then the equation can be rewritten as:

$$P' = \frac{h_2^4}{\left(h_1 - \frac{3}{8}h_2\right)^3} \times \frac{mg}{109 r_B^3}\left(\frac{1-\nu_m^2}{E_m}\right)^{-1/4} \qquad (8.11)$$

If we assume the bracket involving Young's moduli and Poisson's ratio does not vary greatly for most foams during the contact, we may treat this factor as a constant and plot P as a function of h_2 for a given height h_1. The theoretical curve is shown in Figure 8.57. Note: the experimental values of h_2, h_1, m, r_B, ν_m, and E_m from Table 7.3 and 7.4 were used to calculate P by using EQ. 8.11. Figure 8.57 shows the calibration Data (o) and the theoretical P-h_2 curves (full line and dashed line).

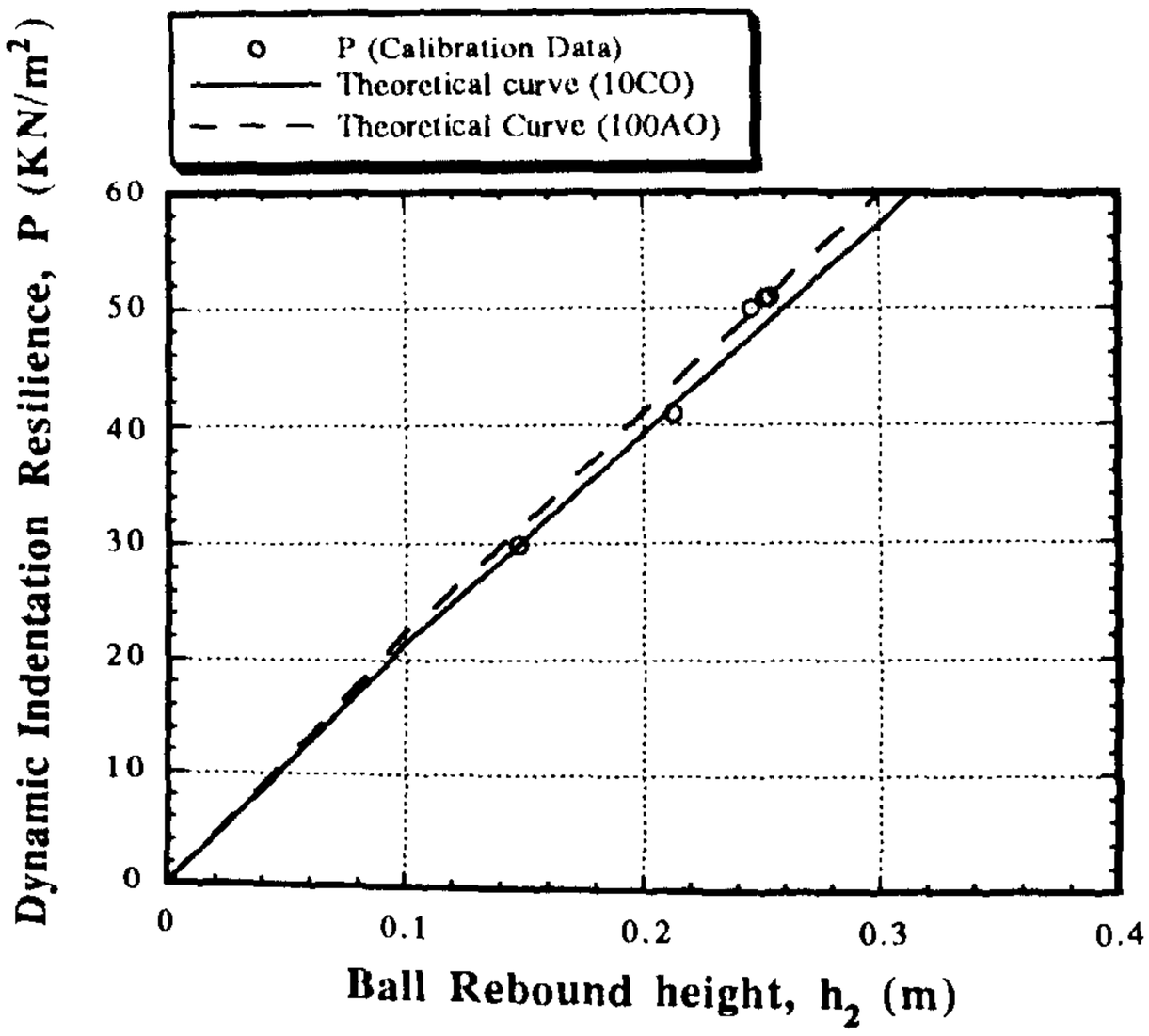

8.57 Dynamic indentation resilience as a function of the height of rebound for a fixed height of fall of 516mm. The equation used to plot the theoretical curves is given in EQ. 7.12.

It can be seen from Figure 8.57 that the dynamic resilience of auxetic foam is higher than its parent conventional foam. Therefore auxetic foam may have good potential as packaging material.

The dynamic indentation resilience of a foam is the pressure with which it resists local indentation by a rapid moving indenter. Under this experimental condition, where the speed of impact is much more higher than the speed of static ball indentation, the dynamic elastic collapse pressure is approximate ten times the static elastic collapse pressure, so that, as with static indentation resilience, dynamic indentation resilience is essentially a measure of the elastic collapse limit of the foam. The actual value of the dynamic elastic collapse pressure, however depends not only

on the size of the indentation as in the Meyer hardness test; it also depends on the velocity of impact and on the way in which it is computed.

8.15 Relate the Loss Tangent with the Ball Rebound Measurements

The viscoelastic deformation of the foam during the ball rebound test, is a shear process, and it is time dependent. The effects of this process on ball rebound measurements has been outlined by Flom (1960) as follows: In determining the elastic loss in a material it is convenient to represent the dynamic shear modulus as a complex quantity, G*. The stress-strain relationship is $\sigma(\omega) = G^*(\omega)\varepsilon(\omega)$ where $G^*(\omega) = G'(\omega) + jG''(\omega)$. The ratio G''/G' is $tan\,\delta$ by which the stress leads the strain and is called the loss tangent. Flom then shows how $tan\,\delta$ can be obtained from the rebound height by the equations:

$$\tan\delta = C\left(\frac{2.303}{\pi}\right)Log\left(h_1/h_2\right) \qquad (8.12)$$

Where: h_1, is the original height of the ball, h_2, is the rebound height of the ball, C, is a constant depending on the geometry of the microstructure. It should be noted that in this analysis Flom assumes that the polymer is not permanently indented by the impact of the ball, and the frequency is assumed to be very low.

If we assume that the frequency of stress in the ball rebound was the same as in the DMTA (10Hz). Then the loss $tan\,\delta$ obtained from the DMTA curves (*Figure* 7.28, 7.29 and 7.30) can be plotted against h_1/h_2 obtained from the ball rebound test (*Table* 7.3, and 7.4) as shown in *Figure* 8.58. For comparison with the experimental results the theoretical equation (EQ. 8.12) is also plotted in the same figure (dashed line).

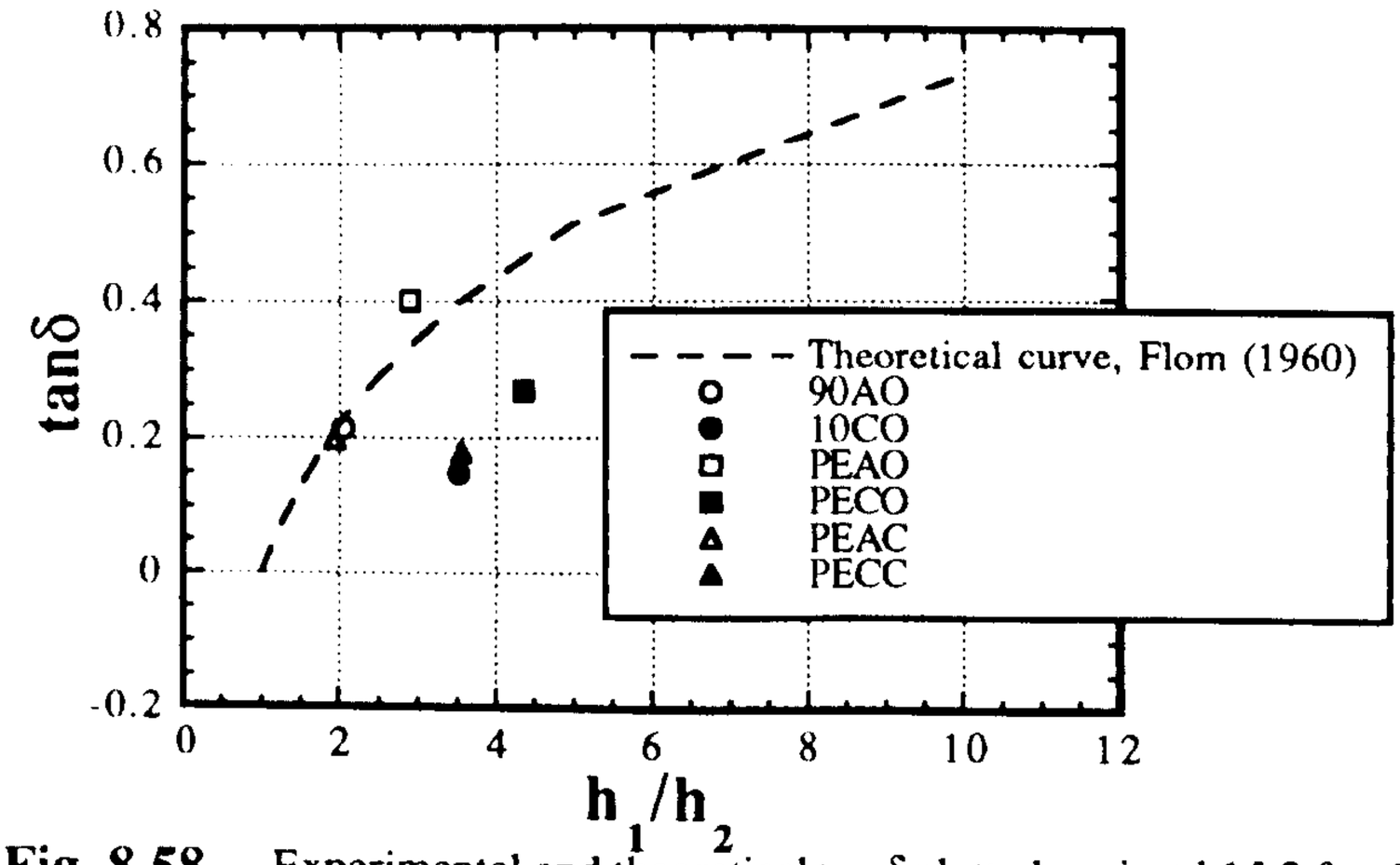

Fig. 8.58 Experimental and theoretical *tan δ* plotted against h1/h2 for the conventional and auxetic foams.

Figures 8.58 shows that the loss $tan\delta$ of an auxetic foam is larger than that for its parent conventional foam. Since the loss tangent, $tan\delta$ is one of the characteristics of a material that determines its dynamic damping capability, then we can see that auxetic foam is better at absorbing dynamic energy.

Figure 8.58 also shows that the ball rebound height for the auxetic foam is higher than its parent conventional foam. Here the foam which we have used is an non-linear viscoelastic material, and actually the frequency of the ball rebound test is much lower than that of the DMTA test. Therefore, it may not be a good idea to compare the result of the ball rebound test with that of DMTA. We would expect the ball rebound measurements to be more closely related to the hysteresis loop than to the Loss tangent. Experiments show that auxetic foams have a larger rebound height and a smaller hysteresis loop.

In order to relate the frictional energy loss with slip at the ball-foam interface, it is necessary to develop a more relevant mathematical model for the loading and the unloading phases of the stress-strain response. This model should not only account for the variation of strain over loaded area but also the non-linear mechanical behaviour and the frequency dependence of the material properties.

Chapter 9 Conclusions and Future Work

9.1 Conclusions

(1) A large block of auxetic foam exhibiting negative Poisson's ratio has been fabricated. The negative Poisson's ratio arises from a re-entrant cell structure. Various features of the re-entrant cell shape are controlled by the processing techniques. Auxetic foams based on thermoplastic polymers (i.e. PUR) were produced by a thermomechanical technique from conventional low density polymeric foams. The 'multi-stage' fabrication method is used to achieve the triaxial compression for the large size foam specimen. The foam cell structure was transformed by a compression, heating, cooling, and relaxing procedure into a re-entrant structure. The required times and temperatures were determined experimentally for each type of foam examined. PUR foam subjected to different permanent volumetric compression ratios can be produced by varying the starting sizes of the foams.

(2) In tension and compression, the transverse expansion and contraction due to the negative Poisson's ratio was observed. By contrast, in the case of a conventional foam, as tensile force is applied in one direction, the cells elongate in that direction and constrict in the orthogonal directions. It was observed that the cell structure become more compact as the permanent volumetric compression was increased. The foam cell structure is very complicated. The cells rotate under the shear stresses.

(3) Results of uniaxial tensile and compressive load-deformation tests revealed significant differences between auxetic and conventional foams, which are known to exhibit three regions of behaviour: (i) an approximately linear behaviour for strain less than about 5%. (ii) a plateau region in which strain increases at constant or nearly constant stress, and (iii) a densification region of the stress-strain curve in which its slope increases markedly with strain. As for an auxetic foam, this study disclosed the absence of a plateau region in the stress-strain curves. Moreover, the tensile and compression stress-strain curves of auxetic foam exhibited a much wider range of linear behaviour.

(4) The auxetic foams exhibited lower Young's modulus. Negative Poisson's ratio and Young's modulus decreases with increasing permanent volumetric compression. The shear modulus of auxetic foam in some directions, (i.e. G_{xy}, G_{yx}, G_{yz}, and G_{zy}) is lower than that of conventional foam. However, in other directions

such as: G_{xy} and G_{yx}, the shear modulus of auxetic foam exhibit higher values. This static testing result is the same as the dynamic testing result obtained from DMTA.

(5) In the indentation of a block of foam by a localised circular pressure distribution of radius a, a foam with a negative Poisson's ratio is more difficult to indent. The reason for this is the local shear strain of the auxetic foam is much less than that of conventional foam. The hexagonal cells with the positive cell angles are very easy to collapse whereas the re-entrant cells will constrict and the cell sizes become smaller.

(6) At small strain and low strain rate, the energy loss of conventional foam is higher than that of auxetic foam. However, at large strain and high strain rate, the hysteresis of auxetic foam exhibits a higher value.

(7) A rhombic dodecahedron model based on foam micro-structure has been developed. Foam can deform by one or any combination of three mechanisms: flexure, hinging, or stretching, and all of these deformation modes can be described by force constant models. The model uses direct measurement of geometric parameters from SEM and optical microscope observation of the specimens. The Young's modulus, Poisson's ratio and shear modulus of both conventional foam and auxetic foams were comparable to those predicted by microstructural analysis based on the deformation of cell ribs. The three dimensional foams have complicated geometries which cannot be completely expressed. The theoretical model for foams can only be an approximate analysis. Models describing the properties of foams in terms of cell rib property and cell geometry can be used to select the most appropriate material for a particular engineering application.

9.2 Future Possibilities and Future Work

Applications of negative Poisson's ratio materials may be envisaged based on either the value of Poisson's ratio itself or another unusual physical property that results from the underlying structural mechanism. Some applications such as: air filters, gaskets, fillings for high way joints, fasteners, and sandwich panels need to be examined experimentally in the future work.

Further experimental studies on auxetic foams are:

(1) Looking for a more accurate way to determine the parameters of the cell geometry (i.e. L, h, and θ).

(2) A model which can be used to predict the mechanical behaviour of foams at large deformation strains requires further development.

(3) An indentation theory on elastic foams requires development.

(4) The foams are made from polymers. At the moment, we are using the property of polymers, i.e. E_s instead of the property of the cell rib. However, actually the foaming process and heat treatment may change the property of the cell ribs. Therefore, we need to find a way to measure the E_s of the foam ribs.

(5) At the present of time, an auxetic foam has to be transformed from a conventional foam. This may give rise to broken or damaged ribs in the cell. Therefore, we need to look for a new way to manufacture auxetic foam, so that it is no longer necessary for an auxetic foam to be converted from a conventional foam, but can be made directly from the expansion process.

References

Abdd EL-sayed, F. K., Jones, R., & Burgens, I, W.,
Composites,
Vol. 10, PP. 209-216, 1979

Alderson, K. L., & Evans, K. E.,
Journal of Materials Science,
Vol. 28, PP. 4092-4098, 1993.

Allen, H. G.,
Trans. J. Plastics Inst.,
PP. 359-363, Feb., 1967.

Almgren, R. F.,
Journal of Elasticity,
Vol. 15, PP. 427-430, 1985.

Ashby, M. F.,
Acta Metall. Mater.,
Vol. 39, No. 6, PP 1025-1039, 1991.

Ashby, M. F.,
Metallurgical Transactions A,
Vol. 14A, PP. 1755-1769, 1983.

Barikani, M., & Hepburn. C.,
Cellular Polymers,
Vol. 6, PP. 41-54, 1987.

Barma, P., Rhodes, M. B., & Salovey, R.,
Journal of Applied Physics.,
Vol. 49, PP. 4985-4991, 1978.

Bhat, B. T., Wang, T. G.,
Journal of Materials Science,
Vol. 25, PP. 5157-5162, 1990.

Benjamin, B, B.,
Civil Eng. Public work Rev., 60(172)
PP. 1646, 1965.

Bigg, D. M.,
Polymer Engineering and Science,
Vol. 21, No. 9, 1981.

Boal, D. H., Seifert, U., & Shillcock, J. C.,
Physical Review E,
Vol. 48, PP. 4274- 4283, 1993.

Brinell, J. A.,
J. Iron & Steel Inst.
Vol. 59, P. 243, 1901. (The first English translation by Wahlberg, A.)

Campbell, G. A.,
Journal of Applied Polymer Science,
Vol. 24, PP. 709-723, 1979.

Chaffanjon, P., & Verhelst, G.,
Cellular Polymers,
Vol. 11, PP. 1-17, 1992.

Challis, K. E., Hall, D. J., & Paul, D. B.,
Cellular Polymers,
Vol. 5, PP. 91-101, 1986.

Chan, Richard., & Nakamura. Masao.,
Journal of Cellular Plastics,
PP. 112-118, Mar.- April/ 1969.

Chen, P. C., & Lakes, R. S.,
Journal of Materials Science,
Vol. 26, PP. 5397-5402, 1991.

Chen, P. C., & Lakes, R. S.,
Journal of Materials Science,
Vol. 28, PP. 4288-4298, 1993.

Chen, P., Anderson, W. , & Lakes, R. S.,
Cellular Polymers,
Vol. 13, No. 1, PP. 17- 32, 1994.

Chessin, N., & Driver, W. E.,
Journal of Cellular Plastics,
PP. 185-191, April, 1967.

Choi, J. B., & Lakes, R. S.,
Cellular Polymers,
10, PP. 205-212, 1991.

Choi, J. B., & Lakes, R. S.,
Journal of Materials Science,
Vol. 27, PP. 4678-4684, 1992.

Choi, J. B., & Lakes, R. S.,
Journal of Materials Science,
Vol. 27, PP. 5375-5381, 1992.

Clark, R. C., & Meinecke, E. A.,
"Mechanical Properties of Polymeric Foams",
Technomic Publishing Co, Inc., 1978.

Clutton, E. Q., & Rice, G. N.,
Cellular Polymers,
Vol. 11, PP. 429-449, 1992.

Cousins, R. R.,
Journal of Applied Polymer Science,
Vol. 20, PP. 2893-2903, 1976.

Crawford, R. J.,
Polymer Testing,
Vol. 3, PP. 37-54, 1982.

Crawford, R. J.,
Polymer Testing,
Vol. 5, PP. 113-136, 1985.

Cunningham, A.,
Cellular Polymers,
Vol. 3, PP. 133-143, 1984.

Davis, G. J., & Zhen, Shu.,
Journal of Materials Science,
Vol. 18, PP. 1899-1911, 1983.

Dawson, J. R., & Shortall, J. B.,
Journal of Materials Science,
Vol. 17, PP. 220-224, 1982.

Dieter, G. E.,
"Mechanical Metallurgy"
McGraw-Hill International Book Company, 1976.

Dubbelday, P. S.,
Journal of American Acoustic Society,
Vol. 91 (3), PP. 1737-1744, 1992.

Dubbelday, P. S.,
NRL/MR/5917-92-719, Naval Research Laboratory, Washington, DC 20375-5000, 1993.

Evans, K. E., & Caddock, B. D.,
Journal of Physics,
D22, P. 1870, 1989.

Evans, K. E., & Hutchinson, I. J.,
Nature,
Vol. 353, Page, 124, 1991.

Evans, K. E.(a),
Composite Structures,
Vol. 17, PP. 95-111, 1991.

Evans, K. E.(b),
Endeavour,
Vol. 15, No. 4, PP. 170-174, 1991.

Evans, K. E.,
Chemistry & Industry,
PP. 654-657, Oct., 1990.

Fatima Vaz, M., & Fortes, M. A.,
Journal of Materials Science Letters,
Vol. 12, PP. 1408-1410, 1993.

Feng, W. W., & Christensen, R. M.,
International Journal of Non-Linear,
Mechanics,
Vol. 17, PP. 355-367, 1982.

Ferry, J. D.,
Viscoelstic Properties of polymers,
Wiley, New York, 1961.

Findley, W. N., & Stanley, C. A.,
Journal of Materials,
Vol. 3, PP. 916-925, 1968.

Flom, D. G.,
Journal of Applied Physics,
Vol. 31, No. 2, PP. 306-314, Feb., 1960.

Friis, E.A., Lakes, R.S., & Park, J. B.,
Journal of Material Science,
Vol. 23, PP 4406-4414, 1988.

Frisch, K. C., & Saunders, J. H.,
Plastic Foams, Part I and II. Marcel
Dekker Inc., New York, 1972.

Gent, A. N., & Thomas, A, G.,
Journal of Applied Polymer Science,
Vol. 1, PP. 107-113, 1959.

Gent, A. N., & Thomas, A, G.,
Rubber Chemistry and Technology,
Vol. 36, PP. 597- 610, 1963.

Gibson, L. J.,
Materials Science and Engineering,
Vol. 67, PP 125-135, 1984.

Gibson, L. J.,
Materials Science & Engineering,
A 110, PP. 1-36, 1989.

Gibson, L. J., Ashby, M. F., Schajer, G. S., & Roberston, C. I.,
Proc. R. Soc. Lond.,
Vol. A382, PP. 25-42, 1982.

Gibson, L. J., & Ashby, M. F.,
Proc. R. Soc. Lond.,
Vol. A382, PP. 43-59, 1982.

Gibson, L. J., & Ashby, M. F.,
" Cellular Solids: Structure &
Properties",

Pergamon Press, London, 1988.

Gibson, L. J., Ashby, M. F., Zhang, J., & Triantafillou, T. C.,
International Journal of Mechanical Science,
Vol. 31, No. 9 PP. 635-663, 1989.

Green, S. J., Shierloh, F. L., Perkins, R. D., & Babcack, S. G.,
Experimental Mechanics,
PP. 103-111, March 1969.

Green, D, J.,
J. Amer. Ceram. Soc.,
Vol. 68, PP. 403-409, 1985.

Gruenbaum, Gad., & Miltz, Joseph.,
Journal of Applied Polymer Science,
Vol. 28, PP. 135-143, 1983.

Gupta, Y. M.,
Polymer Engineering and Science,
Vol. 24, PP. 851-861, 1984.

Hall, R.,
Journal of Reinforced Plastics and Composites,
Vol. 12, PP. 186-197, 1993.

Hanhi, K., & Stenberg, B.,
Cellular Polymer,
Vol. 12, No. 6, PP. 461- 484, 1993.
Vol. 13, No. 1, PP. 33-54, 1994.

Hardy, C., Baronet, C., & Tordion, G. V.,
International Journal of Numerical Methods in Engineering,
Vol. 3, PP. 451-483, 1971.

Harding, R. H.,
Journal of cellular plastics,
Vol. 1, PP. 385-391, 1965.

Harding, R. H.,
Resinography of Cellular Plastics,
ASTM STP414, Am. Soc. Testing Mats., P. 3.

Harrigan, T. P., & Mann, R. W.,
Journal of Materials Science,
Vol. 19, PP. 761-767, 1984.

Hertz, H.,
Miscellaneous Papers, 1896, London.

Hilyard, N. C.,
" Mechanics of Cellular Plastics",
Applied Science Publishers Ltd.,
London, 1982.

Hirotsu, S.,
J. Chem. Phys.,
Vol. 94, PP. 3949-3953, 1991.

Hogg, K. G., and Wasley, R. J.,
Journal of Applied Polymer Science,
Vol. 12, PP. 97- 107 (1969).

Howell, B., Prendergast, P., and Hansen, L.,
DTRC-SME-91/01, David Taylor Research Centre, March, 1991. (AD A235695).

Huang, J. S., & Gibson, L. J.,
Journal of Materials Science,
Vol. 26, PP. 637-647, 1991.

Huang, J. S., & Gibson, L. J.,
Journal of Materials Science Letters,
Vol. 12, PP. 602-604, 1993.

Gibson, L. J., & Huber, A.T.,
Journal of Materials Science,
Vol. 23, PP. 3031-3040, 1988.

Johnson, K. L.,
" Contact Mechanics",
Cambridge University Press, 1985.

Jones, R. W., and Fesman, G.,
Journal of Cellular Plastics,
Vol. 1, PP. 200-205, 1965.

Kanakkanatt, S. V.,
Journal of Cellular Plastics,
PP. 50-53, Jan.- Feb./1973.

Kau, C., Huber, L., Hiltner, A., Baer, E.,
Journal of Applied Polymer Science,
Vol. 44, PP. 2081-2093, 1992.

Kau, C., Huber, L., Hiltner, A., Baer, E.,
Journal of Applied Polymer Science,
Vol. 44, PP. 2069-2079, 1992.

Kelsey, S., Gellatly, R. A., & Clark, B. W.,
Aircraft Engineering.
PP. 294-302, Oct., 1958.

Kelvin, Lord.,
Phil. Mag.,
Vol. 24, P. 503.

Klintworth, J. W., & Stronge, W. J.,
Journal of Materials Science,
Vol. 30, PP. 273-292, 1988.

Klintworth, J. W., & Stronge, W. J.,
International Journal of Mechanical Science,
Vol. 31, PP. 359-378, 1989.

Ko, W. L.,
Journal of Cellular Plastics,
PP. 45-50, Jan. / 1965.

Kolsky, H.,
Stress Waves in Solids, Clarendon,
Oxford, 1953.

Lakes, Roderic,
Science,
Vol. 235, PP. 1038-1040, 1987.

Lakes, Roderic,
Advanced Materials,
Vol. 5, PP. 293-296, 1993.

Lakes, R. S.,
Journal of Materials Science,
Vol. 26, PP. 2287-2292, 1991.

Lakes, R. S., Rosakis, P., & Ruina, A.,
Journal of Materials Science,
Vol. 28, PP. 4667-4672, 1993.

Lakes, R. S., Elms, K.,
Journal of Composite Materials,

Vol. 27, No. 12, PP. 1193-1202, 1993.

Landau, L. D., & Lifshitz, E. M.,
"Theory of Elasticity",
Pergamon Press, 1959.

Lederman, J. M.,
Journal of Applied Polymer Science,
Vol. 15, PP. 693-703, 1971.

Lempriere, B. M.,
AIAA Journal,
Vol. 6, PP. 2226-2227, 1968.

Love, A. E. H.,
Phil. Trans.
Vol. A228, PP 377-420, 1929 and 1944.

Loveridge, P., & Mills, N. J.,
Cellular Polymers,
Vol. 10, PP. 393-405, 1991.

Ludwik, P.,
Die Kegleprobe,
J. Springer, Berlin. 1908.

Mackenzie, J. K.,
Proc. Phys. Soc.,
B63, PP. 2-9, 1950.

Maiti, S. K., Gibson, L. J., & Ashby, M. F.,
ACTA Metallurgica,
Vol. 32, PP. 1963-1975, 1984

Masters, I. G.,
PhD these, the University of Liverpool, the UK. 1994.

Matthews, J. R.,
Acta Metall.,
Vol. 28, PP. 311-318, 1979.

McCrum, N. G., Read, B. E., & Williams, G.,
"Anelastic and Dielectric Effects in Polymeric Solids",
Wiley, London, 1967.

Mehta, B. S., & Colombo, E. A.,
Journal of Cellular Plastics,
PP. 59- 66, Jan.- Feb. / 1976.

Meinecke, E. A., & Schwaber, D. M.,
Journal of Applied Polymer Science.
Vol. 14, PP. 2239-2248, 1970.

Melz, B., & Schneeberger, H.,
Journal of Cellular Plastics,
PP. 85- 89, Mar.- April, 1974,

Menges, G., & Knipschild, F.,
Polymer Engineering and Science,
Vol. 15, PP. 623-627, 1975.

Meyer, E.,
Zeits. d. Vereines Deutsch. Ingenieure,
Vol. 52, PP. 645-835, 1908.

Mills, N. J., & Hwang, A. M. H.,
Cellular Polymers,
Vol. 8, PP. 259-275, 1989.

Milton, G. W.,
Journal of Mechanics and Physics of Solids,
Vol. 40, No. 5, PP. 1105-1137, 1992.

Miltz, Joseph., & Ramon, Ori.,
Polymer Engineering and Science,
Vol. 30, PP. 129-133, 1990.

Miltz, Joseph., & Gruenbaum, Gad.,
Polymer Engineering and Science,
Vol. 21, PP. 1010-1014, 1981.

Moore, D. R., & Couzens, K. H.,
Journal of Cellular Plastics,
PP. 135-139, May - June/ 1974.

Montillet, A., Comiti, J., & Legrand, J.,
Journal of Materials Science,
Vol. 27, PP. 4460-4464, 1992.

Murayama, T.,
" Dynamic Mechanical Analysis of Polymeric Material",
Elsevier Scientific Publishing Company, 1978.

Musgrave, M. J. P.,
" Crystal Acoustics",
Holden-Day, 1970.

Nagy, A., Ko, W. L., & Lindholm, U. S.,
Journal of Cellular Plastics,
PP. 127-174, May - June, 1974.

Neet, T. E.,
Journal of Cellular Plastics,
PP. 45-49, Jan.- Feb./ 1975.

Nkansah, M. A., Evans, K. E., & Hutchinson, I. J.,
Modelling Simulation in Materials Sciences and Engineering,
Vol. 2, PP. 337-352, 1994.

Nye, J. F.,
" Physical Properties of Crystals",
Clarendon Press, 1960.

Okuno, K., & Woodhams, R. T.,
Journal of Cellular Plastics,
PP. 237-244, Sept.- Oct., 1974.

O'neill, H.,
" The Hardness of Metals and Its Measurement",
Chapman & Hall, 1934.

O'Neill, H.,
" Hardness Measurement of Metals and Alloys",
Chapman & Hall, 1967.

Orringer, O., Knadle, K. T., & Mandell, J. F.,
0096-736x/85/9304-0257, Society of Automotive Engineers, Inc.
840866, 1985.

Patel, M. R., & Finnie, I.,
Journal of Materials, JMLSA,
Vol. 5, PP. 909-932, 1970.

Plateau, J. A. F.,
Statique Experimentale et Theorique des Liquides Soumis Aux Seules Force Moleculaires. Ghent. 1873.

Poisson. S. D.,,
Mém. Acad. Sci. Inst. (France)
Vol. 8, PP. 449-451, 1829.

Ramon, O., Mizrahi, S., & Miltz, J.,
Polymer Engineering and Science,
Vol. 30, PP. 197-201, 1990.

Richardson, M. O. W., & Nandra, D. S.,
Cellular Polymers,
Vol. 5, PP. 423-432, 1986.

Richardson, M. O. W., & Nandra, D. S.,
Cellular Polymers,
Vol. 4, PP. 445-462, 1985.

Richardson, M. O. W., & Nandra, D. S.,
Cellular Polymers,
Vol. 4, PP. 279-287, 1985.

Rigbi, Z.,
Applied Polymer Symposia,
No. 5, PP. 1-7, 1967.

Rinde, J. A., & Hogg, K. G.,
Journal of Applied Polymer Science,
Vol. 15, PP. 1377-1395, 1971.

Rinde, J. A.,
Journal of Applied Polymer Science,
Vol. 14, PP. 1913-1926, 1970.

Roark, R. J., & Young, W. C.,
" Formulas for Stress and Strain",
McGraw-Hill, 1975.

Rothenburg, L., Berlin, A. A., & Bathurst, R. J.,
Letters to Nature,
Vol. 354, PP 470-472, 1991.

Roudie,
Le Control de La Durete des Meteux dans L'Industrie, Dunod, Paris. (Tabor, 1959)

Rusch, K.C.,
Journal of Applied Polymer Science,
Vol. 13, PP. 2297-2311, 1969.

Rusch, K.C.,
Journal of Applied Polymer Science,
Vol. 14, PP. 1263-1276, 1970.

Rusch, K.C.,
Journal of Applied Polymer Science,
Vol. 14, PP. 1433-1447, 1970.

Shaw, M. C., & Sata, T.,
International Journal of Mechanical Science,
Vol. 8, PP. 469-478, 1966.

Shore, A. F.,
J. Iron & Steel Inst.
No. 2, PP. 59-65, 1918.

Shuttleworth, R. W.,
Journal of Applied Polymer Science,
Vol. 30, PP. 333-343, 1985.

Schwaber, D. M., & Meinecke, E. A.,
Journal of Applied Polymer Science,
Vol. 15, PP. 2381-2393, 1971.

Shanley, F. R.,
"Strength of Materials",
Mcgraw-Hill, 1957.

Sharp, S. J, Ashby, M. F, & Fleck, N. A.,
Acta Metall. Matera.,
Vol. 41, PP. 685-692, 1993.

Sherwood, J. A.,
Polymer Engineering and Science,
Vol. 32, PP. 1138-1146, 1992.

Sims, G. L. A., & Khunniteekool, C.,
Cellular Polymers,
Vol. 13, No. 2, 1994.

Skochdopde, R. E., & Rubens, L. C.,
Journal of Cellular Plastics,
Vol. 1, PP. 91-99, 1965.

Smith, C. S.,
"Metal interfaces",
American Society of Metals, New York,
P. 108, 1952.

Smolenski, C. P.,
Journal of Cellular Plastics,
PP. 210-214, May -June/ 1984.

Stupak, P. R., & Donovan, J. A.,
Polymer Engineering and Science,
Vol. 34, PP. 857-864, 1994.

Suh, K. W., & Skochdopole, R. E.,
"Foamed Plastics"
Encyclopedia of Chemical Technology,
Vol. 2, 3rd edn. Wiley, New York, P.
82, 1980.

Tabor, D.,
" Hardness of Metals",
Clarendon Press, 1951.

Theocaris, P. S.,
Acta Mechanica,
Vol. 89, PP. 93-121, 1991.

Thompson, D, W.,
"Growth and Form",
Cambridge University Press,
Cambridge, 1961.

Throne, J. L.,
Journal of Cellular Plastics,
Nov.- Dec., PP. 437-442, 1984.

Throne, J. L., Progelhof, R. C., & Kumar, S.,
Journal of Cellular Plastics,
PP. 123-140, Mar.-April/ 1985.

Timoshenko, S. P., & Goodier, J. N.,
" Theory of Elasticity"
McGraw-Hill, 1970.

Tirupataiah, Y., & Sundararajan, G.,
Materials Science and Engineering,
Vol. 91, PP. 169-180, 1987.

Tonyan, T. D., & Gibson, L. J.,
Journal of Materials Science,
Vol. 27, PP. 6371-6378, 1992.

Traeger, R. K.,
Journal of Cellular Plastics,
PP. 405- 418, Sept. / 1967.

Triantafillou, T. C., Zhang, J., Gibson, L. J., & Ashby, M. F.,
International Journal of Mechanical Science,
Vol. 31, PP. 665-678, 1989.

Triantafillou, T. C., & Gibson, L. J.
Materials Science and Engineering,
Vol. 95, PP. 37-53, 1987.

Tsai, J. T.,
Polymer Engineering and Science,
Vol. 22, PP. 545-548, 1982.

Underwood, J. H., O'Hara, G. P., & Zalinka, J. J.,
Experimental Mechanics,
PP. 379-385, Dec., 1986.

Venkataswamy, K., Ard, K., & Beatty, C. L.,
Polymer Engineering and Science,
Vol. 22, PP. 961-967, 1982.

Vickers,
See Smith, R., and Sandland, G.,
Proc. Instn. Mech. Engrs.,
Vol. 1, P. 623, 1925.

Warren, T. L.,
Journal of Applied Physics,
Vol. 67 (12), PP. 7591-7594, 1990.

Warren, W. E., Kraynik, A. M., & Stone, C.,
Journal of Mechanics and Physics of Solids,
Vol. 37, PP. 717-733, 1989.

Warren, W. E., & Kraynik, A. M.,
Mechanics of Materials,
Vol. 6, PP. 27-37, 1987.

Warren, W. E., & Kraynik, A. M.,
Journal of Applied Mechanics,
Vol. 55, PP. 341-346, 1988.

Warren, W. E., & Kraynik, A. M.,
Transactions of ASME,
Vol. 58, PP. 376-381, 1991.

Waterman, N. R., and Phillips, P. J.,
Polymer Engineering and Science,
Vol. 14, PP. 72-78, 1974.

Wei, Gaoyuan.,
Journal of Chemical Physics,
Vol. 96 (4), PP. 3227-3233, 1992.

Wilsea, M., Johnson, K. L., & Ashby, M.,
International Journal of Mechanical Science,
Vol. 17, PP. 457-460, 1974.

Whittaker, R. E.,
Journal of Applied Polymer Science,
Vol. 15, PP 1205-1218, 1971.

William, J. M., Bartons III, J. J., & Wilkerson, M. H.,
Journal of Materials Science,
Vol. 25, PP. 5134-5141, 1990.

William, A., L. & Beltzer, A. I.,
Journal of Acoust. Soc. Am.,
Vol. 84 (6), PP. 2179-2186, 1988.

Wojciechowski, K. W., & Branka, A. C.,
Physical Review A,
Vol. 40 (12), PP. 7222-7225, 1989.

Woolam, W. E.,
Journal of Cellular Plastics,
PP. 79-83, Feb., 1968.

Yossifon, S., & Szanto.,
Journal of Applied Polymer Science,
Vol. 34, PP. 2025-2036, 1987.

Yossifon, S., & Szanto.,
Journal of Applied Polymer Science,
Vol. 38, PP. 1347-1356, 1989.

Yossifon, S., & Szanto.,
Journal of Applied Polymer Science,
Vol. 38, PP. 281-290, 1989.

Zhang, J., & Ashby, M. F.,
Journal of Materials Science,
Vol. 29, PP. 157-163, 1994.